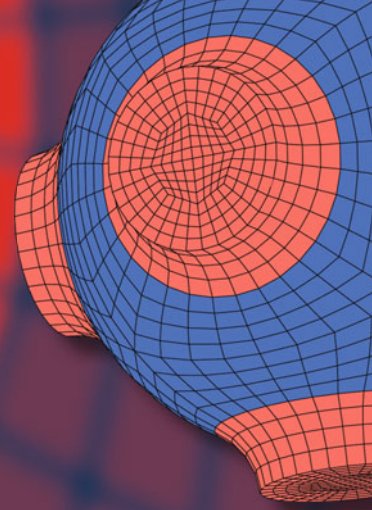


Advanced Structured Materials

Holm Altenbach
Michael Johlitz
Markus Merkel
Andreas Öchsner *Editors*



Lectures Notes on Advanced Structured Materials

 Springer


Advanced Structured Materials

Volume 153

Series Editors

Andreas Öchsner, Faculty of Mechanical and Systems Engineering, Esslingen
University of Applied Sciences, Esslingen, Germany

Lucas F. M. da Silva, Department of Mechanical Engineering, Faculty of
Engineering, University of Porto, Porto, Portugal

Holm Altenbach , Faculty of Mechanical Engineering, Otto von Guericke
University Magdeburg, Magdeburg, Sachsen-Anhalt, Germany

Common engineering materials are reaching their limits in many applications, and new developments are required to meet the increasing demands on engineering materials. The performance of materials can be improved by combining different materials to achieve better properties than with a single constituent, or by shaping the material or constituents into a specific structure. The interaction between material and structure can occur at different length scales, such as the micro, meso, or macro scale, and offers potential applications in very different fields.

This book series addresses the fundamental relationships between materials and their structure on overall properties (e.g., mechanical, thermal, chemical, electrical, or magnetic properties, etc.). Experimental data and procedures are presented, as well as methods for modeling structures and materials using numerical and analytical approaches. In addition, the series shows how these materials engineering and design processes are implemented and how new technologies can be used to optimize materials and processes.


Advanced Structured Materials is indexed in Google Scholar and Scopus.

Holm Altenbach · Michael Johlitz ·
Markus Merkel · Andreas Öchsner
Editors

Lectures Notes on Advanced Structured Materials

 Springer

Editors

Holm Altenbach 
Fakultät für Maschinenbau
Otto-von-Guericke-Universität Magdeburg
Magdeburg, Sachsen-Anhalt, Germany

Markus Merkel 
Institute for Virtual Product Development
Aalen University of Applied Sciences
Aalen, Baden-Württemberg, Germany

Michael Johlitz
Institut für Mechanik
Universität der Bundeswehr München
Neubiberg, Germany

Andreas Öchsner
Faculty of Mechanical and Systems
Engineering
Esslingen University of Applied Sciences
Esslingen, Germany

ISSN 1869-8433

ISSN 1869-8441 (electronic)

Advanced Structured Materials

ISBN 978-3-031-11588-2

ISBN 978-3-031-11589-9 (eBook)

<https://doi.org/10.1007/978-3-031-11589-9>

© The Editor(s) (if applicable) and The Author(s), under exclusive license to Springer Nature Switzerland AG 2022

This work is subject to copyright. All rights are solely and exclusively licensed by the Publisher, whether the whole or part of the material is concerned, specifically the rights of translation, reprinting, reuse of illustrations, recitation, broadcasting, reproduction on microfilms or in any other physical way, and transmission or information storage and retrieval, electronic adaptation, computer software, or by similar or dissimilar methodology now known or hereafter developed.

The use of general descriptive names, registered names, trademarks, service marks, etc. in this publication does not imply, even in the absence of a specific statement, that such names are exempt from the relevant protective laws and regulations and therefore free for general use.

The publisher, the authors, and the editors are safe to assume that the advice and information in this book are believed to be true and accurate at the date of publication. Neither the publisher nor the authors or the editors give a warranty, expressed or implied, with respect to the material contained herein or for any errors or omissions that may have been made. The publisher remains neutral with regard to jurisdictional claims in published maps and institutional affiliations.

This Springer imprint is published by the registered company Springer Nature Switzerland AG
The registered company address is: Gewerbestrasse 11, 6330 Cham, Switzerland

Preface

The postgraduate seminar series “Advanced Structured Materials: Development—Manufacturing—Characterization—Applications” is designed to facilitate teaching and informal discussion in a supportive and friendly environment. The seminar provides a forum for postgraduate students to present their research results and train their presentation and discussion skills, allows for extensive discussion of current research being conducted in the wider area of advanced structured materials, builds a wider postgraduate community and offers networking opportunities for early career researchers.

The first seminar was held in the period 28 February till 3 March 2022 in Malta. The four editors of this volume presented overview lectures related to composite mechanics, experimental mechanics of polymers, additive manufacturing and classical plasticity theory. In addition, 21 postgraduate students attended this seminar and presented their actual research projects. This volume contains the peer-reviewed and revised versions of the submitted manuscripts.

Magdeburg, Germany
Neubiberg, Germany
Aalen, Germany
Esslingen, Germany
June 2022

Holm Altenbach
Michael Johlitz
Markus Merkel
Andreas Öchsner

Contents

Part I Overview Lectures

1 Composite Mechanics	3
Holm Altenbach	
1.1 Preliminary Remarks	3
1.2 Definitions, Classifications and Applications	5
1.3 Laminated Plates	8
1.3.1 Description of Material Behaviour	8
1.3.2 Modelling Levels	8
1.3.3 Modelling Based on Volume and Mass Fraction	9
1.3.4 Combination of Both Approaches	10
1.3.5 Elementary Mixture Rules	11
1.3.6 Effective Properties of a Single Layer	14
1.3.7 Improved Formulas for Effective Moduli	19
1.4 Particle-Reinforced Composites	20
1.4.1 Short-fibre-Reinforced Plastics	20
1.4.2 Spherical Inhomogeneity with Interphase	21
1.5 Functionally Graded Materials	23
1.6 Anti-Sandwich and Nanomaterials	24
1.7 Summary and Outlook	24
References	24
2 Aspects in the Modelling of Heterogeneous Thermo-Oxidative Ageing Using the Example of a Rubber Buffer	29
Bruno Musil and Michael Johlitz	
2.1 Introduction	29
2.2 Chemo-Thermo-Mechanical Simulation of a Rubber Buffer	31
2.2.1 Overview of the Quantities and Equations of the Material Model	31
2.2.2 Results and Discussion	37
2.3 Experimental Investigation on Self-heating in Connection with Ageing of a Rubber Buffer	40

- 2.4 Conclusion 42
- References 42
- 3 Digital Product Development by Additive Manufacturing 45**
 Markus Merkel, Mario Rupp, and Michael Sedlmajer
- 3.1 Introduction 45
- 3.2 AM-Process Within Digital Product Development
 and Manufacturing 46
- References 52
- 4 Theory of Three-Dimensional Plasticity 53**
 Andreas Öchsner
- 4.1 Comments on the Stress Matrix 53
- 4.2 Graphical Representation of Yield Conditions 60
- 4.3 Yield Conditions 64
 - 4.3.1 Mises Yield Condition 65
 - 4.3.2 Tresca Yield Condition 69
 - 4.3.3 Drucker-Prager Yield Condition 74
- 4.4 Flow Rule 78
- 4.5 Hardening Rule 78
 - 4.5.1 Isotropic Hardening 78
 - 4.5.2 Kinematic Hardening 79
- References 79

Part II Specialized Lectures

- 5 Influence of Silicon Content on the Mechanical Properties
 of Additively Manufactured Al-Si Alloys 83**
 Enes Sert, Philippe du Maire, Elmar Schuch, Leonhard Hitzler,
 Ewald Werner, and Andreas Öchsner
- 5.1 Introduction 84
- 5.2 Experimental Methods 85
 - 5.2.1 Sample Preparation 85
 - 5.2.2 Chemical Analysis 86
 - 5.2.3 Flowability 86
 - 5.2.4 Particle Size Distribution 87
 - 5.2.5 Hardness 88
 - 5.2.6 Tensile Tests 88
- 5.3 Results and Discussion 89
 - 5.3.1 Chemical Analysis 89
 - 5.3.2 Flowability 89
 - 5.3.3 Particle Size Distribution 91
 - 5.3.4 Hardness 92
 - 5.3.5 Tensile Properties 93
- 5.4 Conclusions 95
- References 95

- 6 Multi-step Additive Manufacturing Technologies Utilizing the Powder Metallurgical Manufacturing Route 99**
Arne Davids, Lukas Apfelbacher, Leonhard Hitzler, and Christian Krempaszky
 - 6.1 Introduction 100
 - 6.2 Metal Additive Manufacturing 100
 - 6.2.1 Single-Step AM Technologies 100
 - 6.2.2 Multi-step AM Technologies 101
 - 6.3 Summary 112
 - References 113

- 7 A Strategy to Extend the Limits of Unsupported Printing in Laser Powder Bed Fusion by Optimized Process Parameters Selection 119**
Johannes Rottler, Christoph Petroll, Michael Johlitz, Kristin Paetzold, and Alexander Lion
 - 7.1 Introduction and Motivation 120
 - 7.2 Laser Powder Bed Fusion Process 120
 - 7.3 Support Structure 122
 - 7.4 Methods for Minimizing Support Structure 123
 - 7.5 Selecting Process Parameters in LPBF 124
 - 7.5.1 State-of-the-Art Parameter Selection 125
 - 7.5.2 Parameter-Based Strategy to Minimize Support 126
 - 7.6 Conclusion 128
 - References 128

- 8 Influence of Relative Humidity on Thermal Properties of Tool Steel Powder 131**
Garvin Schultheiss, Josef Tomas, and Markus Merkel
 - 8.1 Introduction 131
 - 8.2 Methodology 133
 - 8.3 Experimental Setup 134
 - 8.4 Results 134
 - 8.5 Discussion 136
 - 8.6 Conclusion 137
 - References 137

- 9 An Overview on the 3D Printing of Elastomers and the Influence of Printing Parameters on Their Mechanical Properties 139**
Vivianne M. Bruère, Alexander Lion, Jens Holtmannspötter, and Michael Johlitz
 - 9.1 Introduction 139
 - 9.2 Overview on Additive Manufacturing 141
 - 9.2.1 Definition and Technologies 141
 - 9.2.2 Elastomers in 3D Printing 143

9.2.3	FFF with Elastic Materials	145
9.3	Applied Case on FFF with a TPU Filament	147
9.3.1	Experimental Procedure	147
9.3.2	Results and Discussion	148
9.4	Conclusions	151
	References	152
10	Effects of Reusing Polyamide 12 Powder on the Mechanical Properties of Additively Manufactured Parts	155
	Philippe du Maire, Enes Sert, Matthias Deckert, Michael Johlitz, and Andreas Öchsner	
10.1	Introduction	156
10.2	Methodology	157
10.3	Results and Discussion	160
10.4	Conclusion	164
	References	165
11	On the Influence of Perimeter, Infill-Direction and Geometry on the Tensile Properties of Test Specimen Manufactured by Fused Filament Fabrication	167
	Julian Klingenbeck, Alexander Lion, and Michael Johlitz	
11.1	Introduction	167
11.2	Research Focus	171
11.3	Experimental Setup and Results	172
11.4	Discussion of Tensile Test Results	174
11.5	Conclusion	179
	References	180
12	Design of a Room-in-Room Laboratory Environment for the SLS Printing Process	183
	Dominik Hahne, Alexander Lion, and Michael Johlitz	
12.1	Motivation	183
12.2	Mechanical Design of the Cabin	184
12.2.1	Design Structure	185
12.2.2	Structural Mechanics of the Cabin	186
12.3	Thermal Concept	189
12.4	Extraction System	190
12.5	Summary	192
	References	192
13	Chemical–Mechanical Characterization of Unaged and Aged Additively Manufactured Elastomers	193
	Yvonne Breitmoser, Sebastian Eibl, Tobias Förster, Alexander Lion, and Michael Johlitz	
13.1	Introduction	193
13.2	Material	194
13.3	Methods	195

13.4	Results and Discussion	196
13.4.1	Material Identification and Curing Process	196
13.4.2	Aging Effects	197
13.5	Conclusions	201
	References	202
14	Microstructure and Properties of the Fusion Zone in Steel-Cast Iron Composite Castings	203
	Lukas Apfelbacher, Patrick Hegele, Arne Davids, Leonhard Hitzler, Christian Krempaszky, and Ewald Werner	
14.1	Introduction	204
14.2	Experimental Details	205
14.2.1	Composite Casting	205
14.2.2	Microstructure Observation	207
14.2.3	Hardness Measurement	207
14.3	Results	207
14.3.1	Graphite Morphology	207
14.3.2	Etched Microstructure	208
14.3.3	Hardness	211
14.4	Discussion	211
14.5	Conclusion	215
	References	216
15	Kinetics for Strain-Induced Crystallisation Analysed via Cyclic Loading Simulations	217
	Klara Loos	
15.1	Introduction	217
15.2	Constitutive Model Using a Serial Connection of Amorphous, Non-crystallisable Amorphous and Crystalline Phase	218
15.2.1	Simulation Results: Loading with Various Maximum Stretch	219
15.2.2	Simulation Results: Loading with Different Stretch Rates	221
15.2.3	Simulation Results: Cyclic Loading Varying in Amplitude and Minimum Unloading Stretch	222
15.3	Conclusions and Outlook	226
	References	227
16	Long-Term Storage of Aged NBR in Kerosene in Consideration of Long Material Service Life	229
	Benedikt Demmel, Tobias Förster, Sebastian Eibl, Michael Johlitz, and Alexander Lion	
16.1	Introduction	230
16.2	Materials	230
16.3	Experiments and Methods	232

16.3.1	Elastomer Aging and Preparation	232
16.3.2	Mechanical Testing	232
16.3.3	Gas Chromatography/Mass Spectrometry	232
16.3.4	Sorption Experiments	233
16.4	Results and Discussion	233
16.4.1	Mechanical Properties After Aging	233
16.4.2	Concentration of Stabilizers and Plasticizers	235
16.4.3	Long-Term Sorption Behavior of Kerosene Jet A-1 in Aged NBR	236
16.5	Conclusion	238
	References	239
17	FT-IR Microscopic Analysis of the Chemical Change in the Molecular Structure After Ozone Ageing of Natural Rubber	241
	Caroline Treib, Alexander Lion, and Michael Johlitz	
17.1	Introduction	241
17.2	Experimental	243
17.2.1	Material	243
17.2.2	Artificial Ageing Strategy	243
17.2.3	Fourier Transform Infrared Spectroscopy Method	244
17.3	Results	246
17.3.1	Surface Spectra	246
17.3.2	Cross-Section Spectra	248
17.4	Discussion	250
17.5	Conclusion and Outlook	251
	References	251
18	Investigation of the Viscosity of Liquid Silicone Rubber for Molding Microstructures in the Injection Molding Process	253
	Dennis F. Weißer, Levente Szántó, Dennis Mayer, Johannes Schmid, and Matthias H. Deckert	
18.1	Introduction	254
18.2	Material and Methods	256
18.2.1	Theoretical Approach	256
18.2.2	Experimental Part	267
18.3	Results and Discussion	270
18.3.1	Kinetic Model	270
18.3.2	Rheological Results	270
18.3.3	Dielectrical Results	275
18.3.4	Comparison of the Different Analysis Methods	275
18.3.5	Experimental Results	276
18.4	Conclusion and Outlook	277
	References	280

19 Investigation of Adhesion and Surface Treatments for Thermoplastic—Liquid Silicone Rubber Joints in Multicomponent Injection Molding 283
 Dennis Mayer, Simon J. Heienbrock, Dennis F. Weißer, Johannes Schmid, Sascha Müller, Lothar Kroll, and Matthias H. Deckert

19.1 Introduction 284

19.2 Theoretical Background 285

 19.2.1 Relevant Adhesion Theories for Thermoplastic-LSR Joints 285

 19.2.2 Surface Treatment Methods 286

19.3 Materials and Methods 288

 19.3.1 Materials 288

 19.3.2 Methods 289

19.4 Results and Discussion 295

 19.4.1 Surface Energy of Thermoplastics 295

 19.4.2 Peel Forces of Thermoplastic-LSR Joints 296

 19.4.3 Classification of Surface Treatments 297

19.5 Summary and Outlook 299

References 300

20 Thermoforming: Identification of Process-Relevant Ranges for Strain, Strain Rate, Cooling Rate, and Degree of Crystallinity Through Preliminary Simulations 303
 Sameer Kulkarni, Klara Loos, Alexander Lion, and Michael Johlitz

20.1 Introduction 304

 20.1.1 Thermoforming Process 305

 20.1.2 Crystallization During Thermoforming Process 306

20.2 Simplified Process Simulations 307

 20.2.1 Simulation 1: Cooling 307

 20.2.2 Simulation 2: Forming 309

20.3 Conclusions 313

References 313

21 Examining Lateral Punch Force Effects During Hole Expansion Testing by Means of Numerical Simulations 315
 Tobias Robl, Christian Kremaszky, and Ewald Werner

21.1 Introduction 316

21.2 Modeling 317

 21.2.1 Geometry 318

 21.2.2 Boundary Conditions and Contact Interactions 319

 21.2.3 Material Behavior 319

21.3 Results and Discussion 322

21.4 Conclusions 328

References 329

22 CFD Analysis of Hot Gas Welding of 3D Weld Contours Using Two Different Nozzle Systems 331
 Johannes Schmid, Dennis F. Weißer, Dennis Mayer, Lothar Kroll, Sascha Müller, Rainer Stauch, and Matthias H. Deckert

22.1 The Hot Gas Welding Process 331

22.2 Theory of Impingement Flow 333

22.3 Structure of the CFD Simulation Model for 3D-Shaped Welds 334

22.4 Validation of the Simulation Model 337

22.4.1 Test Setup for Validation of the Simulation 337

22.4.2 Validation of the Simulated Shape of the Molten Polymer 338

22.4.3 Validation of the Simulated Transient Heating Behavior 339

22.5 Investigation of the Influence of 3D-Shaped Weld Contours 341

22.5.1 Simulation Results of Inclined Weld Contours 342

22.5.2 Simulation Results of Hybrid Weld Contours 346

22.6 Summary and Outlook 353

References 354

23 Modeling the Inelastic Behavior of High-Temperature Steels Using a Two-Time-Scale Approach 357
 Katharina Knape and Holm Altenbach

23.1 Introduction 357

23.2 Constitutive Equations 359

23.2.1 Elasticity 359

23.2.2 Inelasticity 360

23.3 Two-Time-Scale Approach 361

23.4 Modeling Creep Behavior 363

23.5 Conclusion 364

References 366

Part I
Overview Lectures

Chapter 1

Composite Mechanics



Holm Altenbach

Abstract Composite materials have become indispensable in engineering today. These were originally developed to combine different material properties. A typical example is a reinforced concrete structure. Attempts were made here to improve the poor tensile properties through the reinforcement. Later, lightweight considerations were dominant. For example, aircraft engines were limited in their performance, so that, e.g., sandwich structures were used for the airplane structure. Similar considerations were also made for space structures. Today, composites are used in almost all areas of technology. This often involves the question of substituting traditional construction materials in order to better meet the requirements of use. In this context, there are also increasing considerations to reduce production costs. The actual focus is therefore on foams and functionally graded materials. This chapter gives a brief overview of selected current developments in composite mechanics. This is supplemented by numerous publications (among them the main references from the author's group), so that one can get a good overview with the references listed within these publications.

Keywords Composites · Reinforcements · Ply · Laminate · Functionally graded materials

1.1 Preliminary Remarks

There is currently an almost unmanageable number of publications in the field of composite mechanics. Taking this fact into account, only selected references will be listed here, which make it easier to familiarize oneself with the various aspects of composite mechanics. The focus is on unidirectional (UD) long-fibre-reinforced composites, short-fibre-reinforced composites, particle-reinforced composites, foams and func-

H. Altenbach (✉)

Lehrstuhl Für Technische Mechanik, Institut Für Mechanik, Fakultät Für Maschinenbau, Otto -von -Guericke -Universität Magdeburg, Magdeburg, Germany
e-mail: holm.altenbach@ovgu.de

© The Author(s), under exclusive license to Springer Nature Switzerland AG 2022
H. Altenbach et al. (eds.), *Lectures Notes on Advanced Structured Materials*,
Advanced Structured Materials 153, https://doi.org/10.1007/978-3-031-11589-9_1

tionally graded materials. In addition, partial problems in the modelling of three-layer plates are dealt with, whereby the so-called anti-sandwich is also considered in addition to the classical sandwich structure.

The basics of the classical laminate theory, some extensions and some remarks with respect to the classical sandwich structures are given, for example, in Altenbach and Becker (2003), Altenbach and Öchsner (2010), Altenbach et al. (2018) (German version: Altenbach et al. (1996)), Altenbach and Öchsner (2020), Cristescu et al. (2003), Jones (2018), Lakes (2020), Mittelstedt and Becker (2016), Mittelstedt (2021), Mikhasev and Altenbach (2019), Öchsner (2021). Among these references are typical textbooks. Altenbach et al. (1996, 2018) offer a systematic introduction to the structural mechanics of composite components—classical and improved models. The structural mechanics analysis is based on strength of materials approaches. It focuses on modelling and calculation of sandwiches and laminated composites, taking into account also anisotropic properties of the material under consideration. All chapters include examples with worked-out solutions. In addition, one can find the basics of analytical and numerical solution methods. Öchsner (2021) provides a systematic and thorough introduction to the classical laminate theory based on the theory for plane elasticity elements and classical (shear-rigid) plate elements. Main attention is paid on unidirectional lamina which can be described based on orthotropic constitutive equations and their composition to layered laminates. In addition to the elastic behaviour, failure is investigated based on the maximum stress, maximum strain, Tsai-Hill and the Tsai-Wu criteria. In Mittelstedt and Becker (2016) is given an introduction to the basics of statics and stability of layered planar laminates. Firstly, a detailed overview of the theory of elasticity of anisotropic structures is presented. Secondly, the calculation of planar laminates using different laminate theories as well as possibilities of evaluating the strength is given. A detailed analysis of the buckling and post-buckling behaviour of laminates is included. Mittelstedt (2021) is a thorough introduction to energy methods in engineering, develops from essential basics to modern numerical simulation methods and provides a huge number of exercises complete with solutions. Jones (2018) balances introduction to the basic concepts of the mechanical behaviour of composite materials and laminated composite structures. It covers topics from micro-mechanics and macromechanics to lamination theory and plate bending, buckling and vibration. Some theory-experiment comparisons and information on the design of composite materials are presented. In Lakes (2020), the principles of the mechanics of solid multiphase systems, the role of heterogeneity and anisotropy in determining physical properties, coupled fields, smart materials, applications in lightweight structures, materials with fibrous, lamellar, particulate, and cellular structures, lattice metamaterials, metamaterials, biomimetic and bio-inspired materials are presented and discussed. Cristescu et al. (2003) is partly a textbook and partly a monograph. The theory behind modern elastic composite materials is discussed. More than 400 problems, many of which are solved, are included. In addition, elements of fracture mechanics related to composites are presented. Other applications are presented in Mikhasev and Altenbach (2019): the stability of composite laminated thin-walled structures and the damping of vibrations and waves in sandwich-type thin-walled structures, adaptive structures and proper-

ties of electrorheological and magnetorheological materials. Finally, in Altenbach and Becker (2020), Altenbach and Öchsner (2010), (2020), actual problems of composites, foams and cellular materials are discussed.

Other references related to the problems considered in this chapter are with focus on:

- classical long-fibre-reinforced composites (Altenbach et al. 1996, 2018; Mittelstedt and Becker 2016; Jones 2018; Lakes 2020; Mittelstedt 2021),
- short-fibre-reinforced composites (Altenbach et al. 2003a,b, 2005; Renner et al. 2005; Altenbach et al. 2007, 2009),
- advanced theories for particle-reinforced composites (Nazarenko and Stolarski 2016; Nazarenko et al. 2016, 2017, 2018),
- functionally graded materials (Altenbach and Eremeyev 2008a,b),
- sandwiches (Altenbach 2000a,b), and
- anti-sandwiches (Schulze et al. 2012; Weps et al. 2013).

1.2 Definitions, Classifications and Applications

The starting point for the definition of composites is the following materials science classification of structural materials. Material science classifies structural materials into three categories (Ashby et al. 2018):

- metals,
- ceramics, and
- polymers.

It is difficult to give an exact assessment of the advantages and disadvantages of these three basic material classes, because each category covers whole groups of materials within which the range of properties is often as broad as the differences between the three material classes. In addition, the microstructure of the three material classes differs significantly, and the possible combinations are consequently different.

Another classification is related to advanced materials that are used in high-tech applications. Among these materials, we have semiconductors, biomaterials, smart materials and nanomaterials:

- Semiconductors are materials, inorganic or organic, which have the ability to control their conduction depending on chemical structure, temperature, illumination and presence of dopants. The name semiconductor comes from the fact that these materials have an electrical conductivity between that of a metal, like copper, gold, etc. and an insulator, such as glass.
- Biomaterials are any substance that has been engineered to interact with biological systems for a medical purpose. These materials must not produce toxic substances and must be compatible with body tissues (i.e. must not cause adverse biological reactions).

- Smart materials are materials that sense and respond to changes in their environments in predetermined manners.
- Nanomaterials are materials that have structural features on the order of a nanometer, some of which may be designed on the atomic/molecular level.

In the case of composites, as usual one starts with the basic materials. The characteristic properties of the three basic types of materials can be described as follows:

- Mostly, metallic materials are of medium to high density. They have good thermal stability and can be made corrosion-resistant by alloying. Metals have useful mechanical characteristics and it is moderately easy to shape and join. For this reason, metals became the preferred structural engineering material.
- Ceramic materials have great thermal stability and are resistant to corrosion, abrasion and other forms of attack. They are very rigid but mostly brittle and can only be shaped with difficulty.
- Polymer materials (plastics) are of low density, have good chemical resistance but lack thermal stability. They have poor mechanical properties, but are easily fabricated and joined. Their resistance to environmental degradation, e.g. the photochemical effects of sunlight, is moderate.

Then, composites can be defined as:

Definition 1 (*Composite Materials*) A composite material (also called composite) is a material which is produced from two or more constituent materials. These constituent materials have notably dissimilar properties and are merged to create a material with properties unlike the individual constituents.

Typical examples of composite materials are:

- reinforced concrete,
- composite wood such as plywood,
- reinforced plastics, such as fibre- and particle-reinforced polymers,
- ceramic-matrix composites,
- metal-matrix composites.

In the focus of this chapter is plate-like structures made from advanced materials:

- composite plates (reinforced by short or long fibres),
- sandwich plates,
- multi-layered plates,
- plates made from cellular materials, etc.

Let us introduce a second definition of composite materials.

Definition 2 (*Composite Materials*) In the most general definition, we can consider a composite as any material that is a combination of two or more materials, commonly referred to as constituents, and have material properties derived from the individual constituents. These properties may have the combined characteristics of the constituents or they are substantially different. Sometimes the material properties of a composite material may exceed those of the constituents.

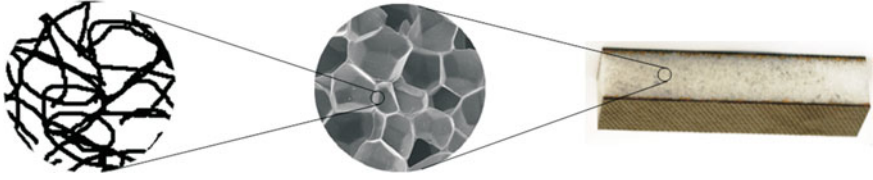


Fig. 1.1 Hierarchy in a foam core sandwich: polymer with chain structure (left), closed-cell foam (middle), sandwich (right)

At first, we have a look on a single ply or lamina. The classification of laminae can be related to the reinforcement (Altenbach et al. 2018): laminate, irregular reinforcement, reinforcement with particles, reinforcement with plate-strapped particles, random arrangement of continuous fibres, irregular reinforcement with short fibres, spatial reinforcement and reinforcement with surface tissues. In structural mechanics with respect to this the laminate can be defined as follows:

Definition 3 (*Laminate*) Laminated structures are composites composed of two-dimensional sheets or panels which are stacked and bonded together with the orientation of the high-strength direction varying with each successive layer.

In addition, a specific kind of a laminate is the classical sandwich structure.

Definition 4 (*Sandwich*) Sandwiches consist of two thin facings (the skins or sheets) enveloping a core. The facings are made of high-strength materials having good properties under tension such as metals or fibre-reinforced laminates, while the core is made of lightweight materials such as foam, resins with special fillers, called syntactic foam, having good properties under compression.

In classical sandwiches, the core can be a foam core, a balsa wood core, a foam core with fillers, a balsa wood core with holes, folded plates core or a honeycomb core (Altenbach et al. 2018). In some applications, we have another type of sandwich structures—the so-called anti-sandwich (Schulze et al. 2012; Weps et al. 2013).

Definition 5 (*Anti-Sandwich*) The anti-sandwiches consist of two thick facings enveloping an extremely thin core. The facings are made of strength materials having good properties under tension, while the core is much weaker. In photovoltaic applications, the face sheets are made of glass and the core is a polymer.

The analysis of laminate and sandwich structures is always associated with different scales. In the case of a foam core sandwich, the scale hierarchy is shown in Fig. 1.1.

It is obvious that the numerical effort increases dramatically as the scale decreases. Therefore, the structural analysis always focuses on homogenization approaches. In addition, in the case of long-fibre-reinforced composites, the anisotropic mechanical properties are obvious. However, even in the case of particle- or short-fibre-reinforced materials, the anisotropy should be considered. The reason for such anisotropy is described, for example, in Saito et al. (2000).

Functionally graded materials have recently become more and more important.

Definition 6 (*Functionally Graded Materials*) In materials science, functionally graded materials (FGMs) may be characterized by the variation in composition and structure gradually over volume, resulting in corresponding changes in the properties of the material.

The FGMs can be designed for specific function and applications. Various approaches based on the bulk processing, preform processing, layer processing and melt processing are used to fabricate the functionally graded materials. Examples of functionally graded materials are materials with an inhomogeneous microstructure like foams and thermal coating.

1.3 Laminated Plates

1.3.1 Description of Material Behaviour

The description of the material behaviour is a big challenge in modern engineering. Let us start with modelling levels. In the case of conventional materials, we can use different approaches which means that the description of the material behaviour can be performed using the materials science approach or the continuum mechanics approach:

- The materials science approach results in a precise description of the deformation and damage mechanisms including the structure-property relationships, however, the constitutive equations are mostly one-dimensional and an extension to three-dimensional equations is difficult.
- In continuum mechanics, the constitutive equations are phenomenologically based as usual resulting in partly rough models, but an extension to three-dimensional equations is rational based or can be realized by engineering assumptions. The main problem is that there is no general approach like the balance equations for formulating the constitutive equations, and consequently, each constitutive equation only specifies the individual response of the concrete material to stresses.

Composite materials consist of two or more constituents and the modelling, analysis and design of structures composed of composites are different from conventional materials. The concept of rheological models (Reiner 1960, 1967) has proven itself here.

1.3.2 Modelling Levels

There are as minimum two levels of modelling:

- At the micro-mechanical level, the average properties of a single-reinforced layer (a lamina or a ply) have to be determined from the individual properties of the

constituents—the fibres and the matrix. The average characteristics include the elastic moduli, the thermal and moisture expansion coefficients, etc. The micro-mechanics of a lamina does not consider the internal structure of the constituent elements, but recognizes the heterogeneity of the ply. Simplifications concern the fibre geometry and packing arrangement, so that the constituent characteristics together with the volume fractions of the constituents yield the average characteristics of the lamina.

- The calculated values of the average properties of a lamina provide the basis to predict the macrostructural properties. At the macro-mechanical level, only the averaged properties of a lamina are considered and the microstructure of the lamina is ignored. The properties along and perpendicular to the fibre direction, these are the principal directions of a lamina, are recognized and the so-called on-axis stress-strain relations for a unidirectional lamina can be developed.

In addition, the loads may be applied not only in-plane but also out-of-plane and the relationships for stiffness and flexibility, for thermal and moisture expansion coefficients and the strength of a ply can be determined. Since the structural elements have anisotropic properties, the behaviour is more complex since more interactions should be considered.

1.3.3 Modelling Based on Volume and Mass Fraction

Let us start with the fibre-matrix relations in the case of UD-reinforced long-fibre composites. In fibre-reinforced composite materials, fibres act as a load carrying medium and the matrix acts as a load transporting medium (Palanikumar 2012). For a single layer (lamina, ply) having a unidirectional long-fibre reinforcement, the proportion of matrix and fibres has a great influence on the effective properties of the ply.

1.3.3.1 Description Based on the Volume Fraction

Let us assume a two-phase composite with the volume V , the matrix volume V_m and the fibre volume V_f . Then,

$$V = V_f + V_m \quad (1.1)$$

and the fibre fraction v_f and matrix fraction v_m can be introduced

$$v_f = \frac{V_f}{V}, \quad v_m = \frac{V_m}{V} \quad (1.2)$$

with

$$v_f + v_m = 1, \quad v_m = 1 - v_f \doteq 1 - \phi. \quad (1.3)$$

The maximum fibre volume fractions $v_{f \max}$ is less than 1. The value depends on the fibre arrangements:

- square or layer-wise fibre packing $v_{f \max} = 0.785$ and
- hexagonal fibre packing $v_{f \max} = 0.907$.

For real UD-laminae, we have $v_{f \max} \approx 0.50 - 0.65$.

1.3.3.2 Description Based on the Mass Fraction

In a similar way the relations for the mass can be introduced, $M = M_f + M_m$, and we have the following relation for the mass fractions

$$m_f = \frac{M_f}{M}, \quad m_m = \frac{M_m}{M} \quad (1.4)$$

with

$$m_f + m_m = 1, \quad m_m = 1 - m_f. \quad (1.5)$$

1.3.4 Combination of Both Approaches

With the relation between volume, mass and density, one can see that the relations are interlinked

$$\begin{aligned} \rho &= \frac{M}{V} = \frac{M_f + M_m}{V} = \frac{\rho_f V_f + \rho_m V_m}{V} = \rho_f v_f + \rho_m v_m = \rho_f v_f + \rho_m (1 - v_f) \\ &= \frac{M}{V_f + V_m} = \frac{M}{\frac{M_f}{\rho_f} + \frac{M_m}{\rho_m}} = \frac{1}{\frac{m_f}{\rho_f} + \frac{m_m}{\rho_m}} = \frac{\rho_f \rho_m}{m_f \rho_m + m_m \rho_f}. \end{aligned} \quad (1.6)$$

Comparing the first and the second line of Eq. (1.6), one obtains

$$m_f = \frac{\rho_f}{\rho} v_f, \quad m_m = \frac{\rho_m}{\rho} v_m \quad \text{or} \quad v_f = \frac{\rho}{\rho_f} m_f, \quad v_m = \frac{\rho}{\rho_m} m_m. \quad (1.7)$$

The effective density ρ is determined by Eq. (1.6). This equation can be easily extended to multiphase composites. The mass fractions are easier to measure in material manufacturing, but volume fractions appear in the theoretical equations for effective properties. Therefore, it is helpful to have simple expressions for shifting from one fraction to the other.

1.3.4.1 Multiphase Composites

The equations can be easily extended to multiphase composites

$$v_1 + v_2 + v_3 + \dots = 1$$

with v_i as the volume fraction of the i th phase. This representation can be used even in the case of porosity

$$v_f + v_m + v_{\text{por}} = 1$$

which results in

$$v_{\text{por}} = 1 - v_f + v_m = 1 - \frac{m_f}{\rho_f} - \frac{m_m}{\rho_m}.$$

The porosity can be included as an additional phase. The quality of a composite material decreases with an increase in porosity. The volume of porosity should be less than 5% for a medium quality and less than 1% for a high quality composite.

If the density ρ_{exp} is measured experimentally and the theoretical density ρ_{theor} is calculated with Eq. (1.6), the volume fraction of porosity is given by

$$v_{\text{por}} = \frac{\rho_{\text{theor}} - \rho_{\text{exp}}}{\rho_{\text{theor}}} \quad (1.8)$$

which is a simple rough estimate of the porosity fraction (or composite quality indicator).

1.3.5 Elementary Mixture Rules

The effective mechanical material moduli for a composite layer can be computed as follows. The estimates are based on some assumptions:

- Unidirectional (UD) layer is a layer of a (endless) fibre-plastic composite in which all fibres are oriented in a single direction and embedded in a plastic matrix.
- Composite layers have at least two different material components which are assumed to be perfect bonded.
- In general, the material response of a composite is determined by the material moduli of all constituents, the volume or mass fractions of the single constituents in the composite material, by the quality of their bonding, i.e. of the behaviour of the interfaces and by the arrangement and distribution of the fibre reinforcement, i.e. the fibre architecture.

Elementary mixture rules for long-fibre-reinforced laminae can be deduced assuming the iso-strain or the iso-stress behaviour. Let us introduce the following notations: E Young's modulus, ν Poisson's ratio, G shear modulus, σ normal stress, ε normal

strain and A cross section area. The subscripts f and m refer to fibre and matrix, the subscripts L \equiv 1, T \equiv 2 refer to the principal (longitudinal) direction (fibre direction) and transverse to the fibre direction and the superscript 0 to the initial (unloaded) state. For stress, strain, stiffness and compliances, the following equations are valid. The extensional strain ε and shear strain γ of a body with the length l_0 and the cross section area A_0 are related assuming a uniform distribution of the forces normal force F and the shear force T and small strains ε and γ to

$$\begin{aligned} \sigma &= \frac{F}{A_0} && \text{normal stress } \sigma, \\ \varepsilon &= \frac{l - l_0}{l_0} = \frac{\Delta l}{l_0} && \text{extensional strain } \varepsilon, \\ \tau &= \frac{T}{A_0} && \text{shear stress } \tau, \\ \gamma &\approx \tan \gamma = \frac{\Delta u}{l_0} && \text{shear strain } \gamma. \end{aligned} \quad (1.9)$$

Δu is the displacement in the transverse direction. In addition, we should connect the stresses with the strains introducing the Hooke's law

$$\begin{aligned} \sigma &= E\varepsilon, \quad E = \frac{\sigma}{\varepsilon}, \quad E \text{ is the elasticity or Young's modulus,} \\ \tau &= G\gamma, \quad G = \frac{\tau}{\gamma}, \quad G \text{ is the shear modulus.} \end{aligned} \quad (1.10)$$

For the longitudinal strained prismatic body, the phenomenon of transverse contraction has to be considered. The ratio of the contraction, expressed by the transverse strain ε_t to the elongation in the strained direction ε , is

$$\varepsilon_t = -\nu\varepsilon, \quad \nu = -\frac{\varepsilon_t}{\varepsilon}. \quad (1.11)$$

For an isotropic bar with an extensional strain $\varepsilon > 0$, a transverse contraction $\varepsilon_t < 0$, it follows that the Poisson's ratio is positive¹. The Hooke's law can be written in the inverse form

$$\varepsilon = E^{-1}\sigma = S\sigma \quad (1.12)$$

$S = E^{-1}$ is the flexibility or compliance modulus.

Let us introduce a bar with stiffness $C_i = E_i A_i$ (i is the number of the layer). The layers can be arranged in parallel and in series (Altenbach et al. 2018). Since

$$\sigma = F/A \quad \text{and} \quad \sigma = E\varepsilon \quad (1.13)$$

¹ The class of auxetic materials that have a negative Poisson's ratio (when stretched, they become thicker perpendicular to the applied force), is not in the focus here. However, such values are possible which follows from the positive definiteness of the strain energy.

one obtains

$$\sigma A = F = EA\varepsilon \quad \text{and} \quad \varepsilon = (EA)^{-1}F. \quad (1.14)$$

EA is the effective tensile stiffness and $(EA)^{-1}$ is the effective tensile flexibility or compliance. If we have the arrangement in parallel, we consider the iso-strain state

$$F = \sum_{i=1}^n F_i, \quad A = \sum_{i=1}^n A_i, \quad \varepsilon = \varepsilon_i \quad (1.15)$$

where F_i is the loading forces on A_i . With

$$F = EA\varepsilon, \quad F_i = E_i A_i \varepsilon, \quad \sum_{i=1}^n F_i = F = \sum_{i=1}^n E_i A_i \varepsilon \quad (1.16)$$

follow the coupling equations for the stiffness $E_i A_i$

$$EA = \sum_{i=1}^n E_i A_i, \quad (EA)^{-1} = \frac{1}{\sum_{i=1}^n E_i A_i}. \quad (1.17)$$

This equal strain treatment is often described as the Voigt² model. For the arrangement in series follows

$$\Delta l = \sum_{i=1}^n \Delta l_i \quad (1.18)$$

together with the iso-force concept $F = F_i$, the elongation Δl of the bar is obtained by addition of the Δl_i of the different parts of the bar with the lengths l_i and the tensile force is equal for all cross-sectional areas. With

$$\Delta l = l\varepsilon = l(EA)^{-1}F, \quad \Delta l_i = l_i \varepsilon_i = l_i (E_i A_i)^{-1}F \quad (1.19)$$

and

$$\sum_{i=1}^n \Delta l_i = \left[\sum_{i=1}^n l_i (E_i A_i)^{-1} \right] F \quad (1.20)$$

it follows the coupling equations for the stiffness $E_i A_i$ arranged in series

$$EA = \frac{l}{\sum_{i=1}^n l_i (E_i A_i)^{-1}}, \quad (EA)^{-1} = \frac{\sum_{i=1}^n l_i (E_i A_i)^{-1}}{l}. \quad (1.21)$$

² Woldemar Voigt (*2 September 1850 Leipzig - †13 December 1919 Göttingen).

This equal stress treatment is described generally as the Reuss³ model.

Comparing both estimates, it is easy to see that the arrangement in parallel results in upper bound stiffness, the arrangement in series in lower bound stiffness. The following mechanical models to calculate the effective properties are based on these two arrangements.

1.3.6 Effective Properties of a Single Layer

Based on these simple mixture rules, the other effective properties of a single layer can be estimated (Altenbach et al. 2018). Let us assume for the UD long-fibre-reinforced composites:

- The bond between fibres and matrix is perfect and no friction is considered.
- The fibres are continuous, homogeneous and parallel aligned in each ply.
- They are packed regularly, i.e. the space between fibres is uniform.
- Fibre and matrix materials are linear elastic, they follow approximately Hooke's law and each elastic modulus is constant.
- Voids are ignored.

The rule of mixtures starting from the iso-strain assumption and the inverse rule of mixtures starting from the iso-stress assumption is based on the statement that the composite property is the weighted mean of the properties or the inverse properties of each constituent multiplied by its volume fraction. In the first case, we have the upper bound effective property, in the second—the lower bound effective properties. These bounds are related to Voigt (1910) and Reuss (1929). Examples of such effective properties are

- the effective longitudinal modulus of elasticity (the strains of the fibres, matrix and composite in the loading direction are the same)

$$E_L = E_f v_f + E_m v_m = E_f v_f + E_m(1 - v_f) = E_f \phi + E_m(1 - \phi) \quad (1.22)$$

with the Young's modulus of the fibres E_f , the Young's modulus of the matrix E_m , the volume fraction of the fibres v_f and the volume fraction of the matrix v_m ,

- the effective transverse modulus of elasticity (the stress resultant, respectively, the stress is equal for all phases)

$$\frac{1}{E_T} = \frac{v_f}{E_f} + \frac{1 - v_f}{E_m} = \frac{v_f}{E_f} + \frac{v_m}{E_m} \quad (1.23)$$

or

$$E_T = \frac{E_f E_m}{(1 - v_f) E_f + v_f E_m} = \frac{E_f E_m}{(1 - \phi) E_f + \phi E_m}. \quad (1.24)$$

³ András (Endre) Reuss (*1 July 1900 Budapest - †10 May 1968 Budapest).

In the further derivations, we use $\phi = v_f$ and $1 - \phi = v_m$ only.

1.3.6.1 Longitudinal Young's Modulus

Assuming the arrangement in parallel, one gets the equilibrium of forces

$$F_L = F_{Lf} + F_{Lm} = \sigma_L A = \sigma_{Lf} A_f + \sigma_{Lm} A_m. \quad (1.25)$$

With the Hooke's law, it follows that

$$\sigma_L = E_L \varepsilon, \quad \sigma_{Lf} = E_f \varepsilon_f, \quad \sigma_{Lm} = E_m \varepsilon_m.$$

With the help of (1.25), we obtain

$$E_L \varepsilon A = E_f \varepsilon_f A_f + E_m \varepsilon_m A_m. \quad (1.26)$$

The iso-strain concept for all phases results in identical strains and, finally, the effective longitudinal Young's modulus can be computed as

$$E_L = E_f \frac{A_f}{A} + E_m \frac{A_m}{A}. \quad (1.27)$$

With

$$\frac{A_f}{A} = \frac{A_f l}{Al} = \frac{V_f}{V} = \phi, \quad \frac{A_m}{A} = \frac{A_m l}{Al} = \frac{V_m}{V} = 1 - \phi \quad (1.28)$$

the effective modulus E_L can be written as follows

$$E_L = E_f \phi + E_m (1 - \phi). \quad (1.29)$$

Equation (1.29) is referred to the Voigt estimate. The predicted values of E_L are in good agreement with experimental results. The part of the load taken by the fibre to the part of the load taken by the composite is a measure of the load shared by the fibre

$$\frac{F_{Lf}}{F_L} = \frac{E_{Lf}}{E_L} \phi. \quad (1.30)$$

Since the fibre's Young's modulus is as usual one or more orders greater than the corresponding matrix value, the second term in (1.29) may be neglected

$$E_L \approx E_f \phi. \quad (1.31)$$

1.3.6.2 Transverse Young's Modulus

The mechanical model to calculate the effective transverse modulus E_T is based on the changes in the transverse direction

$$\Delta b = \Delta b_f + \Delta b_m, \quad \varepsilon_t = \frac{\Delta b}{b} = \frac{\Delta b_f + \Delta b_m}{b}. \quad (1.32)$$

With

$$b = \phi b + (1 - \phi)b = b_f + b_m \quad (1.33)$$

and

$$\varepsilon_t = \frac{\Delta b_f}{\phi b} \frac{\phi b}{b} + \frac{\Delta b_m}{(1 - \phi)b} \frac{(1 - \phi)b}{b} = \phi \varepsilon_{tf} + (1 - \phi) \varepsilon_{tm} \quad (1.34)$$

one can compute the transverse strain for the fibres and matrix as

$$\varepsilon_{tf} = \frac{\Delta b_f}{\phi b}, \quad \varepsilon_{tm} = \frac{\Delta b_m}{(1 - \phi)b}.$$

Using Hooke's law for the fibre, the matrix and the composite

$$\sigma_T = E_T \varepsilon_t, \quad \sigma_{Tf} = E_{Tf} \varepsilon_{tf}, \quad \sigma_{Tm} = E_{Tm} \varepsilon_{tm} \quad (1.35)$$

finally, the transverse modulus can be estimated

$$\frac{1}{E_T} = \frac{\phi}{E_f} + \frac{1 - \phi}{E_m} \quad \text{or} \quad E_T = \frac{E_f E_m}{(1 - \phi) E_f + \phi E_m}. \quad (1.36)$$

Equation (1.36) is the Reuss estimate. The predicted values of E_T are seldom in good agreement with experimental results. However, with $E_m \ll E_f$, one gets the approximation $E_T \approx E_m (1 - \phi)^{-1}$ that means E_T is dominated by the matrix modulus E_m .

1.3.6.3 Major Poisson's Ratio

The mechanical model to calculate the major Poisson's ratio ν_{LT} is based on the following considerations. The major Poisson's ratio is the negative of the ratio of the normal strain in the transverse direction to the normal strain in the longitudinal direction

$$\nu_{LT} = -\frac{\varepsilon_t}{\varepsilon}. \quad (1.37)$$

The transverse strain is equal to

$$-\varepsilon_t = \nu_{LT} \varepsilon = -\frac{\Delta b}{b} = -\frac{\Delta b_f + \Delta b_m}{b} = -[\phi \varepsilon_{tf} + (1 - \phi) \varepsilon_{tm}], \quad (1.38)$$

and with

$$\nu_f = -\frac{\varepsilon_{tf}}{\varepsilon_f}, \quad \nu_m = -\frac{\varepsilon_{tm}}{\varepsilon_m} \quad (1.39)$$

we obtain

$$\varepsilon_t = -\nu_{LT}\varepsilon = -\phi\nu_f\varepsilon_f - (1 - \phi)\nu_m\varepsilon_m. \quad (1.40)$$

The longitudinal strains in the composite, the fibres and the matrix are assumed to be equal (Voigt model of parallel connection)

$$\nu_{LT} = \phi\nu_f + (1 - \phi)\nu_m = \phi\nu_f + (1 - \phi)\nu_m = \phi\nu_f + (1 - \phi)\nu_m. \quad (1.41)$$

The minor Poisson's ratio $\nu_{TL} = -\varepsilon_L/\varepsilon_T$ can be derived with the symmetry condition or reciprocal relationship

$$\frac{\nu_{TL}}{E_T} = \frac{\nu_{LT}}{E_L}. \quad (1.42)$$

This relationship results in

$$\nu_{TL} = \nu_{LT} \frac{E_T}{E_L} = (\phi\nu_f + (1 - \phi)\nu_m) \frac{E_f E_m}{(\phi E_m + (1 - \phi)E_f)(\phi E_f + (1 - \phi)E_m)}. \quad (1.43)$$

The values of Poisson's ratios for fibres or matrix material rarely differ significantly, so that neither matrix nor fibre characteristics dominate the major or the minor elastic parameters ν_{LT} and ν_{TL} .

1.3.6.4 Effective In-Plane Shear Modulus

The mechanical model to calculate the effective in-plane shear modulus G_{LT} is based on the assumption that the shear stresses on the fibre and the matrix are the same, but the shear strains are different

$$\gamma_m = \frac{\tau}{G_m}, \quad \gamma_f = \frac{\tau}{G_f}, \quad \gamma = \frac{\tau}{G_{LT}}. \quad (1.44)$$

The model is a connection in series (Reuss model) and therefore

$$\tau = \tau_f = \tau_m, \quad \Delta = \Delta_f + \Delta_m, \quad \Delta = \hat{b} \tan \gamma = \gamma_f \hat{b}_f + \gamma_m \hat{b}_m \quad (1.45)$$

and with

$$\hat{b} = \hat{b}_f + \hat{b}_m = (\nu_f + \nu_m)\hat{b} = \phi\hat{b} + (1 - \phi)\hat{b} \quad (1.46)$$

it follows that

$$\Delta_f = \gamma_f \phi \hat{b}, \quad \Delta_m = \gamma_m (1 - \phi) \hat{b}. \quad (1.47)$$

Using Hooke's law, we have $\tau/G_{LT} = (\tau/G_m)(1 - \phi) + (\tau/G_f)\phi$ which yields

$$G_{LT} = \frac{G_m G_f}{(1 - \phi)G_f + \phi G_m} \quad (1.48)$$

or by analogy to (1.36)

$$\frac{1}{G_{LT}} = \frac{\phi}{G_f} + \frac{1 - \phi}{G_m}$$

which is again a Reuss estimate. Note that assuming isotropic fibres and matrix material the following relations are valid

$$G_f = \frac{E_f}{2(1 + \nu_f)}, \quad G_m = \frac{E_m}{2(1 + \nu_m)}. \quad (1.49)$$

1.3.6.5 Discussion on the Elementary Mixture Rules

Assuming that $x_2 - x_3$ is the plane of isotropy, we have

$$\begin{aligned} E_1 &= E_L, \quad E_2 = E_3 = E_T, \\ E_4 = G_{23} = G_{TT} &= \frac{E_T}{2(1 + \nu_{TT})}, \quad E_5 = G_{13} = E_6 = G_{12} = G_{LT}, \\ \nu_{12} = \nu_{13} &= \nu_{LT}, \quad \nu_{23} = \nu_{TT}, \quad \nu_{LT} E_T = \nu_{TL} E_L \end{aligned} \quad (1.50)$$

with $E_L, E_T, G_{LT}, G_{TT}, \nu_{LT}$ as the five independent moduli of a transversely isotropic material. Finally, we have four expression that can be found in most textbooks

$$\begin{aligned} E_L &= \phi E_f + (1 - \phi)E_m, \quad E_T = \frac{E_f E_m}{\phi E_m + (1 - \phi)E_f}, \\ G_{LT} &= \frac{G_f G_m}{\phi G_m + (1 - \phi)G_f}, \quad \nu_{LT} = \phi \nu_f + (1 - \phi)\nu_m. \end{aligned} \quad (1.51)$$

The shear modulus G_{TT} corresponds to an iso-shear strain model in the plane of isotropy

$$G_{TT} = \phi G_f + (1 - \phi)G_m. \quad (1.52)$$

Neither the iso-shear stress nor the iso-shear strain condition for G_{LT} and G_{TT} estimation are close to the real situation of shearing loaded fibre-reinforced composites. Very often, fibres material behaviour is transversally isotropic but the matrix material is isotropic. For such cases, simple alternative relations for the effective engineering moduli of the UD-lamina can be given

$$\begin{aligned}
E_L &= \phi E_f + (1 - \phi) E_m, & \nu_{LT} &= \phi \nu_{LTf} + (1 - \phi) \nu_m, \\
E_T &= \frac{E_{Tf} E_m}{\phi E_m + (1 - \phi) E_{Tf}}, & \nu_{TT} &= \frac{\nu_{TTf} \nu_m}{\phi \nu_m + (1 - \phi) \nu_{TTf}}, \\
G_{LT} &= \frac{G_{LTf} G_m}{\phi G_m + (1 - \phi) G_{LTf}}, & G_{TT} &= \phi G_f + (1 - \phi) G_m.
\end{aligned} \tag{1.53}$$

In Eq. (1.53) $E_m, \nu_m, G_m = E_m/2(1 + \nu_m)$ are the isotropic matrix moduli and $E_f, E_{Tf}, G_{LTf}, G_f = E_{Tf}/2(1 + \nu_{TTf}), \nu_{TTf}, \nu_{LTf}$ are transversally isotropic fibre moduli. E_m, ν_m of the matrix material and $E_f, E_{Tf}, G_{LTf}, \nu_{LTf}, \nu_{TTf}$ or G_{TTf} of the fibre material can be chosen as the independent moduli.

1.3.7 Improved Formulas for Effective Moduli

Because the Reuss and Voigt estimates are often not very accurate, several improvements are suggested. The most used improvement is the Halpin-Tsai⁴ model. This is a mathematical model for the prediction of elasticity of composite plies based on the geometry and orientation of the reinforcement and the elastic properties of the filler and matrix. The model is based on the self-consistent field method although. These models are empirical or semi-empirical. In this case, we have

- E_L and ν_{LT} by the law of mixtures Eqs. (1.29) and (1.41)
- For the other moduli (M is, e.g. E_T, G_{LT}, \dots), we have

$$\frac{M}{M_m} = \frac{1 + \xi \eta \phi}{1 - \eta \phi} \quad \eta = \frac{\frac{M_f}{M_m} - 1}{\frac{M_f}{M_m} + \xi}. \tag{1.54}$$

ξ is called the reinforcement factor and depends on

- the geometry of the fibres,
 - the packing arrangement of the fibres and
 - the loading conditions.
- The main difficulty is the determination of the factor ξ by comparing the semi-empirical values with analytical solutions or with experimental results.

More details on the improvements are based on the Halpin-Tsai method which are given in Halpin and Kardos (1976).

Let us make some final remarks:

- In the layer, all moduli are related to the fibre direction and the transverse direction.
- When looking at a laminate, these directions can be different in each layer.
- A transformation of the local directions into a global coordinate system is therefore necessary.

⁴ Stephen Wei-Lun Tsai (*6 July 1929, Beijing).

- The effective stiffness values are then to be considered as the sum of the weighted layer properties in the global system.
- A distinction must be made between in-plane, mixed and out-of-plane stiffness values since symmetries cannot be assumed in the general case.
- The choice of the middle surface should be made based on geometrical assumptions only.
- In the case of sandwich plates, it is helpful to have an additional transverse shear stiffness.

In the classical laminate theory, but also in the non-classical laminate theories (for example, first-order shear deformation theory), the stiffness parameters of the laminate can be estimated as

- sums of weighted properties (for example, laminates),
- as integrals of weighted properties (for example, functional graded materials) and
- sometimes special expressions (for example, for the shear correction).

Typical predictions are presented in Altenbach (2000a, b), Altenbach and Eremeyev (2008a). This approach can be easily extended to viscoelastic systems (Altenbach 1988; Altenbach and Eremeyev 2008b).

1.4 Particle-Reinforced Composites

1.4.1 Short-fibre-Reinforced Plastics

In particle-reinforced composite materials, particles act as a load carrying medium and the matrix acts again as a load transporting medium. The most common particle-reinforced composite is concrete. Here, we have a mixture of gravel and sand usually strengthened by addition of small rocks or sand. Polymers are often reinforced, for example, with short glass fibres. This material is often produced by injection moulding. The particles and the matrix are isotropic materials, however, their combination can result in a quasi-homogeneous anisotropic material. In Saito et al. (2000), the flow-induced orientations of particles during the injection moulding process are discussed. It was established that a rough layered structure can be obtained with different orientation of the glass fibres: in the mid, the orientation is orthogonal to the flow direction, close to the cavity walls, and the orientation is in the flow direction and between “both layers” a chaotic orientation can be established. This kind of anisotropy should be taken into account for global behaviour predictions of structures made of particle-reinforced plastics.

The prediction of the orientation is widely discussed in the literature. One approach is based on the theory of dilute suspensions (Advani and Tucker 1987; Bay and Tucker 1992). If ω is the angular velocity of a single particle, an evolution equation for the fibre microstructure can be developed. Another approach is based on the micropolar theory of concentrated suspensions (Eringen 1991; Altenbach et al.

2003b). Here ω , \mathbf{J} (tensor of inertia) and \mathbf{Q} (rotation tensor) are field quantities and a constitutive equation for the skew symmetric part of $\boldsymbol{\sigma}$ (rotary interactions between fluid and suspended particles) could be established. To verify the corresponding assumptions, studies of the particle motion in homogeneous flow fields are helpful.

Maybe the first paper in this direction was published by Jeffery (1922). He discussed the rotation of an ellipsoid of revolution in a Newtonian fluid. The obtained shear flow yields a periodic orbit. The slender particle results in particle alignment parallel to the streamlines. Later, Bretherton (1962) generalized Jeffery's formula for the angular velocity to axisymmetric particles of various shapes. In both Jeffery's and Bretherton's works, the particle inertia and inertia effects of the fluid flow were ignored.

Considering experimental results, some disagreements with the theoretical results can be established. The particle dynamics in flow fields is presented accounting the fluid inertia, but inertialess particles are assumed (Leal 1980; Subramanian and Koch 2005). Introducing the particle rotation under the influence of rotary inertia, it can be shown that long-time stable orbits do not longer exist (Altenbach et al. 2007). In the case of shear flow, a slender particle may jump over stable alignment (Altenbach et al. 2009). The approximate solution is limited to numerical values for initial angular velocity and particle inertia.

The aim of our further studies was the detailed analysis of the particle rotation in the shear flow. To this end, the governing equations of rigid body dynamics for the slender particle in a homogeneous flow field were deduced, the hydrodynamic moment exerted on the particle was assumed in the form as proposed by Jeffery (1922), the shear flow equations of motion are reduced to a single second-order ordinary differential equation with respect to the angle of rotation about a fixed axis and the phase portrait analysis of this equation was performed. Conclusions about the influence of inertia and the stability of fibre alignment were made. The combined analysis of particle orientation and stiffness distribution was presented. In addition to Altenbach et al. (2003b, 2009), the main results of our investigations are published in Altenbach et al. (2003a, 2005), Renner et al. (2005).

1.4.2 Spherical Inhomogeneity with Interphase

One of the main problems in the description of real composites with reinforcements is the randomness in composites. Special attention must be paid to the interphase, since it is not present in the initial state. Only when matrix and reinforcement material are brought together, the interphase is formed. The randomness in the microstructure of the composite then also has a particular effect on the interphase. To make matters worse, the properties of the interphase are very difficult to determine. At the same time, the failure of the composite is determined to a particular extent by the interphase. The local geometric arrangements and the damage are related to the randomness and the problem of modelling of such materials is a big challenge.

One of the modelling approaches is based on the energy equivalent inhomogeneity concept. The basic ideas are presented, for example, in Hashin (1990, 1991) using the spring layer model of interphase in context with the composite cylinder or the composite sphere models. However, only the equivalent inhomogeneity bulk modulus could be evaluated. In Shen and Li (2005), Sevostianov and Kachanov (2007), the so-called differential approach was used to define equivalent inhomogeneity. Here, the Mori-Tanaka's estimate and Hashin lower bound were used. In Duan et al. (2007), equivalent inhomogeneity properties were obtained by using Eshelby's equivalence principle. The properties depend on the properties of the matrix. A detailed description on some previous works, related to the model presented below, is given in Nazarenko et al. (2015), Nazarenko and Stolarski (2016), Nazarenko et al. (2016, 2017, 2018).

In accordance with Hill (1963), the energy of the inhomogeneity/interphase system can be presented as follows

$$E = \frac{1}{2} \int_{V_i} \boldsymbol{\varepsilon}_i \cdot \mathbf{C}_i \cdot \boldsymbol{\varepsilon}_i dV_i + E_{\text{int}} \quad (1.55)$$

with

$$E_{\text{int}} = \frac{1}{2} \int_{\Omega_{\text{int}}} \boldsymbol{\varepsilon}_{\text{int}} \cdot \mathbf{C}_{\text{int}} \cdot \boldsymbol{\varepsilon}_{\text{int}} d\Omega_{\text{int}}.$$

The equivalent system is presented by the energy

$$E = \frac{1}{2} V_{\text{eq}} \boldsymbol{\varepsilon}_{\text{eq}} \cdot \mathbf{C}_{\text{eq}} \cdot \boldsymbol{\varepsilon}_{\text{eq}} = \frac{1}{2} \boldsymbol{\varepsilon}_{\text{eq}} \cdot \tilde{\mathbf{C}}_{\text{eq}} \cdot \boldsymbol{\varepsilon}_{\text{eq}}. \quad (1.56)$$

$\boldsymbol{\varepsilon}_{\text{int}}$, $\boldsymbol{\varepsilon}_{\text{eq}}$, $\boldsymbol{\varepsilon}_i$ are the strain tensors within the inhomogeneity, interphase and the equivalent inhomogeneity (prescribed). \mathbf{C}_i , \mathbf{C}_{int} , \mathbf{C}_{eq} are the stiffness tensor of the inhomogeneity, interphase and equivalent inhomogeneity, respectively.

The minimization of the potential energy (1.55)

$$\delta E = 0$$

and

$$\boldsymbol{\varepsilon}_i = \mathbf{T}_i \cdot \boldsymbol{\varepsilon}_{\text{eq}}, \quad \boldsymbol{\varepsilon}_{\text{int}} = \mathbf{T}_{\text{int}} \cdot \boldsymbol{\varepsilon}_{\text{eq}}$$

with \mathbf{T}_i , \mathbf{T}_{int} is fourth-order tensors results in the energy of the system at equilibrium

$$E = \frac{1}{2} \boldsymbol{\varepsilon}_{\text{eq}} \cdot \left(\int_{V_i} \mathbf{T}_i^T \cdot \mathbf{C}_i \cdot \mathbf{T}_i dV_i + \int_{\Omega_{\text{int}}} \mathbf{T}_{\text{int}}^T \cdot \mathbf{C}_{\text{int}} \cdot \mathbf{T}_{\text{int}} d\Omega_{\text{int}} \right) \cdot \boldsymbol{\varepsilon}_{\text{eq}}$$

and the stiffness tensor of the equivalent inhomogeneity can be expressed as

$$\tilde{\mathbf{C}}_{\text{eq}} = \int_{V_i} \mathbf{T}_i^T \cdot \mathbf{C}_i \cdot \mathbf{T}_i dV_i + \int_{\Omega_{\text{int}}} \mathbf{T}_{\text{int}}^T \cdot \mathbf{C}_{\text{int}} \cdot \mathbf{T}_{\text{int}} d\Omega_{\text{int}}.$$

Numerical examples are presented in Nazarenko et al. (2015), Nazarenko and Stolarski (2016), Nazarenko et al. (2017, 2018). The applied approach is helpful since the modelling of such a difficult system composed of matrix, particle and interphase is not so easy. It seems that from the point of view of experimental results in chemical-physics, the interphase can have properties weaker than the matrix, stiffer than the filler, but also between of the matrix and filler properties. The reason for this is that measuring the interphase properties is not easy, as they only exist after the matrix and filler has been brought together.

1.5 Functionally Graded Materials

This kind of materials was investigated during the last years since there are many applications of these materials. Foams (metallic or polymeric) are a typical example and a very perspective class of materials for engineering applications. Structural elements made of such materials are applied in civil engineering, in the automotive or aerospace industries since they combine low weight, high specific strength, lower energy effort and excellent possibilities to absorb energy. The technical realization of FGMs is mostly performed as sandwich panels (plates or shells with hard and stiff face sheets and a core layer made of a foam). A foam is a very complex material which has many non-classical properties—some foams have a negative Poisson's ratio (see Lakes 1987). The non-homogeneous foam itself can be modelled as a functionally graded material (FGM) with “smeared” or “homogenized” mechanical properties changing over the thickness direction. Another variant is coatings. In contrast to foams, an asymmetrical distribution of properties can be assumed here. In both cases, however, symmetry and asymmetry with respect to the geometrical mid-surface must be taken into account.

Several publications were made within 2007 and 2016. One of the first is Altenbach and Eremeyev (2008c) discussing first time the full linear elastic isotropic theory of FGMs. The theory presented here can be easily applied to the case of viscoelastic materials (Altenbach and Eremeyev 2011a). Both papers are close to the Cosserat theory (Altenbach et al. 2011). In addition, an overview on generalized two-dimensional continua is given in Altenbach and Eremeyev (2013a, b).

1.6 Anti-Sandwich and Nanomaterials

During the last years, several new applications occurred. At first, with respect of photovoltaic applications, new theories were deduced (Schulze et al. 2012; Weps et al. 2013). A consistent theory was suggested, for example, in Altenbach et al. (2015) and the numerical treatment was discussed in Eisenträger et al. (2015a, b).

Nanomaterials were included in the theoretical, continuum mechanics based concept in Altenbach and Eremeyev (2011b), Altenbach et al. (2012).

1.7 Summary and Outlook

There is a number of open questions that need to be investigated in future:

- the correctness of the assumption of a periodicity in the composite material,
- the uncertainties in the model based on statistical distributions of matrix and reinforcement in the composite material,
- continuum versus discrete approach,
- the correctness of molecular dynamics modelling and
- the assumptions concerning the perfect and real contact conditions.

There is a greater need for research here in the coming years. Questions of failure in particular have not been finally clarified to this day. There are numerous approaches and also experimental results. Unfortunately, there is still now no comprehensive theoretical basis to describe the failure without contradiction.

Acknowledgements This contribution is based on various papers that were created in collaboration with my current and former collaborators (my father Prof. J. Altenbach, Prof. Igor Brigadnov, Prof. Victor A. Eremeyev, Prof. Wolfgang Kissing, Prof. Gennady Lvov, Prof. Konstantin Naumenko, Dr. Lidiia Nazarenko, Prof. Rolands Rikards (†), Prof. Henryk Stolarski, Prof. Pavel Zhilin (†) and former doctoral students (Dr.-Ing. Babara Renner and M.Sc. Sergei Pilipenko).

References

- Advani SG, Tucker CL (1987) The use of tensors to describe and predict fiber orientation in short fiber composites. *J Rheol* 31(8):751–784. <https://doi.org/10.1122/1.549945>
- Altenbach H (1988) Determination of the reduced properties of multilayer viscoelastic sheets. *Mech Compos Mater* 24(1):52–59
- Altenbach H (2000) An alternative determination of transverse shear stiffnesses for sandwich and laminated plates. *Int J Solids Struct* 37(25):3503–3520. [https://doi.org/10.1016/S0020-7683\(99\)00057-8](https://doi.org/10.1016/S0020-7683(99)00057-8)
- Altenbach H (2000) On the determination of transverse shear stiffnesses of orthotropic plates. *Zeitschrift für angewandte Mathematik und Physik ZAMP* 51(4):629–649. <https://doi.org/10.1007/s000330050021>

- Altenbach H, Becker W (2003) Modern trends in composite laminates mechanics. In: CISM international centre for mechanical sciences, vol 448. Springer. <https://doi.org/10.1007/978-3-7091-2544-1>
- Altenbach H, Eremeyev VA (2008) Direct approach-based analysis of plates composed of functionally graded materials. *Arch Appl Mech* 78(10):775–794. <https://doi.org/10.1007/s00419-007-0192-3>
- Altenbach H, Eremeyev VA (2008) On the analysis of viscoelastic plates made of functionally graded materials. *ZAMM - Zeitschrift für angewandte Mathematik und Mechanik* 88(5):332–341. <https://doi.org/10.1002/zamm.200800001>
- Altenbach H, Eremeyev VA (2008c) On the application of Zhilin's theory of simple shells to plates made of functionally graded materials. In: Indeitsev DA, Krivtsov AM (eds) Proceedings of 36 international summer school-conference APM 2008, Institute for Problems in Mechanical Engineering, pp 8–49
- Altenbach H, Eremeyev VA (2011a) Mechanics of viscoelastic plates made of fgms. In: Murín J, Komiš V, Kutiš V (eds) Computational modelling and advanced simulations, computational methods in applied sciences, vol 24. Springer, pp 33–48. https://doi.org/10.1007/978-94-007-0317-9_2
- Altenbach H, Eremeyev VA (2011) On the shell theory on the nanoscale with surface stresses. *Int J Eng Sci* 49(12):1294–1301. <https://doi.org/10.1016/j.ijengsci.2011.03.011>
- Altenbach H, Eremeyev VA (2013a) Cosserat media. In: Altenbach H, Eremeyev VA (eds) Generalized Continua from the theory to engineering applications, CISM international centre for mechanical sciences, vol 541. Springer, pp 65–130. https://doi.org/10.1007/978-3-7091-1371-4_2
- Altenbach H, Eremeyev VA (2013b) Cosserat-type shells. In: Altenbach H, Eremeyev VA (eds) Generalized Continua from the theory to engineering applications, CISM international centre for mechanical sciences, vol 541. Springer, pp 131–178. https://doi.org/10.1007/978-3-7091-1371-4_3
- Altenbach H, Öchsner A (2010) Cellular and porous materials in structures and processes, CISM international centre for mechanical sciences, vol 521. Springer. <https://doi.org/10.1007/978-3-7091-0297-8>
- Altenbach H, Altenbach J, Rikards R (1996) Einführung in die Mechanik der Laminat- und Sandwichtragwerke: Modellierung und Berechnung von Balken und Platten aus Verbundwerkstoffen. Dt. Verl. für Grundstoffindustrie, Stuttgart
- Altenbach H, Naumenko K, Lvov GI, Pilipenko SN (2003) Numerical estimation of the elastic properties of thin-walled structures manufactured from short-fiber-reinforced thermoplastics. *Mech Compos Mater* 39(3):221–234. <https://doi.org/10.1023/A:1024566026411>
- Altenbach H, Naumenko K, Zhilin PA (2003) A micro-polar theory for binary media with application to phase-transitional flow of fiber suspensions. *Continuum Mech Thermodyn* 15(6):539–570. <https://doi.org/10.1007/s00161-003-0133-5>
- Altenbach H, Naumenko K, Pylypenko S (2005) On the numerical prediction of the anisotropic elastic properties in thin-walled structures made from short fiber reinforced plastics. *Comput Assist Mech Eng* 12(4):87–97
- Altenbach H, Naumenko K, Pylypenko S, Renner B (2007) Influence of rotary inertia on the fiber dynamics in homogeneous creeping flows. *ZAMM - Zeitschrift für Angewandte Mathematik und Mechanik* 87(2):81–93. <https://doi.org/10.1002/zamm.200610303>
- Altenbach H, Brigadnov I, Naumenko K (2009) Rotation of a slender particle in a shear flow: influence of the rotary inertia and stability analysis. *ZAMM - Zeitschrift für Angewandte Mathematik und Mechanik* 89(10):823–832. <https://doi.org/10.1002/zamm.200900249>
- Altenbach H, Eremeyev VA, Lebedev LP (2011) Micropolar shells as two-dimensional generalized continua models. In: Altenbach H, Maugin GA, Erofeev V (eds) Mechanics of generalized Continua, advanced structured materials, vol 7. Springer, pp 23–55. https://doi.org/10.1007/978-3-642-19219-7_2

- Altenbach H, Eremeyev VA, Morozov NF (2012) Surface viscoelasticity and effective properties of thin-walled structures at the nanoscale. *Int J Eng Sci* 59:83–89. <https://doi.org/10.1016/j.ijengsci.2012.03.004>
- Altenbach H, Eremeyev VA, Naumenko K (2015) On the use of the first order shear deformation plate theory for the analysis of three-layer plates with thin soft core layer. *ZAMM - Zeitschrift für Angewandte Mathematik und Mechanik* 95(10):1004–1011
- Altenbach H, Altenbach J, Kissing W (2018) *Mechanics of composite structural elements*, 2nd edn. Springer. <https://doi.org/10.1007/978-981-10-8935-0>
- Altenbach H, Öchsner A (2020) *Encyclopedia of Continuum mechanics*, vol 1–3. Springer. <https://doi.org/10.1007/978-3-662-55770-9>
- Ashby M, Shercliff H, Cebon D (2018) *Materials: engineering, science, processing and design*, 4th edn. Butterworth-Heinemann
- Bay RS, Tucker III CL (1992) Fiber orientation in simple injection moldings. Part I: theory and numerical methods. *Polym Compos* 13(4):317–331. <https://doi.org/10.1002/pc.750130409>
- Bretherton FP (1962) The motion of rigid particles in a shear flow at low Reynolds number. *J Fluid Mech* 14:284–304. <https://doi.org/10.1017/S002211206200124X>
- Cristescu ND, Craciun EM, Soós E (2003) *Mechanics of elastic composite*. Chapman and Hall, New York. <https://doi.org/10.1201/9780203502815>
- Duan H, Yi X, Huang Z, Wang J (2007) A unified scheme for prediction of effective moduli of multiphase composites with interface effects. Part I: theoretical framework. *Mech Mater* 39(1):81–93. <https://doi.org/10.1016/j.mechmat.2006.02.009>
- Eisenträger J, Naumenko K, Altenbach H, Köppe H (2015a) Application of the first-order shear deformation theory to the analysis of laminated glasses and photovoltaic panels. *Int J Mech Sci* 96–97:163–171. <https://doi.org/10.1016/j.ijmecsci.2015.03.012>
- Eisenträger J, Naumenko K, Altenbach H, Meenen J (2015b) A user-defined finite element for laminated glass panels and photovoltaic modules based on a layer-wise theory. *Compos Struct* 133:265–277. <https://doi.org/10.1016/j.compstruct.2015.07.049>
- Eringen AC (1991) Continuum theory of dense rigid suspensions. *Rheologica Acta* 30(1):23–32. <https://doi.org/10.1007/BF00366791>
- Halpin JC, Kardos JL (1976) The halpin-tsai equations: a review. *Polym Eng Sci* 16(5):344–352. <https://doi.org/10.1002/pen.760160512>
- Hashin Z (1990) Thermoelastic properties of fiber composites with imperfect interface. *Mechan Mater* 8(4):333–348. [https://doi.org/10.1016/0167-6636\(90\)90051-G](https://doi.org/10.1016/0167-6636(90)90051-G)
- Hashin Z (1991) The spherical inclusion with imperfect interface. *J Appl Mech* 58(2):444–449. <https://doi.org/10.1115/1.2897205>
- Hill R (1963) Elastic properties of reinforced solids: Some theoretical principles. *J Mech Phys Solids* 11(5):357–372. [https://doi.org/10.1016/0022-5096\(63\)90036-X](https://doi.org/10.1016/0022-5096(63)90036-X)
- Jeffery GB (1922) The motion of ellipsoidal particles immersed in a viscous fluid. *Proc Roy Soc Lond Ser A Containing Pap Math Phys Charact* 102(715):161–179. <https://doi.org/10.1098/rspa.1922.0078>
- Jones RM (2018) *Mechanics of composite materials*, 2nd edn. CRC Press, Boca Raton. <https://doi.org/10.1201/9781498711067>
- Lakes R (1987) Foam structures with a negative Poisson's ratio. *Science* 235(4792):1038–1040. <https://doi.org/10.1126/science.235.4792.1038>
- Lakes RS (2020) *Composites and metamaterials*. World Scientific, New Jersey
- Leal LG (1980) Particle motions in a viscous fluid. *Annu Rev Fluid Mech* 12(1):435–476. <https://doi.org/10.1146/annurev.fl.12.010180.002251>
- Mikhasev GI, Altenbach H (2019) *Thin-walled laminated structures: buckling, vibrations and their suppression, advanced structured materials*, vol 106. Springer, Cham. <https://doi.org/10.1007/978-3-030-12761-9>
- Mittelstedt C (2021) *Structural mechanics in lightweight engineering*. Springer, Cham. <https://doi.org/10.1007/978-3-030-75193-7>

- Mittelstedt C, Becker W (2016) *Strukturmechanik ebener Laminate*. Technische Universität Darmstadt, Darmstadt, Studienbereich Mechanik
- Nazarenko L, Stolarski H (2016) Energy-based definition of equivalent inhomogeneity for various interphase models and analysis of effective properties of particulate composites. *Compos Part B Eng* 94:82–94. <https://doi.org/10.1016/j.compositesb.2016.03.015>
- Nazarenko L, Bargmann S, Stolarski H (2015) Energy-equivalent inhomogeneity approach to analysis of effective properties of nanomaterials with stochastic structure. *Int J Solids Struct* 59:183–197. <https://doi.org/10.1016/j.ijsolstr.2015.01.026>
- Nazarenko L, Stolarski H, Altenbach H (2016) Effective properties of short-fiber composites with Gurtin-Murdoch model of interphase. *Int J Solids Struct* 97–98:75–88. <https://doi.org/10.1016/j.ijsolstr.2016.07.041>
- Nazarenko L, Stolarski H, Altenbach H (2017) A model of cylindrical inhomogeneity with spring layer interphase and its application to analysis of short-fiber composites. *Compos Struct* 160:635–652. <https://doi.org/10.1016/j.compstruct.2016.10.024>
- Nazarenko L, Stolarski H, Altenbach H (2018) On modeling and analysis of effective properties of carbon nanotubes reinforced materials. *Compos Struct* 189:718–727. <https://doi.org/10.1016/j.compstruct.2018.01.027>
- Öchsner A (2021) *Foundations of classical laminate theory, advanced structured materials*, vol 163. Springer, Cham. <https://doi.org/10.1007/978-3-030-82631-4>
- Palanikumar K (2012) Analyzing surface quality in machined composites. In: Hocheng H (ed) *Machining technology for composite materials*, Woodhead publishing series in composites science and engineering. Woodhead Publishing, pp 154–182. <https://doi.org/10.1533/9780857095145.1.154>
- Reiner M (1960) *Deformation, strain and flow: an elementary introduction to rheology*. Lewis, London
- Reiner M (1967) *Rheologie in elementarer Darstellung*. Hanser, München
- Renner B, Altenbach H, Naumenko K (2005) Numerical treatment of finite rotation for cylindrical particle. *Technische Mechanik* 25(3/4):151–161
- Reuss A (1929) Berechnung der Fließgrenze von Mischkristallen auf Grund der Plastizitätsbedingung für Einkristalle. *Zeitschrift für Angewandte Mathematik und Mechanik* 9(1):49–58. <https://doi.org/10.1002/zamm.19290090104>
- Saito M, Kukuła S, Kataoka Y, Miyata T (2000) Practical use of statistically modified laminate model for injection moldings. *Mater Sci Eng A* 285(1):280–287. [https://doi.org/10.1016/S0921-5093\(00\)00646-8](https://doi.org/10.1016/S0921-5093(00)00646-8)
- Schulze SH, Pander M, Naumenko K, Altenbach H (2012) Analysis of laminated glass beams for photovoltaic applications. *Int J Solids Struct* 49(15–16):2027–2036. <https://doi.org/10.1016/j.ijsolstr.2012.03.028>
- Sevostianov I, Kachanov M (2007) Effect of interphase layers on the overall elastic and conductive properties of matrix composites. applications to nanosize inclusion. *Int J Solids Struct* 44(3):1304–1315. <https://doi.org/10.1016/j.ijsolstr.2006.06.020>
- Shen L, Li J (2005) Homogenization of a fibre/sphere with an inhomogeneous interphase for the effective elastic moduli of composites. *Proc Roy Soc A Math Phys Eng Sci* 461(2057):1475–1504. <https://doi.org/10.1098/rspa.2005.1447>
- Subramanian G, Koch DL (2005) Inertial effects on fibre motion in simple shear flow. *J Fluid Mech* 535:383–414. <https://doi.org/10.1017/S0022112005004829>
- Voigt W (1910) *Lehrbuch der Kristallphysik (mit Ausschluss der Kristalloptik)*. Springer, Wiesbaden. <https://doi.org/10.1007/978-3-663-15884-4>
- Weps M, Naumenko K, Altenbach H (2013) Unsymmetric three-layer laminate with soft core for photovoltaic modules. *Compos Struct* 105:332–339. <https://doi.org/10.1016/j.compstruct.2013.05.029>

Chapter 2

Aspects in the Modelling of Heterogeneous Thermo-Oxidative Ageing Using the Example of a Rubber Buffer



Bruno Musil and Michael Johlitz

Abstract Elastomers are used in almost all areas of industrial applications. During operation, they are exposed to various environmental influences, especially atmospheric oxygen as well as high temperatures have a significant impact. The resulting irreversible changes in the microstructure of the material, which lead to a change in the structural-mechanical behaviour, are summarised as chemical respectively thermo-oxidative ageing. In the case of thermo-oxidative ageing especially at elevated operating temperatures, the ageing processes run heterogeneously. These effects are referred to as diffusion-limited-oxidation and are associated with the diffusion-reaction behaviour of atmospheric oxygen as well as of antioxidants within the elastomer network. All these phenomena are taken into account in this paper and simulated within the framework of finite viscoelasticity using the example of a rubber buffer using the finite element method. The operating loads lie in a dynamic range as well, so that dissipative heating may occur. The resulting temperature field can lead as an accelerator for chemical reactions, triggering chemical ageing. Thus, the couplings between these two phenomena are considered as well as experimentally investigated.

Keywords Ageing · Diffusion-limited-oxidation · Rubber · Self-heating · Viscoelasticity

2.1 Introduction

If a typical elastomer component like rubber buffer is exposed to environmental conditions, complicated ageing phenomena take place. In this case, the elastomer degenerates and changes its chemical structure in the aged regions (cf. Ehrenstein and

B. Musil (✉)

Institute of Lightweight Design, Universität der Bundeswehr Munich, 85579 Neubiberg, Germany
e-mail: bruno.musil@unibw.de

M. Johlitz

Institute of Mechanics, Universität der Bundeswehr Munich, 85579 Neubiberg, Germany
e-mail: michael.johlitz@unibw.de

Pongratz 2007). As it is widely known, ageing of elastomers results in changes in the internal structure of the network. Influences of external media lead to scission of the primary network of material, i.e. network degradation. In parallel, there is a formation of a secondary network respectively a new crosslinking, i.e. network reformation. Temperature acts as a driver and accelerates this rearrangement of the elastomer network considerably. One of the most significant ageing processes is the reaction of elastomer molecules with oxygen, the so-called thermo-oxidative ageing. This is a diffusion-reaction driven process. In the first step, oxygen diffuses into the polymer material and enters into the chemical structure. After an initialisation phase, chemical reactions are triggered within the elastomer network, which ultimately changes the material properties irreversibly. Possible approaches for modelling homogeneous thermo-oxidative ageing within the framework of finite deformation theory can be found among others in Duarte and Achenbach (2007), Shaw et al. (2005) and Steinke (2013) as well as in Johlitz et al. (2014) and Musil et al. (2018) where the concept of internal variables for ageing modelling has been further developed.

In general, the thermo-oxidative ageing of elastomers proceeds heterogeneously. The oxygen molecules are absorbed from the environment by the elastomer and driven further into the material by diffusion. However, many of the oxygen molecules dissolved at the edge of an elastomer do not penetrate the interior of the material at all, as they have already reacted with the elastomer beforehand. In addition, oxygen diffusion is restricted by the existing and reforming network structure. Likewise, it has been experimentally proven that the oxidation of elastomers causes a reduction in diffusivity (cf. Van Amerongen 1946; Kommling et al. 2016; Musil 2020), which can be explained by the influence of post-crosslinking due to oxidation as well as the incorporation of polar oxygen-containing groups in the elastomer chains. The phenomenon of the resulting heterogeneous oxidation of elastomers is called *diffusion-limited-oxidation* (DLO).

A very important component of a technical rubber mixture is the antioxidant. It inactivates the oxygen-containing radicals produced during ageing and thus slows down the oxidation of the elastomer (cf. Verdu 2012). Musil et al. (2019) showed, that the influence of antioxidants cannot be neglected in the modelling of thermo-oxidative ageing of rubber parts. In the case of heterogeneous oxidation and DLO effect formation, a gradient in antioxidant concentration can also occur, as these antioxidants are consumed faster at the edges, where the highest oxidation prevails. At the same time, there is a diffusion transport of antioxidants from the inner region to the edge region of the component.

A rubber buffer, also known as a silent block or silent bush, is a component consisting mainly of an elastomer block. This is vulcanised to a metal segment on one or both of its edges (see Fig. 2.1). The component is used as a connecting element to decouple the parts connected to it. Examples of applications are engine mounts, the attachment of stabilisers in automotive construction, or the damped decoupling of machines from the building floor.

Due to its technical applications, the component must endure high mechanical as well as thermal stresses during operation. This leads to the triggering or acceleration of the ageing processes to which all technically relevant elastomers are exposed.

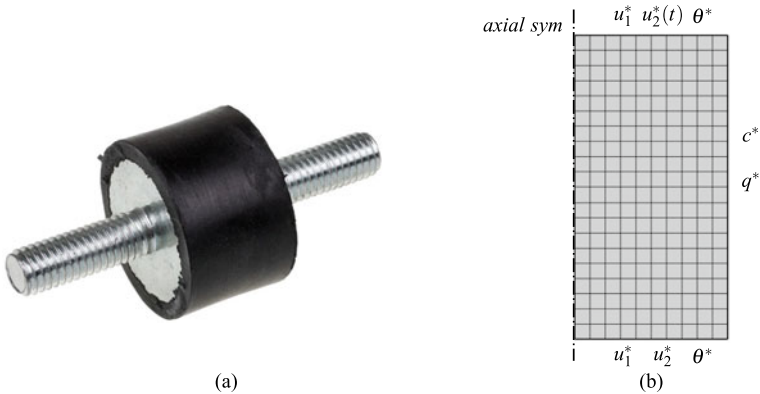


Fig. 2.1 **a** Rubber buffer (silentblock) and **b** finite element model of the rubber buffer with prescribed boundary conditions

Chemical ageing and the associated impairment of the material properties ultimately influence the usability and service life of the rubber buffer in a significant manner. Thanks to the material model presented in the work of Musil et al. (2019), however, the possibility is created to take into account all the phenomena mentioned and thus to be able to make a more accurate service life prediction.

For rubber buffers, however, another coupling direction is also relevant, in that mechanical stresses are converted (dissipated) into heat (cf. Rodas et al. 2014; Dippel 2015; Johlitz et al. 2016). A temperature field resulting from dynamic loads can ultimately trigger or accelerate chemical ageing by driving chemical reactions. In addition, chemical ageing can in turn change the dissipation behaviour of elastomers through its influence on the material properties. How and on which scale this can happen is the subject of an experimental investigation by using the thermal imaging tomography.

2.2 Chemo-Thermo-Mechanical Simulation of a Rubber Buffer

2.2.1 Overview of the Quantities and Equations of the Material Model

In this section, a brief introduction of the differential equations to be solved and the material model developed by Musil et al. (2019) and Musil (2020) is given. In this paper, the commercial software *Comsol Multiphysics* was used for the implementation within the finite element method. All material and model parameters are described in Table 2.1.

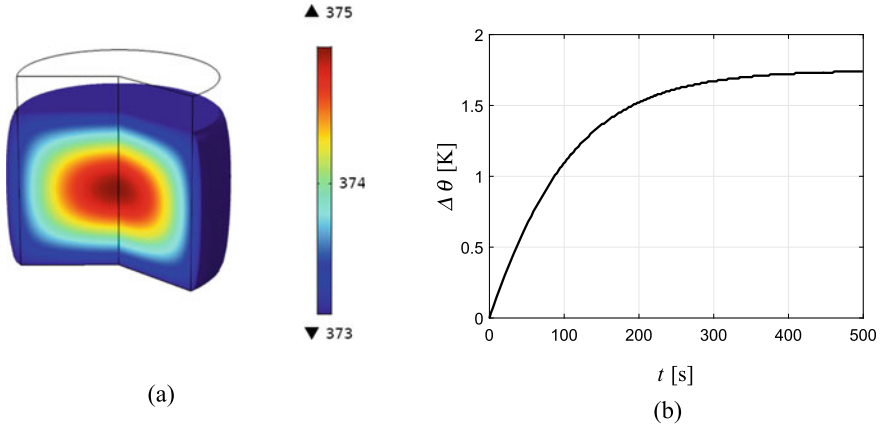


Fig. 2.2 **a** Temperature field θ in K and **b** transient development of self-heating

Kinematics

The deformation gradient tensor

$$\mathbf{F} = \text{Grad } \mathbf{u} + \mathbf{I} \quad (2.1)$$

comprises the gradient of the displacement field \mathbf{u} in the reference configuration and the identity tensor $\mathbf{I} = \delta_{ij} \mathbf{e}_i \otimes \mathbf{e}_j$. A multiplicative split of \mathbf{F} into the thermal part \mathbf{F}_θ , mechanical part \mathbf{F}_M , volumetric part $\bar{\mathbf{F}}$, isochoric part $\hat{\mathbf{F}}$, isochoric inelastic part $\hat{\mathbf{F}}_i$, and isochoric elastic part $\hat{\mathbf{F}}_e$ is carried out:

$$\mathbf{F} = \mathbf{F}_M \cdot \mathbf{F}_\theta \quad (2.2)$$

$$\mathbf{F}_\theta = (\alpha(\theta - \theta_0) + 1) \mathbf{I} = \varphi(\theta) \mathbf{I} \quad (2.3)$$

$$\mathbf{F}_M = \hat{\mathbf{F}} \cdot \bar{\mathbf{F}} \quad (2.4)$$

$$\hat{\mathbf{F}} = \hat{\mathbf{F}}_e \cdot \hat{\mathbf{F}}_i \quad (2.5)$$

$$\hat{\mathbf{F}} = J_M^{-1/3} \mathbf{F}_M \quad (2.6)$$

$$\bar{\mathbf{F}} = J_M^{1/3} \mathbf{I}$$

The determinant of the mechanical part is represented as

$$J_M = \det(\mathbf{F}_M) = \det(\mathbf{F}) \det(\mathbf{F}_\theta^{-1}) = J J_\theta^{-1} \quad (2.7)$$

Following deformation measures are defined:

Table 2.1 Parameters used for the simulation

λ_θ	0.3374	W/(m K)	Heat conduction coefficient
α	1.34e-4	1/K	Coefficient of thermal expansion
A	1.43e3	J/(kg K)	Caloric parameter
B	2.6092	J/(kg K ²)	Caloric parameter
R	8.314	J/(mol K)	Universal gas constant
$\lambda_{c,0}$	1.1e-10	m ² /s	Oxygen diffusion coefficient
γ_c	72.196	–	Oxygen diffusion parameter
λ_a	1.082	m ² /s	Antioxidant diffusion coefficient
E_k	1.0513e5	J/mol	Activation energy of oxygen reaction
k_{01}	2.776e7	1/s	Reaction rate of oxygen
k_{02}	2.136e10	1/s	Reaction rate of oxygen
k_a	2.702e-5	1/s	Reaction rate of antioxidant
μ_d	1.55546e6	Pa	Shear modulus of unaged network
K	1.5546e10	Pa	Bulk modulus
μ_r	567.3e6	Pa	Shear modulus of reformed network
v_d^1	5.396e6	1/s	Rate of network degradation
v_d^2	5.401e7	1/s	Rate of network degradation
E_d^1	8.973e4	J/mol	Activation energy of network degradation
E_d^2	1.036e5	J/mol	Activation energy of network degradation
v_r	8.745e4	1/s	Rate of network reformation
E_r	9.585e4	J/mol	Activation energy of network reformation
τ^1	0.0089	s	
τ^2	0.4753	s	
τ^3	7.4034	s	Relaxation times
μ_e^1	1.065e6	Pa	
μ_e^2	2.704e5	Pa	
μ_e^3	1.762e5	Pa	Elastic shear moduli
c_1^1	1.4053	–	
c_2^1	48.243	K	
c_1^2	0.2613	–	
c_2^2	7.3591	K	
c_1^3	0.1197	–	
c_2^3	4.1892	K	Parameters of the WLF-equation

$$\mathbf{C} := \mathbf{F}^T \cdot \mathbf{F} \quad (2.8)$$

$$\mathbf{C}_M := \mathbf{F}_M^T \cdot \mathbf{F}_M \quad (2.9)$$

$$\hat{\mathbf{C}} = J_M^{-2/3} \mathbf{C}_M \quad (2.10)$$

$$\hat{\mathbf{C}}_e := \hat{\mathbf{F}}_e^T \cdot \hat{\mathbf{F}}_e \quad (2.11)$$

Constitutive and Evolution Equations

The second Piola–Kirchhoff stress tensor \mathbf{S}

$$\begin{aligned} \mathbf{S} = & -p J \mathbf{C}^{-1} \\ & + J_M^{-2/3} \left[\mu_d(q_d) \left(\mathbf{I} - \frac{1}{3} \text{tr}(\hat{\mathbf{C}}) \hat{\mathbf{C}}^{-1} \right) \right. \\ & + \hat{\mathbf{T}}_r - \frac{1}{3} (\hat{\mathbf{T}}_r : \hat{\mathbf{C}}) \cdot \hat{\mathbf{C}}^{-1} \\ & \left. + \mu_e^k(\theta) \left((\hat{\mathbf{C}}_i^k)^{-1} - \frac{1}{3} \text{tr} \left((\hat{\mathbf{C}}_i^k)^{-1} \cdot \hat{\mathbf{C}} \right) \cdot \hat{\mathbf{C}}^{-1} \right) \right] \frac{1}{\varphi^2(\theta)} \end{aligned} \quad (2.12)$$

involves the hydrostatic pressure p

$$p = -\frac{K}{J_\theta} \left[(J_M - 1) + \frac{\ln J_M}{J_M} \right] \quad (2.13)$$

The reformative part of the stress tensor can be calculated via following rate formulation

$$\dot{\hat{\mathbf{T}}}_r = \frac{1}{2} q_r(t) \mathbf{D}_{\text{IV}}^4(t) : \dot{\hat{\mathbf{C}}} \quad (2.14)$$

The associated quantities of this equation are the four-order tensor

$$\mathbf{D}_{\text{IV}}^4 = J_M^{1/3} 4 \frac{\partial^2 w}{\partial \mathbf{C}_M^2} \quad (2.15)$$

with

$$\begin{aligned} \frac{\partial^2 w}{\partial \mathbf{C}_M^2} = & \frac{1}{2} \mu_r J_M^{-2/3} \frac{1}{3} \left[\text{tr}(\mathbf{C}_M) \left(\frac{1}{3} \mathbf{C}_M^{-1} \otimes \mathbf{C}_M^{-1} + (\mathbf{C}_M^{-1} \otimes \mathbf{C}_M^{-1})^{T_{23}} \right) \right. \\ & \left. - \mathbf{C}_M^{-1} \otimes \mathbf{I} - \mathbf{I} \otimes \mathbf{C}_M^{-1} \right] \end{aligned} \quad (2.16)$$

and the rate of the isochoric right Cauchy–Green deformation tensor

$$\dot{\hat{\mathbf{C}}} = J_M^{-2/3} \left(\dot{\mathbf{C}}_M - \frac{1}{3} \text{tr}(\mathbf{C}_M^{-1} \cdot \dot{\mathbf{C}}_M) \mathbf{C}_M \right) \quad (2.17)$$

Solving the evolution equation

$$\dot{\hat{\mathbf{C}}}_i^k = \frac{2}{\tau^k} \left(\hat{\mathbf{C}} - \frac{1}{3} \text{tr}(\hat{\mathbf{C}} \cdot (\hat{\mathbf{C}}_i^k)^{-1}) \hat{\mathbf{C}}_i^k \right) \quad (2.18)$$

leads to the inelastic isochoric right Cauchy–Green deformation tensor $\hat{\mathbf{C}}_1^k$. The elastic shear moduli

$$\mu_e^k(\theta) = \mu_e^k(\theta_0) \exp\left(-\frac{c_1(\theta - \theta_0)}{c_2 + \theta - \theta_0}\right) \quad (2.19)$$

follow a temperature dependence according to Williams et al. (1955). The evolution equations of ageing, i.e. the internal variable of network degradation q_d and network reformation q_r ,

$$\begin{aligned} \dot{q}_d &= v_d e^{-\frac{E_d}{R\theta}} (1 - q_d) c (1 - c_a), & q_d(0) &= 0 \\ \dot{q}_r &= v_r e^{-\frac{E_r}{R\theta}} (1 - q_r) c (1 - c_a), & q_r(0) &= 0 \end{aligned} \quad (2.20)$$

depend on the oxygen concentration c as well as on the antioxidant concentration c_a . The ageing-dependent shear modulus is given as

$$\mu_d(q_d) = \mu_d (1 - q_d) \quad (2.21)$$

The chemical part of the material model involves the reaction term of oxygen

$$\hat{c} = -k c \quad (2.22)$$

and the reaction term of antioxidant

$$\hat{c}_a = -k_a c c_a \quad (2.23)$$

Both the diffusion flux of oxygen

$$\mathbf{j}_0 = -\lambda_c J \mathbf{C}^{-1} \cdot \left(\text{Grad } c - \frac{c}{\theta} \text{Grad } \theta \right) \quad (2.24)$$

and of the antioxidant

$$\mathbf{j}_a^0 = -\lambda_a J \mathbf{C}^{-1} \cdot \left(\text{Grad } c_a - \frac{c_a}{\theta} \text{Grad } \theta \right) \quad (2.25)$$

are described in the reference configuration and are deformation dependent. An ageing-dependent reaction rate of oxygen

$$k = [k_{01}(1 - q_d) + k_{02}(1 - q_r)] e^{-\frac{E_k}{R\theta}} \quad (2.26)$$

as well as an ageing-dependent diffusion coefficient of oxygen

$$\lambda_c = \lambda_{c,0} e^{-\gamma_c q_r} \quad (2.27)$$

are considered. The heat flux of the reference configuration is given as

$$\mathbf{q}_0 = -\lambda_\theta J \mathbf{C}^{-1} \cdot \text{Grad } \theta \quad (2.28)$$

For the sake of completeness, the entropy rate

$$\dot{s} = \frac{1}{\rho_0} \left(\frac{1}{\theta} (A + B \theta) \dot{\theta} - \frac{1}{2} \frac{\partial^2 \mu_c^k(\theta)}{\partial \theta^2} \dot{\theta} \left(\text{tr}(\hat{\mathbf{C}}_c^k) - 3 \right) - \frac{1}{2} \frac{\partial \mu_c^k(\theta)}{\partial \theta} \frac{d}{dt} \text{tr}((\hat{\mathbf{C}}_i^k)^{-1} \cdot \hat{\mathbf{C}}) \right) \quad (2.29)$$

is presented

Governing Equations

The balance of linear momentum, the heat transfer equation and the diffusion-reaction equations are presented in their weak forms. Considering the quasi-static form of the balance of linear momentum in the reference configuration

$$\int_{\Omega} \tilde{\mathbf{S}} : \delta \mathbf{E} \, dV = \int_{\partial \Omega} \tilde{\mathbf{p}} \cdot \delta \mathbf{u} \, dA \quad (2.30)$$

the Total Lagrangian approach is used, with

$$\tilde{\mathbf{S}} = \mathbf{S} + (p - \tilde{p}) J \mathbf{C}^{-1} \quad (2.31)$$

Herein an auxiliary pressure variable \tilde{p} is introduced to avoid volumetric locking. The corresponding incompressibility constraint is given as

$$\int_{\Omega} \frac{1}{K} (p - \tilde{p}) \delta \tilde{p} \, dV = 0 \quad (2.32)$$

Equation (2.30) represents $\tilde{\mathbf{p}}$ the traction vector of the reference configuration. The temperature field θ is obtained solving the heat transfer equation in the form

$$\int_{\Omega} \mathbf{q}_0 \cdot \text{Grad } \delta \theta \, dV - \int_{\Omega} \left(\rho_0 \theta \dot{s} - \frac{1}{2} \mu_c^k(\theta) (\hat{\mathbf{C}}_i^k)^{-1} \cdot \hat{\mathbf{C}} \cdot (\hat{\mathbf{C}}_i^k)^{-1} : \dot{\hat{\mathbf{C}}}_i^k - \frac{1}{2} \mu_0 \left(\text{tr}(\hat{\mathbf{C}}) - 3 \right) \dot{q}_d \right) \delta \theta \, dV = \int_{\partial \Omega} (\mathbf{q}_0 \cdot \mathbf{n}) \delta \theta \, dA \quad (2.33)$$

The diffusion-reaction equation of oxygen

$$\int_{\Omega} \mathbf{j}_0 \cdot \text{Grad } \delta c \, dV - \int_{\Omega} (\dot{c} - \hat{c} - \hat{c}_a) \delta c \, dV = \int_{\partial\Omega} (\mathbf{j}_0 \cdot \mathbf{n}) \delta c \, dA \quad (2.34)$$

and the diffusion-reaction equation of antioxidant

$$\int_{\Omega} \mathbf{j}_a^0 \cdot \text{Grad } \delta c_a \, dV - \int_{\Omega} (\dot{c}_a - \hat{c}_a) \delta c_a \, dV = \int_{\partial\Omega} (\mathbf{j}_a^0 \cdot \mathbf{n}) \delta c_a \, dA \quad (2.35)$$

have been formulated as well and are solved for the fields c and c_a . On the right hand side of Eqs. (2.33)–(2.35) is \mathbf{n} the outward normal surface vector.

2.2.2 Results and Discussion

Regarding the simulation, a finite element model is built in axial-symmetric modus, which is shown in Fig. 2.1. At the lower edge of the component, a fixed constraint is prescribed by $u_1^* = 0$ and $u_2^* = 0$. At the upper edge of the component, $u_1^* = 0$ is valid. In addition, through the Dirichlet boundary condition,

$$u_2^*(t) = u_{20} + \hat{u}_2 \sin(2\pi ft) \quad (2.36)$$

as an oscillating load is applied. Here, the static compressive strain ε_{20} has a value of 20% with a strain amplitude $\hat{\varepsilon}_2$ of 2%. The corresponding displacement values can be calculated using the formula $u = \varepsilon l_0$, where l_0 is the component height. The frequency f was chosen equal 10 Hz. The Dirichlet thermal boundary conditions are prescribed on the upper and lower edges of the component, where direct contact with the metal segment of temperature $\theta^* = 373$ K occurs. Convective boundary conditions are considered on the side surface of the component and are calculated using equation

$$q^* = -\mathbf{n} \cdot \mathbf{q}_0 = -h(\theta - \theta^*) \quad (2.37)$$

Thus, free convection between the elastomer surface and the ambient air is assumed, whereas the associated heat transfer coefficient h in this simulation was chosen according to the study of Sae-Oui et al. (1999). The temperature of the ambient air is also $\theta^* = 373$ K. Since oxygen can diffuse only in the radial direction of the component, a dimensionless oxygen concentration $c^* = 1$ is specified at the lateral surface. Adiabatic boundary conditions of oxygen diffusion at the upper and lower edges of the component represent the barrier of the metal segment.

Initial values of oxygen and antioxidant concentrations are specified for the component as $c = 0$ and $c_a = 1$. This corresponds to an oxygen-unsaturated initial state, with antioxidants present in the material. In addition, adiabatic boundary conditions

are considered for antioxidants, so that no escape or evaporation of antioxidants from the material can occur. The initial temperature of the component is 293 K.

This example is intended to represent a silent block in the engine compartment. First, a static compressive load is applied using u_{20} , followed by a simulation of thermo-oxidative ageing for a duration of $t = 168$ h at 373 K. Thus, a specific ageing state of the mechanically deformed component is achieved. Then, an additional varying mechanical load is applied for a duration of $t = 500$ s, representing engine vibration.

Due to the given dynamic loading, a self-heating of the silent block can be seen, as presented in Fig. 2.2. The transient development of the absolute temperature exhibits a qualitatively similar nonlinear behaviour, as was experimentally determined in Sect. 2.3 (see Fig. 2.8). A dissipative heating of about 2 K can be observed inside the component. The calculated oxygen concentration shown in Fig. 2.3 indicates the DLO effect, which is formed during the ageing of the silent block due to its dimensions. The oxygen concentration profiles along the component radius from Fig. 2.4 represent the evolution of this effect over the ageing time. An increasing oxygen reaction takes place at the edge of the elastomer and reduced oxidation in the interior since the atmospheric oxygen is consumed more quickly at the edges and only the unreacted oxygen is available for further supply by diffusion transport. This

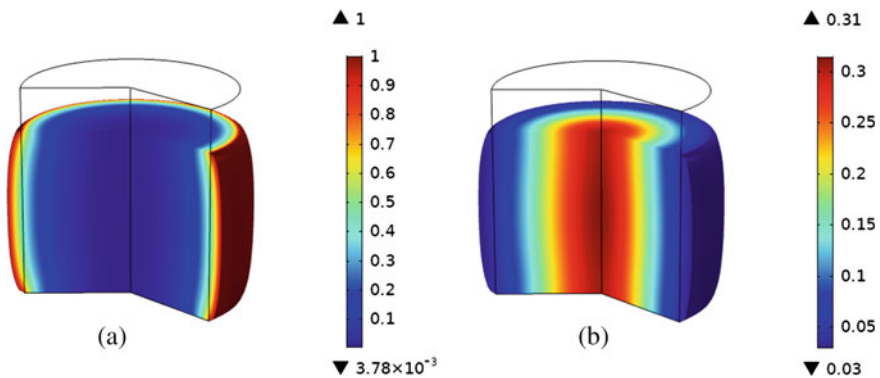
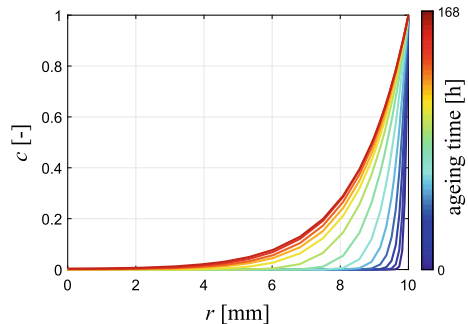


Fig. 2.3 **a** Dimensionless oxygen concentration field c ; **b** dimensionless antioxidant concentration field c_a

Fig. 2.4 Oxygen concentration profiles over ageing time



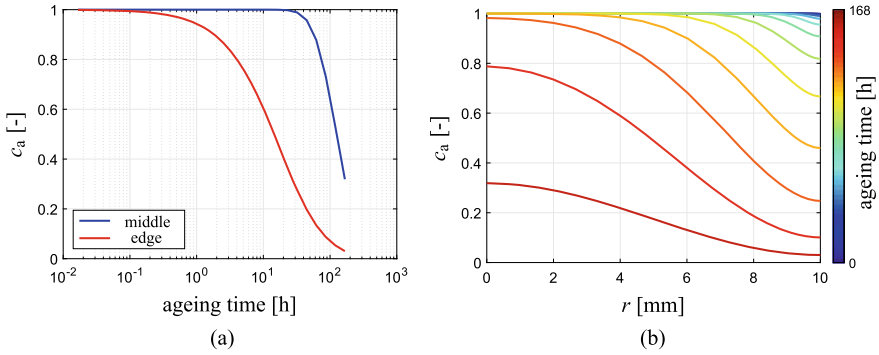
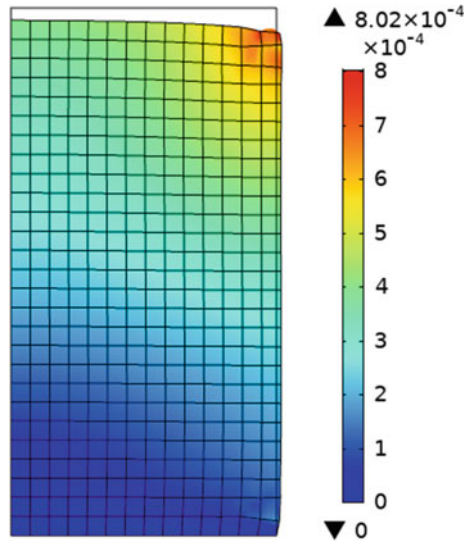


Fig. 2.5 **a** Transient development of the antioxidant concentration; **b** antioxidant concentration profiles over ageing time

Fig. 2.6 Displacement field u [m] of the aged rubber buffer after unloading



effect is of course both dimension and deformation dependent. The ageing-dependent diffusivity also plays a role, as diffusion is slowed down locally.

Heterogeneous oxidation also affects the calculated antioxidant concentration field from Fig. 2.3. As presented in Fig. 2.5, rapid consumption of antioxidants occurs at the component edge, where the greatest oxidation occurs. However, despite the low oxidation inside the component, the antioxidant concentration is also reduced here. This can be explained by the fact that diffusion processes supply the antioxidants to the edge region, where they are subsequently consumed, i.e. they react with oxygen. From a concentration profile of the antioxidants that is constant with respect to the unaged state, a resulting antioxidant distribution is obtained during ageing, as shown in Fig. 2.5 along the component radius for different ageing times. Both the result-

ing oxygen and the antioxidant concentration influence the structural-mechanical behaviour of the rubber component, which is shown in the final simulation step.

Thus, a compression set is calculated. The determination of compression set is often used in seal production and design. For this purpose, the rubber buffer is cooled down to its initial temperature and unloaded. The heterogeneous ageing causes a locally different irreversible change of the elastomer network and leads to locally different stiffness values. As shown in the simulation in Fig. 2.6, the shape of the rubber buffer after unloading depends on this heterogeneity and a permanent deformation can be observed. In addition, the component has lost its original cylindrical geometry and shows greater deformation at the more aged edge of the component.

2.3 Experimental Investigation on Self-heating in Connection with Ageing of a Rubber Buffer

To investigate the influences of thermo-oxidative ageing on dissipative heating, tensile specimens are first stress-free aged in the air at temperatures of 353 K, 373 K and 393 K for two days and one week, respectively. Then the ageing was interrupted and the samples were cooled down to room temperature. Subsequently, the aged specimens are clamped in the DMA testing machine and subjected to the following loads at room temperature: static pre-deformation of 10% and sinusoidal excitation with a dynamic amplitude of 2% and a frequency 25 Hz. Additional ageing during the dynamic test cannot be excluded due to the resulting self-heating of the specimens.

After a certain time, a stationary temperature field is established on the sample surface, which is recorded using a thermal imaging camera. An example is shown in Fig. 2.7. An inhomogeneous temperature field can be observed, where the marked

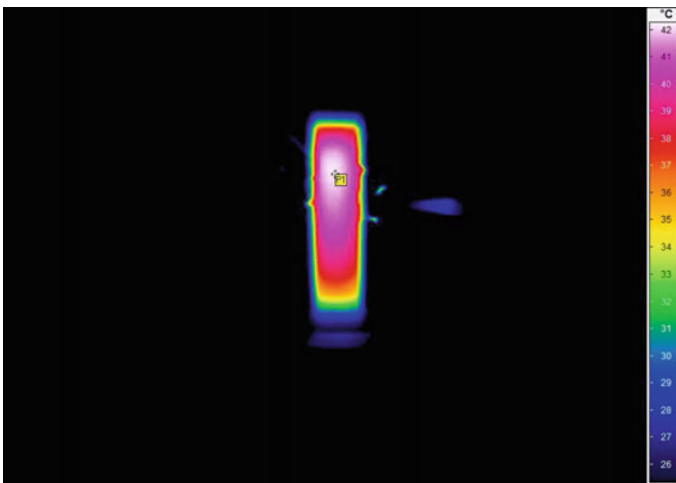


Fig. 2.7 Temperature field due to self-heating during dynamic loading of a rubber sample

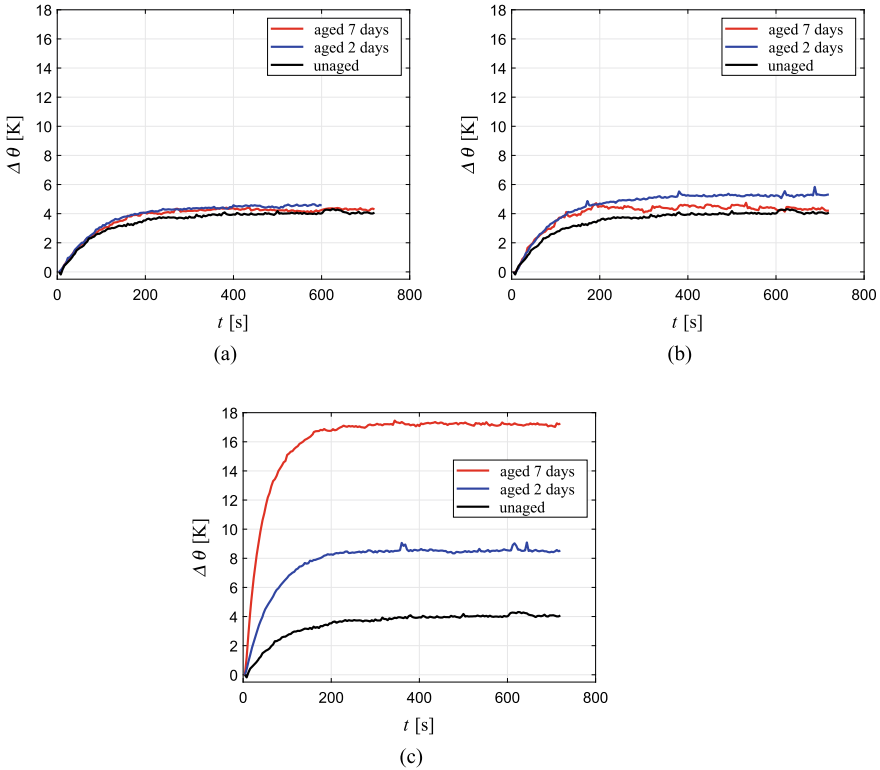


Fig. 2.8 Transient evolution of self-heating of rubber samples pre-aged at **a** 353 K, **b** 373 K, and **c** 393 K

point represents the hottest point of the sample surface. Since the upper edge of the sample is fixed and the excitation occurs only through the lower clamping, turbulent air flows are formed especially in the lower sample region, whereby enhanced convection explains the lower temperatures of the lower sample region. In Fig. 2.8, transient temperature curves at the point of maximum temperature are plotted for differently aged samples. All curves show qualitatively similar transient nonlinear behaviour, with a steady-state occurring after about 200 s. As long as the material has not been distinctly aged, the influences on the dissipative heating do not become particularly significant. However, the more pronounced ageing of the material causes an increasing self-heating under dynamic stress, which is clearly shown in Fig. 2.8c. In this case, a 3.5-fold self-heating was observed compared to the unaged material. This phenomenon shows that the influence of ageing on the viscoelastic material properties cannot be neglected in the case of dynamic loading.

2.4 Conclusion

In this paper, the challenges of heterogeneous thermo-oxidative ageing were introduced and described. Using the example of a rubber buffer under operating loads, the complicated phenomena of heterogeneous ageing were simulated and discussed, taking into account the self-heating of the component. Particular attention was drawn to the formation of the DLO effect in connection with the influence of antioxidants. One type of heterogeneous ageing can also be caused due to a heterogeneous temperature field. As the experimental results of this paper show, the influence of the material changed by ageing on the dissipation properties (viscoelasticity) also plays a relevant role. In the aged zones, there is an increasing self-heating, ergo the material modelling in future should include the influence of ageing on the viscoelastic stiffnesses, in case of modelling cyclically loaded rubber components. For industrial applications, the modelling concept presented in this paper can be used to simulate the heterogeneous thermo-oxidative (chemo-thermo-mechanical) ageing of technical elastomers, taking into account the DLO effect as well as the finite viscoelasticity, which also allows the influence on the material properties to be represented in time, which can be of decisive importance for a service life prediction of the rubber components.

References

- Dippel B (2015) Experimentelle Charakterisierung, Modellierung und FE-Berechnung thermo-mechanischer Kopplungen am Beispiel eines rußgefüllten Naturkautschuks. Ph.D. thesis, Universität der Bundeswehr München
- Duarte J, Achenbach M (2007) On the modelling of rubber ageing and performance changes in rubbery components. *Kaut Gummi Kunstst* 60:172–175
- Ehrenstein G, Pongratz S (2007) *Beständigkeit von Kunststoffen*. Carl Hanser Verlag
- Johlitz M, Diercks N, Lion A (2014) Thermo-oxidative aging of elastomers: a modelling approach based on a finite strain theory. *Int J Plast* 63:138–151
- Johlitz M, Dippel B, Lion A (2016) Dissipative heating of elastomers: a new modelling approach based on finite and coupled thermomechanics. *Contin Mech Thermodyn* 28:1111–1125
- Kömmeling A, Jaunich M, Wolff D (2016) Effects of heterogeneous aging in compressed HNBR and EPDM O-ring seals. *Polym Degrad Stab* 126:39–46
- Musil B (2020) Ein Beitrag zur experimentell gestützten Modellierung der chemothermomechanischen Alterung von Nitrilkautschuk. Ph.D. thesis, Universitätsbibliothek der Universität der Bundeswehr München
- Musil B, Johlitz M, Lion A (2018) On the ageing behaviour of NBR: chemomechanical experiments, modelling and simulation of tension set. *Contin Mech Thermodyn*. <https://doi.org/10.1007/s00161-018-0728-5>
- Musil B, Böhning M, Johlitz M, Lion A (2019) On the inhomogeneous chemo-mechanical ageing behaviour of nitrile rubber: experimental investigations, modelling and parameter identification. *Contin Mech Thermodyn* 32:127–146
- Rodas CO, Zaïri F, Naït-Abdelaziz M (2014) A finite strain thermo-viscoelastic constitutive model to describe the self-heating in elastomeric materials during low-cycle fatigue. *J Mech Phys Solids* 64:396–410
- Sae-Oui P, Freakley P, Oubridge P (1999) Determination of heat transfer coefficient of rubber to air. *Plast Rubber Compos* 28:65–68

- Shaw J, Jones S, Wineman A (2005) Chemorheological response of elastomers at elevated temperatures: experiments and simulations. *J Mech Phys Solids* 53:2758–2793
- Steinke L (2013) Ein Beitrag zur Simulation der thermo-oxidativen Alterung von Elastomeren. VDI-Verlag
- Van Amerongen GJ (1946) The permeability of different rubbers to gases and its relation to diffusivity and solubility. *J Appl Phys* 17:972–985
- Verdu J (2012) Oxydative ageing of polymers. Wiley
- Williams ML, Landel RF, Ferry JD (1955) The temperature dependence of relaxation mechanisms in amorphous polymers and other glass-forming liquids. *J Am Chem Soc* 77:3701–3707

Chapter 3

Digital Product Development by Additive Manufacturing



Markus Merkel , Mario Rupp, and Michael Sedlmajer

Abstract Engineers' work is often linked with the development and production of technical products. In order to improve products and processes, digitalization is more and more applied to each process phase. This upcoming paradigm also is called Industry 4.0. While some disciplines (e.g., design, engineering, quality assurance) successfully implemented digital tools into their daily work, the manufacturing phase was limited by the need for part specific tools. Additive manufacturing (AM) as one of the key enablers of Industry 4.0 is closing this analogous gap. At a very abstract level, the essential ingredients to provide technical products can be reduced to raw material, energy and data. Here, the laser beam powder bed fusion (L-PBF) is taken as process to discuss chances and challenges for the digital manufacturing of metal parts.

Keywords 3D printing · Virtual product development · Engineering applications

3.1 Introduction

Starting from the idea for a new product, the process to realization is described by several disciplines. For a simplified approach, the full digital process is structured by only a few disciplines (see Fig. 3.1). Typically, within design and engineering, the shape and properties of a technical product are defined and optimized due to customers' demand. Here, manufacturing is represented by the L-PBF process as a typical additive process to print metal. Other disciplines (e.g., quality assurance) complete the process chain.

M. Merkel (✉) · M. Rupp · M. Sedlmajer
Institute for Virtual Product Development, Aalen University of Applied Sciences, Beethovenstr. 1,
73430 Aalen, Germany
e-mail: Markus.Merkel@hs-aalen.de

M. Rupp
e-mail: Mario.Rupp@hs-aalen.de

M. Sedlmajer
e-mail: Michael.Sedlmajer@hs-aalen.de

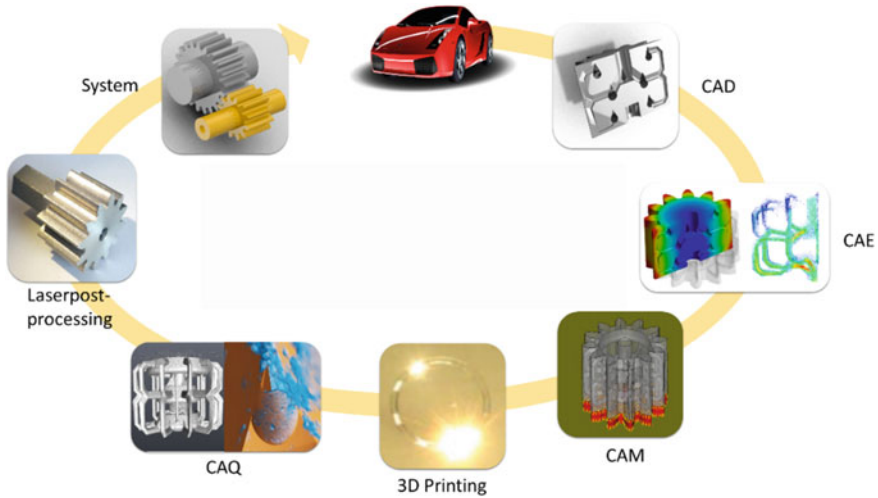


Fig. 3.1 Digital process to realize technical products

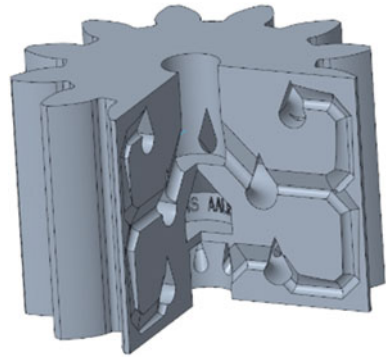
For real engineering applications, the disciplines do not act independently as standalone blocks, and there are overlaps and interactions. Especially, additive manufacturing as an overall philosophy has a strong impact on the geometry and on the properties of a product (Hitzler et al. 2018). Moreover, the additive process has a big impact on technological and economical aspects along the supply chain. Additive manufacturing as a cyber-physical system directly connects the digital CAD data with the physical product and accelerates digitization (Rupp et al. 2021).

With its very agile supply and process chain, costs can be reduced especially for low batch sizes, highly complex geometries and decentralized spare parts (Rupp and Merkel 2021). Additionally, through the layer-wise manufacturing, raw material input and carbon emissions are reduced which leads to a more resource-efficient and sustainable production (Rupp et al. 2022).

3.2 AM-Process Within Digital Product Development and Manufacturing

At the beginning, a strong advantage of additive manufacturing (AM) should be mentioned. The outer as well as the inner contour of a part (CAD) can be defined without any restrictions caused by tooling, e.g., casting enforces special angles to vertical planes or special limits to wall thicknesses (Tomas et al. 2020) and influences the surface quality (Hitzler et al. 2017a). Due to the free definition of geometry, functionalities can be realized within a smaller volume and with more efficiency. Typical examples are porous structures (Ocker et al. 2021a), cooling channels close

Fig. 3.2 Gear wheel with channels for cooling and lubrication: CAD-model



to heated surfaces or arbitrary curved pipes transporting fluids with optimized flow conditions, see Fig. 3.2.

Within engineering (CAE), numerical simulation is used to analyze physical properties, see Fig. 3.3. Multi-objective optimization allows to adapt customer's demands to dimensions of geometric entities like cross-sections of pipes or channels, the volume of cavities or the distribution of mass (Ocker et al. 2021b). Anisotropic material behavior can be enabled by a well-defined AM-process and can be taken into account to further improve material properties for high-precision applications (Hitzler et al. 2017b; Mindermann et al. 2022). Further, high-tech materials as Invar36 are used to expand the field of application of the components (Heine et al. 2022).

The AM-process itself will be discussed later. The quality assurance of additively manufactured parts is also supported by digital tools, e.g., geometric accuracy can be checked by computed tomography (CT), see Fig. 3.4.

An AM-process (CAM) depends on the material (metal, ceramics, plastics) and machines being used. Generally, the process is split into three phases and will be discussed in detail for laser powder bed fused, see Fig. 3.5.

Fig. 3.3 Gear wheel with contour plot of temperature profile (left) and velocities of fluid flow (right)

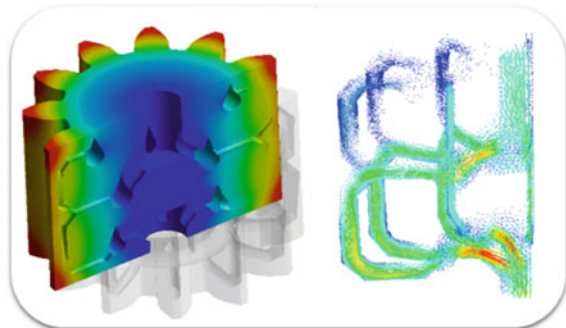


Fig. 3.4 Gear wheel: CT of channels

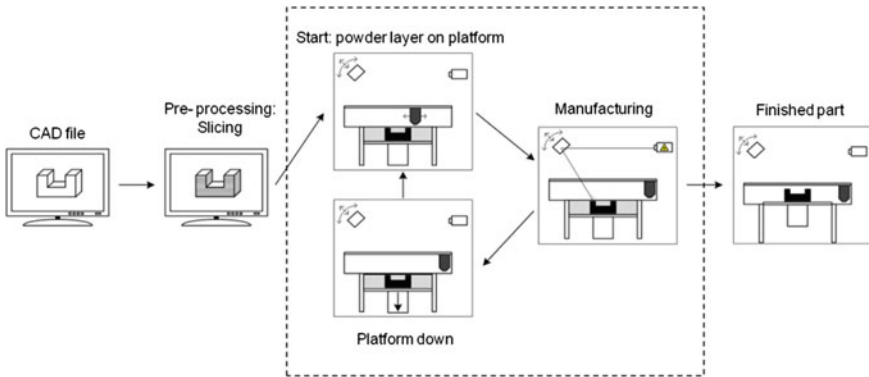
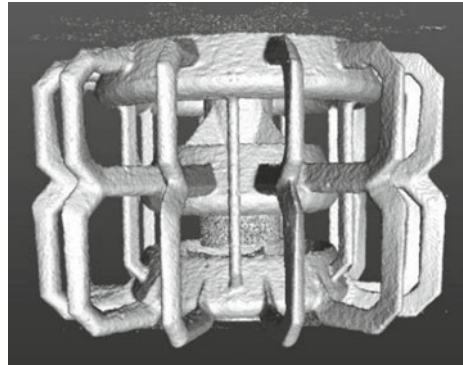


Fig. 3.5 Laser beam powder bed fusion: preprocess, main process and post-process

Within preprocessing the geometry, which is often represented as a 3D-CAD-model, is prepared for layer-wise additive manufacturing. The slicing technique virtually cuts the part in subsequent horizontal slices having the thickness of processed layers. The preprocess covers also the definition of the support structures, see Fig. 3.6.

The main AM-process runs as a loop starting with powder that is continuously distributed over a platform with a constant thickness. In a second step, a laser scans

Fig. 3.6 Gear wheel with support structures: CAD-model

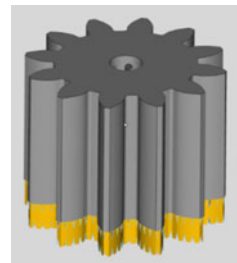
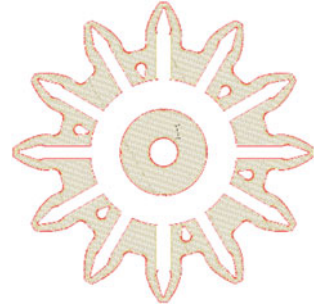


Fig. 3.7 Scanned contours and segments within one layer



the contours and segments of the geometric entities and powder is heated up to local melting, see Fig. 3.7. Typical scanning speeds range from millimeters to meters per second. Depending on the size of the platform, a scan of a layer takes to some minutes and is finalized by a downwards move of the platform.

The process chamber has a cubic or cylindrical volume with ground area of 280 mm × 280 mm or a diameter of 200 mm and a height of 300 mm. The main features are the entry of the laser at the top, which is sometimes completed by a second entry for a camera. The building platform is located at the bottom and the inlet and outlet for the gas flow at the right resp. left side, see front view in Fig. 3.8.

Before the laser scanning starts, a rake guarantees a regular powder bed moving from back to front or vice versa while powder flows out the recoater on the building platform. The gas, argon or nitrogen, is heated while moving from the right to the left side. A weak flow is not able to transport welding splash, a strong flow destroys the regular powder layer, see top view in Fig. 3.9.

A standard platform is heated up to 200 °C or even lower temperature levels at many machines. Knowing that the temperature gradient has a strong influence on the properties of the processed material, the temperature level of the building



Fig. 3.8 Front view to building chamber

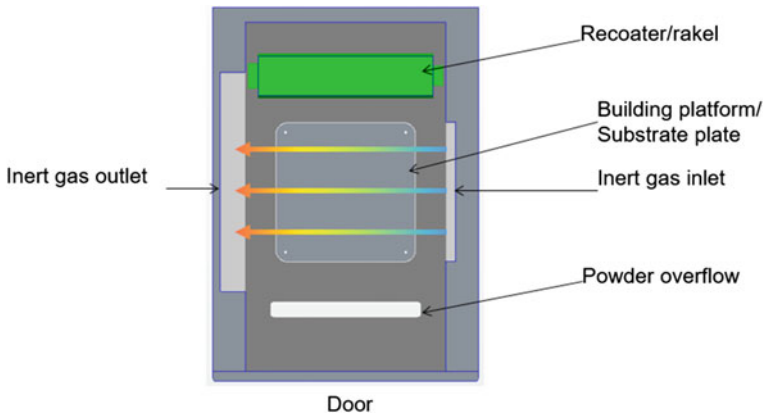


Fig. 3.9 Top view into building chamber, schema

chamber could be adapted to the material in use (Körperich and Merkel 2018). In order to reduce residual stresses, a lower temperature gradient can be achieved by a superheated chamber. This causes structural reorganization of the complete machine, additional insulation is needed, see Fig. 3.10 as a schema in a) and implemented in a SLM-machine in b).

With a superheated chamber, new materials such as tungsten carbide can also be produced in a quasi-melting process (Tomas et al. 2018; Köhn et al. 2021).

The further discussion of the main AM-process is here reduced to counting layers for a simplified example: To print a part with a height of 100 mm by layers with a thickness of 50 μm 2000 loops have to be applied. Afterward, the post-process starts, and parts are still fixed to the platform by support structures and are partially covered by powder, see Fig. 3.11.

As a first step within post-processing, the building platform has to be taken out of the machine, and remaining powder has to be removed and is recycled by separated sieving with a recycling rate up to nearly 100%. The most time consumption is



Fig. 3.10 Heated building chamber a schema b photo of front view

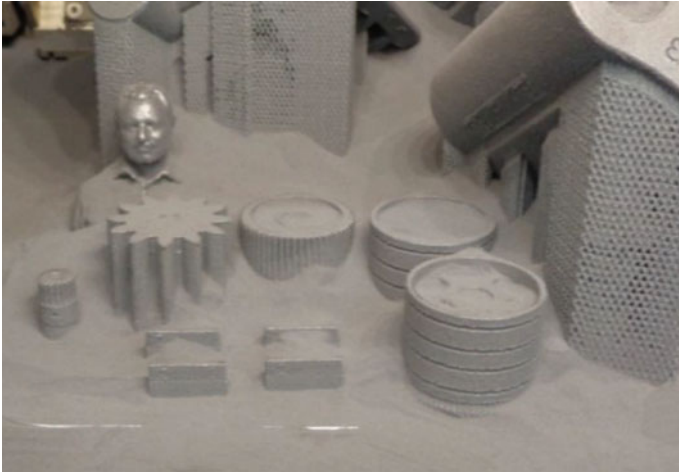


Fig. 3.11 AM-parts fixed on a building platform covered with powder

addressed to removing support structures. While the process is easy, fast and cheap for plastics metal supports enforce special care. In a first step, AM-parts together with supports are separated from the building platform, see Fig. 3.12 left. In a second step, the support structures have to be removed from the AM-parts, see Fig. 3.12 right. Removing support structures for a single part or small batches is often realized by a manual process. Large batches address the need for an automated or at least for a semi-automated process.

AM-products and AM-processes will benefit from detailed investigation of each single step as well from a holistic approach.



Fig. 3.12 Removing support structures: from platform (left) from AM-part (right)

References

- Heine B, Kah A, Sedlmajer M, Ocker C, Merkel M (2022) Impact of corrosion on mechanical properties of additively manufactured Invar 36. *Materialwiss Werkst* 53(3):316–327
- Hitzler L, Hirsch J, Merkel M, Hall W, Öchsner A (2017a) Position dependent surface quality in Selective Laser Melting. *Materialwiss Werkst* 48(5):327–334
- Hitzler L, Merkel M, Hall W, Öchsner A (2018) A review of metal fabricated with powder-bed based additive manufacturing techniques: process, nomenclature, materials, achievable properties, and its utilization in the medical sector. *Adv Eng Mater* 20(5):1–28
- Hitzler L, Hirsch J, Heine B, Merkel M, Hall W, Öchsner A (2017b) On the Anisotropic Mechanical Properties of Selective Laser-Melted Stainless Steel. *Materials* 10(10):1136–1155
- Köhn F, Sedlmajer M, Albrecht J, Merkel M (2021) Additive manufacturing of tungsten carbide surfaces with extreme wear resistivity. *Coatings* 11(10):1240
- Körperich JP, Merkel M (2018) Thermographic analysis of the building height impact on the properties of tool steel in selective laser beam melting. *Materialwiss Werkst* 49(5):689–695
- Liebisch A, Merkel M (2016) On the numerical simulation of the thermal behavior during the selective laser melting process. *Materialwiss Werkst* 47(5–6):521–529
- Mindermann P, Müllner R, Dieringer E, Ocker C, Klink R, Merkel M, Gresser GT (2022) Design of fiber-composite/metal-hybrid structures made by multi-stage coreless filament winding. *Appl Sci* 12(5):2296
- Ocker C, Geyer TF, Czwiolong F, Krömer F, Pannert W, Merkel M, Becker S (2021b) Permeable leading edges for airfoil and fan noise reduction in disturbed inflow. *AIAA J* 59(12):4969–4986
- Ocker C, Czwiolong F, Geyer T F, Paruchuri C, Merkel M, Becker S (2021a) Permeable structures for leading edge noise reduction. *AIAA AVIATION 2021a FORUM: AIAA 2021a–2192*
- Rupp M, Buck M, Klink R, Merkel M, Harrison DK (2022) Additive manufacturing of steel for digital spare parts—A perspective on carbon emissions for decentral production. *J Clean Prod* 4:100069
- Rupp M, Merkel M (2021) Direct digital manufacturing—The role of cost accounting for online hubs to access industry 4.0. *Int Sci J Ind* 4.0 6:102–105
- Rupp M, Schneckenburger M, Merkel M et al (2021) Industry 4.0: a Technological-oriented definition based on bibliometric analysis and literature review. *J Open Innov Technol Mark Complex* 7(1):68
- Tomas J, Hitzler L, Köller M, von Kobylinski J, Sedlmajer M, Werner E, Merkel M (2020) The dimensional accuracy of thin-walled parts manufactured by laser-powder bed fusion. *J Manuf Mater Process* 4(3):91–103
- Tomas J, Schubert T, Bernthaler T, Merkel M, Schneider G, Sellmer D (2018) Laser sintering of tungsten carbide cutter shafts with integrated cooling channels. In: *Proceedings of the 3rd international conferences on progress in additive manufacturing* pp 297–302

Chapter 4

Theory of Three-Dimensional Plasticity



Andreas Öchsner

Abstract This chapter presents a summary of the classical three-dimensional plasticity theory for rate-independent material behavior. The continuum modeling of plastic material behavior in relation to the constitutive equation comprises a yield condition, a flow rule, and a hardening rule. A special emphasis is given on the representation of yield conditions in the so-called invariant space. As typical examples in the context of classical plasticity theory, the conditions according to von Mises, Tresca, and Drucker-Prager are discussed in detail.

4.1 Comments on the Stress Matrix

Let us consider a three-dimensional body which is sufficiently supported and loaded (i.e., by any point or distributed loads) as schematically shown in Fig. 4.1a. Considering the symmetry of the stress matrix, six independent stress components, i.e., three normal and three shear stresses, can be identified, see Fig. 4.1b.

The stress components acting on a differential volume element may have, for example, the values as shown in Eq. (4.1) for the given (x, y, z) coordinate system. A coordinate transformation from the original (x, y, z) to the (x', y', z') coordinate system results in a stress matrix with different stress components, while a principal axis transformation (PAT) calculates the principal stresses σ_i , $(i = 1, 2, 3)$.

$$\sigma_{ij} = \begin{bmatrix} 50 & 0 & 20 \\ 0 & 80 & 20 \\ 20 & 20 & 90 \end{bmatrix}_{(x,y,z)} \xrightarrow{\text{rotation}} \begin{bmatrix} 65 & 15 & 28.28 \\ 15 & 65 & 0 \\ 28.28 & 27 & 90 \end{bmatrix}_{(x',y',z')} \xrightarrow{\text{PAT}} \begin{bmatrix} 110 & 0 & 0 \\ 0 & 70 & 0 \\ 0 & 0 & 40 \end{bmatrix}_{(1,2,3)} \quad (4.1)$$

A. Öchsner (✉)
 Faculty of Mechanical and Systems Engineering, Esslingen University of Applied Sciences,
 Kanalstrasse 33, 73728 Esslingen, Germany
 e-mail: andreas.oechsner@hs-esslingen.de

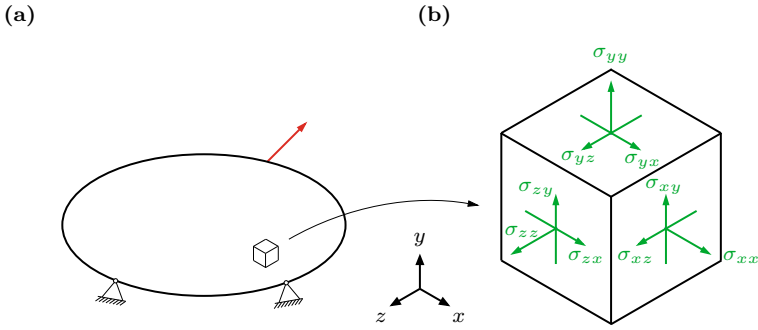


Fig. 4.1 **a** Three-dimensional body under arbitrary load and boundary conditions; **b** infinitesimal volume element with acting normal and shear stress components [see Altenbach and Öchsner (2020)]

Looking at this simple example, the following characteristics of the stress matrix can be summarized:

- The components of the stress matrix depend on the orientation of the user-defined coordinate system.
- There is a specific coordinate system (1, 2, 3) where the shear stresses vanish and only normal stresses remain on the main diagonal, i.e., the so-called principal stresses σ_i ($i = 1, 2, 3$).
- The six or three stress components cannot easily be compared to experimental values from uniaxial tests (e.g., the initial yield stress in tension k_t^{init}).
- A graphical representation of any surface is much easier in a principal stress space (1, 2, 3) with three coordinates than in a space with six coordinates (σ_i).

Further information on continuum mechanics and plasticity theory can be taken from the classical textbooks by Backhaus (1983), Chen and Han (1988), Altenbach (2012), Altenbach et al. (1995), Betten (1987), Itskov (2009), and Itskov and Belyaev (2005). Let us review in the following the determination of the principal stresses and the axes directions of the corresponding (1, 2, 3) coordinate system. From a mathematical point of view, this question can be answered by determining the eigenvalues of the stress matrix (principal stresses) and the corresponding eigenvectors (principal directions). The solution of the so-called *characteristic equation*, i.e.,

$$\det(\sigma_{ij} - \sigma_i \mathbf{1}) = 0, \quad (4.2)$$

gives the three principal stresses σ_i ($i = 1, 2, 3$). Equation (4.2) can be written in components as:

$$\det \left(\begin{bmatrix} \sigma_{xx} & \sigma_{xy} & \sigma_{xz} \\ \sigma_{yx} & \sigma_{yy} & \sigma_{yz} \\ \sigma_{zx} & \sigma_{zy} & \sigma_{zz} \end{bmatrix} - \sigma_i \begin{bmatrix} 1 & 0 & 0 \\ 0 & 1 & 0 \\ 0 & 0 & 1 \end{bmatrix} \right) = \det \left(\begin{bmatrix} \sigma_{xx} - \sigma_i & \sigma_{xy} & \sigma_{xz} \\ \sigma_{yx} & \sigma_{yy} - \sigma_i & \sigma_{yz} \\ \sigma_{zx} & \sigma_{zy} & \sigma_{zz} - \sigma_i \end{bmatrix} \right) = 0. \quad (4.3)$$

The calculation of the determinant ('det') results in the following cubic equation in σ_i :

$$\begin{aligned} & \sigma_i^3 - \underbrace{(\sigma_{xx} + \sigma_{yy} + \sigma_{zz})}_{I_1} \sigma_i^2 \\ & + \underbrace{(\sigma_{xx}\sigma_{yy} + \sigma_{xx}\sigma_{zz} + \sigma_{yy}\sigma_{zz} - \sigma_{xy}^2 - \sigma_{xz}^2 - \sigma_{yz}^2)}_{I_2} \sigma_i \\ & - \underbrace{(\sigma_{xx}\sigma_{yy}\sigma_{zz} - \sigma_{xx}\sigma_{yz}^2 - \sigma_{yy}\sigma_{xz}^2 - \sigma_{zz}\sigma_{xy}^2 + 2\sigma_{xy}\sigma_{xz}\sigma_{yz})}_{I_3} = 0, \end{aligned} \quad (4.4)$$

or in short:

$$\sigma_i^3 - I_1\sigma_i^2 + I_2\sigma_i - I_3 = 0, \quad (4.5)$$

where the three roots ($\sigma_1, \sigma_2, \sigma_3$) of Eq. (4.5) are the principal stresses. Equation (4.4) can be used to define the three scalar so-called principal invariants I_1, I_2 , and I_3 . These tensor invariants are independent of the orientation of the coordinate system (objectivity) and represent the physical content of the stress matrix.

The coordinates of the i th eigenvector (x_i, y_i, z_i)—which correspond to the direction of one of the new (1, 2, 3) coordinate axes—result from the following system of three equations:

$$\begin{bmatrix} \sigma_{xx} - \sigma_i & \sigma_{xy} & \sigma_{xz} \\ \sigma_{yx} & \sigma_{yy} - \sigma_i & \sigma_{yz} \\ \sigma_{zx} & \sigma_{zy} & \sigma_{zz} - \sigma_i \end{bmatrix} \begin{bmatrix} x_i \\ y_i \\ z_i \end{bmatrix} = \begin{bmatrix} 0 \\ 0 \\ 0 \end{bmatrix}. \quad (4.6)$$

Let us mention at this point that the determination of the eigenvalues and eigenvectors is also common in applied mechanics for other tensors or matrices. The second moment of the area tensor (or the moment of inertia tensor) has similar properties as the stress matrix:

$$\begin{bmatrix} I_{xx} & I_{xy} & I_{xz} \\ I_{yx} & I_{yy} & I_{yz} \\ I_{zx} & I_{zy} & I_{zz} \end{bmatrix}_{(x,y,z)} \xrightarrow{\text{PAT}} \begin{bmatrix} I_1 & 0 & 0 \\ 0 & I_2 & 0 \\ 0 & 0 & I_3 \end{bmatrix}_{(1,2,3)}. \quad (4.7)$$

Let us look in the following a bit closer at the stress invariants¹. Another interpretation of the *principal* stress invariants is given by Chen and Han (1988):

¹ It is useful for some applications (e.g., the calculation of the derivative with respect to the stresses) to *not* consider the symmetry of the shear stress components and to work with nine stress components. These invariants are denoted by \underline{I}_i and \underline{J}_i .

Table 4.1 Definition of the three principal (I_i) and basic (J_i) stress invariants of the stress matrix

First stress invariant of σ_{ij}
$I_1 = \sigma_{xx} + \sigma_{yy} + \sigma_{zz}$
$J_1 = \sigma_{xx} + \sigma_{yy} + \sigma_{zz}$
Second stress invariant of σ_{ij}
$I_2 = \sigma_{xx}\sigma_{yy} + \sigma_{xx}\sigma_{zz} + \sigma_{yy}\sigma_{zz} - \sigma_{xy}^2 - \sigma_{xz}^2 - \sigma_{yz}^2$
$J_2 = \frac{1}{2}(\sigma_{xx}^2 + \sigma_{yy}^2 + \sigma_{zz}^2) + \sigma_{xy}^2 + \sigma_{xz}^2 + \sigma_{yz}^2$
Third stress invariant of σ_{ij}
$I_3 = \sigma_{xx}\sigma_{yy}\sigma_{zz} - \sigma_{xx}\sigma_{yz}^2 - \sigma_{yy}\sigma_{xz}^2 - \sigma_{zz}\sigma_{xy}^2 + 2\sigma_{xy}\sigma_{xz}\sigma_{yz}$
$J_3 = \frac{1}{3}(\sigma_{xx}^3 + \sigma_{yy}^3 + \sigma_{zz}^3 + 3\sigma_{xy}^2\sigma_{xx} + 3\sigma_{xy}^2\sigma_{yy} + 3\sigma_{xz}^2\sigma_{xx} + 3\sigma_{xz}^2\sigma_{zz}$ $+ 3\sigma_{yz}^2\sigma_{yy} + 3\sigma_{yz}^2\sigma_{zz} + 6\sigma_{xy}\sigma_{xz}\sigma_{yz})$

– $I_1 =$ sum of the diagonal terms of σ_{ij} :

$$I_1 = \sigma_{xx} + \sigma_{yy} + \sigma_{zz}. \quad (4.8)$$

– $I_2 =$ sum of the two-row main subdeterminants:

$$I_2 = \begin{vmatrix} \sigma_{xx} & \sigma_{xy} \\ \sigma_{xy} & \sigma_{yy} \end{vmatrix} + \begin{vmatrix} \sigma_{yy} & \sigma_{yz} \\ \sigma_{yz} & \sigma_{zz} \end{vmatrix} + \begin{vmatrix} \sigma_{xx} & \sigma_{xz} \\ \sigma_{xz} & \sigma_{zz} \end{vmatrix}. \quad (4.9)$$

– $I_3 =$ determinant of σ_{ij} :

$$I_3 = \begin{vmatrix} \sigma_{xx} & \sigma_{xy} & \sigma_{xz} \\ \sigma_{xy} & \sigma_{yy} & \sigma_{yz} \\ \sigma_{xz} & \sigma_{yz} & \sigma_{zz} \end{vmatrix}. \quad (4.10)$$

Besides these principal invariants, there is also often another set of invariants used. This set is included in the principal invariants and called *basic invariants* [see Backhaus (1983)]:

$$J_1 = I_1, \quad (4.11)$$

$$J_2 = \frac{1}{2}I_1^2 - I_2, \quad (4.12)$$

$$J_3 = \frac{1}{3}I_1^3 - I_1I_2 + I_3. \quad (4.13)$$

The definition of both sets of invariants is given in Table 4.1.

It is common in the framework of the plasticity theory of isotropic materials to decompose the stress matrix σ_{ij} into a pure volume changing (spherical or hydrostatic) matrix σ_{ij}^o and a pure shape changing (deviatoric) stress matrix s_{ij} (cf. Fig. 4.2)²:

² It should be noted that in the case of anisotropic materials, a hydrostatic stress state may result in a shape change (Betten 2001).

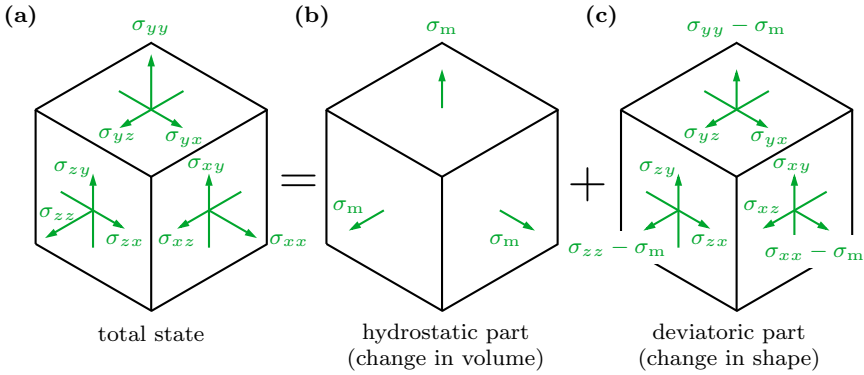


Fig. 4.2 Decomposition of the stress matrix **a** into its spherical **b** and the deviatoric **c** part

$$\sigma_{ij} = \sigma_{ij}^0 + s_{ij} = \sigma_m \mathbf{I} + s_{ij}. \tag{4.14}$$

In Eq. (4.14), $\sigma_m = \frac{1}{3}(\sigma_{xx} + \sigma_{yy} + \sigma_{zz})$ denotes the mean normal stress³ and **I** the identity matrix. Furthermore, Einstein’s summation convention was used [see Moore (2013)].

Equation (4.14) can be written in components as

$$\underbrace{\begin{bmatrix} \sigma_{xx} & \sigma_{xy} & \sigma_{xz} \\ \sigma_{xy} & \sigma_{yy} & \sigma_{yz} \\ \sigma_{xz} & \sigma_{yz} & \sigma_{zz} \end{bmatrix}}_{\text{stress matrix } \sigma_{ij}} = \underbrace{\begin{bmatrix} \sigma_m & 0 & 0 \\ 0 & \sigma_m & 0 \\ 0 & 0 & \sigma_m \end{bmatrix}}_{\text{hydrostatic matrix } \sigma_{ij}^0} + \underbrace{\begin{bmatrix} s_{xx} & s_{xy} & s_{xz} \\ s_{xy} & s_{yy} & s_{yz} \\ s_{xz} & s_{yz} & s_{zz} \end{bmatrix}}_{\text{deviatoric matrix } s_{ij}}. \tag{4.15}$$

It can be seen that the elements outside the diagonal terms, i.e., the shear stresses, are the same for the stress and the deviatoric stress matrix

$$s_{ij} = \sigma_{ij} \quad \text{for } i \neq j, \tag{4.16}$$

$$s_{ij} = \sigma_{ij} - \sigma_m \quad \text{for } i = j, \tag{4.17}$$

and it can be shown that the so-called deviator equation

$$s_{xx} + s_{yy} + s_{zz} = 0 \tag{4.18}$$

holds. The following list summarizes the calculation of the stress deviator components:

³ Also called the hydrostatic stress; in the context of soil mechanics, the pressure $p = -\sigma_m$ is also used.

Table 4.2 Definition of the three principal (I_i°) and basic (J_i°) stress invariants of the hydrostatic stress matrix σ_{ij}°

First stress invariant of σ_{ij}°
$I_1^\circ = 3\sigma_m$
$J_1^\circ = 3\sigma_m$
Second stress invariant of σ_{ij}°
$I_2^\circ = 3\sigma_m^2$
$J_2^\circ = \frac{3}{2}\sigma_m^2$
Third stress invariant of σ_{ij}°
$I_3^\circ = \sigma_m^3$
$J_3^\circ = \sigma_m^3$

Table 4.3 Definition of the three principal (I_i') and basic (J_i') stress invariants of the deviatoric stress matrix s_{ij}

First stress invariant of s_{ij}
$I_1' = 0$
$J_1' = 0$
Second stress invariant of s_{ij}
$I_2' = s_{xx}s_{yy} + s_{xx}s_{zz} + s_{yy}s_{zz} - s_{xy}^2 - s_{xz}^2 - s_{yz}^2$
$J_2' = -I_2'$
Third stress invariant of s_{ij}
$I_3' = s_{xx}s_{yy}s_{zz} - s_{xx}s_{yz}^2 - s_{yy}s_{xz}^2 - s_{zz}s_{xy}^2 + 2s_{xy}s_{xz}s_{yz}$
$J_3' = I_3'$

$$s_{xx} = \sigma_{xx} - \sigma_m = \frac{2}{3}\sigma_{xx} - \frac{1}{3}(\sigma_{yy} + \sigma_{zz}), \quad (4.19)$$

$$s_{yy} = \sigma_{yy} - \sigma_m = \frac{2}{3}\sigma_{yy} - \frac{1}{3}(\sigma_{xx} + \sigma_{zz}), \quad (4.20)$$

$$s_{zz} = \sigma_{zz} - \sigma_m = \frac{2}{3}\sigma_{zz} - \frac{1}{3}(\sigma_{xx} + \sigma_{yy}), \quad (4.21)$$

$$s_{xy} = \sigma_{xy}, \quad (4.22)$$

$$s_{yz} = \sigma_{yz}, \quad (4.23)$$

$$s_{xz} = \sigma_{xz}. \quad (4.24)$$

The definitions of the principal and basic invariants can be applied directly to the hydrostatic and deviatoric part of the stress matrix to obtain a similar representation as provided in Table 4.1, see summary in Table 4.2 for the hydrostatic matrix and the summary in Table 4.3 for the deviatoric matrix.

The hydrostatic part of σ_{ij} has in the case of metallic materials (full dense materials) for temperatures approximately under $0.3 T_{mt}$ (T_{mt} : melting temperature) nearly no influence on the occurrence of inelastic strains since dislocations slip only under the influence of shear stresses (for higher temperatures from 0.3 till $0.5 T_m$ also non-conservative climbing is possible) (Suzuki et al. 1985). On the other hand, the hydrostatic stress has a considerable influence on the yielding behavior in the case of soil mechanics, cellular materials or in damage mechanics (formation of pores, e.g., Gurson (1977)).

The evaluation of the basic invariants for the stress matrix, as well as the hydrostatic and deviatoric part is presented in Table 4.4, expressed in components of σ_{ij} and the principal stresses $\sigma_1, \sigma_2, \sigma_3$.

It can be seen in Table 4.4 that the spherical matrix is completely characterized by its first invariant because the second and third invariant are powers of it. The stress deviator matrix is completely characterized by its second and third invariant. Therefore, the physical contents of the stress state σ_{ij} can be described either by the

Table 4.4 Basic invariants in terms of σ_{ij} and principal values

Invariants	Components of σ_{ij}	Principal stresses $\sigma_1, \sigma_2, \sigma_3$
<i>Stress matrix</i>		
J_1	$\sigma_{xx} + \sigma_{yy} + \sigma_{zz}$	$\sigma_1 + \sigma_2 + \sigma_3$
J_2	$\frac{1}{2} (\sigma_{xx}^2 + \sigma_{yy}^2 + \sigma_{zz}^2)$ $+ \sigma_{xy}^2 + \sigma_{xz}^2 + \sigma_{yz}^2$	$\frac{1}{2} (\sigma_1^2 + \sigma_2^2 + \sigma_3^2)$
J_3	$\frac{1}{3} (\sigma_{xx}^3 + \sigma_{yy}^3 + \sigma_{zz}^3 + 3\sigma_{xy}^2\sigma_{xx}$ $+ 3\sigma_{xy}^2\sigma_{yy} + 3\sigma_{xz}^2\sigma_{xx} + 3\sigma_{xz}^2\sigma_{zz}$ $+ 3\sigma_{yz}^2\sigma_{yy} + 3\sigma_{yz}^2\sigma_{zz} + 6\sigma_{xy}\sigma_{xz}\sigma_{yz})$	$\frac{1}{3} (\sigma_1^3 + \sigma_2^3 + \sigma_3^3)$
<i>Spherical matrix</i>		
J_1^0	$\sigma_{xx} + \sigma_{yy} + \sigma_{zz}$	$\sigma_1 + \sigma_2 + \sigma_3$
J_2^0	$\frac{1}{6} (\sigma_{xx} + \sigma_{yy} + \sigma_{zz})^2$	$\frac{1}{6} (\sigma_1 + \sigma_2 + \sigma_3)^2$
J_3^0	$\frac{1}{27} (\sigma_{xx} + \sigma_{yy} + \sigma_{zz})^3$	$\frac{1}{27} (\sigma_1 + \sigma_2 + \sigma_3)^3$
<i>Stress deviator matrix</i>		
J'_1	0	0
J'_2	$\frac{1}{6} [(\sigma_{xx} - \sigma_{yy})^2 + (\sigma_{yy} - \sigma_{zz})^2$ $+ (\sigma_{zz} - \sigma_{xx})^2] + \sigma_{xy}^2 + \sigma_{yz}^2 + \sigma_{zx}^2$	$\frac{1}{6} [(\sigma_1 - \sigma_2)^2 + (\sigma_2 - \sigma_3)^2$ $+ (\sigma_3 - \sigma_1)^2]$
J'_3	$s_{xx}s_{yy}s_{zz} + 2\sigma_{xy}\sigma_{yz}\sigma_{zx}$ $- s_{xx}\sigma_{yz}^2 - s_{yy}\sigma_{zx}^2 - s_{zz}\sigma_{xy}^2$	$s_1s_2s_3$
With	$s_{xx} = \frac{1}{3} (2\sigma_{xx} - \sigma_{yy} - \sigma_{zz})$	$s_1 = \frac{1}{3} (2\sigma_1 - \sigma_2 - \sigma_3)$
	$s_{yy} = \frac{1}{3} (-\sigma_{xx} + 2\sigma_{yy} - \sigma_{zz})$	$s_2 = \frac{1}{3} (-\sigma_1 + 2\sigma_2 - \sigma_3)$
	$s_{zz} = \frac{1}{3} (-\sigma_{xx} - \sigma_{yy} + 2\sigma_{zz})$	$s_3 = \frac{1}{3} (-\sigma_1 - \sigma_2 + 2\sigma_3)$
	$s_{xy} = \sigma_{xy}, s_{xz} = \sigma_{xz}, s_{yz} = \sigma_{yz}$	

Table 4.5 Basic invariants for the $\sigma_1 - \sigma_2$ and $\sigma - \tau$ space

Invariants	$\sigma_1 - \sigma_2$ space	$\sigma - \tau$ space
J_1^0	$\sigma_1 + \sigma_2$	σ
J_2'	$\frac{1}{3}(\sigma_1^2 + \sigma_2^2 - \sigma_1\sigma_2)$	$\frac{1}{3}\sigma^2 + \tau^2$
J_3'	$\frac{1}{27}(2\sigma_1^3 + 2\sigma_2^3 - 3\sigma_1\sigma_2(\sigma_1 + \sigma_2))$	$\frac{2}{27}\sigma^3 + \frac{1}{3}\sigma\tau^2$

Table 4.6 Basic invariants for a uniaxial (normal) stress (σ) state and a pure shear stress state (τ)

Invariants	Only σ	Only τ
J_1^0	σ	0
J_2'	$\frac{1}{3}\sigma^2$	τ^2
J_3'	$\frac{2}{27}\sigma^3$	0

three basic stress invariants J_i or if we use the decomposition in its spherical and deviatoric part by the first invariant of the spherical matrix and the second and third invariant of the stress deviator matrix. In the following, we will only use these three basic invariants to describe yield and failure conditions. Thus, the physical content of a state of stress will be described by the following set of invariants:

$$\sigma_{ij} \rightarrow J_1^0, J_2', J_3'. \quad (4.25)$$

To derive important special cases of yield conditions, it is also useful to specify the stress invariants for a plane stress state $\sigma_1 - \sigma_2$ and a stress state $\sigma - \tau$ where only one normal and one shear stress is acting. Thus, the stress invariants reduce to the given form in Table 4.5.

Finally, Table 4.6 summarizes the stress invariants for a uniaxial or pure shear stress state.

The representation of a stress state in terms of invariants is also very useful in the context of the implementation of yield conditions into commercial finite elements codes. This significantly facilitates the calculation of derivatives [see Öchsner (2003)].

4.2 Graphical Representation of Yield Conditions

Plastic flow starts in a uniaxial tensile test as soon as the acting tensile stress σ reaches the initial yield stress k^{init} , see Öchsner (2016). In the case of a multiaxial stress state, this simple comparison is replaced by the yield condition. To this end, a scalar value is calculated from the acting six stress components and compared to an experimental scalar value. The yield condition in stress space can be expressed in its most general form ($\mathbb{R}^6 \times \mathbb{R}^{\dim(q)} \rightarrow \mathbb{R}$) as:

$$F = F(\boldsymbol{\sigma}, \mathbf{q}). \quad (4.26)$$

For further characterization, we assume in the following the special case of ideal plastic material behavior (vector of hardening variables $\mathbf{q} = \mathbf{0}$) so that for ($\mathbb{R}^6 \rightarrow \mathbb{R}$)

$$F = F(\boldsymbol{\sigma}) \quad (4.27)$$

depends now only on the stress state. The values of F have—as in the uniaxial case—the following⁴ mechanical meaning:

$$F(\boldsymbol{\sigma}) = 0 \rightarrow \text{plastic material behavior}, \quad (4.28)$$

$$F(\boldsymbol{\sigma}) < 0 \rightarrow \text{elastic material behavior}, \quad (4.29)$$

$$F(\boldsymbol{\sigma}) > 0 \rightarrow \text{invalid}. \quad (4.30)$$

A further simplification is obtained under the assumption that the yield condition can be split in a pure stress part $f(\boldsymbol{\sigma})$ and an experimental material parameter k :

$$F(\boldsymbol{\sigma}) = f(\boldsymbol{\sigma}) - k. \quad (4.31)$$

The yield condition $F = 0$ represents in a n -dimensional space a hypersurface that is also called the yield surface or the yield loci. The number n is equal to the independent stress matrix components. A direct graphical representation of the yield surface is not possible due to its dimensionality, i.e., six variables. However, a reduction of the dimensionality is possible to achieve if a principle axis transformation [see Eq. (4.2)] is applied to the argument σ_{ij} . The components of the stress matrix reduce to the principal stresses σ_1 , σ_2 , and σ_3 on the principal diagonal of the stress matrix and the non-diagonal elements are equal to zero. In such a principal stress space, it is possible to graphically represent the yield condition as a three-dimensional surface. This space is also called the Haigh-Westergaard stress space [see Chen and Zhang (1991)]. A hydrostatic stress state lies in such a principal stress system on the space diagonal (hydrostatic axis). Any plane perpendicular to the hydrostatic axis is called an octahedral plane. The particular octahedral plane passing through the origin is called the deviatoric plane or π -plane [see Chen and Han (1988)]. Because $\sigma_1 + \sigma_2 + \sigma_3 = 0$, it follows from Eq. (4.14) that $\sigma_{ij} = s_{ij}$, i.e., any stress state on the π -plane is pure deviatoric.

The possibility of a representation of a yield condition based on a set of independent stress invariants (e.g., according to Eq. (4.25)) is the characteristic of any isotropic yield condition, regardless of the choice of coordinate system. Therefore, Eq. (4.27) can also be written as

$$F = F(J_1^0, J_2', J_3'). \quad (4.32)$$

⁴ Under the restriction of rate-independent plasticity.

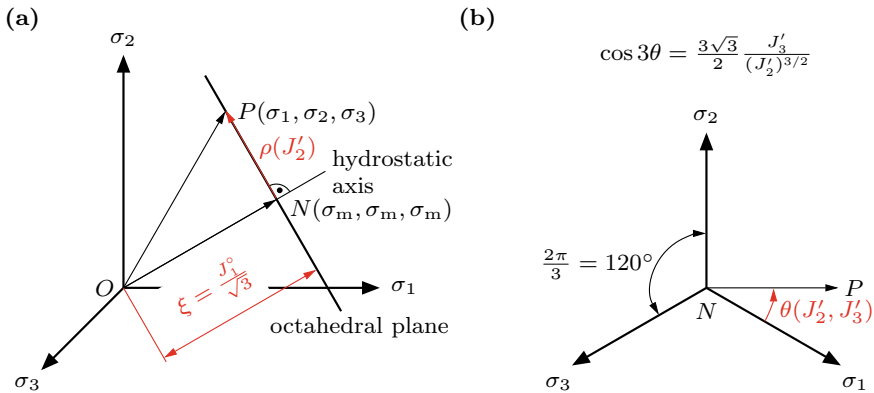


Fig. 4.3 Geometrical interpretation of basic stress invariants: **a** principal stress space; **b** octahedral plane

On the basis of the dependency of the yield condition on the invariants, a descriptive classification can be performed. Yield conditions independent of the hydrostatic stress (J_1^0) can be represented by the invariants J_2' and J_3' . Stress states with $J_2' = \text{const.}$ lie on a circle around the hydrostatic axis in an octahedral plane. A dependency of the yield condition on J_3' results in a deviation from the circle shape. The yield surface forms a prismatic body whose longitudinal axis is represented by the hydrostatic axis. A dependency on J_1^0 denotes a size change of the cross section of the yield surface along the hydrostatic axis. However, the shape of the cross section remains similar in the mathematical sense. Therefore, a dependency on J_1^0 can be represented by sectional views through planes along the hydrostatic axis.

The geometrical interpretation of stress invariants [see Chen and Han (1988)] is given in Fig. 4.3.

It can be seen that an arbitrary stress state P can be expressed by its position along the hydrostatic axis $\xi = \frac{1}{\sqrt{3}} J_1^0$ and its polar coordinates ($\rho = \sqrt{2J_2'}$, $\theta(J_2', J_3')$) in the octahedral plane through P . For the set of polar coordinates, the so-called stress Lode angle θ is defined in the range $0 \leq \theta \leq 60^\circ$ as [see Nayak and Zienkiewicz (1972)],

$$\cos(3\theta) = \frac{3\sqrt{3}}{2} \cdot \frac{J_3'}{(J_2')^{3/2}}. \quad (4.33)$$

It can be concluded from Eq. (4.33) that

$$3\theta = 3\theta(J_2', J_3'), \quad (4.34)$$

or that

$$\theta = \theta(J_2', J_3'). \quad (4.35)$$

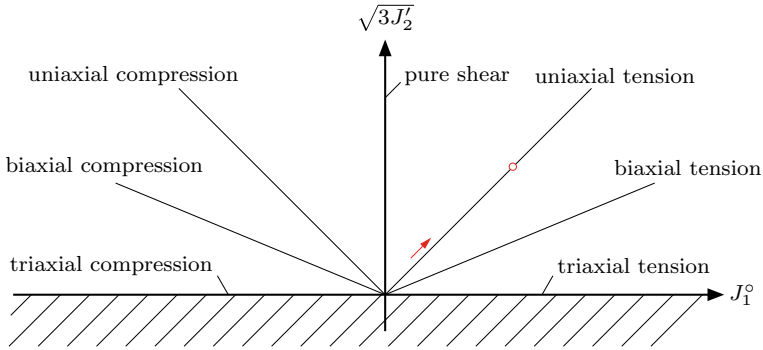
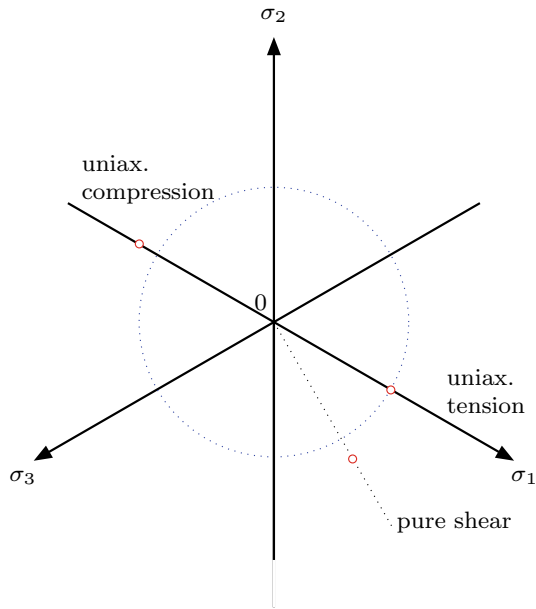


Fig. 4.4 Schematic representation of basic tests in the $J_1^0 - \sqrt{3}J_2^0$ invariant space

Fig. 4.5 Identification of the shape of a yield condition in an octahedral plane ($\sigma_m = \text{const.}$)



The trigonometric identity $\cos(3\theta) = 4 \cos^3(\theta) - 3 \cos(\theta)$ may be used for some transformations.

The set of coordinates $(\xi, \rho, \cos(3\theta))$ is known in the literature as the Haigh-Westergaard coordinates. To investigate the shape of the yield surface, particular experiments, including multiaxial stress states, must be realized and the initial yield points marked and approximated in the Haigh-Westergaard space, the $J_1^0 - \sqrt{3}J_2^0$ invariant space, and octahedral planes, see Figs. 4.4 and 4.5.

Table 4.7 Definition of basic tests in the $J_1^o - \sqrt{3J_2'}$ invariant space

Case	J_1^o	$\sqrt{3J_2'}$	Comment
Uniax. tension (σ)	σ	σ	Slope: 1
Uniax. compression ($-\sigma$)	$-\sigma$	σ	Slope: -1
Biax. tension (σ)	2σ	σ	Slope: 0.5
Biax. compression ($-\sigma$)	-2σ	σ	Slope: -0.5
Triax. tension (σ)	3σ	0	Horiz. axis
Triax. compression ($-\sigma$)	-3σ	0	Horiz. axis
Pure shear (τ)	0	$\sqrt{3} \tau$	Vertical axis

The loading path, for example, for the biaxial tension case in the $J_1^o - \sqrt{3J_2'}$ invariant space (see Fig. 4.4) is obtained as follows (see Table 4.5 for the evaluation of the invariants):

$$\sqrt{3J_2'} = \sigma = \frac{1}{2} J_1^o \quad (4.36)$$

Further load paths for basic experiments in the $J_1^o - \sqrt{3J_2'}$ invariant space are summarized in Table 4.7.

4.3 Yield Conditions

The yield condition can generally be expressed as

$$F(\boldsymbol{\sigma}, \mathbf{q}) \leq 0, \quad (4.37)$$

where $\mathbf{q} = [\kappa \ \boldsymbol{\alpha}]^T$ is the column matrix of internal variables describing the hardening behavior of the material. Parameter κ relates to isotropic hardening, while the matrix $\boldsymbol{\alpha}$ contains the kinematic hardening parameters. The mechanical meaning of F remains as indicated by Eqs. (4.28)–(4.30).

Restricting to isotropic hardening, Eq. (4.37) can be expressed as

$$F(\boldsymbol{\sigma}, \kappa) \leq 0. \quad (4.38)$$

4.3.1 Mises Yield Condition

The total deformation energy per unit volume of a three-dimensional body can be generally expressed as [see Öchsner (2016)]:

$$w = \frac{1}{2} (\sigma_{xx}\varepsilon_{xx} + \sigma_{yy}\varepsilon_{yy} + \sigma_{zz}\varepsilon_{zz} + \tau_{xy}\gamma_{xy} + \tau_{xz}\gamma_{xz} + \tau_{yz}\gamma_{yz}). \quad (4.39)$$

Following the decomposition of the stress matrix in its spherical and deviatoric part as indicated in Fig. 4.2, this deformation energy can be split in its volumetric (w^o) and distortional (w^s) part as:

$$\begin{aligned} w &= \underbrace{\frac{1-2\nu}{6E} (\sigma_{xx} + \sigma_{yy} + \sigma_{zz})^2}_{w^o} + \\ &+ \underbrace{\frac{1+\nu}{6E} [(\sigma_{xx} - \sigma_{yy})^2 + (\sigma_{yy} - \sigma_{zz})^2 + (\sigma_{zz} - \sigma_{xx})^2 + 6(\tau_{xy}^2 + \tau_{yz}^2 + \tau_{xz}^2)]}_{w^s}. \end{aligned} \quad (4.40)$$

The von Mises yield condition states now that plastic deformation starts as soon as the distortional deformation energy per unit volume, i.e.,

$$w^s = \frac{1+\nu}{6E} [(\sigma_{xx} - \sigma_{yy})^2 + (\sigma_{yy} - \sigma_{zz})^2 + (\sigma_{zz} - \sigma_{xx})^2 + 6(\tau_{xy}^2 + \tau_{yz}^2 + \tau_{xz}^2)], \quad (4.41)$$

reaches a critical value ($k_t^2/(6G)$) [see Asaro and Lubarda (2006), Nash (1998)]. This yield condition is commonly applied for ductile metals. The expression in units of stress is given for a general three-dimensional stress state as

$$\begin{aligned} F(\sigma_{ij}) &= \\ &\sqrt{\underbrace{\frac{1}{2} ((\sigma_x - \sigma_y)^2 + (\sigma_y - \sigma_z)^2 + (\sigma_z - \sigma_x)^2) + 3(\sigma_{xy}^2 + \sigma_{yz}^2 + \sigma_{xz}^2)}_{\sigma_{\text{eff}}}} - k_t = 0, \end{aligned} \quad (4.42)$$

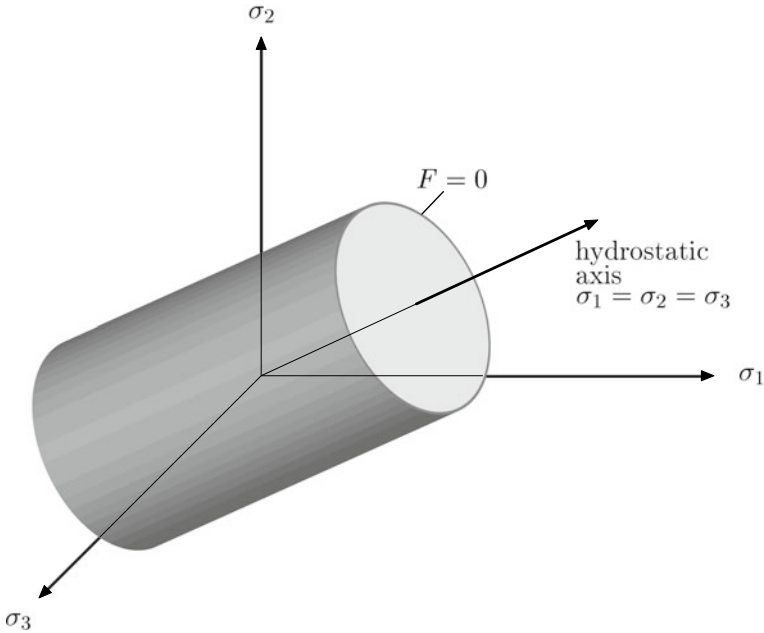


Fig. 4.6 Graphical representation of the yield condition according to von Mises in the principal stress space

or in the principal stress space $(\sigma_1, \sigma_2, \sigma_3)$ with $\sigma_{xy} = \sigma_{yz} = \sigma_{xz} = 0$:

$$F(\sigma_{ij}) = \sqrt{\underbrace{\frac{1}{2}((\sigma_1 - \sigma_2)^2 + (\sigma_2 - \sigma_3)^2 + (\sigma_3 - \sigma_1)^2)}_{\sigma_{\text{eff}}}} - k_t = 0. \quad (4.43)$$

The graphical representation in the principal stress space is given in Fig. 4.6, where a cylinder with its longitudinal axis equal to the hydrostatic axis is obtained.

Expressed with the second invariant of the stress deviator (see Table 4.4), one can write the following formulation:

$$F(J_2') = \sqrt{3J_2'} - k_t = 0. \quad (4.44)$$

The representation in the $\sqrt{3J_2'}-J_1^\circ$ space (see Fig. 4.8) shows that the yield condition is independent of the hydrostatic stress (Fig. 4.7).

The view along the hydrostatic axis is shown in Fig. 4.8 where it can be seen that there is no difference under tension and compression for uniaxial stress states.

Fig. 4.7 Graphical representation of the yield condition according to von Mises in the $\sqrt{3J'_2}-J_1^\circ$ space

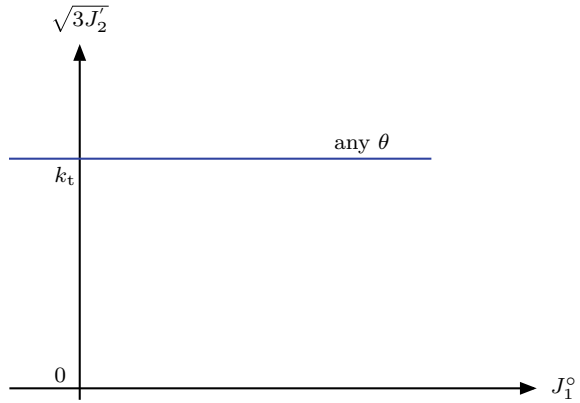
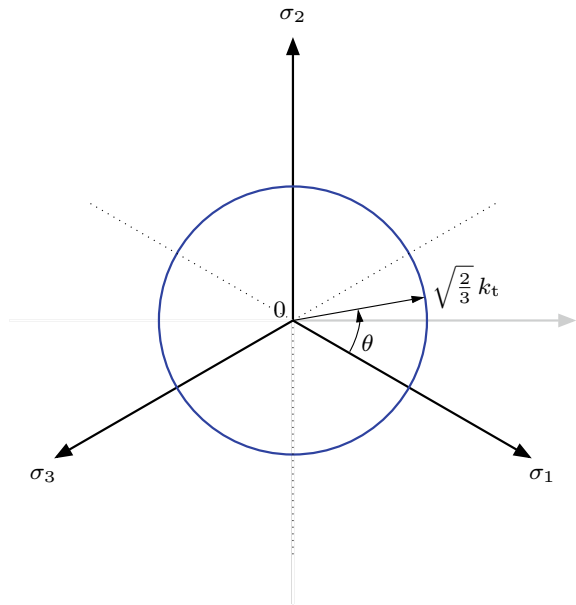


Fig. 4.8 Graphical representation of the yield condition according to von Mises in the octahedral plane



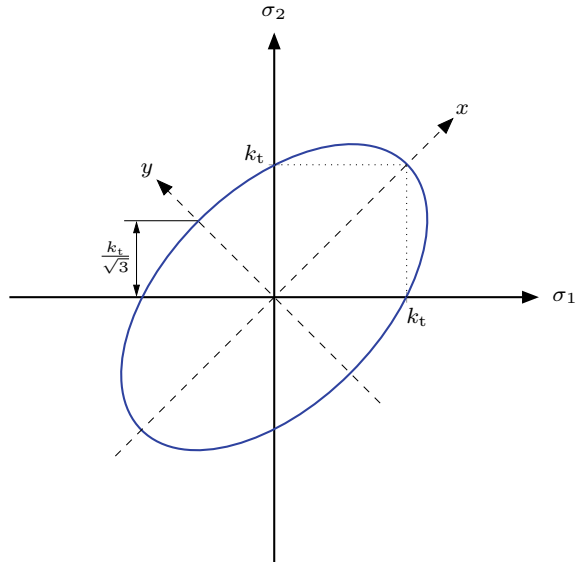
A representation in the two-component principal $\sigma_1-\sigma_2$ space is obtained by substituting the particular basic invariant formulations from Table 4.5 into Eq. (4.44) as (see Fig. 4.9):

$$F_{\sigma_1-\sigma_2} = \sigma_1^2 + \sigma_2^2 - \sigma_1\sigma_2 - k_t^2 = 0, \tag{4.45}$$

or represented in a standard form to easier identify an ellipse (see Fig. 4.9) as

$$F_{\sigma_1-\sigma_2} = \left(\frac{x}{\sqrt{2}k_t}\right)^2 + \left(\frac{y}{\sqrt{2}k_s}\right)^2 - 1 = 0, \tag{4.46}$$

Fig. 4.9 Graphical representation of the yield condition according to von Mises in the σ_1 - σ_2 space



where $x = (\sigma_1 + \sigma_2)/\sqrt{2}$ and $y = (\sigma_2 - \sigma_1)/\sqrt{2}$.

The transformation of Eq. (4.45) into Eq. (4.46) can be obtained in the following way:

$$\sigma_1^2 + \sigma_2^2 - \sigma_1\sigma_2 = k_t^2, \quad (4.47)$$

$$4\sigma_1^2 + 4\sigma_2^2 - 4\sigma_1\sigma_2 = 4k_t^2, \quad (4.48)$$

$$\sigma_1^2 + 2\sigma_1\sigma_2 + \sigma_2^2 + 3(\sigma_1^2 - 2\sigma_1\sigma_2 + \sigma_2^2) = 4k_t^2, \quad (4.49)$$

$$\frac{1}{4}(\sigma_1 + \sigma_2)^2 + \frac{3}{4}(\sigma_2 - \sigma_1)^2 = k_t^2, \quad (4.50)$$

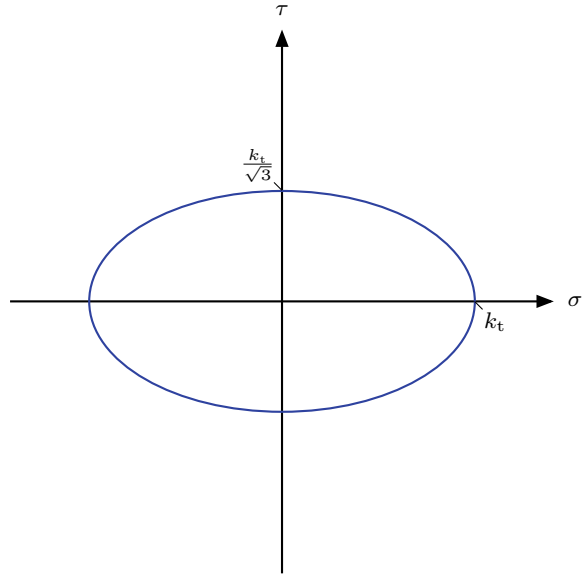
$$\left(\frac{\sigma_1 + \sigma_2}{2k_t}\right)^2 + \left(\frac{\sigma_2 - \sigma_1}{2\frac{k_s}{\sqrt{3}}}\right)^2 = 1. \quad (4.51)$$

A representation in the two-component normal/shear σ - τ space is obtained by substituting the particular basic invariant formulations from Table 4.5 into Eq. (4.44) to finally give the following ellipse (see Fig. 4.10):

$$F_{\sigma-\tau} = \left(\frac{\sigma}{k_t}\right)^2 + \left(\frac{\sqrt{3}\tau}{k_t}\right)^2 - 1 = 0. \quad (4.52)$$

The last formulation allows to identify the relationship between the shear and tensile yield stress. Setting $\sigma = 0$, which means then $\tau \rightarrow k_s$, gives:

Fig. 4.10 Graphical representation of the yield condition according to von Mises in the σ - τ space



$$k_s = \frac{k_t}{\sqrt{3}} \tag{4.53}$$

Based on this relation, it is possible to express the yield condition in terms of the shear yield stress, for example, as:

$$F(J_2') = \sqrt{J_2'} - k_s = 0. \tag{4.54}$$

Table 4.8 illustrates the fact that it is not the right approach to look on single stress components if one has to judge if the stress state is in the elastic or already in the plastic domain. Only the equivalent stress based on a yield condition can answer this question in the case of multiaxial stress states.

4.3.2 Tresca Yield Condition

The Tresca yield condition, also known as the maximum shear stress theory, postulates yielding as soon as the maximum shear stress reaches an experimental value. This yield condition is commonly applied for ductile metals. The expression is given for the principal stresses as

$$\max \left(\frac{1}{2} |\sigma_1 - \sigma_2|, \frac{1}{2} |\sigma_2 - \sigma_3|, \frac{1}{2} |\sigma_3 - \sigma_1| \right) = k_s, \tag{4.55}$$

Table 4.8 Equivalent von Mises stress for different stress states

Stress matrix σ_{ij}	Von Mises stress Eq. (4.43)	Domain ($k_t^{\text{init}} = 150$)
$\begin{bmatrix} 100 & 0 & 0 \\ 0 & 100 & 0 \\ 0 & 0 & 0 \end{bmatrix}$	100	Elastic
$\begin{bmatrix} 100 & 0 & 0 \\ 0 & -100 & 0 \\ 0 & 0 & 0 \end{bmatrix}$	173.2	Plastic
$\begin{bmatrix} 200 & 0 & 20 \\ 0 & 80 & 20 \\ 20 & 20 & 90 \end{bmatrix}$	125.3	Elastic
$\begin{bmatrix} 200 & 0 & 20 \\ 0 & 80 & 20 \\ 20 & 20 & 200 \end{bmatrix}$	129.3	Elastic
$\begin{bmatrix} 100 & 0 & 20 \\ 0 & 80 & 20 \\ 20 & 20 & -80 \end{bmatrix}$	177.8	Plastic

or

$$F(\sigma_i) = \max \left(\frac{1}{2} |\sigma_1 - \sigma_2|, \frac{1}{2} |\sigma_2 - \sigma_3|, \frac{1}{2} |\sigma_3 - \sigma_1| \right) - k_s = 0. \quad (4.56)$$

Expressed with the second and third invariant of the stress deviator, the following formulation is obtained:

$$F(J'_2, J'_3) = 4 (J'_2)^3 - 27 (J'_3)^2 - 36k_s^2 (J'_2)^2 + 96k_s^4 J'_2 - 64k_s^6 = 0. \quad (4.57)$$

The graphical representation in the principal stress space is given in Fig. 4.11, where a prism of six sides with its longitudinal axis equal to the hydrostatic axis is obtained. The view along the hydrostatic axis is shown in Fig. 4.12, where a hexagon can be seen. In addition, it can be concluded that the tensile and compressive yield stresses have the same magnitude.

The representation in the $\sqrt{3}J'_2$ - J'_1 space (see Fig. 4.13) shows that the yield condition is independent of the hydrostatic stress.

For a representation in the two-component principal σ_1 - σ_2 space, the following six straight-line equations can be derived from Eq. (4.55) (see Fig. 4.14):

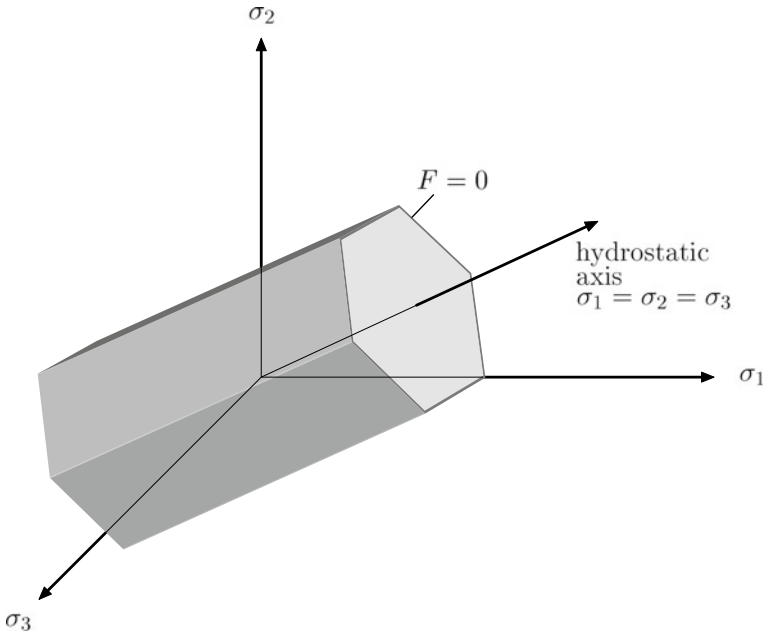


Fig. 4.11 Graphical representation of the yield condition according to Tresca in the principal stress space

Fig. 4.12 Graphical representation of the yield condition according to Tresca in the octahedral plane

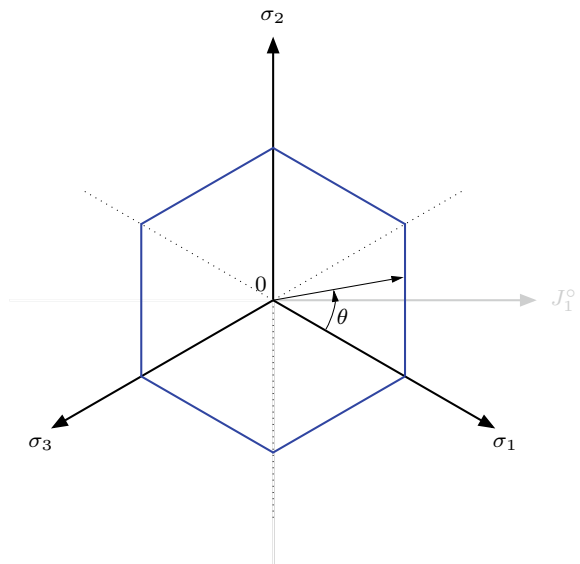
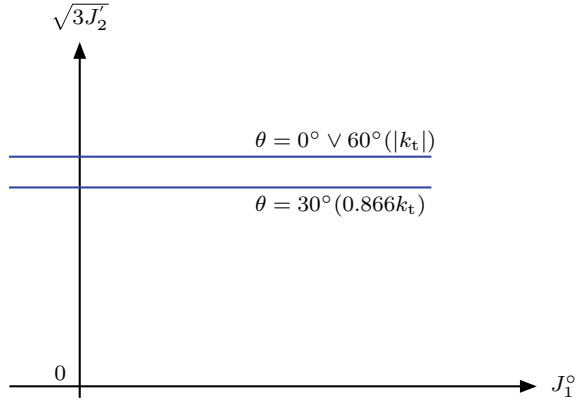


Fig. 4.13 Graphical representation of the yield condition according to Tresca in the $\sqrt{3J_2}'-J_1^\circ$ space



$$\begin{aligned}
 \sigma_2^{(1)} &= \sigma_1 - 2k_s = \sigma_1 - k_t, \\
 \sigma_2^{(2)} &= \sigma_1 + 2k_s = \sigma_1 + k_t, \\
 \sigma_2^{(3)} &= 2k_s = k_t, \\
 \sigma_2^{(4)} &= -2k_s = -k_t, \\
 \sigma_1^{(5)} &= 2k_s = k_t, \\
 \sigma_1^{(6)} &= -2k_s = -k_t.
 \end{aligned}
 \tag{4.58}$$

The principal stresses⁵ σ_1 and σ_2 result from Mohr's circle as

$$\sigma_1 = \frac{\sigma}{2} + \sqrt{\left(\frac{\sigma}{2}\right)^2 + \tau^2} ; \quad \sigma_2 = \frac{\sigma}{2} - \sqrt{\left(\frac{\sigma}{2}\right)^2 + \tau^2}.
 \tag{4.59}$$

Substituting Eq. (4.59) into Eq. (4.55)₁ yields the yield condition in the $\sigma - \tau$ space as

$$F_{\sigma-\tau} = \left(\frac{\sigma}{2}\right)^2 + \tau^2 = k_s^2
 \tag{4.60}$$

or (Fig. 4.15):

$$F_{\sigma-\tau} = \left(\frac{\sigma}{k_t}\right)^2 + \left(\frac{2\tau}{k_t}\right)^2 - 1.
 \tag{4.61}$$

⁵ Mohr's circle gives $\sigma_1 > 0$ and $\sigma_3 < 0$ with $\sigma_2 = 0$.

Fig. 4.14 Graphical representation of the yield condition according to Tresca in the σ_1 - σ_2 space

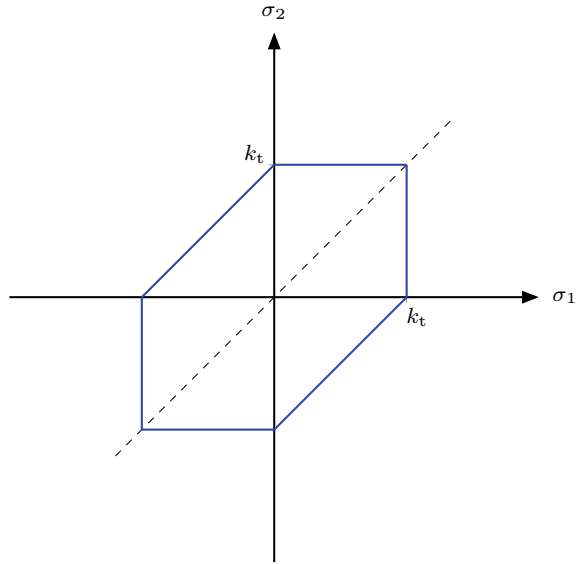
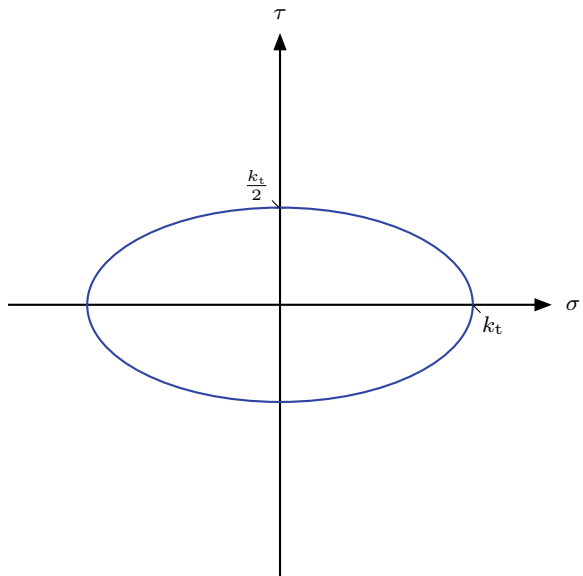


Fig. 4.15 Graphical representation of the yield condition according to Tresca in the σ - τ space



The last formulation allows to identify the relationship between the shear and tensile yield stress as:

$$k_s = \frac{k_t}{2}. \tag{4.62}$$

4.3.3 Drucker-Prager Yield Condition

The Drucker-Prager yield condition is an extension of the formulation according to von Mises [see Eq. (4.54)], which considers the influence of the weighted (factor α) hydrostatic stress (J_1^o):

$$F(J_1^o, J_2') = \alpha J_1^o + \sqrt{J_2'} - k_s, \tag{4.63}$$

where the α and k_s are the material parameters. It should be noted here that the von Mises yield condition is included in Eq. (4.63) for $\alpha = 0$. This condition is usually applied as a failure condition for soils, rocks, and concrete.

The representation in the $\sqrt{J_2'}-J_1^o$ space (see Fig. 4.16) shows that the yield condition is linearly dependent on the hydrostatic stress. This behavior would represent in the principal stress space a right-circular cone.

The view along the hydrostatic axis is shown in Fig. 4.17 where it can be seen that, as in the case of von Mises, a circle is obtained. However, the radius is now a function of the hydrostatic stress, i.e., $r = \sqrt{2}(k_s - \alpha J_1^o)$. This radius reduces in the π -plane, meaning for $J_1^o = 0$ or $\sigma_m = 0$, to $r = \sqrt{2}k_s$, which is identical to the constant radius of the von Mises yield condition, see Fig. 4.8 and relation (4.53).

Fig. 4.16 Graphical representation of the yield condition according to Drucker-Prager in the $\sqrt{J_2'}-J_1^o$ space

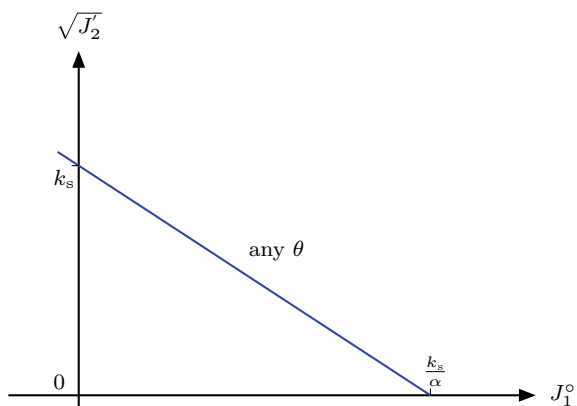
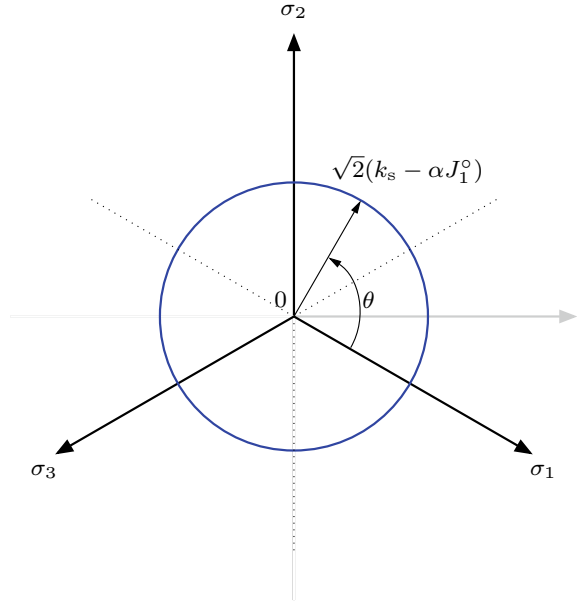


Fig. 4.17 Graphical representation of the yield condition according to Drucker-Prager in an octahedral plane ($\sigma_m = \text{const.}$)



Substituting the equations from Table 4.5 for the basic invariants into Eq. (4.63), the representation in the two-component principal σ_1 - σ_2 space is obtained as

$$F_{\sigma_1-\sigma_2} = (1 - 3\alpha^2) (\sigma_1^2 + \sigma_2^2) - (1 + 6\alpha^2) \sigma_1 \sigma_2 + 6\alpha k_s (\sigma_1 + \sigma_2) - 3k_s^2, \quad (4.64)$$

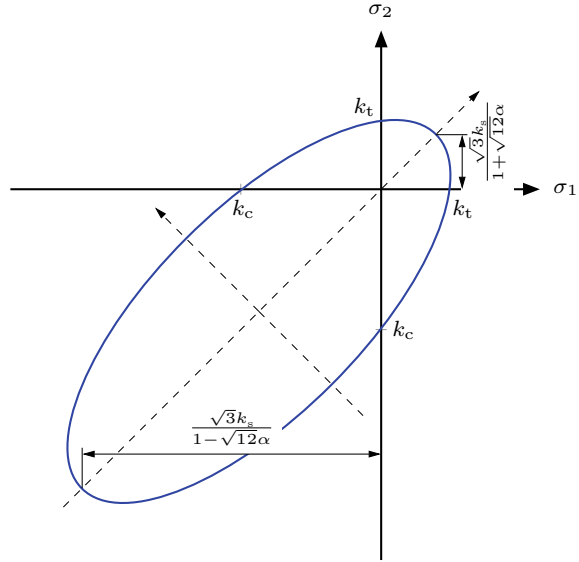
or after some transformations the equation of a shifted and rotated ellipse in the $\sigma_1 - \sigma_2$ space is obtained as (see Fig. 4.18):

$$F_{\sigma_1-\sigma_2} = \left(\frac{x + \frac{6\sqrt{2}k_s\alpha}{1-12\alpha^2}}{\frac{\sqrt{6}k_s}{1-12\alpha^2}} \right)^2 + \left(\frac{y}{\frac{\sqrt{2}k_s}{\sqrt{1-12\alpha^2}}} \right)^2 - 1, \quad (4.65)$$

where

$$x = \frac{1}{\sqrt{2}} (\sigma_1 + \sigma_2), \quad y = \frac{1}{\sqrt{2}} (\sigma_2 - \sigma_1). \quad (4.66)$$

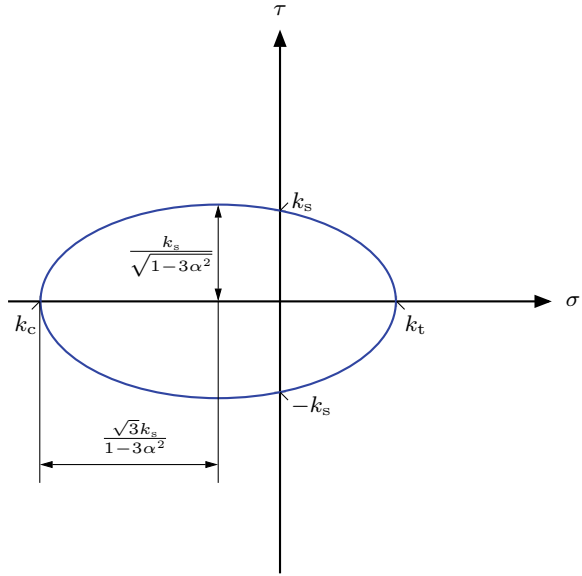
Fig. 4.18 Graphical representation of the yield condition according to Drucker-Prager in the σ_1 - σ_2 space



The transformation of Eq. (4.64) into Eq. (4.65) can be obtained in the following way:

$$\begin{aligned}
 \frac{1}{3}(\sigma_1^2 + \sigma_2^2 - \sigma_1\sigma_2) &= k_s^2 - 2k_s\alpha(\sigma_1 + \sigma_2) + \alpha^2(\sigma_1 + \sigma_2)^2 \quad | \times 12, \\
 4(\sigma_1^2 + \sigma_2^2 - \sigma_1\sigma_2) &= 12k_s^2 - 24k_s\alpha(\sigma_1 + 12\sigma_2) + 12\alpha^2(\sigma_1 + \sigma_2)^2, \\
 \sigma_1^2 + 2\sigma_1\sigma_2 + \sigma_2^2 + 3(\sigma_1^2 - 2\sigma_1\sigma_2 + \sigma_2^2) &= 12k_s^2 - 24k_s\alpha(\sigma_1 + 12\sigma_2) + \\
 &\quad + 12\alpha^2(\sigma_1 + \sigma_2)^2, \\
 (\sigma_1 + \sigma_2)^2 + 3(\sigma_1 - \sigma_2)^2 &= 12k_s^2 - 24k_s\alpha(\sigma_1 + 12\sigma_2) + 12\alpha^2(\sigma_1 + \sigma_2)^2, \\
 (\sigma_1 + \sigma_2)^2 + 3(\sigma_1 - \sigma_2)^2 + 24k_s\alpha(\sigma_1 + 12\sigma_2) - 12\alpha^2(\sigma_1 + \sigma_2)^2 &= \\
 &= \left(\frac{12k_s^2}{1 - 12\alpha^2} - \frac{12\alpha^2 k_s^2}{1 - 12\alpha^2} \right), \\
 3(1 - 12\alpha^2)(\sigma_1 - \sigma_2)^2 + (1 - 12\alpha^2)^2(\sigma_1 + \sigma_2)^2 + \\
 &\quad + 2 \times 12k_s\alpha(1 - 12\alpha^2)(\sigma_1 + \sigma_2) + 12^2\alpha^2 k_s^2 = 12k_s^2, \\
 3(1 - 12\alpha^2)(\sigma_1 - \sigma_2)^2 + ((1 - 12\alpha^2)(\sigma_1 + \sigma_2) + 12k_s\alpha)^2 &= 12k_s^2, \\
 \frac{(1 - 12\alpha^2)(\sigma_1 - \sigma_2)^2}{4k_s^2} + \frac{((1 - 12\alpha^2)(\sigma_1 + \sigma_2) + 12k_s\alpha)^2}{12k_s^2} &= 1. \quad (4.67)
 \end{aligned}$$

Fig. 4.19 Graphical representation of the yield condition according to Drucker-Prager in the σ - τ space



The same procedure yields under consideration of $k_s^2 = \frac{k_t^2}{1-3\alpha^2} - \frac{3\alpha^2 k_c^2}{1-3\alpha^2}$ also to a shifted ellipse in the $\sigma - \tau$ space (see Fig. 4.19):

$$\left(\frac{\sigma + \frac{3k_s\alpha}{1-3\alpha^2}}{\frac{\sqrt{3}k_s}{1-3\alpha^2}} \right)^2 + \left(\frac{\tau}{\frac{k_s}{\sqrt{1-3\alpha^2}}} \right)^2 = 1. \tag{4.68}$$

Setting $\tau \rightarrow 0$ in the last relation allows to extract the relation between the tensile/compressive yield stress and the shear limit ($\sigma \rightarrow k_t \wedge \sigma \rightarrow k_c$) as:

$$k_t = \frac{\sqrt{3}}{1 + \sqrt{3}\alpha} k_s, \quad k_c = \frac{\sqrt{3}}{1 - \sqrt{3}\alpha} k_s. \tag{4.69}$$

Finally, it should be noted here that also the formulation

$$F(J_1^0, J_2^1) = \alpha J_1^0 + \sqrt{J_2^1} - \frac{\bar{\sigma}}{\sqrt{3}}, \tag{4.70}$$

where

$$\bar{\sigma} = (1 + \alpha\sqrt{3})k_t \tag{4.71}$$

and the alternative term linear Mohr-Coulomb can be found in literature.

4.4 Flow Rule

The flow rule, which allows the evaluation of the plastic strain increments, in its general form is given by

$$d\mathbf{e}^{\text{pl}} = d\lambda \mathbf{r}(\boldsymbol{\sigma}, \mathbf{q}), \quad (4.72)$$

where $d\lambda$ is a scalar called the plastic multiplier or consistency parameter and function $\mathbf{r}(\boldsymbol{\sigma}, \mathbf{q}) : (\mathbb{R}^6 \times \mathbb{R}^{\dim(\mathbf{q})}) \rightarrow \mathbb{R}^6$ is the plastic flow direction. The plastic flow direction is often stated in terms of a plastic potential function Q , and the plastic strain increments are given by $d\mathbf{e}^{\text{pl}} = d\lambda \frac{\partial Q}{\partial \boldsymbol{\sigma}}$. The flow is said to be associated if $Q = F$, otherwise non-associated.

The evolution equation for the internal variables \mathbf{q} can be specified in its general form as

$$d\mathbf{q} = d\lambda \mathbf{h}(\boldsymbol{\sigma}, \mathbf{q}), \quad (4.73)$$

where the function $\mathbf{h} : (\mathbb{R}^6 \times \mathbb{R}^7 \rightarrow \mathbb{R}^7)$ describes the evolution of the hardening parameters.

4.5 Hardening Rule

The hardening rule allows the consideration of the influence of material hardening on the yield condition and the flow rule.

4.5.1 Isotropic Hardening

In the case of isotropic hardening, the yield stress is expressed as being dependent on an inner variable κ :

$$k = k(\kappa). \quad (4.74)$$

This results in the effect that the size of the yield surface is scaled but the origin remains unchanged. If the equivalent plastic strain⁶ is used for the hardening variable ($\kappa = \varepsilon_{\text{eff}}^{\text{pl}}$), then one talks about strain hardening.

Another possibility is to describe the hardening being dependent on the specific⁷ plastic work ($\kappa = w^{\text{pl}} = \int \boldsymbol{\sigma} d\mathbf{e}^{\text{pl}}$). Then one talks about work hardening.

⁶ The effective plastic strain is in the general three-dimensional case the function $\varepsilon_{\text{eff}}^{\text{pl}} : (\mathbb{R}^6 \rightarrow \mathbb{R}_+)$ with $\varepsilon_{\text{eff}}^{\text{pl}} = \sqrt{\frac{2}{3} \mathbf{e}^{\text{pl}} \mathbf{e}^{\text{pl}}}$.

⁷ This is the volume-specific definition, meaning $[w^{\text{pl}}] = \frac{\text{N}}{\text{m}^2} \frac{\text{m}}{\text{m}} = \frac{\text{kg m}}{\text{s}^2 \text{m}^2} \frac{\text{m}}{\text{m}} = \frac{\text{kg m}^2}{\text{s}^2 \text{m}^3} = \frac{\text{J}}{\text{m}^3}$.

Fig. 4.20 Flow curve for different isotropic hardening laws. The abscissa is drawn for the case of strain hardening

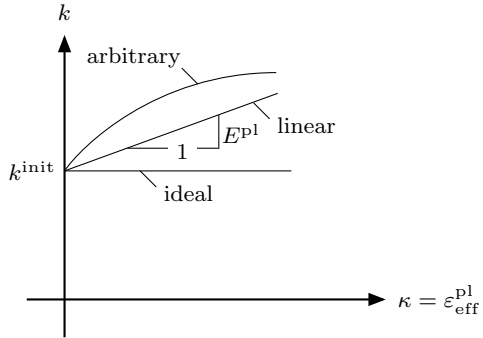


Figure 4.20 shows different modeling approaches for the flow curve, meaning the graphical illustration of the yield stress being dependent on the inner variable for different hardening approaches.

4.5.2 Kinematic Hardening

In the case of pure kinematic hardening, the yield condition is expressed as being dependent on a set of inner variables:

$$F(\boldsymbol{\sigma}, \boldsymbol{\alpha}) = f(\boldsymbol{\sigma} - \boldsymbol{\alpha}) - k = 0, \tag{4.75}$$

where the material parameter k is constant and the kinematic hardening parameters $\boldsymbol{\alpha}$ are dependent on inner variables. These hardening parameters represent the center of the yield surface and result in the effect that the surface translates as a rigid body in the stress space.

References

Altenbach H, Altenbach J, Zolochovsky A (1995) *Erweiterte Deformationsmodelle und Versagenkriterien der Werkstoffmechanik*. Deutscher Verlag für Grundstoffindustrie, Stuttgart

Altenbach H (2012) *Kontinuumsmechanik: Einführung in die materialunabhängigen und materialabhängigen Gleichungen*. Springer, Berlin

Altenbach H, Öchsner A (eds) (2020) *Encyclopedia of continuum mechanics*. Springer, Berlin

Asaro RJ, Lubarda VA (2006) *Mechanics of solids and materials*. Cambridge University Press, Cambridge

Backhaus G (1983) *Deformationsgesetze*. Akademie-Verlag, Berlin

Betten J (1987) *Tensorrechnung für Ingenieure*. Teubner Verlag, Stuttgart

Betten J (2001) *Kontinuumsmechanik*. Springer, Berlin

- Chen WF, Han DJ (1988) Plasticity for structural engineers. Springer, New York
- Chen WF, Zhang H (1991) Structural plasticity: theory, problems, and CAE software. Springer, New York
- Gurson AL (1977) Continuum theory of ductile rupture by void nucleation and growth: part I—yield criteria and flow rules for ductile media. *J Eng Mater-T ASME* 99:2–15
- Itskov M (2009) Tensor algebra and tensor analysis for engineers: with applications to continuum mechanics. Springer, Berlin
- Lurie AI, Belyaev A (2005) Theory of Elasticity. Springer, Berlin
- Moore TA (2013) A general relativity workbook. University Science Books, Mill Valley
- Nash WA (1998) Schaum's outline of theory and problems of strength of material. McGraw-Hill, New York
- Nayak GC, Zienkiewicz OC (1972) Convenient form of stress invariants for plasticity. *J Struct Div-ASCE* 98:1949–954
- Öchsner A (2003) Experimentelle und numerische Untersuchung des elastoplastischen Verhaltens zellulärer Modellwerkstoffe. VDI-Verlag, Düsseldorf
- Öchsner A (2016) Continuum damage and fracture mechanics. Springer, Singapore
- Suzuki H, Ninomiya T, Sumino K, Takeuchi (1985) Dislocation in solids: proceedings of the IX Yamada. VNU Science Press, Utrecht

Part II
Specialized Lectures

Chapter 5

Influence of Silicon Content on the Mechanical Properties of Additively Manufactured Al-Si Alloys



Enes Sert, Philippe du Maire, Elmar Schuch, Leonhard Hitzler,
Ewald Werner, and Andreas Öchsner

Abstract One research area of additive manufacturing is material development and property optimisation, being investigated in our study through static mechanical tests. The materials tested are Al-Si alloys with 8–16 wt.% Si, without any other alloying elements. Tensile strengths achieved for the different materials are between 263 and 411 MPa. For AlSi16, the maximum tensile strength of 411 MPa was achieved at an elongation to fracture of 6.2%. Furthermore, the suitability of the individual powder batches for additive manufacturing was investigated by determining the flow function of the powder batches. Flow properties, particle size distribution and hardness were determined using additively manufactured cubes. A hardness of 149.7 HV10 was achieved for the alloy AlSi16.

Keywords Selective laser melting · Al-Si alloys · Tensile test · Flow properties · Particle size distribution

E. Sert (✉) · P. du Maire · E. Schuch · A. Öchsner
Faculty of Mechanical and Systems Engineering, Esslingen University of Applied Sciences,
73728 Esslingen, Germany
e-mail: enes.sert@hs-esslingen.de

P. du Maire
e-mail: philippe.du-maire@hs-esslingen.de

E. Schuch
e-mail: elmar.schuch@hs-esslingen.de

A. Öchsner
e-mail: andreas.oechsner@hs-esslingen.de

E. Sert · L. Hitzler · E. Werner
School of Engineering and Design, Institute of Materials Science and Mechanics of Materials,
Technical University of Munich, 85748 Garching, Germany
e-mail: hitzler@wkm.mw.tum.de

E. Werner
e-mail: werner@wkm.mw.tum.de

P. du Maire
Faculty of Aerospace Engineering, Universität der Bundeswehr München, 85748 Neubiberg,
Germany

5.1 Introduction

Additive manufacturing offers unique opportunities to produce complex components which are impossible or very difficult to realise using conventional manufacturing processes (Sert et al. 2018). The potential of additive manufacturing of aluminium alloys is already recognised in prototyping, but still holds potential in regard to the optimisation of the materials used and, above all, mass production.

AlSi10Mg represents the most frequently used alloy for selective laser melting (Drossel et al. 2018; Buchbinder et al. 2011; Buchbinder 2013) followed by AlSi12 (Siddique et al. 2015; Rashid et al. 2018). For both alloys, the mechanical properties of die-cast components are well known (Kaufman 1999). First, approaches to investigate the mechanical properties of additively manufactured Al-Si alloys under static and fatigue conditions have been carried out. AlSi10Mg and AlSi12 alloys are not optimised for additive manufacturing, as they were developed and optimised for casting (Drossel et al. 2018; Hitzler et al. 2018). The knowledge of the suitability of these alloys for additive manufacturing is therefore urgent, as in some cases significantly different properties of the material are required.

An examination of the microstructure of these alloys shows very fine-grained structures due to the high cooling rate in selective laser melting (Sert et al. 2019a, b; Olakanmi et al. 2015). In the eutectic or near-eutectic casting alloys AlSi12 and AlSi10Mg, refining alloying elements such as Na, Sr or Sb are added to achieve a fine eutectic. It is to be investigated whether these alloying elements are also necessary for additively produced Al-Si alloys or if they can be avoided. The alloys also contain other alloying elements, e.g. Fe, Mn and Cu, which are mainly added to improve process reliability during casting and may not be necessary in additive manufacturing (DIN EN 1706, 2010). An increase in the strength of additively manufactured AlSi10Mg is not achieved by precipitation hardening via post-heat treatment to the same extent as in their cast counterparts (Buchbinder et al. 2009). Solution annealing leads to coarsening of the very fine microstructure produced by additive manufacturing, especially true for the eutectically formed Si. As a result, strength decreases significantly, whilst ductility increases. Ageing at 150 °C for 10 h following additive manufacturing leads to a slightly better elongation to fracture of 6% compared to 3% in the additively manufactured state without a further loss in strength (Rowolt 2020). Furthermore, the annealing conditions strongly depend on the manufacturing parameters, e.g. the preheating temperature and the dwell time at these elevated temperatures.

Rapid cooling of melts shifts the eutectic point of Al-Si alloys to higher Si contents (Altenpohl 2005; Hanna et al. 1984). As a result, a high proportion of primary Al-Si solid solution is observed in the microstructure of additively produced AlSi12, an alloy that is eutectic at equilibrium cooling conditions (Siddique et al. 2015). The question arises at which Si content, the additively produced Al-Si alloy, shows a purely eutectic microstructure and how its proportion affects the properties of such alloys. The optimum proportions of eutectic and primary α -solid solution must be determined in order to achieve an optimum balance of strength and ductility, since

a minimum proportion of primary α -Al solid solution is required to ensure ductility. The fine-grained microstructure achieved in additive manufacturing gives hope to reach this goal.

Accordingly, from a technical point of view, a strength–ductility-optimised and wear-resistant aluminium alloy without an addition of expensive or structurally weakening alloying elements could be derived.

In this study, five different Al-Si alloys without further alloying elements are investigated. First, the quality and, thus, the applicability for additive manufacturing, specifically in laser powder bed fusion (LPBF), of the different powder batches are examined. Subsequently, hardness measurements and tensile tests are carried out. Finally, the results of these tests are compared to those of available cast aluminium alloys.

5.2 Experimental Methods

5.2.1 Sample Preparation

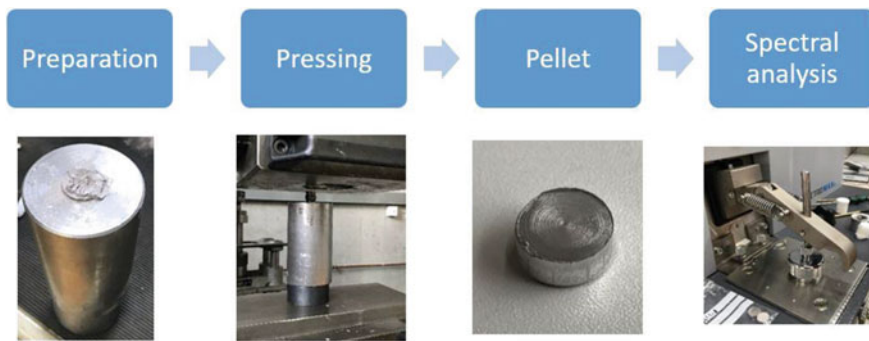
A TruPrint 3000 (TRUMPF Laser- und Systemtechnik GmbH, Ditzingen, Germany) equipped with a 500 W ytterbium fibre laser was employed for the production of the AlSi8, AlSi10, AlSi12, AlSi14 and AlSi16 samples. The laser beam diameter at the focal point was 100 μm , and the available build volume was $\text{\O} 300 \times 400 \text{ mm}^3$. An inert environment was realised with argon, with the residual oxygen content being kept below 0.1%, and the substrate plate was held at 200 °C during production. It should be mentioned that, depending on the component to be tested, the effectiveness of the heat transport via the thermal coupling of the molten bath and the sample material to the support structure varies. Given the fact that the powder bed acts like an insulation compared to solid metal due to its thermal conductivity being magnitudes lower, the thermal coupling is primarily governed by the interaction between the regulation system in the mounting plate and the component, connected via the substrate plate and the support structure. The cooling rate from layer to layer is not constant, and the effective temperature of the actively fabricated layer can deviate from the preset temperature of the installation space, becoming more pronounced with increasing height of the component. Previous experiments have shown a resulting stationary temperature of 130 °C in the powder bed, measured 10 mm above the substrate plate, at a preset temperature of 200 °C (Hitzler et al. 2017). Hence, an effective build temperature of 130 °C is assumed. For the samples (five samples per metal powder batch), five metal powder batches according to the specification of Eckart TLS GmbH with a particle size of 20–60 μm were used. The samples were produced with their longitudinal axis oriented perpendicular to the substrate plate. The process parameter set used is listed in Table 5.1. The nomenclature is in accordance with the standardisation of the samples for comprehensive experiments proposed by Buschermöhle (1995).

Table 5.1 Applied process parameters for the processing of all metal powder batches

	Scanning speed (mm/s)	Laser power (W)	Hatch spacing (mm)	Rotation angle (°)
Core	1750	360	0.05	67

5.2.2 Chemical Analysis

The spectral analysis of the powders (SPECTROMAXx, SPECTRO Analytical Instruments GmbH) was carried out on pressed powder pellets. The pellets were produced by compressing the powder with a force of 250 kN. Three pellets were produced per batch, and three measurements were carried out on each pellet. This results in a total of nine measured values per batch, from which the averaged results were determined. Figure 5.1 shows the processing steps.

**Fig. 5.1** Process steps for the production and analysis of the pellets

5.2.3 Flowability

The analysis of the flow behaviour of the powders was carried out with a Modular Compact Rheometer (Anton Paar Germany GmbH, Ostfildern, Germany). A so-called powder cell was used. In this powder cell, the powder was fluidised by a gas volume flow, which helps to overcome gravity and interparticle forces. This is followed by the transition from static bulk material behaviour to dynamic fluid-like properties. Subsequently, the cohesive strength between powder particles was determined with the help of a two-blade stirrer. The cohesive strength is a measure of the flowability, or the internal flow resistance, of the aerated powder. During the measurement, the torque of the stirrer is recorded, and the average value of the last 20 data points is used to calculate the cohesive strength.

The flowability of a bulk material is characterised by the bulk strength σ_c as a function of the consolidation stress σ_1 and the storage time. The ratio ff_c of consolidation stress σ_1 to bulk strength σ_c is usually used as a characteristic index for flowability (Jenike 1964; Schulze 2019)

$$ff_c = \frac{\sigma_1}{\sigma_c} \quad (5.1)$$

The higher the ff_c is, i.e. the smaller the bulk strength is in relation to the consolidation stress, the better a bulk material flows. In an extension of Jenike's classification (Jenike 1964), the flow behaviour can be characterised according to Schulze as follows (Schulze 2019):

$ff_c < 1$	not flowing
$1 < ff_c < 2$	very cohesive
$2 < ff_c < 4$	cohesive
$4 < ff_c < 10$	easy flowing
$10 < ff_c$	free flowing

In order to classify the flowability via the flow function ff_c , it is necessary to determine the compressive strength. For this purpose, the Warren-Spring cohesion was determined using the rheometer (Ashton et al. 1965). The Warren-Spring cohesion is a measure of the flowability of compacted powders in case of cohesive powders. First, the powder is consolidated with a permeable plate, and then a stirrer with a Warren-Spring geometry is used to penetrate and shear the surface. The maximum of the shear curve represents the beginning of the flow. The resulting maximum shear stress at "failure" (i.e. where the powder starts to flow) is used to calculate the Warren-Spring cohesion. Additionally, it detects changes in formulation by first consolidating and then shearing the powder.

5.2.4 Particle Size Distribution

In order to be able to determine the particle size distribution, the image processing toolbox was used to recognise objects in images with MATLAB. The following list shows the basic steps that are carried out by the MATLAB program:

1. Reading the image into the workspace.
2. Sharpening of the image and preparation of the particle edges.
3. Converting the image into a binary form.
4. Applying a mask to split connected particles.
5. Determine the edges of the particles and draw their outlines.
6. Determine the area and perimeter of the outlined particles.
7. Calculate the maximum distance between two pixels that lie on the perimeter. This distance is the major axis of the ellipse.
8. Calculate the minor axis of the ellipse that is perpendicular to the major axis.

9. Write the values into a text file and read them into the script for statistical evaluation.

5.2.5 *Hardness*

Hardness of the built samples was determined according to the Vickers method (DIN EN ISO 6507-1) with the following settings:

- Test load: 100 N
- Dwell time: 12 s.

In order to eliminate an influence of the support structure on the test results and to ensure comparability across all materials, the surfaces of the built samples were ground in four steps (step 1: SI-C-paper, 120 grit; step 2: SI-C-paper, 320 grit; step 3: SI-C-paper, 600 grit; step 4: SI-C-paper, 1200 grit) and then polished in two steps (step 1: Sigma-paper with diamond lubricant 3 μm ; step 2: SAPHIR VIBRO with Eposil M). The hardness testing machine was manually operated, and it was ensured that the indents were located at sufficient distance from neighbouring indents. In order to be able to characterise the difference between hardness parallel and perpendicular to the layering, the hardness measurements were carried out parallel and perpendicular to the layering.

5.2.6 *Tensile Tests*

The tensile tests were carried out on a Zwick/Roell type Z100 testing machine with a load capacity of 100 kN. Before testing, the specimens were deburred with abrasive paper (Kingspor KL361JF, 320 grit, 25 mm wide) to remove possible crack initiation sites activated during mechanical loading (Sert et al. 2019b, 2020). During the tensile tests, the change in length was measured with a BTC-EXMULTI.010 multi-extensometer. In addition, Young's modulus of each specimen was determined cyclically with five measurements in the linear elastic range, for which the stress was approached to the point of the start of measurement at 10 MPa with 10 mm/min (displacement controlled) and subsequently tested at 20 MPa/s (stress controlled). The upper stress was limited to 100 MPa, and Young's modulus was evaluated between 20 and 80 MPa using the linear regression method. A full tensile test to failure was then carried out to determine the yield strength $R_{p0.2}$, the tensile strength R_m and the elongation at failure A_t according to DIN EN ISO 6892-1: 2017-02.

Table 5.2 Average chemical composition in mass percentage

Materials	Al	STDEV	Si	STDEV	Fe	STDEV
AlSi8	91.744	0.201	7.952	0.219	0.158	0.007
AlSi10	90.230	0.136	9.469	0.123	0.172	0.007
AlSi12	87.994	0.303	11.774	0.300	0.153	0.003
AlSi14	86.671	0.218	13.051	0.217	0.167	0.005
AlSi16	84.489	0.388	15.217	0.385	0.177	0.003

STDEV is the standard deviation

5.3 Results and Discussion

5.3.1 Chemical Analysis

Through spectral analysis, the composition of the bulk material was verified (see Table 5.2). Traces (residues) of other (unwanted) elements should be avoided through the use of elemental aluminium powder. However, we found traces of Fe present in the powder batches. Unfortunately, it was not possible to procure the powder batches without Fe contamination, but since the amount of Fe was less than <0.2%, this contamination could be considered as uncritical.

5.3.2 Flowability

A rheometer with a powder cell was used to determine the cohesion strength and Warren-Spring cohesion of the individual metal powder batches. Figure 5.2 shows the cohesion strength and Fig. 5.3 the Warren-Spring cohesion.

As described in Sect. 5.2.2, the flow function ff_c is defined by the bulk strength and the consolidation stress. The bulk strength is derived from the cohesion strength. The theoretical background of this measurement is based on the Mohr–Coulomb theory on stresses in powder beds. The consolidation stress is derived from the Warren-Spring cohesion. This results in the values for the flowability listed in Table 5.3.

All powder batches are “easy flowing” according to the flow function classification and thus are suitable for additive manufacturing.

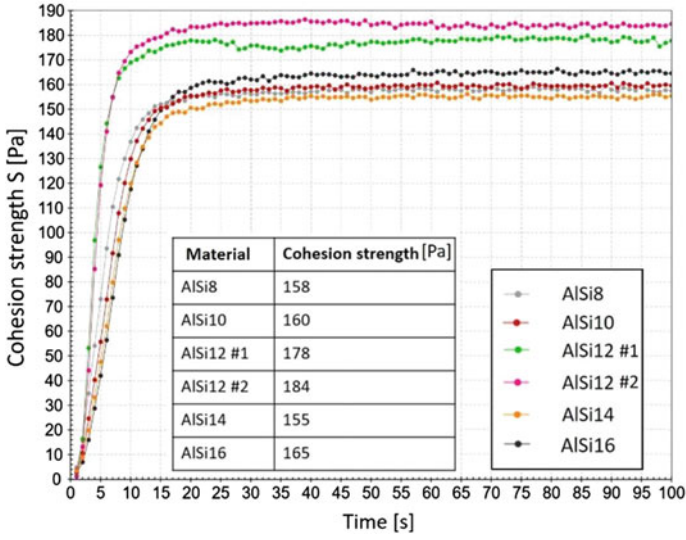


Fig. 5.2 Cohesion strength diagram for all materials

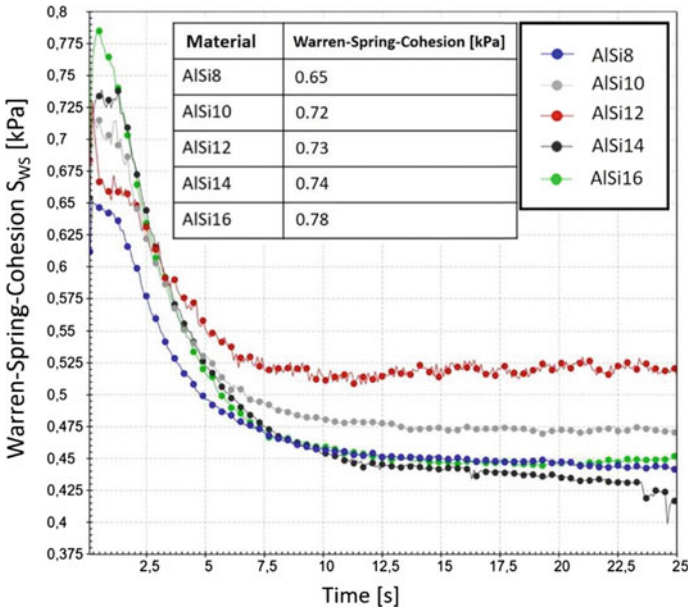


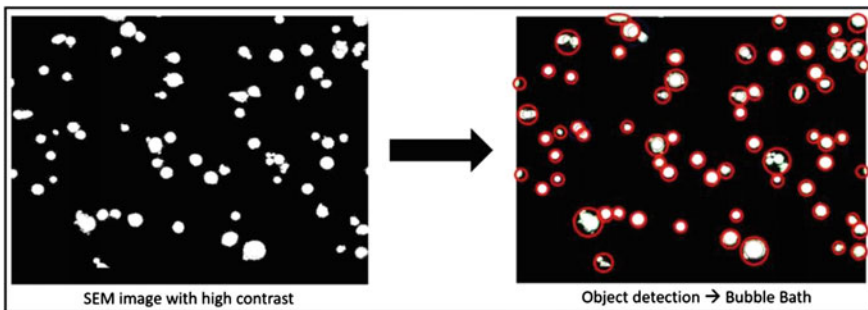
Fig. 5.3 Warren-Spring cohesion diagram for all materials

Table 5.3 Flow function ff_c determined for all five Al-Si alloys

Alloy	ff_c
AlSi8	4.11
AlSi10	4.50
AlSi12	4.10
AlSi14	4.77
AlSi16	4.72

5.3.3 Particle Size Distribution

The verification of the results of the object detection algorithm is important for meaningful statistics. For this purpose, a so-called bubble bath was generated in MATLAB. The program plots white circles on a black background. It should be noted that not all circles are found on closer inspection. Circles that overlap or adhere directly to the outer edge of the image were not detected (see Fig. 5.4).

**Fig. 5.4** SEM image with high contrast and object detection “bubble bath”

The statistical evaluation of the particle size distribution is following the standard ISO 9276-1:1998. The first diagram is a histogram of the particle size. The ordinate shows the relative frequency. The length of the axes of the equivalent ellipses is plotted on the abscissa in units of μm . The second diagram is the approximated distribution of representative ellipses based on their minor axis. The ordinate shows the cumulative relative frequency and the abscissa the length of the major axes in μm . The last diagram according to ISO 9276-1:1998 is the continuous distribution density function.

The normal distribution function of the powder batch AlSi8 according to ISO 9276-1:1998 is shown schematically in Fig. 5.5. The values for all powder batches are listed in Table 5.4. Depending on the consideration of the STDEV, the particular value of the minor axis might get larger than the particular value of the major axis. Thus, the naming should be changed in such a case from minor to major axis.

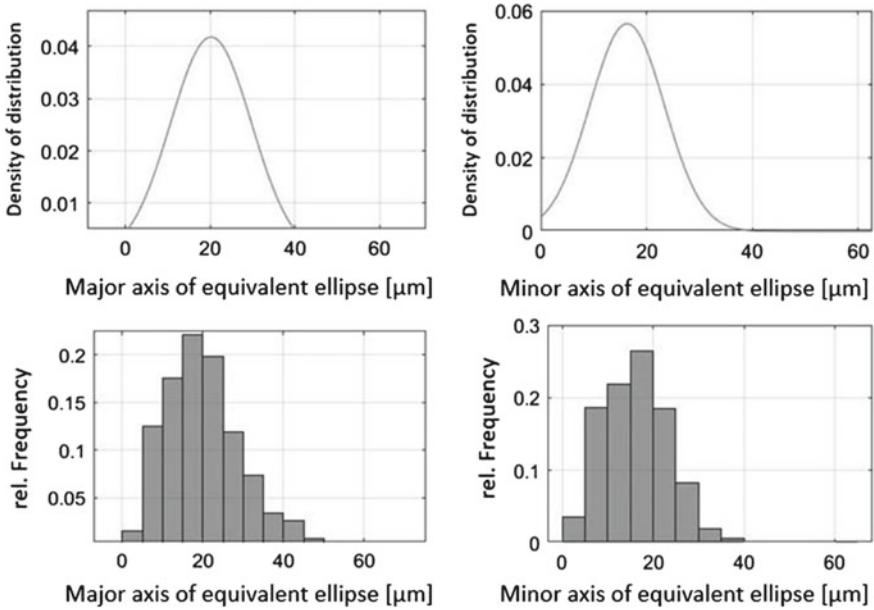


Fig. 5.5 Schematic representation of the particle size distribution of AlSi8 according to the normal distribution function

Table 5.4 Determined particle sizes of all powder batches

Materials	Average major axis of equivalent ellipse (μm)	STDEV	Average minor axis of equivalent ellipse (μm)	STDEV
AlSi8	20.2	9.6	16.3	7.1
AlSi10	18.9	10.8	15.3	8.7
AlSi12	40.5	18.4	33.7	14.9
AlSi14	15.3	10.7	12.4	8.3
AlSi16	11.5	5.4	9.1	4.1

STDEV is the standard deviation

5.3.4 Hardness

Hardness is often employed to estimate the wear resistance of materials. The results of the hardness measurements, performed parallel and perpendicular to the layers, are shown in Fig. 5.6.

The powder batches AlSi8 and AlSi10 are hypoeutectic, whilst AlSi14 and AlSi16 are hypereutectic alloys. The powder batch AlSi12 is the near-eutectic alloy. Comparing the hardness values of the individual powder batches, it is evident that hardness increases with silicon content. The near-eutectic AlSi12 alloy has similar hardness values as the hypereutectic AlSi14 alloy. Sert et al. (2019a) investigated the

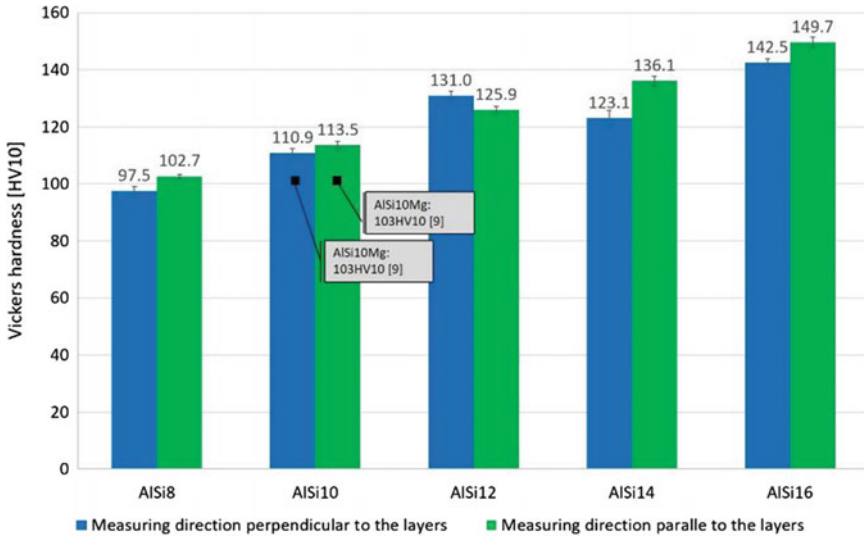


Fig. 5.6 Hardness results of the Al-Si alloys in perpendicular and parallel directions to the layers

hardness of the alloy AISi10Mg containing the common alloying elements. Hardness values of 103HV10 were determined in both perpendicular and parallel directions. Comparing the results with this current study, the hardness of the materials investigated in the study at hand is about 10% higher.

5.3.5 Tensile Properties

The results of tensile tests are given in Table 5.5. Similar to the hardness results, tensile strength increases with silicon content, whilst the elongation at failure decreases.

Table 5.5 Average results for mechanical properties; tensile tests according to DIN EN ISO 6892-1: 2017-02 measured at room temperature

Materials	Young’s modulus E (GPa)		Yield strength $R_{p0.2}$ (MPa)		Ultimate tensile strength R_m (MPa)		Elongation at failure A_t (%)	
	Average	STDEV	Average	STDEV	Average	STDEV	Average	STDEV
AISI8	68.4	0.3	200	0.2	263	0.5	10	1.2
AISI10	70.2	0.3	212	0.7	307	0.6	8.5	0.3
AISI12	72.3	0.1	233	1.7	341	0.9	7.5	1.0
AISI14	72.6	0.4	251	2.1	376	4.2	5.1	1.2
AISI16	73.9	0.3	276	0.9	411	0.9	6.2	0.3

STDEV is the standard deviation

Table 5.6 Comparison of strength values of AlSi10 determined in this study, whilst those reposted in literature for AlSi10Mg

Study	Young's modulus E (GPa)	Yield strength $R_{p0.2}$ (MPa)	Ultimate tensile strength R_m (MPa)	Elongation at failure A_t (%)
	Average	Average	Average	Average
Aboukair et al. (2016)	77.0	268	333	1.4
Aversa et al. (2017)	–	246	362	4.4
Buchbinder et al. (2015)	–	150	250	4.0
Hitzler et al. (2017)	70.4	209	357	3.2
This study	70.2	212	307	8.5

The aim of this study is to investigate the influence of the silicon content on the mechanical properties. Furthermore, a comparison can be made between AlSi10Mg containing the common alloying elements and AlSi10 without alloying elements investigated in this study, as given in Table 5.6.

The chemical composition of the AlSi10Mg alloy influences the mechanical, physical and casting properties. The following can be reported:

- Magnesium (Mg) contributes mainly to the strength of AlSiMg alloys. The formation of precipitation phases during natural or artificial ageing significantly increases strength through the mechanism of precipitation hardening. In addition to the strength properties, hardness also increases with magnesium content. In contrast, the elongation at failure decreases with the content of Mg (Ostermann 2007; Ross and Maile 2002).
- Copper (Cu) improves the machining properties, but a too high copper content leads to a reduction in corrosion resistance and ductility (Tschirnich 2005).
- Manganese (Mn) is used to minimise mould adhesion during die casting. Furthermore, additions above 0.8% degrade mechanical properties as well as castability (Kitaoka 1995).
- Sodium (Na) and strontium (Sr) refine the residual eutectic (eutectic silicon), resulting in a fine-grained structure. The shape of Si particles changes from coarse plates to fine fibres (Closset and Gruzleski 1982).

Manganese is used to improve casting. In additive manufacturing, there is no casting mould; thus, alloying elements that reduce the adhesion of the component on the casting mould can be avoided. The addition of Cu can also be avoided in additive manufacturing, as the problem of lubrication is considered to be less important for higher Si contents. In addition, additive manufacturing is used for near-net-shape production, where machining is minimised as far as possible. Due to the high cooling rates of 10^6 – 10^8 K/s achieved in the laser powder bed fusion, LPBF materials have

extremely fine microstructures, which leads to excellent static mechanical properties in materials that are not prone to stress cracking at high cooling rates. Hence, refining elements such as Na and Sr also can be avoided.

5.4 Conclusions

The basis of this study is Al-Si alloys that exclude the common alloying elements Mg, Cu, Mn, Na and Sr. Powders from these alloys were investigated rheologically to investigate their applicability in selective laser melting. Furthermore, the influence of the silicon content on the strength properties was determined. The following conclusions can be drawn from the results:

1. The exclusion of the alloying elements Mg, Cu, Mn, Na and Sr has no negative influence on the flowability of the powder batches, and therefore, such powders are suitable for selective laser melting.
2. Hardness measurements perpendicular and parallel to the layers showed no significant differences, which seems to be a direct consequence of the homogeneous microstructure.
3. It was found that an increase in silicon content significantly affects strength properties. For example, AlSi16 has a tensile strength of 411 MPa and an elongation to failure of 6.2%.
4. The elongation to failure was also influenced by the silicon content. The elongation to failure decreased continuously from AlSi8 to AlSi14. For AlSi16, an increase in ductility could be observed. This increase will be examined in more detail in ongoing investigations.

Acknowledgements The authors thank BKL Lasertechnik GmbH for producing the samples and Anton Paar GmbH for making the rheometer tests possible and for sharing their knowledge.

This project is supported by the Federal Ministry for Economic Affairs and Climate Action (BMWK) on the basis of a decision by the German Bundestag.

References

- Aboulkhair NT, Maskery I, Tuck C et al (2016) The microstructure and mechanical properties of selectively laser melted AlSi10Mg: the effect of a conventional T6-like heat treatment. *Mater Sci Eng* 667:139–146
- Altenpohl DG (2005) *Aluminium von innen: das Profil eines modernen Metalles*, 5. Neubearbeitete und erweiterte Auflage. Aluminium-Verlag, Düsseldorf
- Ashton MD, Cheng DCH, Farley R et al (1965) Some investigations into the strength and flow properties of powder. *Rheol Acta* 4:206–218
- Aversa A, Lorusso M, Trevisan F et al (2017) Effect of process and post-process conditions on the mechanical properties of an A357 alloy produced via laser powder bed fusion. *Metals* 7(2):68

- Buchbinder D (2013) Selective Laser Melting von Aluminiumgusslegierungen. Dissertation, RWTH Aachen
- Buchbinder D, Meiners W, Wissenbach K et al (2009) Rapid manufacturing of aluminium parts for serial production via selective laser melting (SLM). In: 4th international conference on rapid manufacturing, Loughborough
- Buchbinder D, Meiners W, Brandl E et al (2011) Abschlussbericht—Generative Fertigung von Aluminiumbauteilen für die Serienproduktion. Fraunhofer ILT
- Buchbinder D, Meiners W, Wissenbach K et al (2015) Selective laser melting of aluminum die-cast alloy—correlations between process parameters, solidification conditions, and resulting mechanical properties. *J Laser Appl* 27(S2):S29205
- Buschermöhle H (1995) Vereinheitlichung von Proben für Schwingversuche: Abschlussbericht. FKM-Verlag, Frankfurt a.M.
- Closset B, Gruzleski JE (1982) Structure and properties of hypoeutectic Al-Si-Mg alloys modified with pure strontium. *Metall Mater Trans A* 13(6):945–951
- (DIN) Deutsches Institut für Normung e.V., DIN EN 1706 (2010) Aluminium und Aluminiumlegierungen—Gussstücke—Chemische Zusammensetzung und mechanische Eigenschaften. Beuth, Berlin
- Drossel G, Friedrich S, Kammer C et al (2018) Das Aluminium Taschenbuch 2: Umformen, Gießen, Oberflächenbehandlung, Recycling, 17. Auflage. Beuth, Berlin
- Hanna MD, Lu S-Z, Hellawell A (1984) Modification in the aluminum silicon system. *Metall Trans A* 15(3):459–469
- Hitzler L, Janousch C, Schanz J et al (2017) Direction and location dependency of selective laser melted AlSi10Mg specimens. *J Mater Process Technol* 243:48–61
- Hitzler L, Merkel M, Hall W et al (2018) A review of metal fabricated with laser- and powder-based additive manufacturing techniques: process, nomenclature, materials, achievable properties, and its utilization in the medical sector. *Adv Eng Mater* 20(5):1700658
- Jenike AW (1964) Storage and flow of solids, Bull. No. 123. Engineering Experiment Station, University of Utah, Salt Lake City
- Kaufman JG (1999) Properties of aluminum alloys tensile creep and fatigue data at high and low temperatures. ASM International Materials Park, Ohio
- Kitaoka S (1995) Wear resistant cast aluminium alloy and process of producing same. Patentschrift EP 0 672 760 A1
- Olakanmi EO, Cochrane RF, Dalgarno KW (2015) A review on selective laser sintering/melting (SLS/SLM) of aluminium alloy powders: processing, microstructure, and properties. *Prog Mater Sci* 74:401–477
- Ostermann F (2007) Anwendungstechnologie Aluminium. Springer Verlag
- Rashid R, Masood S, Ruan D et al (2018) Effect of energy per layer on the anisotropy of selective laser melted AlSi12 aluminium alloy. *Addit Manuf* 22:426–439
- Ross E, Maile K (2002) Werkstoffe für Ingenieure—Grundlagen, Anwendungen, Prüfungen. Springer Verlag
- Rowolt C (2020) Untersuchungen zur Wärmebehandlung additiv gefertigter, metallischer Bauteile auf Basis von in-situ Analysen der Phasenumwandlungen. Dissertation, University of Rostock
- Schulze D (2019) Fließigenschaften von Schüttgütern. In: Pulver und Schüttgüter: Fließigenschaften und Handhabung. Springer Berlin Heidelberg, pp 53–98
- Sert E, Hitzler L, Merkel M et al (2018) Entwicklung von topologieoptimierten Adapterelementen für die Fertigung mittels additiver Verfahren: Vereinigung von reinelektrischem Antriebsstrang mit konventionellem Chassis. *Mater Sci Technol* 49(5):674–682
- Sert E, Hitzler L, Heine B et al (2019a) Influence of the heat treatment on the microstructure and hardness of additively manufactured AlSi10Mg samples. *Pract Metallogr* 56(2):91–105
- Sert E, Schuch E, Öchsner A et al (2019b) Tensile strength performance with determination of the Poisson's ratio of additively manufactured AlSi10Mg samples. *Mater Sci Technol* 50(5):539–545
- Sert E, Hitzler L, Hafenstein S et al (2020) Tensile and compressive behaviour of additively manufactured AlSi10Mg samples. *Prog Addit Manuf* 5(3):305–313

Siddique S, Imran M, Walther F (2015) Influence of process-induced microstructure and imperfections on mechanical properties of AlSi12 processed by selective laser melting. *J Mater Process Technol* 221:205–213

Tschirnich M (2005) Einsatz neuer Strategien bei der Werkstoffmodellierung von Aluminiumlegierungen in der Warmumformung. Dissertation, RWTH Aachen

Chapter 6

Multi-step Additive Manufacturing Technologies Utilizing the Powder Metallurgical Manufacturing Route



Arne Davids, Lukas Apfelbacher, Leonhard Hitzler,
and Christian Krempaszky

Abstract Single-step additive manufacturing processes, such as laser powder bed fusion, are capable of producing metal parts within one step by full melting of the feedstock while also generating the geometric shape. However, due to high cooling rates residual stresses and related distortions pose challenges, especially in high strength materials, like tooling steels or hard metals. In multi-step additive manufacturing followed by sintering, components are produced in sequential steps divided into a shaping step achieved by additive manufacturing and a material consolidation step through sintering. Unlike in single-step processes, the material properties obtained by sintering are isotropic, and the extent of residual stresses are uncritical. Additionally, multi-step additive manufacturing is also capable of processing ceramics and metals unsuitable for welding. This review provides an overview about relevant aspects of additive manufacturing categories used in multi-step AM toward sinter-based parts, namely vat photopolymerization (VPP), material extrusion (MEX) and binder jetting (BJ). In principle, these AM technologies are generally similar in utilizing a polymeric binder material as matrix for the powder material, but due to the inherent process differences, the specifications of the binder materials differ significantly, as shown in this study.

A. Davids (✉) · L. Apfelbacher · L. Hitzler · C. Krempaszky
Institute of Materials Science and Mechanics of Materials, Technical University of Munich,
Boltzmannstraße 15, 85748 Garching, Germany
e-mail: arne.davids@tum.de

L. Apfelbacher
e-mail: lukas.apfelbacher@tum.de

L. Hitzler
e-mail: leonhard.hitzler@tum.de

C. Krempaszky
e-mail: krempaszky@tum.de

6.1 Introduction

Additive manufacturing (AM) has become a key technology for the product development process. Predominantly, additive manufacturing is used for rapid prototyping; however, it is increasingly utilized throughout the whole product development and manufacturing process. The broad use of AM technologies is derived from their potential to greatly reduce the number of manufacturing steps to fabricate prototypes or components, for which conventional technologies may need several steps (i.e., different machines, reclamping of the workpiece, tool changes, etc.) to achieve similar part complexity. Other advantages are opportunities of weight saving, material property optimization and embedded functionality without any additional costs. Single-step AM processes which fully melt the feedstock are most wide-spread based on their industrial use and conducted research. However, a downside of these processes are residual stresses and related distortions that are well-known phenomena in welding processes (DebRoy et al. 2018; Hitzler et al. 2018). Since multi-step AM processes utilize a non-metallic binder to generate the part shape and the consolidation takes place in a followed and uniform sintering process, residual stresses are far less. Other driving forces for the adaption of multi-step AM are cost reduction, material availability and continuous innovation.

The aim of the present study is to characterize the multi-step AM technologies vat photopolymerization (VPP), material extrusion (MEX) and binder jetting (BJT) and to provide an overview about their strengths and weaknesses. Apart from describing key-process characteristics, a special focus is set on used binder materials, as it plays a key role in shaping process and also influences the material properties of the final sintered part.

6.2 Metal Additive Manufacturing

Metal AM technologies use metal feedstock, such as powder, wire or metal and binder mixtures to produce three-dimensional (3D) parts by progressively adding material. According to the ISO/ASTM 52900–2022 standard, metal AM technologies can be divided into single-step and multi-step AM processes, see Fig. 6.1.

6.2.1 *Single-Step AM Technologies*

Single-Step AM technologies generate the shape and material properties simultaneously. Metal AM technologies that are considered as single-step AM processes are: powder bed fusion technologies, which fully melt the metal powder; direct energy deposition, which deposits the loose feedstock (powder or wire) together with energy for melting; and material jetting, which ejects molten metal droplets (similar to the

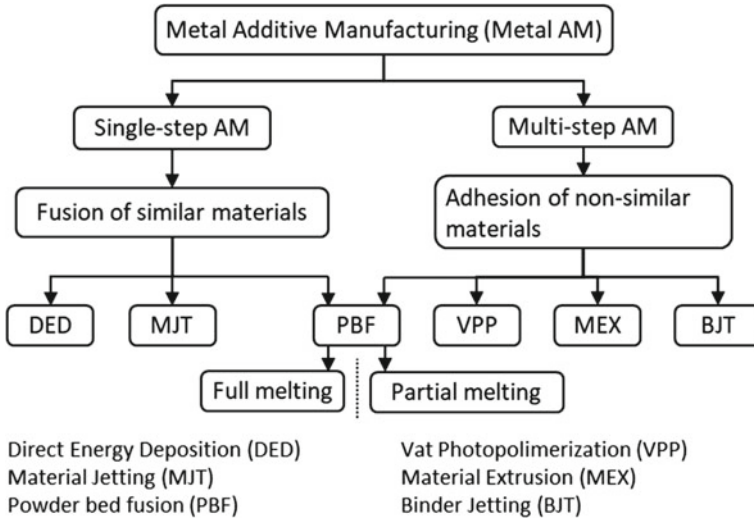


Fig. 6.1 Categorization of selected metal additive manufacturing technologies by the number of manufacturing steps needed to achieve a final metal part (DIN 2022)

inkjet principle). A significant disadvantage of most single-step AM technologies are residual stresses arising due to thermal gradients and shrinkage. These can lead to part imperfections like cracks or deformations (Sames et al. 2016).

6.2.2 Multi-step AM Technologies

Multi-step additive manufacturing technologies include two or more consecutive process steps to produce a final solid part (DIN 2022). These steps are similar to the powder metallurgical manufacturing route shown in Fig. 6.2, and include:

- (1) Shaping: Generating the part shape out of metal powder and binding media utilizing AM technologies.
- (2) Debinding: Removal of the primary binding media.
- (3) Sintering: Removal of the secondary and residual binder while consolidating the metal powder (Bartolo and Gaspar 2008; Suwanpreecha and Manonukul 2022; Ziaee and Crane 2019).

Feedstock:

The feedstock used for multi-step AM, predominantly is a premixed multi-component material, consisting of the metal powder and a binding media. The binding media needs to be specifically tailored to the AM technology. Its main purpose is to support the shaping process and to act as a matrix structure for the metal powder.

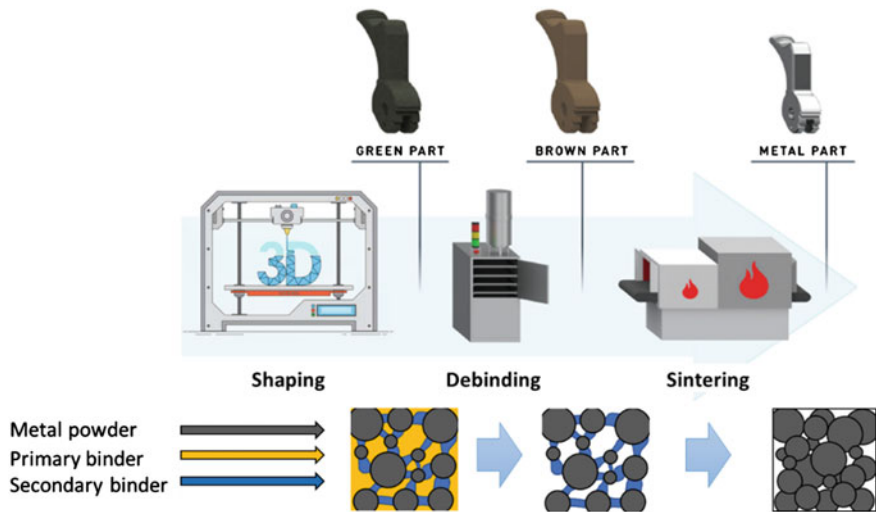


Fig. 6.2 Process scheme of multi-step additive manufacturing technologies; image adopted from (Process—PTI 2022)

The binding media consists of three components: primary binder, secondary binder and additives, such as dispersants or surfactants. The primary binder, also referred to as main binder, accounts for the majority of the volume. It is a low molecular weight polymer, which is easily removable. The secondary binder, also called backbone binder, is a high molecular weight polymer. Its purpose is to maintain the 3D printed shape after debinding and before sintering. (Suwanpreecha and Manonukul 2022).

Shaping:

During shaping, the part geometry is generated. In conventional powder metallurgical processes, this is done by pressing or injecting loose powder or a powder binder mixture into a mold. The utilization of molding techniques usually come with restrictions regarding the part shape and high manufacturing costs (Moon et al. 2021). Additive manufacturing overcomes these restrictions through the layer-by-layer manufacturing principle which allows for more complex designs and without requiring molds. Most intensively researched in that regard are vat photopolymerization, material extrusion and binder jetting processes (Vaezi et al. 2020).

Debinding:

For typical multiple-component binders, the debinding process is split into two stages: primary debinding and secondary debinding. In the first stage, the primary binder is removed. This is done by solvent debinding, immersing the additive manufactured green part into a solvent, or by thermal debinding, which degrades the polymer into volatile products. Most common solvents are water or acetone. The intermediate product is referred to as “brown part”. The secondary debinding is a transition process between debinding and sintering. While the backbone binder

degrades, sintering between the powder particle starts (Ebel 2019; Suwanpreecha and Manonukul 2022). Improper thermal debinding leads to carbonaceous residues that degrade mechanical, optical, thermal, magnetic or electronic properties of the sintered part (Heaney 2019).

Sintering:

Sintering relies on diffusion in solid matter and the principle to reach a lower energy state. Neighboring powder particles in direct contact initially develop necks between each other. This connection gradually widens during the sintering process until a dense part is achieved. At the same time, shrinkage occurs and the density of the part increases. Contrary to the shaping process in which the properties of the binding media are more influential, the sintering process predominantly depends on the metal powder and its properties. Thus, the parameters for the sintering process are material specific. Residual porosity, which is characteristically for sintered parts, can be led back to the particle size of the initial powder and correlated with the green part density. It can, further, be controlled through sintering temperature and time (Šalák 1995). Because the powder consolidation is separate from the AM process and starts uniformly from the part surface, multi-step additive manufacturing followed by sintering inherits less residual stress, compared to single-step AM (DebRoy et al. 2018).

6.2.2.1 Vat Photopolymerization (VPP)

Vat photopolymerization utilizes a liquid photo-reactive polymer, which is selectively polymerized inside a vat (DIN 2022). The process steps for VPP are as follows (detailed in Fig. 6.3): (1) The build platform is lowered into a polymer resin inside a vat, (2) the thin liquid layer gets exposed to UV light, causing the polymer to cure, (3) the build platform is raised again, so new resin flows in and forms a new liquid layer and (4) when the new liquid layer is established, the build platform immerses the last cured layer again into the liquid and the cycle repeats. Most commonly the light source is a laser or a projector system directed by mirrors (Chen et al. 2019).

Table 6.1 gives key-process parameters that can be varied to alter the desired part properties.

Feedstock:

The photo-reactive resin is comprised three components: (1) photo-initiators, which absorb the light and start the curing process, (2) monomers and oligomers, which provide photo-curability and (3) dispersants to maintain low viscosities even in presence of high powder loadings. Additional components may be added to influence the resins rheology, to enhance curability or to ease binder removal (Rasaki et al. 2021; Zimbeck and Rice 2000). For metal stereolithography processing, the typical powder loading is 50 vol-%, higher loadings are generally desirable due to multiple advantages. These include shortening of the debinding time, minimizing the porosity in the sintered part, reducing the risk of part disruption during binder decomposition

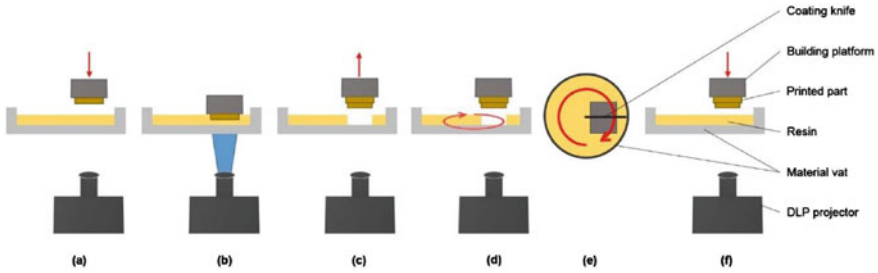


Fig. 6.3 Process steps of the VPP process. **a** Build platform with the already printed layers is immersed into the vat, **b** liquid layer is exposed to UV light and cured, **c** build platform is lifted, **d** Vat surface is recoated with fresh resin, **e** top view of the recoating procedure, and **f** process steps (a) to (e) are repeated until part is finished. Image adopted from (Stögerer et al. 2022)

Table 6.1 Key-process variables in VPP (in accordance with Oh et al. (2020)).

Part placement	Build strategy	Light exposure
<ul style="list-style-type: none"> • Orientation • Support structure 	<ul style="list-style-type: none"> • Layer height • Tool path (only Laser) • Vat temperature 	<ul style="list-style-type: none"> • Exposure duration • Exposure intensity • Light source resolution

and reducing sintering shrinkage (Zimbeck and Rice 2000). Typical resins used for metal VPP as well as powder load and debinding temperature are listed in Table 6.2.

Advantages and Disadvantages:

The biggest advantages of VPP are the high achievable surface quality and accuracy. In addition, VPP utilizes a nonhazardous and easy to handle feedstock. The metal powder is contained within the UV-reactive resin and thus avoids the issues and required safety measures related with loose metal powder. One drawback of powder-filled resins is it being a suspension with limited shelf life due to sedimentation (Zubrzycka et al. 2021). Other limitations of VPP are the rather slow build rate, the

Table 6.2 Binder systems utilized in metal VPP

Binder	Powder loading vol-%	Debinding temperature °C	References
HDDA ^a	50	600	Lee et al. (2006)
Unsaturated polyester and epoxy system	50	n.n	Bartolo and Gaspar (2008)
Acrylate monomers (Di-, tri- and higher)	52	500	Zimbeck and Rice (1998)

1,6-Hexanediol diacrylate

Table 6.3 Advantages and disadvantages of VPP

Advantages	Disadvantages
High surface quality High accuracy and resolution No loose powder handling (power suspension)	Slow build rate Parts are not stackable inside the build chamber Short shelf life of resin Part size limited

need for support structures and the small part sizes due to the restrictions of the light source (see Table 6.3) (Zhou et al. 2016).

Commercially available AM machines:

Commercial systems are available from Incus GmbH (Vienna, Austria), which offer a machine and service for producing VPP-based metal parts. The company started as a spin-off from Lithoz GmbH (Vienna, Austria) and solely focused on processing ceramic powder-filled resins with vat photopolymerization (Boissonneault 2019). Admatec BV (Alkmaar, Netherlands) also offers two systems for processing of metal-filled resins (Admaflex 130 and 300).

6.2.2.2 Material Extrusion (MEX)

The principle of material extrusion is based on the reversible effect of thermoplastic polymers, which become moldable when heated above their glass transition temperature and solidify again upon cooling. In MEX, this mechanism is used to extrude the thermoplastic feedstock through a nozzle onto a build plate and generates a three-dimensional (3D) part by depositing the extrudate onto the already solidified polymer. There are different extrusion concepts to process thermoplastic material. The three basic principles thereof are depicted in Fig. 6.4. Matching feedstock properties and the extruder principle is vital for the shaping process. In a plunger-based approach, the processed material is present in a semi-liquid slurry; therefore, process ability is predominantly driven by the viscosity. To allow easy processing of filament-based material, it is important to ensure a sufficient flexibility of the filament, so it does not break when fed to the extrusion unit. Moreover, it is essential that the cross-section of the filament is in a tight range to maintain a steady material flow. A comprehensive study about problems in filament-based MEX was undertaken by Hsiang Loh et al. (2020). In comparison with the other approaches, the requirements toward pellet material are the lowest due to fewer requirement on the feedstock.

Key-process parameters that influence print quality are listed in Table 6.4.

Feedstock:

The feedstock used in MEX processes is available as pellets, filament or slurry. The metal MEX process is rather similar to metal injection molding (MIM), and thus, the feedstock consists of similar components known from MIM. These are divided into primary polymers with a low molecular weight and secondary polymers with

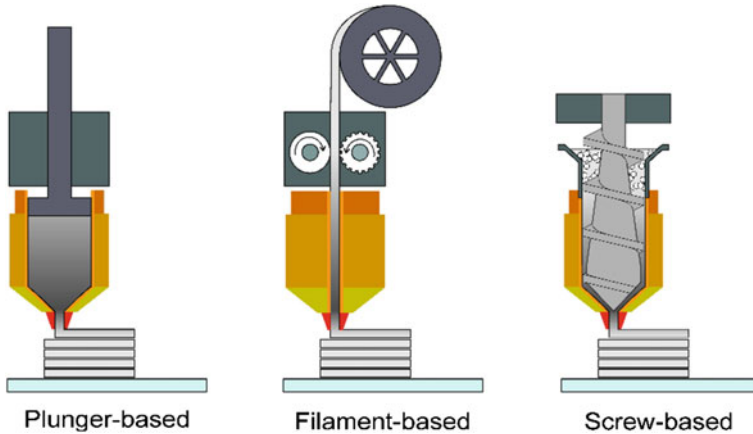


Fig. 6.4 Different extrusion concepts in material extrusion (Gonzalez-Gutierrez et al. 2018)

Table 6.4 Key-process parameter in MEX (in accordance with Oh et al. (2020)).

Part placement	Build strategy	Material extrusion
<ul style="list-style-type: none"> • Orientation • Support structure 	<ul style="list-style-type: none"> • Nozzle diameter • Layer height • Tool path • Travel speed • Build platform temperature 	<ul style="list-style-type: none"> • Volume extrusion rate • Nozzle diameter • Extrusion temperature

a higher molecular weight. Since there is no standardized definition regarding the classification of primary and secondary binder, only a general guideline is provided. Primary binders commonly are based on paraffin or synthetic wax, polyethylene glycol (PEG), thermoplastic elastomers (TPE), styrene-ethylene-butylene-styrene (SEBS) and ethylene–vinyl acetate (EVA). The following components are considered as secondary binder: Polyamide (PA), polypropylene (PP), polyethylene (PE, LDPE, HDPE) and polyoxymethylene (POM) (Kan et al. 2021). An additive that is regularly used as a lubricant is stearic acid (SE). Table 6.5 summarizes reported research on binder materials in MEX.

Advantages and Disadvantages:

The key advantage of MEX is the high material throughput (compared with VPP and BJT), that is achieved with upscaling the extrusion unit. However, this entails a loss in surface quality and resolution, due to the correlation of nozzle diameter to bead size. Since no optical components are utilized in MEX, the initial cost for this technology is lower compared to other AM technologies. Similar to VPP, the metal powder is encapsulated inside the binder material, allowing an easier and nonhazardous material handling. A disadvantage of MEX is that parts cannot be

Table 6.5 Binder materials used in MEX

Feedstock	Binder composition	Solvent debinding		Thermal debinding			References
		Solvent	Temperature in °C	Duration in h	Temperature in °C	Duration in h	
Pellets	PEG and wax	Water	60	12	500	1	H2 with He Lieberwirth et al. (2017), Singh et al. (2021a)
Pellets	TPE and PP	Water and inhibitor	60	48–72	600–800		H2/N2 Lengauer et al. (2019)
Pellets	PEG and wax	Water	60	48–72	500	1	H2 with He Singh et al. (2021b; c), Vishwanath et al. (2021)
Slurry	PEG	Water	60	10	–	–	– Giberti et al. (2016)
Slurry	Embemould K83	Water	40	48	145–300	6	N/A Hassan et al. (2021)
Filament	POM, PP and wax	–	–	–	600	2	N2 Abe et al. (2021)
Filament	TPE and PO	Cyclohexane	70	N/A	600	N/A	H2 Gonzalez-Gutierrez et al. (2019)
Filament	PP, SEBS wax and SA	Cyclohexane	60–70	24	350–440	1–4	H2 or H2 and Ar Kan et al. (2021)
Filament	LDPE, TPE and SA	Cyclohexane	60	N/A	370–470	N/A	H2 Wagner et al. (2022)
Filament	PA	–	–	–	200–450	N/A	N/A Riecker et al. (2016)
Filament	POM and wax	–	–	–	600	2	N2 Kurose et al. (2020)
Filament	TPE, PO and compatibilizer	Cyclohexane	60	3–12	–	–	– Kukla et al. (2017)

(continued)

Table 6.5 (continued)

Feedstock	Binder composition	Solvent debinding		Thermal debinding			References	
		Solvent	Temperature in °C	Duration in h	Temperature in °C	Duration in h		Atmosphere
Filament	TPE and PO	Cyclohexane	65	0.5–57	750	1.5	Vacuum	Thompson et al. (2019)
Filament	POM, PE, DOP, DBP and ZnO (BASF Ultrafuse 316LX)	HNO ₃ gas	110–140	8	450–600	1–2	H ₂	Damon et al. (2019), Ait-Mansour et al. (2020), Liu et al. (2020), Caminero et al. (2021), Jiang and Ning (2021), Rosnitschek et al. (2021)
Filament	POM, PE, DOP, DBP and ZnO (BASF Ultrafuse 316L)	HNO ₃ gas	120	N/A	450–600	1	N/A	Jiang and Ning (2021), Quarto et al. (2021)
Filament	PE and SA	–	–	–	200–425	3	N/A	Wang et al. (2021)
Filament	Polyolefin-based	Aceton	60	24	300–550	N/A	N/A	Zhang et al. (2020)

Table 6.6 Advantages and disadvantages of MEX (Vaezi et al. 2020)

Advantages	Disadvantages
High build rate	Low surface quality
Low initial technology costs	Parts are not stackable inside the build chamber
No loose powder handling	

stacked within the build chamber and support structures are required to manufacture overhangs. This reduces the potential for mass production, due to a low exploitation of the building space and manual labor to remove supports (see Table 6.6) (Vaezi et al. 2020). Overall, the highest potential of MEX is seen in large volume components.

Commercially Available AM Machines:

AM machines based on MEX are widely available for polymer material. While it is generally possible to process highly filled metal feedstock as filament, there are only a few companies that specifically advertise the use of metal powder-filled feedstock. AIM3D GmbH (Rostock, Germany) offers with the ExAM 255 a system with two single screw extruders, capable of processing two different feedstocks (for example build material and support material) at the same time. In addition, Pollen AM (Ivry-sur-Seine, France) offers systems to produce green parts through MEX technology. With their PAM Series P, they offer a 3D printer with open software controls that processes pellet feedstock. As a provider of feedstock BASF SE (Germany) developed a filament feedstock on the basis of their Catamold system, which can be processed by many regular polymer filament 3D printers (Suwanpreecha and Manonukul 2022).

6.2.2.3 Binder Jetting (BJT)

Binder jetting (BJT) is a powder-bed-based AM technology in which a powder is deposited layer-by-layer similar to PBF and selectively joined in each layer with a binding agent that is dispensed via an inkjet printhead. The process steps are divided into three steps. In the first step, a flat powder layer is deposited on the build platform. The flattening is done by a rake or a rotating roller. The unit responsible for the powder deposition and flattening is called recoater (see Fig. 6.5). After powder deposition, a binding agent is selectively applied with a printhead. This step is very similar to the common inkjet printing in which a 2D image is printed onto the powder. Depending on the binding agent, a third step is performed to cure the binder with heat or UV-irradiation.

The part placement is less restrictive than in VPP and MEX, since no support structure is required. During the shaping process, the printed part is surrounded by the powder bed, which stabilizes it. Further, BJT requires less amount of binder to fabricate a green part, because it solely functions as a binding media and not as an auxiliary material for the process (Li et al. 2020). Since the full strength of the part is only achieved after sintering, particular caution needs to be taken to not damage the

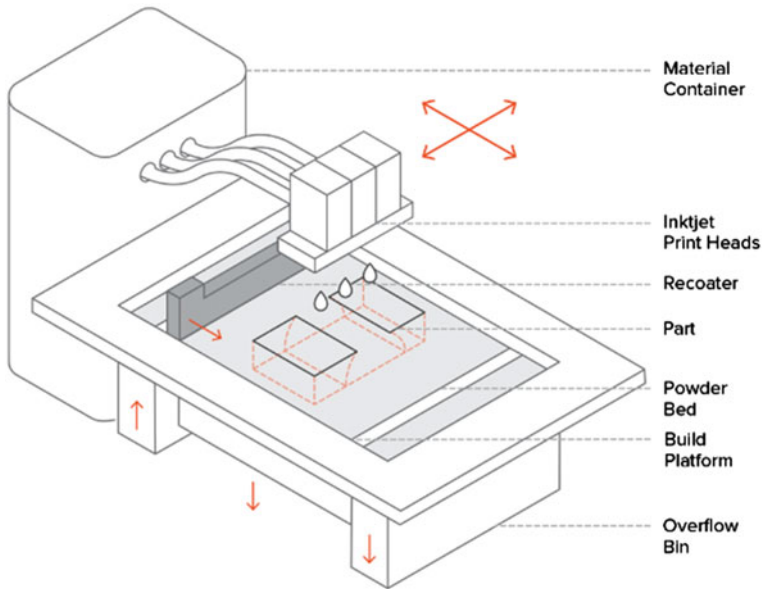


Fig. 6.5 Schematic of a binder jetting machine (3D Hubs Inc 2022)

part in advance. Therefore, recoating speed is limited due to the friction generated during the powder deposition. The main influence of the ink jetting process is on the resolution of the part. This is mostly determined by the nozzle size and the number of the inkjet printhead. When choosing the printhead, it is especially important to ensure the compatibility of the binder ink with the printhead. Table 6.7 gives key-process parameters that can be adapted toward the part geometry, powder material or ink system.

Material:

Regarding the powder deposition, the powder requirements in binder jetting are comparable to other powder bed-based processes. Similar to these, powder particle size, shape and powder bulk density influence the flowability and thus determine the recoating speed and the density of the powder layer. The selection of a suitable binder, compatible with the powder, is critical for successful printing. The two most

Table 6.7 Key-process parameters in BJT (in accordance with Oh et al. (2020)).

Part placement	Powder recoating	Ink jetting
<ul style="list-style-type: none"> • Orientation 	<ul style="list-style-type: none"> • Layer height • Blade traverse speed • Roller rotation speed 	<ul style="list-style-type: none"> • Nozzle diameter • Nozzle number • Binder saturation

important criteria are the wettability and permeation ability which affect the migration of the binder and the strength of the green part (Li et al. 2020). Due to the complexity of binder development, this study can only provide an overview of possible criteria and binder classes that assists in the decision of a binder system.

First and foremost, the binder must be printable with an inkjet printhead. The jettability of a binder is determined by its viscosity, surface tension, viscoelasticity and other properties (Tuladhar 2017). Further, the binder ink needs to be tuned to the employed printhead system. Generally, binder systems are defined as either in-liquid or in-bed binder systems. For an in-liquid solution, all binder components are mixed inside the printed agent. This allows for a greater versatility, but also increases the risk of clogging inside the printhead. An in-bed solution splits the binder components in two parts. One part is in the ink that is printed, the other part is either a solid or liquid and is premixed into the loose powder. Table 6.2 summarizes binder materials used for BJT (Table 6.8).

The binding media is of particular importance, as it needs to be suitable for both feedstock and printhead. Thus, it was observed that many reported studies use proprietary binder systems in their research.

Advantages and Disadvantages:

Table 6.8 Binder media used in BJT

Binder	Curing temperature °C	Curing time h	References
3D systems ZB60	Air dried	1	Sheydaeian et al. (2017)
DEG	200	2	Cordero et al. (2017)
DEG aqueous	100–150	4–6	Li et al. (2017), Paranthaman et al. (2016)
Dextrine/Glycerine	Air dried	24	Fu et al. (2013)
Dextrine/Glycerine	Air dried/70	24	Carrijo et al. (2016)
EG/DEG	200	2	Elliott et al. (2016)
EGBE/IPA/EG	195	2	Do et al. (2017)
EGBE/IPA/EG	195	2	Do et al. (2017)
ExOne EGME/EG	175	N/A	Mostafaei et al. (2016), Mostafaei et al. (2017)
ExOne EGME/EG	175	N/A	Mostafaei et al. (2018)
ExOne LB 04	200	2	Bailey et al. (2016)
ExOne PM-B-SR-04	200	2	Dilip et al. (2017)
ExOne PM-B-SR1-01	170	2	Sun et al. (2009)
ExOne PM-B-SR1-04	190	2	Bai and Williams (2015)
ExOne PM-B-SR2-05	190	2	Bai et al. (2015)
ExOne ProMetal R-1	200	N/A	Levy et al. (2017)
PVA/IPA	IR light	0.33	Williams et al. (2011)
PVA/PVP	Air dried	24	Xiong et al. (2012)

Table 6.9 Advantages and disadvantages of metal BJT

Advantages	Disadvantages
Great variety of processible materials Parts are stackable inside build chamber High build rate	Handling of loose powder Maintenance intensive inkjet printhead Inert atmosphere needed

BJT offers many potential advantages compared to other AM processes (see Table 6.9). It can process most materials available as powder and also combine multiple materials toward functionally graded materials by depositing different materials (Ziaee and Crane 2019). Additionally, BJT systems have a superior productivity due to their high build rate and ability to stack multiple parts on top of each other inside the build chamber. On the downside, the metal powder is present as loose powder, and thus, handling the powder poses health risks and mandates safety measures. Another specific disadvantage for binder jetting is the risk of irreversible clogging of printhead nozzles due to the binder curing inside the nozzles (Du et al. 2020).

Commercially Available AM Machines:

Desktop Metal Inc. (Burlington, USA) offers several metal and ceramic binder jetting machines ranging from a build volume of $350 \times 220 \times 50$ mm up to $800 \times 500 \times 400$ mm (Desktop Metal Inc.). Digital Metal AB (Höganäs, Sweden) offers with its DM P2500 a binder jetting 3D printer with a build volume of $250 \times 217 \times 186$ mm (Digital Metal).

6.3 Summary

In metal multi-step AM followed by sintering, components are produced in sequential steps divided into a shaping step achieved by additive manufacturing, and a material consolidation step through sintering. Unlike in single-step processes, material properties obtained by sintering are isotropic and residual stresses are uncritical. Therefore, multi-step AM present a favorable alternative for processing high strength materials, such as tooling steels or hard metals.

This study reviews the current research on multi-step AM and the fabrication of green parts comprised of binding media and metal powder, suitable for the powder metallurgical manufacturing route to achieve fully-dense metal parts. A comparison of the available and still in development situated technologies vat photopolymerization (VPP), material extrusion (MEX) and binder jetting (BJT) was undertaken. Providing an overview of key-process characteristics, this review focused on binder materials used multi-step AM. While some studies include information about the binder system and debinding process, it was observed that the main focus of investigations are correlations between used metal powder material and as-sintered part properties. Minor efforts were undertaken toward the influence of the binder system

on the green part production, the debinding process and on the as-sintered part properties. The authors of this study strongly recommend further investigation on binding media and compositions and their influence on the properties of the green part, the debinding process and the final (as-sintered) part properties.

References

- Abe Y, Kurose T, Santos MVA, Kanaya Y, Ishigami A, Tanaka S, Ito H (2021) Effect of layer directions on internal structures and tensile properties of 17-4PH stainless steel parts fabricated by fused deposition of metals. *Materials* (Basel, Switzerland), 14(2). <https://doi.org/10.3390/ma14020243>
- Ait-Mansour I, Kretschmar N, Chekurov S, Salmi M, Rech J (2020) Design-dependent shrinkage compensation modeling and mechanical property targeting of metal FFF. *Progress Add Manuf* 5(1):51–57. <https://doi.org/10.1007/s40964-020-00124-8>
- Bai Y, Wagner G, Williams CB (2015) Effect of bimodal powder mixture on powder packing density and sintered density in binder jetting of metals. University of Texas at Austin. <https://repositories.lib.utexas.edu/handle/2152/89376?show=full>
- Bai Y, Williams CB (2015) An exploration of binder jetting of copper. *Rapid Prototyping J* 21(2):177–185. <https://doi.org/10.1108/RPJ-12-2014-0180>
- Bailey AC, Merriman A, Elliott A, Basti MM (2016) Preliminary testing of nanoparticle effectiveness in binder jetting application. *Solid Free Form Fabrication 2016*
- Bartolo PJ, Gaspar J (2008) Metal filled resin for stereolithography metal part. *CIRP Ann* 57(1):235–238. <https://doi.org/10.1016/j.cirp.2008.03.124>
- Boissonneault T (2019) Lithoz spin-off Incus to unveil lithography-based metal 3D printing at Formnext. <https://www.3dprintingmedia.network/lithoz-spin-off-incus-lithography-metal-3d-printing/>
- Caminero MÁ, Romero A, Chacón JM, Núñez PJ, García-Plaza E, Rodríguez GP (2021) Additive manufacturing of 316L stainless-steel structures using fused filament fabrication technology: mechanical and geometric properties. *Rapid Prototyping J* 27(3):583–591. <https://doi.org/10.1108/RPJ-06-2020-0120>
- Carrijo MMM, Lorenz H, Filbert-Demut I, de Oliveira Barra GM, Hotza D, Yin X, Greil P, Travitzky N (2016) Fabrication of Ti₃ SiC₂ -based composites via three-dimensional printing: influence of processing on the final properties. *Ceram Int* 42(8):9557–9564. <https://doi.org/10.1016/j.ceramint.2016.03.036>
- Chen Z, Li Z, Li J, Liu C, Lao C, Fu Y, Liu C, Li Y, Wang P, He Y (2019) 3D printing of ceramics: a review. *J Eur Ceram Soc* 39(4):661–687. <https://doi.org/10.1016/j.jeurceramsoc.2018.11.013>
- Cordero ZC, Siddel DH, Peter WH, Elliott AM (2017) Strengthening of ferrous binder jet 3D printed components through bronze infiltration. *Addit Manuf* 15:87–92. <https://doi.org/10.1016/j.addma.2017.03.011>
- Damon J, Dietrich S, Gorantla S, Popp U, Okolo B, Schulze V (2019) Process porosity and mechanical performance of fused filament fabricated 316L stainless steel. *Rapid Prototyping J* 25(7):1319–1327. <https://doi.org/10.1108/RPJ-01-2019-0002>
- DehRoy T, Wei HL, Zuback JS, Mukherjee T, Elmer JW, Milewski JO, Beese AM, Wilson-Heid A, De A, Zhang W (2018) Additive manufacturing of metallic components—process, structure and properties. *Prog Mater Sci* 92:112–224. <https://doi.org/10.1016/j.pmatsci.2017.10.001>
- Digital Metal. DM P2500. <https://digitalmetal.tech/primer-line/dm-p2500/>
- Dilip J, Miyanaji H, Lassell A, Starr TL, Stucker B (2017) A novel method to fabricate TiAl intermetallic alloy 3D parts using additive manufacturing. *Defence Technol* 13(2):72–76. <https://doi.org/10.1016/j.dt.2016.08.001>

- DIN EV (2022) Additive Fertigung—Grundlagen—Terminologie (DIN EN ISO/ASTM 52900). Beuth, Berlin
- Do T, Kwon P, Shin CS (2017) Process development toward full-density stainless steel parts with binder jetting printing. *Int J Mach Tools Manuf* 121:50–60. <https://doi.org/10.1016/j.ijmactools.2017.04.006>
- Du W, Singh M, Singh D (2020) Binder jetting additive manufacturing of silicon carbide ceramics: development of bimodal powder feedstocks by modeling and experimental methods. *Ceram Int* 46(12):19701–19707. <https://doi.org/10.1016/j.ceramint.2020.04.098>
- Ebel T (2019) Metal injection molding (MIM) of Titanium and titanium alloys. In: *Handbook of metal injection molding*. Elsevier, pp 431–460. <https://doi.org/10.1016/B978-0-08-102152-1.00023-4>
- Elliott A, AlSalih S, Merriman AL, Basti MM (2016) Infiltration of nanoparticles into porous binder jet printed parts. *Am J Eng Appl Sci* 9(1):128–133. <https://doi.org/10.3844/ajeassp.2016.128.133>
- Fu Z, Schlier L, Travitzky N, Greil P (2013) Three-dimensional printing of SiSiC lattice truss structures. *Mater Sci Eng* 560:851–856. <https://doi.org/10.1016/j.msea.2012.09.107>
- Giberti H, Strano M, Annoni M (2016) An innovative machine for fused deposition modeling of metals and advanced ceramics. *MATEC Web Confer* 43:3003. <https://doi.org/10.1051/mateconf/20164303003>
- Gonzalez-Gutierrez J, Arbeiter F, Schlauf T, Kukla C, Holzer C (2019) Tensile properties of sintered 17–4PH stainless steel fabricated by material extrusion additive manufacturing. *Mater Lett* 248:165–168. <https://doi.org/10.1016/j.matlet.2019.04.024>
- Gonzalez-Gutierrez J, Cano S, Schuschnigg S, Kukla C, Sapkota J, Holzer C (2018) Additive manufacturing of metallic and ceramic components by the material extrusion of highly-filled polymers: a review and future perspectives. *Materials (Basel, Switzerland)*, 11(5). <https://doi.org/10.3390/ma11050840>
- Hassan W, Farid MA, Tosi A, Rane K, Strano M (2021) The effect of printing parameters on sintered properties of extrusion-based additively manufactured stainless steel 316L parts. *Int J Adv Manuf Technol* 114(9–10):3057–3067. <https://doi.org/10.1007/s00170-021-07047-w>
- Heaney DF (ed) (2019) Woodhead publishing series in metals and surface engineering. *Handbook of metal injection molding (Second edition)*. WP Woodhead Publishing
- Hitzler L, Merkel M, Hall W, Öchsner A (2018) A Review of metal fabricated with laser- and powder-bed based additive manufacturing techniques: process, nomenclature, materials, achievable properties, and its utilization in the medical sector. *Adv Eng Mater* 20(5):1700658. <https://doi.org/10.1002/adem.201700658>
- Hsiang Loh G, Pei E, Gonzalez-Gutierrez J, Monzón M (2020) An overview of material extrusion troubleshooting. *Appl Sci* 10(14):4776. <https://doi.org/10.3390/app10144776>
- 3D Hubs Inc (2022) How to design parts for binder jetting 3D printing. <https://www.hubs.com/knowledge-base/how-design-parts-binder-jetting-3d-printing/>
- Desktop Metal Inc. Metal family. <https://www.desktopmetal.com/metal-family/>
- Jiang D, Ning F (2021) Additive manufacturing of 316L stainless steel by a printing-debinding-sintering method: effects of microstructure on fatigue property. *J Manuf Sci Eng* 143(9), Article 091007. <https://doi.org/10.1115/1.4050190>
- Kan X, Yang D, Zhao Z, Sun J (2021) 316L FFF binder development and debinding optimization. *Mat Res Express* 8(11):116515. <https://doi.org/10.1088/2053-1591/ac3b15>
- Kukla C, Gonzales-Gutierrez J, Cano S, Hampel S (2017) Fused filament fabrication (FFF) of PIM feedstocks. *Congreso Nacional De Pulvimetalurgia Y I Congreso Iberoamericano De Conferencia (Volume: VI)*
- Kurose T, Abe Y, Santos MVA, Kanaya Y, Ishigami A, Tanaka S, Ito H (2020) Influence of the layer directions on the properties of 316L stainless steel parts fabricated through fused deposition of metals. *Materials (Basel, Switzerland)* 13(11). <https://doi.org/10.3390/ma13112493>
- Lee JW, Lee IH, Cho D-W (2006) Development of micro-stereolithography technology using metal powder. *Microelectron Eng* 83(4–9):1253–1256. <https://doi.org/10.1016/j.mee.2006.01.192>

- Lengauer W, Duretek I, Fürst M, Schwarz V, Gonzalez-Gutierrez J, Schuschnigg S, Kukla C, Kitzmantel M, Neubauer E, Lieberwirth C, Morrison V (2019) Fabrication and properties of extrusion-based 3D-printed hardmetal and cermet components. *Int J Refract Metal Hard Mater* 82:141–149. <https://doi.org/10.1016/j.ijrmhm.2019.04.011>
- Levy A, Miriyev A, Elliott A, Babu SS, Frage N (2017) Additive manufacturing of complex-shaped graded TiC/steel composites. *Mater Des* 118:198–203. <https://doi.org/10.1016/j.matdes.2017.01.024>
- Li L, Tirado A, Conner BS, Chi M, Elliott AM, Rios O, Zhou H, Paranthaman MP (2017) A novel method combining additive manufacturing and alloy infiltration for NdFeB bonded magnet fabrication. *J Magn Magn Mater* 438:163–167. <https://doi.org/10.1016/j.jmmm.2017.04.066>
- Li M, Du W, Elwany A, Pei Z, Ma C (2020) Metal binder jetting additive manufacturing: a literature review. *J Manuf Sci Eng* 142(9):Article 090801. <https://doi.org/10.1115/1.4047430>
- Lieberwirth C, Harder A, Seitz H (2017) Extrusion based additive manufacturing of metal parts. *J Mech Eng Autom* 7(2). <https://doi.org/10.17265/2159-5275/2017.02.004>
- Liu B, Wang Y [Yuxiang], Lin Z, Zhang T (2020) Creating metal parts by fused deposition modeling and sintering. *Mater Lett* 263:127252. <https://doi.org/10.1016/j.matlet.2019.127252>
- Moon AP, Dwarapudi S, Sista KS, Kumar D, Sinha GR (2021) Opportunity and challenges of iron powders for metal injection molding. *ISIJ Int* 61(7):2015–2033. <https://doi.org/10.2355/isijinternational.ISIJINT-2021-050>
- Mostafaei A, Stevens EL, Hughes ET, Biery SD, Hilla C, Chmielus M (2016) Powder bed binder jet printed alloy 625: densification, microstructure and mechanical properties. *Mater Des* 108:126–135. <https://doi.org/10.1016/j.matdes.2016.06.067>
- Mostafaei A, Toman J, Stevens EL, Hughes ET, Krimer YL, Chmielus M (2017) Microstructural evolution and mechanical properties of differently heat-treated binder jet printed samples from gas- and water-atomized alloy 625 powders. *Acta Mater* 124:280–289. <https://doi.org/10.1016/j.actamat.2016.11.021>
- Mostafaei A, Stevens EL, Ference JJ, Schmidt DE, Chmielus M (2018) Binder jetting of a complex-shaped metal partial denture framework. *Addit Manuf* 21:63–68. <https://doi.org/10.1016/j.addma.2018.02.014>
- Oh J-W, Park J, Choi H (2020) Multi-step metals additive manufacturing technologies. *J Korean Powder Metall Inst* 27(3):256–267. <https://doi.org/10.4150/KPMI.2020.27.3.256>
- Paranthaman MP, Shafer CS, Elliott AM, Siddel DH, McGuire MA, Springfield RM, Martin J, Fredette R, Ormerod J (2016) Binder jetting: a novel NdFeB bonded magnet fabrication process. *JOM* 68(7):1978–1982. <https://doi.org/10.1007/s11837-016-1883-4>
- Process—PTI (2022) <http://polymertek.com/inject/metal-mim/process/>
- Quarto M, Carminati M, D’Urso G (2021) Density and shrinkage evaluation of AISI 316L parts printed via FDM process. *Mater Manuf Processes* 36(13):1535–1543. <https://doi.org/10.1080/10426914.2021.1905830>
- Rasaki SA, Xiong D, Xiong S, Su F, Idrees M, Chen Z (2021) Photopolymerization-based additive manufacturing of ceramics: a systematic review. *J Adv Ceram* 10(3):442–471. <https://doi.org/10.1007/s40145-021-0468-z>
- Riecker S, Studnitzky T, Kieback B, Quadbeck P, Andersen O, Clouse J (2016) Fused deposition modeling—Opportunities for cheap metal AM. In: World PM2016 congress and exhibition. <https://www.epma.com/publications/euro-pm-proceedings/product/ep16-3297424>
- Rosnitschek T, Seefeldt A, Alber-Laukant B, Neumeyer T, Altstadt V, Tremmel S (2021) Correlations of geometry and infill degree of extrusion additively manufactured 316L stainless steel components. *Materials* 14(18):5173. <https://doi.org/10.3390/ma14185173>
- Šalák A (1995) *Ferrous powder metallurgy*. Cambridge Internat. Science Publ
- Sames WJ, List FA, Pannala S, Dehoff RR, Babu SS [SS] (2016) The metallurgy and processing science of metal additive manufacturing. *Int Mat Rev* 61(5):315–360. <https://doi.org/10.1080/09506608.2015.1116649>

- Sheydaeian E, Fishman Z, Vlasea M, Toyserkani E (2017) On the effect of throughout layer thickness variation on properties of additively manufactured cellular titanium structures. *Addit Manuf* 18:40–47. <https://doi.org/10.1016/j.addma.2017.08.017>
- Singh G, Missiaen J-M, Bouvard D, Chaix J-M (2021a) Additive manufacturing of 17–4 PH steel using metal injection molding feedstock: analysis of 3D extrusion printing, debinding and sintering. *Addit Manuf* 47:102287. <https://doi.org/10.1016/j.addma.2021.102287>
- Singh G, Missiaen J-M, Bouvard D, Chaix J-M (2021b) Copper additive manufacturing using MIM feedstock: adjustment of printing, debinding, and sintering parameters for processing dense and defectless parts. *Int J Adv Manuf Technol* 115(1–2):449–462. <https://doi.org/10.1007/s00170-021-07188-y>
- Singh G, Missiaen J-M, Bouvard D, Chaix J-M (2021c) Copper extrusion 3D printing using metal injection moulding feedstock: analysis of process parameters for green density and surface roughness optimization. *Addit Manuf* 38:101778. <https://doi.org/10.1016/j.addma.2020.101778>
- Stögerer J, Baumgartner S, Rath T, Stampfl J (2022) Analysis of the mechanical anisotropy of stereolithographic 3D printed polymer composites. *Eur J Mater* 2(1):12–32. <https://doi.org/10.1080/26889277.2022.2035196>
- Sun L, Kim Y-H, Kim D, Kwon P (2009) Densification and properties of 420 stainless steel produced by three-dimensional printing with addition of Si₃N₄ powder. *J Manufac Sci Eng* 131(6):Article 061001. <https://doi.org/10.1115/1.4000335>
- Suwanpreecha C, Manonukul A (2022) A review on material extrusion additive manufacturing of metal and how it compares with metal injection moulding. *Metals* 12(3):429. <https://doi.org/10.3390/met12030429>
- Thompson Y, Gonzalez-Gutierrez J, Kukla C, Felfer P (2019) Fused filament fabrication, debinding and sintering as a low cost additive manufacturing method of 316L stainless steel. *Addit Manuf* 30:100861. <https://doi.org/10.1016/j.addma.2019.100861>
- Tuladhar T (2017) Measurement of complex rheology and jettability of inkjet inks. In: *Handbook of industrial inkjet printing*. John, pp. 409–430. <https://doi.org/10.1002/9783527687169.ch22>
- Vaezi M, Drescher P, Seitz H (2020) Beamless metal additive manufacturing. *Materials* 13(4). <https://doi.org/10.3390/ma13040922>
- Vishwanath AS, Rane K, Schaper J, Strano M, Casati R (2021) Rapid production of AZ91 Mg alloy by extrusion based additive manufacturing process. *Powder Metall* 64(5):370–377. <https://doi.org/10.1080/00325899.2021.1911457>
- Wagner MA, Hadian A, Sebastian T, Clemens F, Schweizer T, Rodriguez-Arbaizar M, Carreño-Morelli E, Spolenak R (2022) Fused filament fabrication of stainless steel structures—from binder development to sintered properties. *Addit Manuf* 49:102472. <https://doi.org/10.1016/j.addma.2021.102472>
- Wang Y, Zhang L, Li X, Yan Z (2021) On hot isostatic pressing sintering of fused filament fabricated 316L stainless steel—evaluation of microstructure, porosity, and tensile properties. *Mater Lett* 296:129854. <https://doi.org/10.1016/j.matlet.2021.129854>
- Williams CB, Cochran JK, Rosen DW (2011) Additive manufacturing of metallic cellular materials via three-dimensional printing. *Int J Adv Manufact Technol* 53(1–4):231–239. <https://doi.org/10.1007/s00170-010-2812-2>
- Xiong Y, Qian C, Sun J (2012) Fabrication of porous titanium implants by three-dimensional printing and sintering at different temperatures. *Dent Mater J* 31(5):815–820. <https://doi.org/10.4012/dmj.2012-065>
- Zhang Y, Bai S, Riede M, Garratt E, Roch A (2020) A comprehensive study on fused filament fabrication of Ti-6Al-4V structures. *Addit Manuf* 34:101256. <https://doi.org/10.1016/j.addma.2020.101256>
- Zhou M, Liu W, Wu H, Song X, Chen Y, Cheng L, He F, Chen S, Wu S (2016) Preparation of a defect-free alumina cutting tool via additive manufacturing based on stereolithography—optimization of the drying and debinding processes. *Ceram Int* 42(10):11598–11602. <https://doi.org/10.1016/j.ceramint.2016.04.050>

- Ziaee M, Crane NB (2019) Binder jetting: a review of process, materials, and methods. *Addit Manuf* 28:781–801. <https://doi.org/10.1016/j.addma.2019.05.031>
- Zimbeck W, Rice R (2000) Stereolithography of ceramics and metals. In: IS&T's 50th annual conference. <https://www.semanticscholar.org/paper/Stereolithography-of-Ceramics-and-Metals-Zimbeck-Annapolis/8d14d3abab6c5ce9fa589932f3329f4342613d46>
- Zimbeck WR, Rice RW (1998) Freeform fabrication of components with designed cellular structure. *MRS Online Proc Libr* 542(1):165–176. <https://doi.org/10.1557/PROC-542-165>
- Zubrzycka P, Radecka M, Graule T, Stuer M (2021) Metal cation complexes as dispersing agents for non-aqueous powder suspensions. *Ceram Int* 47(13):18443–18454. <https://doi.org/10.1016/j.ceramint.2021.03.168>

Chapter 7

A Strategy to Extend the Limits of Unsupported Printing in Laser Powder Bed Fusion by Optimized Process Parameters Selection



Johannes Rottler, Christoph Petroll, Michael Johlitz, Kristin Paetzold, and Alexander Lion

Abstract In additive manufacturing, laser powder bed fusion (LPBF) is a promising fabrication method where components are produced with a laser beam out of a metal powder bed without the requirement for specific tools. However, the process is limited by its low productivity and the poor printability of complex components. This is mainly due to the necessity of additional required support structures. This paper summarizes the knowledge in the context of support structures and state-of-the-art methods for minimizing them. Herby, the potential of an optimized selection of process parameters is identified as a further method to cover future requirements on LPBF printing. For this purpose, the current way for the determination of process parameters and the novel approach of process mapping from academic research is reviewed. For developing a strategy to extend the limits of unsupported printing, the situational effective thermal conductivity around the melt pool region is determined as a key parameter for further recommended research. So printing even complex geometric features without support structure could be enabled.

J. Rottler (✉) · M. Johlitz · A. Lion
Institute of Mechanics, University of the Bundeswehr Munich, Werner-Heisenberg-Weg 39,
85579 Neubiberg, Germany
e-mail: johannes.rottler@unibw.de

M. Johlitz
e-mail: michael.johlitz@unibw.de

A. Lion
e-mail: alexander.lion@unibw.de

C. Petroll
Bundeswehr Research Institute for Materials, Fuels and Lubricants (WIWeB), Institutsweg 1,
85435 Erding, Germany
e-mail: christophpetroll@bundeswehr.org

K. Paetzold
Institute of Machine Elements and Machine Design, TU Dresden, George-Bähr-Straße 3c, 01069
Dresden, Germany
e-mail: kristin.paetzold@tu-dresden.de

7.1 Introduction and Motivation

The development and optimization of additive manufacturing processes are currently gaining importance for both research and industry. Especially rapid prototyping by means of novel methods has reached industry and enhanced product development. Laser powder bed fusion (LPBF) has been identified as a promising approach for rapid manufacturing, rapid tooling, or the generation of high load-bearing prototypes. Compared to conventional rapid prototyping, LPBF still has more limitations due to the less allowable complexity of the component's geometry and poor economic productivity.

As recently stated in the literature, the main reason for the restrictions in LPBF is the mandatory need for a support structure. Consequently, the ratio of additional costs and unproductivity increases due to the additional effort of producing the support structure. Selected use cases demonstrate that up to 48% of the total component costs are caused by the demand for support (Coyne et al. 2021). In detail, this is due to increased working times, material consumption, and required post-processing steps to remove the support structure or to improve surface finish quality. Furthermore, a gap has been identified between state-of-the-art in research and the practical results achieved in development in the industry. However, further research on printability methods in LPBF is needed to gain fundamental process knowledge and identify essential improvements. This will lay the foundation to overcome the existing disadvantages of this printing method and to empower it for widespread application (Coyne et al. 2021; Weber et al. 2021).

In the following, this report focuses on the purpose of support structures in LPBF and examines the current challenges. Therefore, state-of-the-art procedures to minimize support structures are summarized and evaluated. Based on the latest research studies, an approach to improve unsupported printing in LPBF is motivated. This paper aims to give an overview of the current LPBF printing situation and develop a potential roadmap to address this topic.

7.2 Laser Powder Bed Fusion Process

LPBF is an additive manufacturing method where components are generated layer-by-layer out of selectively melted metal powders. A laser beam provides the input energy for heating the metal powder above its melting temperature. Typically, materials used are gas-atomized metal alloys based on aluminum, titanium, and cobalt- and nickel-based steels. In parallel to the term LPBF, other nomenclatures such as selective laser melting (SLM) or laser metal fusion (LMF) are often used. The variety in the nomenclature is caused by the recent parallel developments in machine manufacturing. From a manufacturing point of view, all describe the same process LPBF (Hitzler et al. 2018).

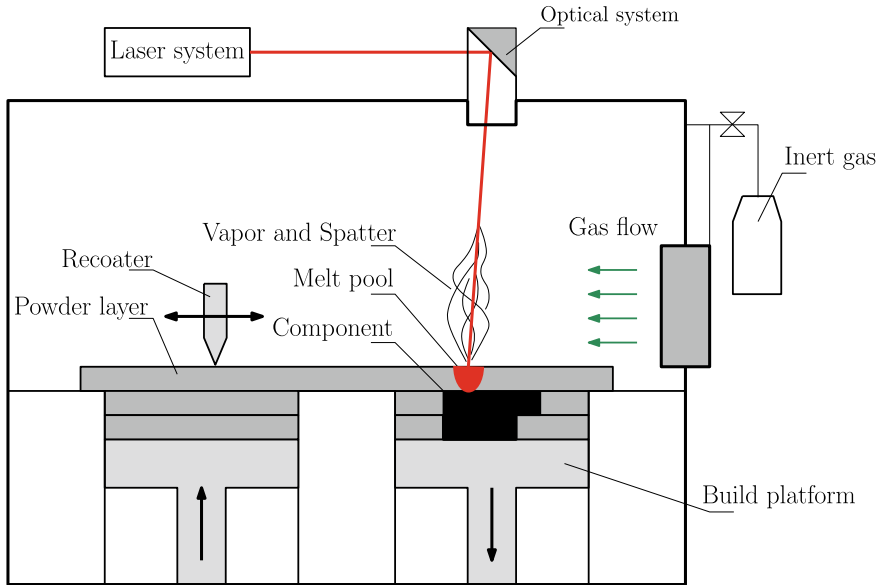


Fig. 7.1 Schematic description of the LPBF process

This process is schematically shown in Fig. 7.1. At the very beginning, the build platform is coated with the first layer of the component material in powder form. In the next step, a photon beam, respectively, laser partially scans the relevant areas of the powder surface. In the focus point, the laser impacts the surface with a spot of a specific diameter of several μm . The most important parameters of the energy input are the laser power in W and the scanning speed in $\frac{\text{mm}}{\text{s}}$. Due to the moving laser beam, the metal powder selectively melts and fusion-welds with the surrounding laser material. If the material close to the melt track was previously melted and solidified, a solid continuum out of the powder material is created. With further layerwise recoating and repetition of the selective melting procedure, a three-dimensional component can be generated in a bed of the loose powder. For the layer-by-layer recoating, the build platform with already processed layers moves downward after each scanning step with a predefined distance, the layer height in μm . This ensures a constant distance between the laser source and the powder surface. The whole printing process is shielded with an atmosphere of an inert gas. To remove both the spatter and the vapor out of the melting zone the gas flows constantly over the powder surface. After finishing the whole print job, the fabricated component has to be removed out of the bed containing the remaining loose powder. During additional post-processing, the component has to be cut from the build platform, including removing the support structure.

7.3 Support Structure

Compared to other additive manufacturing processes dealing with support structure is a unique challenge in LPBF.

Due to evolving vapor in the laser irradiation zone, the recoil pressure ejects molten material from the melt pool. These large spatter particles can solidify on the top surface of neighboring previously solidified melt tracks. Spatter particles on the top surface can lead to contact between the coating unit and the component when recoating the next powder layer (Gong et al. 2014). The component has to be fixed to the build platform while printing to avoid dislocation. The selective energy input with various laser power and scanning speeds causes different temperature fields with pronounced temperature gradients. For example, when printing with Ti-6Al-4V, temperature gradients of about 5–20 $\frac{\text{K}}{\mu\text{m}}$ were measured and cooling rates were 1–40 $\frac{\text{K}}{\mu\text{s}}$ (Hooper 2018). This extreme and fast change in the temperature leads to expansion (during heating) and shrinkage (during cooling) of the material and implies residual stresses. As a result of the residual stress field, the components can tend to deform or even crack during printing. To ensure a successful print job, a support structure reduces the warpage of the component (Kruth et al. 2004). The high difference in thermal conductivity between powder and solid material provokes an anisotropic heat flux which affects microstructure, dimensional accuracy, and surface roughness. Especially in contour and overhanging component areas, the support structure can help to assist the uniform heat dissipation (Cao et al. 2020). Another challenge is to avoid descending an unsupported melt track into the powder bed below due to gravity and capillary forces. This causes lower accuracy and poor surface finish in downfacing areas of the component (Calignano 2014). In summary, the previously mentioned points underline that support structures are currently indispensable for LPBF to achieve an adequate printing quality. Besides ensuring a successful print result, the support structure has to consume only a small amount of material, has to have a low print time, and should be easy to remove (Zhang et al. 2018).

Figure 7.2 shows state-of-the-art types of support structures created in pre-processing. The five types shown are differentiated based on their generic design. All in all, the types differ by contrary differentiation in steadiness and material consumption. The solid block support (see Fig. 7.2a) is the most conservative one. Polyline supports (see Fig. 7.2b) are connecting the component with the build platform with thin walls (lines in cross-section). This can also be applied in patterns (for example, web support, see Fig. 7.2c) or only on the contour of the component (contour support, see Fig. 7.2d). Bar or cone supports (see Fig. 7.2e) are thin rods connecting one anchor point on the downfacing component surface and the build platform. A special type is the tree support, where several anchor points are combined and fixed together on one point at the build platform (Calignano 2014; Zhang et al. 2018). A unique concept of support structures is contact-free support, where a thin powder layer remains unmolten between the support structure and the component (Cooper et al. 2018). Currently, the selection and design of support structures is an iterative process that mainly works on best practices depending on the experience. Up to now,

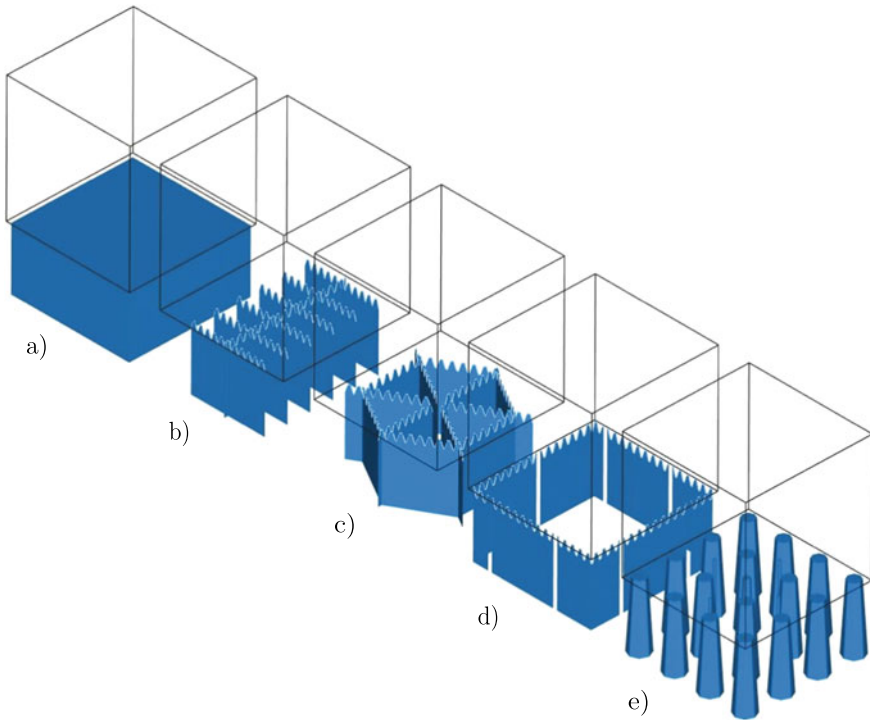


Fig. 7.2 Basic available types in support structure design: Solid block support (a), polyline support (b) with the special designs web support (c) and contour support (d), bar or cone support (e)

there are only a few studies on an optimized design of support structures (Allaire et al. 2020; Calignano 2014; Cloots et al. 2013; Zhang et al. 2018) at which a purposeful approach is still missing.

7.4 Methods for Minimizing Support Structure

State-of-the-art methods for dealing with the controversy of support structures in LPBF were recently presented (Coyné et al. 2021; Weber et al. 2021). Figure 7.3 shows available methods assigned to the respective processing step in the additive manufacturing workflow.

When creating geometry data, a support structure can be avoided by considering the design rules. These regulations define geometrical boundaries of critical features of the component that can be printed unsupported. These critical component features are, for example, inclined overhangs, bridges (horizontal overhangs), thin walls, and horizontal holes. Machine manufacturers use the feasible dimensions of

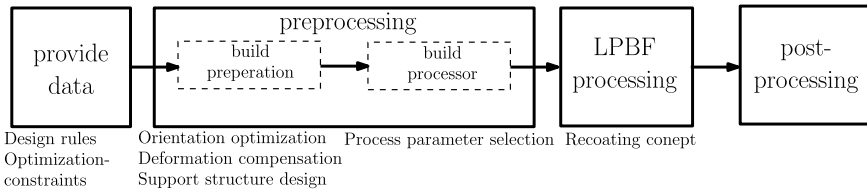


Fig. 7.3 Current methods for minimizing support in LPBF workflow

these critical features to represent the capabilities for unsupported printing of their printers and software. Concrete implementations of this method are rules in mechanical design and additional fabrication constraints in topology optimization. During preprocessing, the first step is the build preparation, in which current the slicing software optimizes the orientation of the component in the powder bed. The software orientates the component in multiple ways and suggests an orientation such less critical overhang regions are achieved. Another procedure is the compensation of deformations. For this purpose, a finite element simulation has to be performed. The design of the support structure is also done during the build preparation. As described in Sect. 7.3 this is an experience-based procedure (Weber et al. 2021).

The second step is the assignment of the process parameters in the build processor, such as laser power and scanning speed. Through a specific selection of the process parameters on weak supported layers and scan tracks, the quality of printed overhangs can be significantly increased (Cloots et al. 2017; Druzgalski et al. 2020; Mertens et al. 2014). A further important aspect in minimizing the support structure is the handling during the printing process. Process monitoring and feedback control systems ensure a precise process stability (Yeung et al. 2019). Low contact or contactless powder recoating reduces the requirement for a massive support structure (Coyné et al. 2021). Most of the methods like design rules, optimization constraints, orientation optimization, and the support structure design are just dealing with the limitation of the LPBF process itself. Hence, a gap between research and the knowledge of machine manufacturers concerning support reduced printing exists, as previously mentioned (Weber et al. 2021). Consequently, further support structure minimization strategies are needed, especially on the process side. Here, a good starting point is the systematic adjustment of the process parameters to build-up critical component features with the minimum support structure.

7.5 Selecting Process Parameters in LPBF

A large number of parameters in the LPBF process influences both the conditions during processing and the print result. In an in-depth analysis, 50 main impact variables were identified and classified into the four main groups: laser and scanning parameters, powder material properties, powder bed properties and recoat parameters, and

build environment parameters. A distinction was made between controllable and predefined parameter settings. The predefined parameters are set due to the configuration of the used LPBF printing machine (Spears and Gold 2016). Before discussing the development of a new strategy, the state of art for determining feasible process parameter combinations is reviewed.

7.5.1 State-of-the-Art Parameter Selection

Process parameters, like the laser power and the scan speed, are assigned during preprocessing. When assigning the process parameters, state-of-the-art preprocessing software (slicing software with build processor) differentiates parameter sets for down skin, up skin, and contour surfaces according to the position and orientation of the component on the build platform. These parameter sets are based on the recommendations of the respective machine manufacturers. In the recent announcements of manufacturers about new possibilities in LPBF printing, the developers refer to new build-up strategies or parameter recipes for printing critical geometric features without support (Cummings and Spink 2019; O’Leary and Schwarze 2021; Wohlfart 2019).

To cover the demand of feasible parameter combinations for new materials, academic research recommends the novel methodology of process mapping (Johnson et al. 2019; Pfaff et al. 2020; Song et al. 2012). The starting point for the process maps is the analysis of single melt tracks printed on a solid base plate with one layer of powder only. To evaluate the processability, the single melt tracks are geometrically measured and quantified in the longitudinal and transverse directions. Parameter combinations that result in uniform and continuous melt tracks are recommended for printing. Furthermore, unsuitable ranges of laser power and scan speed combinations leading to different defect phenomena are identified. Excessive energy input leads to partial evaporation of the melt pool surface, which significantly increases the absorption of the laser energy. Thus, more energy is absorbed, and the melt pool depth increases (Keyholing effect). Proceeded by rapid solidification rates, vapor encloses in the deep melt pool areas promoting pore formation (Dilip et al. 2017; Gong et al. 2014). On the other hand, too small melt pools lead to insufficient bonding with the underlying layers, referred to as lack of fusion. At high scan speeds, discontinuous melt tracks in longitudinal directions occur. This balling behavior is characterized by beading or even melting tracks without connection (Dilip et al. 2017; Gong et al. 2014; Haijun Gong et al. 2014; Johnson et al. 2019; Pfaff et al. 2020). The limits found were evaluated by printing solid test samples. Investigation of the porosity (Dilip et al. 2017; Gordon et al. 2020; Haijun Gong et al. 2014; Pfaff et al. 2020) or microstructure (Pfaff et al. 2020; Song et al. 2012) demonstrated the correlation between the quality of a single melt track and the quality of the component. For the printing of critical features, a rather rough suggestion is given. For example, it is recommended to reduce the volume energy density of the laser energy input to

11–72% and decrease the scanning speed schematically in steps of 10% (Pfaff et al. 2020). Here, the focus was on improving the surface quality or the microstructure, not extending the process limits.

7.5.2 *Parameter-Based Strategy to Minimize Support*

Some research on overhangs states the correlation between the melt pool stability and the quality of overhangs, like the surface roughness (Feng et al. 2021; Skalon et al. 2020) and the dimensional accuracy (Di Wang et al. 2013; Le et al. 2020). Additionally, it is found that the parameter sets intended for the build-up of a solid component are not suitable to print overhangs without a support structure. The deviating melt pool behavior is the situation-dependent condition at the melt pool. As described, the heat conduction from the melt pool determines the cooling rates and, therefore, the solidification of the melt track. Moreover, the thermal history of the material is influenced, and thus the formation of residual stresses can cause warpage. During a print of a component, various conditions of heat transfer situations occur (Clijsters et al. 2012). The difference between melt tracks over solid-supported layers and melt tracks in overhangs is significant (Chen et al. 2017; Mertens et al. 2014; Skalon et al. 2020).

Figure 7.4a shows the top view of a single melt track printed over unsupported powder and a solid supporting substrate. Despite the same energy input parameters, printing over a bulk material results in a continuous melt track (see Fig. 7.4d), while the powder or unsupported melt track tends to balling (see Fig. 7.4b and c). It can be seen that the melt pool behavior is strongly dependent on the situation-individual effective thermal conductivity in the printing area.

A new build-up strategy to extend the limits of unsupported printing based on optimized an process parameter selection should consider the melt pool behaviors in different heat conduction situations. In situ X-ray monitoring showed that in unsupported conditions, a continuous melt pool can be fabricated (Leung et al. 2018). Nevertheless, compared to the melt track over solid material, unsupported tracks tend to sink into the loose powder bed. Herby, the novel process mapping approach should be used with an adapted analysis for weak and unsupported melt tracks. Therefore, Fig. 7.5 shows the new collected influence parameters, including the effective thermal conductivity situation in the powder bed defining the melt pool formation. Based on this, a sound strategy should consider the correlation of these process parameters, which is open to future research. Combined with other methods, this could reduce support structures in LPBF.

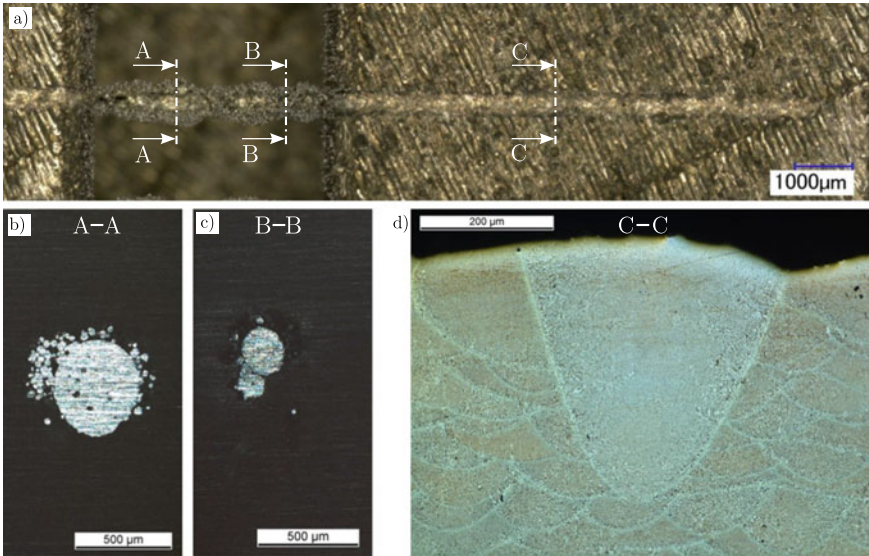


Fig. 7.4 Single melt track printed with 250 W and 250 $\frac{\text{mm}}{\text{s}}$ out of AlSi10Mg powder. The behavior in the unsupported area is shown by the sections with the narrowest width B-B and the widest width A-A. The solid support leads to a melt track with a continuous width and the cross-section C-C

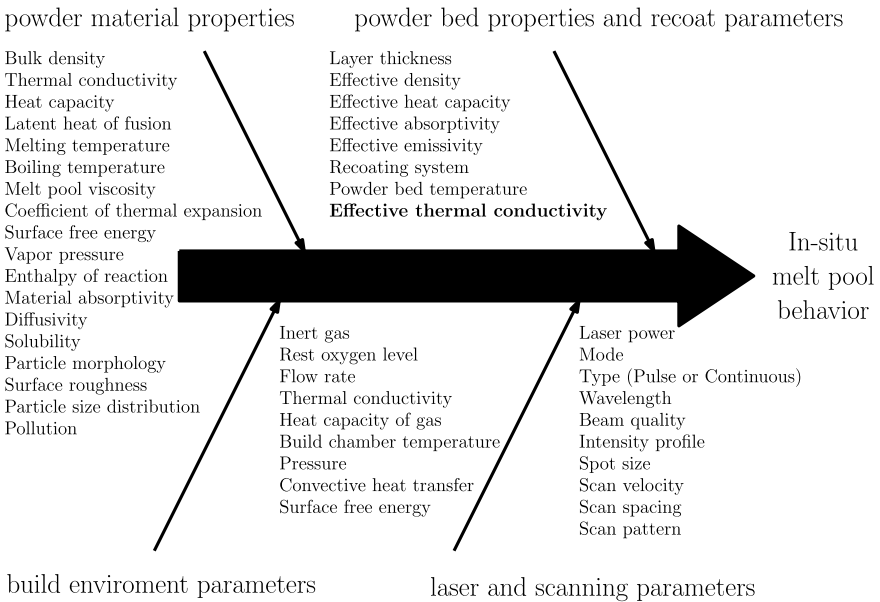


Fig. 7.5 Ishikawa diagram with influencing factors on melt pool behavior including the effective thermal conductivity in a print situation

7.6 Conclusion

Due to specific circumstances, both the productivity and the printability of complex components are limited in LPBF. The reason for this is the requirement of support structures in terms of state-of-the-art manufacturing technology. As shown, the currently applied methods for minimizing the support structure accept the restrictions and aim to improve the component quality. To push the development of LPBF, new build-up strategies for critical component features are needed. A promising technique would be to determine optimized sets of process parameters. The approach of process parameter development based on process mapping was shown as a novel way to analyze the combination of the energy input parameters. Here, the laser power and the scan speed are determined based on the evaluation of single melt tracks printed on a solid base plate with one layer of powder. These parameters are not suitable for printing unsupported overhang regions due to the different heat conduction abilities. A new strategy to extend the limits by optimized parameter selection in LPBF should be based on the melt pool physics and consider the different heat flow situations. Therefore, a collection of influencing parameters for future research is provided.

Acknowledgements This research work were funded by dtcc.bw-Digitalization and Technology Research Center of the Bundeswehr, which we gratefully acknowledge [project FLAB-3Dprint].

References

- Allaire G, Bihl M, Bogosel B (2020) Support optimization in additive manufacturing for geometric and thermo-mechanical constraints. *Struct Multi Optim* 61(6):2377–2399. <https://doi.org/10.1007/s00158-020-02551-1>
- Calignano F (2014) Design optimization of supports for overhanging structures in aluminum and titanium alloys by selective laser melting. *Mater Design* 64:203–213. <https://doi.org/10.1016/j.matdes.2014.07.043>
- Cao Q, Zhang J, Chang S, Fuh JYH, Wang H (2020) The effect of support structures on maraging steel MS1 parts fabricated by selective laser melting at different building angles. *Rapid Prototyping J* 26(9):1465–1476. <https://doi.org/10.1108/RPJ-11-2019-0287>
- Chen H, Gu D, Xiong J, Xia M (2017) Improving additive manufacturing processability of hard-to-process overhanging structure by selective laser melting. *J Mater Process Technol* 250:99–108. <https://doi.org/10.1016/j.jmatprotec.2017.06.044>
- Cloots M, Spierings A, Wegener K (2013) Assessing new support minimizing strategies for the additive manufacturing technology SLM. In: 24th International SFF symposium—an additive manufacturing conference. SFF 2013, pp 631–643
- Cloots M, Zumofen L, Spierings AB, Kirchheim A, Wegener K (2017) Approaches to minimize overhang angles of SLM parts. *Rapid Prototyping J* 23(2):362–369. <https://doi.org/10.1108/RPJ-05-2015-0061>
- Cooper K, Steele P, Cheng B, Chou K (2018) Contact-free support structures for part overhangs in powder-bed metal additive manufacturing. *Inventions* 3(1):2. <https://doi.org/10.3390/inventions3010002>
- Coyne J, Barnes JE, King WE, Slattery K, Cummings C (2021) I want to break free: the journey towards reducing or eliminating support structures. *Metal AM* 7(3):155–163

- Cummings C, Spink B (2019) 5 Advantages of VELO3D's Sapphire: not your average LPBF system-formnext 2019. <https://www.youtube.com/watch?v=n0jV2pZ3C1M>. Accessed 18 Feb 2021
- Wang Di, Yang Y, Yi Z, Su X (2013) Research on the fabricating quality optimization of the overhanging surface in SLM process. *Int J Adv Manuf Technol* 65(9–12):1471–1484. <https://doi.org/10.1007/s00170-012-4271-4>
- Dilip JJS, Zhang S, Teng C, Zeng K, Robinson C, Pal D, Stucker B (2017) Influence of processing parameters on the evolution of melt pool, porosity, and microstructures in Ti-6Al-4V alloy parts fabricated by selective laser melting. *Prog Add Manuf* 2(3):157–167. <https://doi.org/10.1007/s40964-017-0030-2>
- Druzgalski CL, Ashby A, Guss G, King WE, Roehling TT, Matthews MJ (2020) Process optimization of complex geometries using feed forward control for laser powder bed fusion additive manufacturing. *Add Manuf* 34. <https://doi.org/10.1016/j.addma.2020.101169>
- Feng S, Kamat AM, Sabooni S, Pei Y (2021) Experimental and numerical investigation of the origin of surface roughness in laser powder bed fused overhang regions. *Virtual Phys Prototyping* 16:S66–S84. <https://doi.org/10.1080/17452759.2021.1896970>
- Gong H, Rafi K, Gu H, Starr T, Stucker B (2014) Analysis of defect generation in Ti-6Al-4V parts made using powder bed fusion additive manufacturing processes. *Add Manuf* 1–4:87–98. <https://doi.org/10.1016/j.addma.2014.08.002>
- Gordon JV, Narra SP, Cunningham RW, Liu H, Chen H, Suter RM, Beuth JL, Rollett AD (2020) Defect structure process maps for laser powder bed fusion additive manufacturing. *Add Manuf* 36(101):552. <https://doi.org/10.1016/j.addma.2020.101552>
- Haijun Gong, Hengfeng Gu, Kai Zeng, JJS Dilip, Deepankar Pal, Brent Stucker (eds) (2014) Melt pool characterization for selective laser melting of Ti-6Al-4V pre-alloyed powder. University of Texas
- Hitzler L, Merkel M, Hall W, Öchsner A (2018) A review of metal fabricated with laser- and powder-bed based additive manufacturing techniques: process, nomenclature, materials, achievable properties, and its utilization in the medical sector. *Adv Eng Mater* 20(5):1700,658. <https://doi.org/10.1002/adem.201700658>
- Hooper PA (2018) Melt pool temperature and cooling rates in laser powder bed fusion. *Add Manuf* 22:548–559. <https://doi.org/10.1016/j.addma.2018.05.032>
- Johnson L, Mahmoudi M, Zhang B, Seede R, Huang X, Maier JT, Maier HJ, Karaman I, Elwany A, Arróyave R (2019) Assessing printability maps in additive manufacturing of metal alloys. *Acta Mater* 176:199–210. <https://doi.org/10.1016/j.actamat.2019.07.005>
- Kruth JP, Froyen L, van Vaerenbergh J, Mercelis P, Rombouts M, Lauwers B (2004) Selective laser melting of iron-based powder. *J Mater Process Technol* 149(1–3):616–622. <https://doi.org/10.1016/j.jmatprotec.2003.11.051>
- Le KQ, Wong CH, Chua K, Tang C, Du H (2020) Discontinuity of overhanging melt track in selective laser melting process. *Int J Heat Mass Trans* 162(120):284. <https://doi.org/10.1016/j.ijheatmasstransfer.2020.120284>
- Leung CLA, Marussi S, Atwood RC, Towrie M, Withers PJ, Lee PD (2018) In situ X-ray imaging of defect and molten pool dynamics in laser additive manufacturing. *Nature Commun* 9(1):1355. <https://doi.org/10.1038/s41467-018-03734-7>
- Mertens R, Clijsters S, Kempen K, Kruth JP (2014) Optimization of scan strategies in selective laser melting of aluminum parts with downfacing areas. *J Manuf Sci Eng* 136(6). <https://doi.org/10.1115/1.4028620>
- O'Leary S, Schwarze D (2021) SLM solutions free float-the big live launch. <https://freefloat.slm-solutions.com/factsheet>. Accessed 18 Feb 2021
- Pfaff A, Jäcklein M, Schlager M, Harwick W, Hoschke K, Balle F (2020) An empirical approach for the development of process parameters for laser powder bed fusion. *Mater* (Basel, Switzerland) 13(23). <https://doi.org/10.3390/ma13235400>
- S Clijsters, T Craeghs, J-P Kruth (eds) (2012) A priori process parameter adjustment for SLM process optimization. Taylor & Francis Group

- Skalon M, Meier B, Gruberbauer A, Amancio-Filho ST, Sommitsch C (2020) Stability of a melt pool during 3d-printing of an unsupported steel component and its influence on roughness. *Mater* (Basel, Switzerland) 13(3). <https://doi.org/10.3390/ma13030808>
- Song B, Dong S, Zhang B, Liao H, Coddet C (2012) Effects of processing parameters on microstructure and mechanical property of selective laser melted Ti6Al4V. *Mater Design* 1980–2015(35):120–125. <https://doi.org/10.1016/j.matdes.2011.09.051>
- Spears TG, Gold SA (2016) In-process sensing in selective laser melting (SLM) additive manufacturing. *Integrating Mater Manuf Innov* 5(1):16–40. <https://doi.org/10.1186/s40192-016-0045-4>
- Weber S, Montero J, Bleckmann M, Paetzold K (2021) Support-free metal additive manufacturing: a structured review on the state of the art in academia and industry. Cambridge University Press. <https://doi.org/10.1017/pds.2021.542>
- Wohlfart M (2019) Can you Build a 100 mm Support-free Horizontal Disk? <https://www.linkedin.com/pulse/can-you-build-100-mm-support-free-horizontal-disk-michael-wohlfart/>. Accessed 18 Feb 2021
- Yeung H, Lane B, Fox J (2019) Part geometry and conduction-based laser power control for powder bed fusion additive manufacturing. *Add Manuf* 30. <https://doi.org/10.1016/j.addma.2019.100844>
- Zhang K, Fu G, Zhang P, Ma Z, Mao Z, Zhang DZ (2018) Study on the geometric design of supports for overhanging structures fabricated by selective laser melting. *Mater* (Basel, Switzerland) 12(1). <https://doi.org/10.3390/ma12010027>

Chapter 8

Influence of Relative Humidity on Thermal Properties of Tool Steel Powder



Garvin Schultheiss, Josef Tomas, and Markus Merkel 

Abstract The ever-increasing demands on component properties have been inspiring research in the additive manufacturing sector for years, driving it to gain a greater understanding of process phenomena in order to find new creative solutions for industrial applications. Due to the peculiarities of the selective laser melting process, anisotropic component properties often occur, which are usually undesirable and on the prevention of which a great deal of research focuses. Current research topics focus mainly on the properties of iron alloys in particular tool steel. The moisture of the powder has an influence on the flowability. With the change of relative humidity, the thermal properties of the powder also change. The question arises as to how the influence of the relative humidity affects the thermal properties of the powder. In this work, the influence of relative humidity on the thermal conductivity of tool steel powder is investigated. The transient plane source method is used to determine thermal transport mechanisms of the material.

8.1 Introduction

The additive manufacturing industry has achieved a growth of 7.5% in 2020 compared to 2019. In 2020, sales of metals for AM grew by 15.2% compared to the previous year (Wohlers et al. 2021). The possibilities of this production process are far from exhausted. In particular, the difficulty of thermal effects during the process makes it difficult to reliably produce components with known thermal and mechanical properties (Hitzler et al. 2017). For this reason, components are often subjected to thermal post-treatment to homogenize the microstructure and reduce residual stresses, which

G. Schultheiss · J. Tomas (✉) · M. Merkel
Aalen University of Applied Sciences, Beethovenstr. 1, 73430 Aalen, Germany
e-mail: josef.tomas@hs-aalen.de

G. Schultheiss
e-mail: garvin.schultheiss@hs-aalen.de

M. Merkel
e-mail: markus.merkel@hs-aalen.de

© The Author(s), under exclusive license to Springer Nature Switzerland AG 2022
H. Altenbach et al. (eds.), *Lectures Notes on Advanced Structured Materials*,
Advanced Structured Materials 153, https://doi.org/10.1007/978-3-031-11589-9_8

negates some efficiency gained through the process. During the construction process, a lot of heat is introduced by the laser, which is for the most part being dissipated through the part. The surrounding powder bed and the constant addition of more energy make it difficult for the heat to dissipate evenly due to the insulating effect of the powder.

Hadley et al. (1986) have examined experimentally and theoretically the thermal conductivity of the binary powder system brass and 316L stainless steel under various gas pressures ranging from vacuum to 2 MPa. Measurements were made with loose powder up to a theoretical density of 90% with the steady-state comparator method. This method uses a one-dimensional constant heat flow, guided through a series of disks with known thermal properties inside a pressure vessel. The sample is placed between the identical standard disks, so the conductivity can be determined through any drops in temperature, which are registered by thermocouples alongside the vessel. The research of Hadley et al. (1986) measured the thermal conductivity for 316L stainless steel powder of 0.331 W/(mK) at ambient pressure and 0.588 W/(mK) in a vacuum. Suggesting that the thermal conductivity of powder is mainly dependent on the thermal conductivity on the interstitial gas.

Gruzdev et al. (1990) have conducted thermal conductivity measurements of two binary, compressed powder systems, Al–Ni and Al–Zr. The powder mixtures were pressed into round test specimens at a pressure of 5 t and then measured depending on their porosity using an automatic λ -calorimeter with the linear heating method. The test specimen is placed between a metallic block and the calorimetric unit in an adiabatic environment. Because the thermal properties of the metal block are well known, the thermal conductivity of the specimen can be calculated from the drop in temperature between the two measuring elements. Gruzdev et al. (1990) could show that less dense specimens have a significantly lower thermal conductivity. This is mainly due to the reduced contact area of the particles.

Shapiro et al. (2004) used a stationary method to measure the thermal conductivity of different materials including alumina under the influence of various infiltrating gasses (Helium, Air, Argon) and gas pressures. It follows the same principle as Hadley et al. (1986). The metal powder is being filled into a cylindrical adiabatic cavity on top of a known reference specimen and mechanical pressure varying from 3.9 to 18.8 kPa is being applied. Powder and specimen are subjected to unidirectional heat flux, and temperature differences alongside the two are registered by thermocouples. The experiments were conducted inside a pressure chamber. Experimental data was extended with a simplified version of the model of Bauer and Schlünder (1978) to be able to make a statement about contact surfaces and heat conduction resistances of bulk materials. Results show that the infiltrating gas, the gas pressure and the bulk density have a significant impact on the thermal conductivity of powders.

Alkahari et al. (2012) used the laser ash technique and a self-developed theoretical model to determine the influence of bulk density and particle diameter on the thermal conductivity of different metal powders and powder mixtures. They were able to show that the thermal conductivity increases with increasing particle diameter and density.

Table 8.1 Chemical composition of tool steel powder

Fe	C	Cr	Mn	Mo	NiCu	P	S	Si	V
Bal.	0.32– 0.45	4.75– 5.50	0.20– 0.60	1.10– 1.75	0.75	0.03	0.03	0.80– 1.25	0.80– 1.20

In the study of thermal conductivities of diverse metal powders under the influence of different inert gases (Argon, Nitrogen and Helium) was done by Wei et al. (2018). For conducting the experiments, the transient hot wire method was used. A platinum wire was immersed into a powder that lies inside a rectangular test section made from copper. The whole setup was then covered with a glass bell jar, which has connections for a vacuum pump and gas supply. They found that the type of inert gas and its pressure have a significant influence on the thermal conductivity of the powder. However, the powder material has a very small influence.

The influence of the relative humidity of the metal powder on its thermal transport properties is not evident from the literature. In this work, the influences of relative humidity on thermal properties of tool steel powder are examined. For the gas in the interstices, air was used since powder bed fusion process is mostly run on nitrogen, and the ambient air consists of 78% of it.

8.2 Methodology

Gas atomized tool steel powder (tool steel 1.2344/ A681 H13/ H13, SLM Solutions Group AG), which is also used in laser powder bed fusion process, with a theoretical density of $8 \text{ g}/(\text{cm})^3$ was used. The chemical composition is given in Table 8.1. The shape of the entire powder is spherical.

In order to determine the thermal transport characteristics, a “Hot Disk TPS 2500 S” thermal constants analyser (Tomas et al. 2021) is used for this research. It covers an extensive range of materials of various geometries and meets ISO standard 22007-2. The device is compatible with different modules. This allows the thermal properties of isotropic as well as anisotropic materials to be measured. In addition, one-dimensional measurements can be made on rods, and it is also capable of doing measurements in the surface of thin film test specimens. The great advantages of this method over other measurement methods are the simplicity with which the experiments can be carried out and the versatility of its use.

To be able to use the transient source plane method on powders, a powder holder was constructed and then manufactured out of AlCuMgPb, Fig. 8.1. The powder is filled from the top-up to the slit, then the sensor is inserted from the side and the rest of the vessel is filled with powder. Then the container can be closed.

Fig. 8.1 Powder holder for thermal properties measurement



8.3 Experimental Setup

To determine this influence experimentally, the sample holder chamber was hermetically sealed. Inside, moist tool steel powder was placed in an open powder holder 8.1 with an embedded 9.868 mm hot disk sensor (HD 8563). To extract the moisture from the powder, two 100 g silica gel packs were placed inside the sample holder chamber. The setup is shown in Fig. 8.2. The same packs are being used to dry the powder before adding it to the process. Additionally, a humidity sensor (HYTELOG-RS232) was placed inside the measuring chamber, to monitor the relative humidity of the air inside. The tests carried out previously have shown that 100 g of silica gel is sufficient for the amount of powder to reduce the moisture content of the powder, and the moisture will be removed from the powder after a certain time. This experiment was conducted over 24 h to make sure that the relative humidity of the powder can equalize with the relative humidity of the air inside the test setup. Relative humidity cannot be monitored in the powder sample directly because the added humidity sensor would change the thermal properties of the powder sample, and the measuring room is very limited in size, so an additional container with the same powder could not be placed inside. The temperature sensor of the hot disk device was also placed inside the setup. The “Hot Disk TPS 2500 S S” thermal constants analyser from Hot Disk AB was used to carry out the following measurements. The thermal conductivity, thermal diffusivity, specific heat capacity as well as the relative humidity of the powder were measured prior to the experiment. After closing the setup and thus starting the experiment, the measurement was done every 30 min, to give the sample enough time to equalize its temperature.

8.4 Results

The absolute change in thermal conductivity over the test period was recorded as 0.0038 W W/(mK), the maximum difference in thermal conductivity over measurement period is 0.0126 W W/(mK). The thermal diffusivity behaved very similarly, but only changed by a hundredth, see Fig. 8.3. The relative humidity of the air in

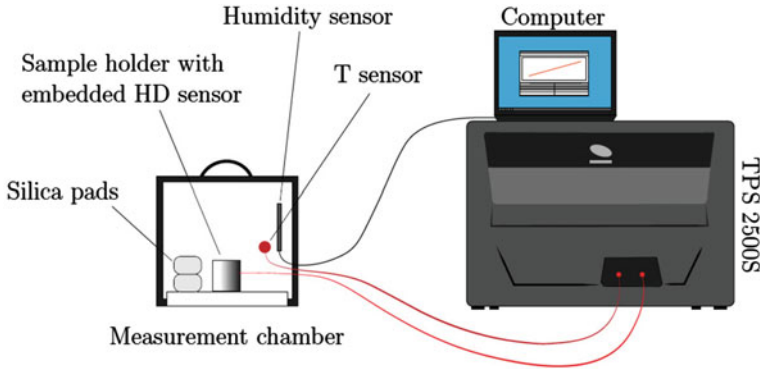


Fig. 8.2 Experimental setup to determine the influence of relative humidity on tool steel powder (HD: hot disk, T: temperature)

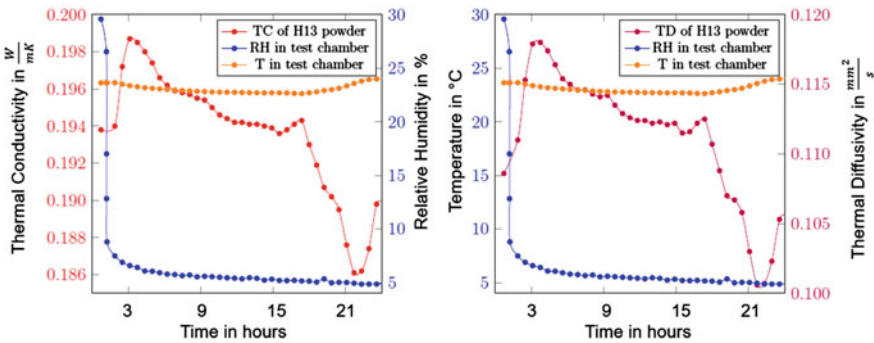


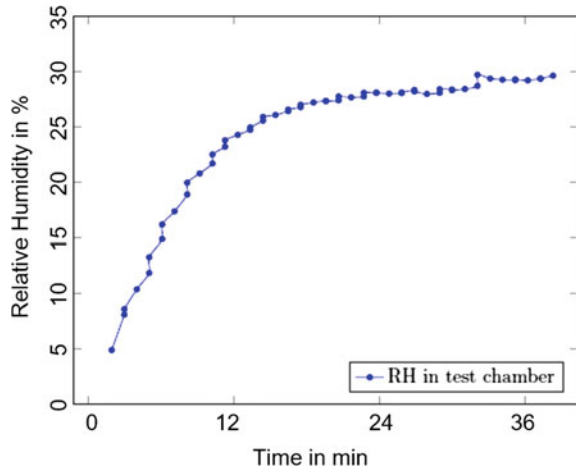
Fig. 8.3 Thermal conductivity and diffusivity of tool steel relative humidity in test chamber over 24 h (TC: thermal conductivity, TD: thermal diffusivity, RH: relative humidity, T: Temperature at $(23.15 \pm 1.00)^\circ\text{C}$)

test chamber dropped rapidly and reached a value below 10% within 30 min. Within 270 min, relative humidity of less than 6% was recorded. In the further course of the measurement, relative humidity stabilized at a value of about 5%.

The thermal conductivity of the powder rises to its maximum after 120 min and then sinks steadily over the course of the measurement. It reaches its low point of $0.1861 \text{ W W}/(\text{mK})$ and then rises again to $0.19 \text{ W}/(\text{mK})$ for the last measured point. The temperature of the powder remained in the range of $(23.15 \pm 1.00)^\circ\text{C}$ over the course of the measurement.

After the setup was opened, the relative humidity of the powder was measured as 4.96%. The humidity sensor now remained in the powder sample until the humidity of the powder had adapted to the environment. This moisture absorption took 30 min as shown in Fig. 8.4. This was measured to see how long the powder needs at room temperature (here: 23.15°C) to reach the maximum relative humidity. For additive manufacturing, it is of great importance how long the powder may be exposed to

Fig. 8.4 Increase in relative humidity in the powder due to the contact with ambient air (RH: relative humidity)



humidity because from a relative humidity of approx. 20%, the powder has only limited flowability, depending on the particle size and is therefore not suitable for manufacturing.

8.5 Discussion

It can be seen an increase in thermal conductivity and diffusivity, then a decrease over a long period of time followed by a rise after it hit its low turning point. The increase at the beginning could be a stabilization process. Although the following steady decrease in thermal conductivity suggests that the change in relative humidity in the powder leads to a decrease in the thermal conductivity of the powder, the difference is just 1.9% and hence lies within the range of uncertainty of the method (Gustafsson 1991). It can therefore not be accepted as a fact without further investigation. It is also possible, that the difference in thermal conductivity comes from the small changes in the sample temperature or subtle changes in the bulk. Mahapatra et al. (2011) have studied the influence of relative humidity on the thermal conductivity properties of rice flour. This can only be compared with metal powders to a limited extent, but the opposite behavior of thermal diffusivity and relative humidity could be found. This does not coincide with the observations made here for tool steel. Other than that, no published research could be found to compare the results on the relative humidity influence on powder.

8.6 Conclusion

With the experiment to determine the humidity dependency of the thermal conductivity of tool steel, the change in thermal conductivity and diffusivity over 24 h was measured while the relative humidity of the powder sample was reduced from 29.58 to 4.96%. The results show that the thermal properties of the loose powder change only slightly during the test. The changes could not be related with certainty to the changes in relative humidity. To make a better statement, the methods used must be improved.

Acknowledgements This work was financially supported by the Ministry of Science, Research and the Arts of the State Baden-Wuerttemberg (Germany).

References

- Alkahari MR et al (2012) Thermal conductivity of metal powder and consolidated material fabricated via selective laser melting. *Key Eng Mater Trans Tech Publ* 523:244–249
- Bauer R (1978) Effective radial thermal conductivity of packings in gas flow. *Int Chem Eng* 18:181–204
- Gruzdev VA, Kovalenko YA (1990) Thermal conductivity of pressed metal powder materials. *Exp Heat Transf Int J* 3(2):149–158
- Gustafsson SE (1991) Transient plane source techniques for thermal conductivity and thermal diffusivity measurements of solid materials. *Rev Sci Instrum* 62(3):797–804
- Hadley GR (1986) Thermal conductivity of packed metal powders. *Int J Heat Mass Transf* 29(6):909–920
- Hitzler L et al (2017) On the anisotropic mechanical properties of selective laser melted stainless steel. *Materials* 10(10):1136
- Mahapatra A, Lan Y, Harris D (2011) Influence of moisture content and temperature on thermal conductivity and thermal diffusivity of rice flours. *Int J Food Prop* 14(3):675–683
- Shapiro M et al (2004) Characterization of powder beds by thermal conductivity: effect of gas pressure on the thermal resistance of particle contact points. *Part Part Syst Charact Meas Description Part Prop Behav Powders Other Disperse Syst* 21(4):268–275
- Tomas J, Öchsner A, Merkel M (2021) Experimental study on thermal properties of hollow sphere structures. *Defect Diffus Forum Trans Tech Publ* 407:185–191
- Wei LC et al (2018) Thermal conductivity of metal powders for powder bed additive manufacturing. *Addit Manuf* 21:201–208
- Wohlers T et al (2021) Wohlers report 2021: 3D printing and additive manufacturing: global state of the industry. Fort Collins, Wohlers Associates

Chapter 9

An Overview on the 3D Printing of Elastomers and the Influence of Printing Parameters on Their Mechanical Properties



Vivianne M. Bruère , Alexander Lion, Jens Holtmannspötter, and Michael Johlitz

Abstract Additive manufacturing (AM) technologies show a great potential to revolutionize the fabrication and logistics of components. However, the field of elastomers is a rather unexplored topic regarding 3D printing compared to other types of materials. To enlarge the scientific knowledge of 3D printing of elastomeric parts, this work starts with a literature overview and a discussion of AM in general. Subsequently, AM of elastomers is presented with the focus on fused filament fabrication (FFF) particularities. Characteristics and limitations as well as relevant aspects to be considered when dealing with thermoplastic elastomers in FFF printers are addressed. A quantitative analysis follows, investigating the primary effect of the infill raster orientation on the tensile behavior of samples printed in a FFF printer using thermoplastic polyurethane. A minor influence of unidirectional (0° , 45° , 90°) and alternating (45° – 135°) orientations was verified for strains below 400%, which becomes more significant for the higher strain range and the resulting ultimate tensile stress.

Keywords Elastomers · Fused filament fabrication · Raster orientation · Tensile behavior · Thermoplastic polyurethane

9.1 Introduction

In present-day, additive manufacturing (AM) is manifested by the visible rapid improvement of processing technologies and the constant expansion of material libraries. Originated in the prototyping field, AM has broadened its applications to in-service products. AM allows a quick adaptation to new market needs. A recent example is the role AM played in the outbreak of the current coronavirus

V. M. Bruère (✉) · A. Lion · M. Johlitz
Institute of Mechanics, University of the Bundeswehr Munich, Neubiberg, Germany
e-mail: vivianne.bruere@unibw.de

J. Holtmannspötter
Bundeswehr Research Institute for Materials, Fuels and Lubricants, Erding, Germany

disease 2019 (COVID 2019). The shortage of both personal protective equipment (PPE) and medical devices due to the unpredictable evolution of the pandemic and the global disruption of linear supply chains led to the emergency fabrication of this medical equipment. Universities, companies and even hobbyists were directly involved, voluntarily or not, assisting in the fast decentralized production of 3D printed parts, e.g., face shields, masks, suits, nasopharyngeal swabs, respirators and ventilators (Advincula et al. 2020; Parry and Banks 2020; Tareq et al. 2021).

The pandemic showed the relevance of AM and illustrated some of its great advantages: on-demand, local manufacturing with low lead times. Aside from this, 3D printing allows the fabrication of customized and complex parts without individual tooling. In addition, waste and post-processing can be reduced (Klahn et al. 2015; Bikas et al. 2016; Ford and Despeisse 2016; Januszewicz et al. 2016). In contrast, the challenges concerning product safety, standardization and regulation (Parry and Banks 2020), as well as reliability and quality consistency (Joshi and Sheikh 2015; Liu et al. 2017) hinder a wider application of AM for manufacturing purposes. For some technologies and materials, the inferior mechanical properties compared to those from established conventional fabrication methods are still an issue (Lukić et al. 2016; Ligon et al. 2017). Therefore, research and testing of the capabilities of AM technologies and associated materials are essential for a better understanding and their further application as a manufacturing route.

A recent topic of interest is 3D printing of elastomeric materials. They are of great importance for complex machines and have to fulfill multiple requirements. Components such as seals, bushings, membranes, hoses and rubber sleeves are manufactured with elastomers, which suffer fatigue and aging during operation and, therefore, require frequent replacement. These components may as well be subjected to aging during storage, resulting in significant warehousing costs. Challenges in logistics must be considered, particularly for demands in remote locations, for instance, in case of military operations. Hence, AM of elastomeric parts could lead to major economical improvements. A relevant drawback is that conventional elastomers are not easily processable in AM, since the printing technology dictates the type and nature of the material used.

With this in mind, this work aims to introduce the reader to the field of AM, showing material requirements and general particularities, then analyzing the possibilities for printing elastomeric materials. An overview of some of the currently available 3D printing technologies is presented. The focus is later placed on the fabrication of rubber-like parts and existing alternatives. A further discussion of the capabilities and challenges of elastic filaments for fused filament fabrication (FFF) is conducted. An applied case study of a thermoplastic polyurethane filament is thereafter carried out, with the objective of verifying the influence of the infill orientation on the material behavior by means of tensile tests. This work, therefore, contributes to the investigation of elastomers in the AM scenario for a greater comprehension on the subject, as well as paving the way for future studies towards material characterization, modeling and numerical applications.

9.2 Overview on Additive Manufacturing

9.2.1 Definition and Technologies

The American Society of Testing and Materials (ASTM) defines AM as a “process of joining materials to make objects from 3D model data, usually layer upon layer” (ASTM 2012). This manufacturing process, commonly known as 3D printing, starts with the creation of a three-dimensional computer-aided design (CAD) model of an object, where STL has become the standard file format in this field. The CAD geometry is imported into a specific software (named “slicer”), then sliced into a series of layers according to the printing parameters. Each AM technology has an appropriate slicer and corresponding parameters to be used, generating the printing instructions for each layer. These instructions are stored in a G-code file and read by the 3D printer for the fabrication of the desired part. The process stages are illustrated in Fig. 9.1. Post-processing operations for product enhancement may be needed, depending on the technology, the geometry or even the printing resolution and requirements. Those include: removal of support or excess material, washing, curing, polishing, sanding and painting.

The various AM technologies differ mainly in the mode of the layer deposition, the operating principle and the material feasibility. A common classification based on the layer deposition mechanism (ASTM 2012) can be seen in Fig. 9.2. Regarding polymers, all except direct energy deposition (typically for metals) are applicable. In Table 9.1, some examples of AM technologies are summarized.

As observed in Table 9.1, each technology has its particularities, and the 3D printing process dictates the type of employed material, also affecting the quality of the final part. Some AM technologies use thermoplastics; others use thermosets (either thermally or UV-cured). SLA, on the one hand, provides great resolution; on

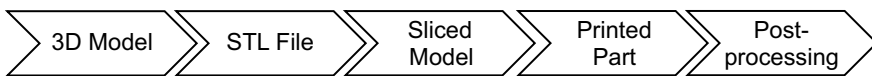


Fig. 9.1 Steps of 3D printing

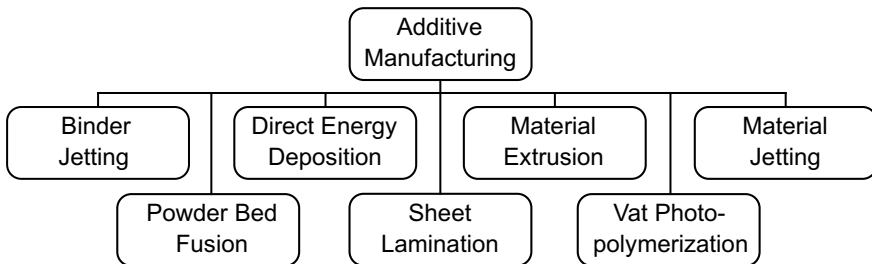


Fig. 9.2 Classification of AM processes according to the layer deposition mechanism

Table 9.1 Description of commercially available AM technologies

Technology	Classification	Description	Material
Selective laser sintering (SLS)	Powder bed fusion	Powder is selectively sintered by a laser	Thermoplastic powder
Fused filament fabrication (FFF)	Material extrusion	Material is extruded through a heated nozzle, melted and deposited in a bed	Thermoplastic filament or pellets
Liquid additive manufacturing (LAM)	Material extrusion	Highly viscous material is extruded onto a build plate, then cured by heat	High viscosity thermosetting liquid (silicone, polyurethane)
PolyJet	Material jetting	Multiple nozzles deposit droplets of material that are then cured by UV light	UV-cured resin (photopolymer)
Stereolithography (SLA)	Vat photopolymerization	Resin in a vat is selectively cured by an UV laser	UV-cured resin (photopolymer)
Digital light processing (DLP)	Vat photopolymerization	Resin in a vat is selectively cured by a digital light projector	UV-cured resin (photopolymer)

the other hand, the mechanical properties of the printed materials often show weak spots and, generally, post-curing is required. DLP allows faster printing compared to SLA but leads to a lower accuracy. LAM exhibits similar material properties as manufacturing by injection molding but is restricted to highly viscous materials and support structures cannot be printed. Support is not needed in SLS, as the unsintered powder acts as such; however, shrinkage effects rough surfaces are drawbacks. PolyJet prints with dissolvable support material and low viscosity inks, also allowing multi-material and colored parts. Finally, FFF is the least expensive and most familiar 3D printing technology. Due to low emissions, it can be used even in offices and there is a great variety of FFF filaments. However, accuracy is low and the adhesion between consecutive layers limits the strength of the print. The specific geometry of the component in service and its application should be taken into account for a proper selection of the 3D printing technology.

9.2.2 Elastomers in 3D Printing

AM has already achieved a considerable progress in the technical field for metals and high-performance polymers, which are especially used in the aerospace industry and offer a good combination of quality consistency and reproducibility. However, the 3D printing of elastomers is still comparably in its early stages, mostly restricted to prototyping and research. Typical examples of elastomers are natural rubber, styrene-butadiene rubber (SBR) and silicone. As a rule, these materials are not suitable for the current AM technologies due to the required nature of the material (mainly thermoplastics or UV-cured resins). Vulcanization cannot be easily transferred to 3D printing processes as well. An exception is LAM, which uses a conventional two-component liquid silicone rubber (LSR). Hence, alternative rubber-like materials, whether already existing or newly developed, are generally employed in AM to fulfill the process requirements. Elastic photopolymers are frequently applied in vat photopolymerization, material jetting and binder jetting machines; thermoplastic elastomers (TPEs)—specifically, thermoplastic polyurethanes (TPUs)—are the choice for powder bed fusion and filament extrusion printers.

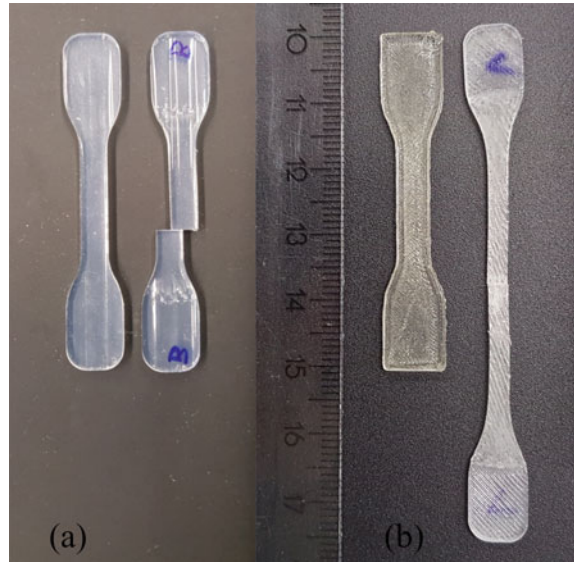
Due to the wide range of material options, the variety in the resulting material properties is large. Table 9.2 gives a brief outline of the tensile properties for the TPU Recreus Filaflex 70A from company Recreus (Elda, Spain) (Recreus 2022a), for the combined photopolymer TangoBlackPlus with VeroClear from Stratasys® (Rehovot, Israel) with two grades of hardness (Stratasys 2022), and for a LSR supplied by Dow® (Midland, MI, USA) called SILASTIC™ LC 3335 (Dow 2018).

It can be observed that the shore hardness values for the considered materials do not correlate with the tensile strength. Silastic is highly elastic and return to its original size after stress release (Fig. 9.3a). TPU Filaflex filaments are flexible and can also reach high strain levels, but exhibit plastic deformation (ca. 50% in Fig. 9.3b). In addition, parts printed with thermoplastics cannot withstand high operational temperatures. As to the Tango+ photopolymers, they present lower mechanical strengths. Exposure to natural sunlight also accelerates the aging process, leading to a brittle behavior in a shorter amount of time compared to the other elastic materials. Moreover, they usually show some tackiness as well as a characteristic smell which may be unpleasant for some users and should be considered for applications in case of contact with humans.

Table 9.2 Tensile properties of 3D printing materials from manufacturers

Materials	Filaflex 70A	Tango+ 70	Tango+ 50	Silastic
Technology	FFF	PolyJet	PolyJet	LAM
Tensile strength (MPa)	32	3.5–5.0	1.9–3.0	9.5
Elongation at break (%)	900	65–80	95–110	480
Hardness (Shore A)	70	70	50	50

Fig. 9.3 Comparison of original size to size after tensile test for **a** Silastic and **b** Filaflex 70A



There are still several manufacturing limitations for the 3D printing of elastomers. These limitations are not only the restriction of the type and nature of the material for the investigated technology and their resulting mechanical strength, but also the printing process itself. For elastic materials, printing of complex geometries is more challenging compared to stiff materials, since support structures cannot be easily removed. Another critical aspect is moisture absorption. In a previous work (Loos et al. 2021), the influence of water absorption on samples printed with the above mentioned materials was investigated and verified. Filaflex 70A and Tango+ presented a significant mass gain above 2.8%, while Silastic showed a low moisture absorption below 0.2% at saturation. Likewise, the mechanical behaviors of the studied TPU and photopolymers were affected on a larger scale in comparison with LSR. This information is relevant for printed parts used in moist environments or water applications. Moisture absorption is also to be considered before and during the printing process. For instance, in FFF printers, the temperature of the nozzle required for the filament melting and extrusion is above the water evaporation temperature. If the filament contains moisture, voids in the streaming are created and extrusion failures take place.

Each AM technology has its own particular printing conditions and post-processing procedures. Process deviations affect the quality and the mechanical performance of the final prints. Post-curing of rubber-like thermosets and the choice of the deposition path in material extrusion techniques are some examples. To overcome the discussed shortcomings, the market is constantly developing in the field of materials science and technologies to improve the mechanical capabilities of the used materials. Improvements are also achievable by scientific research, the direction

in which this work is oriented. In the following sections, the focus is the 3D printing process FFF and its peculiarities when dealing with a TPU filament.

9.2.3 *FFF with Elastic Materials*

As previously mentioned, the operation of FFF 3D printers with elastomeric materials require the use of thermoplastic elastomers. Among several types of TPEs, TPU is one of the most advantageous material for printing flexible geometries. This is the result of physical crosslinks between hard, isocyanate-based segments and soft, polyester/polyether chain segments (Drobny 2014), allowing large deformation and bending. For this reason, printing with TPU, especially with remote extruders, is challenging due to their lack of stiffness that the FFF extrusion process demands to successfully compress the filament and push it through the hot nozzle. Buckling is a typical aspect affecting the print control (Gilmer et al. 2018). Some relevant attributes for printing with FFF concerning the technology itself and the use of TPU filaments can be found in Table 9.3.

When dealing with TPU filaments, the main issue is extrusion failure, more specifically, under-extrusion. All materials are potentially subjected to under-extrusion. Common solutions include an increase in printing temperature and/or flow (more material is then extruded), a reduction in printing speed and/or retraction settings, as well as the use of the correct filament diameter and a clean nozzle. Particularly for TPUs, higher printing speeds may deliver more under-extruded parts. As for retraction, it should be minimal for elastic filaments, and at times, disabled. In order to compensate the low retraction settings without inducing too much stringing, faster print head movements in the x–y plane can be applied. Another alternative is to set the printing process by keeping the flow as constant as possible in order to avoid extrusion interruptions and consequent retraction points.

Under-extrusion has not only a mechanical source (e.g., buckling), but also a physical source, in the case of moisture. Buckling is low for stiff filaments but predominant for soft elastic materials. The extruder motor pushes the filament in a way that it can act like a piston and be extruded through the heated nozzle; nevertheless, the low Young's modulus of TPUs offers resistance and hinders the uniform flow. For this reason, direct extruders are preferred to Bowden (remote) extruders. Although with more weight on the print head and consequent mass vibrations, direct extruders enable a better printing control due to the reduced filament length. Consequently, increased reproducibility can be achieved. Buckling during the printing of elastic materials can, however, be eliminated using pellet-based systems. TPU filaments are also very sensitive to moisture, as previously mentioned. Moist filaments processed in FFF lead to steam formation at the hot end, since the printing temperatures are generally above 100 °C. Therefore, the streaming leads to voids, and a lower quality of the printed part including bubbles trapped inside and induced cracks. Filament drying is necessary to avoid these issues, as well as filament storage before/after and, depending on the environment humidity, during printing.

Table 9.3 Attributes typical in FFF and typical of TPU filaments

Attribute	General or specific	Consequence	Comments and solution
Single nozzle deposition	General to FFF	Time-consuming print	C: common nozzle diameters of 0.25–0.8 mm
Limited build plate	General to FFF	Limited print size	S: print larger, separate parts and assemble
Interlayer adhesion	General to FFF	Low adhesion: lower quality and performance (line detachment)	S: reduce layer height, increase printing temperature
Intralayer adhesion	General to FFF	Low adhesion: lines in the same layer not attaching to each other	C: evidence of under-extrusion S: increase flow
Adhesion plate-part	General to FFF For TPUs: no issues	Low adhesion: print does not stick to plate	S: coat plate with an adhesive, increase contact area and/or plate temperature
Printing of complex geometries with support structures	General to FFF For TPUs: an issue	Printing of bridges and overhangs possible	C: check material compatibility (limited for TPUs), compromised surface on contact area (cannot be easily broken away for TPUs)
Filament buckling	Typical of TPUs	Extrusion failures, discontinuous flow, under-extrusion	C: due to TPU's low elastic modulus S: reduce printing speed, reduce/remove retraction, keep flow constant, choose Direct extruder
Moisture in the filament before print	Typical of TPUs	Extrusion failures, non-uniformity of the flow, under-extrusion, induced flaws	C: TPUs are hygroscopic S: filament drying, proper material storage before, during and after printing

A further consideration for FFF printing with TPUs is the unfeasibility of printing with support material. The compatibility with other materials to act as support is more limited and their elastic nature hinders the support removal, even for support materials of the same type. The use of brims fits into this matter; in the case of stiff materials, the breakaway of the plate-part adhesion features is easily performed, which is not the case for TPUs. Moreover, for TPUs there are no issues regarding plate-part adhesion as well as shrinkage effects, exempting the need of plate heating or use of adhesives. Thus, skirts surrounding the geometry are sufficient to ensure a good flow before

printing the object, preventing the removal of excess material connected to the part and consequent compromised surfaces. Knowledge as such, whether acquired within the 3D printing community or through experience, was considered for the following investigation.

9.3 Applied Case on FFF with a TPU Filament

For the FFF process, the raster orientation, i.e., the direction of the material deposition, was primarily investigated. The aim was to study the influence of this printing parameter on the tensile behavior of the printed samples. Two investigations were carried out: in the first, denoted by A, analyzed the unidirectional raster orientation, while the second, referred to as B, focused on the alternating orientation for two printing temperatures. The experimental methods of both studies and the results are discussed in the following sections.

9.3.1 *Experimental Procedure*

The samples investigated were printed in a German RepRap $\times 500$ 3D printer, equipped with a 0.4 mm nozzle and a direct drive extruder for filament diameters of 1.75 mm. The used material was the TPU Filaflex 82A (Recreus, Spain) (Recreus 2022b), which is a polyether polyurethane. The definition of the printing parameters was based on a combination of manufacturer suggestions and personal experiences from parameter adjustments to the used machine. The printing speed is set to a lower value of 10 mm/s, which is essential when dealing with elastic filaments. From experience, higher printing speeds led to under-extruded parts. Other applied parameters for investigations A and B are presented in Table 9.4. In addition, three different raster orientations of 0° , 45° and 90° relative to the tensile direction for investigation A were used. In investigation B, the samples were manufactured at the alternating directions 45° – 135° . The geometry consisted of a S3A dumbbell specimen taken from the German Standard DIN 53504 (DIN 2017). Since no indications of moisture were detected, drying prior to the printing was not required.

The tensile tests were performed on a Zwick Roell universal testing machine with a force sensor of 500 N at ambient temperature, and a displacement rate of 0.25 mm/s was applied. In every investigation, 3 specimens per sample were analyzed. From the experimental data, the ultimate strength and the elongation at break were evaluated for all samples.

Table 9.4 Printing parameters for the applied case

Parameters	A	B
Printing temperature (°C)	230	210, 230
Bed temperature (°C)	25	25
Printing speed (mm/s)	10	10
Layer thickness (mm)	0.48	0.48
Layer height (mm)	0.2	0.2
Contour lines (-)	1	2
Flow (%)	120	120
Infill percentage (%)	100	100
Infill angles (°)	0, 45, 90	45–135

9.3.2 Results and Discussion

The stress–strain curves from investigation A are presented in Fig. 9.4, while the ultimate stress values with their respective elongation at break can be found in Table 9.5. It can be observed that the 0° orientation exhibits a superior tensile strength and a higher ultimate strain. The 45° and 90° orientations had similar values, the latter being slightly higher. Their percentage errors for ultimate stress with reference to the 0° orientation are 22.7% and 20.1%, respectively. The shape of the curves, however, are similar. The 45° orientation shows a higher stiffness, that becomes more prominent for deformations beyond ca. 400%.

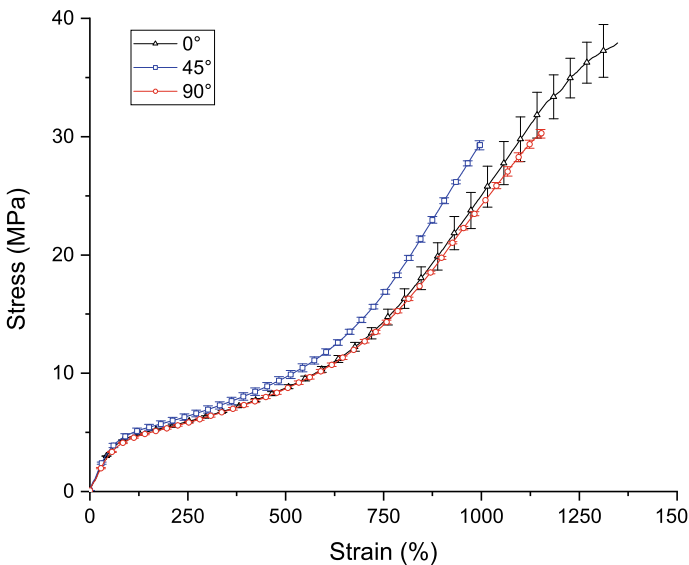


Fig. 9.4 Tensile stress curves for investigation A

Table 9.5 Ultimate tensile stress for investigation A

Raster angle	Stress (MPa)	Strain (%)
0°	37.92 ± 2.61	1348.26
45°	29.30 ± 0.42	996.66
90°	30.28 ± 0.35	1153.35

Moreover, all samples exhibited quite high elongations at break, as well as plasticity, withstanding a minimum of 28 MPa in stress. Figure 9.5 shows the failure patterns for the three orientations. The failure in the deposition direction for the angles of 45° and 90° is particularly noticeable. This indicates the weaker bond between the lines within a layer as the determinant failure cause. In fact, line adhesion is a common issue in FFF printed parts due to the extrusion mechanism of oval strands, which affects the bonding of side-by-side lines. No delamination between consecutive layers was observed, verifying the impact of infill orientation in the specimen failure. Overall, it can be affirmed that the influence of the unidirectional raster orientation is a fact to be considered when dealing with high deformations, since in the lower strain range (<400%) no significant differences among the samples were observed.

For investigation B, Fig. 9.6 shows a sample printed at 210°C before and after the tensile test. It can be observed that the intralayer adhesion, i.e., the adhesion between the lines within the same layer, was insufficient. Although the unloaded sample shows considerable gaps between the outer and the inner contour lines but minor gaps in the infill, these minor gaps increase substantially after the tensile loading and demonstrate the inadequate line adhesion in the infill as well. The interlayer adhesion, though, was effective: the outer contour line detached completely from the inner contour line with their successive layers well connected.

Another interesting fact is that the angle alternation of consecutive layers led to a better integrity of the sample. The lower layer shifted in 90° helped in keeping the lines of the upper layer from immediately breaking the sample. Figure 9.7 displays a sample printed with 230 °C before and after the tensile test. In this case, the intralayer adhesion was effective, with no visible gaps in any stage. In fact, the higher printing temperature allowed more material to flow out of the nozzle, rectifying the under-extrusion and low adhesion observed in the 210 °C case (as presented in Table 9.3).



Fig. 9.5 Break pattern of samples with a 0°, b 45° and c 90° orientation

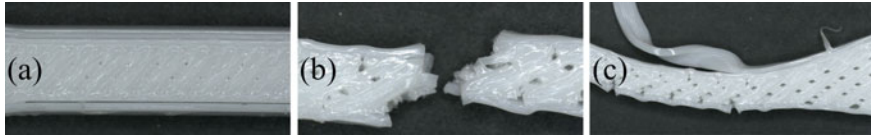


Fig. 9.6 Sample printed at 210 °C for investigation B **a** before and **b** after the tensile test with **c** detachment of the outer contour line

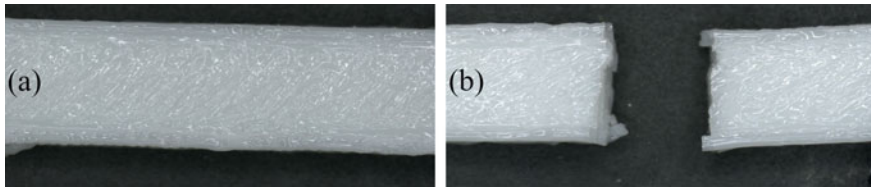


Fig. 9.7 Sample printed at 230 °C for investigation B **a** before and **b** after the tensile test

The tensile test results for investigation B are visualized in Fig. 9.8 and Table 9.6. The increase in the ultimate strength in almost 45% by applying a higher printing temperature becomes evident. Nevertheless, the under-extruded 210 °C sample still shows an acceptable ultimate stress, inferring that the alternating orientation between consecutive layers is advantageous, as it plays an important role in keeping the sample integrity. In addition, the 230° case revealed a slight increase in stiffness, which is a reflection of the better-adhered lines leading to a stronger part.

Similar to investigation A, the 45°–135° samples exhibited a high elongation at break as well as plastic deformation. The ultimate stress for the stronger 45°–135° sample, printed at 230 °C, was found to be 11.6% lower than for the unidirectional 0° sample, but higher than the other unidirectional cases. They also present a similar shape of the stress–strain curve and a comparable stiffness up to strains of 500%, after which the alternating oriented sample reaches higher stress values. This is relevant when the component demands higher strains during operation, as the infill orientation influences its premature failure, as well as the achievable tensile stresses. The best outcome is observed for rasters at 0°, even though the 45°–135° orientation is similar in performance and in case of failing line adhesion the alternating rasters better ensure the unity of the part. The behavior of the samples regarding the failure mode is a result of the infill parameter selection, while the plasticity is intrinsically related to hard segments in the material.

It should be considered that the samples from investigation B were printed with two contour lines, while the samples from A had only one. Due to the same deposition angle, this printing parameter does not affect the 0° samples but the same cannot be affirmed for the other orientations and may offer different results, which are worthy of consideration in future studies. The absence of contour lines is also to be considered. The contour lines act as tie points for the infill and will definitely have an impact on the 90° orientation, as the line adhesion is one of the key causes for the sample

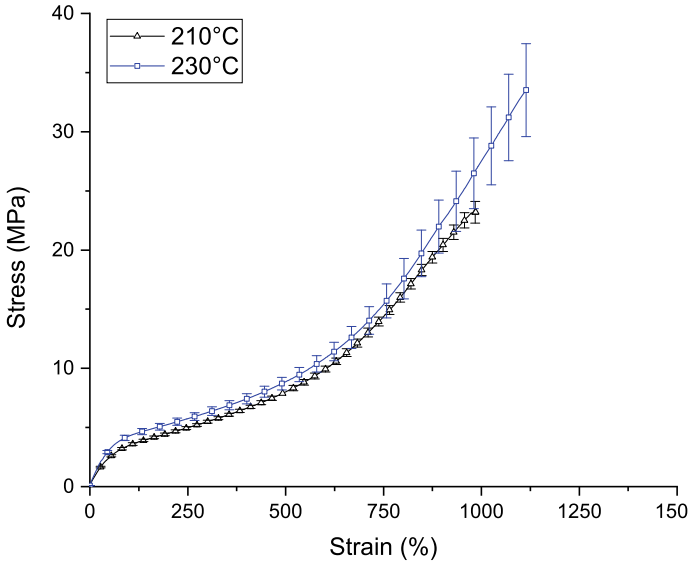


Fig. 9.8 Tensile stress curves for investigation B

Table 9.6 Ultimate tensile stress for investigation B

Temperature (°C)	Stress (MPa)	Strain (%)
210	23.20 ± 0.93	985.47
230	33.52 ± 3.92	1114.26

failure. Moreover, it should be remarked that the FFF technology shows a wide range of process parameters to be provided. Such a broad parameter selection results in a large variation of the quality of the printed parts regarding integrity and accuracy, directly affecting their mechanical behavior. Finally, the specific application of the printed geometry is essential matter for selecting the printing parameters: if the service deformations are below 400%, for example, then the material behavior is similar and the printing orientation does not show a significant influence on the performance.

9.4 Conclusions

This work was a combination of a scientific discussion in the topic of 3D printing of elastomers and an investigation of different printing strategies for a TPU filament with respect to the mechanical behavior. The first portion provided a summary of additive manufacturing regarding the commercially available technologies, with a detailed discussion in the field of elastomers. Relevant traits of three of the possible

elastomeric materials for 3D printing were briefly reported, including some of their current limitations. The focus on the FFF process using thermoplastic polyurethanes gathered several attributes to be considered, as well as issues that they may result in unsatisfactory conditions, which have to be dealt with. Notable attention should be paid to extrusion failures due to filament buckling and/or moisture, besides the application of lower printing speeds to promote better printing control.

The second portion of this contribution studies the influence of unidirectional and alternating raster orientations in FFF. It was revealed that the type and the orientation angle play an important role in the range of higher strains. Unidirectional deposition paths parallel to the tensile direction led to the best mechanical properties. Nevertheless, up to deformations of 400–500% no substantial effect was detected and the stiffness changes were low. In addition, since the rupture of the samples under tensile loading is highly affected by the adhesion between the lines in the same layer, the alternating 45°–135° orientation was found to be an interesting option in cases of under-extruded parts. The change in the orientation is beneficial in maintaining the same layer lines bonded to the print and avoiding a premature tensile failure.

Those investigations illustrate the capabilities of 3D printing with an elastomeric material, as well as highlights the influence of the printing parameters on their mechanical response. For FFF, these parameters are numerous, and they deserve consideration in subsequent studies. In this way, a larger database of knowledge on the technology and the use of elastic filaments along with a consequent optimization of the process is to be obtained. Thereby, the use of AM elastomers in several fields of technical applications is expected to be expanded, as this already takes place for other types of materials.

References

- Advincula RC, Dizon JRC, Chen Q et al (2020) Additive manufacturing for COVID-19: devices, materials, prospects, and challenges. *MRS Commun* 10(3):413–427
- ASTM (2012) ASTM F2792-12a: standard terminology for additive manufacturing technologies. ASTM International, West Conshohocken, PA
- Bikas H, Stavropoulos P, Chryssolouris G (2016) Additive manufacturing methods and modelling approaches: a critical review. *Int J Adv Manuf Tech* 83:389–405
- DIN Deutsches Institut für Normung eV (2017) DIN 53504:2017-03 testing of rubber—determination of tensile strength at break, tensile stress at yield, elongation at break and stress values in a tensile test. Beuth Verlag GmbH, Berlin, Germany
- Dow (2018) SILASTIC™ 3D 3335 Liquid silicone rubber (LSR). <https://www.dow.com/en-us/pdf/silastic-3d-3335-liquid-silicone-rubber-lsr.4137603z.html>. Accessed 20 Feb 2022
- Drobny JG (2014) Handbook of thermoplastic elastomers. Elsevier
- Ford S, Despeisse M (2016) Additive manufacturing and sustainability: an exploratory study of the advantages and challenges. *J Clean Prod* 137:1573–1587
- Gilmer EL, Miller D, Chatham CA et al (2018) Model analysis of feedstock behavior in fused filament fabrication: Enabling rapid materials screening. *Polymer* 152:51–61
- Januszewicz R, Tumbleston JR, Quintanilla AL et al (2016) Layerless fabrication with continuous liquid interface production. *P Natl Acad Sci USA* 113(42):11703–11708

- Joshi SC, Sheikh AA (2015) 3D printing in aerospace and its long-term sustainability. *Virtual Phys Prototyp* 10(4):175–185
- Klahn C, Leutenecker B, Meboldt M (2015) Design strategies for the process of additive manufacturing. *Proc CIRP* 36:230–235
- Ligon SC, Liska R, Stampfl J et al (2017) Polymers for 3D printing and customized additive manufacturing. *Chem Rev* 117(15):10212–10290
- Liu R, Wang Z, Sparks T et al (2017) Aerospace applications of laser additive manufacturing. Elsevier. In: Brandt M (ed) *Laser additive manufacturing: materials, design, technologies, and applications*. Woodhead Publishing
- Loos K, Bruère VM, Demmel B et al (2021) Future-oriented experimental characterization of 3D printed and conventional elastomers based on their swelling behavior. *Polymers* 13:4402
- Lukić M, Clarke J, Tuck C et al (2016) Printability of elastomer latex for additive manufacturing or 3D printing. *J Appl Polym Sci* 133(4)
- Parry EJ, Banks CE (2020) COVID-19: additive manufacturing response in the UK. *J 3D Print Med* 4(3):167–174
- Recreus (2022a) Filaflex 70A. <https://recreus.com/gb/filaments/6-filaflex-70a.html>. Accessed 20 Feb 2022a
- Recreus (2022b) Filaflex 82A. <https://recreus.com/gb/filaments/9-filaflex-82a.html>. Accessed 20 Feb 2022b
- Stratasys (2022) Tango. <https://www.stratasys.com/en/materials/materials-catalog/polyjet-materials/tango>. Accessed 20 Feb 2022
- Tareq MS, Rahman T, Hossain M et al (2021) Additive manufacturing and the COVID-19 challenges: an in-depth study. *J Manuf Syst* 60:787–798

Chapter 10

Effects of Reusing Polyamide 12 Powder on the Mechanical Properties of Additively Manufactured Parts



Philippe du Maire, Enes Sert, Matthias Deckert, Michael Johlitz,
and Andreas Öchsner

Abstract Series production of the future is facing the challenge of ever higher demands for individualised and complex products. Thus additive manufacturing is one of the key technologies to meet these demands. A major challenge in the selective laser sintering process is the reuse of the powder leftover after the building process as only 5–20% of the powder is used to produce the component. This research investigates the effects on the mechanical properties when reusing the unsintered powder remaining in the process chamber. Tensile test specimens are fabricated out of PA12 and investigated. The study shows a decreasing tensile strength and an increasing elongation at break with repeated reuse of the remaining powder. A high mechanical anisotropy can be determined as tensile strength, and elongation at break are highly dependent on the orientation of the specimen in the construction chamber. The reasons might be found in the process parameters. The powder particles show an increased cracking with repeated reuse of the remaining PA12 powder.

P. du Maire (✉) · E. Sert · M. Deckert · A. Öchsner
Faculty of Mechanical and Systems Engineering, Esslingen University of Applied Sciences,
Kanalstrasse 33, 73728 Esslingen, Germany
e-mail: philippe.du-maire@hs-esslingen.de

E. Sert
e-mail: enes.sert@hs-esslingen.de

M. Deckert
e-mail: matthias.deckert@hs-esslingen.de

A. Öchsner
e-mail: andreas.oechsner@hs-esslingen.de

M. Johlitz
Faculty of Aerospace Engineering, Institute of Mechanics, Universität der Bundeswehr München,
Werner-Heisenberg-Weg 39, 85577 Neubiberg, Germany
e-mail: michael.johlitz@unibw.de

10.1 Introduction

Initially developed in the 1980s at the University of Texas at Austin in the USA, the selective laser sintering (SLS) technology is already in use for over 25 years (Schmid 2015). It belongs to the powder-based additive manufacturing technologies which use polymer powder as base material to build up parts layer by layer. Up to now, the SLS is mainly applied in the field of prototyping in industry and research but according to Breuninger et al. and others, it is currently at the transition stage from prototype tooling to series production (Bourell et al. 2014; Breuninger et al. 2013; Ligon et al. 2017; Schmid 2015). The advantages of additive manufacturing technologies are obvious. The process allows for a high degree of individualised products, as well as the production of highly complex geometries in one processing step without tool changing or the need for assembling several parts. In addition, additive manufacturing enables the integration of functions during its construction process. With all these advantages, additive manufacturing processes meet the demands of series production in future and therefore represents a key technology for tomorrow's production environment (Bonten 2020; Breuninger et al. 2013).

The functionality of the SLS process is as simple as it is ingenious. Using three dimensional (3D) computer-aided design (CAD) files which are converted into stereolithography (STL) file format, the parts can be directly built from the CAD files (Ajoku et al. 2006). The STL file contains all relevant data about the surface geometry necessary for the SLS process to build up the component. As already described before, the SLS process uses polymer powder as base material, which is applied to the construction area, also known as part bed, in thin layers of around 100 μm . With the aid of a CO_2 laser, the powder is locally melted according to the 3D model to create the component. The molten polymer solidifies bonds with the former part slices and thus forms each layer fragment of the part (Abts 2020). Subsequently, the construction area is lowered about one layer thickness, new powder is applied to the part bed and again melted by the laser. This routine is repeated until the whole component is built up layer by layer beginning from bottom to top.

In order to avoid warpage due to fast cooling, the part bed as well as the powder feedstock are preheated by process chamber heaters (Breuninger et al. 2013; Dadbakhsh et al. 2017; Pham et al. 2008). Furthermore, this minimises the laser energy required to melt the polymer particles. For this reason, the powder in the part bed is preheated to a temperature just below the melting point of the material. This means the laser only has to achieve a small increase in temperature, about a few degrees, to melt up the polymer. However, these high temperatures in the process chamber also lead to drawbacks and challenges for the processing of the material as they cause a thermal degradation of the unsintered powder. The thermal degradation or often called thermal ageing results in a limited reusability of the unsintered powder because of decreasing mechanical properties and a decreasing surface quality of the sintered parts (Ligon et al. 2017; Schmid et al. 2014). In fact, the deteriorating surface quality is the main problem, as this is no longer acceptable for industrial applications due to the formation of the so-called orange peel. The importance of reusability becomes

clear when looking at the process itself. In each processing cycle, only 5–20% (Dadbakhsh et al. 2017; Dotchev and Yusoff 2009) of the powder is molten to build the component, which means a high amount of powder remains unsintered. In industry, the leftover powder is not directly discarded but is usually refreshed with a certain amount of virgin powder, allowing for limited reuse. Clearly, the refreshing cannot be extended to infinity as the thermal degradation still increases with repeated use of the powder mixture. This underlines the necessity for a proper recycling technology for the leftover powder. In order to develop a recycling process, the effects of thermal degradation have to be investigated more in detail.

In this study, the effects of thermal ageing on the mechanical properties of test specimens made out of PA12 powder are investigated. For the examination, two test series of tensile test specimens are produced with different thermal ageing states of the base material and investigated regarding their mechanical properties. The results are compared to each other. Different powder qualities are achieved by reusing the remaining powder several times, distinguishing this research from previous studies. Several authors have already investigated the mechanical properties of SLS components regarding virgin, aged and mixed powder or different powder manufacturers (Caulfield et al. 2007; Dadbakhsh et al. 2017; Zarringhalam et al. 2006). However, the following study is focused on the repeated use and hence the increasing thermal ageing state of the base material, while sticking to one powder manufacturer. Furthermore, the particle shape, i.e. morphology of the powder is analysed using a Schottky field emission scanning electron microscope.

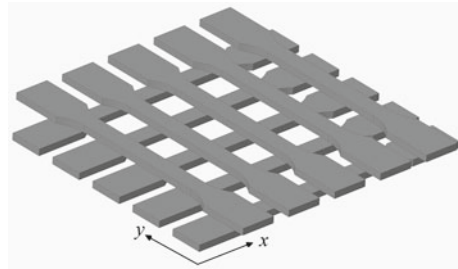
10.2 Methodology

In order to evaluate the effects of thermal ageing during the building process, tensile test specimens are produced with different qualities of the powder using a Vanguard HS selective laser sintering system from the company 3D-Systems Inc. The SLS printer is equipped with a 100 W CO₂ laser, and the process chamber is flooded with nitrogen as inert gas during the building process. A build volume of 380 × 330 × 275 mm³ is used for the production of the samples. The tensile test specimens are built out of the polyamide (PA) DuraForm PA from the manufacturer 3D-Systems Inc. DuraForm PA belongs to the PA12 polymers, which are mostly used in industries (Breuninger et al. 2013; Dotchev and Yusoff 2009; Goodridge et al. 2012; Ligon et al. 2017; Schmid 2015). Schmid 2015 estimates the market share of PA12 at 95%. The dimensions chosen for the specimens can be taken from Table 10.1.

To control the ageing state of the powder and ensure the reproducibility, the test specimens are fabricated in several process cycles. Starting with virgin PA12 powder in the first production process, the leftover powder in the building chamber is collected after each built job and reused to produce the next set of tensile test specimens. This means only the leftover powder is used after producing the first set of specimens and, no virgin or other powder materials are added into the process anymore. The process parameter and number of produced parts are kept the same for every production cycle which enables a detailed determination of the thermal load

Table 10.1 Dimensions of the test specimen according to DIN EN ISO 527-2 Type 1A

Dimension	Description	Value	Unit
l_1	Length of the narrow part	80	mm
l_2	Distance between the wide parallels	110	mm
l_3	Overall length	170	mm
b_1	Width of the narrow part	10	mm
b_2	Width at the ending	20	mm
h	Thickness	5	mm

Fig. 10.1 Positioning of the tensile test specimens in the process chamber

on the powder. Furthermore, samples of the unsintered powder are taken after each building process to investigate the morphology of the powder particles.

In order to ensure a proper data set and clear investigation, the powder is reused four times to produce the first series samples, which means there will be five sets of tensile test specimens fabricated with increasing thermal load of the powder. One set was produced with virgin powder, and four other sets were produced with up to four times reused powder from the process chamber. In addition to that, another built process is carried out using a powder mixture of 60% used powder and 40% virgin powder, which represents a typical refreshing rate used in industries. A further series of tests are carried out in which the powder is reused twice more, i.e. up to six times. The second test run serves as validation test to examine the repeatability of the results. Each set of samples consist out of ten tensile test specimen. Five are fabricated with its test direction along the x -axis, and five specimens are produced perpendicular to that, with its test direction along the y -axis. It has to be noted, that the powder application direction is parallel to the x -axis. The position of the samples in the building chamber is visualised in Fig. 10.1. A layer thickness of 100 μm is chosen for the production of the components, and the temperature of the process chamber heaters is set to a value of 177 $^{\circ}\text{C}$ to avoid shrinkage effects due to rapid cooling of the molten polymer powder.

The building process is structured in the following steps. At the beginning of each build, a warm up layer with a total powder height of 12.5 mm is applied to the building platform, followed by another 2 mm powder which serves as a base layer. Subsequently, the tensile test specimens are produced as described before and visualised in Fig. 10.1. Each build ends with a cool down layer of 2.54 mm to ensure a

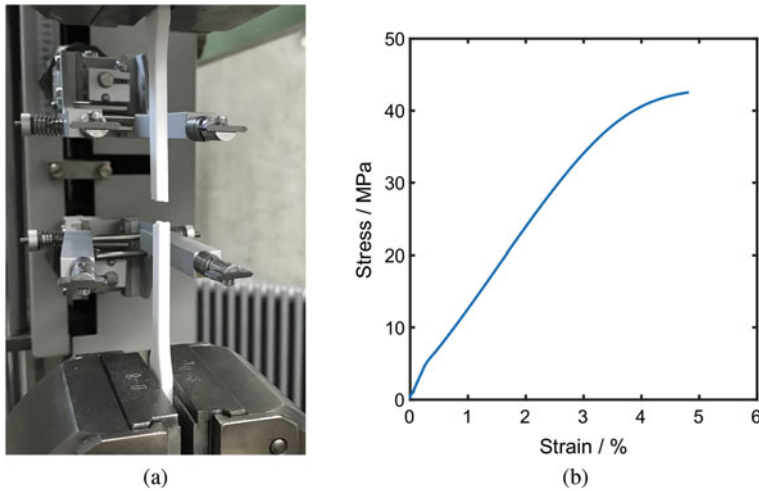


Fig. 10.2 a Clamped tensile test specimen and b exemplary stress-strain curve

controlled and slow cool down and avoid shrinkage. In order to characterise the influences of the thermally aged PA12 powder on the mechanical properties of potentially built components, the specimens are investigated regarding their tensile strength and their elongation at break. The testing set-up is exemplarily displayed in Fig. 10.2 with the clamped tensile test specimen shown in Fig. 10.2a and the corresponding stress-strain curve in Fig. 10.2b.

The investigations are carried out on a Zwick 1445-02, 10 kN universal testing machine, using modular sensor arm extensometers in order to obtain more accurate values for the strains in the range of Young's modulus. After the Young's modulus has been detected with a testing speed of 1 mm/min, the extensometers are moved away, and the measurements are taken via the traverse path. This serves as protection against possible damages caused by the sudden breakage of the test specimen when the ultimate tensile strength is reached. After the Young's modulus has been detected, the further testing is executed using a testing speed of 50 mm/min. To receive a clear appraisal of the mechanical properties, at least three specimens are tested for each building direction and each manufacturing process. The two remaining samples serve as spares in the event of an invalid test run, to ensure a data set of at least three valid test runs. In addition to the mechanical properties, the morphology of the powder particles is investigated using the samples of unsintered powder taken after each manufacturing process. The morphology, i.e. particle shape is investigated with the aid of a Schottky field emission scanning electron microscope (SEM) JSM-7200F from the company Jeol GmbH. As the microscopic examination via SEM requires a conductive surface and since polyamide belongs to the non-conductive materials, sputtering of the PA12 samples is necessary to visualise the particles (Ehrenstein 2020). For this reason, the powder samples are prepared using a thin gold coating.

The coating is applied with a Leica sputter coater EM ACE 200 using a sputter time of 20 s, which creates a gold layer of roughly 10–15 nm.

10.3 Results and Discussion

Investigating the ultimate tensile strength (UTS) at room temperature for the first test series shows a decrease in strength with multiple reuse of the leftover powder. The resulting mean values of the UTS are displayed as bars in Figs. 10.3 and 10.4. Furthermore, the minimum and maximum values of each set of tensile test specimens are indicated by failure bars.

The loss in strength can be seen for both, the components produced in x -direction and the components produced in y -direction. It is striking that the UTS increases again for specimens produced with four times reused powder (Fig. 10.3). This can be clearly seen for the complete data set and also for the components produced perpendicular to the powder application direction. The impression arises that this trend could continue. Although the test results are evident, this behaviour and a possible trend cannot be confirmed by the results of the second test series (Fig. 10.4) in which the powder is reused twice more. When comparing the resulting trend of the UTS for the second test series, shown in Fig. 10.4 and the one of the first test series it can be clearly seen that the increase after the fourth reuse of the powder is only an anomaly and can therefore be neglected. It has to be noted that the results for the second and third reuse of the first test series also differ, which might lead to the impression that the tensile strength seems to increase again for the fourth reuse. The data sheet specifies a maximal tensile strength of 43 MPa according to ASTM D638, which can be clearly confirmed and reached with both test series for the components produced along the y -direction. An average tensile strength of 48.3 MPa is obtained for the first test series and 45.55 MPa for the second one. On the other

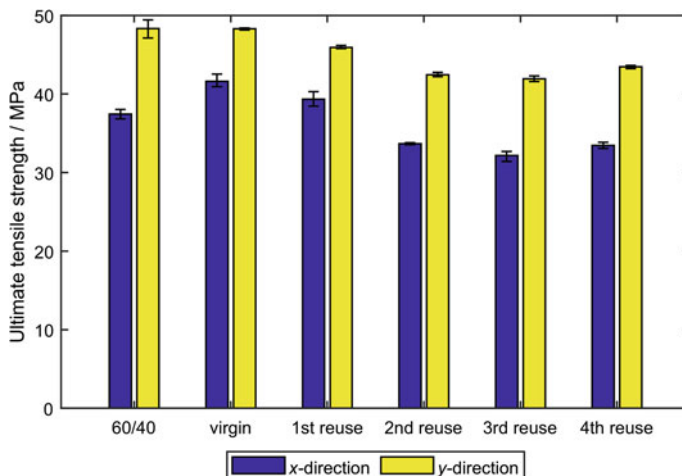


Fig. 10.3 Ultimate tensile strength of the first test series

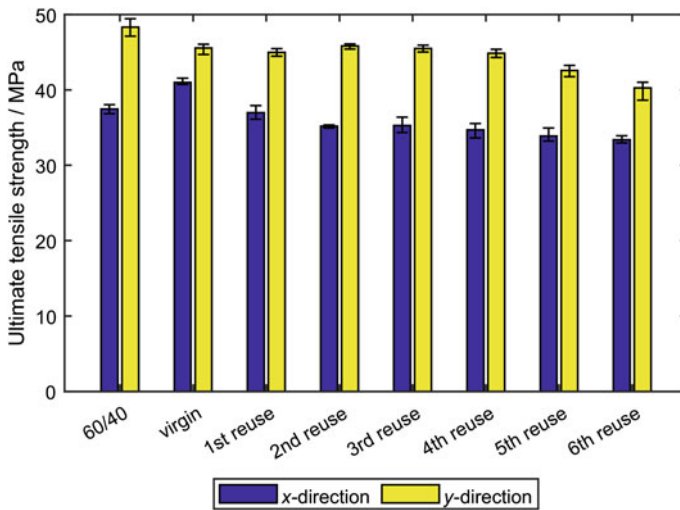
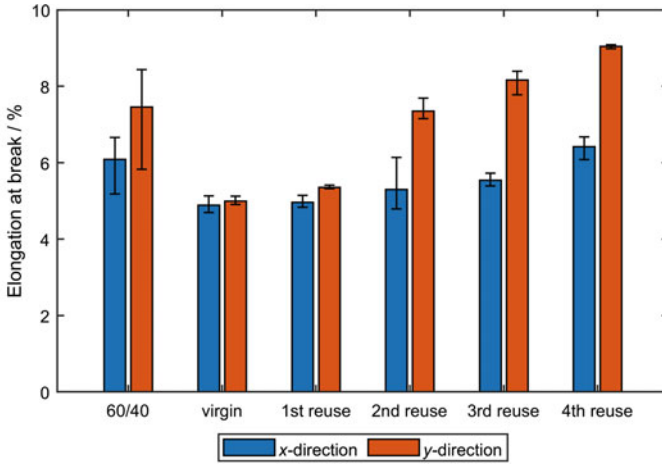


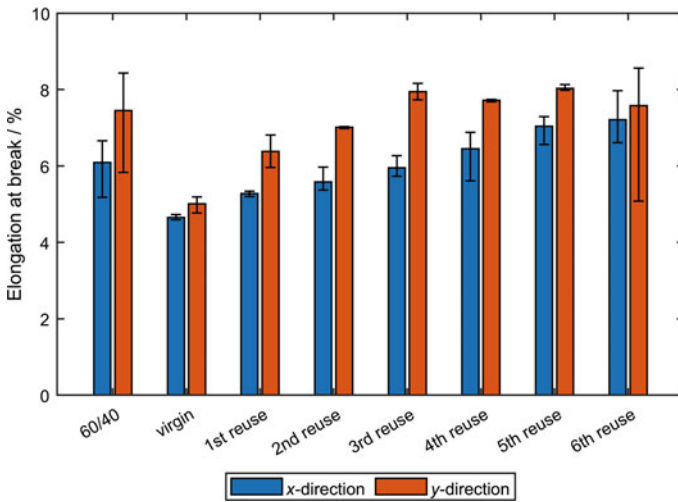
Fig. 10.4 Ultimate tensile strength of the first test series

hand, the tensile strength determined for the specimens produced in x -direction is slightly below the specification of the data sheet with values of 41.61 MPa (first test series) and 41.0 MPa (second test series). These differences between the strength values obtained for the samples produced in x - and y -direction will be discussed in more detail below. Looking at the UTS obtained by the second series of tests (see Fig. 10.4), a decreasing strength with an increasing number of reusing cycles can be seen. The more often the powder is reused, the longer it is exposed to thermal stress in the construction chamber, resulting in higher thermal ageing of the powder and thus lower strength values of the produced components. Evaluating the tensile strength for the specimen produced with a powder mixture of 60% used powder and 40% virgin powder shows that the resulting UTS lies close to the UTS investigated for the samples made out of virgin powder. Both, the first and the second series of tests show this behaviour and thus confirm the 60/40 mixture as a good refreshing rate for the reuse of the leftover powder.

Similar to the differences found for the strength values for the virgin powder, it is striking out that the tensile strength of the entire components built up along the powder application direction (y -direction) is significantly higher compared to the one produced perpendicular to that (x -direction). This behaviour can be noticed in both test series when comparing the results for the UTS shown in Figs. 10.3 with 10.4. In the additive manufacturing, the mechanical anisotropy in z -direction is a characteristic behaviour and is already investigated in other studies (Ajoku et al. 2006; Gibson and Shi 1997; Rybachuk et al. 2017), but the reason for the different strength in x - and y -direction cannot be confirmed finally and has to be further investigated as the results are evident in both series of tests. A possible reason could be found in different scanning times of the laser and thus different melting times during the building process. The powder is melted in the x -direction, i.e. the scanning direction



(a) First test series



(b) Second test series

Fig. 10.5 Elongation at break for different thermal ageing states of the PA12

corresponds to the *x*-axis. Therefore, a complete scan of a component built up along the *y*-direction demands less time than a scan of a part placed in *x*-direction. The shorter melting time might lead to better bonding between the particles. In fact, the strength decreases in mean by an average of 24% for the specimen orientated along the *x*-axis compared to the one produced perpendicular to that in the first series of tests. The same holds for the second series of tests, which underlines the importance of the component positioning in the process chamber. For the design of components,

this high dependence of the ultimate tensile strength on the orientation in the process chamber has to be considered.

Investigating the elongation at break leads to a similar behaviour like the tensile strength. Again the values for the components fabricated along the x -direction are lower than those for the y -direction. The results are displayed in Fig. 10.5.

Also in this case, the results are clear and appear in both test series. In contrast to the tensile strength, the elongation at break increases with repeated reuse. For the first test series, the elongation at break increases by an average of 31% (x -direction) for the fourth reuse compared to the elongation obtained for the samples made out of virgin powder. In case of the y -direction, the increase is far greater and, with a value of 81%, is almost twice as high. Evaluating the second test series shows similar results. The elongation at break for the x -direction increases about 55% in average and about 51% for test specimens produced along the y -direction when reusing the PA12 powder seven times. It has to be noted that the maximal increase occurs for the fifth reuse.

The results of the SEM microscopy of the virgin powder and the maximum reusing states of the first and the second test series are displayed in Fig. 10.6. Each of the powder samples investigated exhibits the characteristic potato-like particle shape. However, the morphology of the virgin powder denotes a smooth and spherical surface (see Fig. 10.6a), a cracking of the powder particles can be seen in Fig. 10.6b, c for the aged powder at a resolution of 1000.

Evaluating the samples, it can be seen that the particles seem to show an increased cracking with increasing thermal load, i.e. number of reusing cycles of the powder. The powder particles, which have been reused seven times show the deepest cracks and an increasing number of cracking (see Fig. 10.6c). Looking at the particles, which have been reused four times (see Fig. 10.6b) does not show such deep cracks. Also the total number of cracks is lower. Even if the virgin powder seems to show no cracking, it has to be noted that also for the virgin powder a small amount of cracked powder particles can be determined.

The increasing cracking of the particles might influence the flowability of the powder and thus effect the reusability of the leftover powder negatively, as a reduced flowability might favour the appearance of orange peel. Subsequently, the compo-

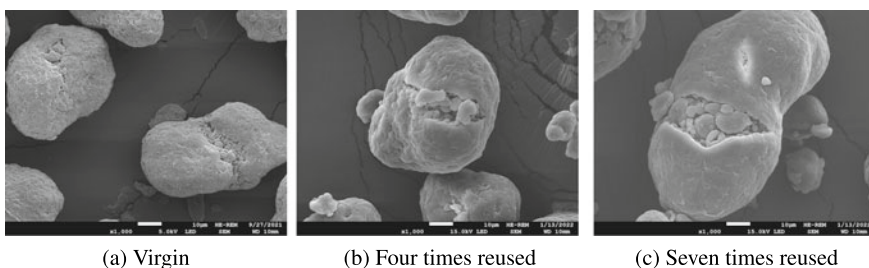


Fig. 10.6 SEM pictures of different thermal ageing states of the PA12 powder

nents are no longer usable due to the unacceptable surface quality of the orange peel. The occurrence of an increasing cracking has also been investigated by (Dadbakhsh et al. 2017).

10.4 Conclusion

The investigated samples show a strong mechanical anisotropy, which appears in both, the first as well as the second test series. All tensile test specimens built along the y -direction, which is perpendicular to the direction of the powder application show a significantly higher ultimate tensile strength compared to those fabricated along the x -direction, i.e. parallel to the powder application. This behaviour cannot be explained by the literature, which is why the only justification may be found in process-related influences. A similar anisotropy can be determined for the elongation at break. However, the ultimate tensile strength decreases with repeated reuse of the unsintered material, and the elongation at break shows a strong increase. But also for the elongation at break, the values for components fabricated along the y -direction are higher than those produced along the x -direction.

Using a powder refreshing rate of 60% aged powder and 40% virgin powder to produce the specimens leads to an ultimate tensile strength which lies close to the strength of components made out of virgin powder. This behaviour can also be observed repeatedly in the second test series and thus confirm the 60/40 mixture as an appropriate refreshing rate for the reuse of the unsintered powder. In general, it can be observed that the ultimate tensile strength decreases and the elongation at break increases with repeated reuse of the remaining unsintered powder.

Analysing the powder particles with the aid of a scanning electron microscope showed an increasing cracking of the powder particles with repeated reuse of the leftover powder, i.e. increasing thermal load. This might reduce the flowability of the powder and thus favours the appearance of orange peel which is a rejection criterion for the industrial application as it represents an unacceptable surface quality. The reduction of the flowability should therefore be confirmed with further investigations like the analysis of the particle size distribution, the bulk density or rheological examinations of the powder.

Acknowledgements The author acknowledges the staff of the laboratory for polymer technologies at the Esslingen University for the kind support to realise the experiments and the usage of the laboratory equipment. Many thanks to the company 4D Concepts GmbH for providing the tensile test specimens.

This Project is supported by the Federal Ministry for Economic Affairs and Climate Action (BMWK) on the basis of a decision by the German Bundestag. It is a cooperative research project with the companies 4D Concepts GmbH and M.J. Additive GmbH.

References

- Abts G (2020) *Kunststoff-Wissen für Einsteiger*, 4, aktualisierte. Hanser, München
- Ajoku U, Saleh N, Hopkinson N, Hague R, Erasenthiran P (2006) Investigating mechanical anisotropy and end-of-vector effect in laser-sintered nylon parts. *Proc IMechE* 220:1077–1086
- Bonten C (2020) *Kunststofftechnik Einführung und Grundlagen*, 5, aktualisierte. Hanser, München
- Bourell DL, Watt TJ, Leigh DK, Fulche B (2014) Performance limitations in polymer laser sintering. *Phys Procedia* 56:147–156
- Breuninger J, Becker R, Wolf A, Rommel S, Verl A (2013) *Generative Fertigung mit Kunststoffen*. Springer, Berlin
- Caulfield B, Mc Hugh PE, Lohfeld S (2007) Dependence of mechanical properties of polyamide components on build parameters in the SLS process. *J Mater Process Technol* 182:477–488
- Dadbakhsh S, Verbelen L, Verkinderen O, Strobbe D, Van Puyvelde P, Kruth J-P (2017) Effect of PA12 powder reuse on coalescence behaviour and microstructure of SLS parts. *Eur Polym J* 95:250–262
- Dotchev K, Yusoff W (2009) Recycling of polyamide 12 based powders in the LS process. *Rapid Prototyp J* 15:192–203
- Ehrenstein GW (2020) *Mikroskopie*. Hanser, München
- Gibson I, Shi D (1997) Material properties and fabrication parameters in selective laser sintering process. *Rapid Prototyp J* 4:129–136
- Goodridge RD, Tuck CJ, Hague R (2012) Laser sintering of polyamides and other polymers. *Prog Mat Sc* 57:229–267
- Ligon SC, Liska R, Stampf J, Gurr M, Mülhaupt R (2017) Polymers for 3D printing and customized additive manufacturing. *Chem Rev* 117:10212–10290
- Pham DT, Dotchev KD, Yusoff WAY (2008) Deterioration of polyamide powder properties in the laser sintering process. *Proc IMechE* 222:2163–2176
- Rybachuk M, Mauger CA, Fiedler T, Öchsner A (2017) Anisotropic mechanical properties of fused deposition modeled parts fabricated by using acrylonitrile butadiene styrene polymer. *J Polym Eng* 37:699–706
- Schmid M (2015) *Additive Fertigung mit Selektivem Lasersintern (SLS)*. Springer, Wiesbaden
- Schmid M, Amando A, Wagner K (2014) Materials perspective of polymers for additive manufacturing with selective laser sintering. *J Mater Res* 29:1824–1832
- Zarringhalam H, Hopkinson N, Kamperman NF, de Vlieger JJ (2006) Effects of processing on microstructure and properties of SLS Nylon 12. *Mater Sci Eng A* 435–436:172–180

Chapter 11

On the Influence of Perimeter, Infill-Direction and Geometry on the Tensile Properties of Test Specimen Manufactured by Fused Filament Fabrication



Julian Klingenbeck, Alexander Lion, and Michael Johlitz

Abstract Fused filament fabrication is an additive manufacturing method commonly used in home and industrial application. The quality of the print is dependent on the printing parameters, which have been a repeated focus in scientific research. This contribution concerns itself with the investigation of two parameters (perimeters and infill connection) influencing the geometry of printed tensile samples and their impact on the measurement of the ultimate tensile strength and the Young's modulus. The samples were manufactured out of polylactic acid (PLA) with raster angles of 0 and 90 °C. Furthermore, the influence of the manufacturing method was investigated by comparing directly printed samples with samples routed out of printed plates. Test results showed a significant dependence on infill connection and perimeter, the exact nature of which in turn dependent on raster angle.

11.1 Introduction

Additive manufacturing (AM), colloquially referred to as 3D printing, is an umbrella term for a variety of different manufacturing processes. Their uniting feature being that a part/component is build up through repeatedly adding new material to the already existing part, thereby growing the part until the final geometry is created. This definition therefore stands in contrast to conventional manufacturing methods, where a part is either produced as a whole (casting) or through repeated subtraction of material from a blank. The umbrella of AM comprises a host of technologies,

J. Klingenbeck (✉) · A. Lion · M. Johlitz
Institut für Mechanik, Universität der Bundeswehr München, 85579 Neubiberg, Germany
e-mail: julian.klingenbeck@unibw.de

A. Lion
e-mail: alexander.lion@unibw.de

M. Johlitz
e-mail: michael.johlitz@unibw.de

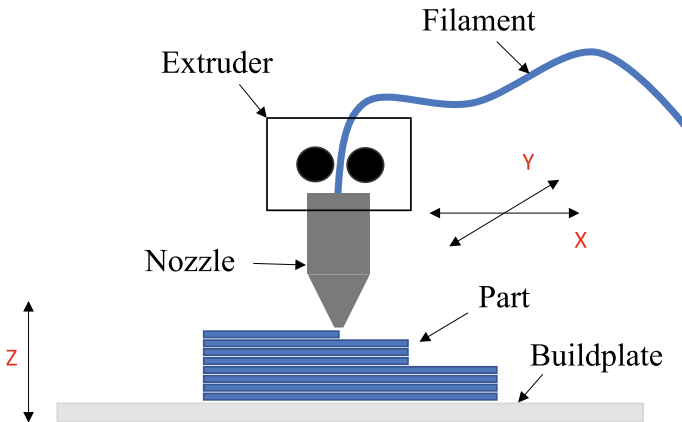


Fig. 11.1 Schematic representation of a FFF printer

often specific to the materials used, utilizing different methods for processing and depositing the base materials. As it stands today, the list of printable materials include metals, polymers and ceramics as well as more specialized materials like concrete and composite materials (fibre reinforcement, metal alloys, wood fibre, etc.) (Gebhardt et al. 2018; Gibson et al. 2015).

One commonly used printing technology for hobbyist/home as well as industrial applications is fused filament fabrication (FFF). In this method, as depicted schematically in Fig. 11.1, a prefabricated polymer strand, called filament, is plastified in an extruder unit and subsequently deposited onto a build platform. Through relative movements between the extruder and the build plate, the desired geometry is created in a layer wise fashion (Gebhardt et al. 2018; Gibson et al. 2015).

The nature of the printing process results in a microstructure or characteristic internal geometry, as exemplary depicted with the fracture surface of a tensile test specimen in Fig. 11.2c. Although the specific internal structure of a part depends on the travel path of the extruder, as prescribed by the user, the individual polymer strands as well as airgaps between them remain clearly visible after printing.

Typically, printed parts are build up out of two distinct regions. The shell and the infill. The shell is generated, as the printer deposits a defined number of polymer strands in a concentric fashion following the outer and inner contours of the part in each printed layer. These contours are generally referred to as perimeters. The remaining inner regions of the part are printed with so-called infills, which can be realized in a variety of different geometries, such as parallel lines, grids, triangles, etc. Beyond that, 3D printing offers the ability to reduce the global infill density to save weight, material and printing time, by adjusting the proportion of gaps in the infill geometry. An infill density of 100% is only achievable with a line-type infill. Although it is possible to manufacture parts solely out of perimeters or infill, the combination of both is common practice.

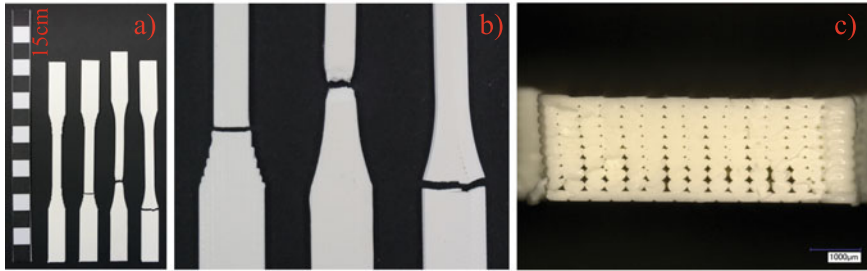


Fig. 11.2 **a** whole specimen **b** break location (from left to right: 0D,0P,UN—0D,1P,UN—P,90D,6P,UN) **c** fracture surface

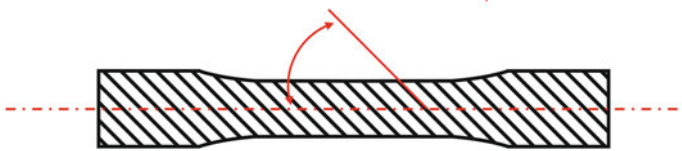


Fig. 11.3 Schematic depiction of raster angle in a tensile specimen measured against length axis

It is a well established fact, that the manufacturing parameters, in the context of 3D Printing also referred to as printing parameters, greatly influence the outcome of the printing process. Suboptimal parameter sets may reduce the quality of the printed part, while inadequate parameters may prevent a successful print. The effect of a variety of different printing parameters on different part properties has already been studied using a variety of different printers as well as different materials, such as polylactic acid (PLA) and acrylonitrile butadiene styrene (ABS). Table 11.1 provides a selection of publications, researching the impact of different printing parameters on several observable properties of the printed parts as well as the printing process. For a summation of the most important printing parameters and their influences, the reader is referred to the reviews by Dey and Yodo (2019), Popescu et al. (2018) and Wang et al. (2020b).

One of the most impactful parameters in FFF printing is the raster angle, also referred to as infill angle or infill orientation as depicted in Fig. 11.3. This parameter is only applicable in case of a line-type infill, where the individual infill layers are deposited as parallel lines with the infill density determining the distance between the parallel polymer strands. The direction of the infill lines may be kept identical or altered over the layers of the part. In the following, the raster angle is measured in relation to the longitudinal axis of the test specimen, i.e. in relation to the loading direction. It is generally accepted in literature (Ahn et al. 2002; Gebisa and Lemu 2019; Hu et al. 2021; Kiendl and Gao 2020), that, in the case of unidirectional line infill, a raster angle of 0° , i.e. in loading direction, develops the highest values of tensile strength, while a 90° orientation results in the weakest.

Table 11.1 Table of selected literature

Author	Material	Parameters	Observed property
Ahn et al. (2002)	ABS	Air gap, line width, extruder temp., raster angle, colour	Tensile strength
Camposco-Negrete (2020)	ASA	Layer height, infill pattern, build orientation, orientation angle, buildplate position	Build time, energy consumption, dimensions
Ćwikła et al. (2017)	ABS	Infill density, shell thickness, extrusion multiplier, infill pattern	Tensile strength
García-León et al. (2021)	PC, PA + CF	Printing speed, layer height, infill density	Impactbreak energy
Gebisa and Lemu (2019)	PEI	Air gap, line width, raster angle, perimeter count, Perimeter line width	Tensile strain, tensile strength
Hu et al. (2021)	PEEK, SCF + PEEK	Nozzle diameter, extruder temp., raster angle	Tensile strength, tensile modulus
Kamaal et al. (2021)	SCF + PLA	Build orientation, infill density, layer height	Tensile strength, Impact strength
Kiendl and Gao (2020)	PLA	Raster angle	Tensile modulus, tensile strength, toughness
Kim et al. (2018)	PLA	Printing speed	Surface roughness
Kozior and Kundera (2017)	ABS	Orientation angle	Relaxation stress
Liu et al. (2019)	PEEK	Layer height, infill density, perimeter count	Print time, material consumption, storage modulus
McLaggart et al. (2020)	ABS, CF + ABS	Gamma radiation dose	Tensile modulus, maximum elongation, flexural strength, flexural modulus, flexural strain, hardness
Mohamed et al. (2016a)	PC + ABS	Air gap, layer height, raster angle, build orientation, line width, perimeter count	Build time, material consumption, dynamic flexural modulus
Mohamed et al. (2016b)	PC + ABS	Air gap, layer height, raster angle, build orientation, line width, perimeter count	Storage modulus, loss modulus, mechanical dampening
Pant et al. (2020)	PLA	Layer height, build orientation, extruder temp.	Wear rate
Pérez et al. (2018)	PLA	Layer height, printing speed, extruder temp., wall thickness	Surface roughness
Radhwan et al. (2019)	PLA	Layer height, printing speed, infill density	Surface roughness
Rybachuk et al. (2017)	ABS	Build orientation, gauge thickness	Tensile modulus, compressive modulus, tensile strength, compressive strength, yield strength, elongation, hardness Rockwell
Samykano et al. (2019)	ABS	Layer height, raster angle, infill density	Tensile strength, Tensile modulus
Wang et al. (2020a)	PEEK, CF + PEEK, GF + PEEK	Extruder temp., buildplate temp., printing speed, layer height	Tensile strength, flexural strength, impact strength

A possible explanation for this behaviour is, that in a 0° orientation, the force acts along the deposited polymer strands, which individually can be assumed to be homogenous and isotropic approaching a tensile strength close to injection moulded specimens (Ahn et al. 2002). For a 90° orientation, the load is carried across the boundaries between the polymer strands. Since, as depicted in Fig. 11.2, the individual polymer strands are not perfectly connected, and the adhesive properties of the boundary areas are possibly lower than the cohesive properties of the bulk material, and the overall strength is expected to be lower than for 0° samples.

The paper is structured as follows. In Sect. 11.2, the research question, based on the theoretical background laid out in Sect. 11.1, will be elaborated. Section 11.3 presents the experimental setup employed followed by the discussion of the testing results in Sect. 11.4. A summary is given in Sect. 11.5.

11.2 Research Focus

A commonly utilized test to study the influence of the printing parameters on the mechanical properties is the uniaxial tensile test. It allows the measurement of several material properties such as Young's modulus, ultimate tensile strength and elongation. Tensile tests have been used frequently in preceding research to establish the impact of different printing parameters on the material properties (Ahn et al. 2002; Ćwikła et al. 2017; Gebisa and Lemu 2019; Hu et al. 2021; Kiendl and Gao 2020; Samykano et al. 2019; Wang et al. 2020a).

The geometries used for tensile testing are either rectangular strips or dogbone-shaped test specimens as defined, for example, in DIN EN ISO 527-2 (2012-06). Although these are standardized geometries, it is unclear how test specimen should be manufactured in the context of 3D printing, specifically FFF, to achieve best results, as some printing parameters impact the geometry of the printed parts, resulting in a divergence from the desired geometry.

This paper aims to provide a contribution to better understanding the influence of certain manufacturing parameters for tensile test specimen. For better comparability with previous research, it was elected to focus on tensile samples with a line-type infill, 100% infill density and raster angles of 0° and 90° . The parameters explored in this study are the manufacturing method as well as two factors influencing the geometry of a printed part: perimeters and infill connection.

Perimeters

Should the samples be printed with or without a perimeter? Utilizing perimeters allows to match the desired geometry more closely. Printing without perimeter (i.e. only printing infill) makes it impossible to create a smooth surface following the desired geometry in curved regions, as depicted in Fig. 11.4. Thus, a stepwise surface with the resolution dependent on the line width of the deposited polymer strands is created. If, on the other hand, the samples are printed with a raster angle unequal to 0° , the implementation of perimeters results in areas with different raster angles.

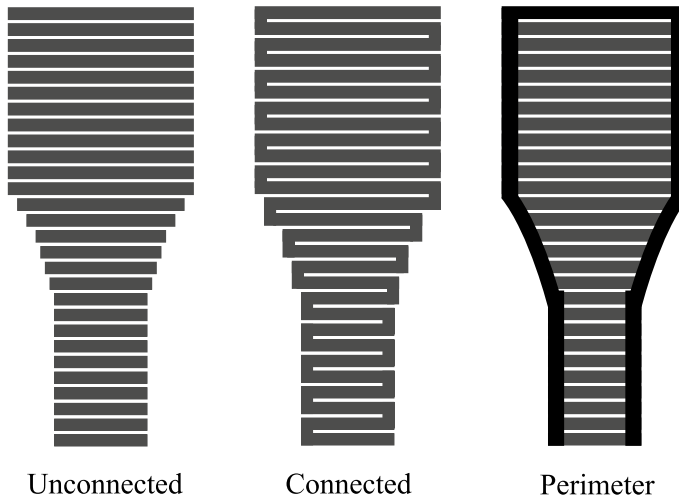


Fig. 11.4 Schematic depiction of the influence of infill connection and perimeters on part geometry

Since the orientation of the polymer strands is one of the most impactful parameters with regard to the mechanical properties of a printed part, it stands to reason that perimeters could influence the results of tensile tests. This could prove problematic, if solely the behaviour of the infill structure needs to be measured, for example to establish experimental data for the purpose of modelling and simulation.

Infill Connection

If the samples are printed without perimeters, a further option is available for the line-type infill. The individual polymer strands can be connected, effectively printing the layer in one unbroken line, or unconnected as depicted in Fig. 11.4. Both options result in a distinct stepwise appearance in the curved regions of the tensile specimen.

Manufacturing Method

Another point of interest is the manufacturing method. Should the samples be printed directly, presumably being a closer representation of a 3D printed part, or cut out of printed plates? The latter allows to match the sample geometry as defined in DIN EN ISO 527-2 (2012-06) without the need for a perimeter.

11.3 Experimental Setup and Results

Tensile tests in accordance with DIN EN ISO 527-1 (2012-06) were performed in two separate test series to measure both ultimate tensile strength as well as the Young's modulus. In the first test series, the impact of the manufacturing method (printed, routed) and the geometry altering print parameters (infill line connection, perimeter)

Table 11.2 Varied printing parameters for tested groups

Group name	Manufacturing method	Infill connection	Raster angle	Perimeter count
0D,0P,UN	Printed	Unconnected	0°	0
0D,0P,C	Printed	Connected	0°	0
0D,1P,UN	Printed	Unconnected	0°	1
0D,Routed	Routed	–	0°	–
90D,0P,UN	Printed	Unconnected	90°	0
90D,0P,C	Printed	Connected	90°	0
90D,1P,UN	Printed	Unconnected	90°	0
P,90D,1P,UN	Printed	Unconnected	90°	1
P,90D,2P,UN	Printed	Unconnected	90°	2
P,90D,3P,UN	Printed	Unconnected	90°	3
P,90D,4P,UN	Printed	Unconnected	90°	4
P,90D,5P,UN	Printed	Unconnected	90°	5
P,90D,6P,UN	Printed	Unconnected	90°	6

was investigated. In a second test series, the influence of perimeters was investigated further, by testing samples manufactured with an increasing number of perimeters, reaching from 1 to 6 (the maximum possible amount for the given geometry). The second test series were performed with samples with a raster angle of 90° only (in the following also referred to as 90D). As it was expected, based on literature, the 90° samples would perform worse than those with a raster angle of 0° (in the following also referred to as 0D), therefore making the potential effects of perimeters more visible.

The samples were dimensioned as proposed by the German standard DIN EN ISO 527-2 (2012-06) Type 1BA and produced on an Ultimaker s5 FFF printer. The material used was white polylactic acid (PLA, Ultimaker); a thermoplast widely used in FFF printing. The varied printing parameters, as discussed above, as well as a selection of the most important parameters which were kept constant and their values are given in Tables 11.2 and 11.3. The parameters were set during the slicing process with the Cura software (Ver. 4.11.0). Until testing, samples were stored at room temperature (approx. 21 °C) in a container with controlled relative humidity of 30%.

Uniaxial tensile tests were performed until failure on a Zwick Roell Z020 testing machine with a 2.5 kN force sensor.

A preload of 1 N and a strainrate of 1%/min were prescribed. The displacement of the traverse was used to adjust the strain rate. All tests were performed at room temperature (21 °C) and 30% relative humidity.

Five specimens were tested per group, and the Young's moduli were evaluated as defined in DIN EN ISO 527-1 (2012-06) (between 0.25% and 0.05% strain). The

Table 11.3 Printing parameters kept constant for all tested groups

Parameter	Value
Layer height	0.2 mm
Line width	0.42 mm
Top/bottom layers	0
Infill density	100%
Extruder temperature	205 °C
Buildplate temperature	60 °C
Printing speed	30 mm/s
Cooling	Enabled
Z-seam alignment	Sharpest corner

Table 11.4 Average values and standard deviations of Young's modulus and ultimate tensile strength for all testes groups

Groups	Mean	Std. deviation	Mean	Std. deviation
0D,0P,UN	3170.25	52.62	52.48	1.39
0D,0P,C	3060.99	43.83	53.17	0.96
0D,1P,UN	3130.83	21.31	57.66	0.35
0D,Routed	2964.09	28.68	47.72	3.34
90D,0P,UN	2544.20	120.10	29.57	2.18
90D,0P,C	2844.51	36.66	38.65	0.91
90D,1P,UN	2959.25	51.74	40.18	1.25
P,90D,1P,UN	3029.62	40.08	40.08	1.04
P,90D,1P,UN	2809.99	96.80	37.36	2.23
P,90D,1P,UN	3033.81	23.17	46.44	0.98
P,90D,1P,UN	2968.42	24.67	45.95	1.51
P,90D,1P,UN	2800.55	30.14	45.47	1.81
P,90D,1P,UN	2906.89	35.75	52.32	2.17

average values of the Young's modulus and the ultimate tensile strength as well as the corresponding standard deviations are given in Table 11.4 for all groups.

11.4 Discussion of Tensile Test Results

The results are compared in the following boxplots. The influence of the sample geometry as well as of the manufacturing method is illustrated in Fig. 11.5 for both the 0D and the 90D groups. Regardless of the polymer strand orientation, the highest mean tensile strength, for each orientation respectively, is measured for the samples

printed with one perimeter, followed by those without perimeter and connected infill. Samples with unconnected infill (without perimeter) register an even lower mean tensile strength. Regarding the Young's modulus, no clear trend could be established for the 0D groups. For the 90D groups, however, a trend analogous to that of the ultimate tensile strength can be identified. The results of a comparison of the three groups (for 0D and 90D samples) with pairwise t-tests (Kühlmeier and Kühlmeier 2001) are shown in Fig. 11.6. The level of significance was set to 5%. The Bonferroni correction (Abdi 2006) was applied to compensate for multiple testing, effectively reducing the level of significance to only 1.6%. These comparisons serve to statistically substantiate the claims made previously.

It was found, that for a raster angle of 0° , no significant difference in the tensile strength between connected and unconnected infill could be established, while the use of a perimeter proved to be statistically relevant. For the 90° samples, no significant difference could be established between the connected infill and the use of a perimeter. The samples with unconnected infill, however, display significantly lower values of tensile strength.

Although statistically relevant differences in the Young's modulus of the 0° groups could be established, no clear trend emerges. For a raster angle of 90° , a significant increase in the Young's modulus was observed following the order of unconnected infill, connected infill and samples with perimeter.

A possible explanation for this difference in tensile strength may be, as mentioned previously, the variation in geometry between the samples with and without perimeter. Specimens without perimeter exhibit sharp edges in the curved section of the geometry. It can be expected, that local stresses peak at these edges, resulting in premature failure of the sample. This would suggest that the results for directly printed samples without perimeters are systematically underestimated.

The routed specimens, despite matching the desired geometry most closely, show the lowest tensile strength, with considerable spread in the individual measurements (see Fig. 11.5).

Further, it can be observed, that all groups with a raster angle of 0° , i.e. with polymer strands oriented in load direction, can withstand greater loads and display higher Young's moduli than those with a raster angle of 90° for all groups. This behaviour as well as the measured values correlate well with those found in previous studies (Kiendl and Gao 2020). The contrast between the 0° and 90° groups is further visualized in Fig. 11.7.

The qualitative behaviour (of all but two groups) is aptly represented by the stress-strain response of the group 0D,0P,UN as shown in Fig. 11.8.

Although the material generally displays a nonlinear stress-strain response, it is well approximated by a linear shape, especially at low strains. As the sample approaches its ultimate tensile strength, the nonlinear behaviour becomes more pronounced. After the maximum stress is reached, a drop in the engineering stress is measured until failure occurs soon after. No pronounced necking is observed. The fracture surfaces (Fig. 11.2) of these samples support this observation. Exhibiting clean breaks with little to no deformation and indicative of a brittle fracture.

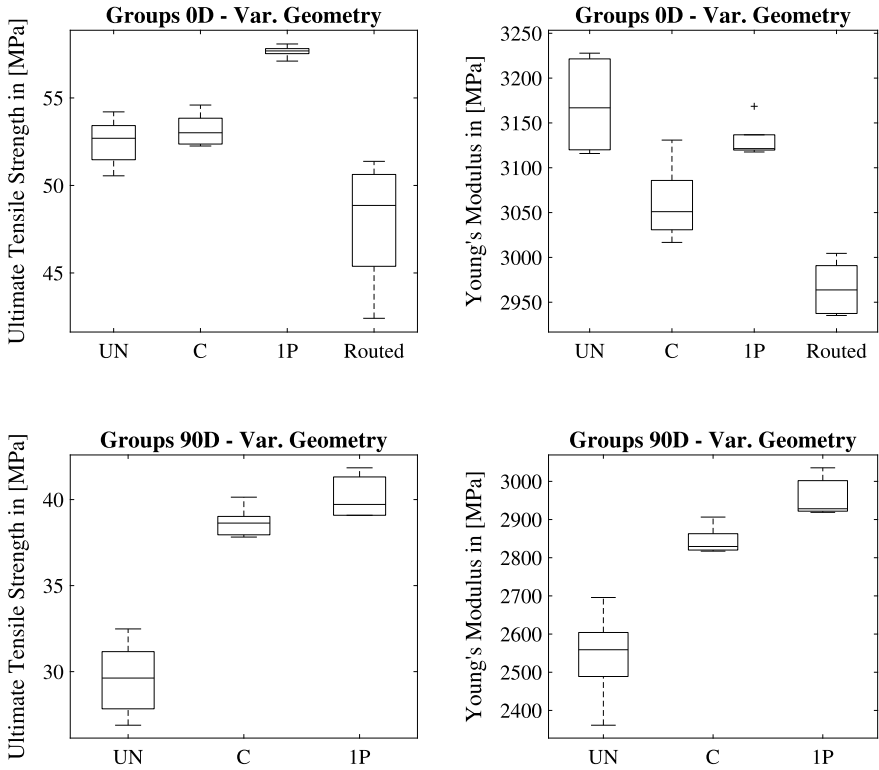


Fig. 11.5 Ultimate tensile strength and Young's modulus for different geometry factors, manufacturing methods and raster angles

Groups 0D

Ultimate Tensile Strength				Young's Modulus			
	UN	C	1P		UN	C	1P
UN	1	0.3881	0.0005	UN	1	0.0073	0.1811
C		1	0.0002	C		1	0.0185
1P			1	1P			1

Groups 90D

Ultimate Tensile Strength				Young's Modulus			
	UN	C	1P		UN	C	1P
UN	1	0.0004	8E-05	UN	1	0.0031	0.0009
C		1	0.0636	C		1	0.0049
1P			1	1P			1

Fig. 11.6 Comparison of the UN, C and 1P groups for 0° and 90° raster angles with pairwise t-tests (level of significance: 0.0166)

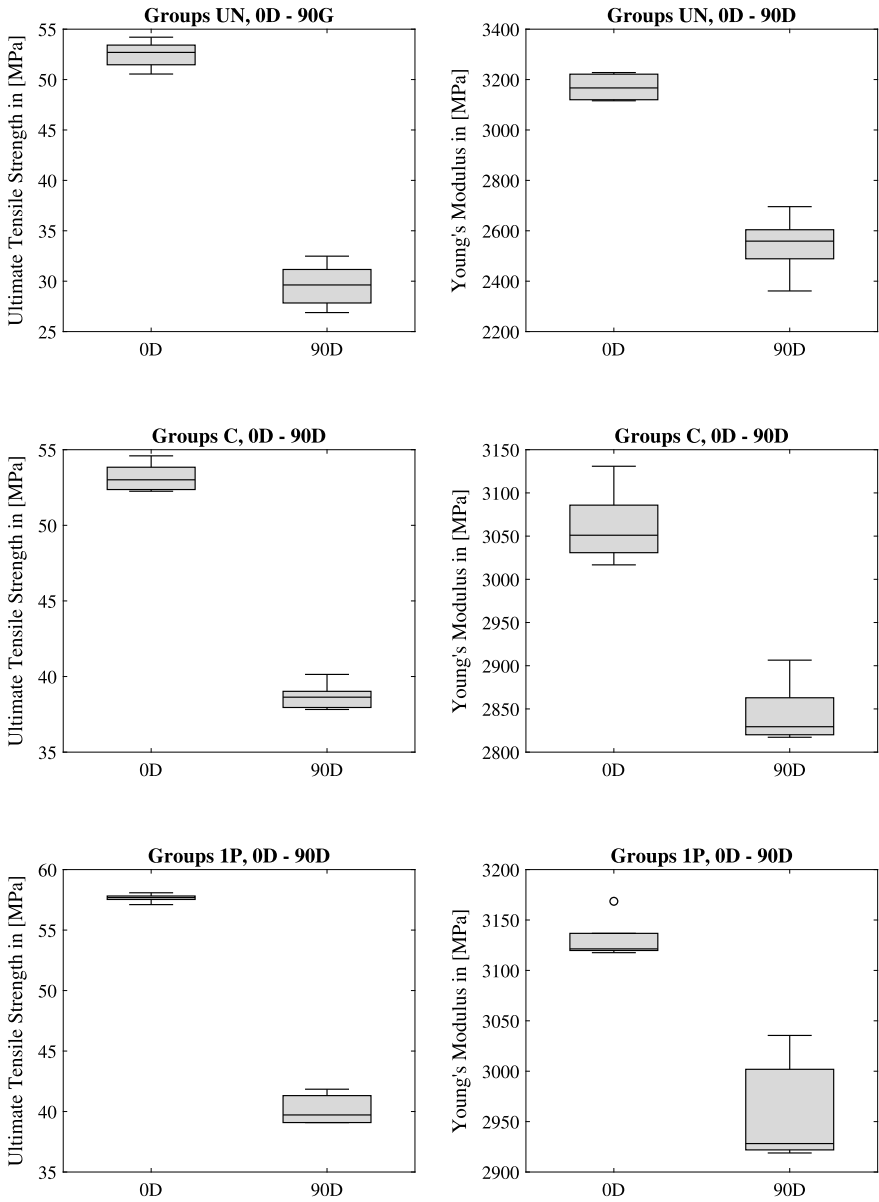


Fig. 11.7 Comparison of ultimate tensile strength and Young's modulus for raster angles 0° and 90° at varying geometric parameters

Fig. 11.8 Stress-strain behaviour for samples of group 0D,0P,UN

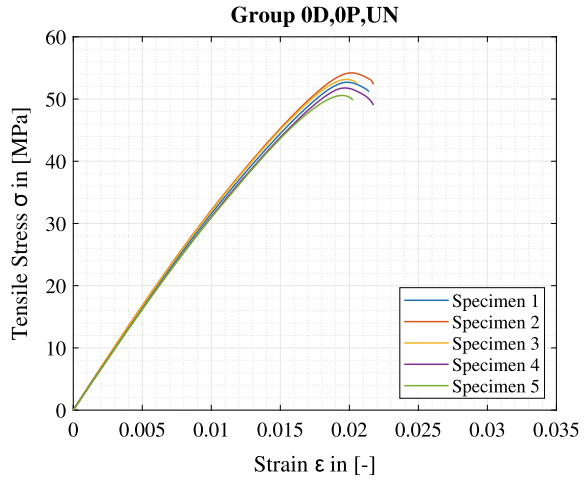
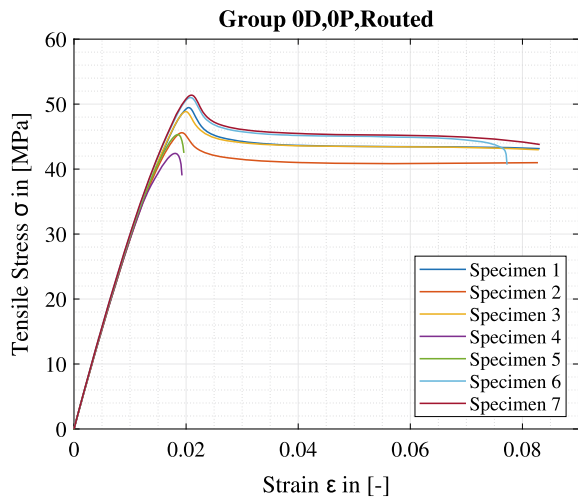


Fig. 11.9 Stress-strain behaviour for samples of group 0D,Routed



For the groups 0D,Routed and 0D,1P,UN, the qualitative behaviour differs. This is exemplarily depicted in Fig. 11.9 for the routed samples. Although the stress-strain curve behaves similar initially, after the maximum stress is reached necking is clearly observable as the measured stress drops at first rapidly and then settles on a stationary value until failure. A further matter to note is that the individual samples of the 0D, Routed and 0D,1P,UN groups do not exhibit identical behaviour. While some exhibit the ductile behaviour described, others show brittle fracture behaviour as described further above. This inconsistency in behaviour might indicate an insufficient (printing) parameter set or irregularities in the internal structure of the samples. As shown in Fig. 11.2, there exist gaps between the individual polymer strands inside a FFF printed part. Although not visible in a singular cross-section, the size of these gaps

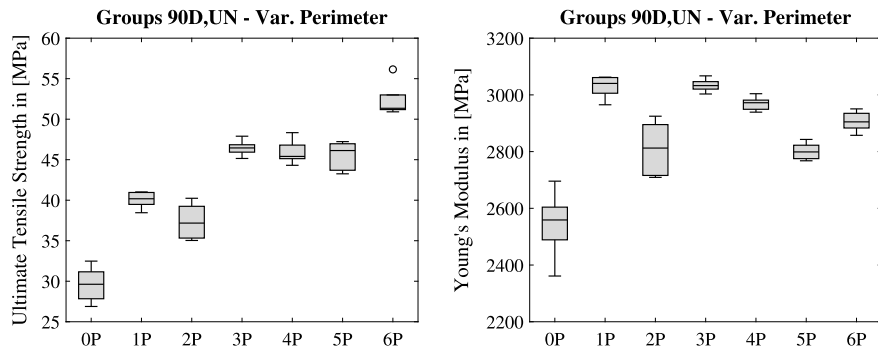


Fig. 11.10 Ultimate tensile strength and Young’s modulus for samples with varying perimeter count

is not consistent along the entire length of the printed polymer strand. It is therefore possible that the effective cross-sectional area in a given sample exhibits a minimum, leading to a local weak point and allowing for brittle fracture.

The results of the second test series are summarized in Fig. 11.10. Regarding the tensile strength, a general trend can be identified with an increasing number of perimeters resulting in higher values. An analysis of variance (ANOVA test) (Kühlmeier and Kühlmeier 2001) confirms the significance of perimeters with a p -value of $6.29e-12$ for a level of significance of 5%. However, the results of the groups 1P and 2P as well as 3P,4P and 5P show no substantial difference between each other. Concerning the Young’s moduli, no clear trend can be established. Although the presence of perimeters leads to higher values of the Young’s modulus, no clear trend emerges in relation to the number of perimeters. It further has to be noted, that all samples printed with 6 perimeters, the maximum geometrically possible number, broke inside the clamp of the testing machine (see Fig. 11.2). A possible explanation is provided by the now varying raster angles along the part geometry. While a raster angle of 0° persists through the entire gage length of the samples, a substantial amount of the clamping region is still printed with a raster angle of 90° . Since, as shown above, the tensile strength of the 90° samples only approaches between 56 and 70% of that of the 0° samples, the clamping region might exhibit weaker material properties than the gage length. This, in combination with the additional stresses introduced through the clamping forces, might have lead to the reliable failure of the samples in the clamping region.

11.5 Conclusion

In this work, the FFF printing process was briefly outlined. The importance of the printing parameters was highlighted, and an overview about current research in the field has been provided. Tensile tests in accordance with DIN EN ISO 527-1

(2012-06) were performed for samples with varying printing parameters. Samples were manufactured on an Ultimaker s5 out of PLA. The results of these comparisons can be summarized as follows:

- Routed samples showed lower values for both Young's modulus and ultimate tensile strength than their printed counterparts with wide spread in the individual results.
- Samples with a raster angle of 0° displayed a higher ultimate tensile strength as well as Young's modulus than their 90° counterparts for all tested parameter variations.
- For a raster angle of 0° , the infill connection had no significant effect on tensile strength, while the use of a perimeter leads to an increase in tensile strength. Regarding Young's modulus, no trend could be established.
- For a raster angle of 90° , the use of both connected infill as well as perimeters increases tensile strength compared to a unconnected infill. Regarding Young's modulus a trend emerges, with measurement results increasing in the order of unconnected infill, connected infill and samples with perimeter.
- The number of perimeters used was shown to increase the measured tensile strength. The use of perimeters leads to an increase in the Young's modulus as well, although no trend regarding the number of perimeters emerged.

It has been shown that perimeters have considerable impact on ultimate tensile strength possibly because the use of perimeters allows to achieve the desired geometry, while samples printed without exhibit a stepwise transition in the curved regions of the geometry. Thus, creating sharp edges, resulting in stress peaks and premature failure of the sample.

Based on these results, a further points of interest would be to study the tensile behaviour of rectangular, stripe-shaped specimens, as they are defined, for example, in DIN EN ISO 527-4 (1997-07) for the testing of fibre-laminates. The use of this geometry would avoid the geometric problems discussed in this contribution, warranting a comparison with dogbone-shaped test specimens.

Acknowledgements This research work is funded by dtcc.bw-Digitalization and Technology Research Center of the Bundeswehr which we gratefully acknowledge [project FLAB-3Dprint].

References

- Abdi H (2006) Bonferroni test. In: Encyclopedia of measurement and statistics, a Sage reference publication, vol 1. SAGE, Thousand Oaks
- Ahn SH, Montero M, Odell D, Roundy S, Wright PK (2002) Anisotropic material properties of fused deposition modeling ABS. Rapid Prototyp J 8(4):248–257. <https://doi.org/10.1108/13552540210441166>

- Camposeco-Negrete C (2020) Optimization of FDM parameters for improving part quality, productivity and sustainability of the process using Taguchi methodology and desirability approach. *Prog Add Manuf* 5(1):59–65. <https://doi.org/10.1007/s40964-020-00115-9>
- Ćwikła G, Grabowik C, Kalinowski K, Paprocka I, Ociepka P (2017) The influence of printing parameters on selected mechanical properties of FDM/FFF 3D-printed parts. In: IOP conference series: materials science and engineering 227. <https://doi.org/10.1088/1757-899X/227/1/012033>
- Dey A, Yodo N (2019) A systematic survey of FDM process parameter optimization and their influence on part characteristics. *J Manuf Mater Process* 3(3):64. <https://doi.org/10.3390/jmmp3030064>
- DIN EN ISO 527-1 (2012-06) Kunststoffe—Bestimmung der Zugeigenschaften—Teil 1: Allgemeine Grundsätze (ISO 527-1:2012)
- DIN EN ISO 527-2 (2012-06) Kunststoffe—Bestimmung der Zugeigenschaften—Teil 2: Prüfbedingungen für Form- und Extrusionsmassen (ISO 527-2:2012)
- DIN EN ISO 527-4 (1997-07) Kunststoffe—Bestimmung der Zugeigenschaften—Teil 4: Prüfbedingungen für isotrop und anisotrop faserverstärkte Kunststoffverbundwerkstoffe (ISO 527-4:1997)
- García-León RA, Rodríguez-Castilla M, Quintero-Quintero W (2021) Experimental analysis of impact resistance of 3D polycarbonate and nylon + carbon fiber specimens. *J Mater Eng Performance*. <https://doi.org/10.1007/s11665-020-05422-4>
- Gebhardt A, Kessler J, Thurn L (2018) 3D Printing: understanding additive manufacturing, 2nd edn. Hanser Publications, Cincinnati
- Gebisa AW, Lemu HG (2019) Influence of 3D printing FDM process parameters on tensile property of ULTEM 9085. *Procedia Manuf* 30:331–338. <https://doi.org/10.1016/j.promfg.2019.02.047>
- Gibson I, Rosen D, Stucker B (2015) Additive manufacturing technologies: 3D printing, rapid prototyping and direct digital manufacturing, 2nd edition edn. Springer, New York. <https://www.loc.gov/catdir/enhancements/fy1617/2014953293-b.html>
- Hu B, Xing Z, Wu W, Zhang X, Zhou H, Du C, Shan B (2021) Enhancing the mechanical properties of SCF/PEEK composites in FDM via process-parameter optimization. *High Performance Polym* 095400832110036. <https://doi.org/10.1177/09540083211003654>
- Kamaal M, Anas M, Rastogi H, Bhardwaj N, Rahaman A (2021) Effect of FDM process parameters on mechanical properties of 3D-printed carbon fibre-PLA composite. *Prog Add Manuf* 6(1):63–69. <https://doi.org/10.1007/s40964-020-00145-3>
- Kiendl J, Gao C (2020) Controlling toughness and strength of FDM 3D-printed PLA components through the raster layout. *Compos Part B Eng* 180. <https://doi.org/10.1016/j.compositesb.2019.107562>
- Kim MK, Lee IH, Kim HC (2018) Effect of fabrication parameters on surface roughness of FDM parts. *Int J Precision Eng Manuf* 19(1):137–142. <https://doi.org/10.1007/s12541-018-0016-0>
- Kozior T, Kundera C (2017) Evaluation of the influence of parameters of FDM technology on the selected mechanical properties of models. *Procedia Eng* 192:463–468. <https://doi.org/10.1016/j.proeng.2017.06.080>
- Kühlmeyer M, Kühlmeyer C (2001) Statistische Auswertungsmethoden für Ingenieure: Mit Praxisbeispielen. VDI-Buch, Springer, Berlin. <https://doi.org/10.1007/978-3-642-56776-6>
- Liu H, Cheng X, Yang XH, Zheng GM, Guo QJ (2019) Experimental study on parameters of 3D printing process for PEEK materials. In: IOP conference series: materials science and engineering, p 504. <https://doi.org/10.1088/1757-899X/504/1/012001>
- McTaggart R, Rankouhi B, Letcher T (2020) Effects of gamma irradiation on mechanical properties of 3D-printed carbon fiber-reinforced ABS. *Int J Adv Manuf Technol* 111(7–8):1917–1927. <https://doi.org/10.1007/s00170-020-06243-4>
- Mohamed OA, Masood SH, Bhowmik JL (2016) Mathematical modeling and FDM process parameters optimization using response surface methodology based on Q-optimal design. *Appl Math Modell* 40(23–24):10052–10073. <https://doi.org/10.1016/j.apm.2016.06.055>
- Mohamed OA, Masood SH, Bhowmik JL, Nikzad M, Azadmanjiri J (2016) Effect of process parameters on dynamic mechanical performance of FDM PC/ABS printed parts through design of

- experiment. *J Mater Eng Perform* 25(7):2922–2935. <https://doi.org/10.1007/s11665-016-2157-6>
- Pant M, Singari RM, Arora PK, Moona G, Kumar H (2020) Wear assessment of 3-D printed parts of PLA (polylactic acid) using Taguchi design and Artificial Neural Network (ANN) technique. *Mater Res Express* 7(11). <https://doi.org/10.1088/2053-1591/abc8bd>
- Pérez M, Medina-Sánchez G, García-Collado A, Gupta M, Carou D (2018) Surface quality enhancement of fused deposition modeling (FDM) printed samples based on the selection of critical printing parameters. *Mater (Basel, Switzerland)* 11(8). <https://doi.org/10.3390/ma11081382>
- Popescu D, Zapciu A, Amza C, Baci F, Marinescu R (2018) FDM process parameters influence over the mechanical properties of polymer specimens: a review. *Polym Test* 69:157–166. <https://doi.org/10.1016/j.polymertesting.2018.05.020>
- Radhwan H, Shayfull Z, Farizuan MR, Effendi MSM, Irfan AR (2019) Optimization parameter effects on the quality surface finish of the three-dimensional printing (3D-printing) fused deposition modeling (FDM) using RSM. In: AIP conference proceedings, applied physics of condensed matter (APCOM 2019), AIP Publishing. <https://doi.org/10.1063/1.5118163>
- Rybachuk M, Alice Mauger C, Fiedler T, Öchsner A (2017) Anisotropic mechanical properties of fused deposition modeled parts fabricated by using acrylonitrile butadiene styrene polymer. *J Polym Eng* 37(7):699–706. <https://doi.org/10.1515/polyeng-2016-0263>
- Samykano M, Selvamani SK, Kadirgama K, Ngui WK, Kanagaraj G, Sudhakar K (2019) Mechanical property of FDM printed ABS: influence of printing parameters. *Int J Adv Manuf Technol* 102(9–12):2779–2796. <https://doi.org/10.1007/s00170-019-03313-0>
- Wang P, Zou B, Ding S, Li L, Huang C (2020) Effects of FDM-3d printing parameters on mechanical properties and microstructure of CF/peek and GF/peek. *Chin J Aeronaut.* <https://doi.org/10.1016/j.cja.2020.05.040>
- Wang Y, Müller WD, Rumjahn A, Schwitalla A (2020b) Parameters influencing the outcome of additive manufacturing of tiny medical devices based on peek. *Materials (Basel, Switzerland)* 13(2). <https://doi.org/10.3390/ma13020466>

Chapter 12

Design of a Room-in-Room Laboratory Environment for the SLS Printing Process



Dominik Hahne, Alexander Lion, and Michael Johlitz

Abstract This contribution presents a solution for generating an encapsulated environment for the selective laser sintering printing process. All relevant subroutines—such as unpacking, sieving, powder mixing, and conveying—can be done in a controlled and sealed environment. The exposure to harmful temperature and humidity conditions of the sensitive powder materials is avoided by accurate climate control. According to finite element calculations, the evaluated structural solution is modular, flexible, and robust.

12.1 Motivation

Selective laser sintering (SLS) is a mature additive manufacturing (AM) technology that can generate prototypes and serial parts. It is often seen as a replacement for conventional manufacturing processes (e.g., injection moulding). However, its tool-less, layer-by-layer printing process offers design engineers an additional degree of freedom (Kruth et al. 2007). For quantities between 100 and 10.000 parts, investigations show the economic benefits of SLS over conventional production methods (Hopkinson et al. 2006). Nevertheless, there are several research questions regarding the printing process itself. The main concerns are the ageing of the material (mainly PA12) due to the thermal history of the powder (Wudy and Drummer 2019), temperature differences on the building platform leading to position-dependent mechanical properties (Wegner and Witt 2013), and the detailed interaction between the CO₂-laser and powder (Greiner et al. 2021).

However, this contribution focuses on preparatory and follow-up work of the printing process. A used and virgin powder mixture is typically used in industrial applications

D. Hahne (✉) · A. Lion · M. Johlitz
Universität der Bundeswehr, Werner-Heisenberg-Weg 39, 85577 Neubiberg, Germany
e-mail: dominik.hahne@unibw.de

A. Lion
e-mail: alexander.lion@unibw.de

M. Johlitz
e-mail: michael.johlitz@unibw.de

© The Author(s), under exclusive license to Springer Nature Switzerland AG 2022
H. Altenbach et al. (eds.), *Lectures Notes on Advanced Structured Materials*,
Advanced Structured Materials 153, https://doi.org/10.1007/978-3-031-11589-9_12

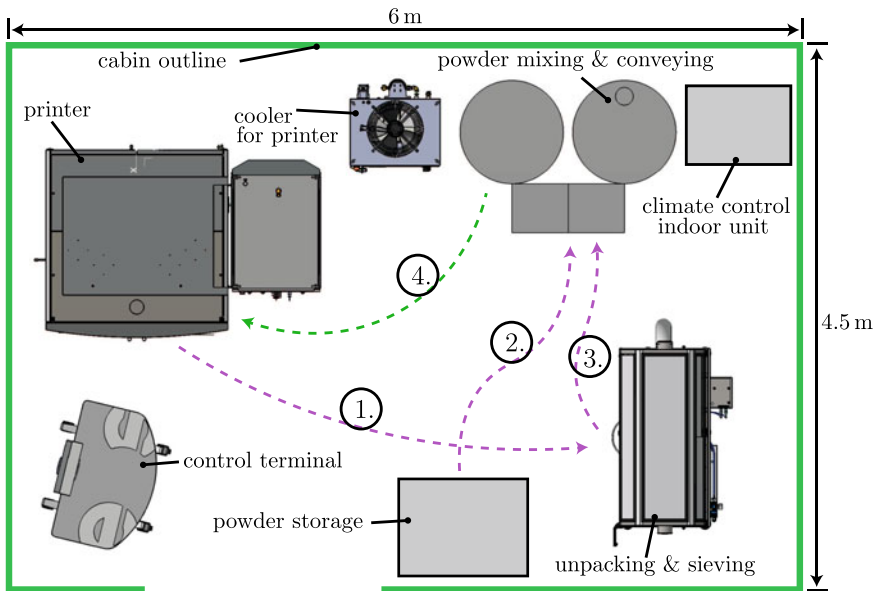


Fig. 12.1 Subroutines of SLS process with powder path (dashed lines)

to reduce costs while maintaining consistent part quality. In many SLS systems, the mixing procedure and the machine's feeding are manual processes. Every manual process can potentially negatively manipulate the tools and materials, e.g. exposure to inadmissible temperatures and humidity conditions or entering of dirt and foreign objects. A room-in-room laboratory is built around the SLS machine to avoid those influences as much as possible. The balance of time, costs, and availability of accurate laboratory facilities is considered. Figure 12.1 shows the subroutines of the SLS process.

1. Transfer of printed parts from the printer to the unpacking & sieving station
2. Transportation of the virgin powder
3. Transportation of the used powder
4. Feeding of the machine (automated process).

The target is to create a laboratory environment with stable temperature and humidity conditions for all SLS-subroutines.

12.2 Mechanical Design of the Cabin

Temperature and humidity are crucial for the SLS process itself and the preparatory and follow-up work, such as powder mixing and transportation, unpacking of

the parts, and powder sieving. Therefore, the necessity for building a cabin around the printing system is seen as a chance to create an optimized printing and handling environment for the SLS process. Following a classical, sequential approach of product development (planning and clarifying the task, concept, design, and elaboration) (Feldhusen and Grote 2016) would not agree with the dynamic setting of the project, leading to a more simultaneous engineering process. Nevertheless, an overview of the main requirements must be given at the beginning. Even though the main task is already stated, several aspects need to be concerned. The laboratory environment should be built up in a short period, meaning that all parts must be available within an acceptable range of approximately eight weeks. Further, the cabin is sought to be modular, scalable, and reuseable to be adapted and transferred to fulfil more or other tasks in future. All named aspects conclude that a solution using as many standardized components as possible is best to fulfil all requirements.

12.2.1 Design Structure

The cabin framework is built from extrusion moulded aluminium profiles because they are used widely in the industrial and scientific sectors to build test benches and machine housings. The availability is ensured, and the handling is familiar. The design is simplified by taking the predefined geometries from the manufacturers' websites or engineering tools¹. Construction works start by roughly sketching the outline, estimating the deformation due to deadweight and external loads, choosing the suitable geometries of the profiles (i.e., width and height) and finally getting more and more into detail with the design. Aligning the profiles in an installation-friendly way, choosing the fasteners between the profiles and generating a regular profile pattern for simplifying the housing plates is part of the detailing process and is subject to several iterations. As long as there is no chance of compensating tolerances between the profiles, all contact points between the framework and floor need to be adjustable in height. Figure 12.2 shows the isometrical view of the cabin's basic framework and the fully covered cabin.

The upstream (unpacking and sieving) and downstream (powder mixing and conveying) steps of the printing process should be integrated inside the cabin. The cabin dimensions ($6 \times 3 \times 4.5 \text{ m}^3$ W \times H \times D) are evaluated by roughly sketching the components inside the footprint. 3D models made it possible to create an assembly with all components involved, as shown in Fig. 12.2.

In Fig. 12.2, one can see intermediate support for the roof in the centre of the cabin, which was placed in the conceptual phase. The main reasons are the dead weight of the roof profiles ($\approx 210 \text{ kg}$) and the powder conveying system, which is mounted on the roof as the printer is fed from the top.

¹ There are several companies offering aluminium profiles. Engineering tools and geometries are offered on their websites.

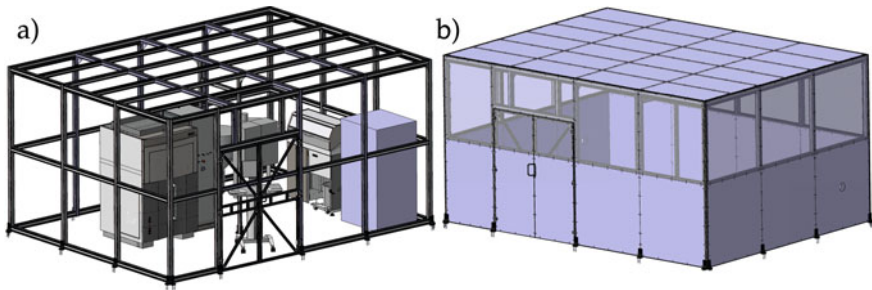


Fig. 12.2 a Components placed inside the cabin, b Fully covered cabin

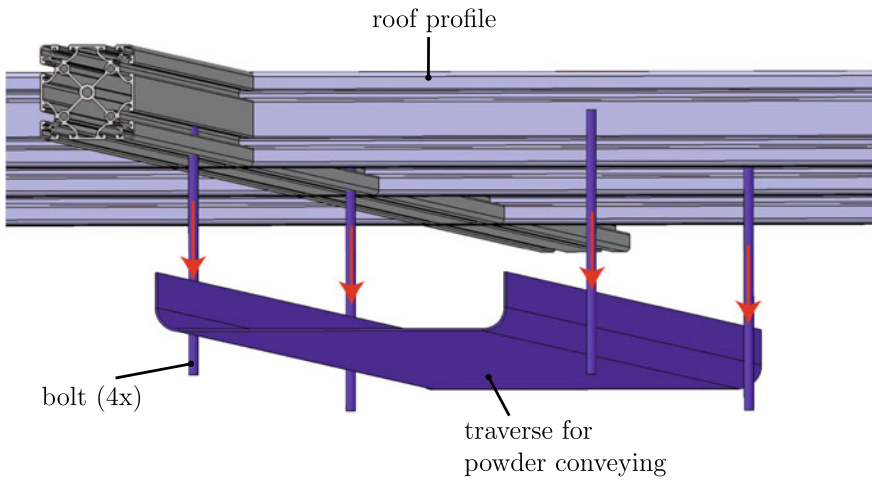


Fig. 12.3 Sketch of traverse for powder conveying

12.2.2 Structural Mechanics of the Cabin

The load capacity of the roof is the primary concern regarding stresses and deformations of the cabin framework. The powder conveying system is mounted onto a traverse connected to the roof with four M8 threaded bolts and is placed above the printer. Bolt load (1.000 N) and positioning are given by printer specification. Figure 12.3 shows the principal sketch of the traverse and the load.

The interface design between the bolts and the roof profiles of the cabin was straightforward and aligned with the availability of profiles in the mechanical workshop. Flexibility to slightly change the position of the bolts is ensured with different fastening points (Fig. 12.4).

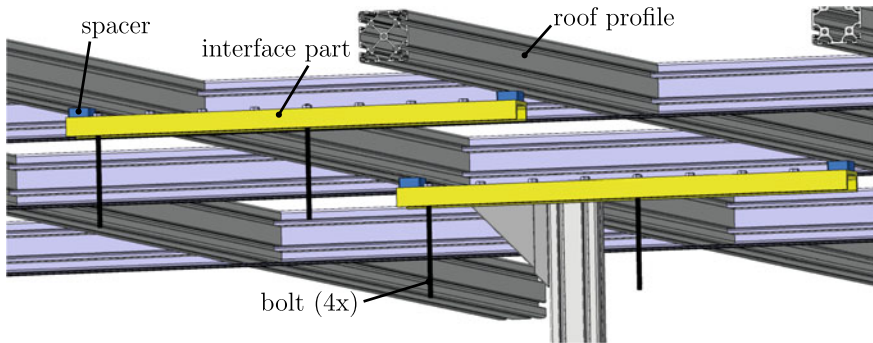


Fig. 12.4 Interface part between powder conveying system and cabin roof

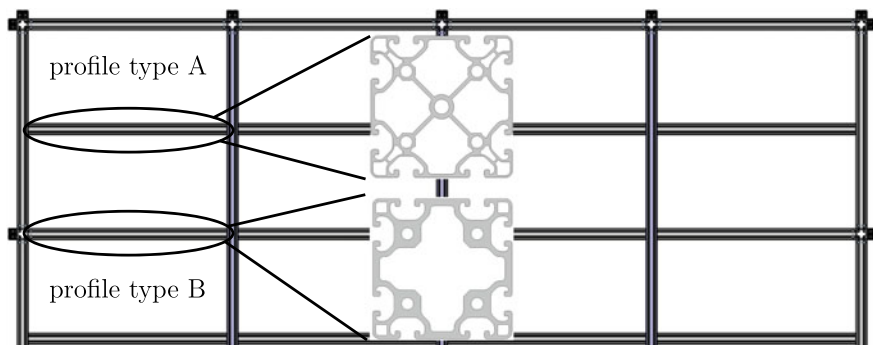


Fig. 12.5 Cabin roof and types of profiles

12.2.2.1 FE-Calculation of the Cabin Roof

The cabin's roof is subjected to its dead weight and the bolt load of the traverse indirectly through the interface part. The fine structure of roof profiles requires fine meshes to achieve accurate results. The aim is to generate at least three elements across the thickness of the profile walls. The different geometries of the profiles are subjected to a 3-point-bending test to establish which standard profile is suitable according to the moment of inertia. Choosing two different types of profiles for the roof results from an optimization regarding the ratio of stiffness and dead weight in the detailed design phase (Fig. 12.5). Figure 12.6 shows the results of the FE-calculation and the equivalent diameter for a circular profile. All calculations are linear-elastic. Small deformations are expected.

Simulating the whole framework with detailed profile geometry leads to many elements and high computing time. After repatriating the continuous casting section to a standard profile, the whole cabin can be modelled as a 2D-beam structure. The density of the standard profile is modified according to the cross-sectional area compared to the casting profile to generate the correct dead weight. Figure 12.7 shows

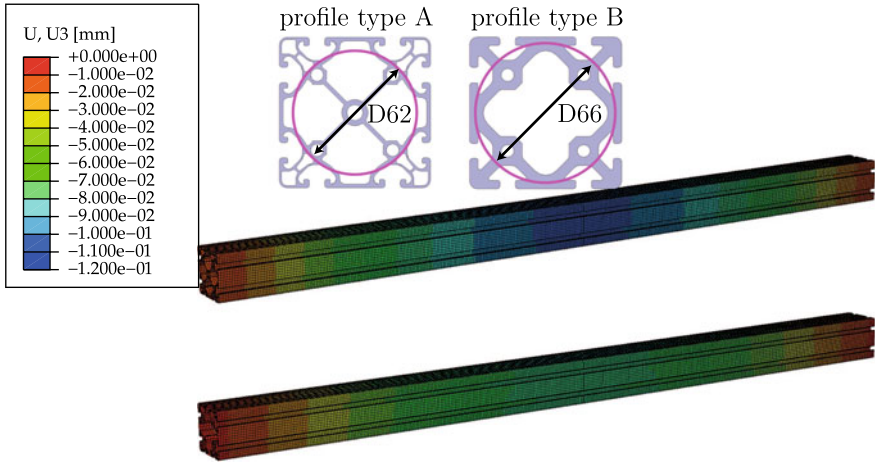


Fig. 12.6 FE-result profiles and cylindrical equivalent

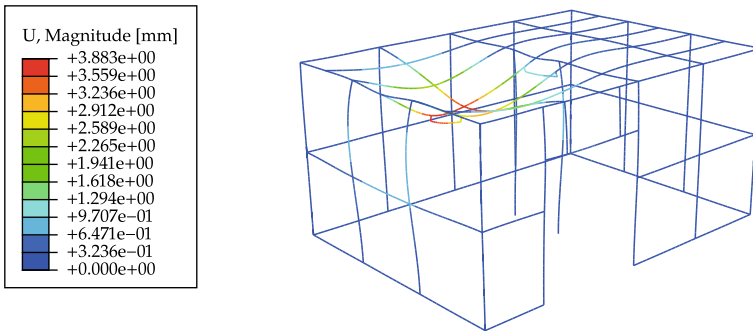


Fig. 12.7 Simulated deformations of the the cabin roof

the deformation of the cabin roof subjected to the load of the powder conveyor and its dead weight. The connections between the profiles are modelled as tied joints. The additional supporting effect of the double-walled housing was not considered, as there is no material model for both materials, and the computing effort for nonlinear materials exceeds the expected benefit in this case.

12.2.2.2 FE-Calculation of the Interface Part for Powder Conveying

The deformations and stresses of the interface part are simulated in a separate step. The bolt joint between the interface part and cabin roof is considered with a stiffness of $c = 2.58 \times 10^5 \frac{\text{N}}{\text{mm}}$ following a classical calculation approach from machine elements literature (Wittel et al. 2021). The required force of 1.000 N ($2\times$) is applied in worst-case positions. Deformation and stresses of the interface part are within acceptable limits (Fig. 12.8). Peak stresses can be found near the bolt joints (Fig. 12.9).

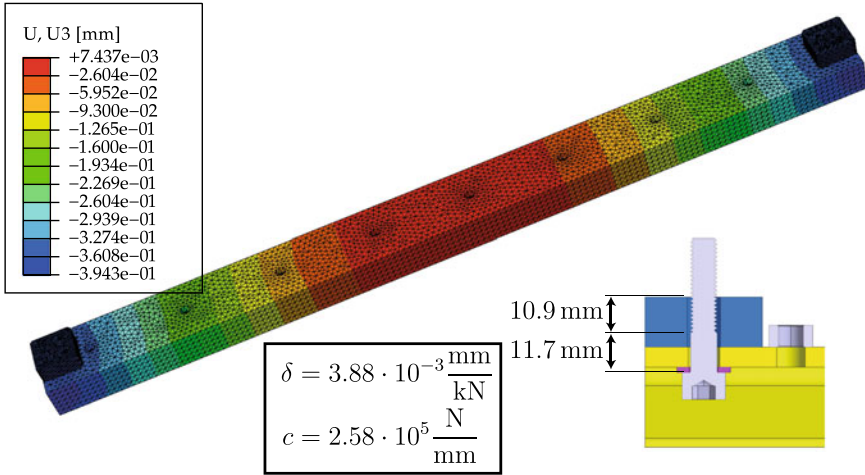


Fig. 12.8 Simulated deformations of the interface part

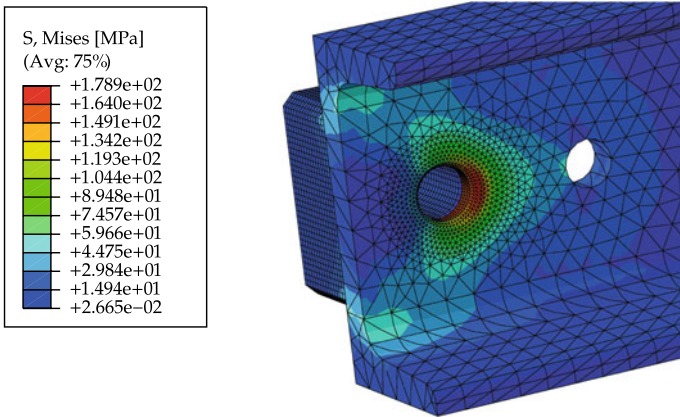


Fig. 12.9 Maximum stresses near bolt joints

12.3 Thermal Concept

The build-up of the cabin within an existing facility leads to a room-in-room construction. The cabin itself has climate control, the building around has a heating system.

The housing of the cabin is double-walled to improve the thermal insulation. The walls are made from PET-G and resin-saturated cellulose fibre. The aluminium profiles need to be covered as much as possible to avoid thermal bridges (Fig. 12.2).

Table 12.1 Thermal conductivity of cabin materials

Materials	Thermal conductivity	Acc. to standard
Aluminium	$\approx 160 \frac{\text{W}}{\text{mK}}$	
PET-G (transparent)	$0.2 \frac{\text{W}}{\text{mK}}$	DIN EN ISO 22007-1
resin-saturated cellulose fibre	$0.3 \frac{\text{W}}{\text{mK}}$	DIN EN ISO 22007-1

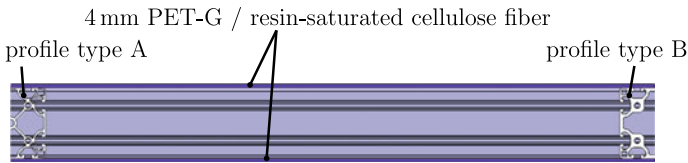
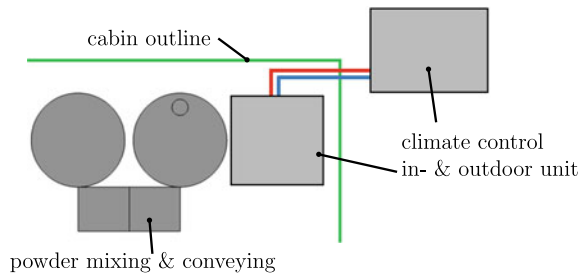
**Fig. 12.10** Sectional view of the cabin roof**Fig. 12.11** Basic sketch of climate control

Figure 12.10 shows a section through the roof of the cabin. The thermal conductivity of the involved materials can be taken from Table 12.1².

The climatization is done by a split system (Fig. 12.11) specially designed for high thermal loads and optimized for laboratory environments. The system has a data logger next to heating, cooling, and (de-)humidifying. The humidity and temperature inside the cabin can be traced for every print job, unpacking, sieving, and powder conveying process. According to printer specifications, the maximum waste heat is 10 kW. The climate control system has a cooling capacity of 14 kW.

12.4 Extraction System

The SLS printer may only be operated in conjunction with an extraction system because inhalation of vapours from the thermal decomposition of powder can lead to adverse health effects. Like the interface part for powder conveying, the extraction system can be seen as an additional feature added after finishing the basic framework and housing. As the holes in the housing need to be added in the workshop,

² Material data are provided by the manufacturer.

Fig. 12.12 Components of the extraction system

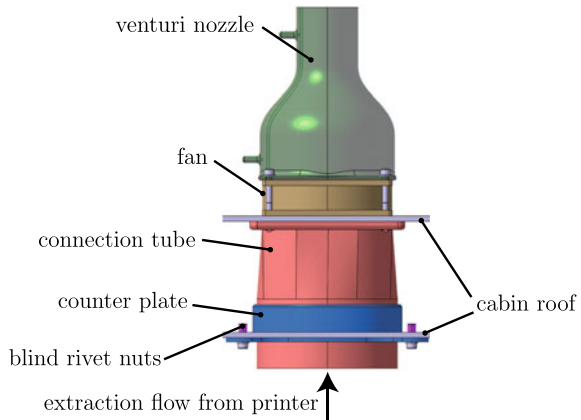
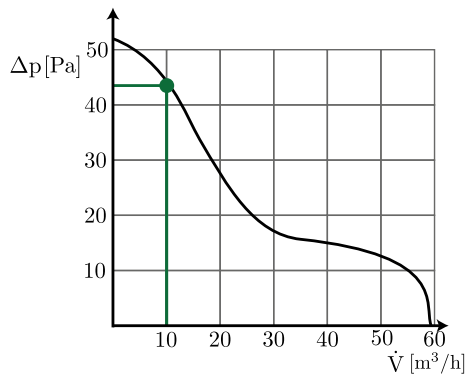


Fig. 12.13 Characteristic curve of fan



equalization of tolerances is the primary concern and an assembly with connection tube and counter plate is chosen for air routing through the double-walled cabin roof. A volume flow of $10 \frac{\text{m}^3}{\text{h}}$ needs to be ensured. The connection tube through the double-walled cabin roof is fabricated via fused filament fabrication (FFF). The printer’s specification gives the diameter of the tube (100 mm). Figure 12.12 shows the components of the extraction system.

The fan can be adjusted to the correct volume flow rate with a simple PWM control. Volume flow is calculated using Bernoulli’s equation—assuming incompressibility and lack of friction—and measuring the pressure difference in the Venturi nozzle. Figure 12.13 shows the characteristic curve of the fan. If the pressure difference within the extraction system exceeds 40 Pa, the fan is not able to deliver the required volume flow rate. In this case, a second fan will be mounted in series.

12.5 Summary

A concept for generating a climate-controlled environment for printing and all relevant subroutines is designed. Regarding schedule, costs, and modularity, only standard components were used for building the housing. FE-calculations of the critical parts show acceptable values for stresses and deformations of the cabin framework and related parts. The extraction system is added as an additional feature using standard and self-printed parts. Humidity and temperature are kept in a small and accurate range by a 14 kW split climate control for technical environments.

Acknowledgements This paper is funded by dtec.bw—Digitalization and Technology Research Center of the Bundeswehr, which we gratefully acknowledge [project FLAB-3Dprint].

References

- Feldhusen J, Grote KH (2016) Pahl/Beitz Konstruktionslehre, 8th edn. Springer, New York
- Greiner S, Jaksch A, Drummer D (2021) Understanding cylinder temperature effects in laser beam melting of polymers. Lecture notes in mechanical engineering. Springer, New York
- Hopkinson N, Hague R, Dickens P (2006) Rapid manufacturing: an industrial revolution for the digital age. Wiley, Chichester England
- Kruth JP, Levy G, Klocke F, Childs T (2007) Consolidation phenomena in laser and powder-bed based layered manufacturing. CIRP Ann 56(2):730–759
- Wegner A, Witt G (2013) Ursachen für eine mangelnde reproduzierbarkeit beim laser-sintern von kunststoffbauteilen. RTejournal 10
- Wittel H, Jannasch D, Spura C (2021) Roloff/Matek Maschinenelemente: Normung, Berechnung, Gestaltung/Herbert Wittel, Christian Spura, Dieter Jannasch. Springer
- Wudy K, Drummer D (2019) Ageing effects of polyamide 12 in selective laser sintering: molecular weight distribution and thermal properties. Add Manuf 25:1–9. ISSN 2214-8604

Chapter 13

Chemical–Mechanical Characterization of Unaged and Aged Additively Manufactured Elastomers



Yvonne Breitmoser, Sebastian Eibl, Tobias Förster, Alexander Lion, and Michael Johlitz

Abstract Aging phenomena of additively manufactured components produced by multi jet modeling (MJM) are investigated using chemical and mechanical analysis methods. To obtain knowledge on the long-term behavior of the investigated urethane acrylates, dependencies of chemical and mechanical properties on aging are investigated in depth. For this purpose, infrared spectroscopic studies were performed to elucidate the chemical change due to aging. The resulting changes in mechanical properties were investigated by means of differential scanning calorimetry, tensile tests, and hardness measurements. The results show that with progressive aging, the chemical composition in the components changes, causing a decrease in mechanical properties.

13.1 Introduction

Additive manufacturing (AM) is an emerging technology that is gaining more and more acceptance. Printing on demand or at a specific location, as well as great time and cost savings for small series are arguments in favor of this technology. AM is already widely used in medical applications to create customized implants or

Y. Breitmoser (✉) · A. Lion · M. Johlitz
Institute of Mechanics, Universität der Bundeswehr München, Werner-Heisenberg-Weg 39, 85577 Neubiberg, Germany
e-mail: yvonne.breitmoser@unibw.de

A. Lion
e-mail: alexander.lion@unibw.de

M. Johlitz
e-mail: michael.johlitz@unibw.de

Y. Breitmoser · S. Eibl · T. Förster
Wehrwissenschaftliches Institut für Werk- und Betriebsstoffe, Institutsweg 1, 85435 Erding, Germany
e-mail: sebastianeibl@bundeswehr.org

T. Förster
e-mail: tobiaslfoerster@bundeswehr.org

anatomical models (Haryńska et al. 2018; Herzberger et al. 2019; Peltola et al. 2008). In the automotive sector, sealants and interiors (Herzberger et al. 2019; Shahrubudin et al. 2019) and in aerospace, air vents and probes (Singamneni et al. 2019; Wiese et al. 2020) are printed.

In addition to metals and stiff polymers such as polyamide (Kennedy and Christ 2020; Ligon et al. 2017; Ngo et al. 2018) or polylactic acid (Kennedy and Christ 2020; Ligon et al. 2017; Ngo et al. 2018), soft and elastic polymers (Herzberger et al. 2019) are also increasingly coming into focus for AM. The currently available manufacturing processes, however, prevent the use of conventional vulcanized elastomers. Therefore, there are significant differences in the chemical compositions of the AM elastomers available on the market compared to conventional ones. Nevertheless, since they have to fulfill similar material requirements, it is necessary to investigate the applicability of these new types of elastomers. To find applications as a substitute for conventional parts, the chemical structure must be elucidated to be able to correlate this with the mechanical properties. In addition, the long-term behavior of these polymers, especially in terms of aging, must also be investigated.

One possibility for producing components additively is the multi jet modeling (MJM) process. An inkjet head with several nozzles ejects small droplets of a photopolymer. After applying a layer, the created layer is cured with UV light, and the process is repeated (Ligon et al. 2017). Multiple inkjet heads enable three-dimensional multi-material or multi-color components. Thus, components with hard and soft segments and even with hardness gradients can be produced. The aim of this study is to investigate the aging behaviors of MJM processed polymers. A basic material identification is first performed to correlate chemical and mechanical properties. Accelerated aging tests focusing on thermally induced changes in chemical composition and mechanical properties are described.

13.2 Material

The acrylic formulations VeroClear™ and TangoBlackPlus™, abbreviated as TangoBlack+, both supplied by Stratasys® were used in the experiments. Further, two blends were investigated, abbreviated as VeroTango 95 and VeroTango 70, both consisting of VeroClear and TangoBlack+ in different mixing ratios, which can be set via the printer software. VeroClear is a stiff transparent polymer with a hardness of 85 Shore D, whereas TangoBlack+ is a black elastomer with a hardness of 25 Shore A. The blends VeroTango 95 and VeroTango 70 have black color and a hardness of 95 Shore A and 70 Shore A, respectively. The material specifications provided by the manufacturer are given in Table 13.1.

Dumbbell-shaped test specimens (S2) made of the materials were produced using the Stratasys Objet500 Connex3™ MJM printer. The hardness grades of VeroTango 95 and VeroTango 70 were generated by the printer itself through drop-wise dithering patterns of the two main materials VeroClear and TangoBlack+.

Table 13.1 Properties of investigated materials provided by the manufacturer

Property	VeroClear	VeroTango 95	VeroTango 70	TangoBlack+
Tensile strength (MPa)	50–65	8.5–10	3.5–5.0	0.8–1.5
Elongation at break (%)	10–25	35–45	65–80	170–220
Hardness (Shore)	83–86 D	92–95 A	68–72 A	26–28 A

All samples were printed with support material, which was removed after completion of the printing process. Careful cleaning of the support material was possible with a spatula. Then, the remaining adhering material was removed under flowing water, and the specimens were dried at room temperature for a period of two days.

The thermal aging tests according to DIN 53508 were performed at aging temperatures of 70 and 100 °C for 24, 72, and 168 h in a thermal air-flow-oven Binder ED56.

13.3 Methods

To characterize the polymers, ca. 5 mg of each of the uncrosslinked resins VeroClear and TangoBlack+ were added with ca. 1 g of acetone, from which a gas chromatography/mass spectrometry (GC/MS) analysis was performed. An Agilent 7890A gas chromatograph with a 30 m DB 5MS column (0.25 mm inner diameter and 0.25 µm film thickness) coupled with an Agilent 5975 MSD mass spectrometer was used.

A fivefold measurement was performed for each subsequent test. To observe the progressive aging chemically, Fourier transform infrared (FTIR) spectra were recorded with an attenuated total reflectance (ATR) unit with a diamond crystal. 32 individual scans were averaged for one spectrum. Measurements were taken with a Bruker Tensor 27 system in the range between 4000 and 400 cm⁻¹.

Differential scanning calorimetry (DSC) can be used to quantify the aging process. To this end, the DSC 204 F1 Phoenix by Netzsch was used. The measurements were done with a heating rate of 10 K min⁻¹ in the range of –80 to 90 °C.

Due to the different strengths of the materials used and the resulting use of different load cells, the tensile tests were performed on two tensile testing machines. VeroClear was tested using the UPM Zwick Z020 according to DIN EN ISO 527, the remaining materials were tested with the Zwick Roell 1445 according to DIN 53504.

The Shore hardness values for Shore AM and Shore D were determined with a Digitest of Bareiss according to DIN ISO 48-4.

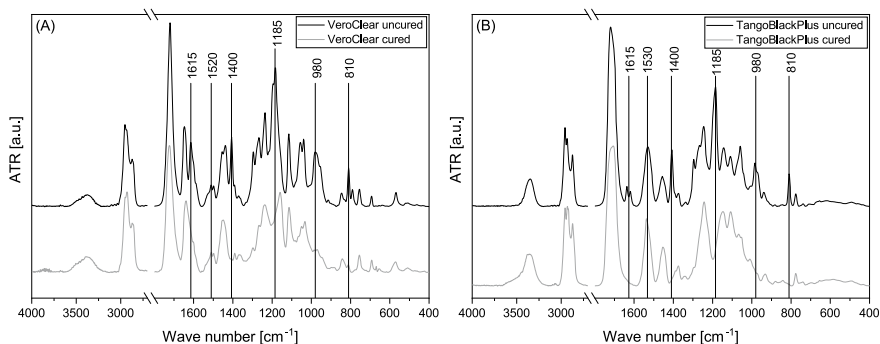


Fig. 13.1 FTIR spectra of uncured and cured **a** VeroClear and **b** TangoBlack+

13.4 Results and Discussion

13.4.1 Material Identification and Curing Process

Because the formulations of the materials are proprietary, chemical analysis was performed by GC/MS and FTIR analysis of the liquid resin and by FTIR analysis of the printed samples. The resulting IR spectra are given for VeroClear in Fig. 13.1a and for TangoBlack+ in Fig. 13.1b. Some characteristic functional groups of the monomers could be identified from their absence after polymerization. The terminal $C=CH_2$ vinyl group in acrylates with expected bands at about 1615, 1400, 1180, 980, and 810 cm^{-1} , was observed in both monomeric resins, while it decreased significantly after polymerization. In addition, urethane groups can be identified by bands around 1530 cm^{-1} .

The spectrum of VeroClear indicates a material consisting mainly of acrylate with a low content of urethane groups. That of TangoBlack+, compared to VeroClear, shows an increased amount of urethane groups (1530 cm^{-1}). This indicates that TangoBlack+ consists mainly of urethane groups and has a lower content of acrylate. Compared to the urethanes, acrylates form more harder and more brittle materials, in which urethane groups might act as spacers. An increase in the amount of urethane added softens the specimens and makes them more elastic. Thus, the hardness gradient of the specimen materials used can be explained. VeroClear, mainly made of acrylate, is hard. When mixed with TangoBlack+, the blends VeroTango 95 and VeroTango 70 exhibit softer and more elastic properties than VeroClear. Since the urethane content is highest in TangoBlack+, it is the softest and most elastic.

Gas chromatography/mass spectrometry (GC/MS) measurements of uncured VeroClear and TangoBlack+ showed that the used photopolymers are urethane acrylates. Comparison with the NIST-database (NIST Mass Spectrometry Data Center, 2017) shows that isobornyl acrylate and the photoinitiator 1-hydroxycyclohexyl-phenylketone are essential components. The presence of urethane groups can also be confirmed by detecting characteristic mass fragments of isocyanate groups in

the mass spectra. Whether these originate from urethane monomers or are formed during analysis cannot safely be differentiated yet and will be the subject of future investigations. Other components cannot be identified in detail. Re-evaluation of the FTIR spectra identified the isobornyl acrylate detected by GC/MS.

The results of GC/MS and FTIR analysis give detailed insights into photoinitiated radical polymerization process. The polymerization reaction is schematically shown in Fig. 13.2. At the beginning of the crosslinking reaction, a UV light-induced radical cleavage of the photoinitiator takes place. The free radicals formed react with isobornyl acrylate (schematically shown as n monomers), urethane spacer (schematically shown as m monomers), and trifunctional acrylates to form a network. The hardness depends on the amount of urethane spacer. More spacer increases the distance between the individual chains, thus the plastic becomes softer, and less spacer let the chains get closer together, thus it becomes harder.

13.4.2 Aging Effects

13.4.2.1 IR Spectroscopic Analysis

For the chemical investigation of the aging phenomena, FTIR spectra were recorded for each material. Baseline correction and normalization to the CH_2 deformation vibration at 1449 cm^{-1} were applied to the spectra. Figure 13.3 shows the internally normalized IR spectra of VeroClear (a) and TangoBlack+ (b) in a pristine and aged state at 100°C for 168 h.

VeroClear and TangoBlack+ both show a chemical change due to thermal aging. A decrease in intensity in the band regions around 1530 cm^{-1} in the TangoBlack+ spectrum suggests a break in the C-N bond in the urethanes. As a result of thermal aging, oxidation products are formed in the samples due to reactions with oxygen. Accordingly, the bands should increase at 1720 cm^{-1} (C=O), 1250, 1150, and 1105 cm^{-1} (C-O). This is the case for both materials.

These chemical changes result in a yellowish discoloration of the VeroClear samples. TangoBlack+ shows no discoloration as the samples are black. Furthermore, the hardness should increase, this was confirmed with hardness measurements, see Sect. 13.4.2.2.

The evaluation of VeroClear and TangoBlack+ at 70°C aging temperature and for the blends VeroTango 95 and VeroTango 70 for both temperatures were performed analogously to this evaluation. The results also show a similar chemical change. In addition, the decreases and increases of the bands are smaller at 70°C than at 100°C .

13.4.2.2 Thermal and Mechanical Investigations

To quantify the aging process, the results of the DSC analyses are shown in Fig. 13.4. In the unaged state, VeroClear exhibits the highest glass transition temperature (T_g) at

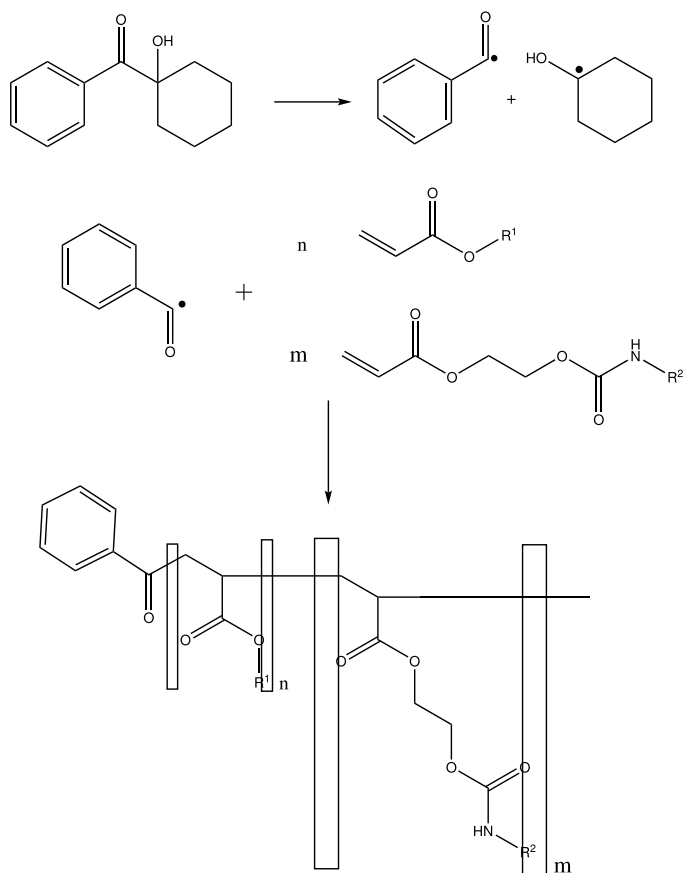


Fig. 13.2 Schematic photoinitiated radical polymerization. Top: Activation of the photoinitiator. Bottom: Chain growth reaction

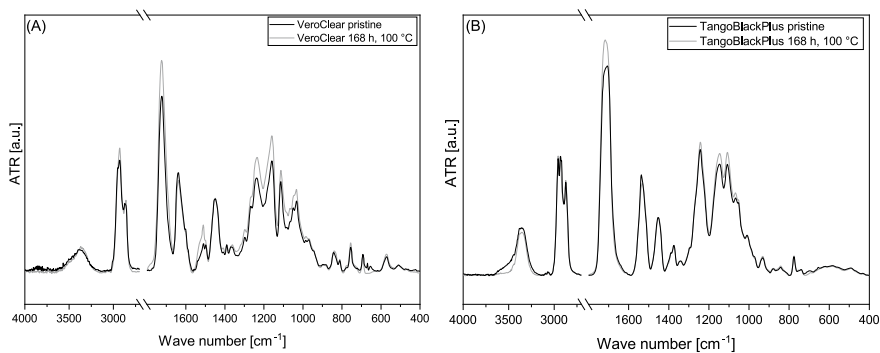


Fig. 13.3 FTIR spectra of **a** VeroClear and **b** TangoBlack+ showing the effect of aging at 100 °C after 168 h

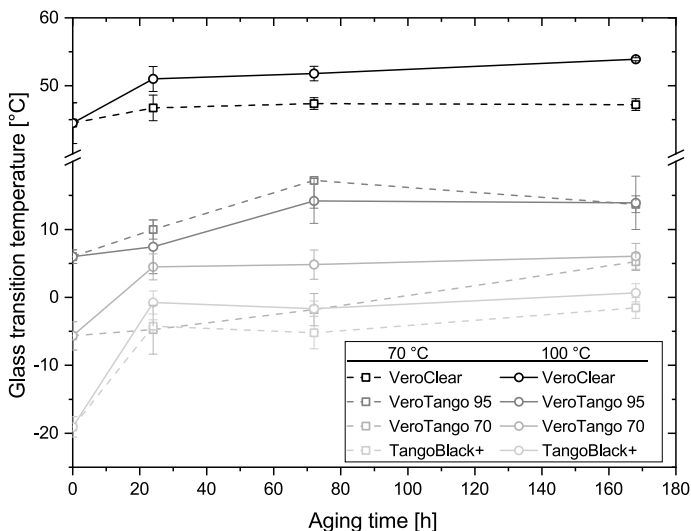


Fig. 13.4 Glass transition temperature as a function of aging time and temperature. Samples: black: VeroClear; dark gray: VeroTango 95; gray: VeroTango 70; light gray: TangoBlack+; squares □: 70 °C; circles ○: 100 °C

44.5 °C, whereas with increasing TangoBlack+ content, the T_g decreases to -19.1 °C for TangoBlack+. VeroClear has a T_g above room temperature and shows inelastic behavior. The blends VeroTango 95 and VeroTango 70 as well as TangoBlack+ show a T_g below room temperature and thus soft elastic behavior. This can be explained by the different chemical compositions and the associated varying amounts of urethane.

All materials show an increase in T_g after aging. The chain mobility of the polymers is influenced by thermal aging, as well as post-crosslinking by thermally formed radicals. The inhibition of chain mobility by oxidation products or by the formation of new linkages results in an increase of T_g , hardness, and tensile properties.

In its pristine state, VeroClear shows a very high tensile strength and a low elongation at break compared to the other tested materials because it has poor elastic properties. Increasing the amount of the elastic TangoBlack+ leads to a significant reduction in tensile strength and an increase in elongation at break, see Table 13.2. The comparison with the manufacturer's data from Table 13.1 shows certain differences. This may be due to the age of the uncured materials used, as they were close to their expiration date.

Figure 13.5 shows the results of tensile strength (A) and elongation at break (B) of the aged specimens. During aging, the tensile strength of VeroClear and VeroTango 95 initially increases in the first 24 h, but as aging progresses, the values hardly change. In the case of elongation at break, artificial aging causes a decrease in these values for VeroClear and VeroTango 95. This can be explained by a post-crosslinking reaction, leading to a decrease in chain mobility. The values of VeroTango 70 and TangoBlack+ show an increase. This is probably related to the different oxidation behavior of acrylate and urethane.

Table 13.2 Tensile strength, elongation at break, and hardness of the pristine materials

Property	VeroClear	VeroTango 95	VeroTango 70	TangoBlack+
Tensile strength (MPa)	61.1 ± 1.7	7.5 ± 0.3	2.5 ± 0.1	0.8 ± 0.1
Elongation at break (%)	9.3 ± 2.4	56.6 ± 1.3	67.9 ± 1.1	145.1 ± 9.2
Hardness (Shore)	80.3 ± 0.7 D	78.7 ± 4.6 AM	50.5 ± 2.9 AM	23.2 ± 0.7 AM

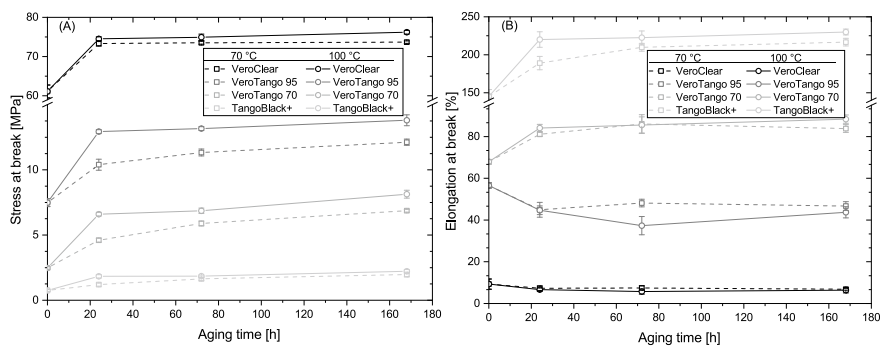


Fig. 13.5 **a** Tensile strength and **b** elongation at break in dependency on time and temperature. Samples: black: VeroClear; dark gray: VeroTango 95; gray: VeroTango 70; light gray: TangoBlack+; squares \square : 70 °C; circles \circ : 100 °C

Since the VeroTango 95 and 70 materials are a mixture of VeroClear and TangoBlack+, the increase or decrease in elongation at break depends on the amount of the monomer ratio used for polymerization. The change in the stress at break is also dependent on the VeroClear and TangoBlack+ content.

As already shown in the IR investigations, the structure of the polymer changes chemically, which also can be found by the hardness measurements, see Fig. 13.6. The hardness increases with aging. The hardness values for the pristine materials are given in Table 13.2. The difference to the manufacturer's data is due to the age of the uncured materials used, as they were close to their expiration date.

The hardness measurements confirm that as aging progresses, the hardness of the specimens increases. Figure 13.6 shows results for the materials VeroTango 95, VeroTango 70, and TangoBlack+. It can be clearly seen that the increase at 100 °C is higher than at 70 °C. VeroClear shows no change in hardness during thermal exposure and remains at the range of 80 Shore D.

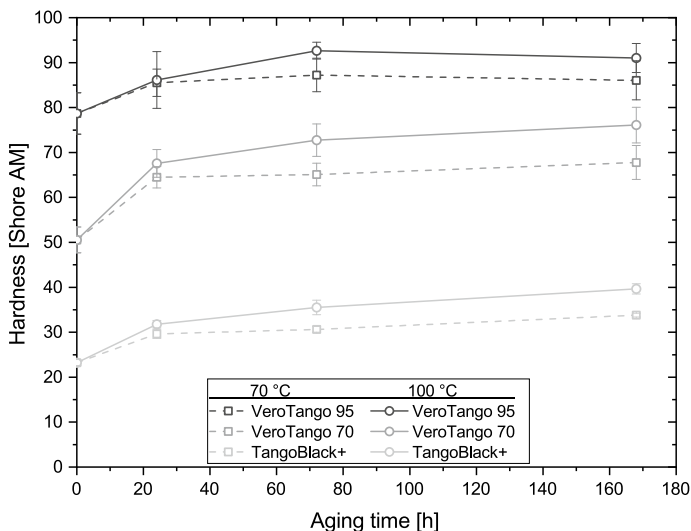


Fig. 13.6 Shore hardness for VeroTango 95, VeroTango 70, and TangoBlack+ as function of aging time and temperature. Samples: black: VeroClear; dark gray: VeroTango 95; gray: VeroTango 70; light gray: TangoBlack+; squares \square : 70 °C; circles \circ : 100 °C

13.5 Conclusions

The aging behavior of materials printed by MJM was investigated after thermal aging. Chemical characterization was performed by infrared spectroscopy (IR) and gas chromatography coupled with mass spectrometry (GC/MS). In all materials, the thermal formation of oxidation products was detected with IR spectroscopy. This results in an increase in glass transition temperature, tensile strength, and hardness, and a decrease in elongation at break. The materials with higher TangoBlack+ content show an increase in both tensile strength and elongation at break. The increase in tensile strength can be explained by a post-crosslinking reaction.

Chemical analyses provide useful chemical information about the detailed chemical structure of monomers and allow a deep understanding of the polymerization mechanism. Thus, this information can explain the mechanical properties and aging behavior. The urethane groups are most likely responsible for softness. Certain degrees of hardness can be adjusted by selective addition to the acrylate matrix. The properties of additively manufactured urethane acrylates change with composition. Large amounts of acrylate increase breaking stress, glass transition temperature, and hardness, but also reduce elongation at break. High amounts of urethane do the opposite, decreasing breaking stress, glass transition temperature, and hardness, and increasing elongation at break. The properties also change as the polymer ages, as evidenced by an increase in hardness, glass transition temperature, and breaking stress. Infrared spectroscopic analysis (IR) confirms the formation of chemical

species resulting from oxidation processes. This allows a direct correlation between the chemical structure and the changed material properties. In the near future, an increasing number of parts will be produced with additive manufacturing, which makes this topic interesting for experimental investigations.

Acknowledgements We acknowledge scientific cooperation with the Bundeswehr Research Institute for Materials, Fuels and Lubricants, Erding, Germany. Special thanks to Stephan Forster and Jonas Perzl.

References

- Deutsches Institut für Normung eV (2000) DIN 53508:2000-03, Testing of rubber—accelerated ageing
- Deutsches Institut für Normung eV (2012) DIN EN ISO 527–2:2012–06; Plastics—determination of tensile properties—part 2: test conditions for moulding and extrusion plastics (ISO 527–2:2012). German version EN ISO 527–2:2012
- Deutsches Institut für Normung eV (2017) DIN 53504:2017–03; Testing of rubber—determination of tensile strength at break, tensile stress at yield, elongation at break and stress values in a tensile test
- Deutsches Institut für Normung eV (2019) DIN EN ISO 527–1:2019–12; Plastics—determination of tensile properties—part 1: general principles (ISO 527–1:2019). German Version EN ISO 527–1:2019
- Deutsches Institut für Normung eV (2021) DIN ISO 48-4:2021-02, Rubber, vulcanized or thermoplastic—determination of hardness—part 4: indentation hardness by durometer method (Shore hardness) (ISO 48-4:2018)
- Haryńska A, Gubanska I, Kucinska-Lipka J, Janik H (2018) Fabrication and characterization of flexible medical-grade TPU filament for fused deposition modeling 3DP technology. *Polymers (Basel)* 10(12):1304
- Herzberger J, Sirrine JM, Williams CB, Long TE (2019) Polymer design for 3D printing elastomers: recent advances in structure, properties, and printing. *Prog Polym Sci* 97(101):144
- Kennedy ZC, Christ JF (2020) Printing polymer blends through in situ active mixing during fused filament fabrication. *Add Manuf* 36(101):233
- Ligon SC, Liska R, Stampfl J, Gurr M, Mülhaupt R (2017) Polymers for 3D printing and customized additive manufacturing. *Chem Rev* 117(15):10212–10290
- Ngo TD, Kashani A, Imbalzano G, Nguyen KT, Hui D (2018) Additive manufacturing (3D printing): a review of materials, methods, applications and challenges. *Compos Part B Eng* 143:172–196
- NIST Mass Spectrometry Data Center (2017) NIST/EPA/NIH EI and NIST Tandem Mass Spectral Library
- Peltola SM, Melchels FPW, Grijpma DW, Kellomäki M (2008) A review of rapid prototyping techniques for tissue engineering purposes. *Ann Med* 40(4):268–280
- Shahrubudin N, Lee T, Ramlan R (2019) An overview on 3D printing technology: technological, materials, and applications. *Procedia Manuf* 35:1286–1296
- Singamneni S, LV Y, Hewitt A, Chalk R, Thomas W, Jordison D, (2019) Additive manufacturing for the aircraft industry: a review. *J Aeronaut Aerosp Eng* 08(01):214
- Wiese M, Thiede S, Herrmann C (2020) Rapid manufacturing of automotive polymer series parts: a systematic review of processes, materials and challenges. *Add Manuf* 36(101):582

Chapter 14

Microstructure and Properties of the Fusion Zone in Steel-Cast Iron Composite Castings



Lukas Apfelbacher, Patrick Hegele, Arne Davids, Leonhard Hitzler,
Christian Kremaszky, and Ewald Werner

Abstract Casting is an established way to manufacture metal components with complex geometry and high wall thickness at low cost. However, the possibilities for locally modifying material properties are limited in conventional casting processes. These limitations can be remedied by utilizing composite casting. Within this study, a lamellar graphite cast iron melt was poured into low carbon steel shells comprised the steels S235JR and 25CrMo4, differing in their mechanical properties and their thermal conductivity, with the aim to form a material bond. Three different temperatures for the steel shells at the time of pouring were investigated: 293, 383 and 583 K. After preheating, the shells were embedded in unheated sand moulds, which were then filled with an EN-GJL-250 melt. The resulting fusion zone was characterized using optical microscopy, and the mechanical properties were assessed by Brinell hardness tests. The properties and microstructural morphology around the fusion zone strongly depend on the initial temperature of the shell at the time of casting. For shell temperatures of 293 K, no proper bonding was achieved between shell and core. A pearlite layer with a thickness of up to 500 μm was formed at a temperature of 583 K, whilst the adjacent region of the cast iron became decarburized. The hardness of the fusion zone reached a maximum of 275 HBW for a shell temperature of 383 K with an overall span from 235 to 275 HBW.

L. Apfelbacher (✉) · P. Hegele · A. Davids · L. Hitzler · C. Kremaszky · E. Werner
School of Engineering and Design, Institute of Materials Science and Mechanics of Materials,
Technical University of Munich, 85748 Garching, Germany
e-mail: l.apfelbacher@tum.de

P. Hegele
e-mail: patrick.hegele@tum.de

A. Davids
e-mail: arne.davids@tum.de

L. Hitzler
e-mail: Leonhard.hitzler@tum.de

C. Kremaszky
e-mail: kremaszky@tum.de

E. Werner
e-mail: ewald.werner@tum.de

Keywords Composite casting · Compound casting · Grey cast iron · Fusion zone · Material-fit connection

14.1 Introduction

Joining two different materials in one part to locally combine and tailor different properties can be achieved either by a form-fit, a force-fit or a material-fit connection mechanism (Khrebtov 2011; DIN 8593:2003). Form-fit connections include, for example, bolted and riveted connections. Crimped connections are an example of a force-fit connection. Material-fit connections *inter alia* include adhesive or welded joints (Moro 2022; DIN 8593:2003). A solid bond can be achieved via all three aforementioned mechanisms, each with its specific advantages and disadvantages.

All these mechanisms can be exploited in joining metallic constituents by composite casting (Noguchi 2008). This process is characterized by casting melt onto an insert or into a mould, which at least partially becomes the final component itself. In doing so, a form-fit connection is achieved when the solidified melt interlocks with serrations in the insert or the shell. This is the dominant joining mechanism in high pressure die casting (HPDC), where steel inserts are recast with an aluminium melt to increase the mechanical properties of the composite (Elliott 1988, Schittenhelm 2018). Furthermore, differences in the thermal expansion coefficients (CTE) of composite casting constituents can be utilized for joining by the force-fit mechanism. An industrially established example based on this principle is the connection of steel tubes with cast aluminium joints for automotive applications (Dörr and Wibbeke 2008). Finally, a connection in composite casting can also be established by a material fit. A typical process employing this mechanism exhibits a bond formation in three mostly simultaneous stages: (i) partial fusing of the metallic inserts due to the thermal capacity of the added melt, (ii) mixing of the atomic constituents mainly amongst the involved liquids by interdiffusion and convection, and (iii) adherent solidification onto the residuals of the inserts by heterogeneous nucleation or grain growth. The resulting connections are microstructurally smooth and, hence, exhibit a gradual transition in macroscopic properties (e.g. in Young's modulus, CTE or chemical potential).

This is expected to be advantageous in comparison with sharp transitions created by the aforementioned composite casting approaches concerning mechanical and thermal load-bearing capabilities as well as in corrosive environments. Furthermore, material-fit composite casting enables new design possibilities—regarding the material thickness and accessibility of bonds—not feasible within related conventional joining technologies like welding.

Nevertheless, similar to welding processes, design limitations for material-fit composite casting have to be considered. For example, excessively thin metal shells bear the risk of softening during the process leading to leakage of melt. This risk increases, if the superheating of the melt becomes higher in comparison with the melting point of the shell. Ideally, just a marginal but sufficient amount of the shell is

fused to form a dense alloy layer without unnecessarily affecting its overall properties. Moreover, it is evident that chemically similar materials are more suited for composite casting with the aim for a material-fit bond, due to the fact that the remelting of the shell required for fusion is more likely to happen without the need for extensive pre-treatment (IBleib et al. 1995).

Despite considering these limitations, the formation of a reproducible and distinct transition zone and, hence, a reliable material bond is not necessarily given (Buchmayr and Weligoschek 2010; Krause 1990). For example, in conventional sand casting metallic inserts, called chills, are used to control the solidification of the cast. They increase heat dissipation locally without forming a proper bond with the cast material and can be removed after casting (Jaromin et al. 2019). Therefore, a series of pre-treatment steps is commonly applied to achieve a bonding and to overcome differences in the thermo-physical properties. Viable results have been achieved with metallic coatings (Bakke et al. 2022). However, coating of the shells can be tedious and costly. A new approach is based on preheating the shells.

To study this processing route in detail, the effect of three different shell temperatures at the time of pouring on the bond formation between low carbon steel shells and a lamellar grey iron cast was investigated in this work.

Fe-based alloys were selected for both joining partners to enhance the probability to form a sufficient bond. Nevertheless, these material classes are quite different in their material properties. On the one hand, low carbon steels can be formed easily to thin wall thickness to become the casting mould whilst retaining sufficient structural strength during casting. On the other hand, lamellar grey iron offers increased thermal conductivity and vibration damping but suffers from significantly lower mechanical properties. The combination of the two material classes offers the possibility to achieve better thermo-physical properties, compared to a single-material part, which can be even further tuned by a tailored selection of alloys within the specific material classes. To investigate the influence of this fine-tuning on the transition zone, examinations were applied to shells comprised two distinct low carbon steels.

14.2 Experimental Details

14.2.1 Composite Casting

The grey iron EN-GJL-250 (DIN EN 1561:2012-01) was obtained from recycled material. The thickness ratio of melt to steel was 20:1, with a wall thickness of the steel shells of 5 mm. One shell was made of a S235JR alloy and the second one of 25CrMo4 with a thermal conductivity of 40 W/mK and 49 W/mK, respectively (Gruppo Lucefin 2012; DEW 2011). In Table 14.1, the chemical composition of the employed materials, determined via optical emission spectroscopy (Spectromaxx-LMX06, SPECTRO Analytical Instruments GmbH), is provided.

Table 14.1 Chemical composition of shell and cast materials in wt.%

Material	C	Si	Mn	Mo	Cu	Cr	Ni	Ti	Fe
EN-GJL-250	3.44	1.94	0.64	0.03	0.24	0.16	–	0.16	Balance
S235JR	0.08	0.01	0.52	0.01	0.02	0.01	0.01	–	Balance
25CrMo4	0.24	0.23	0.61	0.18	0.21	0.96	0.19	–	Balance

The steel shells were pre-treated by shot blasting with alumina (0.25–0.5 mm). Preheating was conducted in a Nabertherm L3/11 electrical resistance furnace in air (Nabertherm GmbH). Three shell temperatures T_{shell} were targeted at the time of the pouring: 293, 383 and 583 K. To accomplish these, the steel shells were superheated approximately 50 K above the desired T_{shell} in a furnace. Then, the superheated steel shells were placed without delay into the copes of the two-part casting flasks, which themselves were not preheated to reflect industrial production conditions. After the targeted shell temperature, which was measured with K-type thermocouples brazed to the shells, was reached, the moulds were filled with the grey cast iron melt. For inoculation 0.15 wt.% FeSi (Elkem SuperSeed 75, Elkem ASA, Norway) was placed in the sprue. This step, in addition to the increased Si content of the cast iron, was taken to avoid metastable carbide formation (chill) and secure grey solidification. The resulting microstructure is expected to be fully pearlitic with graphite lamellae. Figure 14.1 shows a schematic sketch of an assembled flask, including the embedded steel shell. The melt was poured into the cup to ensure a rising cast.

Table 14.2 outlines the shell materials and the targeted temperatures T_{shell} of these inserts at the time of pouring for the samples. The temperature of the melt at pouring was 1673 K for all samples produced.

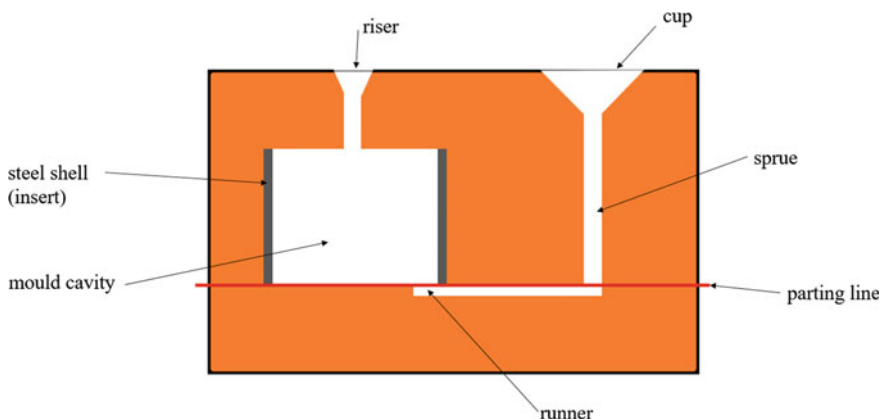


Fig. 14.1 Schematic sketch of the flask, consisting of the heated steel shell embedded in the unheated green sand mould

Table 14.2 Configurations of the fabricated samples, material combination and shell temperature

Sample	1	2	3	4	5	6
Shell	S235JR	25CrMo4	S235JR	25CrMo4	S235JR	25CrMo4
T_{shell} (K)	293	293	383	383	583	583

Table 14.3 Preparation steps for metallographic sections

Disc	Abrasive	Lubricant	rpm	Force (N)	Time (min)
SiC 220	–	Water	300	180	Till plane
MD Allegro	9 μm	DP lubricant blue	150	180	4
MD-Dac	3 μm	DP lubricant blue	150	180	4
MD-Mol	1 μm	–	150	120	6

14.2.2 Microstructure Observation

A metallographic preparation was applied to sections of the samples that were within a plane perpendicular to the outer surface of the shell and located around the fusion zone and half of the mould in filling direction. The preparation is detailed in Table 14.3. A light optical microscope Axio Scope.A1 (Zeiss) was used for image acquisition. The graphite structure was analysed according to EN ISO 945-1:2019, and, after etching with 3% alcoholic nitric acid (Nital), the microstructure was evaluated according to DIN 50600:2017-10.

14.2.3 Hardness Measurement

The measurement of Brinell hardness (HBW 5/750) was performed according to EN ISO 6506-1:2014, utilizing a Dia Testor 2Rc (Otto Wolpert-Werke). Measurements were taken from three different areas, namely the cast iron core, the fusion zone and the steel shell. Ten hardness indentations distributed over the entire height of the samples for each of the three microstructural zones were evaluated.

14.3 Results

14.3.1 Graphite Morphology

The graphite morphology was assessed in accordance with DIN EN ISO 945-1:2019. The graphite forms present are depicted in Fig. 14.2, whilst Fig. 14.3 shows the different arrangements of graphite lamellae. Figures 14.4 and 14.5 show the graphite

Fig. 14.2 Graphite forms IV (left) and V (right). Excerpt from: directional series diagrams for main forms of graphite in cast iron according to DIN EN ISO 945-1:2019

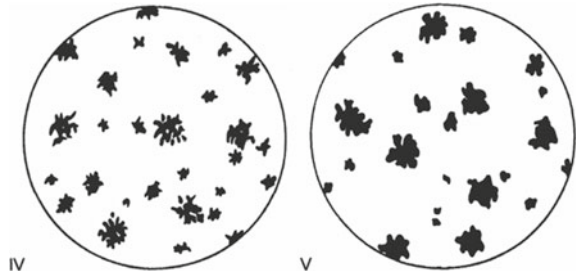


Fig. 14.3 Graphite arrangements A (left), D (middle) and E (right). Excerpt from: directional series diagrams for arrangement of graphite in cast iron according to DIN EN ISO 945-1:2019

morphology of the composite samples. For the unheated shell, no continuous bonding between the steel shell and the cast iron core was achieved. Spherical graphite precipitates were evident in the dendritic microstructure of the cast iron core. These irregular graphite spheres could be assigned to the graphite forms IV and V (Figs. 14.4a and 14.5a). In addition, small areas with D-graphite (interdendritic graphite with random orientation) were present. After pouring the melt into the shell preheated to 383 K, nearly only D-graphite was present in the fusion zone (Figs. 14.4b and 14.5b). Graphite lamellae of arrangement A only occurred isolated for sample 3 (Fig. 14.4b) and in a few areas in sample 4, near the bonding line (Fig. 14.5b). A shell temperature of 583 K led to the graphite morphology typical for EN-GJL-250, consisting of long lamellae of type A- and E-graphite (Figs. 14.4c and 14.5c).

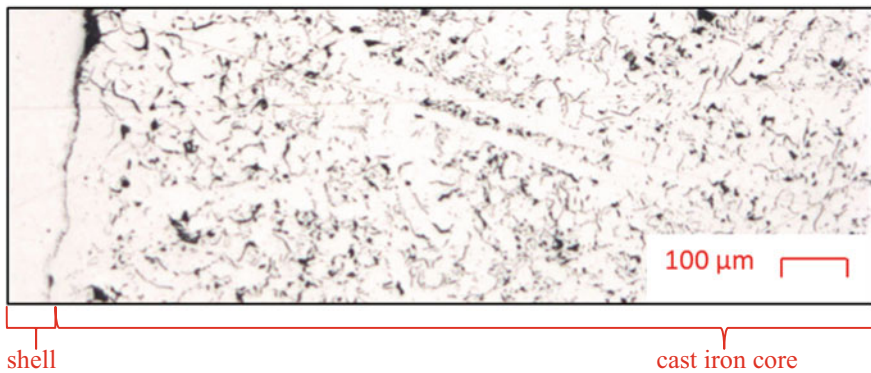
14.3.2 Etched Microstructure

Figures 14.6 and 14.7 show the microstructure after etching. For samples cast at a shell temperature of 293 K, no fusion zone was evident, irrespective of the shell material used. The cast iron contained some ferritic structures in the region adjacent to the fusion zone for both shell materials (Figs. 14.6a and 14.7a). These structures were significantly more pronounced in the 25CrMo4 sample, where local ferrite seams formed near the gap between the two materials. In the same area, the steel

(a) Sample 1 (S235JR, 293 K)



(b) Sample 3 (S235JR, 383 K)



(c) Sample 5 (S235JR, 583 K)

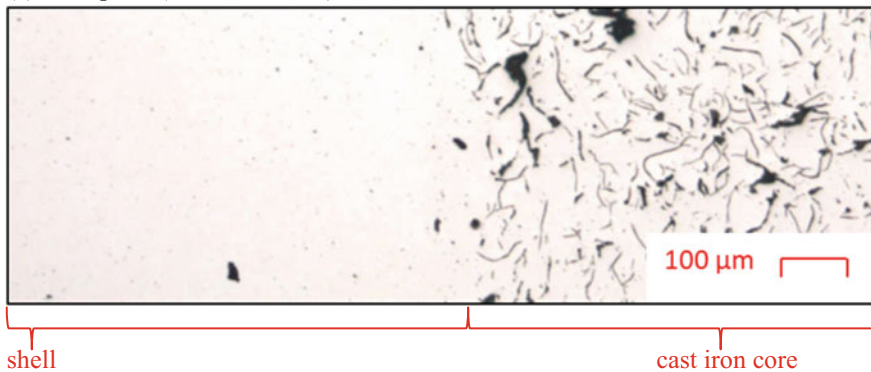
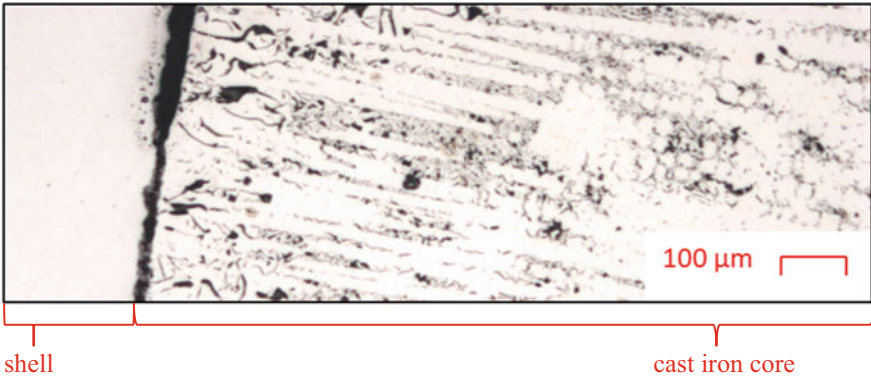
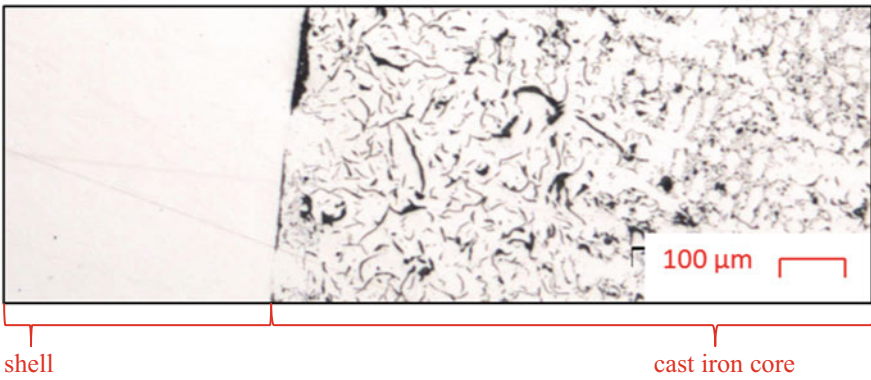


Fig. 14.4 Micrographs of the composite samples with nomenclature according to Table 14.2, showing the graphite morphology in the fusion zone for the shell temperatures at the time of the pouring. **a** 293 K, **b** 383 K, **c** 583 K. The shell material S235JR is seen on the left, the EN-GJL-250 cast iron core on the right

a) Sample 2 (25CrMo4, 293 K)



b) Sample 4 (25CrMo4, 383 K)



c) Sample 6 (25CrMo4, 583 K)

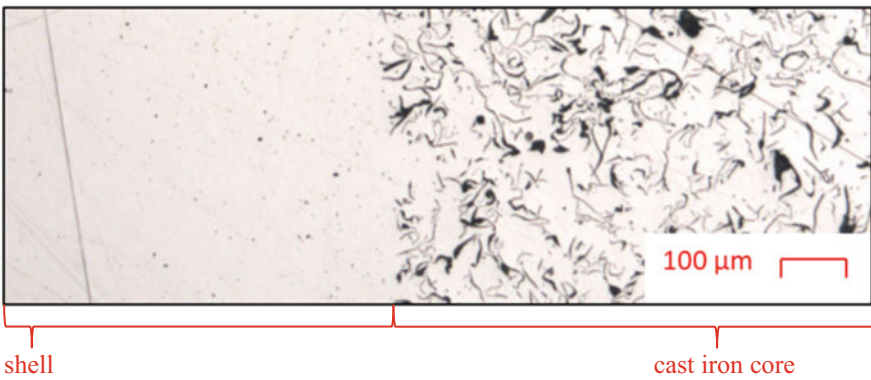


Fig. 14.5 Micrographs of the composite samples with nomenclature according to Table 14.2, showing the graphite morphology in the fusion zone for the shell temperatures at the time of the pouring. **a** 293 K, **b** 383 K, **c** 583 K. The shell material 25CrMo4 is seen on the left, the EN-GJL-250 cast iron core on the right

shell also becomes decarburized (Fig. 14.7a). A shell temperature of 383 K led to the formation of a bonding layer over large parts of the samples, whereby a pearlitisation of approximately 300 μm into the steel shell was noted (Figs. 14.6b and 14.7b). The microstructure of the cast iron core consisted of pearlite. A shell temperature of 583 K led to a completely pearlitic cast microstructure in the examined area near the fusion zone. In addition, the steel shell underwent a pearlitic transformation. The transformed zone had a thickness of approximately 500 μm . For both shell materials, a coarsening of the grains in the steel could be observed at 583 K in comparison with the lower shell temperatures (Figs. 14.6c and 14.7c).

14.3.3 Hardness

The hardness of the samples with a S235JR shell is shown in Fig. 14.8a. The hardness of the cast iron ranged between 190 and 235 HBW, which are typical values for EN-GJL-250¹ (DIN EN 1561:2012-01). The hardness of the shell material was 120 HBW. This is in agreement with the technical data sheet provided by the supplier (Gruppo Lucefin 2012). At a shell temperature of 293 K, no bonding between the shell and the cast iron could be achieved. Therefore, no hardness could be determined for the fusion zone in these instances. A shell temperature of 383 K resulted in a fusion zone with hardness values between 235 and 295 HBW. For a shell temperature of 583 K, the hardness of the fusion zone ranged between 250 and 260 HBW, which was only slightly above the hardness of the cast iron core. Figure 14.8b shows the hardness values for the sample with the 25CrMo4 shell. The hardness values for the cast iron core and the fusion zone were similar to those of the S235JR shell sample in Fig. 14.8a. The hardness of the 25CrMo4 steel shell was 210 HBW, which is in agreement with the technical data sheet provided by the supplier (DEW Witten 2011).

14.4 Discussion

In this study, the influence of the chemical composition of the shell and the shell temperature at the time of the pouring T_{shell} on the resulting fusion zone were investigated.

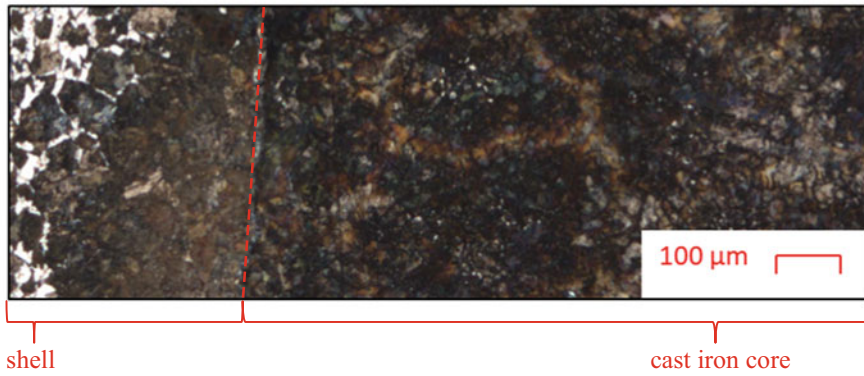
The microstructure of the samples was significantly influenced by the initial temperature of the steel shells. For $T_{\text{shell}} = 293$ K (samples 1 and 2), no bonding between the cast iron and the shell was achieved. In the adjacent cast iron area, cementite needles formed and graphite is present in the form of irregular spheres. Moreover, the matrix of the cast iron core solely comprised pearlite, as expected for the chosen

¹ Hardness values for cast iron depend on the wall thickness of the casting and the production process parameters (DIN EN 1561:2012-01).

(a) Sample 1 (S235JR, 293 K)



(b) Sample 3 (S235JR, 383 K)



(c) Sample 5 (S235JR, 583 K)

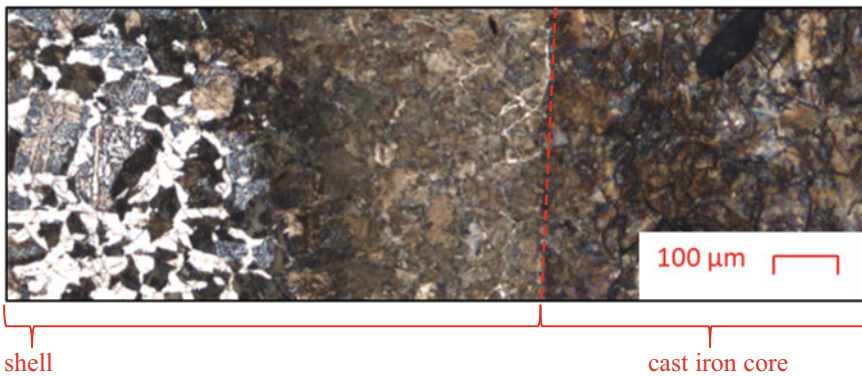
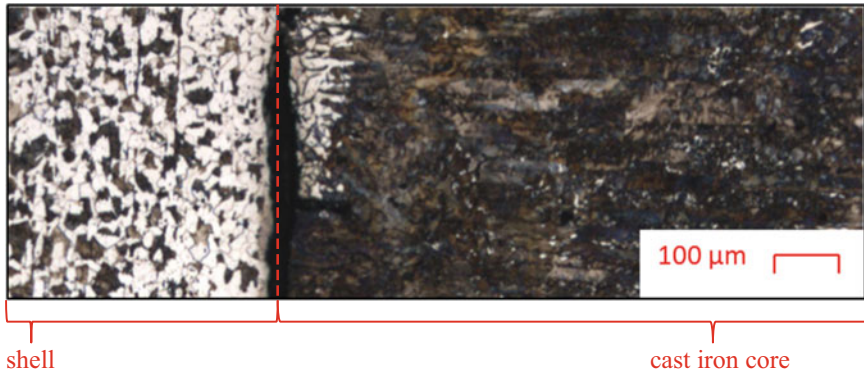
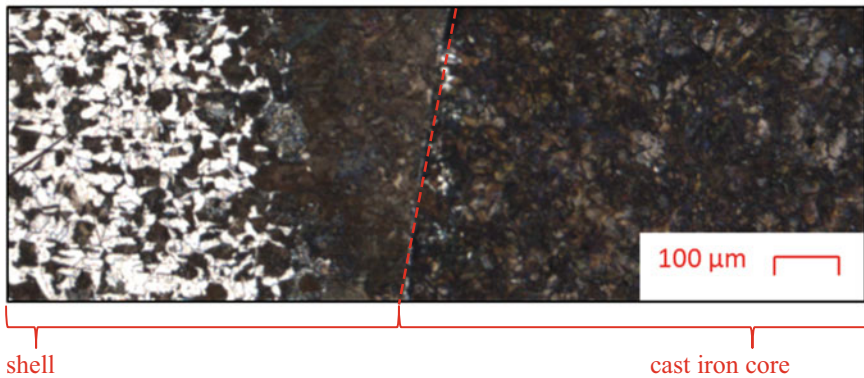


Fig. 14.6 Sections of the etched samples with nomenclature according to Table 14.2, showing the microstructure in the fusion zone for the shell temperatures at the time of the pouring. **a** 293 K, **b** 383 K, **c** 583 K. The shell material S235JR is seen on the left, the EN-GJL-250 cast iron core on the right. The red line indicates the fusion layer

(a) Sample 2 (25CrMo4, 293 K)



(b) Sample 4 (25CrMo4, 383 K)



(c) Sample 6 (25CrMo4, 583 K)

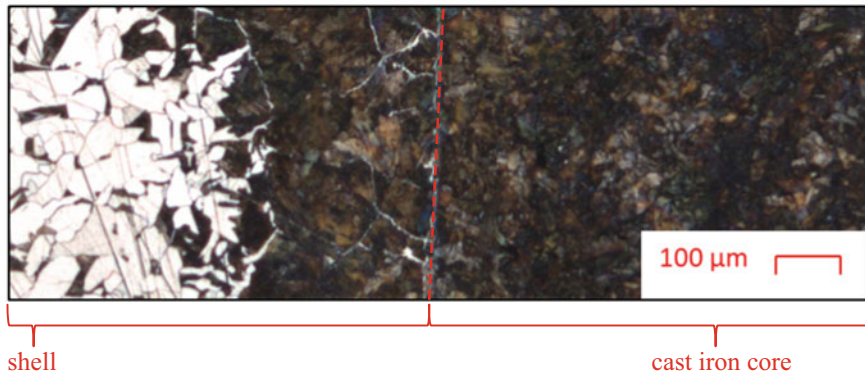


Fig. 14.7 Sections of the etched samples with nomenclature according to Table 14.2, showing the microstructure in the fusion zone for the shell temperatures at the time of the pouring. **a** 293 K, **b** 383 K, **c** 583 K. The shell material 25CrMo4 is seen on the left, the EN-GJL-250 cast iron core on the right. The red line indicates the fusion layer

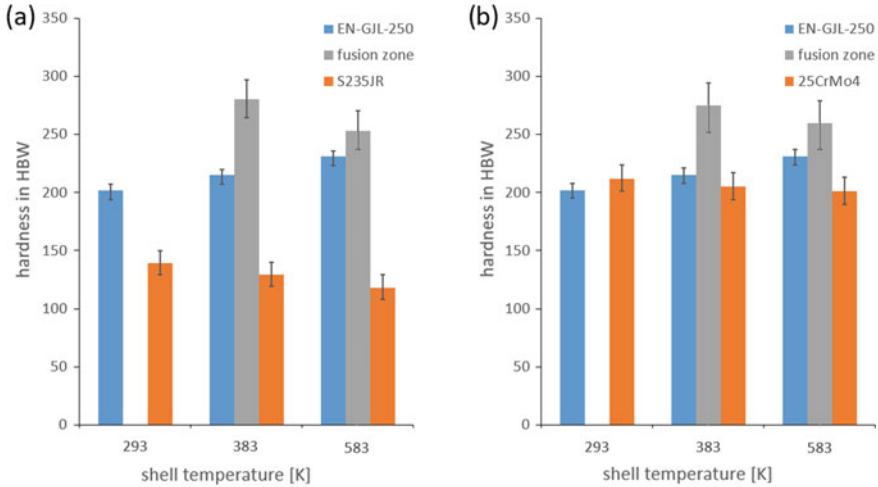


Fig. 14.8 Hardness results for samples created at different preheating temperatures and shell materials **a** shell material S235JR, **b** shell material 25CrMo4

experimental setup (detailed in Sect. 14.2.1). Therefore, the shell likely acted as a chill and increased the cooling rate to such an extent, that it outweighed the graphitization potential of the melt and the influence of inoculation on the formation of stable graphite morphologies. Ferrite seams were present in sample 2. Their formation was promoted by the presence of D-graphite, which provided short diffusion paths for carbon (Elliott 1988; Berns and Theisen 2008). Another possible explanation could be the transition of carbon into the gap between the two materials under the formation of carbon-oxides. This assumption is supported by the fact that the steel shell in this area also becomes decarburized.

Increasing T_{shell} to 383 K (samples 3 and 4) resulted in a non-continuous material-bond connection between the steel shell and the cast iron core. The matrix of the cast iron core was fully pearlitic, and the steel shell underwent a pearlitic transformation up to a depth of 300 μm . The graphite morphology in the fusion zone mainly consisted of supercooled graphite of form D. Only individual graphite lamellae of form A were visible in sample 3, whilst in sample 4 this graphite morphology could be observed locally in the fusion zone. This is somewhat unexpected, as one would correlate the formation of graphite lamellae with a lower cooling rate in this area, whilst the formation of the supercooled graphite further into the cast iron core indicates a high cooling rate. One reason could be the imperfect formation of the fusion zone, where the cooling rate was initially quite low. This could allow for the solidification of a thin cast iron layer with lamellar graphite. After solidification of these fringe areas, they could act as a heat bridge and increase the supercooling of the subsequent areas. D-graphite forms when the cooling rate favours metastable solidification, but this is counteracted by a sufficiently high Si concentration. Although the increase in T_{shell} led to the formation of a diffusion layer, the presence of undesired D-graphite

is an indication for an insufficient shell temperature to ensure the desired graphite morphology (Elliott 1988; Berns and Theisen 2008).

For $T_{\text{shell}} = 583$ K (samples 5 and 6), a continuous fusion zone with a pearlitic matrix was achieved. Pearlinitisation of the steel shell occurred and reached $500 \mu\text{m}$ into the shell, whilst the cast iron core was fully pearlitic. The predominant graphite shape was assigned to form A, with a lesser amount of form E. This was consistent with the typical graphite morphology for EN-GJL-250, although the percentage of IA-graphite is slightly higher in an ideal EN-GJL-250 microstructure (Elliott 1988; Berns and Theisen 2008).

The lack of a fusion zone at 293 K for both shell materials seems to be due to the chilling effect of the steel insert on the solidification of the cast iron melt. At $T_{\text{shell}} = 583$ K, the increase in hardness in comparison with the cast iron core can be attributed to either a fine pearlitic microstructure and/or to cementite present in this layer due to the chill effect of the steel shell. A shell temperature of 583 K only led to a minor increase in hardness compared to the cast iron core. The reason is the reduced chilling effect of the steel shell due to the increased temperature of the contact surface, leading to a coarser pearlitic microstructure compared to samples 3 and 4 (Elliott 1988; Berns and Theisen 2008).

An influence of the shell material (S235JR or 25CrMo4) on the fusion zone was not detected, even though the shell materials differed by about 60 HBW in hardness and also in their thermal conductivity. However, both shell materials are rather similar and both belong to the category of low carbon steels. Therefore, it can be concluded that the difference in thermal conductivity of the steels employed as shell materials does not alter the formation of the bonding zone and its properties.

No breakthrough of the melt through the shell was detected. Thus, even with a shell temperature of 583 K at the time of pouring, the local superheating during casting did not result in a leakage of the shell.

14.5 Conclusion

Low carbon steel shells were filled with lamellar graphite cast iron, and the occurring fusion zone was examined. The quality of this zone significantly depends on the temperature of the contact surface between the steel shell and the cast iron melt at the time of pouring. Insufficient preheating of the shell either leads to no material bonding or to undesired microstructural constituents in the area adjacent to the bonding line, such as needle-shaped cementite or ferrite seams. For the setup used in this study, the selected shell temperature of 583 K was sufficient to create a fusion zone that solely consists of pearlite in both the steel shell and the cast iron core. At this temperature, the depth of the fully pearlitic layer extended up to $500 \mu\text{m}$ into the steel shell. It can, therefore, be concluded that a solid bonding between low carbon steel and cast iron can be achieved without the need for any extensive surface treatments, like metallic coatings. The quality of the fusion zone depends almost entirely on the temperature of the contact surface between the shell and the melt. The chemical composition of

the steel shell had no dominant influence on the fusion zone. However, it should be mentioned that for this study only two similar steels were used with a simple geometry and the melt-to-shell ratio was kept constant at 20:1. In an industrial scenario, there are further influencing factors on the microstructure and the properties of the fusion zone in composite casting. These include, but are not limited to, the pouring temperature and chemical composition of the melt and the heat transfer through the mould.

Acknowledgements This project is supported by the Federal Ministry for Economic Affairs and Climate Action (BMWK) on the basis of a decision by the German Bundestag.

References

- Bakke et al (2022) Sn-aided joining of cast aluminum and steel through a compound casting process. *Metall Mater Trans B* 53:60–70
- Berns H, Theisen W (2008) *Eisenwerkstoffe—Stahl und Gusseisen*, 8th edn. Springer, Berlin, pp 31–35
- Buchmayr B, Weligoschek T (2010) Untersuchungen zum Verbundgießen warmfester Legierungen. *Berg Huettenmann Monatsh* 155:318–324
- DIN 50600:2017-10 (2017) Prüfung metallischer Werkstoffe—Metallographische Gefügebilder—Abbildungsmaßstäbe. Beuth, Berlin
- DIN 8593:2003 (2003) *Fertigungsverfahren Fügen*. Beuth, Berlin
- DIN EN 1561:2012-01 (2012) *Gießereiwesen—Gusseisen mit Lamellengraphit*. Beuth, Berlin
- DIN EN ISO 6506-1:2014 (2014) *Metallische Werkstoffe—Härteprüfung nach Brinell—Teil 1: Prüfverfahren*. Beuth, Berlin
- DIN EN ISO 945-1:2019 (2019) *Mikrostruktur von Gusseisen—Teil 1: Graphitklassifizierung durch visuelle Auswertung*. Beuth, Berlin
- Dörr J, Wibbeke M (2008) Publication number DE 10 2008 020467 A1. Deutsches Patent- und Markenamt, Bochum
- Elliott (1988) *Cast iron technology*. Butterworth & Co. Ltd, London, pp 1–4, 11–12, 104–105
- Ißleib et al (1995) *Verbundgießen von Eisen-Kohlenstoff-Legierungen—grundlegende metallurgische Reaktionen an der Grenzfläche—Teil I. Gießerei-Praxis* 15(16):286–289
- Jaromin et al (2019) Influence of type and shape of the chill on solidification process of steel casting. *Arch Foundry Eng* 1:35–40
- Khreibtov (2011) *Neuartiges Verfahren zur Online—Prozessüberwachung und—Fehlerklassifizierung beim Durchsetzfügeverbinden von Blechen*. Doctoral thesis, Technical University Clausthal-Zellerfeld
- Krause (1990) *Verbundgießverfahren zur Herstellung spezieller Gussstücke aus Eisenwerkstoffen*. *Gießerei-Praxis* 17:279–282
- Moro (2022) *Fügen durch Stoffvereinigen*. In: *Baukonstruktion—vom Prinzip zum Detail*. Springer, Berlin, pp 314–319
- Noguchi (2008) Trends of composite casting technology and joining technology for castings in Japan. *Int J Cast Met Res* 21:219–225
- Schittenhelm (2018) *Topologieoptimierter Verbund von Aluminium und Stahl zur lokalen Steifigkeitserhöhung von Druckgussbauteilen*. Doctoral thesis, University Bremen
- Technical data sheet 25CrMo4 according to EN 10083-3. Deutsche Edelstahlwerke, Witten (2011)
- Technical data sheet S235JR according to EN 10025-2: 2004. Gruppo Lucefin, Esine (2012)

Chapter 15

Kinetics for Strain-Induced Crystallisation Analysed via Cyclic Loading Simulations



Klara Loos

Abstract A thermodynamically consistent concept to model the strain-induced crystallisation phenomenon using a multiphase approach is presented in Loos et al. (Contin Mech Thermodyn 33:1107–1140, 2021). This follow-up contribution demonstrates the time dependence of the model within cyclic simulations. The stress as well as crystallinity evolution over stretch with various maximum stretch up to $\lambda = 6$ show good concordance with the experimental data concerning maximum values of stress and crystallinity, the hysteresis appearance, the area of hysteresis, the onset of crystallisation λ_{SIC} and melting stretch λ_{m} . Simulations using different strain rates of $\dot{\lambda} = 2 \times 10^{-3}$ to -5×10^{-3} 1/s show the model's time dependence in the way the higher the strain rate, the less total crystallinity evolves, as proved by literature experimental data. Using different scenarios, the concurring dependence of the cyclic behaviour is demonstrated using various amplitudes, and minimum unloading and maximum loading points concerning stretch. The simulation results reveal the ability of the model to reproduce real material behaviour.

Keywords Strain-induced crystallisation · Natural rubber · Material modelling · Strain rate dependence · Viscoelasticity · Cyclic simulations

15.1 Introduction

A vehicle tyre is a highly sophisticated component made from various materials in many production steps. The vehicle tyre is the essential connection between the vehicle and the road and is thus mainly responsible for the transmission of drive and braking forces. In today's world, where there are more and more electrically powered cars, production is as resource-efficient as possible and increasingly relies on recycled raw materials, the reduction of tyre wear through fine dust reduction and the reduction of rolling noise, and there are many reasons for a deep understanding of materials to

K. Loos (✉)

Institute of Mechanics, Faculty of Aerospace, Universität der Bundeswehr München,
Werner-Heisenberg-Weg 39, 85577 Neubiberg, Germany
e-mail: klara.loos@unibw.de

optimise future tyres. Extending the life of tyres is economically and environmentally motivated, but is limited by, among other things, the formation of micro-cracks in the material. One phenomenon that naturally counteracts the propagation of cracks in rubbery material is strain-induced crystallisation (SIC). This research concerns the modelling of SIC, which occurs particularly in natural rubber (NR). Here, a unfilled natural rubber 0NR1.2 is investigated.¹ For a uniaxial tensile experiment, strain-induced crystallisation occurs when loading to high strains around $\lambda_{\text{SIC}} \approx 4.3$ and melts during unloading at strains of $\lambda_{\text{m}} \approx 3$ where all crystallites melt. The values are extracted from Candau (2014, p. 132), which considers the exact same mixture. For similar measurements, the reader is referred to Trabelsi et al. (2004).

This research studies the cyclic behaviour of an existing model for SIC including a special phenomenon internally called polarisation. The meaning of *polarisation* in the context of SIC is the behaviour of the material to cyclic loading in dependence of the amplitude of the cycles and the mean value around which the cycles take place. Transferred to the application of a rolling tyre, the cyclic loading is of special interest. The fully unloaded case $\lambda = 1$ like in a classical uniaxial tensile test is never reached due to its characteristic application of a pressure-inflated rolling tyre. In the sense of crystallites, it makes a difference if a crystallite forms from the fully amorphous state or if it grows from an already existent crystal.

The following contribution first introduces the basic concept of the existent material model as presented in Loos et al. (2021). Next, its time dependence is demonstrated using simulations varying in their stretch rates. After this, three kinds of cyclic loadings are presented and discussed in detail. Moreover, they are compared to experimental literature results. Finally, conclusions and ideas for future simulations are stated.

15.2 Constitutive Model Using a Serial Connection of Amorphous, Non-crystallisable Amorphous and Crystalline Phase

Figure 15.1 illustrates the fundamental idea of the presented model considering three different phases. First, during any deformation, the material consists mainly of the amorphous phase. This amorphous phase is again divided into two parts: a crystallisable fraction with length l_a (orange) and a non-crystallisable fraction with length l_n (dark blue). The crystalline phase (light blue) evolves at high stretches to its length l_c . A linear dependence between the non-crystallisable and the crystalline phase is assumed. Due to the serial connection, the total length l comprises the individual lengths $l(t) = l_a(t) + l_n(t) + l_c(t)$ and the total stress is equal to the stresses of the single phases $\sigma = \sigma_a = \sigma_n = \sigma_c$. Its density in reference configuration is ρ_R . The crystallinity is depicted to the ratio between crystalline length and total length and therefore related to the volume. The set of constitutive equations for stress σ , the

¹ The exact mixture includes 100 phr rubber, 3 phr 6PPD, 2 phr stearic acid, 1.5 phr zinc oxide, 1.9 CBS, and 1.2 phr sulphur.

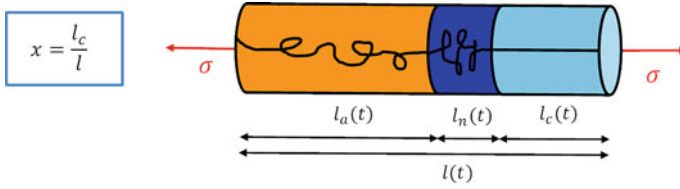


Fig. 15.1 Stretched elastomer part in serial connection in the current configuration: the crystallisable amorphous phase with its length l_a (left, orange), the non-crystallisable amorphous phase with its length l_n (middle, dark blue) and the crystalline phase with its length l_c (right, light blue)

internal state three variables: crystallinity index x , stretch of the crystalline phase λ_c and stretch of the non-crystallisable amorphous phase λ_n are given as

$$\sigma = \rho_R \left(1 - \frac{x}{x_0}\right)^{-1} \frac{\partial \psi}{\partial \lambda_a}, \quad (15.1)$$

$$\dot{x} = \beta(\theta, \dots) \left[-\rho_R \frac{\partial \psi}{\partial x} + \left(-\frac{1}{x_0} \lambda_a + \left(\frac{1}{x_0} - 1 \right) \lambda_n + \lambda_c \right) \sigma \right], \quad (15.2)$$

$$\dot{\lambda}_c = \frac{x}{\eta_c} \left(\sigma - \rho_R x^{-1} \frac{\partial \psi}{\partial \lambda_c} \right) \quad \text{and} \quad (15.3)$$

$$\dot{\lambda}_n = \frac{1}{\eta_n} \left(\frac{x}{x_0} - x \right) \left(\sigma - \rho_R \left(\frac{x}{x_0} - x \right)^{-1} \frac{\partial \psi}{\partial \lambda_n} \right), \quad (15.4)$$

where ψ is the Helmholtz-type free energy, $x_0 \leq 1$ is the scalar maximum crystallinity, $\beta(\theta, \dots) \geq 0$ is a positive prefactor, and $\eta_c, \eta_n > 0$ are scalar proportional prefactors. The reader is referred to Loos et al. (2021) for detailed derivation of the constitutive model. This set of partial differential equations is solved via a discretisation scheme, and the three-dimensional stress and crystallinity response is compared with experimental results. The stretches of the non-crystallisable amorphous fraction and crystalline fraction are internal, non-measurable variables.

15.2.1 Simulation Results: Loading with Various Maximum Stretch

To analyse the hysteresis behaviour of stress and crystallinity with its unique onset of crystallisation for high stretches, cycles with increasing stretch of $\Delta\lambda = 1$ for each cycle and a stretch rate of $\dot{\lambda} = 4.2 \times 10^{-3} 1/s$ are simulated. This load case is compared to one single cycle with maximum stretch of $\lambda = 6$ in Fig. 15.2. The material's stress and crystallinity answer of the fifth cycle with maximum stretch of $\lambda = 6$ is identical to the one with maximum stretch of $\lambda = 6$ and increasing stretch.

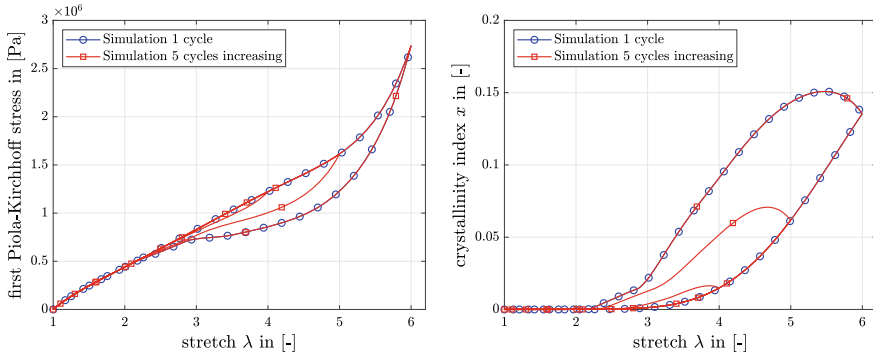


Fig. 15.2 Stress and crystallinity simulation of increasing cycles, stretch rate: $\dot{\lambda} = 4.2 \times 10^{-3}$ 1/s. Predefined stretch served as input for the simulation

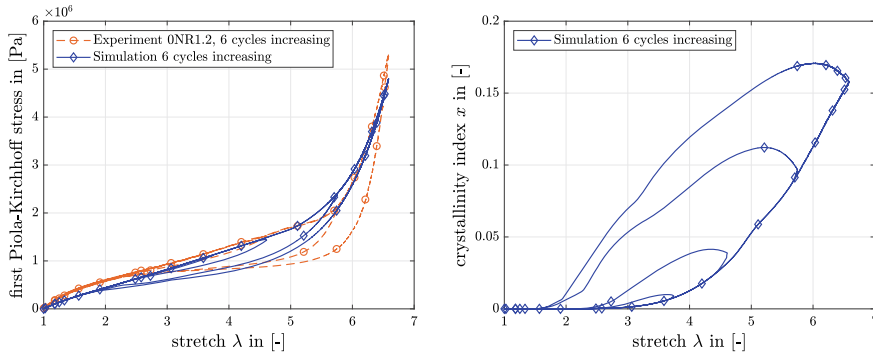


Fig. 15.3 Stress and crystallinity simulation of increasing cycles, stretch rate: $\dot{\lambda} = 1 \times 10^{-2}$ 1/s. Experimental data by Loos (2018)

The model is independent from its deformation history and stress softening also known as Mullins effect is not included in the model.

Next, in contrast to use predefined stretch as simulation input, the stretch from a uniaxial experiment up to $\lambda_{max} \approx 6.5$ serves as input for the simulation. The high concordance is observed in Fig. 15.3. The simulation shows real material behaviour: a hysteresis in the stress response develops only after a critical stretch has been exceeded. The magnitude of the hysteresis in the simulation corresponds to that in the experiment. The experimentally measured stretch with video-extensometry served as input for the simulation.

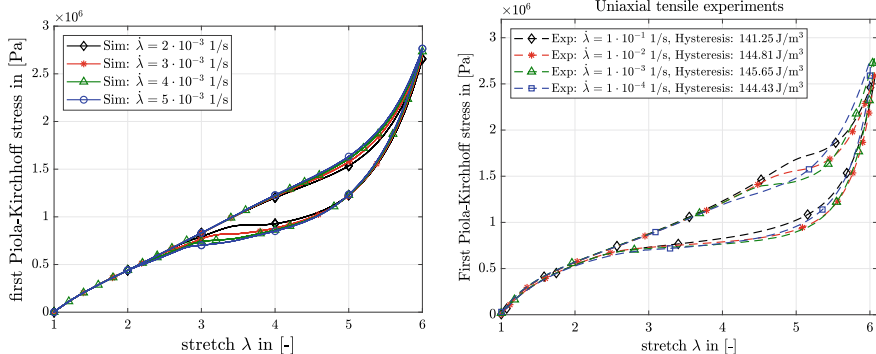
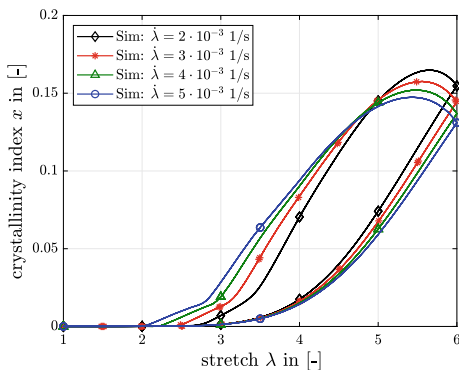


Fig. 15.4 Stress simulation of uniaxial cyclic loading with various stretch rates from $\dot{\lambda} = 2 \times 10^{-3}$ to 5×10^{-3} 1/s. Experimental data on the right partially published in Loos et al. (2020)

Fig. 15.5 Crystallinity simulation of uniaxial loading with various stretch rates from $\dot{\lambda} = 2$ to 5×10^{-3} 1/s



15.2.2 Simulation Results: Loading with Different Stretch Rates

The presented viscoelastic model depends on time and, therefore, is stretch rate dependent. The simulations in Figs. 15.4 and 15.5 are conducted with constant stretch rate varied from $\dot{\lambda} = 2 \times 10^{-3}$ to 5×10^{-3} 1/s. The stress response agrees with the experimental data: the smaller the stretch rate, the smaller the stress hysteresis and the closer the stress response to the equilibrium stress showing no hysteresis.

The simulated crystallinity agrees with the experimental data of Amnuaypornsrri et al. (2012) reprinted with permission in Fig. 15.6 for vulcanised NR. The higher the stretch rate, the lower the total crystallinity and the lower the crystallisation rate. The stretch rate dependence of the model is higher than in the experimental data when comparing the absolute stretch rates. For the simulation, the onset of crystallisation occurs at approximately the same stretch for all stretch rates, as displayed in the experimental data.

Fig. 15.6 Experimental results of various stretch rates (a) 5 mm/min to (d) 40 mm/min. Reprinted from Amnuayporn Sri et al. (2012), Copyright (2012), with permission from Elsevier

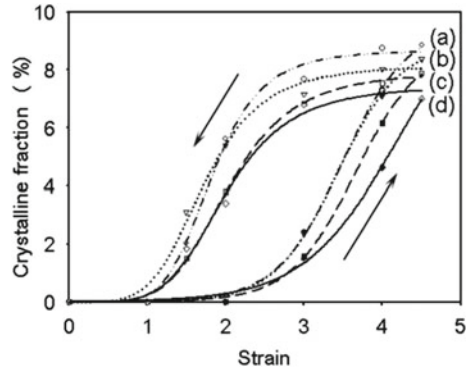
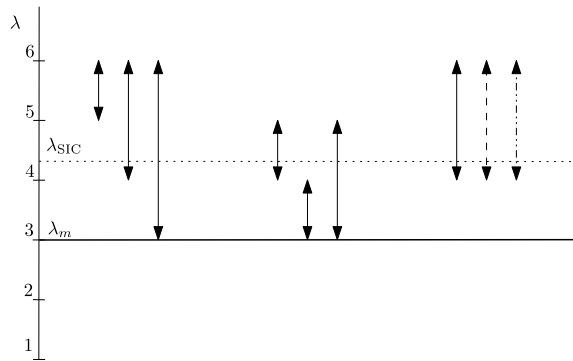


Fig. 15.7 Overview of three cyclic loading scenarios. λ_{SIC} is the stretch of crystallisation onset and at stretch λ_m all crystallites melt during unloading



15.2.3 Simulation Results: Cyclic Loading Varying in Amplitude and Minimum Unloading Stretch

The focus of the presented simulations is the materials dependence on cyclic loading histories. The stretch of crystallisation onset is identified to $\lambda_{SIC} \approx 4.3$ for a stretch rate of $\dot{\lambda} = 4.2 \times 10^{-3}$ 1/s, and the stretch of total melting of the crystallites during unloading is identified to $\lambda_m \approx 3$ (Candau 2014, p. 189) for the investigated material. The maximum and minimum stretch of the cycles are chosen regarding these values. The quantities *stretch amplitude* $\Delta\lambda$ and, thus, the *minimum* and *maximum stretch* are varied in the analysis $\Delta\lambda = \lambda_{max} - \lambda_{min}$. The stretch rate is $\dot{\lambda} = 4.2 \times 10^{-3}$ 1/s, if not specifically defined. Figure 15.7 gives an overview of the following cyclic simulations. First, the influence of the minimum stretch in the unloading is investigated. Second, the influence of stretching below or above λ_{SIC} is analysed. Third, cycles with various stretch rate $\dot{\lambda}$ are investigated.

The results of the first uniaxial cyclic simulation are shown in Figs. 15.8 and 15.9, where the maximum stretch is kept constant to $\lambda_{max} = 6$. The amplitude of the cyclic tests and, thus, the minimum achieved stretch during the cycles is changed from $\lambda_{min} = 5, 4, 3$.

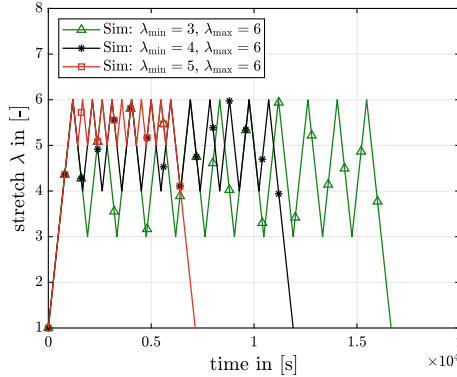


Fig. 15.8 Simulation of uniaxial cyclic loading. Equal maximum stretch $\lambda_{\max} = 6$, different cycling amplitude $\Delta\lambda = 1, 2, 3$, equal stretch rate $\dot{\lambda} = 4.2 \times 10^{-3}$ 1/s. Stretch over time

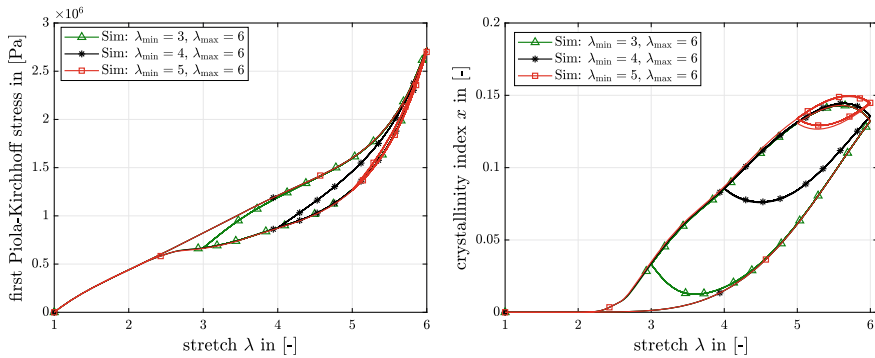


Fig. 15.9 Simulation of uniaxial cyclic loading. Equal maximum stretch, different cycling amplitude $\Delta\lambda = 1, 2, 3$, equal stretch rate $\dot{\lambda} = 4.2 \times 10^{-3}$ 1/s. Stress and crystallinity over stretch

The stress at the highest stretch is initially equal. With the beginning of the cyclic unloading, all three examples follow the same unloading path. Depending on the reversal point and, thus, the minimum deformation during the cycles, different behaviour of the material is observed. Both stress and crystallinity of the most unloaded material ($\Delta\lambda = 3$, green) reach the initial path in the following load within $\Delta\lambda = 1$. The remaining crystals, thus, hardly influence the re-stretching. At a minimum stretch of $\lambda_{\min} = 4$ (i.e. a residual crystallinity index of 8%), the original and the reloading path do not merge. The crystallinity is always higher than the initial degree of crystallinity. Concretely, at a stretch of $\lambda = 5$, the crystallinity related to the original load path is 6%, and at reloading, it is 8.5%. The remaining crystals in the material, therefore, influence the re-crystallisation and accelerate it. At a small load relief of $\Delta\lambda = 1$, the total crystallinity at maximum load reaches a value of crystallinity that is 1% higher in absolute value.

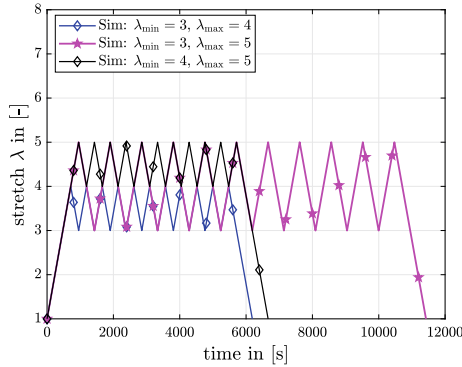


Fig. 15.10 Simulation of stress for uniaxial cyclic loading. Different maximum stretch $\lambda_{\max} = 4, 5$, different cycling amplitude $\Delta\lambda = 1, 2$

However, if one considers the stress response of these simulations, under cyclic loading of $\Delta\lambda = 1$, hardly any hysteresis occurs. The relief and loading of the cyclic load completely follow the unloading path. Only with higher unloading, hysteresis develops in the stress response. Similar to the behaviour of crystallinity, the stress response of the material further unloaded reaches the original load path within $\Delta\lambda = 1$. In contrast, the reloading path of the specimen unloaded by $\Delta\lambda = 2$ reaches the original loading only at the highest point of loading. The maximum stress value for the stretch of $\lambda_{\max} = 6$ is identical for all cycles. The change in crystallinity at the maximum load point has only an imperceptible effect on the stress response, namely a stress relaxation of 0.04 MPa, which is $\approx 1.5\%$ of the maximum stress.

The next simulation scenario demonstrates similar behaviour illustrated in Figs. 15.10 and 15.11. In the scenario of the demonstrated black curve, the material is cyclically unloaded from a maximum stretch of $\lambda_{\max} = 5$ by $\Delta\lambda = 1$ with $\lambda_{\min} = 4 > 3 = \lambda_m$. The crystallinity increases with each cycle, which is an indication that the material is not in a state of equilibrium. The model thus includes the dependence of re-crystallisation on the level of unloading, exactly as observed in experimental data.

The next scenario investigates the stretch rate dependence during cycling simulations in Figs. 15.12 and 15.14. The stretch rate at initial loading and final unloading is equal to $\dot{\lambda} = 4.2 \times 10^{-3}$ 1/s. A simulation with double stretch rate and one with a half stretch rate were performed with equal amplitude of $\Delta\lambda = 2$ starting from $\lambda_{\max} = 6$. The cyclic loading reveals low stress hysteresis and pronounced crystallisation hysteresis along the unloading path. The half stretch rate simulations, marked by a red solid line and stars in Fig. 15.12, indicate a flatter stress hysteresis. The maximum stress value is slightly below the initial maximum value. The higher the stretch rate, the steeper the stress hysteresis slope. In Fig. 15.13, similar experimental data published by Candau et al. (2015) is shown for comparison. These experiments were performed using a self-built dynamic tensile machine with frequencies in the range from 2 to 80 Hz. The frequencies in the experiments by Candau et al. are higher than

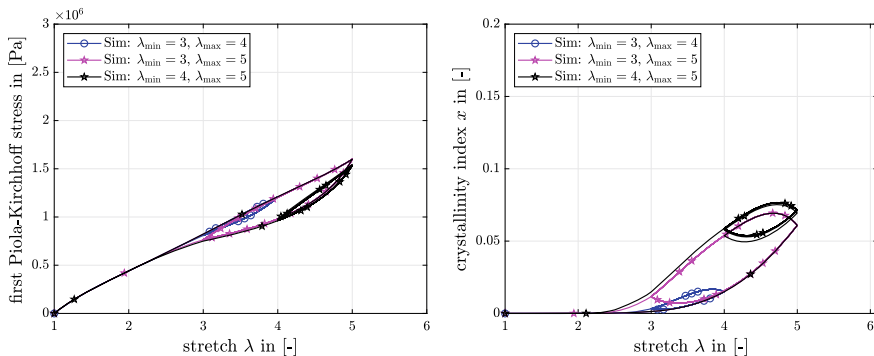
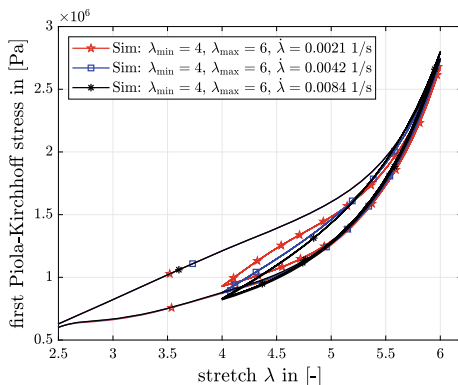


Fig. 15.11 Simulation of uniaxial cyclic loading. Different maximum stretch $\lambda_{\max} = 4, 5$, different cycling amplitude $\Delta\lambda = 1, 2$. Stress and crystallinity over stretch

Fig. 15.12 Stress simulation with equal maximum stretch $\lambda_{\max} = 6$, equal cycling amplitude $\Delta\lambda = 2$ and different stretch rates during cycling



in the shown simulations. The cyclic simulation and the experiment in Fig. 15.12 show high agreement for the slope of hysteresis and the maximum and minimum values. When it comes to the crystallinity response, the lower the stretch rate the higher the maximum value of crystallinity during cyclic loading. The more time the polymer chains have to form a regular pattern, the more crystallinity evolves. For the simulations with half stretch rate, the crystallinity hysteresis is narrower and steeper. Moreover, the minimum crystallinity is lower. At a low stretch rate, the crystals have time to develop and also time to melt (Fig. 15.14).

The simulations with the double stretch rate marked by blue solid lines with squares display the opposite behaviour: the maximum value of the stress is higher, as well as the slope of the stress hysteresis, whereas the crystallinity hysteresis is flatter and the maximum value of the crystallinity is smaller. The evolution of the crystals cannot follow the stretch rate; the development and melting of the crystals are lower.

Fig. 15.13 Stress response during cyclic experiments 2 Hz (thin blue solid line) 20 Hz (thin green dashed line). The thick grey line shows a single uniaxial cycle with low strain rate of $\dot{\lambda} = 4.2 \times 10^{-3}$ 1/s. Reprinted with permission from Candau et al. (2015)

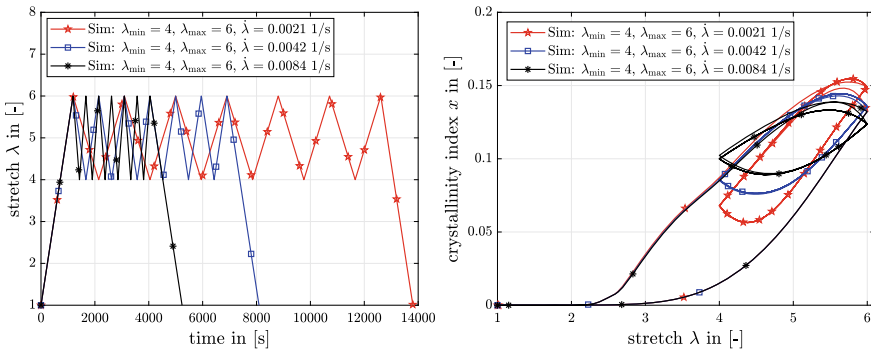
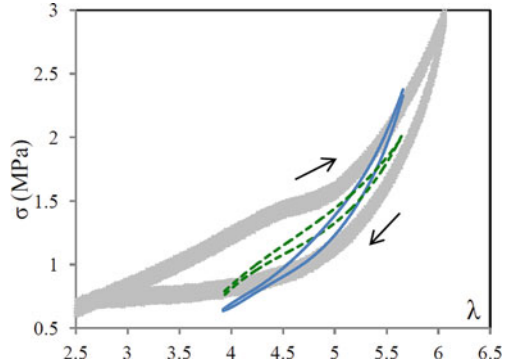


Fig. 15.14 Simulation of uniaxial cyclic loading. Equal maximum stretch $\lambda_{max} = 6$, equal cycling amplitude $\Delta\lambda = 2$, different stretch rates during cycling. Stretch over time and crystallinity over stretch

15.3 Conclusions and Outlook

In the present research work, three kinds of process dependencies of a previously presented material model are investigated. First, the dependence of the stress and crystallisation hysteresis on the maximum stretch is confirmed. Furthermore, the strain rate dependence is demonstrated by simulations with 4 different strain rates. The faster the loading, the higher the stress response and the smaller the total crystallinity. The crystallisation behaviour is successfully compared with literature values. The cyclic behaviour is investigated using three different scenarios with the parameters amplitude, mean value around which the cycles run, and again strain rate. The simulation is able to represent the true growth and melting of the crystallites. The crystallisation kinetics depends on the initial state. Whether the crystal forms from the completely amorphous state or whether it grows from an already existing crystal makes a considerable difference. The comparison with literature values is consulted at several points and agrees with the simulation results.

References

- Amnuaypornsi S, Toki S, Hsiao BS, Sakdapipanich J (2012) The effects of endlinking network and entanglement to stress-strain relation and strain-induced crystallization of un-vulcanized and vulcanized natural rubber. *Polymer* 53:3325–3330
- Candau N (2014) Compréhension des mécanismes de cristallisation sous tension des élastomères en conditions quasi-statiques et dynamiques. PhD thesis
- Candau N, Chazeau L, Chenal JM, Gauthier C, Ferreira J, Munch E, Thiaudiere D (2015) Strain induced crystallization and melting of natural rubber during dynamic cycles. *Phys Chem Chem Phys* 17:15331–15338
- Loos K, Aydogdu AB, Lion A, Johlitz M, Calipel J (2020) Strain-induced crystallisation in natural rubber: a thermodynamically consistent model of the material behaviour using a multiphase approach. *Contin Mech Thermodyn* 32:501–526
- Loos K, Aydogdu AB, Lion A, Johlitz M, Calipel J (2021) Strain-induced crystallisation in natural rubber: a thermodynamically consistent model of the material behaviour using a serial connection of phases. *Contin Mech Thermodyn* 33:1107–1140
- Trabelsi S, Albouy PA, Rault J (2004) Stress-induced crystallization properties of natural and synthetic CIS-polyisoprene. *Rubber Chem Technol* 77:303–3016

Chapter 16

Long-Term Storage of Aged NBR in Kerosene in Consideration of Long Material Service Life



**Benedikt Demmel, Tobias Förster, Sebastian Eibl, Michael Johlitz,
and Alexander Lion**

Abstract Elastomeric parts with long service lifetimes and contact to fuels or oils are exposed to aging. Acrylonitrile-butadiene-rubber (NBR) with acrylonitrile contents of 18, 28, and 39 wt%, sulfur- and peroxide-cured, is the subject of this study. The impact of the accelerated aging, induced by storage of specimens at 120 °C in air, on mechanical properties, the additive composition, and long-term sorption experiments in Jet A-1 kerosene for up to 423 days is investigated. Peroxide-cured NBR shows different tensile properties and sorption behavior compared to the sulfur cured analog. The investigated mechanical properties for varying acrylonitrile contents degrade similarly with increasing aging durations. The uptakes and uptake rates of Jet A-1 in sorption experiments correlated inversely with the acrylonitrile content. Aging-caused crosslinking leads to a reduction in equilibrium mass uptakes and the fuel uptake rate. In severely aged samples, soluble polymer fragments are extracted from the elastomer. With regard to the evaluation of long-term use of elastomer parts, it is challenging that for high acrylonitrile contents and aged samples, the static sorption equilibrium is not reached after 423 days.

Keywords NBR · Aging · Fuel · Diffusion · Long-term · Compatibility · GC/MS · Mechanical testing

B. Demmel (✉) · M. Johlitz · A. Lion

Universität der Bundeswehr München, Fakultät für Luft- und Raumfahrttechnik, Institut für Mechanik, Werner-Heisenberg-Weg 39, 85577 Neubiberg, Germany
e-mail: benedikt.demmel@unibw.de

M. Johlitz

e-mail: michael.johlitz@unibw.de

A. Lion

e-mail: alexander.lion@unibw.de

B. Demmel · T. Förster · S. Eibl

Wehrwissenschaftliches Institut für Werk- und Betriebsstoffe (WIWeB), Institutsweg 1, 85435 Erding, Germany
e-mail: Tobias1Foerster@bundeswehr.org

S. Eibl

e-mail: SebastianEibl@bundeswehr.org

16.1 Introduction

Elastomers are used as barrier materials in a variety of applications such as seals, tank linings, hoses, or membranes (Röthemeyer and Sommer 2013). To fulfill its barrier properties, the choice of an appropriate elastomer that is compatible with the surrounding media is mandatory. Acrylonitrile-butadiene-rubber (NBR) exhibits high resistance toward the penetration of non-polar organic liquids according to Starmer (1993), which originates from its polarity due to its structurally inherent cyano group (Lachat et al. 2009). Thus, NBR is typical for parts with contact to non-polar fuels or oils in the aircraft. The properties of NBR are mainly influenced by its acrylonitrile content, which typically varies between 15 and 50 wt%. With increasing acrylonitrile contents, the cold flexibility decreases, whereas the resistance toward non-polar liquids increases. Further, the network structure, determined by the curing mechanisms or aging-induced crosslinking reactions, is influential (El-Nemr 2011; Mathai and Thomas 1996). Although other inert sealing materials like fluorosilicone rubbers (FVMQ) or hydrogenated NBR (HNBR) are available on the market NBR is highly relevant due to its good properties, widespread use, and cost. Especially in the military sector, due to high maintenance frequencies, long service times are achieved. Therefore, NBR in use may undergo some degree of aging accompanied by a change in the material properties, e.g., chemical changes, see Pazur et al. (2014), hardness, tensile strength, elongation at break, see Delor-Jestin et al. (2000), additive composition, and swelling behavior toward surrounding liquids (Buckley and Roland 2014; Loos et al. 2021). For sustainable use of elastomeric parts, influencing factors that reduce the lifetime and to which degree must be identified. Fuel or oil characteristics are dependent on their chemical composition, and especially a high concentration of aromatic hydrocarbons promotes high swelling degrees in NBR of low acrylonitrile content (Förster and Blivernitz 2021; Graham et al. 2006). Focus is laid on structure-to-property relationships and their change in dependency of the aging of the elastomer. This work contributes to the safe use of the investigated elastomer/fuel combinations and fuels with a similar composition, especially in an aged condition of the elastomer, by evaluating the factors that reduce the long-term service life.

16.2 Materials

Sulfur-cured, carbon black filled, and stabilized acrylonitrile-butadiene-rubbers (NBR) with acrylonitrile contents of 18, 28, and 39 wt% in the rubber are used in the experiments and are abbreviated as NBR18, NBR28, and NBR39. Further, carbon black filled NBR with 28 wt% acrylonitrile content in the rubber, which is cured with peroxide reagents and stabilized with a differing antioxidant, is used and abbreviated as NBR28p. The chemical structural formula of uncured poly(acrylonitrile-*co*-butadiene) is depicted in Fig. 16.1. The acrylonitrile-derived unit is polar and causative for good fuel resistance, while the butadiene-derived units are causative

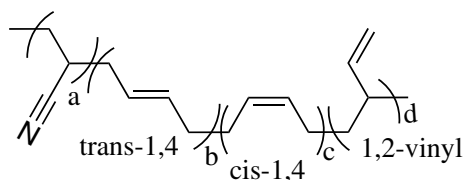


Fig. 16.1 Chemical structural formula of uncured poly(acrylonitrile-*co*-butadiene) **a** acrylonitrile-derived unit, **b–d** butadiene-derived units

Table 16.1 Composition of the investigated NBR elastomers in phr

Component	Content/phr			
	NBR18	NBR28	NBR39	NBR28p
Perbunan 1846	100			
Perbunan 2845		100		
Perbunan 3945			100	
Perbunan 2845				100
Di(2-ethylhexyl) phthalate (DEHP)		20		20
<i>N</i> -(1,3-dimethylbutyl)- <i>N'</i> -phenyl- <i>p</i> -phenylenediamine (6PPD)		2		0
2,6-Di- <i>tert</i> -butyl-4-methylphenol		0		2
Carbon black (type: N550)		60		60
Zinc oxide		5		0
Stearic acid		1		0
Sulfur		2		0
<i>N</i> -Cyclohexyl-2-benzothiazole sulfenamide (CBS)		1.5		0
TMTM-80 ^a		0.5		0
Perkadox BC-40K-pd ^b		0		7.5
TAC/S ^c		0		4.3

^a80% tetramethylthiuram monosulfide, 20% elastomer binder and dispersing agents

^b40% dicumylperoxide, 60% kaolin

^c70% triallyl cyanurate, 30% silicic acid

for the elastomer flexibility and its relative properties (Röthemeyer and Sommer 2013). All elastomers are supplied by Deutsches Institut für Kautschuktechnologie (DIK) and the detailed compositions are given in Table 16.1 reported as parts-per-hundred rubber (phr). Conventional Jet A-1 kerosene with an aromatics content of 16.2 vol% and a density of 0.8117 g cm⁻¹ is used as an immersion liquid for sorption experiments. The fuel properties are reported in the publications Blivernitz (2019), Scheuermann et al. (2017) and Zschocke et al. (2012).

16.3 Experiments and Methods

16.3.1 *Elastomer Aging and Preparation*

The elastomer samples with a dimension of $60 \times 10 \times 1 \text{ mm}^3$ and dumbbell-shaped S2 specimens are aged thermo-oxidatively in air in a Binder ED56 oven at $120 \text{ }^\circ\text{C}$ with natural convection. The durations are 1, 2, 3, 5, 7, and 14 days in order to cover light and strong degradation of the samples as it is expected for materials in long-term applications. For subsequent sorption experiments, the rectangular samples are extracted for two days in acetone using a soxhlet apparatus to remove any soluble additives. The samples are dried at room temperature for two days in a fume hood, stored in the laboratory climate to equilibrate, and are cut to a length of 30 mm. Samples for mechanical characterization and the determination of additive contents are left without further treatment.

16.3.2 *Mechanical Testing*

Hardness Shore A is determined on three different locations at the surface of five samples for each aging duration on a digi test II, by bareiss[®] equipped with a Micro Shore A test head after 3 s measurement time according to ISO 7619-1:2010 (Deutsches Institut für Normung e.V., 2012). Tensile testing is performed as a five-fold determination with dumbbell S2 specimens. A Zwick Roell 1445 universal testing machine is used with a force sensor of 500 N and the optical extension sensor ProLine lightX-tens 2–1000 at ambient temperature, a preload of 0.1 MPa, and a strain rate of 200 mm min^{-1} , according to the Standard DIN 53504:2017-03 (Deutsches Institut für Normung e.V., 2017). The tensile test specimens are not pre-conditioned under cyclic load to conserve the changes in the network structure due to aging prior to testing.

16.3.3 *Gas Chromatography/Mass Spectrometry*

Samples of the investigated elastomers after different aging durations are prepared for the analysis in a solid-liquid extraction of 8–12 mg elastomer with acetone for five days. The acetone extracts are analyzed with gas chromatography/mass spectrometry (GC/MS) using automated liquid injection. An Agilent 7890A gas chromatograph coupled with an Agilent 5975 MSD mass spectrometer was used to perform the GC/MS analysis. The column was a 30 m DB-5MS (0.25 mm inner diameter and $0.25 \text{ }\mu\text{m}$ film thickness). The GC oven was heated with 50 K min^{-1} from 50 to $320 \text{ }^\circ\text{C}$ and held for 5 min at $320 \text{ }^\circ\text{C}$. The concentrations of the stabilizers and the plasticizers

in the elastomers are determined with an external calibration using standards with known concentrations and are referred to as the non-extractable elastomer mass m_0 .

16.3.4 Sorption Experiments

Sorption experiments are performed gravimetrically at 22 °C for up to 423 days which corresponds to approximately $6000\text{ s}^{0.5}$. The samples are weighed prior to the experiments to obtain the non-extractable elastomer mass m_0 . Subsequently, they are immersed in the respective storage fuels. After a time t , the samples are taken out, and the excess fuel is removed by dipping the sample quickly ($<1\text{ s}$) in low boiling benzine and drying it with a lint-free paper cloth. The samples are weighed, where m_t represents the absolute mass of the elastomer and the absorbed fluid at the time t and stored again in the fuels. Mass uptakes are determined as $\Delta m_t = (m_t - m_0)/m_0 \cdot 100\text{ wt\%}$, and the equilibrium mass uptake is denoted as Δm_{eq} . The sorption times are reported in $t^{0.5}$ to account for Fickian diffusion.

16.4 Results and Discussion

16.4.1 Mechanical Properties After Aging

The influence of the aging of the specimens at elevated temperatures in air is reflected in the mechanical properties of the elastomers. In Fig. 16.2, the development of hardness is shown in dependency of the aging duration at 120 °C. The pristine samples of the NBRs show hardnesses in the range of 68–72 Shore A. For NBR18 and NBR28, the hardness increases linearly with $2.0\text{ Shore A d}^{-1}$ at 120 °C. The increase rate of the hardness is $1.9\text{ Shore A d}^{-1}$ for NBR39 and $1.3\text{ Shore A d}^{-1}$ for NBR28p. Firstly, because of the aging-induced crosslinking of NBR that takes place at elevated temperatures, the hardness of the specimens increases. The crosslinking proceeds either through reactions of oxygen with unsaturated bonds in the butadiene unit of the elastomer or through conversion of polysulfide linkages to di- or monosulfide bonds, which yields shorter but numerically more crosslinks. Secondly, the elastomer loses the plasticizer (see Fig. 16.6), which further increases the hardness. The hardness increase is slower for NBR28p, as it contains less plasticizer according to the GC/MS analysis in Fig. 16.6, and post-crosslinking only occurs through thermo-oxidative reactions. The reason for that is that peroxide-cured NBR28p is more thermally stable since it does not contain sulfur, which can produce crosslinks through conversion reactions. Furthermore, the peroxide-derived crosslinks do not participate in re-crosslinking reactions at these aging conditions.

The elongation at break ε_B and stress at break σ_B , determined with tensile tests, are shown in Figs. 16.3 and 16.4. According to Fig. 16.3, the elongation at break of sulfur-

Fig. 16.2 Micro-hardness Shore A for the investigated elastomers in dependency of the aging duration

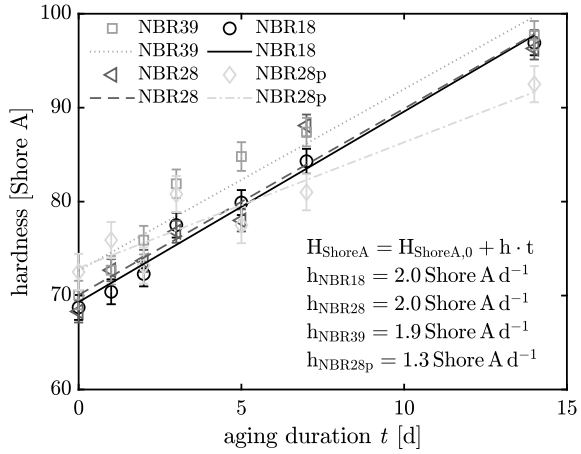
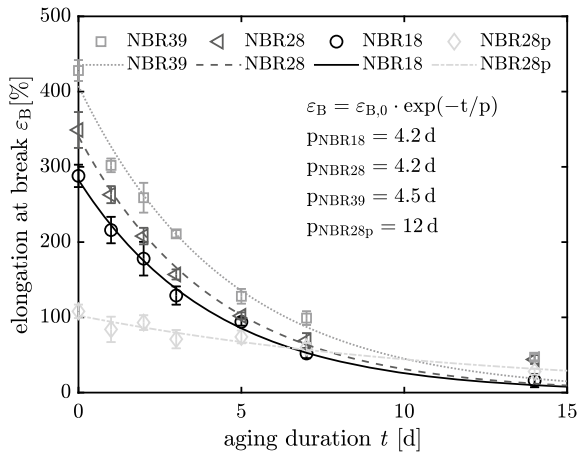


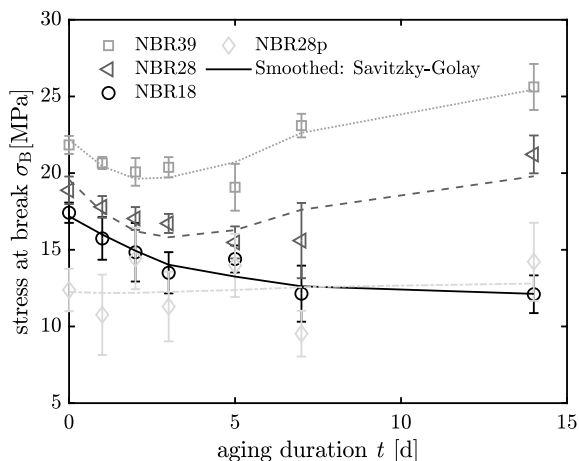
Fig. 16.3 Elongation at break for the investigated elastomers in dependency of the aging duration



cured pristine elastomers is highest for NBR39 and decreases in correlation with the acrylonitrile content to NBR18. The physical intermolecular interactions between the cyano groups result in higher cohesive forces in the elastomer and contribute in this way to higher ε_B for higher acrylonitrile contents. In the direct comparison of both NBRs with 28 wt% acrylonitrile, the peroxide-cured NBR exhibits significantly lower ε_B . Peroxide curing produces shorter linkages between the macromolecules resulting in lower possible ε_B . When aging progresses, the elongation at break ε_B decreases for all elastomers. The decay constants for the exponential decrease in ε_B are 4.2 d for NBR18 and NBR28, 4.5 d for NBR39, and 12 d for NBR28p. Lower ε_B caused by longer residence times at 120 °C is attributed to the additional crosslinking. The additional crosslinks restrict the elongations and cause breakage at lower elongations.

Figure 16.4 shows the stress at break σ_B for the investigated NBR elastomers. For pristine samples, the highest σ_B is attributed to NBR39, followed by NBR28,

Fig. 16.4 Stress at break for the investigated elastomers in dependency of the aging duration

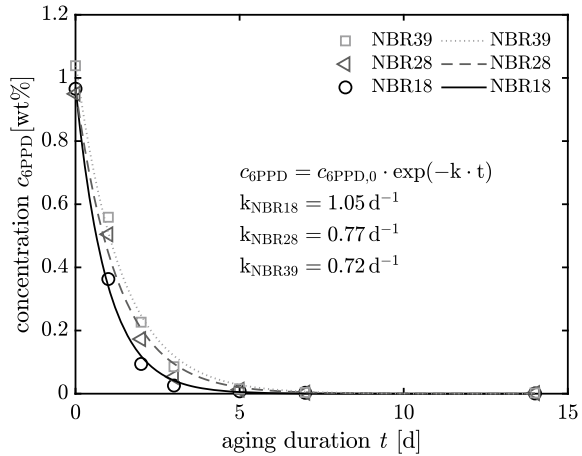


NBR18, and NBR28p exhibits the lowest σ_B . The polar interactive forces between the cyano groups in NBR contribute to intramolecular cohesive forces. Therefore, the stress at break σ_B of NBR39 is higher than that of NBR18 with its lower proportion of cyano groups in the rubber. As illustrated by the development of σ_B of NBR39, the stress at break is at first decreased for short aging durations, passes a minimum, and increases again for long aging durations. Oxidation, bond cleavage, and crosslinking reactions take place simultaneously in the elastomer (Musil et al. 2018; Zaghdoudi and Jaunich 2019). The cleavage reactions lead to a reduced polymer-polymer and polymer-filler interaction, with the consequence of lower σ_B . Contrarily, crosslinking increases the number of bonds in the elastomer and thus leads to higher σ_B . The stress at break increases again when the crosslinking exceeds cleavage. The location of the minimum is shifted to longer durations for NBR28 and NBR18, and the increase is not observable for NBR18. Stress at break σ_B of NBR28 and NBR39 rises exactly after the stabilizer is consumed completely after 5–7 days (see Fig. 16.5). The curve of NBR28p contrarily increases continuously without a minimum. Possibly due to small polymer chain distances, many of the radicals which are formed by cleavage reactions recombine. The tensile behavior of NBR28p differs strongly from the sulfur-cured analog owing to the divergent curing mechanism.

16.4.2 Concentration of Stabilizers and Plasticizers

The concentrations of the stabilizer 6PPD are depicted in Fig. 16.5 for NBR39, NBR28, and NBR18. Since NBR28p contains a different stabilizer, for which no calibration standard is available, the concentrations are not quantified. For all investigated elastomers, the initial concentrations are ca. 1 wt% related to m_0 . With increasing aging durations, the stabilizer concentrations decrease exponentially, following

Fig. 16.5 Concentration of 6PPD for the investigated elastomers in dependency of the aging duration



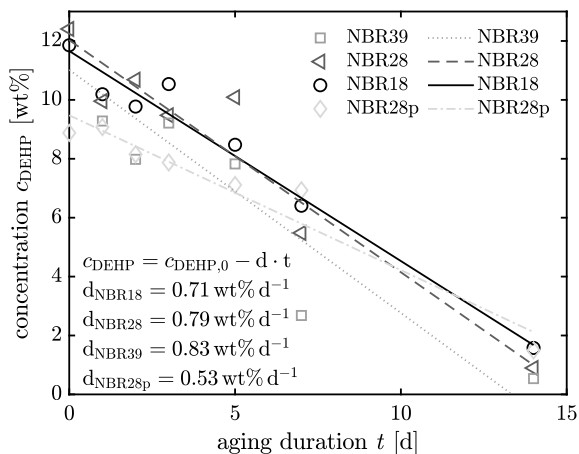
a first-order kinetic. The stabilizer reacts with oxygen, which diffuses into the elastomer and is consumed in this reaction. The decrease rate is lowest for NBR39 and highest for NBR18. The degree of unsaturation decreases in the order NBR18 > NBR28 > NBR39. The higher proportion of double bonds in NBR18 makes it more prone to oxidation, which causes a faster consumption of the stabilizer. Additionally, according to the literature, the gas permeability of oxygen decreases with increasing acrylonitrile content (Röthemeyer and Sommer 2013). After 5–7 days, the stabilizer is consumed completely in all samples.

The concentrations of the plasticizer DEHP are plotted in Fig. 16.6. The elastomers NBR18, NBR28, and NBR39 contain 11.9, 12.4, and 13.2 wt% DEHP related to m_0 , respectively, and NBR28p contains 8.9 wt% DEHP. The concentrations decrease linearly with the aging duration, which corresponds to a zero-order kinetic. The rate constant of NBR28p is significantly lower than those of the sulfur-cured NBRs. The loss of plasticizer occurs through diffusion-controlled thermal desorption. Different desorption rates are attributed to different intermolecular interactions between DEHP and NBR and the plasticizer mobility in the elastomer.

16.4.3 Long-Term Sorption Behavior of Kerosene Jet A-1 in Aged NBR

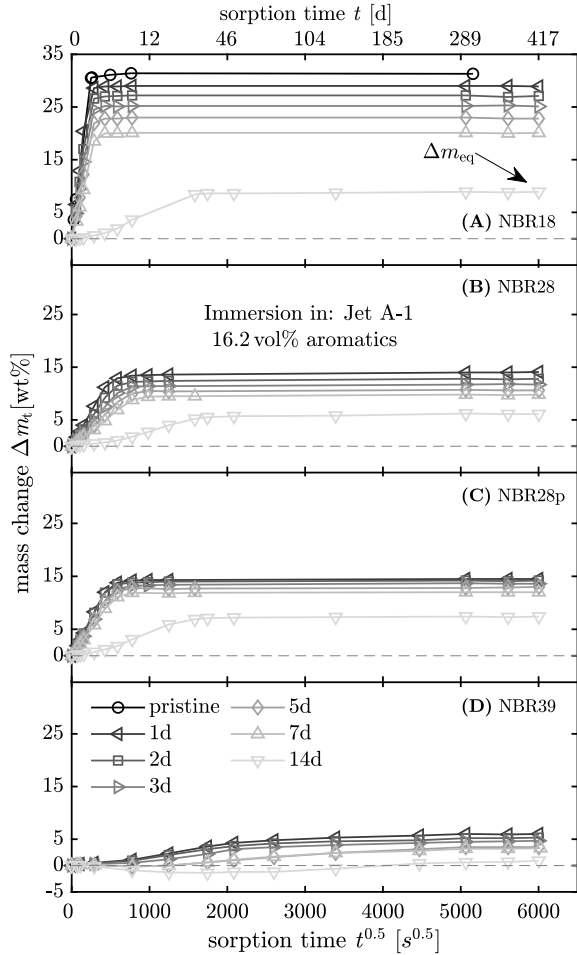
Results of the long-term sorption experiments with NBR18, NBR28, NBR28p, and NBR39 in kerosene Jet A-1 for up to 423 days are shown in Fig. 16.7. The mass uptakes are plotted versus the square root of the sorption time $t^{0.5}$ to account for the Fickian diffusion law. For reasons of clarity, additionally, the sorption time is added to the abscissa at the top of the graph. Equilibrium mass uptakes Δm_{eq} are the constant values at the end of the sorption experiment and lie in the range 31.3–8.9 wt% for

Fig. 16.6 Concentration of DEHP for the investigated elastomers in dependency of the aging duration



NBR18, 14.1–6.1 wt% for NBR28, 14.5–7.5 wt% for NBR28p, and 6.0–0.9 wt% for NBR39. It is known that aromatic hydrocarbons exhibit high swelling potentials in NBR elastomers, especially with low acrylonitrile contents. In the set of a–d, the acrylonitrile content from NBR18 (a) to NBR39 (d), i.e., the elastomer polarity increases in the order NBR18 < NBR28 = NBR28p < NBR39. With increasing acrylonitrile contents, the equilibrium mass uptakes Δm_t , and the initial slopes of the sorption curves decrease. Reasons for that are that the equilibrium mass uptakes Δm_{eq} decrease with increasing aging durations because of crosslinking. Also, the uptake rate of fuel, which is represented by the initial slope of the sorption curves, decreases with increasing aging durations. In the direct comparison of NBR28 and its peroxide-cured analog NBR28p, the reduction in Δm_{eq} for NBR28p proceeds less sharply, attributed to aforementioned superior thermal stability of NBR28p (see Sect. 16.4.1). For severely aged samples (14 d and 7 d at 120 °C) of NBR39 (see Fig. 16.7d), the uptake of fuel is convoluted with the extraction of soluble components, expressed by the negative slope at the beginning of the sorption curve and negative mass changes Δm_t for up to 4000 s^{0.5}. As described in Sect. 16.3.1, the soluble plasticizers and stabilizers are extracted with acetone prior to the sorption experiments. Therefore, the intermittent mass loss must originate in the extraction of soluble polymer fragments and poorly soluble reaction reagents. For samples that are aged shortly or moderately (1–5 days) also, an extraction of soluble components is possible, but due to the fast uptake of fuel and fast extraction processes, it is not visible in the shape of the sorption curve. The uptake and extraction kinetics are very slow for NBR39 since the mass uptakes after 423 days are not constant. Especially in consideration of long service lifetimes of elastomeric construction parts, it is important to conduct sufficiently long-lasting sorption experiments to correctly determine the static sorption equilibrium Δm_{eq} .

Fig. 16.7 Sorption curves of the elastomers in Jet A-1 in dependency of the aging of the elastomers: **a** NBR18, **b** NBR28, **c** NBR28p, **d** NBR39. The acrylonitrile content increases from top to bottom: **a** < **b** = **c** < **d**



16.5 Conclusion

This study investigates the material behavior of aged acrylonitrile-butadiene-rubbers (NBR) with acrylonitrile contents of 18–39 wt% for sulfur as well as peroxide-cured networks. The aging changes the mechanical properties of the elastomers. Longer residence times at 120 °C lead to increased hardness and decreased elongation at break. The proportion of the polar cyano group and the number of double bonds in the elastomer are determined by the acrylonitrile content. Aging occurs faster in NBR with lower acrylonitrile contents due to the higher amount of double bonds, which are more prone to oxidation. The stabilizer 6PPD is consumed following a first-order kinetic and the plasticizer DEHP is desorbed thermally following a zero-order kinetic. The interaction of fuels and aged NBR is characterized by gravimetric sorp-

tion experiments. Fuels with high aromatic contents, represented by the kerosene Jet A-1, exhibit high swelling potentials in NBR. The equilibrium mass uptakes are relatively low for high acrylonitrile contents and increase for low acrylonitrile contents. Crosslinking as a consequence of the elastomer aging reduces the equilibrium mass uptakes Δm_{eq} and the fuel uptake rate. Special care has to be taken in the evaluation of NBR with high acrylonitrile contents since the sorption equilibrium does not set in after 423 days, and in short-term swelling experiments, the swelling equilibrium may be evaluated inaccurately. According to the hardness and tensile tests, the elastomer is severely degraded after 3–5 days. The equilibrium mass uptakes of Jet A-1 in the aged NBRs relatively decrease less sharply for longer aging durations than the tensile properties. In the light of the swelling equilibrium, the elastomers are more durable, and lower swelling degrees in some cases are even favorable. Peroxide-cured NBR is less prone to aging, reflected in the decrease rate of the tensile properties and reduction of Δm_{eq} . It is therefore recommended for long-term use, provided its tensile properties are sufficient for the respective application.

Acknowledgements The scientific cooperation between the Universität der Bundeswehr, Fakultät für Luft- und Raumfahrttechnik, Institut für Mechanik and Wehrwissenschaftliches Institut für Werk- und Betriebsstoffe (WIWeB), Erding is gratefully acknowledged.

References

- Blivernitz A (2019) Untersuchung der Verträglichkeit von Elastomeren mit synthetischen Flugturbinenkraftstoffen anhand ablaufender Diffusionsprozesse. PhD thesis, Universität der Bundeswehr München
- Buckley GS, Roland CM (2014) Influence of liquid media on lifetime predictions of nitrile rubber. *J Appl Polym Sci* 131(11):40296
- Delor-Jestin F, Barrois-Oudin N, Cardinet C, Lacoste J, Lemaire J (2000) Thermal ageing of acrylonitrile-butadiene copolymer. *Polym Degrad Stab* 70(1):1–4
- Deutsches Institut für Normung eV (2012) DIN ISO 7619-1:2012-02: rubber, vulcanized or thermoplastic—determination of indentation hardness—part 1: durometer method (shore hardness) (ISO 7619-1:2010)
- Deutsches Institut für Normung eV (2017) DIN 53504:2017-03: testing of rubber—determination of tensile strength at break, tensile stress at yield, elongation at break and stress values in a tensile test
- El-Nemr KF (2011) Effect of different curing systems on the mechanical and physico-chemical properties of acrylonitrile butadiene rubber vulcanizates. *Mater Des* 32(6):3361–3369
- Förster T, Blivernitz A (2021) Migration of mineral oil in elastomers. *J Rubber Res* 24(2):257–269
- Graham JL, Striebich RC, Myers KJ, Minus DK, Harrison WE (2006) Swelling of nitrile rubber by selected aromatics blended in a synthetic jet fuel. *Energy Fuels* 20(2):759–765
- Lachat V, Varshney V, Dhinojwala A, Yeganeh MS (2009) Molecular origin of solvent resistance of polyacrylonitrile. *Macromolecules* 42:7103–7107
- Loos K, Bruère VM, Demmel B, Ilmberger Y, Lion A, Johlitz M (2021) Future-oriented experimental characterization of 3D printed and conventional elastomers based on their swelling behavior. *Polymers* 13(24):4402
- Mathai AE, Thomas S (1996) Transport of aromatic hydrocarbons through crosslinked nitrile rubber membranes. *J Macromol Sci Phys* 35(2):229–253

- Musil B, Johlitz M, Lion A (2018) On the ageing behaviour of NBR: chemomechanical experiments, modelling and simulation of tension set. *Contin Mech Thermodyn* 32(2):369–385
- Pazur RJ, Cormier JG, Korhan-Taymaz K (2014) The effect of acrylonitrile content on the thermo-oxidative aging of nitrile rubber. *Rubber Chem Technol* 87(1):53–69
- Röthemeyer F, Sommer F (2013) *Kautschuk Technologie*. Hanser
- Scheuermann SS, Forster S, Eibl S (2017) In-depth interpretation of mid-infrared spectra of various synthetic fuels for the chemometric prediction of aviation fuel blend properties. *Energy Fuels* 31(3):2934–2943
- Starmer PH (1993) Swelling of nitrile rubber vulcanizates—part 3: factors affecting maximum swelling. *J Elastom Plast* 25:188–215
- Zaghdoudi K, Jaunich W (2019) Scission, cross-linking, and physical relaxation during thermal degradation of elastomers. *Polymers* 11(8):1280
- Zschocke A, Scheuermann S, Ortner J (2012) High biofuel blends in aviation (HBBA). https://ec.europa.eu/energy/sites/ener/files/documents/final_report_for_publication.pdf. Cited 27 Feb 2022

Chapter 17

FT-IR Microscopic Analysis of the Chemical Change in the Molecular Structure After Ozone Ageing of Natural Rubber



Caroline Treib, Alexander Lion, and Michael Johlitz

Abstract Natural rubber (NR) is a polymer relevant for many industrial applications, e.g., for its beneficial resistance against crack growth. However, applied as hose, sealing or tyre side wall it is not permanently resistant against inevitable environmental influences like UV-light, oxygen, or ozone. The latter is considered in this contribution. Ozone attack results in a fast surface crack development therefore antiozonants are added to NR compounds to reduce the velocity of degradation. Structural change is measured in Fourier transformed infrared (FT-IR) spectra of the ozone-aged surface. They show peaks assigned to oxidation products that evolve and change after artificial ageing. To discover the depth of change in molecular structure, a map of IR spectra is recorded in the cross-section by FT-IR microscopy. NR without antiozonants shows an ageing front line and a gradient of ageing intensity. Compounds including antiozonants change less pronounced in their FT-IR spectra. Therefore, other methods, e.g., differential scanning calorimetry is going to be applied to these compounds.

Keywords FT-IR · Ozone · NR (Natural rubber) · Antiozonants · Ageing

17.1 Introduction

Ozone ageing severely deteriorates natural rubber (NR), published as early as 1945 by Newton (1945). As a result, reduction in component lifetime has remained a discussed issue as the review of Mars and Fatemi (2005) shows.

C. Treib (✉) · A. Lion · M. Johlitz

Fakultät für Luft- und Raumfahrttechnik, Institut für Mechanik, Universität der Bundeswehr München, Werner-Heisenberg-Weg 39, 85577 Neubiberg, Germany

e-mail: caroline.treib@unibw.de

URL: <https://www.unibw.de/lrt4>

A. Lion

e-mail: alexander.lion@unibw.de

M. Johlitz

e-mail: michael.johlitz@unibw.de

Ozone concentration is measured either as mass per volume in $\mu\text{g}/\text{m}^3$, which is common for long measurements in meteorological stations, or as volume fraction in parts per hundred million (pphm) typically used in laboratory devices. At a given air pressure of 1013 hPa and a temperature of 20 °C, the relation calculates to:

$$1 \text{ pphm} \hat{=} 20 \mu\text{g}/\text{m}^3 \quad (17.1)$$

Maximum ground-level ozone concentrations have been measured by 6 German meteorological stations over $300 \mu\text{g}/\text{m}^3$, respectively, 15 pphm in the summer of 2019 in the South and West of Germany (Bundesumweltamt 2019). Long-term average values measured by Bavarian meteorological stations range from 30 to $70 \mu\text{g}/\text{m}^3$ (Bayerisches Landesamt für Umwelt (LfU) 2020). The ambient ozone concentration is always the result of simultaneous production and decay of ozone molecules, stated by Seinfeld (1989). Local accumulations of air pollution especially by volatile organic compounds or nitrogen dioxide increase the steady state ozone level. In contrast, nitric oxide reacts with ozone reducing the ozone level. Thus, the measured equilibrium concentration is dependent on time and location. Energy to enhance the photolytic creation reaction in favour of ozone can be drawn from sunlight as Huntink et al. (2004) state or else from electric emissions, e.g., in industrial sites. Temperature merely influences ozone creation stated by Huntink et al. (2004). In contrast, increasing the temperature is a common approach to accelerate the oxidation of rubber, see Neuhaus et al. (2017) or Herzig (2020). Accelerated thermo-oxidative ageing is achieved at temperatures of 70 °C and more according to Herzig et al. (2017). Tamm (2002) published measurements that show a rapid acceleration in decay of ozone in exhaust gas catalysts at about 60 °C.

Crack development is observed on the surface with cracks being lateral to the strain direction as stated by several authors (Andrews and Braden 1961; Lake 1970; Huntink et al. 2004). According to Cataldo (2019), its initiation is caused by the combination of mechanical strain and cleavage during ozonolysis of alkenes, studied by Criegee (1975). To avoid the cleavage in the main chains, antiozonants such as *p*-phenylenediamines (PPD) or paraffinic wax are added. Both reduce chain scission; however, PPDs are most popular according to Huntink et al. (2004) and Cataldo (2018). Paraffinic wax migrates to the surface to form a physical barrier towards ozone attack according to Lake (1970), whereas PPDs react with ozone faster than rubber and forms an additional barrier with the reaction products, as described by Cataldo (2018). Still, neither of the two antiozonants prevents degradation caused by ozone enough to inhibit crack formation under dynamic mechanic loading completely. Moreover, their effect depends on migration efficiency, stated by Ignatz-Hoover et al. (2003). A procedure to categorise the ozone resistance given in DIN-ISO1431 (2017) takes crack length, shape, and number into account.

In contrast to plenty publications dealing with cracks in rubber due to ozone, no publications are known to the authors that examine the depth to which ozone attacks natural rubber ahead of crack initiation. Thus, this study analyses the chemical change in the molecular structure of NR via Fourier transformed infrared (FT-IR)

Table 17.1 Natural rubber compounds

Component (phr ^a)	<i>M1</i>	<i>M2</i>	<i>M3</i>
NR CV 60		100	
Carbon black N330		40	
Zinc oxide		3	
Stearic acid		1	
Accelerator TBBS		1	
Sulphur		2	
6PPD	3	3	0
Paraffin wax	3	0	0

^aParts per hundred rubber

spectroscopy. In addition to single points on the surface of aged samples, spectral mappings in the cross-section show the ageing depth and its gradient for different artificial ageing intensities.

17.2 Experimental

17.2.1 Material

Three compounds of natural rubber are investigated differing solely in antiozonants added. The mixing ratios are given in Table 17.1. The vulcanisation system is based on zinc oxide, stearic acid, sulphur, and the accelerator TBBS.¹ Two widely applied antiozonants, popular in industry as stated by Huntink et al. (2004) and Cataldo (2018), are included: 6PPD² and paraffin wax. The latter migrates to the surface to build a physical barrier to ozone attack. The diamine 6PPD reacts with ozone molecules as a scavenger and leaves reaction products behind that offer an additional physical barrier (Cataldo 2019). Besides 6PPD, compound *M1* is mixed with the physically protecting paraffin wax. Compound *M2* contains solely the chemical antiozonant, and compound *M3* is completely free of antiozonants.

17.2.2 Artificial Ageing Strategy

To properly reproduce natural degradation in a laboratory, an artificial acceleration is necessary to reduce the time scale of a component's true lifetime (Mitra et al. 2006).

¹ *N*-tert-Butyl-2-benzothiazolesulfenamide.

² *N*-(1,3-dimethylbutyl)-*N'*-phenyl-*p*-phenylenediamine.

Table 17.2 Ageing parameters ozone concentration and ageing time

Ageing times	(h)	4	12	37	111
Ozone concentrations	(pphm)	25	36	52	75

Since an increase in temperature correlates to an accelerated ozone decay, a constant temperature of 40 °C is applied in the experiments in accordance with standard DIN-ISO1431 (2017).

To regulate an ozone climate simulator, a faster measurement of ozone concentration compared to a meteorological station is necessary. Regarding an ensured precision of about 5 pphm, applied concentrations start at 25 pphm resulting in an acceleration by increased concentration. To avoid the risk of not only accelerating the ageing process but changing its behaviour, no more than 75 pphm ozone concentration is applied. In between the range, a logarithmic distribution is chosen as for the range of ageing times applied, listed in Table 17.2.

17.2.3 *Fourier Transform Infrared Spectroscopy Method*

The method of Fourier transform infrared spectroscopy (FT-IR) is based on molecular vibrations in response to infrared radiation. Molecular mass and binding strength influence the vibration so that characteristic spectra can be recorded for different materials or states of a material. Functional groups as well as main chains of the polymer depending on its composition result in absorbed bands. Therefore, an identification of chemical change in molecular structure, as it occurs after different ageing times, can be identified.

A preliminary test records FT-IR spectra on the surface of artificially aged samples to gain information about the changes in molecular structure due to the ageing with ozone. These are conducted with an attenuated total reflectance (ATR) unit ‘*Platinum ATR*’ by *Bruker* on the ‘*Vertex70*’ model that uses a monolithic diamond crystal. A general scheme of the measurement is shown in Fig. 17.1. An IR beam is directed through an ATR crystal towards the rubber sample. The sample is pressed with the ozone-aged surface to the crystal to ensure sample-crystal contact. The IR beam hits the sample to create an evanescent wave that refracts the IR beam to be collected by a detector. The range of wavelength is 400–4000 cm^{-1} with a resolution of 4 cm^{-1} . Each measurement consists of 32 scans.

Subsequently, an FT-IR microscope with an attenuated total reflectance (ATR) attachment called *LUMOS II* by *Bruker* is used to conduct experiments on the cross-section of the material. The recorded spectra cover wavelengths from 750 to 4000 cm^{-1} with a resolution of 1.6 cm^{-1} . For each spectra, the mean of 5 scans is calculated. The cryo-cooled germanium crystal maps a field of 40 times 40 μm

Fig. 17.1 Diagram of the measurement setup of the single spectrum ATR FT-IR device

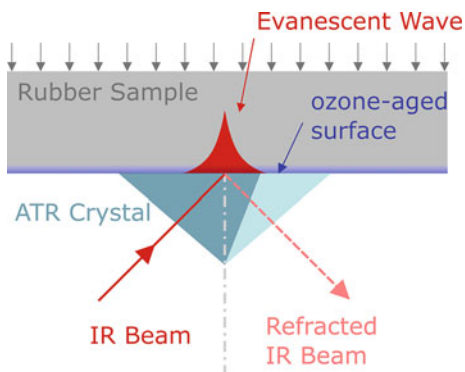
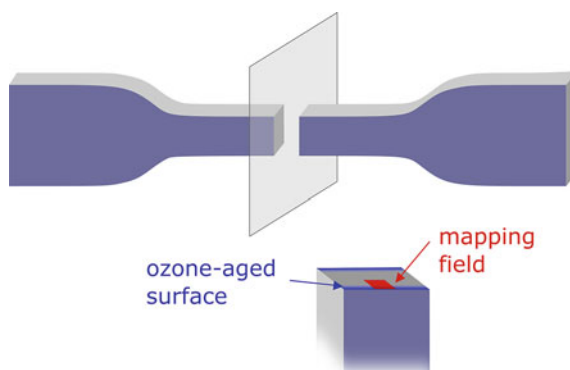


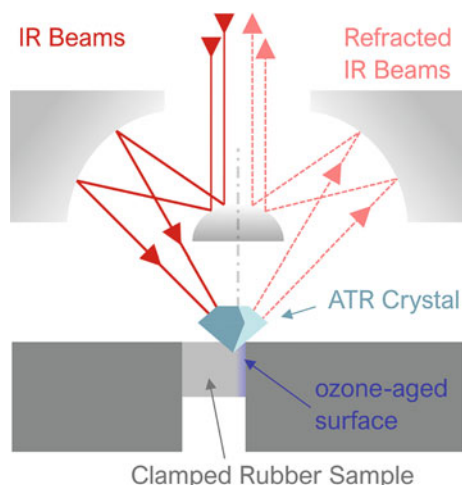
Fig. 17.2 Cutting plane through ozone-aged sample and mapping field for FR-IR microscopy



dissolved into 32 times 32 points with distinct spectra recorded. A general sketch of the method is shown in Fig. 17.3 that shows the incoming IR beams are directed and collected via mirrors in order to cover the mapping field. The cutting plane through a previously ozone-aged sample is pictured in Fig. 17.2. To measure a gradient in the spectra of the cross-section, the mapping field is chosen to cover the aged surface area and some part of the sample centre. Cutting the sample with a sharp scalpel delivered the best results in terms of surface smoothness, that is crucial to obtain optimal results. Then the rubber sample is clamped with the prepared cross-section facing up.

Moisture and carbon dioxide cause interference in the measurement of the spectra, since the samples are surrounded by ambient air of the laboratory. Thus, the response of a measured base line in air is automatically eliminated in subsequent measurements by the device. In both devices, a base line is taken ahead of each measurement.

Fig. 17.3 Diagram of the objective of the ATR FT-IR microscope on the sample



17.3 Results

The intensity of FT-IR spectra depends strongly on the contact pressure between crystal and sample material. Therefore, the y -axis description of the absorbance is of arbitrary unit without relevance in absolute value. Despite different intensities, comparing aged to pristine spectra reveals evolving and dissolving peaks. Thus, a structural degradation gradient is proven between pristine and ozone-aged NR compounds.

17.3.1 Surface Spectra

Strongly changing bandwidth due to ozone ageing is detected by FT-IR spectra of the surface of the three NR compounds given in Table 17.1. The absorbance is compared before and after ageing in a concentration of ozone of 15 ppm for 48 h. This extremely high concentration of ozone is chosen to ascertain a strong change in molecular structure in order to detect bandwidth of wave numbers where peaks change due to ageing.

For each NR compound, Fig. 17.4 shows a spectrum of the pristine bulk material in comparison with a spectrum of the aged surface. The peaks correlating to the main polymer branches, according to Hummel (1968), are present in all three compounds. Besides, several evolving peaks are detected given in an overview in Table 17.3.

Main polymer chains are present in all compounds for both pristine and aged condition. Hence, their correlating vibration peaks remain in the spectra after ageing. Compared to peaks at larger wavelengths present in pristine and aged spectra at 1370, 1435, and 825 cm^{-1} lower ones at 2962, 2920, and 2850 cm^{-1} are more pronounced.

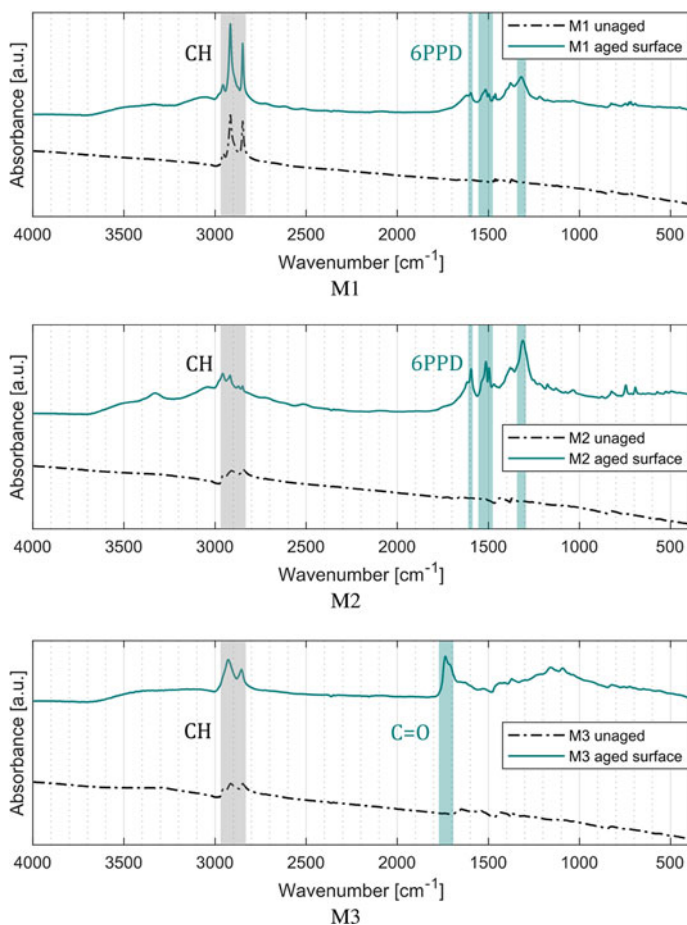


Fig. 17.4 FT-IR spectral difference between pristine bulk and aged surface after 48 h at 15 ppm

Table 17.3 Wavelength correlation to vibration of molecular functional groups

		Main polymer branches					
Wavelength (cm ⁻¹)	2962	2920	2850	1370	1435	825	
Functional groups	$\nu_a\text{CH}_3$	$\nu_a\text{CH}_2$ CH	$\nu_s\text{CH}_2$ CH	$\delta_a\text{CH}_3$	$\delta_s\text{CH}_3$	$\delta = \text{CH}_2\text{O}$	
		Peaks that evolve after ageing					
Wavelength (cm ⁻¹)	1740	1740–1660		1600	1518, 1500, 1320		
Functional groups	C=O	Oxidised side groups		C–O, C–C, C=C–C=C	6PPD		

According to Hummel (1968), they correlate to the symmetrical and asymmetrical stretching vibrations of $\nu_a\text{CH}_3$, $\nu_a\text{CH}_2$, $\nu_s\text{CH}_2$, $\delta_a\text{CH}_3$, $\delta_s\text{CH}_3$, $\delta = \text{CH}_2$, CH .

However, some peaks are evolving after ozone loading. Due to the intense artificial ageing, 6PPD is expected to have migrated to the surface. The assigned spectral response is evolving peaks about 1518, 1500, and 1320 cm^{-1} . They are present in the spectra of the aged NR compound *M1* and *M2*. NR compound *M1* contains wax in addition to 6PPD, which forms a thin, stretchable, and protective layer by migration of wax to the surface, stated, e.g., by Lake (1970). The additional wax to 6PPD on the surface might be causing the reduced peak intensity compared to the main polymer chain peaks, since the main peaks of paraffin wax at 2900–3000 cm^{-1} overlap with the main polymer chain peaks.

An increase in intensity of a peak at 1600 cm^{-1} may correlate to C–C or C–O bonds after Hummel (1968); however, Zheng et al. (2021) assigns the peak to the vibration of the group C=C–C=C. Consistent with the results of Zheng et al. (2021), a strong peak forms after ageing the unprotected NR compound *M3* at about 1740 cm^{-1} , a wave number correlating to carbonyl compounds (C=O). Carbonyl compounds such as ketone groups are as well stated by Criegee (1975) to arise from disrupted vinyl groups in the process of ozonation of alkenes as in polyisoprene.

17.3.2 Cross-Section Spectra

In the surface spectra, bandwidths of interest are detected. To compare neighbouring measurement points in the FT-IR microscopy to each other, evolving peak areas are related to persistent main chain peak areas, that should not change much due to ozone ageing. Subsequently, for every measurement point in FT-IR microscopy, the evolved peak areas and the consistent peak areas of the main polymer chains are integrated. The relative change of peak areas to the main chain peak areas eliminates differences in intensity of the single spectra in the mapping field.

Figure 17.5 shows a sample of natural rubber compound *M3* after 111 h at 75 pphm. The peak area of C=O between the wave numbers 1700–1780 cm^{-1} and the consistent main chain peak areas between 2830 and 2980 cm^{-1} are depicted. To eliminate differences in intensity, the C=O peak areas are divided by CH peak areas. The results are displayed for one line perpendicular to the sample surface located in the first few μm on the x -axis. Towards the sample surface (Fig. 17.5) the oxidation intensity, respectively the C=O peak area, increases fast. The total depth of molecular change due to ozonation reaches about 20 μm .

Examining the mapped field not only in one line but the whole area as shown in Figs. 17.6 and 17.7, the smoothness of the oxidation boarder is visible. Four different ageing states of material compound *M3* are shown in Fig. 17.6: 75 pphm for ageing times of 111, 37, 12, and 4 h. In contrast, Fig. 17.7 depicts the results for different ozone concentrations of 75, 52, 36, and 20 pphm at an ageing time of 111 h. The samples' oxidised surfaces are located on the right hand side of the image sections. They are adjacent to the clamping system's rubber coated jaws that mark the samples'

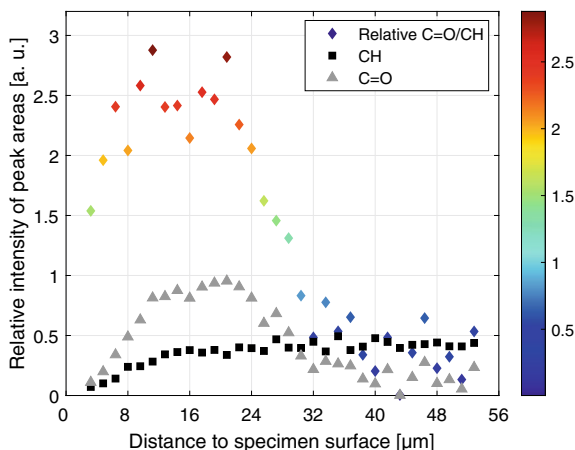


Fig. 17.5 Relative increase of carbonyl compound peak areas (C=O) to main chain peak areas (CH) in compound *M3* after 111 h at 75 ppm towards the sample surface (0 μm)

ends. The clamping rubber shows a spotted area as there is no significant difference in the calculated peak relation but only measurement noise.

As in Fig. 17.5, the colour shows an increase in relative C=O peak areas to main chain peak areas towards red. Figure 17.7b, c show an overlap at the edge of two measurement points. Since the ATR crystal points to the rubber surface at a contact pressure, the deformation of the rubber is leading to an overlap of the mapping squares.

The shape of the ageing front line seems to be parallel to the surface but not always homogeneous. Except for Figs. 17.6d and 17.7d no measurement shows a homogeneous and parallel ageing front line. A reduction in ageing time, see Fig. 17.6, leads to less intense relative peaks of C=O. In addition, shortening the ageing time reduces the ageing depth from about 20 μm after 111 h to about 10 μm after 4 h of exposure. Comparing 37–111 h of exposure the depth seems similar but the intensity of ageing rises for the latter. Lowering the ozone concentration, see Fig. 17.7, has no significant influence on the ageing depth, but the ageing intensity rises with increasing ozone concentration. Thus, both intensity and depth of the ageing, assessed as C=O peak areas, are dependent on the ageing parameters time and concentration.

Attempts to measure a similar gradient in NR compound *M1* and *M2* in the relation of peak areas at 1560–1640 to 2830–2980 cm^{-1} failed. Carbon black, part of all three compounds analysed, disturbs the IR measurement due to its high index of refraction close to that of the diamond. Thus, the measurement noise induced might cover possible changes of spectra inside the protected rubber compounds. Moreover, the protective layer, built by the antiozonants without mechanical strain present during ageing, obstructs the migration of ozone into the bulk. Only the spotted colour correlating with the samples' ends is visible in the results of the FT-IR mappings, shown in Fig. 17.8.

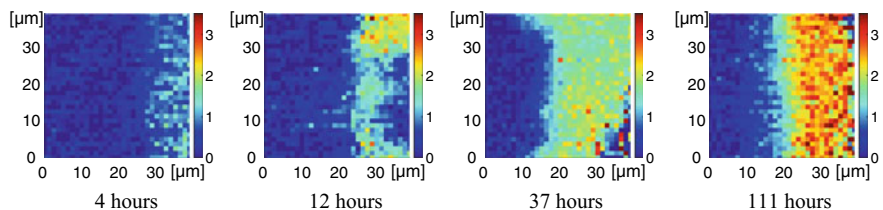


Fig. 17.6 Mappings of relative carbonyl compound ($\text{C}=\text{O}$, $1700\text{--}1780\text{ cm}^{-1}$) peak size in surface area of NR compound *M3* samples after 75 pp hm for ageing times of 4, 12, 37, and 111 h

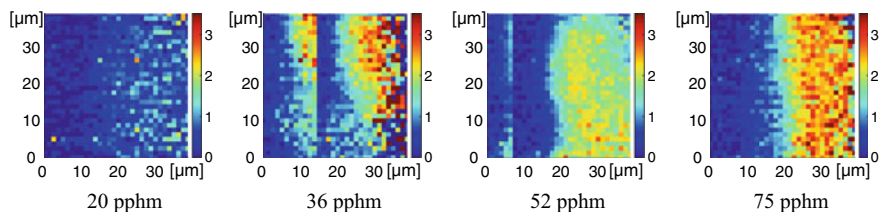


Fig. 17.7 Mappings of relative carbonyl compound ($\text{C}=\text{O}$, $1700\text{--}1780\text{ cm}^{-1}$) peak size in surface area of NR compound *M3* samples after the ageing time of 111 h at ozone concentrations of 20, 36, 52, and 75 pp hm

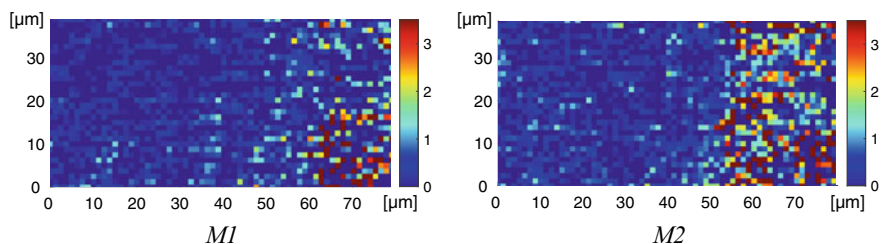


Fig. 17.8 Mappings of relative peak size $1560\text{--}1640$ to $2830\text{--}2980\text{ cm}^{-1}$ in surface area of NR compounds *M1* and *M2* after the ageing time of 111 h at ozone concentration of 75 pp hm

17.4 Discussion

All NR compounds show changes in FT-IR spectra after exposure to ozone. Even the compound *M1*, protected by wax and 6PPD, clearly changes its IR spectra on the surface after ageing, as both other compounds do. The main polymer chains persist, whereas the chemical reaction affects the molecular structure so that characteristic side groups change depending on the antiozonants applied. The unprotected NR compound *M3* forms $\text{C}=\text{O}$ sidegroups, whereas the addition of 6PPD seems to hinder further reaction after $\text{C}=\text{C}-\text{C}=\text{C}$, $\text{C}-\text{C}$, and $\text{C}-\text{O}$ are built.

As the FT-IR microscopy shows the ageing depth and intensity is not overall homogeneous but depends on the ozone exposure in terms of ozone concentration

and ageing time. After 111 h at 75 ppm ozone concentration, the oxidised carbonyl groups in compound *M3* reach to a depth of 20 μm . Ozonation depth and intensity of the evolving peaks of oxidised sidegroups reduce with lower ozone concentration and shorter ageing time. The ozone concentration seems to have a stronger influence on the ozonation intensity in contrast to the ageing time that also influences the depth of the ageing front line.

17.5 Conclusion and Outlook

The results of the FT-IR spectral analysis show that the unloaded NR compounds, though lacking cracks after ozone ageing, undergo a molecular change. The sample bulk shows no molecular change, visible by means of the FT-IR method, but towards the surface change is detected. The depth of the molecular change depends foremost on the ageing time. Whereas, both ageing time and ozone concentration influence the intensity of the molecular change. Adding antiozonants, 6PPD and paraffin wax, the surface spectra change but no gradient is obtained by the FT-IR method. Thus, further experiments are planned to gain extended insight on a possible ageing gradient or changing mechanical properties in protected NR compounds. First, differential scanning calorimetry might show changes in thermo-mechanical properties such as glass-transition temperature. Second, the overall increase of the amount of oxygen in the samples after ozone exposure will be assessed with nuclear magnetic resonance measurements.

Acknowledgements We thank Dr. rer. nat. Lara Greiner (*Wehrwissenschaftliches Institut für Werk- und Betriebsstoffe*) for the supply of FT-IR equipment and assistance with spectroscopy techniques for FT-IR microscopy. Parts of this research paper are funded by dtec.bw—Digitalization and Technology Research Center of the Bundeswehr which we gratefully acknowledge [project FLAB-3Dprint].

References

- Andrews EH, Braden M (1961) The reaction of ozone with surfaces of natural rubber, and its dependence upon strain. *J Polym Sci*
- Bayerisches Landesamt für Umwelt (LfU) (2020) Langzeitverläufe der Schadstoffbelastung an den bayerischen LÜB-Messstationen. www.lfu.bayern.de. Accessed 16 Nov 2021
- Bundesumweltamt (2019) Aktuelle Luftdaten. www.umweltbundesamt.de/daten/luft/luftdaten/karten. Accessed 16 Nov 2021
- Cataldo F (2018) Early stages of p-phenylenediamine antiozonants reaction with ozone: radical cation and nitroxyl radical formation. *Polym Degrad Stabil* 147:132–142
- Cataldo F (2019) Protection mechanism of rubbers from ozone attack. *Ozone Sci Eng* 41(4):358–368
- Criegee R (1975) Mechanism of ozonolysis. *Angew Chem Int Ed* 14

- DIN-ISO1431 (2017) Elastomere oder thermoplastische Elastomere—Widerstand gegen Ozonrisbildung—Teil 1: Statische und dynamische Dehnungsprüfung (ISO 1431-1:2012). Beuth-Verlag, Berlin
- Herzig A (2020) Thermo-oxidative ageing of elastomers. A contribution to the experimental investigation and modelling. PhD thesis, Universität der Bundeswehr München
- Herzig A, Sekerakova L, Johlitz M, Lion A (2017) A modelling approach for the heterogeneous oxidation of elastomers. *Contin Mech Thermodyn*. <https://doi.org/10.1007/s00161-017-0568-8>
- Hummel DO (1968) *Atlas der Kunststoffanalyse*. Hanser
- Huntink NM, Datta RN, Noordermeer JWM (2004) Addressing durability of rubber compounds. *Rubber Chem Technol* 77(3):476–511
- Ignatz-Hoover F, To BH, Datta RN, De Hoog AJ, Huntink NM, Talma AG (2003) Chemical additives migration in rubber. *Rubber Chem Technol* 76(3):747–768
- Lake GJ (1970) Ozone cracking and protection of rubber. *Rubber Chem Technol* 43(5)
- Mars WV, Fatemi A (2005) Multiaxial fatigue of rubber: part II: experimental observations and life predictions. *Fatigue Fract Eng Mater Struct*
- Mitra S, Ghanbari-Siahkali A, Almdal K (2006) A novel method for monitoring chemical degradation of crosslinked rubber by stress relaxation under tension. *Polym Degrad Stab* 91:2520–2526
- Neuhaus C, Lion A, Johlitz M, Heuler P, Barkhoff M, Duisen F (2017) Fatigue behaviour of an elastomer under consideration of ageing effects. *Int J Fatigue* 104:72–80. <https://doi.org/10.1016/j.ijfatigue.2017.07.010>
- Newton RG (1945) Mechanism of exposure-cracking of rubbers. With a review of the influence of ozone. *Rubber Chem Technol*
- Seinfeld JH (1989) Urban air pollution: state of the science. *Science* 243(4892):745–752. American Association for the Advancement of Science
- Tamm U (2002) Beseitigung von organischen Schadstoffen in Abgasen durch Oxidation mit Ozon. PhD thesis, Martin-Luther-Universität Halle-Wittenberg
- Zheng T, Zheng X, Zhan S, Zhou J, Liao S (2021) Study on the ozone aging mechanism of natural rubber. *Polym Degrad Stabil* 186(109):514. <https://doi.org/10.1016/j.polymdegradstab.2021.109514>

Chapter 18

Investigation of the Viscosity of Liquid Silicone Rubber for Molding Microstructures in the Injection Molding Process



Dennis F. Weißer, Levente Szántó, Dennis Mayer, Johannes Schmid, and Matthias H. Deckert

Abstract The processing of liquid silicone rubber (LSR) in the injection molding process is becoming increasingly important. The reasons for this are its outstanding properties and economic processability. The functionalization of surfaces through nano- or microstructures introduced directly in the injection mold opens up new fields of application. For example, antibacterial, self-cleaning or tribologically and haptically optimized surfaces can be produced directly during injection molding. To ensure process-reliable molding of the microstructures, the influence of various process settings on moldability is investigated in this work. The viscosity of the LSR plays a decisive role. If it is too high, the LSR cannot lay into the nano- and microstructures and the structures will not be completely imprinted. The viscosity of LSR is influenced by several overlapping factors during processing. While the shear stress and the initial temperature input reduce the viscosity, the crosslinking reaction starts after the incubation time at a certain temperature, which abruptly increases the viscosity. Dynamic differential scanning calorimetry (DSC), oscillating rheometer tests and dielectric thermal analysis (DEA) measurement methods are used to investigate the properties of LSR during processing. Incubation times and crosslinking reactions are determined and compared for rheometer and DSC measurements. An attempt has also been made to define a gel point. Here, a clear distinction must be

D. F. Weißer (✉) · D. Mayer · J. Schmid · M. H. Deckert
Esslingen University of Applied Sciences, Kanalstraße 33, 73728 Esslingen, Germany
e-mail: dennis.weisser@hs-esslingen.de

D. Mayer
e-mail: dennis.mayer@hs-esslingen.de

J. Schmid
e-mail: johannes.schmid@hs-esslingen.de

M. H. Deckert
e-mail: matthias.deckert@hs-esslingen.de

L. Szántó
Freiburger Materialforschungszentrum, Stefan-Meier-Straße 21, 79104 Freiburg im Breisgau, Germany
e-mail: levente.szanto@yahoo.com

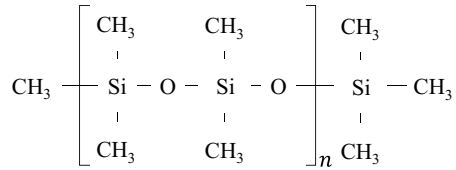
made between physical gel, consisting of entanglements and intermolecular interactions, and chemical gel, consisting of covalent bonds due to crosslinking. Since the physical gel recedes very quickly after destruction by shear stress, it is difficult to determine the chemical gel point using rheometry. Here DSC and DEA measurements help to determine the chemical crosslinking behavior. In addition to material characterization, microstructures are produced in an injection molding process with varying mold temperatures and injection speeds. Afterward, the microstructures are characterized for their degree of molding. It is shown that LSR molds the microstructures very reliably, even with poorly selected process parameters. This can be justified by the additional volume dilation, which is not taken into account in any of the measurement methods investigated. The viscosity of the injected, cold LSR has already decreased due to the shear stress. In addition, the temperature input initially reduces the viscosity. While the incubation time prevents immediate crosslinking as the temperature rises, the low-viscosity LSR expands due to thermal expansion and pushes into the nanostructures or microstructures. This is when the crosslinking reaction begins, during which the viscosity increases abruptly. The structures were not completely formed only at very high mold temperatures and low injection speeds. Here, it is helpful to cool the mold surface briefly and locally using variothermal tempering before injection.

Keywords Liquid silicone rubber (LSR) · Injection molding · Processing · Crosslinking · Nanostructure · Rheology · Gel point · DEA · Viscosity · Incubation time

18.1 Introduction

The importance of liquid silicone rubber (LSR), a rubber developed especially for injection molding in the 1970s, has increased continuously in recent years. The reasons for this are its unchanging mechanical and electrical properties over a wide temperature range, biocompatibility, good resistance to aging, UV, ozone and chemicals (Osswald et al. 2018; Jerschow 2001; Beyer and Wolf 2015; Ratner 2013; Tomanek 1990; The Dow Chemical Company 2012; Moretto et al. 2010). This allows LSR to be used for seals in the automotive and aerospace industries, as cable insulation for the electrical industry, baking dishes and pacifiers for the food industry, and even medical implants and devices (Tomanek 1990; Lambrecht et al. 2003; Wolf et al. 2008; Owen and Dvornic 2012). Added to this are the excellent optical properties, which enable its use in LEDs and matrix headlights (Dow Corning Corporation 2019). In addition to the outstanding application properties, there are also advantages in processing: LSR can be precisely processed in the injection molding process in short cycle times, sometimes without post-curing, and yet has a long pot life at room temperature (Harkous et al. 2016). Due to the low viscosity, which varies between that of honey and water depending on the type, complex and thin-walled components with long flow path lengths can also be realized with LSR.

Fig. 18.1 Base polymer poly (dimethyl) siloxane PDMS ($n = 0, 1, \dots$) with terminal vinyl groups



LSR is produced from two components, A and B, in a platinum-catalyzed addition reaction. The base polymer is poly (dimethyl) siloxane (PDMS) shown in Fig. 18.1, which can be adapted to the requirement profile by substitution of various functional groups. One of the two components, usually component A, contains polymer and the catalyst (platinum complex) necessary for the reaction, the other component B contains polymer and the crosslinking agent (H-Siloxane) (Tomanek 1990; Verheyen et al. 2016). The crosslinking reaction of LSR can be described by the Chalk–Harrod catalysis cycle (Beyer and Wolf 2015). The advantage of the addition reaction over the peroxide crosslinking also used is that no low-molecular, volatile components are released (Röthemeyer and Sommer 2013). The degree of crosslinking can be determined by the chain length and the definition of a certain number of functional groups in the starting components during the chemical production process (Beyer and Wolf 2015; Wacker Chemie and von Siliconen 2020). The crosslinking reaction in LSR, as in all heat-activated thermoset materials, is exothermic and irreversible, forming a three-dimensional network of covalent bonds. By adding a reaction retarder, the so-called inhibitors, the reaction can be adjusted to the injection molding process. In the initial state, the platinum catalyst is first deactivated by the inhibitor, which in the case of LSR is usually alkynols. An increase in temperature deactivates the platinum-inhibitor complex and crosslinking begins (Beyer and Wolf 2015).

It can be observed that the manufacture of plastic products with microstructures using injection molding has increased significantly in recent times. Producing functional surfaces with high precision and reproducibility in mass production with a short cycle time is particularly attractive (Attia and Alcock 2010). On the one hand, this can involve downscaling and functionalization of fluidic systems and microsystems technology, for example, in analytical applications like lab-on-a-hip applications (Rapp 2017). On the other hand, there is the field of surface structures. In this field, surface properties are deliberately influenced by microstructures, as is the case with the lotus flower (Nosonovsky and Bhushan 2008), moth eye (Boden and Bagnall 2012), the antibacterial wings of the cicada (Pogodin et al. 2013) or the tribologically optimized skin of the snake (Baum et al. 2014). Because of its low viscosity in the uncured state, compared to molten thermoplastics, LSR is particularly suitable for accurate contour molding. To reproduce the smallest contours or microstructures of the mold surface as precisely as possible in LSR in the injection molding process, the first moments after injection are particularly interesting. Then the viscosity of the LSR compound is still low enough to permeate the fine surface structures. Since the crosslinking reaction of the fast-curing LSR is extremely accelerated when the hot

mold is touched, leading to an increase in viscosity, this presents a particular challenge. In contrast to the rarely investigated field of LSR processing, there is already experience in molding microstructures in thermoplastics in literature (Kuhn et al. 2010; Kübler 2010).

Following the investigation and modeling of the heat transfer and the degree of crosslinking in a previous publication (Weißer et al. 2020), this paper investigates the rheological properties of the LSR component during processing and consider its ability to form micro- and nanostructures. For this purpose, a rheological approach with the determination of viscosity and the gel point as well as thixotropic properties, a thermal approach to determine the degree of crosslinking and a dielectric approach to determine the ion viscosity are investigated. All methods are compared, and finally, the results are verified with practical investigations and measurements on injection-molded parts with microstructures.

18.2 Material and Methods

18.2.1 Theoretical Approach

18.2.1.1 Process-Dependent Viscosity

To make a statement about the quality of the impression of nano- and microstructures in LSR, depending on various injection molding process parameters, information is needed about the viscosity of the LSR at the beginning of the injection molding process. This is because above a certain viscosity, the material can no longer be pressed into the nanostructures and thus they are no longer molded; see Fig. 18.2a. If the viscosity is low enough, the material can penetrate the nanostructures and form them accurately; see Fig. 18.2b.

The viscosity of LSR depends on several factors: (Osswald and Rudolph 2014; Henze 1999).

- Temperature: As the temperature increases, the viscosity decreases in general, but as the crosslinking accelerates the viscosity increases (Bont et al. 2021; Buyl et al. 2013).
- Shear rate: LSR exhibits shear-thinning behavior. The greater the shear rate, the lower the viscosity of the LSR (Moretto et al. 2010; Haberstroh et al. 2002; Bont et al. 2021).
- Degree of crosslinking: The greater the degree of crosslinking, the higher the viscosity.
- Pressure: The higher the pressure, the greater the viscosity (GÖTTFERT Werkstoff-Prüfmaschinen GmbH 2021).
- Filler content: The greater the filler content, the higher the viscosity (Geng et al. 2017).

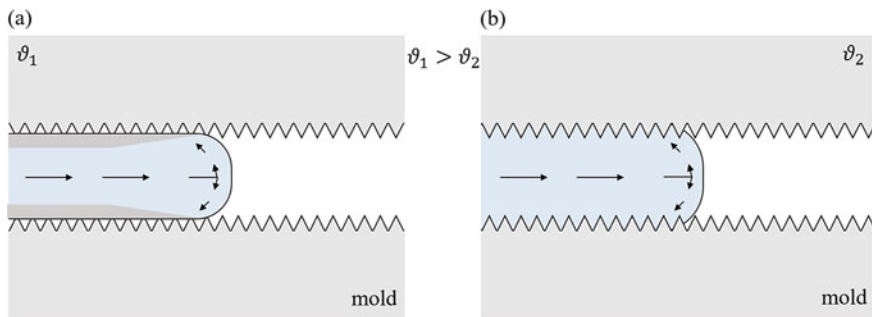
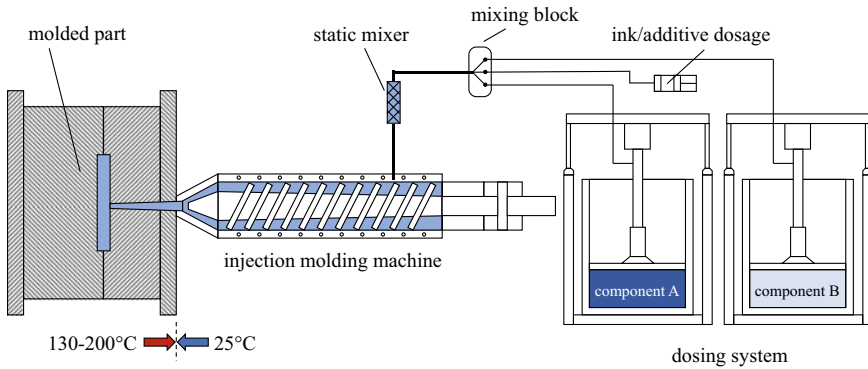


Fig. 18.2 Impression principle of nanostructures in LSR. **a** Incomplete molding due to high viscosity. **b** Complete molding of the nanostructures. Figure is derived from Klaiber (2010) who defined it for thermoplastics, but swelling flow theory is, according to Eyerer (Eyerer et al. 2008), also applicable to LSR

In reality, all these effects overlap and influence the viscosity of the LSR. When LSR is processed via injection molding process, shown schematically in Figs. 18.3 and 18.4, it is present in its initially state at room temperature and is conveyed from two containers (component A and component B) through thick hoses to the injection molding machine with the aid of a metering system. Shortly before reaching the injection unit, components A and B are combined and mixed in the static mixer. This is where the first intensive shearing of the material takes place. In the injection unit, the material is conveyed by the screw toward the mold and metered. A second shear stressing of the LSR material takes place. The viscosity decreases due to the shear stress, as physical bonds such as entanglements, hydrogen bonds and van der Waals forces are loosened. However, as the material remains in the injection unit after the metering process until the next shot, these physical bonds are re-established after a certain time and viscosity increases again; see Fig. 18.4. This time-dependent effect is also known as thixotropy (Beyer and Wolf 2015).

Subsequently, the material is injected into the hot injection mold. Here it flows under high pressure due to the narrow gate geometry and experiences the greatest shear stress during the injection molding process. Although this is highly dependent on the gate design. While in thick gating systems, shear due to, e.g., high injection speeds has no influence on the material (Beyer and Wolf 2015; Hempel 2001; Bont et al. 2021), and in thin-walled gating systems, the material temperature can rise by up to 100 °C due to the pressure loss occurring and the high shear rate (Capellmann et al. 2003). As long as the crosslinking reaction has not yet started, an increase in temperature leads to a reduction in viscosity. In addition to the thin-walled gating system, molds with cold runner systems are also subject to higher shear stress during injection due to the narrow opening of the valve gate nozzle.

By the time it hits the hot mold wall, the LSR material has ideally not yet undergone any temperature increase, or the temperature introduced is not sufficient to start the temperature-dependent crosslinking reaction. Only the shear stress affects the viscosity, which drops sharply due to the shear introduced during injection. The shear



mold	plastification unit	static mixer	dosing system
1000-10,000 [s ⁻¹]	10-1000 [s ⁻¹]	1-10 [s ⁻¹]	0,1-1 [s ⁻¹]

Fig. 18.3 LSR injection molding principle with occurring shear rates increasing from metering system to mold

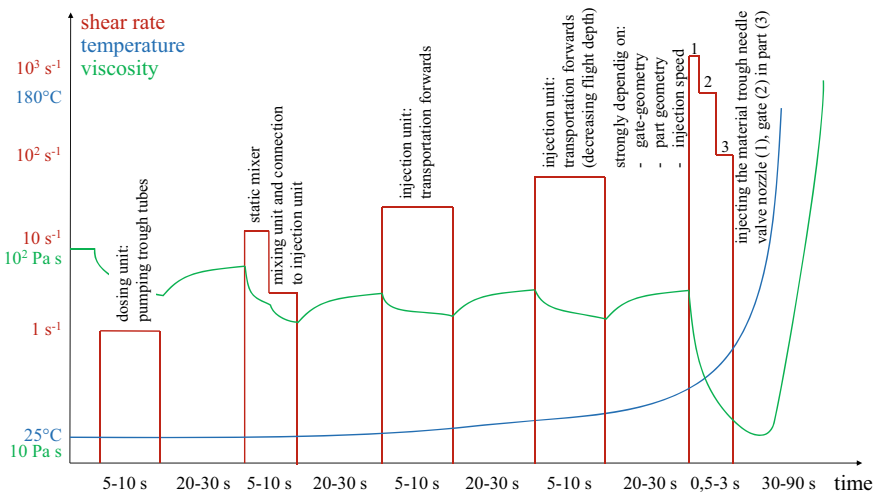


Fig. 18.4 Schematic representation of the shear stress of a virtual LSR particle that is conveyed via the metering unit into the mold. In addition to the schematic shear stress, the resulting temperature and viscosity are shown schematically

rates occurring during the injection molding of LSR throughout the entire process, from the metering unit to the mold, are shown in Figs. 18.3 and 18.4. During this process, the viscosity of the LSR can drop to values of approx. 1–10 Pa·s at high shear rates for standard silicones (Henze 1999).

There are various models to describe viscosity depending on temperature and shear rate (Cross-WLF, Carreau, Cross-Arrhenius). The Carreau–Yasuda model is

an often chosen model to describe the shear rate and temperature-dependent viscosity due to its great flexibility, Eq. (18.1) (Ou et al. 2017b; Aho and Syrjälä 2008):

$$\eta(\dot{\gamma}, T) = \eta_0(T) \left(1 + \left(\frac{\eta_0(T)\dot{\gamma}}{\tau} \right)^A \right)^{\frac{n-1}{A}} \quad (18.1)$$

where η describes the shear viscosity and η_0 is the apparent shear viscosity at zero shear rate. T describes the temperature, $\dot{\gamma}$ the shear rate, τ the critical shear stress which is roughly characterizing the transition of shear stress from the Newton range to the shear-thinning region. A stands for the width of the transition region, and n is the power-law index, defined by the slope of the viscosity curve concerning shear rate in the shear-thinning region. For the shear-thinning and fluid-like LSR, n is between 0 and 1.

Other models, like the Castro–Macosko viscosity model, describe the viscosity as a function of temperature and degree of crosslinking, Eq. (18.2) (Castro and Macosko 1982):

$$\eta(\alpha, T) = \eta_0 \left(\frac{\alpha_g}{\alpha_g - \alpha(t)} \right)^{(C_1 - C_2\alpha(t))} \quad (18.2)$$

with:

$$\eta_0 = A_\eta e^{\left(\frac{T_b}{T(t)}\right)} \quad (18.3)$$

where α describes the degree of crosslinking at time t and α_g is the degree of crosslinking at gel point. C_1 , C_2 , T_b and A_η are material-specific constants that are obtained from fitting experimental reactive and non-reacting viscosity data.

Still, other models, like the Cross model, describe the viscosity as a function of temperature, shear rate and pressure, Eq. (18.4) (Cross 1965):

$$\eta'(T, \dot{\gamma}, P) = \frac{\eta_0}{1 + \left(\frac{\eta\dot{\gamma}}{\tau^*}\right)^{1-n}} \quad (18.4)$$

with:

$$\eta_0 = B e^{\left(\frac{T_b}{T}\right)} e^{(\beta P)} \quad (18.5)$$

where τ^* is a material-specific constant that is numerically fitted and related to the transition between Newtonian and power-law regions of the shear dependence. B , β and T_b are material-specific constants that are obtained from fitting experimental viscosity data.

By substituting the Cross component defined in Eq. (18.4) into η_0 in the Castro–Macosko model in Eq. (18.2), the influence of shear rate can be combined with

the temperature and degree of crosslinking dependence. By substituting Eq. (18.5) instead of Eq. (18.3), also the pressure dependence can be included (Ziebell and Bhogesra 2016; Bont et al. 2021).

As soon as the LSR is in the mold and no longer under shear stress, physical bonds begin to form again via secondary valences and the viscosity increases. At the same time, the LSR comes into contact with the hot mold surface. Heat transfer begins to heat up the LSR, previously kept at room temperature. The LSR can thereby undergo heating rates of 300–1800 K min⁻¹ (Walde 1996). Although the viscosity initially decreases again as the temperature rises, since the chains become more mobile, at the same time the crosslinking reaction begins as soon as a certain temperature is exceeded. In addition, the LSR expands in the mold due to the heat input resulting heat dilatation.

The time during which the temperature rises and no crosslinking reaction takes place is called the incubation time. During this time, the so-called inhibitors first repel the free radicals that want to start the crosslinking reaction. Once the inhibitors have been used up, the irreversible crosslinking reaction starts (Schneider 1986; Röttemeyer and Sommer 2013). Only the addition of inhibitors enables the processing of the reactive LSR materials. The material is adjusted in such a way that, on the one hand, unproblematic mold filling without crosslinking is ensured and, on the other hand, economical process times can be realized. The term incubation time, like the scorch time and the scorch index, is known primarily from elastomer processing. The scorch index is a mathematical description of the occurrence of crosslinking and takes values between 0 and 1; see Eqs. (18.6) and (18.7). The scorch index is formed as the ratio of elapsed (injection) time and incubation time. A safe filling process is achieved when the scorch index remains below 1 at all points of the component. Then premature crosslinking is avoided (Hopmann et al. 2018). According to Ou (Ou et al. 2017b), the scorch time is defined as the duration until a crosslinking degree of 5% is reached. In injection molding simulation software, such as SIGMASOFT[®], this value is defined to 2% crosslinking degree. In other references, the scorch time is linked to the torque increase of the encoder used. For example, according to ISO 6502-3:2018-07 for a biconical cavity curemeter, an increase in torque of 0.1 N·m over minimum torque at ± 0.5° oscillation curve marks the reaching of the scorch time. Combined with incubation time, the scorch index $S(t)$ is defined by the following Eq. (18.6):

$$S(t) = \int_0^t \frac{1}{t_i(T(t))} dt \quad (18.6)$$

where t_i describes the incubation time, which can be determined using the Arrhenius approach written in Eq. (18.7) (Capellmann et al. 2003; Kim 2020):

$$t_i(T(t)) = t_i(T_0) * e^{\frac{E_{ti}}{R} \left(\frac{1}{T_0} - \frac{1}{T(t)} \right)} \quad (18.7)$$

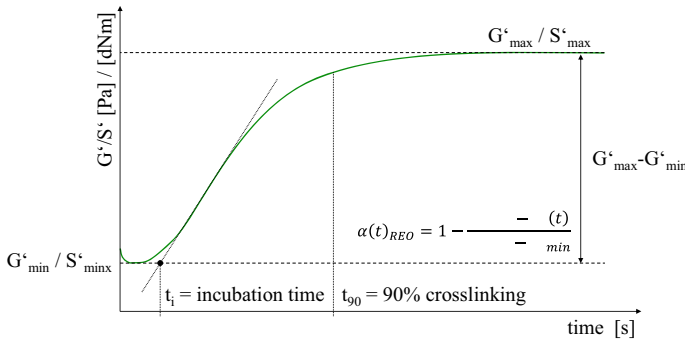


Fig. 18.5 Determination of the isotherm curing of a rubber compound without reversion according to DIN 53529-2 including the incubation time t_i and the time t_{90} to achieve 90% crosslinking

where E_{ti} stands for the activation energy for incubation time, R for the general gas constant and T_0 for the reference temperature.

Experimentally, the incubation time can be read from the vulcameter curve, which is known mainly from rubber processing and is determined using vulcameters (DIN 53529-2:1983-03). According to Röthemeyer, it can also be determined from the turnover function plotted over time (Röthemeyer and Sommer 2013). The intersection of the tangent at the inflection point of the vulcameter curve or turnover function with the minimum of the curve describes the incubation time; see Fig. 18.5 (Dick 2014; DIN 53529-2:1983-03; Röthemeyer and Sommer 2013; Verheyen 2019; Mezger 2020).

After the incubation period is reached, the flexibility decreases due to the build-up of an irreversible, crosslinked network until the LSR is no longer a liquid but a solid state. The point marking this phase transition is called the gel point and will be studied in more detail in this work.

The diagram in Fig. 18.6a is known from thermoset processing (Tran 2020). According to Buyl (Buyl et al. 2013), however, the temperature dependence also applies to LSR material; in addition, the shearing of the material lowers the viscosity (Beyer and Wolf 2015). For the processing of LSR in the injection molding process, the diagram shows the principal influences of temperature effect and shear versus crosslinking on the viscosity of LSR over time. The diagram in Fig. 18.6b describes the influence of viscosity, incubation time and crosslinking time of the processing on LSR at different mold temperatures (Hopmann et al. 2018). It shows that shortening the incubation time (4) shifts the injection boundary to the left so that less time is available to inject the material while the mold temperature remains the same. At the same time, an increase in viscosity also means higher pressure losses during the injection process, which can be converted into heat. The temperature input into the mold shortens the incubation phase, and the injection boundary shifts to the left (1). The additional temperature input in turn shortens the heating time (3). If the shear stress during the injection phase is to be prevented, or if the pressure limit of the machine is reached due to the higher viscosity, the injection speed is reduced and the

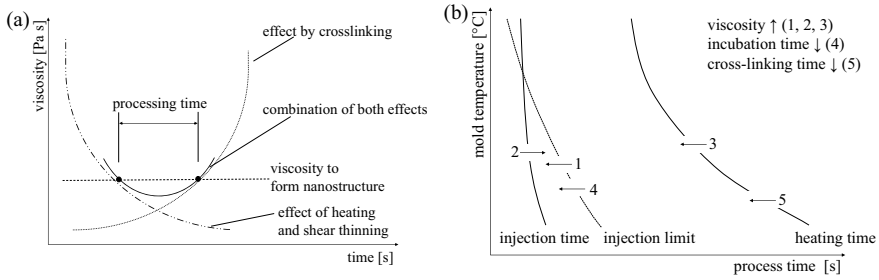


Fig. 18.6 Influence on processing LSR. **a** Influence of temperature, shear rate and crosslinking on viscosity during processing of LSR, according to (Tran 2020). **b** Influence of viscosity, incubation time and crosslinking time on processing of LSR depending on different mold temperatures, similar to (Hopmann et al. 2018; Röthemeyer and Sommer 2013)

injection time is extended accordingly, which means a shift of the curve to the right (2). A material (-batch) with a shorter crosslinking time shortens the heating time (5); however, the injection phase is not affected.

Consequently, to be able to state whether nano- or microstructures with certain parameters are molded or not, the viscosity must be known. For this purpose, measuring instruments such as the rotational rheometer or an instrument for dielectric analysis (DEA) are suitable to analyze the viscosity of LSR. Since the increase in viscosity of LSR in the injection mold is significantly related to crosslinking, the limiting viscosity for molding nanostructures can also be determined indirectly via the degree of crosslinking. Using a differential scanning calorimetry (DSC) measuring device, the crosslinking reaction can be measured and the degree of crosslinking calculated with the measurement results.

18.2.1.2 Determination of the Gel Point

During the transition of a liquid to a solid, the formation of a chemical or physical network as viscosity increases results in a state known as a gel. A distinction is made between chemical and physical gels. Chemical gels are formed by the formation of chemical network points, for example in crosslinking materials such as epoxies, elastomers and silicones. The network formed is permanent and consists of covalent formations. In contrast, in physical gels, a temporary network is formed due to secondary valences (van der Waals forces, hydrogen bonds and entanglements) (Beyer and Wolf 2015; Osswald and Rudolph 2014). The physical network can briefly be dissolved by shear stress, which is accompanied by a reduction in viscosity. If the material is subsequently no longer stressed, the physical network rebuilds after a certain time. If the rebuilding of the network is time dependent, the phenomenon is called thixotropy. This effect also occurs in LSR (Beyer and Wolf 2015). Therefore, in rheological investigations of systems such as LSR, which form both physical and chemical networks, it is essential to consider the previous history of the material.

If the rheological measurement is to be used to analyze the LSR under practical processing conditions during the injection molding process, it must be presheared before the measurement to first destroy the physical network. Thus, Fig. 18.3 shows the typical shear rates that occur during injection molding of LSR.

The gel point is regarded as an important parameter when measuring crosslinking systems. It is considered to be the point at which a reactive system changes from the liquid to the solid state. Nishinari gives a good overview of the different approaches to define gels or the gel point (Nishinari 2009). Ehrenstein (Ehrenstein 2011) gives the gel point for resins depending on their chemical conversion. Thus, for unsaturated polyester resins (UP), only 5–10% of the reactive double bonds have reacted at the gel point, while for epoxies it is already 60–70% of the epoxy groups.

Practically, it is not trivial to determine the gel point of a material exactly. Several approaches to determine the gel point can be found in literature. Isothermal measurements are performed with a rotational rheometer, where the storage modulus (G') and loss modulus (G'') are measured at a defined, low frequency. The point where G' and G'' intersect is called the gel point; see Fig. 18.7 (Nosonovsky and Bhushan 2008; Pogodin et al. 2013).

At this point, the loss factor becomes $\tan\delta = G''/G' = 1$. (Winter 1987) Since G' and G'' are frequency-dependent and the intersection of G' and G'' often does not reflect the gel point, Winter and Chambon propose measurements at different frequencies, each of which records the $\tan\delta$. The point where all $\tan\delta$ curves meet is defined as the gel point, Fig. 18.8 (Winter and Chambon 1986; Guan et al. 2016; Harkous et al. 2016; Nishinari 2009; Winter 2002). Furthermore, Winter describes that the growth of G' cannot be used to determine the gel point, as this occurs well before the actual gel point (Hoffmann et al.).

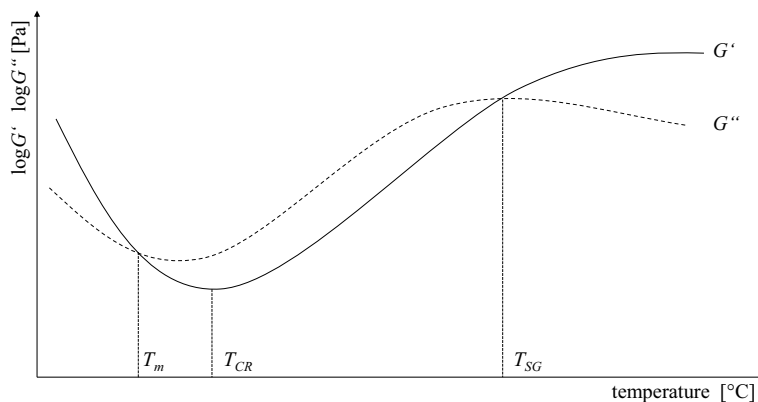


Fig. 18.7 Schematic, general data of G' and G'' dependent on temperature of a curing polymer with T_m melting point, T_{CR} onset chemical reaction and T_{SG} sol/gel transition that equals the gel point according to (Mezger 2020)

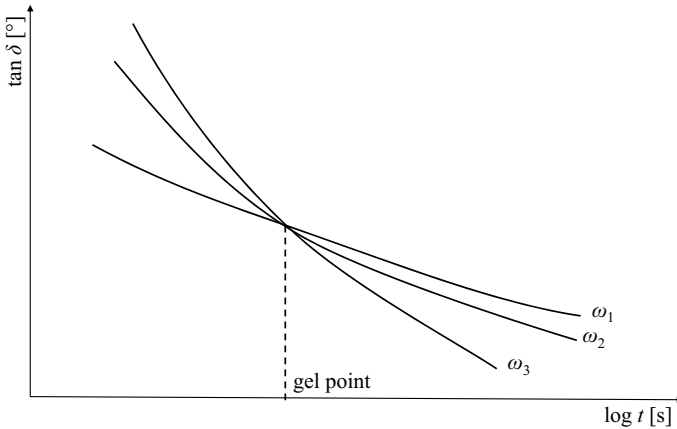


Fig. 18.8 Schematic representation of the gel point determination according to (Winter 2002): The intercept of loss factor ($\tan \delta = G''/G'$) for different frequencies equals the gel point

18.2.1.3 Determining Viscosity and the Degree of Crosslinking

As already described in Sect. 2.1.1, the viscosity of LSR depends on various influencing parameters. The increase in viscosity is mainly related to the start of the crosslinking reaction. For this reason, knowledge of a maximum degree of crosslinking is essential to make a statement about when the molding of nano- and microstructures is no longer possible. In order to determine the degree of crosslinking of LSR, the rheological and the thermal examinations of the material are particularly suitable (Harkous et al. 2016).

Rheological Approach

The rotational rheometer is particularly appropriate for measuring viscosity changes. Since uncrosslinked LSR exhibits viscoelastic behavior, G' and G'' are interesting variables to measure for they enable statements about the elastic or viscous behavior (Mezger 2020).

For crosslinking systems, as LSR is, it is suggested to heat up the sample in the rheometer with a constant heating rate, in the following called temperature sweeps. Here, there is the possibility to detect the gel point by the time courses of G' and G'' , which have identical values at the gel point (Winter and Chambon 1986; Pahl et al. 1995). Alternatively, the gel point can also be detected by an intersection of the G' and G'' curves during a frequency sweep.

The loss factor $\tan \delta$ is defined as G''/G' . Accordingly, the gel point is reached when loss factor $\tan \delta = 1$ or face angle $\delta = 45^\circ$. Figure 18.7 shows the typical, temperature-dependent course of G' and G'' as well as the prominent points. Thus, at T_{CR} the chemical crosslinking reaction starts, and T_{SG} marks the sol/gel transition,

or the so-called gel point (Mezger 2020). It has been shown that G' and G'' depend on the frequency. Therefore, it is recommended to use the multi-wave mode for gel point determination. The multi-wave mode merges multiple oscillation frequencies simultaneously into one waveform.

To find out the degree of crosslinking from the rheological measurements, measurements with constant deformation and constant frequency are carried out. From the measured storage modulus G' , the degree of crosslinking α can then be found using Eq. (18.8) (Harkous et al. 2016; Saražin et al. 2020; Guan et al. 2016; Hempel 2001; Ou et al. 2017b, 2017a; Leroy et al. 2013; Čop et al. 2015; Pelz 2001):

$$\alpha(t)_{\text{REO}} = 1 - \frac{S'_{\text{max}} - S'(t)}{S'_{\text{max}} - S'_{\text{min}}} = 1 - \frac{G'_{\text{max}} - G'(t)}{G'_{\text{max}} - G'_{\text{min}}} \quad (18.8)$$

where S'_{min} describes the minimum, S'_{max} the maximum torque of the measuring device. $S'(t)$ is the value of the torque of the measuring device at time t . G'_{min} describes the minimum storage shear modulus, G'_{max} the maximum storage shear modulus and $G'(t)$ the value of storage modulus at time t .

Dielectrically Approach

Dielectric thermal analysis (DTEA or DEA for short) can be used to specifically investigate crosslinking reactions by measuring the dielectric properties of the material. Information can be obtained about flow behavior, reactivity and the curing process. During the measurement, the sample is brought into contact with two electrodes to which a sinusoidal voltage is applied. The measurement can be carried out at different measuring frequencies. The applied voltage forces the charge carriers in the material under investigation, often ions such as catalysts or impurities, to move: positive particles migrate to the negative pole and vice versa. In addition, the dipoles in the electric field align themselves. The result is a sinusoidal current with a specific amplitude and phase shift relative to the applied measurement signal, which describe the ion and dipole mobility of the material. If the crosslinking reaction progresses, the viscosity increases, which in turn is reflected in a reduced mobility of the charge carriers and thus a reduced amplitude and a larger phase shift. From this, four dielectric properties can be calculated: the permittivity ε' , also known as the dielectric constant, the loss factor ε'' , the dissipation factor $\delta = \varepsilon''/\varepsilon'$ and the ionic conductivity σ . The higher the dielectric loss factor ε'' , the better the conductivity of the sample, resulting in an attenuation of the electric field, Eq. (18.9) (NETZSCH Analysieren and Prüfen 2022):

$$\sigma = \varepsilon'' * \omega * \varepsilon_0 \quad (18.9)$$

where ε_0 equals the permittivity of free space ($8.854 \times 10^{-12} \text{ F m}^{-1}$) and ω describes the angular frequency ($2\pi f$). ε'' stands for the loss factor and f for the given frequency.

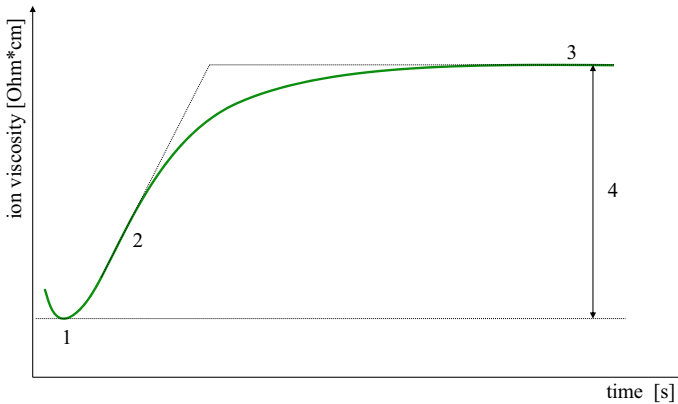


Fig. 18.9 Schematic progression of ion viscosity for a crosslinking material, based on (NETZSCH Analysieren and Prüfen 2022)

As resulting measurands, for measurements with a defined heating rate, the dissipation factor (ε'') and the ion viscosity are given versus time and temperature, respectively (NETZSCH Analysieren and Prüfen 2022; Haines 2002; Brown 2004; Mezger 2020). The ion viscosity can be calculated using Eq. (18.10):

$$\nu = \frac{1}{\sigma} \quad (18.10)$$

Figure 18.9 shows the schematic course of the ion viscosity: A minimum of the ion viscosity, point (1), means best rheological flow behavior. The slope of the ion viscosity describes the reactivity of the material, (2). If the slope is zero, the material is fully cured; see (3). The maximum vertical distance of the ion viscosity indicates the crosslinking density; see (4).

Thermal Approach

The degree of curing can be determined by differential scanning calorimetry (DSC) measurements (Hülдер 2008). Since the curing normally takes place exothermically due to forming of covalent bonds, the reaction heat released can be detected as an increase in the specific heat flow of the sample mass. The amount of heat released corresponds to the area of the completely exothermic peak of the heat flow curve. If the amount of heat released at time t is set to the maximum amount of heat released, the reaction conversion α , hereinafter also referred to as the degree of crosslinking, can be determined (Ehrenstein et al. 1997).

The curing rate increases enormously with increasing temperature. This effect can be detected using measurements with a DSC measuring device at different heating rates. This makes it possible to determine how much energy is released at which point

in time by the exothermic crosslinking reaction. The thermal approach has already been described in detail in a previous paper (Weißer et al. 2020). Here, the empirical approach according to Kamal–Sourour was chosen to describe the reaction kinetics, Eq. (18.11):

$$\frac{d\alpha}{dt} = (k_1(T) + k_2(T) \cdot \alpha^m) \cdot (1 - \alpha)^n \quad (18.11)$$

where m and n describe the reaction order, $k_1(T)$ and $k_2(T)$ are temperature-dependent constants.

18.2.2 Experimental Part

18.2.2.1 Material

In this study, we used a commercial two-component LSR material by Momentive (SILOPREN™ LSR 2050) with a hardness of 50 Shore A. The components A and B were mixed in a 1:1 ratio.

18.2.2.2 Characterization of the Material Properties

Procedure Rheological Measurements

A stress-controlled rheometer with a parallel plate geometry, model Physica MCR 301 (Anton Paar), was used to measure the rheological properties. A plate diameter of 25 mm was used; the material was always freshly mixed using a two-component syringe with static mixer and applied with a gap of 0.9 mm. The temperature around the measurement point was precisely controlled using a TC30 convection heating system and liquid nitrogen. All measurements were performed in the linear viscoelastic region. To determine the linear viscoelastic region, at first an amplitude sweep was performed. For this, at constant 5 °C the deformation was changed logarithmically from 0.01–100% with 10 rad s⁻¹ measuring angular velocity.

The measurements to determine the gel point were performed with a constant deformation of 0.1% in multi-wave mode. Different frequencies were approached for each measurement point (1, 2, 4, 8 Hz). The temperature sweeps were performed at 1 Hz and 0.5% deformation. Therefore, the temperature was increased from 25 to 150 °C at rates of 1, 2 and 5 K min⁻¹. Before this, the material was presheared at 1000 Pa shear stress for 60 s.

Isothermal time sweep measurements were performed at room temperature (25 °C) to determine the gel point as well as at higher temperatures (80, 90, 100, 110 and 120 °C) to determine the crosslinking reaction. For these heating experiments, as uniform procedure, all samples were applied at 5 °C and then heated with 20 K min⁻¹

while applying constant shear stress of 1000 Pa. After reaching the test temperature, the LSR was presheared with shear rate 25 s^{-1} for 20 s, then the actual time sweep measurement began. This procedure is intended to clear the sample history before measurement (Beyer and Wolf 2015). Also it provides a more realistic measurement, since the material is initially subjected to high shear forces in the injection molding machine, and then cures directly afterward in the hot injection mold.

Procedure of the Dielectric Analysis

The dielectric measurements were performed on a NETZSCH DEA 288 Ionic (NETZSCH-Gerätebau GmbH) with the IDEX 115/35 T sensor in static air. The temperature was increased from 25 to 200 °C at a heating rate of 3 K min^{-1} , and the measuring frequencies 10, 100, 1000 and 10,000 Hz were used. However, the best results were achieved with a frequency of 10 Hz. The result from the 10 Hz measurement was derived to determine out the area of the largest slope (maxima in the derivative).

Procedure of the Thermal Measurement

The calorimetric measurements of the LSR mass were carried out with the DSC 214 Polyma dynamic differential calorimetry analyzer from NETZSCH-Gerätebau GmbH. The dynamic measurements were performed for sample masses of 10 mg at four different heating rates (1, 2.5, 5 and 10 K min^{-1}) in sealed and once pierced aluminum pans. As a reference, an also pierced and sealed empty pan was used. First, heating was carried out at the corresponding heating rate from -70 to 220 °C, then cooled down again to -70 °C, this temperature was held for 15 min to allow thermal equalization, and then heated up again to 220 °C. The second heating curve is therefore recorded to determine whether the sample has crosslinked completely in the first heating cycle. Each measurement was performed at least twice. The material under investigation was stored at -20 °C to prevent pre-crosslinking. For the preparation of the LSR samples, 20 min were observed in each case from taking the samples out of the fridge until the start of the DSC measurement. During all measurements, the samples were purged with nitrogen. For the evaluation of the DSC curves, only the two heating curves are used.

For lower heating rates, the peak shifts toward lower temperatures, and for faster heating rates it shifts toward higher temperatures. The total amount of heat released was determined by drawing a straight line before and after the peak, connecting the baselines and integrating the resulting area under the peak. For all heating rates, the crosslinking area remains largely the same. The average amount of heat released during crosslinking was determined to be 5.3 J kg^{-1} .

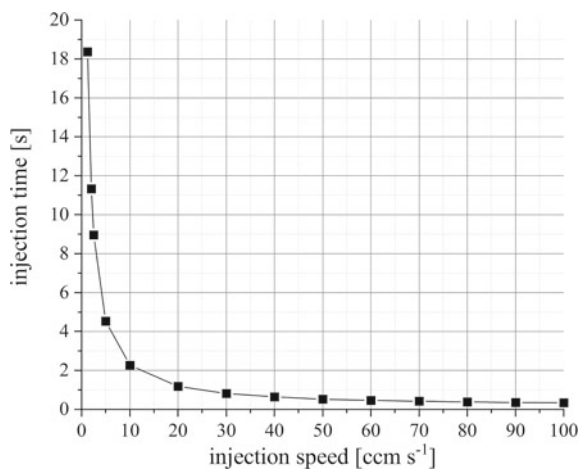
18.2.2.3 Experimental Setup

The LSR was processed on an Arburg 420 C 1000 injection molding machine, which is specially equipped for processing liquid silicone rubber. Using a special dosing system, the pumpable, pasty components A and B are transported separately to the static mixer, shortly before the dosing unit of the injection molding machine. Only immediately before the actual processing, the two components are mixed, dosed and injected into the hot mold via the injection unit, which is temperature-controlled to 25 °C. The material samples for further investigation of the LSR (rheological, thermal or dielectric) were taken directly from the dosing unit of the injection molding machine after production. This ensured that the material properties corresponded to the actual production conditions. The usual mold temperatures for the injection molding process range from 130 to 200 °C. Figure 18.10 shows the dependence of the injection time on the injection speed for the used test mold, which has no cold runner but a relatively thick curing sprue. Figure 18.11a shows the injection mold used with the injection-molded part. In Fig. 18.11b, the microstructure is shown schematically that was introduced in the mold insert by ultra-short pulse laser structuring. The height of 25 μm was used as the relevant evaluation criterion.

In this study, the influence of the process parameters mold temperature (130, 140, 150, 160, 180, 200 °C) and injection speed (2, 5, 10, 50, 100 ccm s^{-1}) was investigated. For this purpose, a full factorial design of experiment (DoE) was run. The produced LSR components were examined and qualified by white light interferometer NewView™ 9000 from ZYGO.

A special feature of the mold used is the possibility of briefly cooling down the structured mold insert in a targeted manner. For this purpose, cold compressed air at a pressure of 2 bar flows for 10 s through the cooling channels behind the 2-mm-thick mold insert. This allows the mold insert to be cooled down from 180 to 20 °C in the process.

Fig. 18.10 Dependence of the injection time on the selected injection speed for the test mold



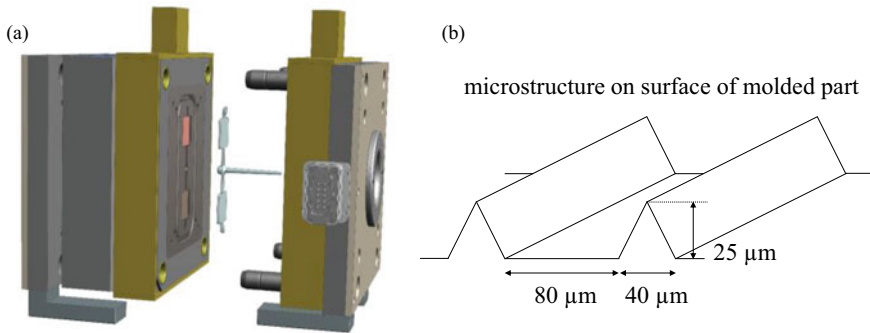


Fig. 18.11 a Injection mold with LSR part and options for two differently structured mold inserts with a size of 40 mm × 40 mm. b Schematic representation of the ideal plastic surface after injection molding with microstructure

18.3 Results and Discussion

18.3.1 Kinetic Model

With the data of the dynamic DSC measurements at different heating rates described in Sect. 2.2.2, the kinetic constants of the Kamal–Sourour model presented in Sect. 2.1.3 were calculated. The model parameters are fitted until they describe the crosslinking process for all measured heating rates as accurately as possible. The diagram in Fig. 18.12a shows the measured DSC data and the calculated data according to the Kamal–Sourour model for the corresponding heating rates. For the mathematical modeling, the parameters listed in Fig. 18.12b were used, to which no physical significance can be attributed.

With the calculated model data, prediction calculations can be carried out for various scenarios; see Fig. 18.13a. Thus, the filling process in the injection mold can be simulated realistically: Cold, uncrosslinked material is injected into a hot mold in a short time. Subsequently, the crosslinking reactions can be investigated with the prediction model for different isothermal mold temperatures. By evaluating the inflection point of the turnover curve, compare to Fig. 18.5 in Sect. 2.1.1, the incubation time at different mold temperatures can be read from the crosslinking isotherms. The incubation times calculated from these data for different mold temperatures are shown in Fig. 18.13b.

18.3.2 Rheological Results

At the beginning of the rheological investigations, the linear viscoelastic region was investigated with an amplitude sweep. As can be seen in Fig. 18.14, $G'' > G'$. This

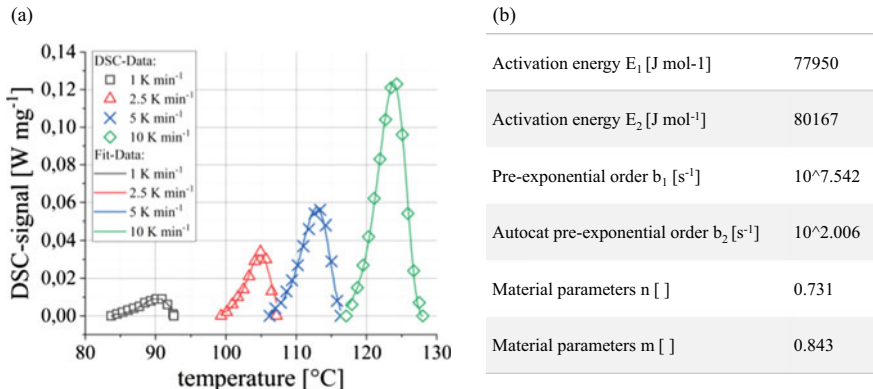


Fig. 18.12 **a** Result of DSC measurements and fitted data kinetic model for Silopren 2050: Temperature-dependent representation of crosslinking for different heating rates. **b** Parameters used for the mathematical modeling of Kamal–Sourour model

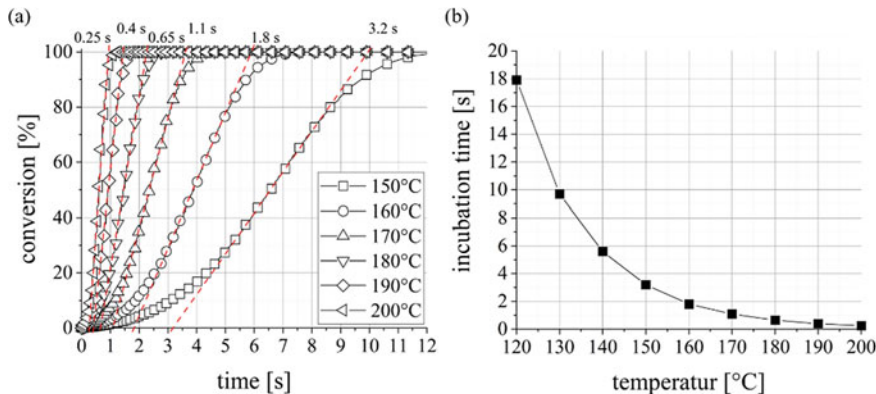


Fig. 18.13 **a** Predictions of curing at different, isothermal mold temperatures, based on DSC measurements at different heating rates. The red dashed lines show the tangents at the inflection point for evaluation of the incubation time. **b** Estimated incubation time for different mold temperatures

means that uncrosslinked LSR shows liquid-like behavior, i.e., the viscous behavior dominates the elastic behavior. For further rheological investigations, a deformation of 0.1% was selected in order to remain in the linear viscoelastic region.

In order to determine the gel point of the LSR, originated from physical entanglements or secondary valences, multi-wave measurements with 0.1% deformation at 25 °C were performed. As Fig. 18.15 reveals, after the preshearing, that removes the physical crosslinking, the LSR reached the gel point after only 120 s. Nevertheless, the material is still 0% crosslinked and the built-up network can be destroyed again

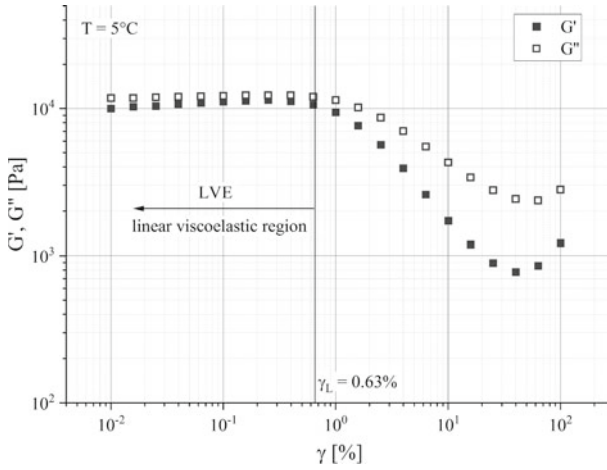
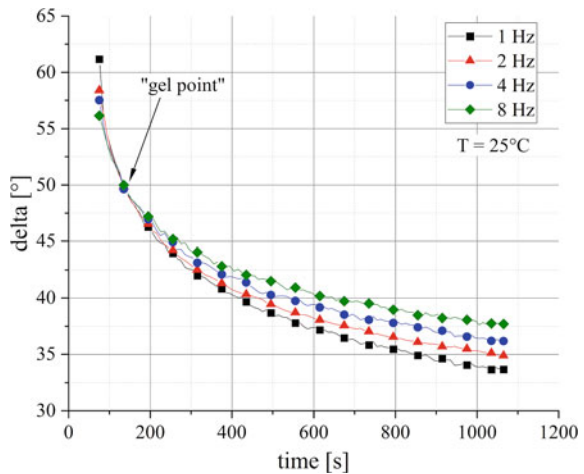


Fig. 18.14 Amplitude sweep ($\gamma = 0.01\%$ to 10%) to define the linear viscoelastic region conducted at 5°C material temperature to exclude chemical crosslinking and angular velocity $\omega = 10\text{ rad s}^{-1}$

by shear stress. This shows that it is essential to distinguish between chemical and physical gel when determining the “gel point”.

In Fig. 18.16a, the two individual components A and B are examined without preshear at a heating rate of 2 K min^{-1} from 30 to 180°C in a temperature sweep. It can be seen that a gel is already present at 30°C ($G' > G''$, or $\delta < 45^\circ$). In addition, a crosslinking reaction occurs in the single-component B as well, however only at higher temperatures. This is because component B contains the crosslinker, but component A contains the catalyst, which accelerates the reaction at lower temperatures. Figure 18.16b on the right shows temperature sweeps for the mixed LSR

Fig. 18.15 Time sweep at constant temperature of 25°C and shear strain of $\gamma = 0.1\%$, measured in multi-wave mode (1, 2, 4 and 8 Hz) after preshearing with a shear stress of 1000 Pa for 60 s



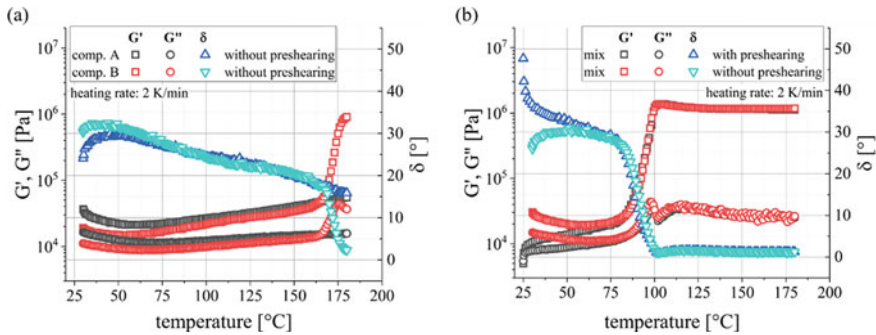


Fig. 18.16 **a** Temperature sweep for components A and B at heating rate 2 K min^{-1} , $\gamma = 0.1\%$ and $\omega = 10 \text{ rad s}^{-1}$. **b** Temperature sweep for the mixture (1:1) at heating rate 2 K min^{-1} , $\gamma = 0.1\%$ and $\omega = 10 \text{ rad s}^{-1}$, the presheared material was preloaded with a shear stress of 1000 Pa for 60 s

from 25 to $180 \text{ }^\circ\text{C}$ without and with preshear ($\dot{\gamma}$ up to 10 s^{-1}) at a heating rate of 2 K min^{-1} . It can be seen that at the start of the measurement, the presheared material has a gel point ($\delta = 45^\circ$), and the non-presheared material is already solid-like from the beginning of the measurement. While G' and G'' of the presheared material increase constantly until the start of the crosslinking reaction, these values initially decrease for the unsheared material. This can be explained by the fact that the viscosity of the material decreases due to the heat input. From approx. $75 \text{ }^\circ\text{C}$, the presheared and unsheared curves overlap again.

To determine the crosslinking reaction, measurements were made at different constant temperatures. Figure 18.17a shows the curves of the storage modulus G' for the temperatures $80, 90, 100, 110, 120 \text{ }^\circ\text{C}$. It can be seen that at temperatures 80 and $90 \text{ }^\circ\text{C}$, a constant G' -level cannot be reached after 1000 s of measurement time. In this case, crosslinking is not yet complete or even not yet started. As well at an isothermal temperature of $100 \text{ }^\circ\text{C}$, the G' level of higher temperatures isn't reached as is the case for higher temperatures. This can be explained by the fact that the reaction proceeds more slowly due to the lower temperature, and the radicals do not reach the crosslinking points due to lower molecular movements. In addition, above a certain degree of crosslinking, the molecular movements are so restricted by chemical bonds that it takes a long time to achieve complete crosslinking. It can be seen that G' of the $100 \text{ }^\circ\text{C}$ curve increases slowly but steadily. For closer investigations, only the temperatures $100, 110$ and $120 \text{ }^\circ\text{C}$ were used to evaluate the crosslinking reaction; see Fig. 18.17b. The Eq. (18.8) was used for this purpose, also displayed in Fig. 18.17b. To analyze the course of the $100 \text{ }^\circ\text{C}$ measurement, G'_{max} of 110 and $120 \text{ }^\circ\text{C}$ was used. This is the reason, that for $100 \text{ }^\circ\text{C}$ temperature, 100% crosslinking is not reached after 700 s .

The evaluation of the temperature sweep at different heating rates supports the previous results; see Fig. 18.18. For 1 K min^{-1} , the complex viscosity increases abruptly from about $85 \text{ }^\circ\text{C}$, which means that the LSR changes from the viscous to the elastic range. The sharp increase in complex viscosity means that a chemical

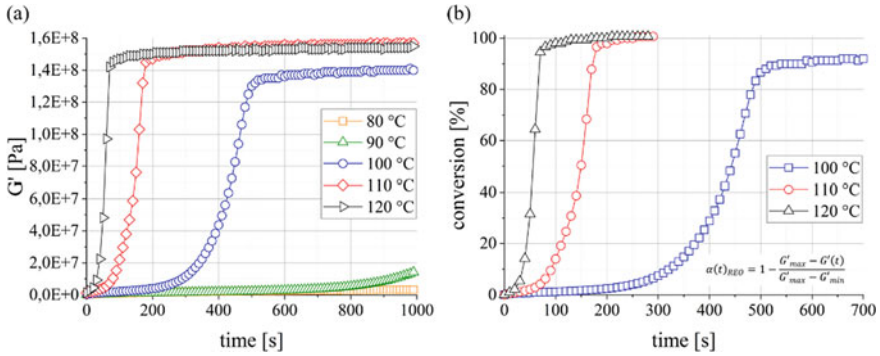


Fig. 18.17 **a** Storage module for different isothermal temperatures, $f = 1$ Hz and $\gamma = 0.1\%$. Before the measurement, the material was presheared with a shear stress of 1000 Pa during heating and with a shear rate of 25 s^{-1} for 20 s. **b** Conversion of the 1 Hz measurement of G' depicted in Fig. 18.17a by the given formula into the degree of crosslinking α at constant temperatures 100, 110 and 120 °C

network is formed here due to the starting crosslinking reaction, which is fully formed at 100 °C. Further, it can be seen that for higher heating rates, the range of the abrupt viscosity increase shifts further to higher temperatures, due to bad thermal conductivity ($\alpha = 0.22 \text{ W m}^{-1} \text{ K}^{-1}$). Thus, at a heating rate of 5 K min^{-1} , it is already 105 °C at which the complex viscosity increases. In the injection mold, significantly higher heating rates of $300\text{--}1800 \text{ K min}^{-1}$ occur, which is why it can be assumed that the crosslinking reactions shift even further to higher temperatures (Walde 1996).

Fig. 18.18 Complex viscosity during temperature sweep measurements at heating rates of 1, 2 and 5 K min^{-1} a deformation of 0.5% and a measurement frequency of 1 Hz. Before the measurement, the material was presheared with a shear stress of 1000 Pa for 60 s

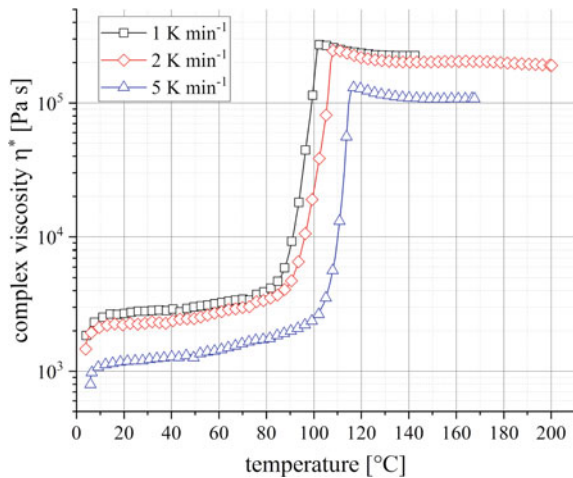
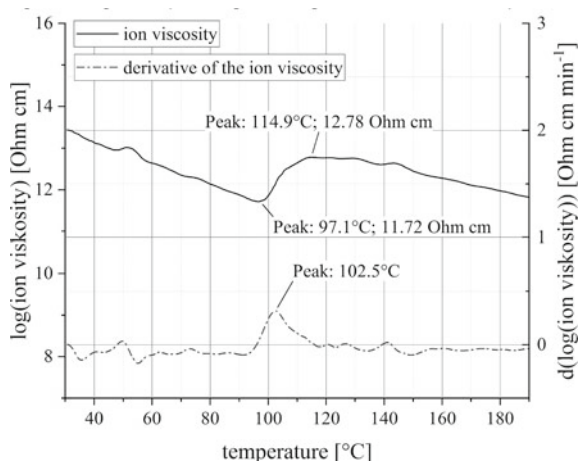


Fig. 18.19 Result of the DEA measurement for heating from 30 to 190 °C with 3 K min⁻¹ and a frequency of 10 Hz



18.3.3 Dielectrical Results

The DEA measurements, displayed in Fig. 18.19, showed the course of the ion viscosity for a measuring frequency of 10 Hz. The material reaches the lowest viscosity at 97.1 °C and thus has the best flow behavior. Then the crosslinking reaction begins, which—as can be seen from the maximum of the first derivative—exhibits its maximum conversion rate at 102.5 °C. At 114.9 °C, the ion viscosity reaches its maximum value, thus the crosslinking is completed. The subsequent drop can be explained by the temperature dependence of the ion viscosity.

18.3.4 Comparison of the Different Analysis Methods

Figure 18.20 compares the three measurement methods for heating rates from 1 to 5 K min⁻¹ with respect to the start time of the crosslinking reaction. It can be seen that the DEA measurement fits perfectly into the rheometer measurements. Although the DSC measurements show a similar trend toward higher crosslinking reaction start-temperatures with increasing heating rates, the data is 15–20 °C lower than the rheometer and DEA measurements. Deviations arise, for example, because the DSC measurement (10 mg) uses much smaller masses than the rheometer measurement (980 mg) and the DEA measurement, which must be heated. Due to the poor thermal conductivity of LSR (0.22 W m⁻¹ K⁻¹), the increasing ambient temperature in the measurement with constant heating rates causes the thermal energy to be introduced more slowly into the LSR material under investigation.

When measuring with constant temperatures, the rheometer measurement reaches its limits in temperature ranges of interest for production, since crosslinking starts so quickly that often the constant measurement temperature has not even been reached

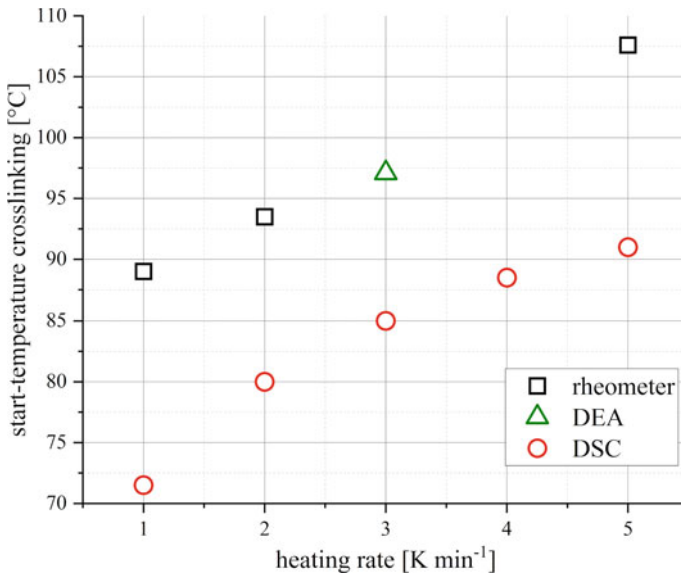


Fig. 18.20 Comparison of the three measurement methods used to determine the starting temperature of the crosslinking reaction depending on the heating rate used from 1–5 K min⁻¹

despite the high heating rate. The measurements carried out as part of this work have shown that 120 °C is the maximum possible isothermal measurement temperature for the rheometer investigation. The predictions for different temperature scenarios calculated from dynamic DSC measurements were simulated with the real temperature profile for comparison with the rheometer measurements. This was performed starting at 20 °C and heating up to 120 °C at a rate of 20 K min⁻¹; compare Fig. 18.21a and b. It can be seen that toward the end, the measuring device no longer manages the set heating rate of 20 K min⁻¹. In order to be able to compare the two measuring methods nevertheless, the DSC data were calculated with exactly the same temperature profile from the rheometer measurement. The two crosslinking curves obtained agree surprisingly well. In conclusion, it can be stated that the DSC measurement is more suitable for determining the crosslinking behavior, as already stated by Harkous (Harkous et al. 2016).

18.3.5 Experimental Results

The LSR parts produced at different mold temperatures and different injection speeds were measured using a white light interferometer. The results of the degrees of impression obtained (measured height in μm vs. the maximum height of mold insert = 25 μm) were unexpectedly good. Only for 180 and 200 °C mold temperature, bad results were obtained with very low injection speeds. Figure 18.21 shows the

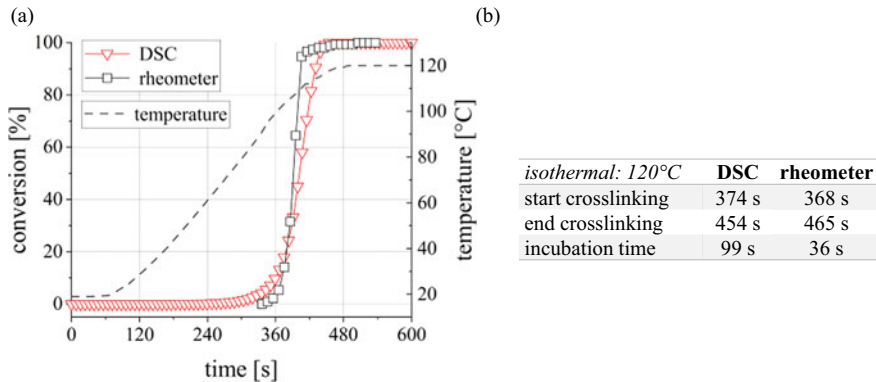


Fig. 18.21 **a** Comparison of the calculated crosslinking curve from the rheometer measurements and the crosslinking predicted from dynamic DSC measurements. The kinetic prediction is based on the real temperature profile from the measurement with the rheometer. **b** Values read concerning start and end of crosslinking as well as incubation time for the chosen temperature program

percentage degree of impression depending on the two process parameters—mold temperature and injection speed.

As shown in Fig. 18.22, for high mold temperatures and low injection speeds, the degree of molding of the microstructures is very poor. For this reason, variothermal temperature control was used to cool down the mold surface on which the microstructures are inserted using compressed air for 10 s before injection. For 180 °C mold temperature, the mold insert was thus cooled down locally to an actual 160 °C. Despite a low injection speed of only 2 ccm s⁻¹, the microstructures could be molded 100% compared to the process without variothermal temperature control; compare to Fig. 18.23.

18.4 Conclusion and Outlook

In order to investigate the moldability of micro- and nanostructures in LSR, various measurement methods were carried out to characterize the influencing parameters, such as viscosity and degree of crosslinking. Investigations into the determination of the gel point of LSR have shown that this is difficult under near-production conditions, where several effects overlap. The gel point, which is typically detected by rheometer measurements, describes only the reversible physical gel, but not the relevant, chemical gel, which influences the impression of microstructures. The physical gel can be destroyed by shear stress, which constantly acts on the material during the processing of LSR in the injection molding process. Thus, it is necessary to conduct further investigations on the physical gel point formation depending on the preshearing of the material.

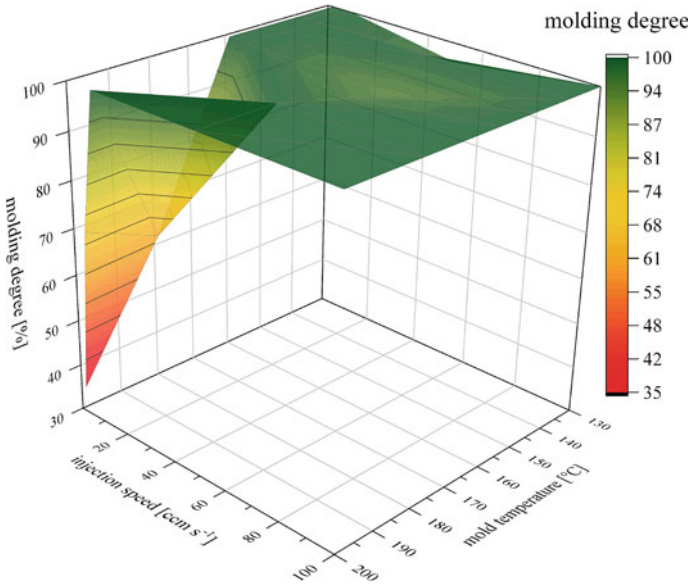
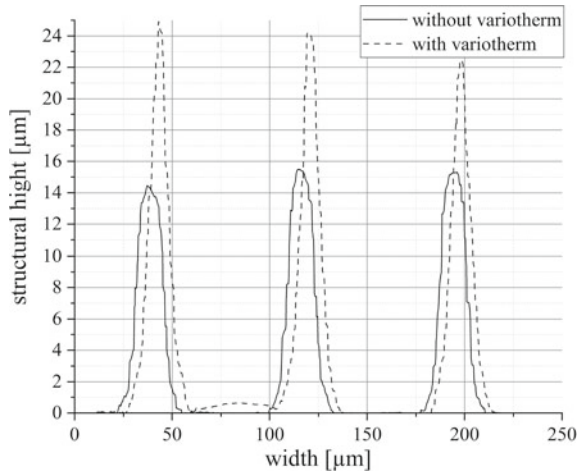


Fig. 18.22 3D representation of the influencing parameters injection speed and mold temperature on the degree of impression of microstructures (related to 25 μm structure height)

Fig. 18.23 Comparison of the same process conditions (180 °C mold temperature, 2 cm s⁻¹ injection speed, 60 s curing time) with and without variothermal temperature control



Using thermal DSC measurements, it was possible to create the well-fitting Kamal–Sourour model. This was used to calculate predictions of the expected crosslinking reaction at different isothermal mold temperatures, based on which the incubation time was determined. The mold temperature-dependent incubation time was correlated with the actual injection speed-dependent injection times of the test

mold used and as shown in three dimensions in Fig. 18.24. This has enabled a theoretical prediction of whether nano- or microstructures are possible with the selected setting parameters of mold temperature and injection speed. The practical investigations carried out as part of this work have shown that microstructures are even formed for higher mold temperatures and lower injection speeds. This is believed to be due to a combination of a reduction in viscosity during shear stress caused by the injection process and temperature input from the hot mold. This is because as the temperature increases, the viscosity initially decreases additionally, and at the same time thermal expansion (dilatation) takes place due to temperature increase. In addition, this thermal expansion presses the still low-viscosity and uncrosslinked LSR material into the nano- and microstructures in the mold. In further investigations, the pressure curve in the mold as a function of temperature will be studied in detail.

Furthermore, the practice tests have shown that in borderline areas where the microstructures cannot be molded well due to high mold temperature and low injection speed, a reversal of the variothermal temperature control known so far for thermoplastics can help. In this process, the hot mold is cooled down locally for a short time at the desired location before the injection process. The lower mold surface temperature obtained in this way then enables clean molding of the desired surface. In this work, the mold insert was cooled with cold compressed air, but significantly higher cooling rates are also possible when water is used.

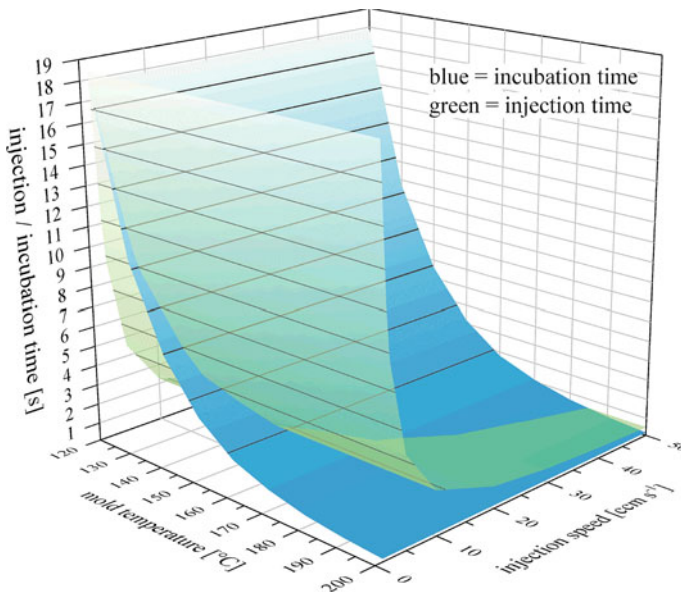


Fig. 18.24 3D representation of mold temperature-dependent incubation time (blue area) and injection speed-dependent injection time (green area) to assess process limits for molding nano- and microstructures

Acknowledgements D. Weisser would like to acknowledge the support of *Baden-Württemberg Stiftung gGmbH* within the scope of “Biofunctional materials and surfaces” research program. He would also like to thank NETZSCH-Gerätebau GmbH for performing the DEA measurements and Freiburger Materialforschungszentrum FMF for the measurement capabilities at the rheometer.

References

- Aho J, Syrjäälä S (2008) On the measurement and modeling of viscosity of polymers at low temperatures. *Polym Test* 27:35–40
- Attia UM, Alcock JR (2010) Integration of functionality into polymer-based microfluidic devices produced by high-volume micro-moulding techniques. *Int J Adv Manuf* 48:973–991
- Baum MJ, Heepe L, Gorb SN (2014) Friction behavior of a microstructured polymer surface inspired by snake skin. *Beilstein J Nanotechnol* 5:83–97
- Beyer P, Wolf HP (2015) Effizienz und Qualität durch eine neue Generation rheologieoptimierter Flüssigsiliconelastomere. *GAK Gummi Fasern Kunstst* 68:676–683
- Boden SA, Bagnall DM (2012) Moth-eye antireflective structures. In: Bhushan B (ed) *Encyclopedia of nanotechnology*. Springer Netherlands, Dordrecht
- Bont M, Barry C, Johnston S (2021) A review of liquid silicone rubber injection molding: process variables and process modeling. *Polym Eng Sci* 61:331–347
- Brown ME (ed) (2004) *Introduction to thermal analysis. Techniques and applications*. Kluwer Academic Publishers (Springer eBook Collection Chemistry and Materials Science, 1), Dordrecht
- Buyl F de, Beukema M, van Tiggelen K (2013) Innovations in silicones for LED application. In: *Silicone elastomers 2013*. 10–12 June 2013, Hilton Munich City, Munich, Germany. Smithers Rapra Ltd; Conference Silicone Elastomers Shawbury
- Capellmann R, Haberstroh E, Häuser T et al (2003) Development of Simulation software for the injection moulding of liquid silicone rubber. *Int Polym Sci Technol* 30:1–8
- Castro JM, Macosko CW (1982) Studies of mold filling and curing in the reaction injection molding process. *AIChE J* 28:250–260
- Čop M, Gospodarič B, Kempainen K et al (2015) Characterization of the curing process of mixed pine and spruce tannin-based foams by different methods. *Eur Polym J* 69:29–37
- Cross MM (1965) Rheology of non-Newtonian fluids: a new flow equation for pseudoplastic systems. *J Colloid Sci* 20:417–437
- Dick J S (2014) *Rubber technology. Compounding and testing for performance*. 2. Aufl. Carl Hanser Fachbuchverlag, s.l.
- DIN 53529-2:1983-03 Prüfung von Kautschuk und Elastomeren; Vulkametrie; Bestimmung des Vulkanisationsverlaufes und reaktionskinetische Auswertung von Vernetzungsisothermen
- Dow Corning Corporation (2019) Formbare optische Silikone von SILASTIC™ ermöglichen bahnbrechendes LED-Scheinwerferdesign von Hella KGaA Hueck & Co. Dow Corning Corporation. <https://www.google.com/search?client=firefox-b-d&q=Formbare+optische+Silikone+von+SILASTIC%E2%84%A2+erm%C3%B6glichen+bahnbrechendes+LED-Scheinwerferdesign+von+Hella+KGaA+Hueck+%26+Co>. Accessed 04 Apr 2022
- Ehrenstein GW (2011) *Polymer-Werkstoffe. Struktur; Eigenschaften; Anwendung*. 3. Aufl. Carl Hanser Fachbuchverlag, s.l.
- Ehrenstein GW, Bittmann E, Hoffmann L (1997) *Duroplaste. Aushärtung–Prüfung–Eigenschaften*. Hanser, München
- Eyerer P, Hirth T, Elsner P (2008) *Polymer engineering. Technologien und Praxis*. Springer, Berlin, Heidelberg
- Geng C, Zhang Q, Lei W et al (2017) Simultaneously reduced viscosity and enhanced strength of liquid silicone rubber/silica composites by silica surface modification. *J Appl Polym Sci* 134:45544

- GÖTTFERT Werkstoff-Prüfmaschinen GmbH Druckabhängigkeit der Viskosität. <https://www.goettfert.de/anwendungen-wissen/rheo-info/fuer-kapillarrheometer/druckabhaengigkeit-der-viskositaeet>. Accessed 06 Dec 2021
- Guan D, Cai Z, Liu X et al (2016) Rheological study on the cure kinetics of two-component addition cured silicone rubber. *Chin J Polym Sci* 34:1290–1300
- Haberstroh E, Michaeli W, Henze EK (2002) Simulation of the filling and curing phase in injection molding of liquid silicone rubber (LSR). *J Reinf Plast Compos* 21:461–471
- Haines P (2002) Principles of thermal analysis and calorimetry. Royal Society of Chemistry, Cambridge
- Harkous A, Colomines G, Leroy E et al (2016) The kinetic behavior of liquid silicone rubber: a comparison between thermal and rheological approaches based on gel point determination. *React Funct Polym* 101:20–27
- Hempel J (2001) Elastomere werkstoffe, Weinheim, Germany
- Henze EK (1999) Verarbeitung von Flüssigsilikonkautschuk (LSR) zu technischen Formteilen. Verlag Mainz, Wissenschaftsverlag, Aachen, Aachen
- Hoffmann K, Dumaine et al General discussion
- Hopmann C, Menges G, Michaeli W et al (2018) Spritzgießwerkzeuge. Auslegung, Bau, Anwendung. 7., neu bearbeitete Auflage. Hanser; Ciando, München
- Hülder G (2008) Zur Aushärtung kalthärtender Reaktionsharzsysteme für tragende Anwendungen im Bauwesen, 1st edn. Univ, Erlangen-Nürnberg, Lehrstuhl für Kunststofftechnik, Erlangen
- Jerschow P (2001) Silicone elastomers. Rapra Technology Ltd., Shawbury, U.K
- Kim D (2020) Curing kinetic and viscosity behavior of liquid silicone rubber for reaction injection molding analysis, vol. 3, 3. SPE ANTEC (2015: Orlando, Fla.) SPE ANTEC 2015, pp 2316–2320
- Klaiber F (2010) Entwicklung einer Anlagen- und Prozesstechnik für die Herstellung superhydrophober Oberflächen im Spritzgießverfahren. Development of a machine and process technique for the production of superhydrophobic surfaces by injection moulding. Zugl.: Aachen, Techn. Hochsch., Diss., 2010. 1. Aufl. Mainz, Aachen
- Kübler M (2010) Verfahrensentwicklung zur Herstellung gebrauchsbeständiger kleinststrukturierter Kunststoffbauteile. Zugl.: Berlin, Techn Univ, Diss., 2010. Univ.-Verl. der TU Berlin, Berlin
- Kuhn S, Burr A, Kübler M et al (2010) Study on the replication quality of micro-structures in the injection molding process with dynamical tool tempering systems. *Microsyst Technol* 16:1787–1801
- Lambrecht J, Wolf HP, Gerlach E (2003) Chemische Eigenschaften von Silicnelastomeren. In: Kindersberger J (ed) Silikonelastomere. [Elektronische Ressource]: VDE Verl, Berlin
- Leroy E, Soud A, Sarda A et al (2013) A knowledge based approach for elastomer cure kinetic parameters estimation. *Polym Test* 32:9–14
- Mezger T (2020) The rheology handbook. For users of rotational and oscillatory rheometers. 5th revised edition. Vincentz Network, Hannover
- Moretto H-H, Schulze M, Wagner G (2010) Silicones. In: Ullmann's encyclopedia of industrial chemistry. Wiley, Chichester
- NETZSCH Analysieren & Prüfen (2022) Dielektrische Analyse (DEA). <https://www.netzsch-thermal-analysis.com/de/contract-testing/methoden/dielektrische-analyse-dea/>, updated on 1/10/2022. Accessed 10 Jan 2022
- Nishinari K (2009) Some thoughts on the definition of a gel. In: Gels: Structures, properties, and functions. Springer, Berlin
- Nosonovsky M, Bhushan B (2008) Biologically inspired surfaces: broadening the scope of roughness. *Adv Funct Mater* 18:843–855
- Osswald T A, Rudolph N (2014) Polymer rheology. Fundamentals and applications. Hanser, Munich
- Osswald TA, Baur E, Rudolph N (2018) Plastics handbook. The resource for plastics engineers. 5. Auflage. Hanser Publications, Cincinnati, Ohio
- Ou H, Sahli M, Barriere T et al (2017a) Experimental characterisation and modelling of rheokinetic properties of different silicone elastomers. *Int J Adv Manuf* 92:4199–4211

- Ou H, Sahli M, Barrière T et al (2017b) Multiphysics modelling and experimental investigations of the filling and curing phases of bi-injection moulding of thermoplastic polymer/liquid silicone rubbers. *Int J Adv Manuf Technol* 92:3871–3882
- Owen MJ, Dvornic PR (2012) *Silicone surface science*. Springer, Dordrecht
- Pahl M, Gleißle W, Hans-Martin L (eds) (1995) *Praktische Rheologie der Kunststoffe und Elastomere*. 4., überarb. Aufl., Düsseldorf. VDI-Verl. (Kunststofftechnik)
- Pelz PF (2001) Die Rheologie Kautschukmischung. In: Hempel J (ed) *Darmsstadt (Elastomere Werkstoffe)*. <http://tubiblio.ulb.tu-darmstadt.de/36244/>. Accessed 16 Feb 2021
- Pogodin S, Hasan J, Baulin VA et al (2013) Biophysical model of bacterial cell interactions with nanopatterned cicada wing surfaces. *Biophys J* 104:835–840
- Rapp BE (2017) *Microfluidics. Modeling, mechanics, and mathematics*. William Andrew, Kidlington, United Kingdom
- Ratner BD (ed) (2013) *Biomaterials science. An introduction to materials in medicine*. 3. ed., Amsterdam, Heidelberg, Elsevier
- Röthemeyer F, Sommer F (2013) *Kautschuk-Technologie. Werkstoffe–Verarbeitung—Produkte*. 3., neu bearb. und erw. Aufl. Hanser, München
- Saražin J, Schmiedl D, Pizzi A et al (2020) Bio-based adhesive mixtures of pine tannin and different types of lignins. *BioRes* 15:9401–9412
- Schneider C (1986) *Das Verarbeitungsverhalten von Elastomeren im Spritzgießporens*. Dissertation. Rheinisch-Westfälischen Technischen Hochschule Aachen, Aachen. Fakultät für Maschinenwesen
- The Dow Chemical Company (2012) *Liquid injection molding. Processing guide for SILASTIC™ liquid silicone rubber (LSR) and SILASTIC™ fluoro liquid silicone rubber (F-LSR)*. The Dow Chemical Company. <https://www.dow.com/content/dam/dcc/documents/en-us/app-tech-guide/45/45-10/45-1014-01-liquid-injection-molding-processing-guide.pdf?iframe=true>, updated on 2020. Accessed 30 Aug 2021
- Tomanek A (1990) *Silicone & Technik. Ein Kompendium für Praxis, Lehre und Selbststudium*
- Tran NT (2020) *Creating material properties for thermoset injection molding simulation process*. Universitätsverlag Chemnitz, Chemnitz
- Verheyen F, Giesen R-U, Heim H-P (2016) Characterizing the rheological behavior of liquid silicone rubber using a high pressure capillary rheometer
- Verheyen F (2019) *Die extrusion von Festsilikonkautschuk*. With assistance of Universität Kassel Wacker Chemie AG, von Siliconen H (2020) <https://www.chem2do.de/c2d/de/silicone/herstellung/herstellung.jsp>. Accessed 21 Jan 2020
- Walde H (1996) *Beitrag zum vollautomatischen Spritzgießen von Flüssigsilikonkautschuk*. Basics of automatic injection moulding of liquid silicone rubber. 1. Aufl. Verl. der Augustinus-Buchh, Aachen
- Weißer DF, Walz D, Schmid J et al (2020) Calculating the temperature and degree of cross-linking for liquid silicone rubber processing in injection molding. *Jnl Adv Manuf Process*. <https://doi.org/10.1002/amp2.10072>
- Winter HH (1987) Can the gel point of a cross-linking polymer be detected by the $G' - G''$ crossover? *Polym Eng Sci* 27:1698–1702
- Winter HH, Chambon F (1986) Analysis of linear viscoelasticity of a crosslinking polymer at the gel point. *J Rheol* 30:367–382
- Winter HH (2002) The critical gel. In: R Borsali, R Pecora (eds) *Structure and dynamics of polymer and colloidal systems*. Springer Netherlands, Dordrecht
- Wolf A, Andriot M, Chao S-H et al (2008) Chapter 2—Silicones in industrial applications. In: Gleria M, de Jaeger R (eds) *Silicon-based inorganic polymers*. Nova Science Publishers, New York
- Ziebell R, Bhogesra H (2016) LIM simulation modeling using newly developed chemorheological methods. In: *International silicone conference*. International Silicone Conference. Akron, OH, 17-18 May 2016

Chapter 19

Investigation of Adhesion and Surface Treatments for Thermoplastic—Liquid Silicone Rubber Joints in Multicomponent Injection Molding



Dennis Mayer, Simon J. Heienbrock, Dennis F. Weißer, Johannes Schmid, Sascha Müller, Lothar Kroll, and Matthias H. Deckert

Abstract An initiation of adhesion between standard thermoplastic injection molding materials and non-adhesion-modified optical grade liquid silicone rubber (LSR) was achieved via physical surface treatments. In this study, peel test specimens of thermoplastic and liquid silicone rubber were produced in a two-component injection mold. Both surface treatments, atmospheric pressure plasma jet and sili-cating were studied on their influence on the substrate surface. It was shown that the surface energy was significantly increased, which also had the effect of initiating and increasing adhesion of the joint. A classification of the surface treatments, based on their influence on polar surface energy and peel force, was carried out. Such classifications can help to better understand surface treatments influence in

D. Mayer (✉) · D. F. Weißer · J. Schmid · M. H. Deckert
Faculty of Mechanical and Systems Engineering, Esslingen University of Applied Sciences,
Kanalstr. 33, 73728 Esslingen am Neckar, Germany
e-mail: dennis.mayer@hs-esslingen.de

D. F. Weißer
e-mail: dennis.weisser@hs-esslingen.de

J. Schmid
e-mail: johannes.schmid@hs-esslingen.de

M. H. Deckert
e-mail: matthias.deckert@hs-esslingen.de

S. J. Heienbrock
Department of Development and Innovation, Wilhelm Weber GmbH & Co. KG, Boppenäckerstr.
10, 73734 Esslingen am Neckar, Germany
e-mail: s.heienbrock@weber-esslingen.de

S. Müller · L. Kroll
Department of Lightweight Structures and Polymer Technology, Chemnitz University of
Technology, Reichenhainer Str. 31/33, 09126 Chemnitz, Germany
e-mail: sascha.mueller@mb.tu-chemnitz.de

L. Kroll
e-mail: lothar.kroll@mb.tu-chemnitz.de

the context of thermoplastic-liquid silicone rubber joints and to estimate potential adhesive properties of the joining components.

Keywords Adhesion · Surface treatment · Liquid silicone rubber · LSR · Multicomponent injection molding · Plasma · Silicating · Surface energy · Peel test

19.1 Introduction

For today's plastic components, the integration of functions plays an increasing role. This often requires the use of several materials with different properties. Hard–soft compounds are often used where the combination of stiffness and strength properties in combination with flexible, elastic, sealing, or haptic properties is advantageous (Goodship and Love 2002). In the field of polymer hard–soft compounds, combinations of thermoplastics and thermoplastic elastomers (TPE) are widely used and have been sufficiently studied (Jaroschek 1993; Kuhmann 1999; Schuck 2009). The use of TPE can be problematic in applications with high operating temperature requirements (Ronnewinkel 2000; Schlitt 2018). Here, as in the specific case of an optical application, the use of liquid silicone rubber (LSR) becomes highly interesting. At this point, two challenges in the processing of LSR must be stated. One challenge is the multi-component molding of thermoplastics in combination with LSR (Ronnewinkel 2000; Seitz 2015; Goodship and Love 2002; Wilcik et al. 2011). A sophisticated temperature control concept must be realized that enables both materials to be processed in a way that is suitable for the material. On the one hand, in the exemplary case of a polyamide66, the thermoplastic melt (300 °C) must be solidified at a mold temperature of 100 °C. On the other hand, the crosslinking of LSR must take place in the same mold at, for example, 160 °C after the liquid is injected at room temperature.

A much greater challenge is posed by material compatibility and the resulting adhesion in thermoplastic-LSR joints (Ronnewinkel 2000; Thust 2014; Seitz 2015; Schlitt 2018). This is even more significant if the LSR cannot be modified in terms of adhesion, as it is the case within this work. For this reason, the authors identified a demand to initiate this publication.

The objective of the present study involves the initiation of adhesion for standard thermoplastic materials in combination with an optical grade, non-adhesion modified LSR. For this purpose, two surface treatment methods are to be investigated in detail. The treatment methods are to be characterized in terms of their influence on the surface energy of the treated surface and the adhesion generated for the material joint in the form of the peel force. A final classification of the treatment methods in terms of their influence on the surface energy and peel force is intended to provide a possibility for estimating the adhesion to be expected for a specific material combination. The basis for this is the modification of the thermoplastic surface, and its resulting influences on the surface energy.

For this purpose, the theoretical background covers adhesion theories relevant for thermoplastic-LSR joints. Furthermore, the surface treatments via atmospheric pressure plasma jetting and silicating are introduced. The following section presents the materials used as well as the experimental setup and implementation. This includes the production of the two-component test specimens, the surface treatment methods, the measurement of the surface energies, and the determination of the adhesion of the material joints. Furthermore, the results of the determined surface energies of the solids as well as the achieved adhesion forces are presented in order to classify the effects of the surface treatments. At the end of this work, summarizing conclusions are made, and an outlook on further research objectives is given.

19.2 Theoretical Background

19.2.1 *Relevant Adhesion Theories for Thermoplastic-LSR Joints*

Adhesion is interpreted differently and used as a synonym for a surface or material property, a process, a state or a phenomenon, depending on the view. This could be due to the complex interaction of several different and not yet fully understood mechanisms and interactions. Different theories and approaches exist to explain basic adhesion models at the molecular level, and no universal explanation for these processes can be found (Härtig 2012). A superposition of the individual adhesion models is likely, which is why they can only explain the adhesion between two components in their entirety (Seitz 2015).

For plastic-plastic joints, four adhesion theories are generally of particular relevance for the formation of adhesion. These are mechanical adhesion in the form of undercuts, diffusion theory in the form of interdiffusion, polarization theory, and adsorption theory (Schuck 2009). For adhesion mechanisms in thermoplastic-LSR joints in particular, there is little established understanding. No theory provides a complete description of the interactions and adhesion mechanisms, which in turn highlights the complexity of adhesion (Ronnewinkel 2000; Thust 2014).

According to (Thust 2014), mainly radical-initiated hydrogen abstraction and crosslinking reactions across the interface are plausible for adhesion in thermoplastic-elastomer joints. Furthermore, various surface treatments are used to initiate adhesion for thermoplastic-LSR joints (Schlitt 2018; Seitz et al. 2016). Here, the thermoplastic surfaces can be modified with reactive groups, which in turn promote covalent bonds (Lake 2009). This modification can also occur through the formulation of the LSR. Thus, the formation of chemical bonds in the form of hydrogen abstraction between the thermoplastic and LSR can also occur if the LSR contains a radical-forming crosslinking agent (Thust, 2014; Seitz et al. 2016). Chemical modification of the LSR is not possible in the specific application and therefore will not be further discussed in this study.

The prerequisite for the relevant theories and approaches to describe adhesion is good wetting of the adherent by the adhesive (Kühnert 2005; Thust 2014). That in turn depends significantly on the intermolecular interactions in the phase surface of a material. The greater the attraction of the partners, the lower the interfacial tension and the better the wetting (Kopczynska 2008; Schuck 2009). In order to manipulate the surface energy of plastics, surface treatment methods are introduced.

19.2.2 Surface Treatment Methods

Plastics are classified as low-energetic in terms of interface terminology. In addition, the surface energy levels of various plastics are very similar, which is why low wetting must generally be assumed for plastic-plastic joints (Habenicht 2009). To still enable good wetting and to utilize additional adhesion-relevant effects, surface treatment of the substrate surface becomes obvious. Treatment processes can expose or create physically or chemically reactive spots on the surface, which in turn represent the prerequisite for the required atomic and molecular interactions (Roth 2001; Habenicht 2009).

According to (Habenicht 2009), the known and common surface treatment methods for plastic-plastic joints can be assigned to three categories.

- **Mechanical treatments:** Processes such as cleaning and roughening remove adhesion-inhibiting boundary layers and increase the effective surface area of the interface.
- **Chemical treatments:** Processes such as pickling, gas-phase fluorination, sulfonating, and ozonation are used to form and enrich polar groups in the surface. The basic principle is the installation of electronegative elements that form dipoles.
- **Physical treatments:** Processes such as plasma treatment, corona discharge, flame treatment, laser treatment, and ion etching also represent chemical modifications of the surface. However, the processes are based on basic physical principles, which is why a distinction is made at this point between chemical and physical processes. (Habenicht 2009)

In the following, the physical surface treatment methods: plasma treatment and silicating, as a special process of flame treatment, are presented.

19.2.2.1 Surface Treatment via Atmospheric Pressure Plasma Jet

Plasma can be understood as the fourth state of matter and refers to a gas excited into energetic states consisting of atomic, molecular, ionic, free radical as well as metastable species (Kinloch 1987; Tiwari and Soucek 2014). Plasma technologies can be differentiated among others according to process pressures, thermal impact as well as the type of energy coupling. For this study, the atmospheric pressure plasma jet is relevant and will be considered in the following.

Here the energy for the plasma is supplied by a generator. The atmospheric pressure plasma is generated by a high-voltage discharge in the nozzle, which is equipped with electrodes. Air is used as process gas. The plasma exits due to the nozzle geometry in a directional manner (Schuck 2009). Since the surface to be treated is only briefly in contact with the plasma jet, the thermal effect on the surface is small and the treatment does not lead to thermally damaging the base material (Roth 2001; Gil'man 2003; Habenicht 2009; Tiwari and Soucek 2014). For this reason, the use of the process is particularly suitable for the treatment of plastic surfaces.

The influence of treatment with atmospheric pressure plasma jet on the plastic surface is multifaceted, and the impact of the plasma jet leads to both physical and chemical effects. The physical effect of the plasma jet is due to the energy of the ions that act on the surface and result in the fine cleaning effect. The chemical effect of the plasma jet is understood as the reaction of the surface with the reactive gas components occurring in the plasma jet, which leads to an activation of the surface in the form of higher reactivity due to free radicals. In addition, the radiation occurring during plasma treatment is capable of intensifying these effects (Habenicht 2009; Tiwari and Soucek 2014). Depending on the composition of the process gas as well as the polymer to be treated, chemical changes occur on the surface. In an oxygen atmosphere, dipoles are formed which significantly change the wetting properties and through their integration, the polymer surface obtains polar properties (Roth 2001; Gil'man 2003; Habenicht 2009).

Another effect of atmospheric pressure plasma treatment on polymer surfaces is the cleaning or removal of low molecular weight contaminants (Kinloch 1987; Roth 2001). The treatment can be further characterized by the fact that no ions or atoms are injected under the treated surface (no ion implantation), that no material is removed (no etching), and that the treatment does not lead to any significant addition of monolayers (no deposition). It has been shown that surface treatment by plasma can replace adhesion additives at least as well, whereas overtreatment can have the opposite effect on polycarbonates and reduce adhesion. (Roth 2001; Lau 2006).

19.2.2.2 Surface Treatment via Silicating

Silicating is a special form of flame treatment. Flame treatment has been known since 1952 as the Kroidl process and involves directing the surface to be treated through a premixed gas-oxygen flame, which shortly leads to temperatures of 200–400 °C on the surface. This results in oxidation of the uppermost molecular layers of the plastic surface. Similar to plasma treatment, this chemical and physical modification leads to the formation of various C-O groupings in the surface area. These groups exhibit significantly stronger intermolecular interactions than the non-polar hydrocarbon chain. Thus, flame treatment is not a purely thermal process, but rather the utilization of the chemical activity of the flame. It has been shown that the activation of the surface is reversible and rapidly decreases to its initial state. To achieve a stable hydrolytic bond, the surface can be modified more fundamentally by the application

of coating layers. In this way, layers can achieve various properties that the original surface does not exhibit. (Habenicht 2009; Richter and Tiller 2004).

The process of silicating is characterized by the addition of substances to the flame. These substances react in combination with the flame and deposit as a layer on the surface. The addition of organosilicon compounds to the flame results in the silicating of the surface. In this process, a 5–100 nm thick layer of amorphous silicon oxides is deposited in the form of a dense and firmly adhering layer (Habenicht 2009; Sura Instruments GmbH 2022). As an alternative to pickling and etching techniques for the pretreatment of metals for plastic coatings, the process was developed in the 1980s and introduced under the brand name Pyrosil® (Richter and Tiller 2004).

The adhesion-relevant effects of silicating can be divided into two mechanisms. Due to the treatment, there is a high reactivity of the layer, which results in chemical bonding possibilities for organic components. In addition to that, the silicon dioxide (SiO₂) layer has a microporous surface structure (Sura Instruments GmbH 2022; Richter and Tiller 2004). Depending on the process parameters of the silicating, the structure of the surface can be specifically adjusted. It has been shown that layers for specific applications can be obtained by adjusting the surface porosity and structure (Struppert et al. 2012). The authors illustrated a dense and smooth SiO₂ barrier layer with a Ra roughness of about 2 nm as well as an antireflective layer with a relatively high roughness of about 20 nm. The selective adjustment of porosity and surface roughness can be used in the context of adhesion to maximize the interface area and to improve the wetting.

19.3 Materials and Methods

19.3.1 Materials

The following five thermoplastic materials are used to investigate the influence of surface modifications on the adhesion between thermoplastics and liquid silicone rubber, see Table 19.1.

Table 19.1 Thermoplastic materials investigated within this study

Material	Manufacturer	Polymer	Properties
Makrolon® 2405	Covestro	PC	Standard type and low viscosity
Plexiglas® Satinice df20 8 N	Roehm	PMMA	Good diffusing power and light transmittance
Terluran® GP-22	Ineos Styrolution	ABS	High resistance to impact and heat distortion
Zytel® 101L	Dupont	PA66	Standard type
Zytel® 70G35HSL	Dupont	PA66-GF35	Heat stabilized and 35% glass fiber reinforced

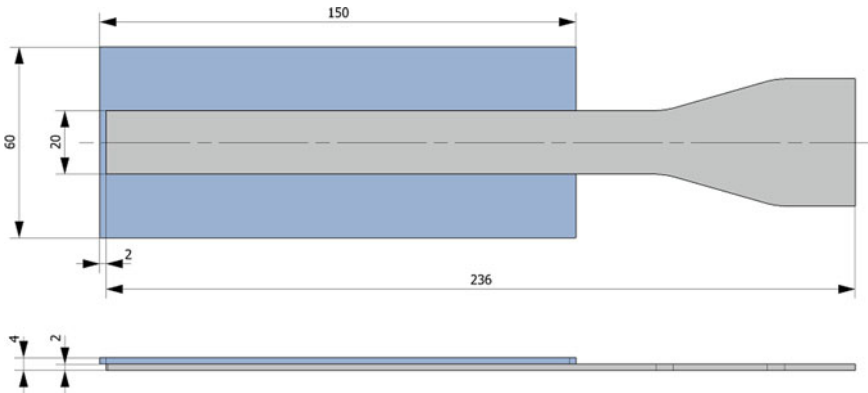


Fig. 19.1 Two-component peel test specimen in accordance with (Verein Deutscher Ingenieure 2016)

These injection molding grades are studied in terms of adhesion in combination with the optical grade polydimethylsiloxane (PDMS) Dowsil® MS-1002 moldable silicone by The Dow Chemical Company. It is a medium viscosity, high Shore A hardness and fast curing optical molding resin. Applications for this LSR grade include primary or secondary lenses, light pipes, light guides, and other optic devices.

19.3.2 Methods

19.3.2.1 Two-Component Peel Test Specimen

To evaluate the adhesion between the thermoplastic and the silicone material, a two-component peel specimen is used. The specimen is described in the guideline 2019 by the Association of German Engineers (VDI) and is originally defined for testing the adhesion of thermoplastic elastomers (TPE) on substrates (Verein Deutscher Ingenieure 2016). The guideline is nevertheless widely used to quantify adhesion for hard–soft joints in general (Seitz 2015; Schlitt 2018; Baumgart et al. 2014, 2016; Kühr et al. 2014) (Fig. 19.1).

19.3.2.2 Injection Molding

Injection Molding Machine

A two-component injection mold for processing thermoplastics and LSR into peel test specimen was produced. The mold is designed to fit an Arburg Allrounder 420 °C vertical/horizontal two-component injection molding machine. The machine has a

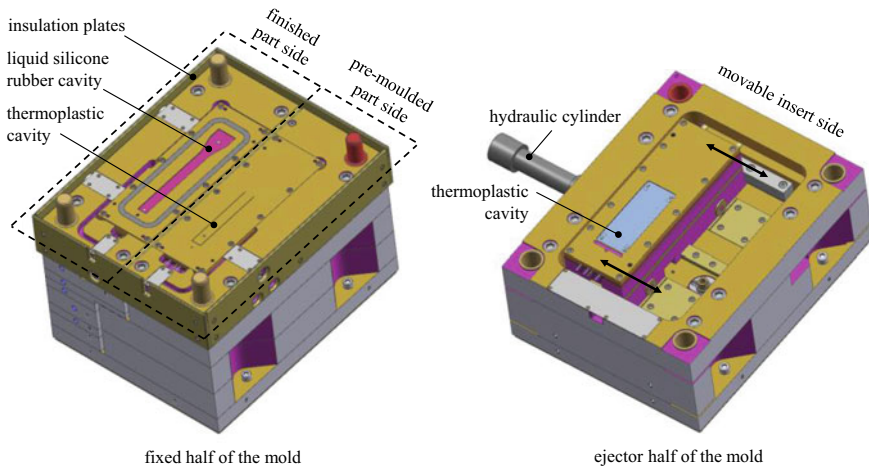


Fig. 19.2 Layout of the two-component injection mold for the production of peel test specimens

tie bar distance of 420 mm and a clamping force of 1000 kN. The vertical injection unit for processing LSR is fed with material via a dosing unit. The metering unit pumps the LSR components *A* and *B* in a ratio of 1:1, mixes them via a static mixer to form a homogeneous mass and feeds it to the injection unit.

Injection Mold

The injection mold is divided into two parts on the fixed side and has an insert package on the ejector side which can be moved by means of a hydraulic core pull. The mold design is shown in Fig. 19.2. The temperature control of the mold is a challenge when processing thermoplastics and liquid silicone in one process. While thermoplastic molding compounds are injected hot and cooled by the mold walls, the temperature control is reversed for LSR. The liquid silicone, which is cooled until it enters the hot cavity, cross-links as a result of the heat input. In order to be able to control the temperature management in the injection mold, the injection mold was designed variothermally. By using seven separately controllable electrical heating circuits and seven corresponding water-cooling circuits, the mold wall temperatures can be adjusted as required.

The pre-mold insert on the fixed mold half and the insert on the ejector half for producing the thermoplastic pre-mold, each have three heating and cooling circuits, which can heat and cool the cavity close to the contour. The ability to control the circuits individually allows for example, the contact surface of the pre-molded part, which is later flooded by the LSR, to be heated or cooled in a controlled manner. In addition, the finished part side of the fixed half is equipped with a heating and cooling circuit.

For precise monitoring and evaluation of the injection molding process, the mold is equipped with three cavity pressure sensors from Kistler Instrumente GmbH. One sensor of type 6157C is located near the sprue in the thermoplastic pre-mold cavity and two further sensors of type 6152B are located near and far from the sprue in the finished mold cavity for LSR. The associated process monitoring is performed by the ComoNeo system from Kistler.

Two-Component Injection Molding Process

The first section of the fixed half consists of a pre-mold side, which is used to produce the thermoplastic pre-mold. Here, the hot melt is fed from the vertical injection unit via a hot runner into the cavity on the ejector side. According to the manufacturers, mold temperatures in this area, for the thermoplastics already listed, range from 30 (minimum) to 130 °C (maximum), depending on the material processed. After the holding pressure and cooling time phase, the mold is opened 10 mm wide. The hydraulic core pull then moves the ejector side insert together with the thermoplastic pre-molded part to the finished part side. In order to limit the dissipation of heat during this opening, the insulating plates on the fixed half around the mold overhang the parting line by 15 mm. As a result, the mold remains thermally closed at an opening of 10 mm.

The second section of the fixed half consists of the finished part side with the LSR cavity. The cold runner nozzle feeds the liquid from the horizontal injection molding unit, which is always cooled to room temperature, into the cavity, which in turn is tempered to 160 °C. The finished part cavity on the fixed half is surrounded by a sealing strip, which is needed to build up a vacuum to prevent air from entering the silicone component. In the second step of the process sequence, the mold is now closed and a vacuum is applied at the same time. Once the cavity is vacuumed to a pressure level of less than 0.1 bar, the LSR is injected onto the thermoplastic pre-molded part. After the LSR has crosslinked, the mold is opened and the two-component peel specimen is ejected.

19.3.2.3 Surface Treatments

Preliminary tests involving the listed thermoplastics and the optical grade LSR MS-1002 showed that no adhesion at all was achieved for ABS, PC, and PMMA in two-component injection molding. For PA66 and PA66-GF35, low levels of adhesion could be achieved. Due to various aspects such as the required treatment time, the possibility of process integration in injection molding, and possible negative influences on the thermoplastic substrate, the surface treatment processes of atmospheric pressure plasma jet, and Pyrosil® silicating are the focus of the following investigations.

Within the scope of this study, both processes could only be carried out on a laboratory scale. If the treatment processes were to be applied to series production

components, they would have to be integrated into the two-component injection molding process. In this context, the treated thermoplastic plates were inserted into the injection mold at room temperature and overmolded with LSR. At this point, it must be mentioned that the influence of the thermoplastic temperature on the subsequent joint strength could not be investigated. It is assumed that the temperature of the thermoplastic during overmolding with LSR has an influence on the adhesion-relevant effects and thus influences the adhesion between the components.

Surface Treatment via Atmospheric Pressure Plasma Jet

The thermoplastic plates were treated by Plasmatrete GmbH using its atmospheric pressure plasma jet technology Openair-Plasma® (Plasmatrete GmbH 2022). Compressed air with a flow rate of 45 l min^{-1} was used as process gas. The later contact surface between thermoplastic and LSR was treated with a rotary nozzle type RD1004 which sufficiently covers the width of the contact surface of 20 mm and treats it uniformly. Treatment was performed on one cycle with a translational feed rate of 9 m min^{-1} and a distance of 10 mm between nozzle and thermoplastic substrate.

Surface Treatment via Silicating

The treatment of the thermoplastic plates was carried out externally by the company Sura Instruments GmbH. The flame pyrolytic deposition of silicon dioxide is based on the company's Pyrosil® process and can be assigned to the surface treatment silicating. Here, the treated thermoplastic surface was run over with a gas flame into which the Pyrosil precursor is dosed. The silicon containing precursor burns and deposits on the thermoplastic surface as an amorphous silicon dioxide layer. (Sura Instruments GmbH 2022).

The translational speed at which the flame was moved over the substrate surface was 600 mm s^{-1} . Four deposition cycles were carried out with a delay of 10 s each. The distance between the flame and the substrate was 25 mm. The resulting silicon dioxide layer has a calculated thickness of 22 nm. The treated thermoplastic plates were processed the next day where they were placed in the injection mold at room temperature and overmolded with LSR.

19.3.2.4 Measurement of Surface Energy

To determine the wettability of the thermoplastic plates, their surface tension was measured. The OCA 20 contact angle measuring device from Data physics was used for this purpose. A defined drop of a test liquid is deposited via a dosing device on the surface to be measured. A camera system detects the deposited drop on the substrate

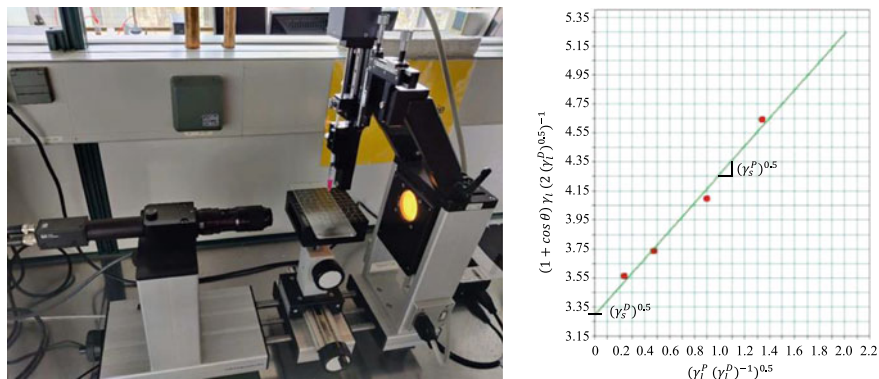


Fig. 19.3 Setup up of the contact angle measurement system (left) and exemplary measurement result consisting of four test liquids

surface. The opposite lighting helps to increase the contrast of the drop. The contact angle measuring device with its setup is shown in Fig. 19.3 on the left.

Using drop geometry analysis software, the contact angle of the test liquid on the substrate surface at the 3-phase point is determined by evaluating the circular tangents. Four test liquids were used in this study. Each of the liquids has different polarities. The used test liquids with their surface energy as well as their disperse and polar surface energy components are listed in Table 19.2.

Contact angles were determined with four different test liquids on the untreated and treated thermoplastic plates. Each contact angle determination consisted of at least five measurements per liquid and substrate surface. The subsequent determination of the surface energy was carried out according to the method of geometric mean derived by Owens, Wendt, Rabel, and Kaelble (OWRK). The surface energy of the thermoplastic surface is now determined via linear regression using the measured contact angles and the known disperse and polar surface energy components of the test liquids. An exemplary evaluation is shown in Fig. 19.3 on the right. The disperse surface energy component is calculated from the square of the ordinate intercept, the polar surface energy component via the square of the slope of the straight line.

Table 19.2 Test liquids used with their total surface energy as well as their disperse and polar surface energy components

Test liquid	Total surface energy [mN m ⁻¹]	Disperse component [mN m ⁻¹]	Polar component [mN m ⁻¹]
Water	72.8	21.8	51.0
Diiodomethane	50.8	50.8	0.0
Ethylene glycol	47.7	30.9	16.8
Dimethyl sulfoxide	44.0	36.0	8.0

19.3.2.5 Determination of Peel Force

Fixture

A peel device based on VDI guideline 2019 is used to quantify the adhesion between thermoplastics and LSR. This device is used to determine the peel force of the inserted peel specimen on a Zwick/Roell 14450 universal tensile testing machine. After installation of the measuring device, the tensile testing machine has a remaining traverse path of 650 mm. If silicones with high elongation are used, the traverse path can be a limiting factor in the peel test, since it can be fully exploited. The peel device was designed in-house and adapted to the requirements of the guideline. It consists of a linear guide with slide, two holders for fixing the thermoplastic plate on the slide, and a pulley that ensures vertical removal of the LSR component. During the design process, special emphasis was placed on the smooth running of the slide as well as the pulley in order to avoid overlapping of the slide resistance and the actual peel forces. Furthermore, the two holders are equipped with individually adjustable underlays to compensate for the different shrinkage of the various thermoplastic materials.

Implementation

The fixture is attached via the tension rod of the tensile testing machine. In the next step, a peel specimen is attached to the slide via the thermoplastic plate. As shown in Fig. 19.4 on the left, the LSR component is clamped into the clamping jaw. The tensile testing machine now peels the LSR component from the thermoplastic component at a constant traverse speed of 100 min^{-1} at 90° to the adherent surface. Meanwhile, the test routine records the force level of the load cell as well as the traverse path. The test is finished when the LSR component has been completely pulled off the thermoplastic component or material failure occurs.

Analysis

The adhesion of the joint is evaluated by means of the recorded force/traverse path curve during the test. An example is shown in Fig. 19.4 on the right. ISO 6133 specifies the analysis of multi-peak traces obtained in determinations of tear strength and adhesion strength. According to the standard, the determination of the average force depends on the curve shape and the number of peaks. Thus, a distinction is made between five cases: curves with less than 5 (a), between 5 and 20 (b), and more than 20 (c) peaks. Further, a distinction is made in curves with too many dense peaks (e) as well as curves with wavy course (d) (DIN 2017).

For the scope of this study, only the evaluation method (d) is relevant. In this case, the arithmetic mean is stated as the midpoint between maximum and minimum. As can be seen in the figure, a constant force level is established first after an increase up to about 20% of the total traverse path. This increase can be explained by the

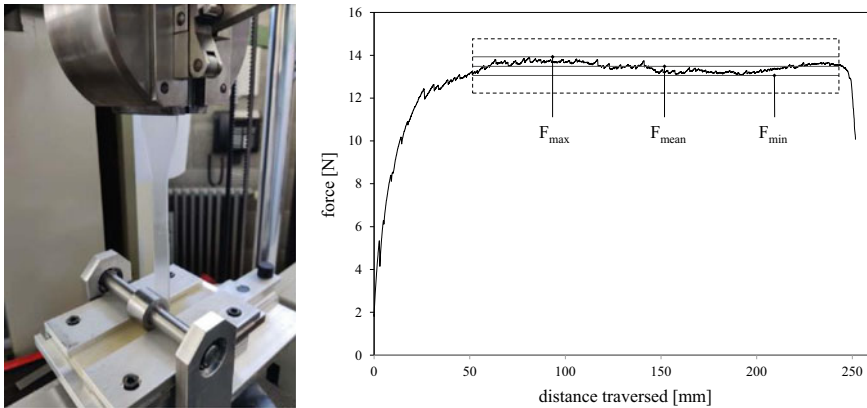


Fig. 19.4 Peel test of a PA66-GF35/MS-1002 peel specimen (left) and exemplary graph of the force over the traverse path including the evaluation range, maximum, minimum as well as average peel force (right)

superposition of tensile forces in the silicone and the force caused by adhesion. This range is irrelevant for the evaluation of the average peel force.

19.4 Results and Discussion

19.4.1 Surface Energy of Thermoplastics

For the determination of surface energy, several plates were selected for each of the five thermoplastic materials and treatment methods. The surface energy was determined with five measurements for the untreated, atmospheric pressure plasma jet treated, and silicized conditions. The results of the determination of the surface energy as disperse and polar components can be seen in Fig. 19.5. The measured contact angles were all in the range of $\pm 2.8^\circ$, and the corresponding surface energies show an almost consistent picture. An increase in the total surface energy from the untreated to the plasma-treated to the silicized state can be observed for all materials investigated. Only a slight increase in surface energy was observed for ABS after plasma treatment with 48.6 mN m^{-1} and after silicating 49.0 mN m^{-1} . The same trend is also seen in the increase of the polar surface energy component for all materials. Increasingly from the untreated to the plasma-treated to the silicized state, the percentage of the polar component to the total surface energy increases. For example, the silicized ABS has the highest percentage of polar to total surface energy of 69.0%, whereas PA66-GF35 has with 60.7% the highest percentage for the plasma treatment. An opposite trend can be observed for the disperse component. Thus, the disperse component decreases from the untreated to the plasma-treated

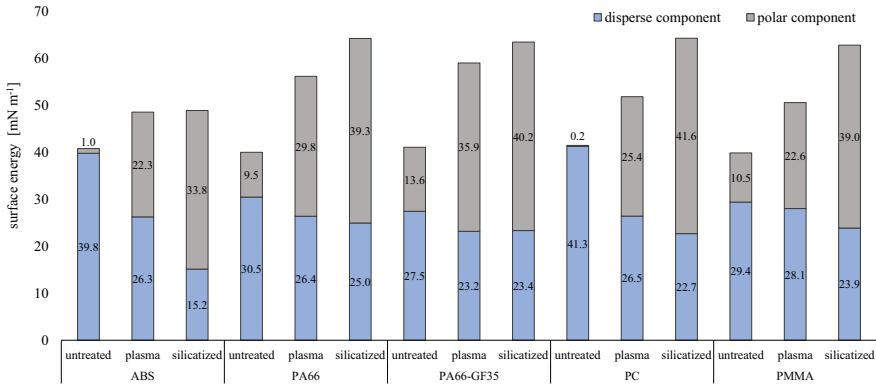


Fig. 19.5 Results of the determination of the disperse and polar surface energy components for the materials ABS, PA66, PA66-GF35, PC, and PMMA in the untreated, plasma-treated, and silicized state

to the silicized state for four of the five materials investigated. An exception is PA66-GF35, which shows a slight increase from the plasma-treated state with 23.2–23.4 mN m⁻¹ in the silicized state.

19.4.2 Peel Forces of Thermoplastic-LSR Joints

After overmolding, the untreated and treated thermoplastic plates with LSR, the contact zone was examined. The joints showed no air inclusions or defects at the interface, which is why it was possible to perform the peel tests according to (VDI 2016). The peel specimens evaluated all exhibited the same fracture pattern, which can be attributed to a pure adhesive failure. The LSR component could be peeled off from the thermoplastic substrate without leaving any residue.

The results of the peel tests are shown in Fig. 19.6. As already investigated in the preliminary tests, PMMA, ABS, and PC in the untreated state do not adhere to the MS-1002. On the other hand, the use of polyamide66 with and without glass fiber reinforcement leads to peel forces in the range of 5.47 and 5.88 N. At this point, it should be mentioned that there might have been adhesion with PMMA, ABS, and PC, which was so low that the joint was already separated when the specimen was ejected from the mold.

The picture is different for substrates treated with atmospheric pressure plasma jet. For PMMA, ABS, and PC, the treatment leads to an initial initiation of adhesion. However, for PMMA (4.24) and PC (4.55 N), this is below the force level obtained for the two polyamides66 without treatment. Together with ABS, both PA66 and PA66-GF35 exhibit fairly similar peel forces in the range of 8.04–9.02 N. Overall, the plasma treatment leads to an increase in peel force compared to the untreated state

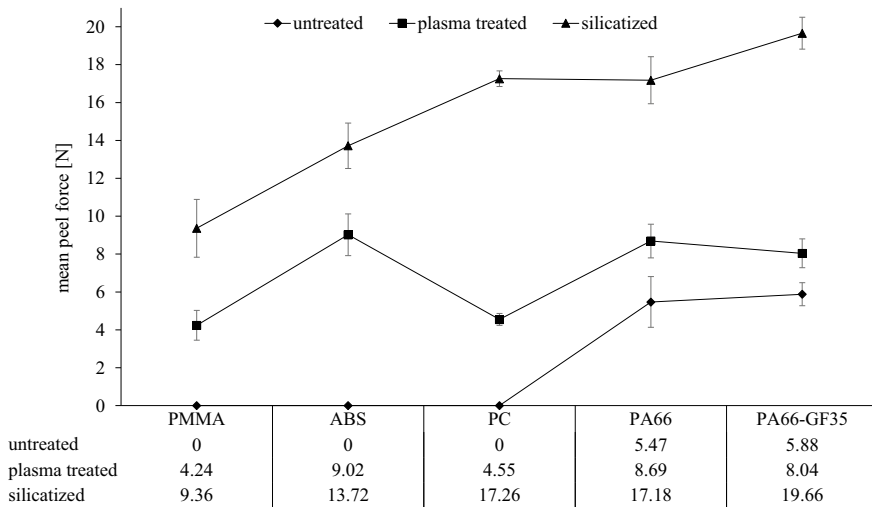


Fig. 19.6 Mean peel forces of the thermoplastic substrates in combination with MS-1002 for the applied surface treatments

for PA66 and PA66-GF35 as well as to an initial initiation of adhesion for PMMA, ABS, and PC.

When the thermoplastic substrates are silicized, a significant increase in joint strength compared to plasma treatment can be observed for all tested specimens. ABS shows an increase in peel strength from 4.7 to 13.72 N. For PMMA and PA66, the peel forces achieved approximately doubles to 9.36 N for PMMA and 17.18 N for PA66. Polycarbonate shows a 279% increase in peel force to 17.26 N compared to the plasma treatment. The highest peel force level of all samples was observed for the silicized PA66-GF35. The peel force of 19.66 N represents an increase of 145% compared to the plasma treatment and 234% compared to the untreated condition.

19.4.3 Classification of Surface Treatments

The influence of surface energy on adhesion in polymer–polymer joints has already been described in Sect. 2.1. Furthermore, it was discussed in Sect. 2.2 that the increase of the surface energy has a significant influence on thermoplastic-liquid silicone rubber joints and that non-polar plastics exhibit significantly better adhesion properties after enrichment of polar groups at the surface. Based on the measured surface energies of the treated thermoplastic substrates and the determined peel forces of the thermoplastic-LSR joints, a classification of the surface treatments is now to be carried out. For this purpose, the peel forces are plotted against the polar components of the surface energy for all surface treatments and materials. The classification of the surface treatments is shown in Fig. 19.7.

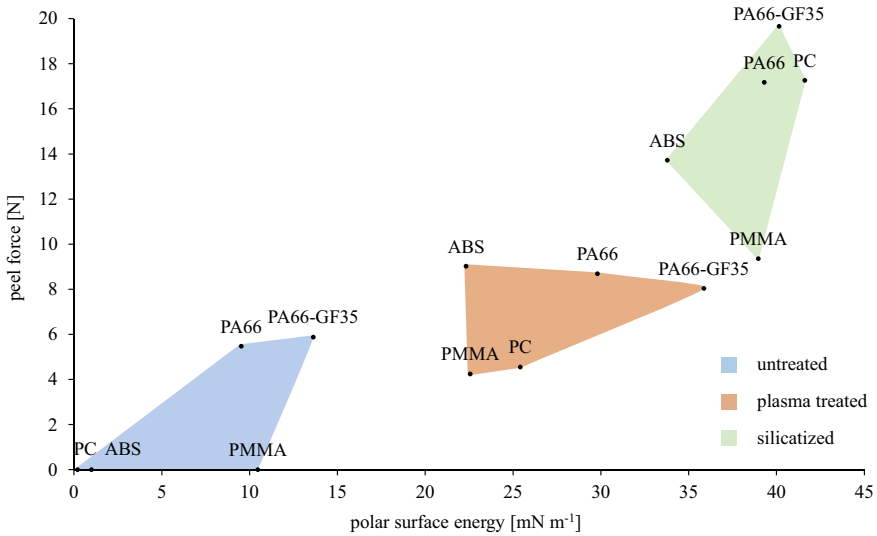


Fig. 19.7 Classification of surface treatments according to surface energy und peel force

Three clearly separated areas reflecting the surface treatments can be seen. This clustering illustrates the relation of polar surface energy component and achieved peel force. As expected, the untreated thermoplastics form the section with the lowest polarity. Moreover, only the two polyamides66 with and without reinforcement exhibit adhesion with the non-adhesion-modified LSR. The substrates treated with atmospheric pressure plasma jet are found to be in the range of 22.3–35.9 mN m⁻¹ and associated mean peel forces of 4.24–9.02 N. The peeling forces of the studied joints increase to their maximum values for treatment via silicating, which in turn has the largest polar surface energy components in the range of 33.8–41.6 mN m⁻¹ and peel forces ranging from 9.36–19.66 N. In addition to clustering the surface treatment methods, the influence of the treatments on the materials with resulting polarity and adhesion can be seen. Thus, an increase in polarity and peel force can be observed for each material.

The increased adhesion and the simultaneous increase in polar surface energy can be explained by the effects generated in the thermoplastic surface by the surface treatments. As described, treatment with an atmospheric pressure plasma jet leads to activation of the surface in the form of higher reactivity. The integration of dipoles in the form of carbonyl, carboxyl, or hydroxyl groups generates secondary valent binding forces and improves the wetting properties (Habenicht 2009). In the case of silicating, in addition to the radicals generated, which bind to the broken fractures in the plastic molecules during treatment, another phenomenon is used to explain the adhesion: the mechanical adhesion due to roughness and increased surface area (Schlitt 2018). Thus, the still liquid silicone wets the rough surface and cures within the voids and undercuts. Nevertheless, the adhesion occurring in these joints cannot be clearly assigned to particular adhesion theories.

19.5 Summary and Outlook

Within the scope of the study, the influence of surface treatments via atmospheric pressure plasma jet and silicating on the adhesion between standard thermoplastics and optical grade liquid silicone rubber was investigated. For this purpose, two-component peel test specimens were produced in a specially made injection mold on a horizontal/vertical two-component injection molding machine. Since the treatments were performed off-site, the thermoplastic pre-molded specimen were inserted into the mold and overmolded with LSR. The adhesion initiated by the treatments was quantified on an in-house developed peel device in terms of peel force. Furthermore, the influence of the treatments on the surface energy was determined via contact angle measurements.

The results show an increase in total and especially polar surface energy by both treatment methods. This is mainly explained by the modification of the substrate surface with reactive groups. Thus, plasma treatment leads to an increase in the polar surface energy from plus 12.1 mN m^{-1} for PMMA to plus 25.2 mN m^{-1} for PC. Silicating also leads to an increase in surface polar energy from plus 26.6 mN m^{-1} for PA66-GF35 to up to plus 41.4 mN m^{-1} for PC compared to the untreated state. Both treatments also lead to an increase in peel strength for the joint with MS-1002, compared to the untreated state, as well as to the initial initiation of adhesion. Atmospheric pressure plasma jet treatment of PMMA, ABS, and PC leads to the initial initiation of adhesion. The peel force level here is in the range of 4.24 N for PMMA and 9.02 N for ABS. Silicating of the thermoplastic substrates leads to an increase in the peel force for each of the materials studied. Thus, the averaged peel forces are in the range of 9.36 N for PMMA and 19.66 N for PA66-GF35. By plotting the peel forces obtained against the determined polar surface energy components of all treatment methods and materials, the influences of the surface treatments are clearly visible.

The classification of the surface treatments according to their effects on the surface energy and adhesion can help to better understand their influence in the context of thermoplastic-LSR joints. In the future, the tests will be extended to more thermoplastic materials and to their combination with other LSR. Furthermore, the use of additional surface treatments will be investigated. This extension to additional materials and surface treatments should help to provide an orientation as to which adhesion strength in joints can be expected on the basis of the material combination and surface treatment used.

Acknowledgements D. Mayer would like to acknowledge the support of Federal Ministry for Economic Affairs and Energy. They funded this research project between Wilhelm Weber GmbH & Co.KG and Esslingen University of Applied Sciences on thermoplastic—liquid silicone rubber joints within their programm “Zentrale Innovationsprogramm Mittelstand (ZIM)” (funding code: ZF4166302DN8). He would also like to acknowledge Sura Instruments GmbH and Plasmatreat GmbH for performing surface treatments.

References

- Baumgart C, Krug K, Altstädt V (2014) Hitzebeständige 2K-Verbunde. *Kunststoffe* 10:134–137
- Baumgart C, Weiß D, Altstädt V (2016) Influence of different tempering conditions on the adhesion properties of thermoplastic/liquid silicone rubber combinations. *Polym Eng Sci* 56(8):849–855
- DIN Deutsches Institut für Normung e.V (2017) DIN ISO 6133:2017-04, Rubber and plastics—analysis of multi-peak traces obtained in determinations of tear strength and adhesion strength. Beuth Verlag GmbH, Berlin
- Gil'man AB (2003) Low-temperature plasma treatment as an effective method for surface modification of polymeric materials. *High Energy Chem* 37:17–23
- Plasmatreat GmbH (2022) Openair-plasma® technique. Atmospheric pressure plasma solutions for surface treatment. <https://www.plasmatreat.com/plasma-technology/openair-atmospheric-plasma-technique.html>. Accessed 18 Feb 2022
- Goodship V, Love JC (2002) Multi-material injection moulding. Rapra Technology, Shrewsbury, U.K
- Habenicht G (2009) Kleben. Springer, Berlin Heidelberg, Berlin, Heidelberg
- Härtig T (2012) Stoffübertragung beim Spritzgießen. Dissertation, Chemnitz
- Jaroschek CS (1993) Injection moulding of articles out of multiple components. Dissertation, Aachen
- Kinloch AJ (1987) Adhesion and Adhesives. Springer, Netherlands, Dordrecht
- Kopczynska A (2008) Oberflächenspannungssphänomene bei Kunststoffen - Bestimmung und Anwendung. Dissertation, Erlangen-Nürnberg
- Kuhmann K (1999) Prozeß- und Materialeinflüsse beim Mehrkomponentenspritzgießen. Dissertation, Erlangen
- Kühnert I (2005) Grenzflächen beim Mehrkunststoffspritzgießen. Dissertation. FKTU, Chemnitz
- Kühr C, Spörrer A, Altstädt V (2014) Determination of adhesion between thermoplastic and liquid silicone rubbers in hard-soft-combinations via mechanical peeling test. *AIP Conf Proc* 1593:142–145
- Lau K (2006) Plasmagestützte Aufdampfprozesse für die Herstellung hafter optischer Beschichtungen auf Bisphenol-A Polycarbonat. Dissertation, Halle (Saale)
- Lake M (ed) (2009) Oberflächentechnik in der Kunststoffverarbeitung: Vorbehandeln, Beschichten, Funktionalisieren und Kennzeichnen von Kunststoffoberflächen. Hanser, München
- Richter T, Tiller H-J (2004) CVD of silica as an alternative method to vakuum treatment. *Vak Forsch Prax* 16(2):85–87
- Ronnwinkler C (2000) Multi-component injection moulding of liquid silicone rubber, thermoplastic combinations. Dissertation. Mainz, Aachen
- Roth JR (2001) Industrial plasma engineering. Inst. of Physics Publ, Bristol
- Schlitt C (2018) Thermoplasten und Flüssigsilikonem mit unterschiedlichen Mechanismen zur Initiierung der Vernetzung hergestellt im Mehrkomponenten-Spritzgießverfahren. Dissertation. Kassel University Press GmbH, Kassel
- Schuck M (2009) Kompatibilitätsprinzipien beim Montagespritzgießen. Dissertation. LKT, Erlangen
- Seitz V, Arzt K, Mahnel S et al (2016) Improvement of adhesion strength of self-adhesive silicone rubber on thermoplastic substrates – Comparison of an atmospheric pressure plasma jet (APPJ) and a Pyrosil® flame. *Int J Adhes Adhes* 66:65–72
- Seitz V (2015) Kleinflächige, polymere Hart-Weich-Verbindungen. Dissertation, München
- Struppert T, Heft A, Grünler B (2012) Thin functional films by combustion chemical vapour deposition (C-CVD). *Thin Solid Films* 520(12):4106–4109
- Sura Instruments GmbH (2022) Pyrosil®-Verfahren. <https://www.sura-instruments.de/en/technologies/pyrosil-process>. Accessed 09 Feb 2022
- Thust T (2014) Rezeptur- und Prozesseinflüsse auf das Haftverhalten beim Mehrkomponentenspritzgießen von Thermoplast-Elastomer-Verbundbauteilen am Beispiel PA6.6—HNBR. Dissertation, Halle

- Tiwari A, Soucek MD (eds) (2014) Concise encyclopedia of high performance silicones. Scrivene Publishing/Wiley, Hoboken New Jersey.
- VDI Verein Deutscher Ingenieure (2016) Testing the adhesion of thermoplastic elastomers (TPE) on substrates. Beuth Verlag GmbH, Düsseldorf
- Wilcik V, Dull G, Johnson T et al (2011) Self-adhesive LSR in 2K injection molding. Rubber World 245:20–24

Chapter 20

Thermoforming: Identification of Process-Relevant Ranges for Strain, Strain Rate, Cooling Rate, and Degree of Crystallinity Through Preliminary Simulations



Sameer Kulkarni, Klara Loos, Alexander Lion, and Michael Johlitz

Abstract Advanced materials are essential for improving modern automobiles' fuel efficiency while maintaining performance and safety. The automobile's body and chassis weight can be significantly reduced by replacing traditional metallic components with composite materials. Additionally, many composite materials exhibit excellent resistance to corrosion, wear, and high temperature. In recent years, thermoforming of composite sheets made of continuous fiber reinforcements is becoming increasingly popular for mass production. This research project focuses on developing a novel, thermo-mechanically coupled material model for a composite laminate made of unidirectional fiber-reinforced thermoplastic tapes (UD-tapes), intending to correctly simulate the thermoforming process. A multi-scale modeling approach is used to model the composite material, where the composite's effective properties at the macro-scale are derived from the individual matrix, fiber properties, and the underlying composite micro-structure through homogenization procedures. Hence, in the first step, the material parameters of the matrix material are identified based on extensive thermal and mechanical experiments over the entire process-relevant temperature range, 80–260 °C. However, prior to conducting the experiments, it is essential to identify the magnitude of the experimental inputs, such as strains, strain rates, and anticipated cooling rates specific to the thermoforming process. In order to find these inputs, simplified simulations are performed in the commercial

S. Kulkarni (✉) · K. Loos · A. Lion · M. Johlitz
Fakultät für Luft- und Raumfahrttechnik, Institut für Mechanik, Universität der Bundeswehr München, Werner-Heisenberg-Weg 39, 85577 Neubiberg, Germany
e-mail: sameer.kulkarni@unibw.de

K. Loos
e-mail: klara.loos@unibw.de

A. Lion
e-mail: alexander.lion@unibw.de

M. Johlitz
e-mail: michael.johlitz@unibw.de

finite element software ANSYS with standard material models and using the material parameters from the literature. In this contribution, the simulation results and their implications for material characterization experiments are presented.

Keywords Thermoforming · PA6 · Semi-crystalline thermoplastics · Crystallization · Forming simulation · Finite element analysis · Ansys

20.1 Introduction

Future-oriented resource-saving technologies rely on the development of advanced materials. To improve the fuel efficiency of present-day automobiles and maintain their safety and performance, the use of lightweight and advanced materials has become crucial. A 10% reduction in the vehicle weight can improve the fuel efficiency by 6–8%. The use of lightweight metal alloys and fiber-reinforced polymers can substantially reduce the weight of a vehicle's body and chassis, thereby reducing a vehicle's fuel consumption significantly (OEERE 2014).

In recent years, the thermoforming of composite sheets made of continuous fiber reinforcements, also known as organic sheets, has become an essential technology for mass production. The excellent formability, easy storage, and handling of the organic sheets make the thermoforming process suitable for various applications. In particular, thermoforming of thermoplastics is attractive since the components can be reheated, molded, and cooled multiple times, allowing a high level of recyclability (Stamopoulos et al. 2021). Moreover, thermoforming offers a great cost-benefit and has a short processing time (Pyatov et al. 2021). Currently, thermoforming is used in many industries, including packaging, medical, automotive, and aerospace (Namdari and Mosaddegh 2019).

Although thermoforming has significant advantages over other processing techniques, some concerns are still to address. Various effects such as thermal gradients, fiber-matrix interactions, and the complex crystallization behavior during solidification of the polymer may result in excessive residual stresses in the components. The selection of non-optimal process parameters can result in undesirable defects such as buckling, wrinkles, and tears, making it challenging to ensure the process's stability (Pyatov et al. 2021; Doebrich et al. 2014). Trial-and-error approaches are traditionally used to optimize the thermoforming process, where the mold design, the temperature of the molds and the organic sheets, plug speed, displacement are altered until a part of the desired quality is produced (Koziey et al. 1997).

Recently, advances in computer technology made it possible to use finite element methods to simulate the thermoforming process. With finite element simulations, a detailed and realistic prediction of the forming result is possible. Such a simulation can include all constitutive equations, boundary conditions, and material parameters. These capabilities eliminate the need to perform expensive trial-and-error procedures (Koziey et al. 1997). However, the aforementioned thermal-mechanical effects make thermoforming highly complex to model.

The current research project focuses on developing a novel thermo-mechanically coupled material model for a composite laminate made of unidirectional fiber-reinforced thermoplastic tapes (UD-tapes), based on an extensive experimental investigation, with the overall aim of correctly simulating the thermoforming process. This model should cover the entire process-relevant temperature range in order to compute the residual stresses that arise due to the aforementioned physical effects. To develop such a model of the composite material, a multi-scale modeling approach will be used. In this approach, the effective properties of the composite are derived based on the individual matrix, fiber properties, and the underlying micro-structure through homogenization procedures. Hence, in the first step, the material parameters of the matrix (PA6) are being identified based on thermal and mechanical experiments over the process-relevant temperature range, 80–260 °C. To describe the matrix, a thermo-mechanical constitutive framework developed by Felder et al. (2019), which incorporates coupled thermal, mechanical, and crystallization effects, shall be used.

The organic sheets investigated in this project consist of continuous glass fiber textiles impregnated with a PA6 (Nylon 6) matrix. However, the proposed approach shall be developed in such a general way that it is also suitable for other related materials.

20.1.1 Thermoforming Process

Thermoforming is a manufacturing process in which a sheet of thermoplastic material is first heated to its softening temperature, usually with the help of an infrared radiant heater panel. Following this, the sheet is pressed against the mold with the help of either pneumatic or mechanical means. The sheet receives the shape of the mold contours during continuous cooling. After forming is finished, the formed part is allowed to cool down close to the glass transition temperature θ_g of the polymer. Finally, the sheet is removed from the mold, and the excess material is trimmed off (Pyatov et al. 2021; Namdari and Mosaddegh 2019; Schug 2019). The process is depicted schematically in Fig. 20.1.

The forming temperature is a critical parameter in thermoforming. For a thermoplastic polymer to deform, it should be soft but not so soft that it leads to sagging. On the other hand, the temperature should be high enough to sufficiently

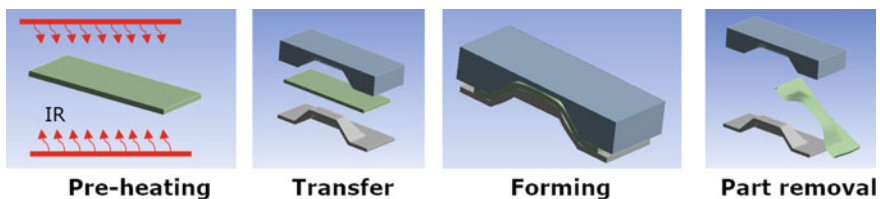


Fig. 20.1 Schematic of the thermoforming process

soften the polymer so that it deforms under the plug, yet not too high that the polymer flows out of the organic sheet (Morris 2016). Amorphous thermoplastics typically become sufficiently soft around 30–60 °C above θ_g . As a result, they do not need to be heated to their melting temperature θ_m during forming. Most of the thermoforming markets are working with amorphous thermoplastics such as PVC, PP, HIPS, PS, ABS, PETG, PVDC, EVOH, and PMMA (Koziey et al. 1997).

The semi-crystalline thermoplastics, however, become pliable either slightly below or above θ_m . They have a narrow forming temperature window and require a higher forming pressure. Thermoplastic sheets of ordinary semi-crystalline PA6 are extremely difficult to thermoform, both below as well as above θ_m . They remain stiff and dimensionally stable below θ_m . Above θ_m , they become too viscous, which leads to sagging and thinning during the thermoforming process (Bayer 2001). However, newer PA6 grades, which are specially branched polyamides and reinforced with glass fibers, can be formed above θ_m due to their enhanced melt viscosity (Bayer 2001). The forming temperature for PA6 is between 225 and 290 °C (Astrom 1997).

20.1.2 Crystallization During Thermoforming Process

Crystallinity refers to the structural order of a solid. In a crystalline structure, atoms or molecules are arranged in a repetitive and consistent pattern. When a semi-crystalline polymer solidifies from the melt, its molecular chains partially align. Depending on crystallization nuclei, the molecular chains fold together and form orderly crystalline lamellae (NETZSCH 2001). Figure 20.2 shows typical crystalline and amorphous phases of semi-crystalline polymers. Compared with the disordered amorphous phase, the ordered crystalline phase has a higher density and stiffness but less entropy (Lion and Johlitz 2016).

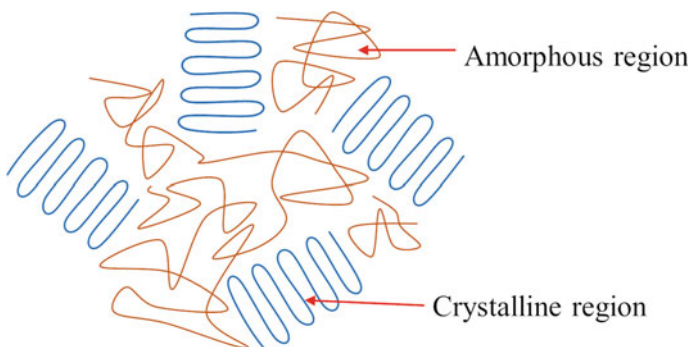


Fig. 20.2 Structure of a semi-crystalline polymer

Prior to the thermoforming, the polymer sheet is heated above its melting temperature θ_m . The sheet is then continuously cooled during the forming process. This leads to crystallization of the polymer under non-isothermal conditions. Crystallization, being an exothermic process, releases heat to the surrounding. The amount of this heat is proportional to the resulting degree of crystallinity in the polymer. The faster the cooling takes place, the less crystallinity is established. Additionally, the temperature at which crystallization initiates and ends are dependent on the cooling rate. During thermoforming, the cooling takes place unevenly in the polymer along the thickness of the sheet. The sheet cools down faster on its surface than in the inner region. Consequently, crystallization occurs inhomogeneously along the thickness. Considering all these aforementioned points, a thorough investigation of the crystallization kinetics over a wide range of cooling rates is necessary.

To model the material behavior during thermoforming, it is also necessary to reliably determine the material's mechanical properties as a function of the amount of crystallinity in the polymer. For this purpose, test specimens with distinct and fixed degrees of crystallinities are produced using a specific innovative blend strategy. With these specimens, mechanical tests can be performed over the process-relevant temperature range below θ_m .

20.2 Simplified Process Simulations

In order to develop a suitable material model, the input parameters of the material characterization experiments must be based on reality. This applies to the temperature rates, degrees of crystallinity, deformations, and deformation rates occurring within the component to be simulated.

20.2.1 *Simulation 1: Cooling*

To estimate the cooling rates and the degrees of crystallinity evolved in PA6 during the thermoforming, a simplified simulation model for a transient heat conduction problem is set up in the commercial FEM software ANSYS.

20.2.1.1 Simulation Setup

A PA6 layer of 4 mm thickness is located between two steel plates of thickness 10 mm each, as illustrated in Fig. 20.3. A homogeneous temperature of 260 °C, above the melting temperature θ_m of PA6, which is typically 225 °C, is applied to the polymer layer. The surrounding steel plates have initial temperatures of 80 °C. These initial temperature boundary conditions are set in accordance with LANXESS's process guidelines (LANXESS 2019), a company that manufactures organic sheets. The whole assembly is then exposed to an environment at 23 °C. The resulting space-

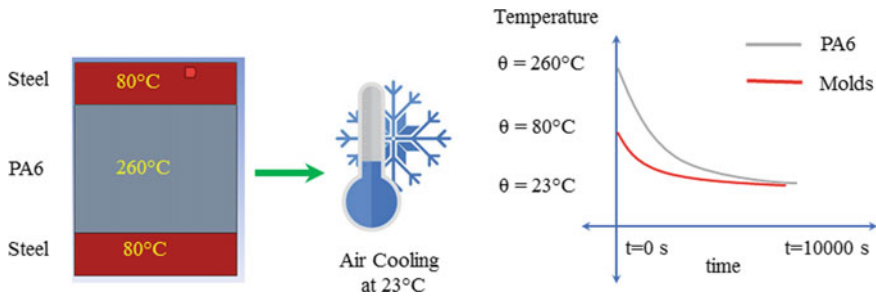


Fig. 20.3 Temperature boundary conditions in the cooling simulation

and time-dependent temperature field in the polymer layer is analyzed. The thermal expansion effects are neglected in this simulation.

The heat transfer between polymer and steel takes place due to conduction and that from steel to the surrounding environment due to convection and radiation. For this simplified simulation, the heat transfer only in a single direction—along the thickness is considered. The density of PA6 is linearly interpolated between 932 kg m^{-3} at 240°C and 1140 kg m^{-3} at 23°C . The air convection coefficient and the emissivity are taken to be $25 \text{ W m}^{-2}\text{K}^{-1}$ and 0.8, respectively. The thermal contact conductance between polymer sheets and steel is taken to be $5000 \text{ W m}^{-2}\text{K}^{-1}$. The material properties—specific heat capacity at constant pressure c_p and thermal heat conductivity k are taken from (Santos et al. 2013). This setup allows to estimate typical values of the cooling rates that occur in the production of organic sheet components.

20.2.1.2 Results and Discussion

In Fig. 20.4b, the simulated cooling rates in $^\circ\text{C s}^{-1}$ are plotted against instantaneous temperatures in $^\circ\text{C}$. The simulation is analyzed spatially resolved, at 0.5 mm incremental distances from the center of the polymer plate to the boundary, as depicted in Fig. 20.4a. The data reveals high cooling rates close the steel plate boundary. The cooling rates decrease with increasing distance from the steel plates. Their maximum values, which only occur in the very thin boundary layers to the steel plates, at locations $>3.5 \text{ mm}$, are estimated to be irrelevant for the component behavior and are therefore not taken into account. The highest cooling rate observed, at a distance of 0.5 mm away from the boundary, is 54°C s^{-1} . As anticipated, the cooling rates are highest at the beginning of the process, and they decrease as the temperature of the sheet decreases.

To estimate the degrees of crystallinity that are likely to emerge for such a dynamic cooling process, results from one experimental study (Parodi et al. 2017) are used along with the simulation results from this study. In Parodi et al. (2017), the author conducted several cooling experiments on pure PA6 over a wide range of constant cooling rates to determine the resulting degree of crystallinity and peak crystalliza-

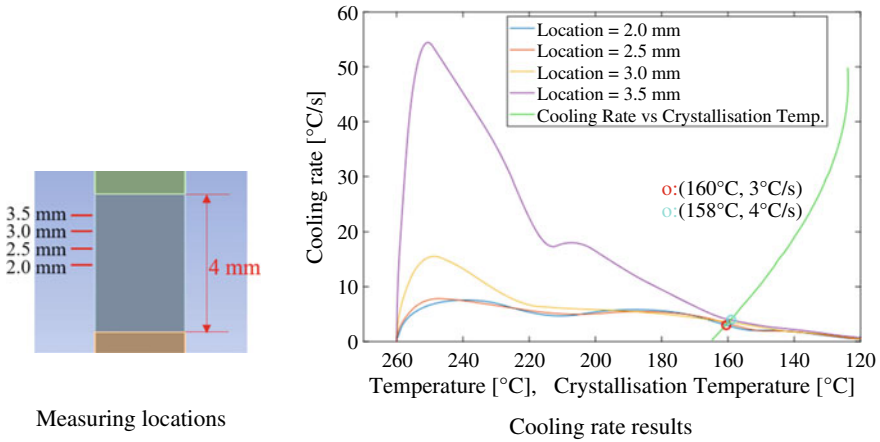


Fig. 20.4 Cooling simulation results

tion temperature as functions of constant cooling rates. The green curve in Fig. 20.4b, reproduced from these experimental results, is overlapped with the dynamic cooling rate results, such that the intersection points give a prediction of the peak crystallization temperatures and the instantaneous cooling rates when the sheet material is actually expected to crystallize. With these instantaneous cooling rates now known, the corresponding degree of crystallinity is estimated by comparing it with the results in Parodi et al. (2017). This same approach is also used by Jariyavidyanont et al. (2018) for identifying the crystallization temperature in the injection molding process.

As seen in Fig. 20.4b, for the two extreme locations, 2 mm and 3.5 mm on the sheet, the instantaneous cooling rates during the crystallization are predicted to reach 3 °C s^{-1} and 4 °C s^{-1} , respectively. According to Parodi et al. (2017), cooling rates of 3 °C s^{-1} and 4 °C s^{-1} result in 30% and 28% crystallinity, respectively. This difference of 2% in crystallinity between the two extreme locations is insignificantly small.

The simulation was repeated for two more sheet thicknesses, 2 and 8 mm, but the cooling rate results measured near the boundary and in the center remained nearly identical to those for the 4 mm thick sheet. Hence, in these two sheets, nearly the same range of crystallinity in the thickness can be expected as in the 4 mm sheet.

20.2.2 Simulation 2: Forming

The strain and strain rates to be covered in the validation experiments are estimated by a qualitative simulation of the thermoforming process. Based on the simulated strain values, the range for the tension, compression, and shear tests will be defined. The

strain rates will be used as inputs for the rate-dependent mechanical tests, dynamic mechanical analysis (DMA), and rheometer measurements.

The process parameters for the simulations are chosen based on LANXESS's process guidelines (LANXESS 2019). At the beginning of the thermoforming process, the organic sheet is heated above the matrix's melting temperature θ_m and is transferred to the preheated molds. The forming process occurs when the matrix is semi-solid. After the forming is finished, the matrix material solidifies due to continuous cooling. During this period of consolidation, the sheet experiences only thermal strains, which are much smaller than the earlier developed mechanical strains. Next, during the removal of the produced component, stress is released, and thus the strain is reduced. Consequently, only the forming step is considered in this simulation study.

20.2.2.1 Simulation Setup

For this analysis, a 2D-plane strain transient implicit simulation scheme was employed. Since the goal of the simplified simulation is to find strains and strain rates, a kinematic simulation scheme is used, where the strain result is always similar regardless of the chosen material model for the sheet. Hence, the strains in the polymer sheet in this simulation primarily depend on the tool geometry. Consequently, the strain rates depend on the tool geometry and the plug speed. An isotropic material with an elasticity modulus of 200 MPa and a Poisson's ratio of $\nu = 0.35$, typical for PA6 at 170 °C, is chosen for the sheet. The tool geometry, the sheet thickness, and the process conditions in this simulation are chosen according to the final experimental test setup planned for validating the thermoforming process simulation in the future. The simulation is set up from the moment the plug is in contact with the sheet. The plug, the mold, and the clamps are modeled as rigid bodies, while the sheet is the only deformable component. During the forming step, the plug descends onto the sheet at a speed of 5 mm/s. Hence to form a 10 mm depth, it takes 2 s. This forming time is relatively short compared to the total cooling time of 20–60 s typically. Consequently, the forming step is assumed to be isothermal in the simulation, and thermal strains are neglected.

In the actual process, before forming, the sheet is first stretched using springs to avoid sagging of the semi-solid sheet. In a real composite, the strains resulting from this pre-stretching are negligible due to the presence of extremely stiff fibers. Pre-stretching is therefore skipped in this simulation, instead clamps are used as shown in Fig. 20.5 to guide the material as close to reality.

As shown in Fig. 20.5, a displacement boundary condition is used to apply the plug descent. A friction coefficient of $\mu = 0.15$ is applied between the plug and sheet as well as between the sheet and the mold according Fetfatsidis et al. (2011). The draft angle is set to 45°. For all internal corners, a radius of 1 mm is used.

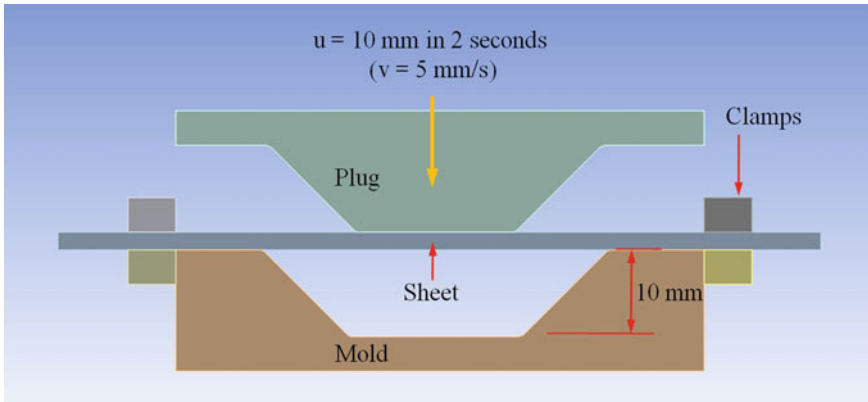


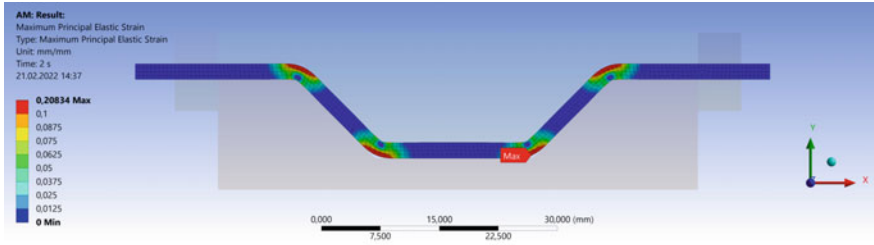
Fig. 20.5 Forming simulation setup

20.2.2.2 Results and Discussion

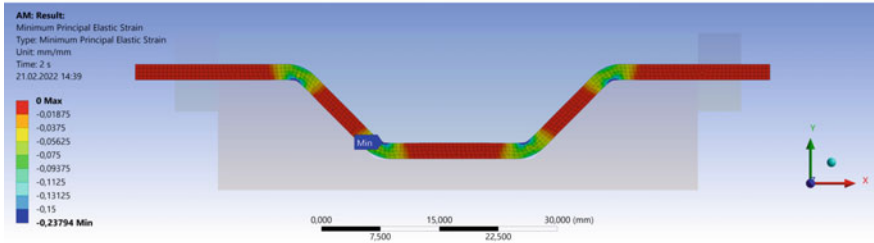
Various studies on modeling thermoforming process (Schug 2019; Dörr et al. 2020; Stamopoulos et al. 2021; Ropers et al. 2017; Doebrich et al. 2014; Pyatov et al. 2021) suggest that there exist three main deformation mechanisms in the thermoforming, namely inter-ply slippage, intra-ply shear, and out-of-plane bending. Hence, for correctly modeling the thermoforming process, an accurate characterization of the bending and shear behavior is essential.

Figure 20.6a–c illustrate the simulation results for the first principal strain ε_1 , the third principal strain ε_3 , and the maximum shear strain γ_{\max} , respectively, in the sheet at the end of the forming. The first principal strain results correspond to the local maximum tensile strain values. Its maximum value $\varepsilon_{1,\max} = 0.2083 \approx 21\%$ occurs on the outer boundary of the formed sheet and represents the maximum bending tensile strain in this case. The average value of the first principal strain over the entire sheet is $\varepsilon_{1,\text{avg}} = 1.94\%$. The absolute value of the third principal strain relates to the local maximum compressive strains induced in the sheet. Its maximum and average values are $\varepsilon_{3,\max} \approx 24\%$ and $\varepsilon_{3,\text{avg}} \approx 2.2\%$, respectively. Contrary to the maximum tensile strain, the maximum compressive strain occurs on the inner boundary of the formed part. The maximum value of the shear strain in the sheet is $\approx 31\%$, and its average value in the sheet is 3.86% .

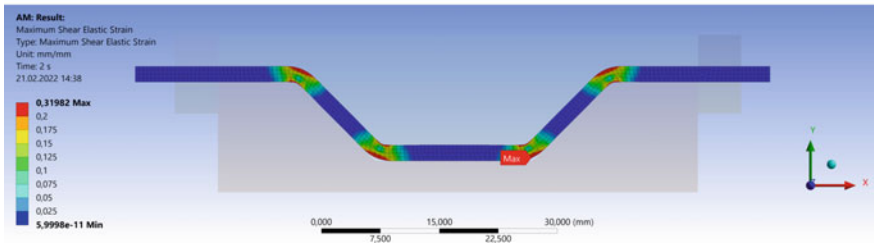
To determine the process-relevant strain rates, the evolution of the maximum shear strain γ_{\max} in the sheet is analyzed. In Fig. 20.7b, the maximum shear rates at three distinct points as shown in Fig. 20.7b, are plotted against time. While the sheet is being formed, the strain rate remains within ± 0.1 or $\pm 10\%$ for most of the time. As the material reaches its final shape as per the contours of the mold cavity, high strain rates of up to 1.7 or 170% are observed in the corner regions.



Plot: First principal strain ϵ_1



Plot: Third principal strain ϵ_3



Plot: Maximum shear strain γ_{max}

Fig. 20.6 Forming simulation result: strain

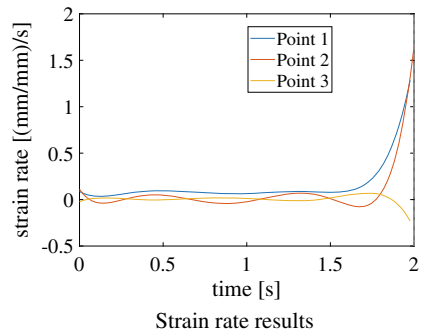
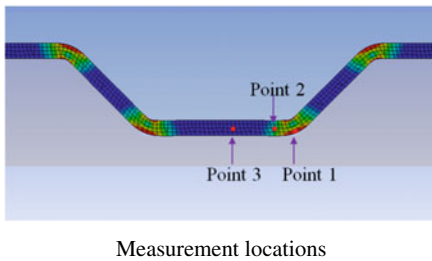


Fig. 20.7 Forming simulation result: strain rate

20.3 Conclusions

In this study, simplified finite element simulations are carried out to identify the range of the inputs for future material characterization experiments.

In the first simulation, the cooling rates expected in the organic sheet during thermoforming are determined. The resultant cooling rates range from 0 to $54\text{ }^{\circ}\text{C s}^{-1}$, and are functions of the location along the sheet thickness and the time/instantaneous temperature at that location. As the sheet cools down, a phase change or crystallization of PA6 is estimated to occur as the instantaneous cooling rate in the sheet drops to $3\text{--}4\text{ }^{\circ}\text{C s}^{-1}$. The degree of crystallization in the PA6, as a result of the determined cooling pattern, is estimated to be between 28 and 30%. For the characterization of the crystallization kinetics, non-isothermal DSC and flash-DSC caloric experiments for the pure PA6 as well as for the fiber-reinforced PA6 are planned.

In the second simulation, the forming process is simulated in a simplified manner to determine the expected strains and strain rates in the organic sheets. Using a sheet of 2 mm thickness, a mold with a draft angle of 45° , and a plug velocity of 5 mm/s, the maximum tensile ε_1 , maximum compressive $|\varepsilon_3|$ and maximum shear strains are estimated to be 21%, 24%, and 34%, respectively. To characterize the material's visco-elastic behavior in the semi-solid state, dynamic mechanical analysis (DMA) and rheometer measurements are planned. These tests will be conducted within the range of strain rates identified in the presented simulations. For the material in the solid state, tension, compression, and shear tests will be conducted mainly in the process-relevant temperature range of $60\text{--}170\text{ }^{\circ}\text{C}$.

References

- Astrom BT (1997) Thermoplastic composite sheet forming: materials and manufacturing techniques. In: Bhattacharyya D (ed) Composite sheet forming, 1st edn. Elsevier Science BV, Amsterdam
- Bayer AG (2001) Bayer: Thermoformen von Platten aus Polyamid 6 erstmals möglich. chemie.de. <https://www.chemie.de/news/1195/bayer-thermoformen-von-platten-aus-polyamid-6-erstmal-moeglich.html>. Accessed 20 Feb 2022
- Doeblich O, Gereke T, Diestel O, Krzywinski S, Cherif C (2014) Decoupling the bending behavior and the membrane properties of finite shell elements for a correct description of the mechanical behavior of textiles with a laminate formulation. *J Ind Text* 47(1):70–84
- Dörr D, Gergely R, Ivanov D, Kärger L, Henning F, Hrymak A (2020) On the applicability of thermoforming characterization and simulation approaches to glass mat thermoplastic composites. *Procedia Manuf* 47:118–125
- Erich NETZSCH GmbH and Co. Holding KG (2001) Crystallinity/degree of crystallinity. <https://analyzing-testing.netzsch.com/en/training-know-how/glossary/crystallinity-degree-of-crystallinity>. Accessed 10 May 2022
- Felder S, Holthausen H, Hesseler S, Pohlkemper F, Gries T, Simon W, Reese S (2019) Incorporating crystallinity distributions into a thermo-mechanically coupled constitutive model for semi-crystalline polymers. *Int J Plast* 132:102751

- Fetfatsidis KA, Jauffrès D, Sherwood JA, Chen J (2011) Characterization of the tool/fabric and fabric/fabric friction for woven-fabric composites during the thermostamping process. *Int J Mater Form*. <https://doi.org/10.1007/s12289-011-1072-5>
- Jariyavidyanont K, Williams JL, Rhoades AM, Kühnert I, Androsch R (2018) Crystallization of polyamide 11 during injection molding. *Polym Eng Sci* 58(7):1053–1061
- Koziey BL, Ghafur MO, Lachopoulos JV, Mirza FA (1997) Computer simulation of thermoforming. In: Bhattacharyya D (ed) *Composite sheet forming*, 1st edn. Elsevier Science BV, Amsterdam
- LANXESS (2019) Tepex processing guideline: tepex dynalite x02. <https://techcenter.lanxess.com/scp/emea/en/products/tepex/35952181/uniarticle.jsp?docId=35952181>. Accessed 20 Feb 2022
- Lion A, Johlitz M (2016) A thermodynamic approach to model the calorific properties of semicrystalline polymers. *Contin Mech Thermodyn* 28:799–819
- Morris BA (2016) *The science and technology of flexible packaging*, 1st edn. Elsevier, New York
- Namdari N, Mosaddegh P (2019) Experimental and simulation studies on the mold replicability in the thermoforming process. *J Polym Eng* 39(4):397–405
- Office of Energy Efficiency and Renewable Energy (2014) *Lightweight materials for cars and trucks*. <https://www.energy.gov/eere/vehicles/lightweight-materials-cars-and-trucks>. Accessed 10 May 2022
- Parodi E, Govaerta LE, Petersa GW (2017) Glass transition temperature versus structure of polyamide 6: a flash-DSC study. *Thermochim Acta* 657:110–122
- Pyatov N, Natarajan HK, Osswald TA (2021) Experimental investigation of in-plane shear behaviour of thermoplastic fibre-reinforced composites under thermoforming process conditions. *J Compos Sci* 5(9):248
- Ropers S, Sachs U, Kardos M, Osswald TA (2017) A thermo-viscoelastic approach for the characterization and modeling of the bending behavior of thermoplastic composites—part II. *Compos A Appl Sci Manuf* 90:22–32
- Santos WN, Sousa JA, Gregorio R Jr (2013) Thermal conductivity behaviour of polymers around glass transition and crystalline melting temperatures. *Polym Test* 32(5):987–994
- Schug AF (2019) *Unidirectional fibre reinforced thermoplastic composites: a forming study*. PhD thesis, The Technical University of Munich, Munich
- Stamopoulos AG, Ilio AD, Genova LG (2021) Simulation of the thermoforming process of glass fiber-reinforced polymeric components: investigation of the combined effect of the crosshead speed and material temperature. *Int J Adv Manuf Technol* 117:2987–3009

Chapter 21

Examining Lateral Punch Force Effects During Hole Expansion Testing by Means of Numerical Simulations



Tobias Robl, Christian Krempaszky, and Ewald Werner

Abstract Hole expansion testing is suitable to study the stretchability of sheared edges of sheet metal for the automotive industry. During testing, a square specimen with a circular center hole is clamped and a conical punch is pressed into the hole. The movement of the punch is stopped when the first through-thickness crack appears at the hole edge. For symmetry reasons, no lateral punch force should occur before the first through-thickness crack appears. Even before a crack appears, however, lateral punch force components can be recorded during testing. They may be caused by an imperfect test setup or an imperfect specimen. In this contribution, the influence of a displaced specimen, a specimen with an eccentric prehardened zone due to punching of the hole, a tilted test setup and a specimen with a tilted hole axis on the lateral punch force is studied by means of numerical simulations. The results of the simulations indicate the influence of a lateral displacement of the specimen with respect to the punch axis being most significant. This is also indicated by experimental results gathered in hole expansion tests performed in a laboratory. The influence of the other imperfections mentioned is of minor importance.

Keywords Hole expanding test · Sheet metal · Formability · Material testing · Numerical simulation

T. Robl (✉) · C. Krempaszky · E. Werner
Department of Materials Engineering, TUM School of Engineering and Design, Institute of Materials Science and Mechanics of Materials, Technical University of Munich, Munich, Germany
e-mail: tobias.robl@tum.de

C. Krempaszky
e-mail: krempaszky@tum.de

E. Werner
e-mail: ewald.werner@tum.de

21.1 Introduction

Hole expansion testing is suitable to study the stretchability of sheared edges of sheet metal (ISO 16630 2017). The results of the test can be used to improve cutting processes or the selection of suitable metallic sheet materials, both with regard to edge cracking (Krempaszky et al. 2014).

During testing, a square specimen with a center hole is clamped between an upper and a lower die. Then, a conical punch is pressed into the hole (Fig. 21.1). The movement of the punch is stopped when the first through-thickness crack appears at the hole edge. The specimen is removed from the test setup and the hole expansion ratio,

$$\lambda = \frac{d_1 - d_0}{d_0}, \quad (21.1)$$

is determined from the initial hole diameter, d_0 , and the actual hole diameter, d_1 . The hole expansion ratio represents a characteristic measure to evaluate the edge stretchability of sheet metal (Krempaszky et al. 2014). Among others, the hole expansion ratio strongly depends on the condition of the hole edge and the microstructure of the sheet metal (Karellova et al. 2007a, b, 2009a).

Determining the hole expansion ratio according to ISO 16630 (2017) is subject to uncertainties. Because the occurrence of the first through-thickness crack cannot be predicted in advance, the test is ended usually a short period of time after the crack appears. Furthermore, spring back of the deformed sheet occurs when the specimen is removed from the test setup (Robl et al. 2021). To address both aspects, an improved test setup has been established at the Institute of Materials Science and Mechanics of Materials (Technical University of Munich). By using a camera system, the hole edge is monitored during testing. By this, the end of the test and the actual hole diameter, d_1 , at the end of the test can be determined more precisely (Krempaszky et al. 2014; Dünckelmeyer et al. 2009; Karellova et al. 2009b).

With the improved test setup, it is possible to evaluate the axial and the lateral punch force during testing. Even before the first through-thickness crack appears, lateral punch force components can be recorded as will be shown and discussed later in this work (Fig. 21.9). They may be caused by an imperfect test setup or by an imperfect specimen. The lateral punch force components are affected strongly by the appearance of the first through-thickness crack, while the axial punch force is affected less severely (Krempaszky et al. 2014).

For a perfect test setup and a perfect specimen, no lateral punch force is expected to occur before the first through-thickness crack appears, and it seems consistent to consider the evolution of the lateral punch force to evaluate if testing is carried out properly. As the lateral punch force is affected strongly by the appearance of the first through-thickness crack, this force component might also be considered as a criterion to define the end of the test. With regard to both aspects, it is of high interest to identify imperfections of the test setup and the specimen, which affect the lateral punch force significantly.

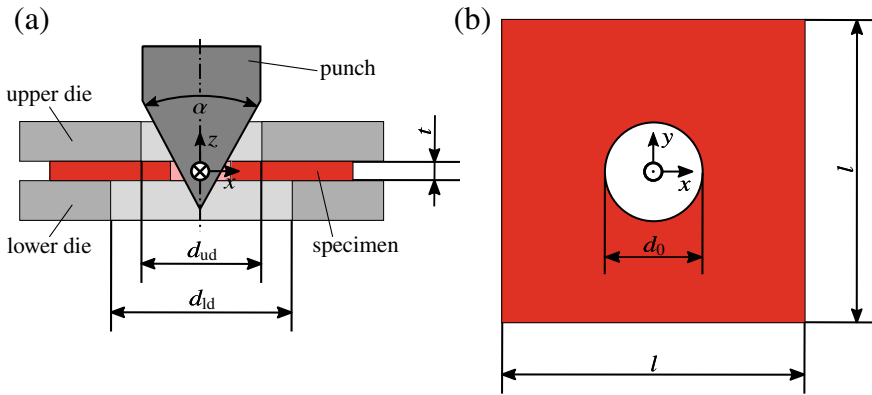


Fig. 21.1 Schematic representation of test setup (a) and specimen (b): thickness, t , initial hole diameter, d_0 , and edge length, l , of specimen; inside diameter of upper die, d_{ud} , and lower die, d_{ld} ; punch tip angle, α

In this contribution, the influence of a displaced specimen, a specimen with a prehardened zone due to punching of the hole, a tilted test setup and a specimen with a tilted hole axis is studied (Fig. 21.2). To examine the impact of these factors on the lateral punch force, numerical simulations are carried out using the commercial finite element code Abaqus/Explicit (Smith 2019). In one additional numerical simulation, the appearance of a crack is considered to study the influence of a through-surface crack on the lateral punch force in the numerical experiment. The results of all numerical studies are compared to experimental results. As hole expansion testing is typically used to characterize the formability of sheet metal for the automotive industry, the numerical studies are carried out with material parameters for the cold rolled and annealed dual-phase automotive steel grades DP590 (HCT590X) and DP600 (HCT600X) (Perez-Velasquez et al. 2020; Chinara et al. 2022).

21.2 Modeling

Within the computational model, upper die, lower die, punch and specimen are represented (Fig. 21.3a). Upper die, lower die and punch are modeled as surface models and as rigid bodies. For the numerical simulation considering the appearance of a crack, the specimen is represented as a volume model. The crack path is specified by one layer of cohesive elements (Fig. 21.3b). For the numerical studies, in which the appearance of a crack is not considered, the specimen is represented as a combined surface and volume model (Fig. 21.3c). Within the numerical studies, clamping of the specimen and pressing the punch into the hole are considered.

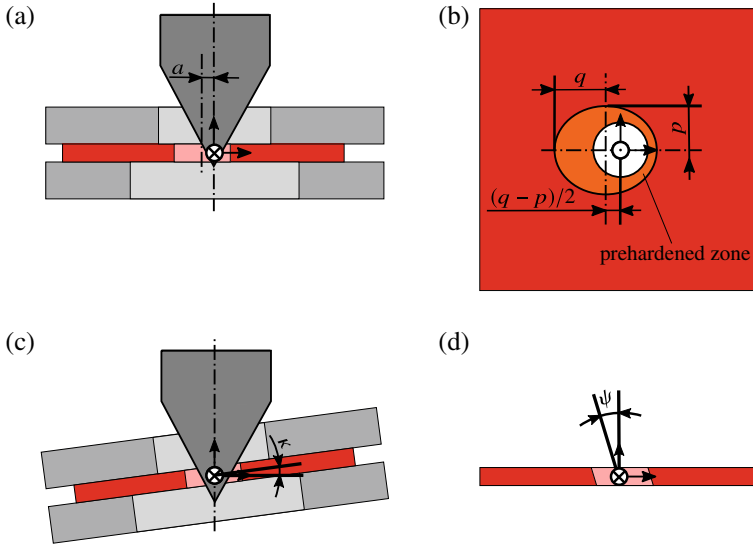


Fig. 21.2 Imperfections of test setup and specimen: displaced specimen (a), eccentric prehardened zone due to punching of the hole (b), tilted test setup (c) and tilted hole axis (d): displacement of specimen, a ; dimensions of prehardened zone, q , p ; tilt angle of test setup, κ ; and tilt angle of hole axis, ψ

Table 21.1 Geometry data for specimen, upper die, lower die and punch (cf. Fig. 21.1): thickness, t , initial hole diameter, d_0 , and edge length, l , of specimen; inside diameter of lower die, d_{ld} , and upper die, d_{ud} ; diameter of punch, d_p , and punch tip angle, α

t (mm)	d_0 (mm)	l (mm)	d_{ld} (mm)	d_{ud} (mm)	d_p (mm)	α (°)
1.36	10	100	69	42	42	60

21.2.1 Geometry

The dimensions of upper die, lower die, punch and specimen are given in Table 21.1. The crack path is approximated as a cuboid (length 43 mm, height 1.36 mm, thickness 0.002 mm) as shown in Fig. 21.3b. To represent the geometry of the hole edge accurately, the thickness of the crack path is chosen three orders of magnitude smaller than the initial hole diameter, d_0 . C3D8R elements (linear, three-dimensional stress/displacement continuum element with 8 nodes and reduced integration) are used to mesh the volume regions of the specimen, and S4R elements (linear, three-dimensional stress/displacement shell element with 4 nodes and reduced integration) to mesh the surface regions. The crack path is meshed with one layer of COH3D8 elements (linear, three-dimensional cohesive element with 8 nodes) (Smith 2019).

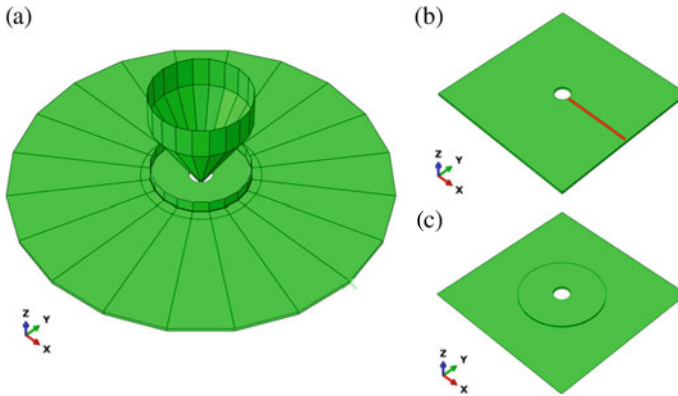


Fig. 21.3 Model geometry (a) and specimens for the numerical studies (b, c). Volume model of specimen with predefined crack path highlighted in red (b) as well as combined volume and surface model (c)

21.2.2 Boundary Conditions and Contact Interactions

While the degrees of freedom of the lower die are restrained in all spatial directions, i.e., in x -, y - and z -directions, the degrees of freedom of the upper die are locked only transversely to the punch axis, i.e., in x - and y -directions. The punch is supported elastically in the x - and y -directions. The stiffness of the support, $k_x = k_y = 750$ N/mm, corresponds to the transverse stiffness of the experimental setup used (Krempaszky et al. 2014).

The following displacement and force boundary conditions are applied to the model geometry: To push the upper die down, the displacement u_{ud} is applied. Then the clamping force, $F_{ud} = 100$ kN, is applied to the upper die. The punch is pushed down by specifying the punch stroke, u_p .

The specimen forms a contact pair each with the punch, the upper and lower dies, respectively. For all contact pairs, the friction coefficient is assumed to be $\mu = 0.2$ (Chinara et al. 2022). The two parts of the combined volume and surface model of the specimen are coupled via the inner hole edge of the specimen part modeled as a surface and the outer circumferential face of the specimen part modeled as a volume (Fig. 21.3c). The displacements of the cohesive elements and of the specimen are coupled in the contact areas (Fig. 21.3b).

21.2.3 Material Behavior

Elastic-plastic material behavior is assigned to the specimen. Young's modulus and Poisson's ratio are assumed as $E = 210$ GPa and $\nu = 0.3$. Both are typical values for steel. Due to thermo-mechanical processing, sheet metal for the automotive industry

exhibits a pronounced anisotropic plastic material behavior (Kalpakjian et al. 2011). Therefore, the Hill yield criterion and the associated flow rule are used to describe the plastic material behavior (Hill 1948). For Cartesian coordinates, the flow criterion

$$f(\underline{\underline{\sigma}}) = \left[F(\sigma_{yy} - \sigma_{zz})^2 + G(\sigma_{zz} - \sigma_{xx})^2 + H(\sigma_{xx} - \sigma_{yy})^2 + 2L\tau_{yz}^2 + 2M\tau_{zx}^2 + 2N\tau_{xy}^2 \right]^{1/2} \quad (21.2)$$

can be formulated depending on the material parameters

$$F = \frac{1}{2} \left(\frac{1}{R_{zz}^2} + \frac{1}{R_{yy}^2} - \frac{1}{R_{xx}^2} \right), \quad G = \frac{1}{2} \left(\frac{1}{R_{zz}^2} + \frac{1}{R_{xx}^2} - \frac{1}{R_{yy}^2} \right), \quad (21.3)$$

$$H = \frac{1}{2} \left(\frac{1}{R_{yy}^2} + \frac{1}{R_{xx}^2} - \frac{1}{R_{zz}^2} \right), \quad L = \frac{3}{2R_{yz}^2}, \quad M = \frac{3}{2R_{xz}^2}, \quad N = \frac{3}{2R_{xy}^2}.$$

Plastic flow occurs, if the yield condition,

$$f(\underline{\underline{\sigma}}) = Y, \quad (21.4)$$

applies. For the steel grade DP590, the flow stress in rolling direction of the sheet,

$$Y = Y_0 + A \cdot \varepsilon_p + B \cdot (1 - e^{-\beta \varepsilon_p}), \quad (21.5)$$

is given as a function of plastic strain, ε_p , and depends on the parameters $Y_0 = 500$ MPa, $A = 410$ MPa, $B = 340$ MPa and $\beta = 9.8$ (Chinara et al. 2022; El-Magd and Abouridouane 2014; Paul et al. 2014). The anisotropic yield stress ratios,

$$R_{xx} = \frac{Y_{xx}}{Y} = 1.0000, \quad R_{yy} = \frac{Y_{yy}}{Y} = 1.0385, \quad R_{zz} = \frac{Y_{zz}}{Y} = 0.9930 \quad (21.6)$$

$$R_{xy} = \frac{k_{xy}}{k} = 1.0966, \quad R_{xz} = \frac{k_{xz}}{k} = 1.0000, \quad R_{yz} = \frac{k_{yz}}{k} = 1.0000,$$

have been determined using tensile tests (Chinara et al. 2022). The anisotropic yield stress ratios are given with respect to the yield stress of the sheet metal in rolling direction, $Y_{xx} = Y$, transverse to the rolling direction, Y_{yy} , and in sheet thickness direction, Y_{zz} , as well as to the shear flow stresses, k_{xy} , k_{xz} , k_{yz} , and the reference shear flow stress $k = Y/\sqrt{3}$.

According to Eq. (21.5), the yield stress is given by $Y = Y_0 = 500$ MPa. This seems to be too high as undeformed dual-phase steels show a continuous initial flow behavior starting at a much smaller stress. The initial flow behavior, which is associated to plastic flow on grain level even for very small macroscopic strains, can be related to residual stresses and predeformations on grain level induced by heat treatment during sheet metal production (Robl et al. 2021; Fillafer et al. 2014).

However, during hole expansion testing the sheet metal is deformed far beyond this strain range. For this reason, we consider the description of the flow stress according to Eq. (21.5) as sufficiently accurate in the context of the investigated problem.

The elastic material behavior of the cohesive elements,

$$\underline{t} = \begin{bmatrix} t_n \\ t_s \\ t_t \end{bmatrix} = \begin{bmatrix} E & 0 & 0 \\ 0 & \frac{E}{2(1+\nu)} & 0 \\ 0 & 0 & \frac{E}{2(1+\nu)} \end{bmatrix} \cdot \begin{bmatrix} \varepsilon_n \\ \varepsilon_s \\ \varepsilon_t \end{bmatrix} = \underline{\underline{E}} \cdot \underline{\varepsilon}, \quad (21.7)$$

is specified via the elasticity matrix $\underline{\underline{E}}$. The elasticity matrix relates the normal stress component acting perpendicularly to the crack plane, t_n , and the shear stress components in the crack plane, t_s , t_t , to the strain components,

$$\varepsilon_n = \frac{\delta_n}{w_c^0}, \quad \varepsilon_s = \frac{\delta_s}{w_c^0}, \quad \varepsilon_t = \frac{\delta_t}{w_c^0}. \quad (21.8)$$

The strain components are defined with respect to the corresponding relative displacements of top and bottom faces of a cohesive element, δ_i , and the initial thickness of the element, w_c^0 . As the crack path is discretized by one layer of cohesive elements, the initial thickness of the elements corresponds to the initial thickness of the crack path. Damage initiates, if one of the stress components, t_i , reaches a critical value, t_i^0 , and therefore,

$$\max \left\langle \frac{\langle t_n \rangle}{t_n^0}, \frac{t_s}{t_s^0}, \frac{t_t}{t_t^0} \right\rangle = 1 \quad (21.9)$$

applies (Smith 2019). With the total mixed-mode relative displacement (Camanho and Davila 2002),

$$\delta_m = \sqrt{\langle \delta_n \rangle^2 + \delta_s^2 + \delta_t^2}, \quad (21.10)$$

damage evolution can be described by the damage variable (Smith 2019),

$$D = \frac{\delta_m^f (\delta_m^{\max} - \delta_m^0)}{\delta_m^{\max} (\delta_m^f - \delta_m^0)}. \quad (21.11)$$

In Eq. (21.11), the total mixed-mode relative displacement at the moment of damage initiation is given by δ_m^0 , the largest total mixed-mode relative displacement so far by δ_m^{\max} and the total mixed-mode relative displacement at the moment of total failure by

$$\delta_m^f = \frac{2 \cdot G^C}{t_m^0}. \quad (21.12)$$

The total mixed-mode relative displacement at the moment of total failure is given with respect to the fracture energy, G^C , and the effective traction at damage initiation, t_m^0 , whereby the effective traction in general is given as

$$t_m = \sqrt{\langle t_n \rangle^2 + t_s^2 + t_t^2}. \quad (21.13)$$

At the moment of damage initiation, i.e., for $\delta_m^{\max} = \delta_m^0$, the damage variable is 0. $D = 1$ applies at the moment of total failure, i.e., for $\delta_m^{\max} = \delta_m^f$. Within the range of $0 < D < 1$, the elastic material behavior,

$$\underline{t} = \underline{\tilde{E}} \cdot \underline{\varepsilon}, \quad (21.14)$$

depends on the modified elasticity matrix,

$$\underline{\tilde{E}} = (1 - D) \cdot \underline{E}. \quad (21.15)$$

If $D = 1$ applies, the cohesive elements are deleted (Smith 2019). In the context of the investigated problem, the cohesive elements are loaded predominantly in normal direction, i.e., perpendicularly to the crack plane. Therefore, $\delta_m = \delta_n$ and $t_m = t_n$ apply. The material parameters $G^C = 500$ N/mm and $t_n^0 = 680$ MPa have been determined for the steel grade DP600, which is very close to the steel grade DP590 (Perez-Velasquez et al. 2020).

21.3 Results and Discussion

To study the influence of a through-thickness crack on the lateral punch force and of different imperfections regarding test setup and specimen (cf. Fig. 21.2), numerical studies were conducted. The results of these studies are shown in Figs. 21.4, 21.5, 21.6, 21.7 and 21.8.

In Fig. 21.4a, b, the lateral and the axial punch force, F_x, F_z , are shown as a function of the punch stroke, u_p for a perfect test setup and a perfect specimen. For the specimen without a predefined crack path, no lateral punch force occurs. The evolution of the axial punch force is typical for hole expansion testing (Krempaszky et al. 2014). For a punch stroke less than $u_p \approx 12$ mm, the deformation of the specimen is dominated by geometrical nonlinear, elastic-plastic bending of the region around the hole. For $u_p > 12$ mm, the axial punch force is dominated by geometrical effects and strain hardening of the material (Krempaszky et al. 2014). For the specimen with a predefined crack path, an increase of the lateral punch force can be reported when damage of the cohesive elements initiates (Fig. 21.4b, c). Initiating damage of the cohesive elements does also influence the axial punch force significantly (Fig. 21.4a, c).

The results of additional numerical studies are shown in Fig. 21.5a–e. These studies examine the influence of displaced specimens, specimens with a prehardened zone around the hole, tilted test setups and specimens with a tilted hole axis on the lateral punch force (cf. Fig. 21.2). In Fig. 21.5f, the lateral punch force is shown for one specific parameter combination ($\kappa = 1^\circ$, $a = 0.2$ mm, $\epsilon_p = 50\%$, $q/p = 5.95$ mm/5.40 mm) and varying sheet thickness, t . The following observations can be made:

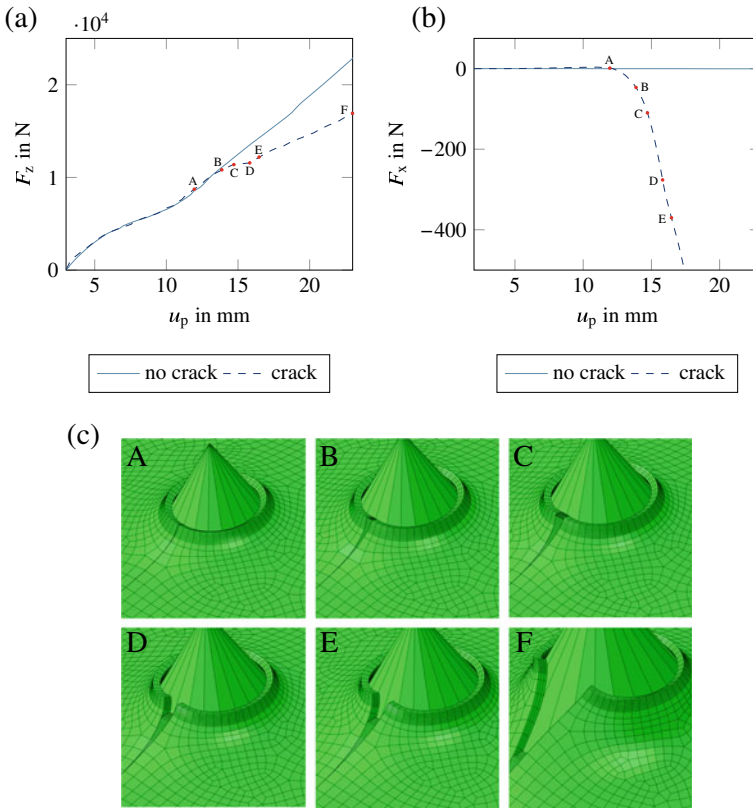


Fig. 21.4 Axial punch force, F_z , (a) and lateral punch force, F_x , (b) as a function of the punch stroke, u_p , for specimens with and without predefined crack path. Deformed specimen with predefined crack path shown for different punch strokes, u_p , (c)

- For displaced specimens and for specimens with a tilted hole axis (Fig. 21.5a, e), the lateral punch force drops abruptly to the local minimum at the beginning of the punch stroke. Then, it increases to a local maximum before reaching a steady state value. For increasing values of a and ψ , the lateral punch force level increases.
- Also for tilted test setups (Fig. 21.5d), the lateral punch force drops abruptly to the local minimum at the beginning of the punch stroke. Then, it increases to the global maximum. After the global maximum has been reached, the lateral punch force decreases again. The lateral punch force level at low and high punch strokes increases with increasing values of κ .
- For specimens with a prehardened zone around the hole (Fig. 21.5b, c), only a small lateral punch force can be reported at the beginning of the punch stroke. For $u_p > 5$ mm, the lateral punch force increases to the local maximum. After the local maximum, the lateral punch force decreases and reaches a steady state

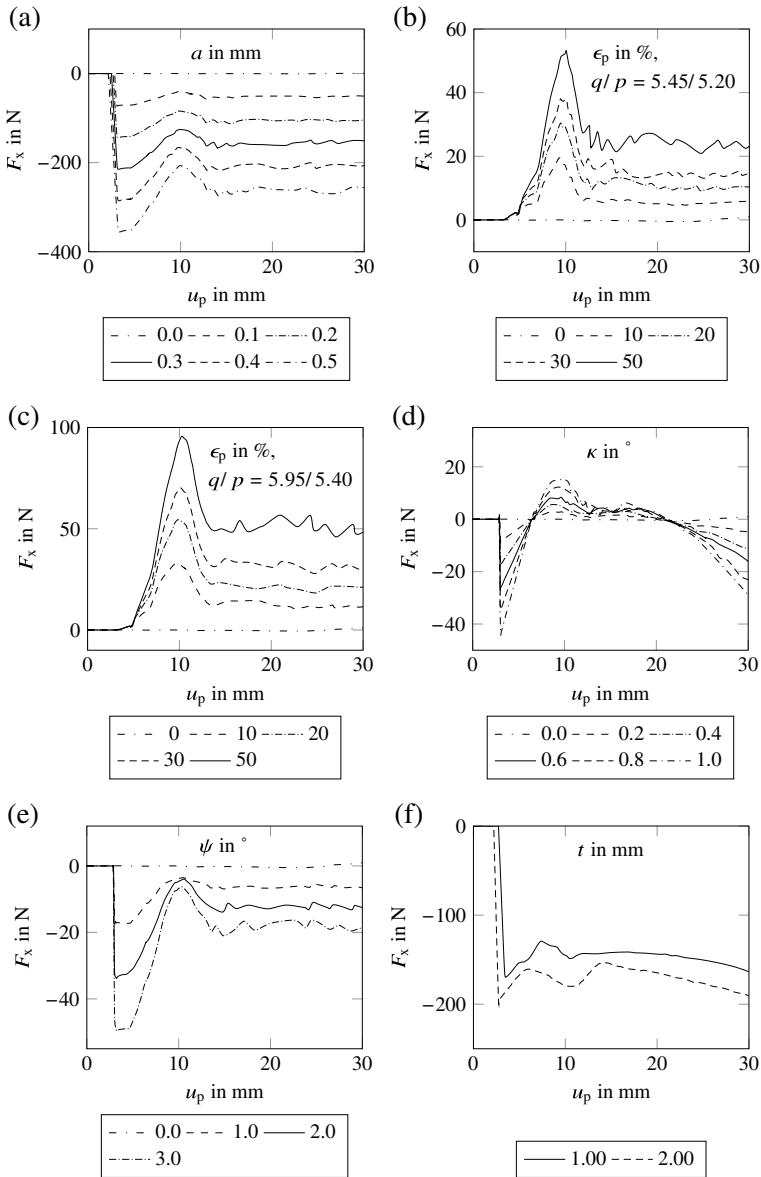


Fig. 21.5 Lateral punch force, F_x , as a function of the punch stroke, u_p , for displaced specimens (a), specimens with prehardened zone around the hole (b, c), tilted test setups (d), specimens with a tilted hole axis (e) and specimens with varying sheet thickness, t , for which $\kappa = 1^\circ$, $a = 0.2$ mm, $\epsilon_p = 50\%$ and $q/p = 5.95$ mm/5.40 mm applies (f)

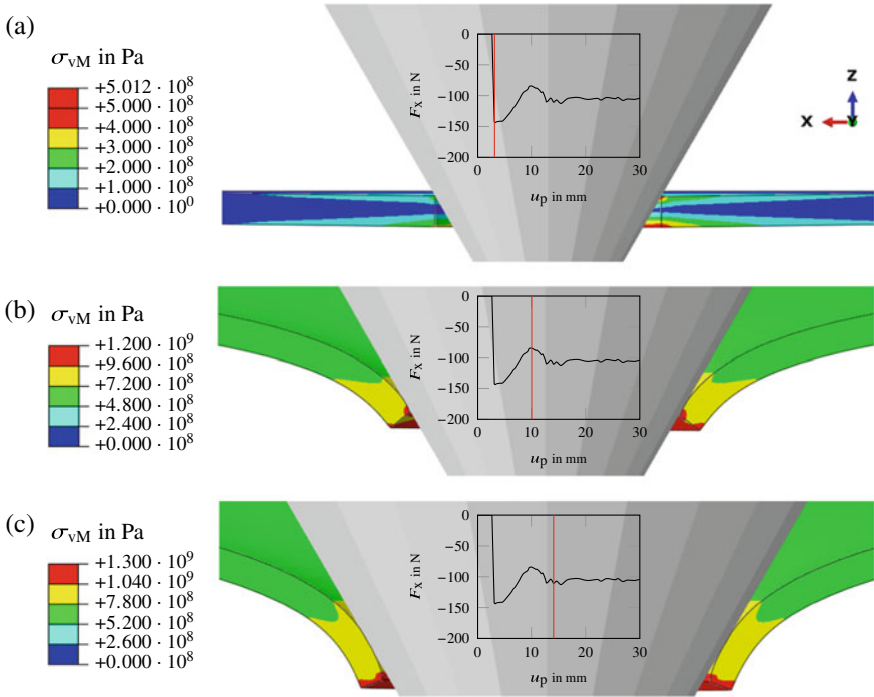


Fig. 21.6 Test setup with displaced specimen ($a = 0.2$ mm): equivalent stress according to von Mises, σ_{vM} , in Pa for different punch strokes, u_p (specimen displayed in sectional view)

value. With increasing prehardening and increasing size of the prehardened zone, the lateral punch force level increases.

- For the specific parameter combination (Fig. 21.5f), the lateral punch force drops abruptly to the local minimum. Then, it increases to a local maximum. For $u_p > 10$ mm, the lateral punch force decreases. The lateral punch force level increases with increasing sheet thickness, t .

These observations can be explained as follows:

- For displaced specimens, tilted test setups and specimens with a tilted hole axis, a single-point contact between the hole edge and the punch can be observed at the beginning of the punch stroke (Fig. 21.6a). With increasing punch stroke, this single-point contact progressively becomes sickle-shaped but is still one-sided. The punch is deflected in the negative x -direction and the lateral punch force decreases. As soon as the contact zone becomes increasingly circumferential and ring-shaped, also the transverse force increases. The lateral punch force increases until the hole edge detaches completely from the punch surface. At last, the part of the hole edge detaches, which came into contact with the punch surface last. A local, viz., a global maximum is reached because the resistance against elastic-

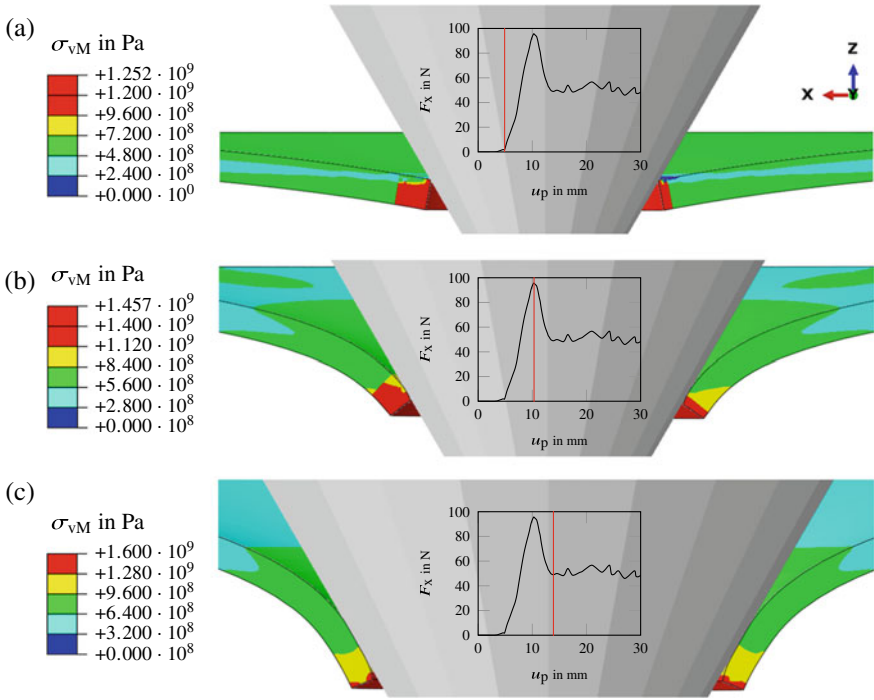


Fig. 21.7 Specimen with prehardened zone ($\epsilon_p = 50\%$, $q/p = 5.95 \text{ mm}/5.40 \text{ mm}$): equivalent stress according to von Mises, σ_{VM} , in Pa for different punch strokes, u_p (specimen displayed in sectional view)

plastic bending of the specimen is higher before the hole edge detaches from the punch surface than after detaching (Fig. 21.6b). Constant values of the lateral punch force, F_x , for displaced specimens and for specimens with a tilted hole axis, which are predicted for punch strokes, u_p , higher than approx. 15 mm, can be associated with the eccentricity of the hole, viz., the deviation of the hole axis from the punch axis (Fig. 21.6c). Decreasing values of F_x for tilted test setups can be related to different effective punch tip angles in the range of positive and negative x -values.

- The specimens with a prehardened zone are deformed elastically at the beginning of the punch stroke. Then, plastic flow occurs predominantly within the prehardened zone. Due to the isotropic elastic and orthotropic plastic material behavior of the whole specimen, the lateral punch force is zero (Fig. 21.7a). The lateral punch force increases, if plastic deformation within the prehardened zone is influenced by the surrounding material. That is, if plastic flow occurs also outside the prehardened zone. Then, due to the averaged yield stress level, the resistance of the specimen against plastic deformation is lower in the region of positive x -values than in the region of negative x -values. Therefore, the lateral punch force

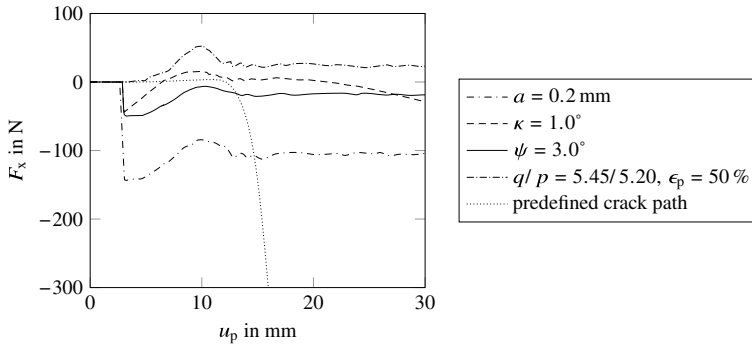


Fig. 21.8 Lateral punch force, F_x , as a function of the punch stroke, u_p , for models with different imperfection types and for the model with predefined crack path

increases (Fig. 21.7b). The maximum of the lateral punch force is reached before the prehardened zone in the area of negative x -values detaches from the punch (Fig. 21.7c).

In Fig. 21.8, the lateral punch force, F_x , is shown as a function of the punch stroke, u_p , for models with different imperfection types and for the model with a predefined crack path. For the chosen parameter values, the results indicate that the lateral punch force during testing is affected strongest by displaced specimens before a crack appears. After a crack occurs, the lateral punch force is affected predominantly by the crack itself. Obviously, strong variations of the lateral punch force at the beginning of the punch stroke are related to displaced specimens, tilted test setups and specimens with a tilted hole axis. An eccentric, prehardened zone around the hole affects the lateral punch force later in the numerical experiment.

In Fig. 21.9, experimental data from hole expansion testing is shown, i.e., the lateral punch force components, F_x , F_y , as a function of the punch stroke, u_p . The hole expansion tests were conducted on three sets of specimens made from the steel grade HCT780X, which is a cold rolled and annealed automotive dual-phase steel with a tensile strength of at least 780 MPa. The holes of two specimens each were manufactured by punching, laser cutting or electrical discharge machining, respectively. Due to punching of the hole, a prehardened zone around the hole or a tilted hole axis may be present for the corresponding specimens.

For all three types of specimen, a similar characteristic of at least one lateral punch force component can be observed before the first through-thickness crack occurs. This characteristic as well as the lateral punch force level in general indicate that the specimens most probably were displaced during testing by approx. 0.1–0.2 mm (cf. Fig. 21.5). This is surprising as an adequate positioning of the specimens has been ensured by lowering the punch before clamping. Due to lowering the punch, the hole edge has been in contact with the punch surface during clamping. However, this procedure is obviously subject to uncertainties. From the results in Fig. 21.9, a significant influence of a tilted test setup cannot be identified. This is also the case for the influence of a prehardened zone around the hole and a tilted hole axis (Fig. 21.9c, d).

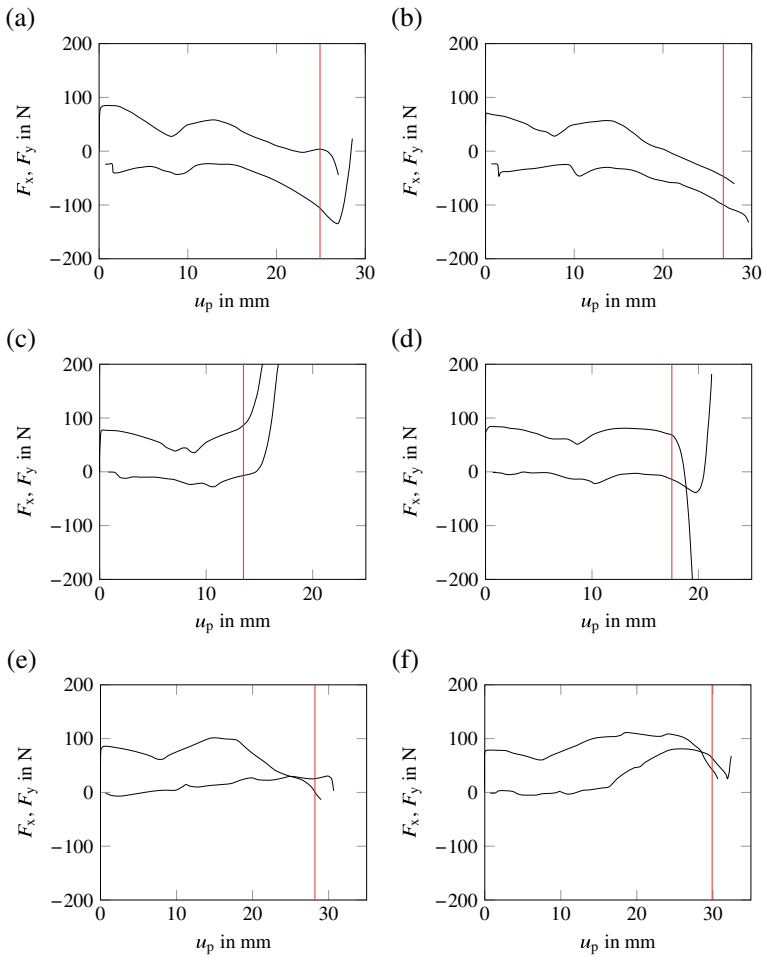


Fig. 21.9 Lateral punch force components, F_x , F_y , as a function of the punch stroke, u_p , for specimens made out of the automotive sheet metal grade HCT780X (thickness, $t = 1.8$ mm, initial hole diameter, $d_0 = 10$ mm). Occurrence of the first through-thickness crack marked with red line. Holes of the specimens manufactured by laser cutting (**a**, **b**), punching (**c**, **d**) and electrical discharge machining (**e**, **f**). Further geometry parameters of the test setup: punch tip angle, $\alpha = 60^\circ$, inside diameter of lower die, $d_{id} = 70$ mm

21.4 Conclusions

In this contribution, the influence of a displaced specimen, a specimen with a pre-hardened zone due to punching of the hole, a tilted test setup and a specimen with a tilted hole axis on the lateral punch force during hole expansion testing has been studied by means of numerical simulations. The simulations indicate the influence of a displaced specimen being most significant before the first through-thickness crack

appears. This is also indicated by experimental results. The influence of other imperfection types, such as an eccentric prehardened zone due to punching of the hole, a tilted test setup or a tilted hole axis, seems to be of minor importance. The numerical and the experimental results indicate, that it may be useful to examine the lateral punch force components during testing to verify if testing is carried out properly. In contrast, it only seems useful to define a reliable criterion for the end of the test based on the evolution of the lateral punch force, if nearly perfect testing conditions are assured. With regard to both aspects, a validation of the numerical results by experimental investigations should be carried out at first. To define improved guidelines for proper testing conditions, it is furthermore of high interest, in which manner the hole expansion ratio is affected by the different imperfection types. The clarification of these questions is focus of ongoing experimental and numerical investigations.

References

- Camanho PP, Davila CG (2002) Mixed-mode decohesion finite elements for the simulation of delamination in composite materials. Research report (report number: NASA/TM-2002-211737). NASA Langley Research Center, Hampton, VA
- Chinara M, Paul SK, Chatterjee S, Mukherjee S (2022) Effect of planar anisotropy on the hole expansion ratio of cold-rolled DP 590 steel. *Trans Indian Inst Met* 75:535–543
- Düncelmeyer M, Karelova A, Kremaszky C, Werner E (2009) Instrumented hole expansion test. In: Proceedings of international doctoral seminar, Smolenice
- El-Magd E, Abouridouane M (2014) Influence of strain rate and temperature on the flow behavior of magnesium alloy AZ80. *Z Metallkd* 92:1231–1235
- Fillafer A, Werner E, Kremaszky C (2014) On phase transformation induced effects controlling the initial flow behavior of ferritic-martensitic dual-phase steels. *Mater Sci Eng A* 708:556–562
- Hill R (1948) A theory of the yielding and plastic flow of anisotropic metals. *Proc R Soc A* 193:281–297
- ISO 16630 (2017) Metallic materials—sheet and strip—hole expanding test. Switzerland
- Kalpajian S, Schmid SR, Werner E (2011) *Werkstofftechnik*, 5th edn. Pearson, Munich
- Karelova A, Kremaszky C, Werner E, Hebesberger T, Pichler A (2007a) Influence of the edge conditions on the hole expansion property of dual-phase and complex-phase steels. In: Fekete J, Garcia I, Speer J, Walp M (eds) Proceedings of materials science & technology 2007. Automotive. Association for Iron & Steel and TMS, Warrendale, PA
- Karelova A, Kremaszky C, Werner E, Hebesberger T, Pichler A (2007b) Influence of microstructure and tensile properties on hole expansion property of dual-phase and complex-phase high strength steels. In: Proceedings of international doctoral seminar, Trnava
- Karelova A, Kremaszky C, Werner E, Tsipouridis P, Hebesberger T, Pichler A (2009a) Hole expansion of dual-phase and complex-phase AHS steels—effect of edge conditions. *Steel Res Int* 80:71–77
- Karelova A, Kremaszky C, Düncelmeyer M, Werner E, Hebesberger T, Pichler A (2009b) Formability of advanced high strength steels determined by instrumented hole expansion testing. In: Proceedings of materials science & technology 2009. Steel processing, product and application symposium. Association for Iron & Steel and TMS, Warrendale, PA
- Kremaszky C, Larour P, Freudenthaler J, Werner E (2014) Towards more efficient hole expansion testing. In: Sfar H, Maillard A (eds) Proceedings of international deep drawing research group conference (IDDRG conference), Paris

- Paul SK, Mukherjee M, Kundu S, Chandra S (2014) Prediction of hole expansion ratio for automotive grade steels. *Comput Mater Sci* 89:189–197
- Perez-Velasquez C, Avendano-Rodriguez D, Narvaez-Tovar C, Roncery LM, Roriguez-Baracaldo R (2020) Fatigue crack growth and fracture toughness in a dual phase steel: effect of increasing martensite volume fraction. *Int J Autom Mech Eng* 17:8086–8095
- Robl T, Kremaszky C, Fillafer A, Werner E (2021) Examining the unloading behavior of dual-phase steels by means of microstructure simulations. *Mater Sci Eng A* 823:141744
- Smith M (2019) ABAQUS/standard user's manual. Dassault Systemes Simulia Corp, Waltham, MA

Chapter 22

CFD Analysis of Hot Gas Welding of 3D Weld Contours Using Two Different Nozzle Systems



Johannes Schmid, Dennis F. Weißer, Dennis Mayer, Lothar Kroll, Sascha Müller, Rainer Stauch, and Matthias H. Deckert

Abstract A nozzle system (top nozzle system) for hot gas welding, which encloses the weld seam during heating, was developed with the help of computational fluid dynamics (CFD) simulations. The significantly more controlled flow behavior of the hot gas improves the processing window, increases the reproducibility and achieves a significantly more efficient heating time of the polymer weld seam. The CFD simulations used to develop the new nozzle system are validated by temperature measurements in the hot gas welding process with IR camera and thermocouples. The simulations carried out with the round and top nozzle system on inclined and hybrid weld contours show that the top nozzle can reliably heat the polymer even at increasing angles of up to 45°. In contrast, the heating behavior of the round nozzle shows a more significant temperature drop at the surface with increasing angles. Furthermore, the heating times for the round nozzle are 100% longer and the temperature range on the polymer surface is up to 70% higher.

Keywords Hot gas welding · Plastic welding · CFD simulation · Nozzle · Heating of the polymer · 3D weld contours

22.1 The Hot Gas Welding Process

To join technical polymer components, both non-contact welding processes, such as infrared (Rattke and Natrop 2007; Gehde et al. 2008; Fuhrich et al. 2011a, b; Fuhrich and Gehde 2014), laser welding (Klein 2001; Schulz 2002) and contacting processes,

J. Schmid (✉) · D. F. Weißer · D. Mayer · R. Stauch · M. H. Deckert
Faculty of Mechanical and Systems Engineering, Esslingen University of Applied Sciences,
Kanalstr. 33, 73728 Esslingen am Neckar, Germany
e-mail: Johannes.Schmid@hs-esslingen.de

M. H. Deckert
e-mail: Matthias.Deckert@hs-esslingen.de

L. Kroll · S. Müller
Department of Lightweight Structures and Polymer Technology, Chemnitz University of
Technology, Reichenhainer Strasse 31/33, 09126 Chemnitz, Germany

such as vibration (Schlarb 1989; Friedrich 2014) and ultrasonic welding, have become established in series production (Mochev and Endemann 2016). However, joining processes that melt the thermoplastic without contact, e.g., by radiation or convection heating have been increasingly investigated and developed in the recent years (Rattke and Natrop 2007, 2008; Fuhrich and Gehde 2014; Barkhoff and Happel 2019). The reason is the absence of the formation of particles, e.g., in friction welding or the adhesion of plastic melt in hot plate welding. The heating of components that is not free of particles is increasingly becoming a criterion for exclusion when selecting a suitable joining process for engineering polymers (Rattke and Natrop 2007; Potente et al. 2010; Belmann, 2017).

Hot gas welding is a further development of the widely used hot plate welding (Egen 1985; Kreiter 1987; Bonten 1998; Tüchert 2005; Potente et al. 2008; Friedrich and Schöppner 2012; Baudrit et al. 2014). The advantage of hot gas welding is not only the non-contact heating but it is also the free design of the weld seam. In contrast to the usual welding processes such as ultrasonic or vibration welding, three-dimensional weld seams can be produced comparatively easily (Mochev 2018; Deckert et al. 2019; Rzepka 2021). The disadvantages of the process are the highly complex tools, relatively long cycle times, and high-energy consumption (Mochev and Endemann 2018; Rzepka 2021). For hot gas welding, the complete welding contour of both halves of the component to be joined is reproduced with small, closely spaced tubes on the so-called hot gas tool. The tubes' hot gas flow melts the polymer at the joining surfaces. After that, the components joined under pressure (Fig. 22.1).

Today hot gas welding processes often show limited processing windows and therefore are difficult to adjust and control. The currently used conventional “round nozzle” creates an impingement flow, which heats the joining zone of the component only selectively and creates a crater-like structure (Albrecht et al. 2020, 2021). This type of nozzle produces comparatively high heat losses, and the surface temperatures are difficult to control. Furthermore, the round nozzle system has long heating times because the hot gas flows uncontrollably away from the polymer surface after

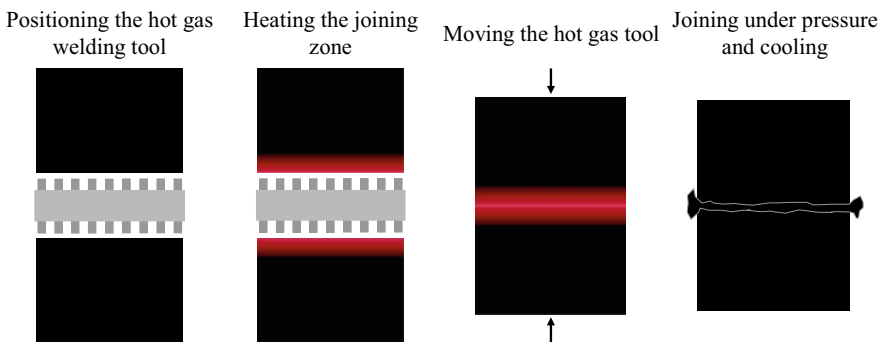


Fig. 22.1 Hot gas welding sequences

impinging it (Schmid et al. 2021a, 2021b, 2021c). The newly developed “top nozzle” overcomes the mentioned drawbacks. With this next generation nozzle design, the weld joint is entirely covered by the nozzle itself (GMB Kunststoffteile GmbH 2020). As a result, the heat loss is minimized and the hot gas flow can be controlled much better. For polyamides with different base polymers and different glass fiber contents, an average reduction in heating time of up to 50% is possible. The achieved weld strengths for the tested materials are comparable or higher with the top nozzle system (Schmid et al. 2021a, 2021b, 2021c).

22.2 Theory of Impingement Flow

The flow field between the nozzle and the solid can be divided into three different regions (sections). As can be seen in Fig. 22.2, a free jet is formed directly after the nozzle exit. This free jet is broadened and delayed by the interaction with the surrounding gas. The free jet changes into a stagnation flow at a certain distance from the solid (VDI 2013). In the area where the jet is affected by the wall (stagnation area), the wall-normal component of the velocity decreases to zero. In contrast, the wall-parallel component increases from zero to a maximum value at a certain distance from the stagnation point (Hofmann 2005). At the stagnation point, the velocity is zero. The wall jet (downstream zone) and the free jet increase in jet thickness due to mixing with the ambient fluid, and therefore, the velocity of the hot gas decreases. At a distance of one to two nozzle diameters from the center point of the nozzle, the maximum of the wall-parallel velocity can be detected (Hofmann 2005).

Schabel and Martin studied single round nozzles and two-dimensional nozzle arrays (x - and y -direction) (VDI 2013). In the hot gas welding process studied in this paper, only one-dimensional nozzle arrays (x - or y -direction) are used.

The Reynolds number for the simulations carried out with the investigated round nozzle is calculated according to Eq. (22.2.1) and ranges from $Re_{\text{round nozzle}} =$

Fig. 22.2 Impingement flow from a slot or round nozzle (VDI 2013)

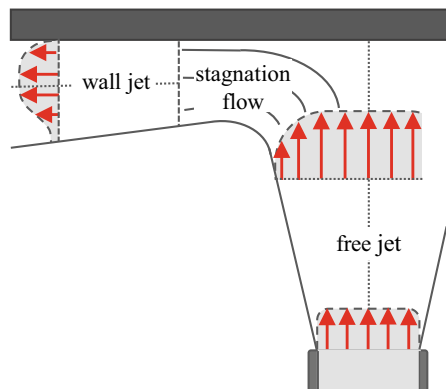


Table 22.1 Comparison of the Reynolds number and geometrical dimensions according to (VDI 2013)

Validity limits from (VDI 2013)	Hot gas welding process
$2.5 \leq \frac{r}{D} \leq 7.5$	$\frac{r}{D} = \frac{2.0\text{mm}}{1.7\text{mm}} = 1.2$
$2.0 \leq \frac{H}{D} \leq 12$	$\frac{H}{D} = \frac{2.0-4.5\text{mm}}{1.7\text{mm}} = 1.2 - 2.65$
$2000 \leq \text{Re} \leq 400.000$	$\text{Re} = 263 - 557$

263–371 in the studied areas. For the simulations carried out with the top nozzle, the Reynolds number is calculated according to Eq. (22.2.2) and ranges from $\text{Re}_{\text{top nozzle}} = 394\text{--}557$ in the studied areas. Hereby, c_F describes the flow velocity, d the hydraulic diameter of the nozzle and ν the kinematic viscosity in the investigated temperature. The kinematic viscosity of nitrogen with respect to the gas temperature is taken from (VDI 2013) and interpolated accordingly.

$$\text{Re}_{\text{roundnozzle}} = \frac{c_F \cdot d}{\nu} = \frac{(8.97 \dots 12.69 \frac{\text{m}}{\text{s}}) \cdot 1.7 \cdot 10^{-3} \text{m}}{58 \cdot 10^{-6} \frac{\text{m}^2}{\text{s}}} = 263 \dots 371 \quad (22.2.1)$$

$$\text{Re}_{\text{topnozzle}} = \frac{c_F \cdot d}{\nu} = \frac{(13.46 \dots 19.04 \frac{\text{m}}{\text{s}}) \cdot 1.7 \cdot 10^{-3} \text{m}}{58 \cdot 10^{-6} \frac{\text{m}^2}{\text{s}}} = 394 \dots 557 \quad (22.2.2)$$

The range of validity of the Reynolds number for the calculation of the Nusselt number for the impingement flow for a single circular nozzle or a circular nozzle array specified in (VDI 2013) is $\text{Re} > 2000$ (Table 22.1). The hot gas welding process lies beyond the validity limits mentioned in (VDI 2013) with respect to the Reynolds number and the geometrical dimensions (Table 22.1). For these reasons, it is impossible to rely on existing knowledge, and a CFD analysis of the existing flow problem is necessary. Furthermore, the reduction of the calculation of the Nusselt number from the two-dimensional array of (VDI 2013) to the case of a one-dimensional nozzle field studied here is not straightforward. In addition, the influence of impingement flows on inclined welds with a certain angle is investigated in this paper.

22.3 Structure of the CFD Simulation Model for 3D-Shaped Welds

The CFD software “Simcenter STAR-CCM + 2020.1” is used to perform the CFD simulations. The simulation model of the round nozzle system (Fig. 22.3 left) consists of four tubes (fluid), a polymer with a surface angle varying from 0° to 45° (solid) and the free flow area. The top nozzle system (Fig. 22.3 right) consists of four tubes with top nozzle (fluid), a polymer with a surface angle varying from 0 to 45° (solid) and the free flow area. The individual tubes have an inner diameter of $d_{\text{inside}} = 1.7 \text{ mm}$ ($d_{\text{outside}} = 2.0 \text{ mm}$) and a distance of $\Delta x = 3.3 \text{ mm}$. The model is symmetric at the front and back (symmetry plane—blue area in Fig. 22.3) to simulate an infinitely

long weld. The simulation is limited to heat transfer by convection. Superimposed heat transfer by radiation is very low due to the low visibility factor between the tube and the polymer and can therefore be neglected.

The three steps of the simulation and the stored properties for the simulation model round nozzle and top nozzle are given in Table 22.2. The simulation steps contain a creation of the computational mesh and the calculation of the steady-state flow to initiate a flow field for the subsequent transient simulation. The transient simulation for a specified physical time of the heating behavior of the polymer by the hot gas is the third and the last step.

According to (Gardon and Akfirat 1965), an impingement flow is considered turbulent if the Reynolds number is larger than 2000 ($Re > 2000$). The investigation

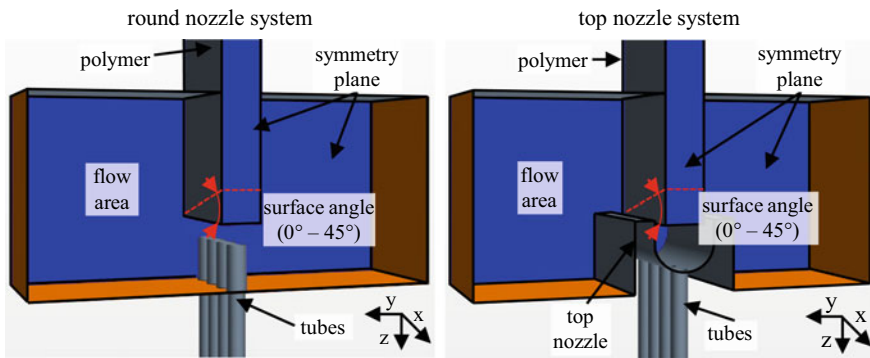


Fig. 22.3 Illustration of the used simulation models

Table 22.2 Overview of the steps and the stored properties of the simulation model

The steps of the simulation process	Properties of the CFD model
<ul style="list-style-type: none"> • Creation of the computational mesh • Calculation of the steady-state flow without heat transfer processes in the polymer (→ initial flow field for transient simulation) • Transient simulation of the heating of the polymer for an appropriate time 	<ul style="list-style-type: none"> • Laminar flow • Calculation of the gas (nitrogen) properties (temperature dependent) <ul style="list-style-type: none"> – Polynomial density and specific heat – Dynamic viscosity – Thermal conductivity • Calculation of the polymer properties (temperature dependent) <ul style="list-style-type: none"> – Polynomial density and specific heat – Thermal conductivity • Polyhedral cells: <ul style="list-style-type: none"> – 5.4 million (round nozzle system) – 5.1 million (top nozzle system) • Physical time: <ul style="list-style-type: none"> – 25.0 s (round nozzle system) – 12.5 s (top nozzle system) • Time step = 0.01 s

of the Nusselt number in (Gardon and Akfirat 1965) shows that impingement flows for $Re < 2000$ and a nozzle-to-plate-spacing of $H/D < 5.5$ are laminar. According to Simionescu (Simionescu et al. 2017), impingement flows are fully laminar between $Re = 300$ and 1000. Depending on the process parameters for the round nozzle system, Reynolds numbers between 263 and 371 and nozzle-to-plate-spacing of 1.2 appear for the hot gas welding process. Reynolds numbers between 394 and 557 and nozzle-to-plate-spacing of 2.65 appear for the hot gas welding process with the top nozzle system, depending on the process parameters. Due to low Reynolds numbers and the low nozzle-to-plate-spacing, laminar CFD simulations are performed. In the region of interest for the heat transfer of the welding process, the predominantly laminar character of the hot gas flow can also be seen in Fig. 22.4 (round nozzle system) and Fig. 22.5 (top nozzle system).

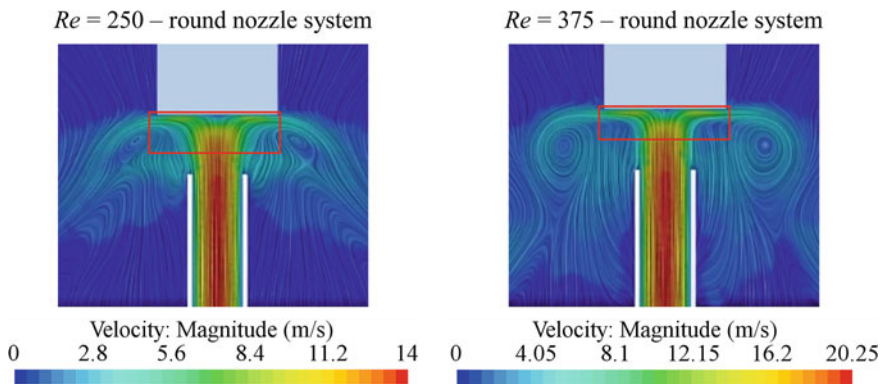


Fig. 22.4 Flow field of the investigated hot gas welding process with the round nozzle system

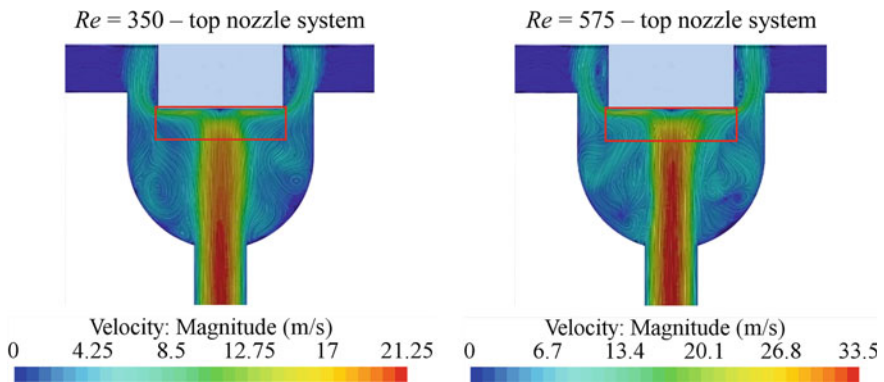


Fig. 22.5 Flow field of the investigated hot gas welding process with the top nozzle system

22.4 Validation of the Simulation Model

Temperature measurements are carried out to validate the simulation results with an infrared camera system (IR) and with disposable thermocouples. The validation of the simulation is done by temperature measurements with thermocouples and an IR camera system at horizontal plates with a thickness of 4 mm. Furthermore, the melting behavior of the polymer of the top nozzle system is validated.

22.4.1 Test Setup for Validation of the Simulation

Temperature measurements are performed to analyze the heating of the polymer in the welding process with the top nozzle. The hot gas welding system (type: VDP 2012, manufacturer: KVT Bielefeld GmbH, Bielefeld) is equipped with pressure sensors and an IR camera system, Fig. 22.6, right. The heating of the polymer is measured with thermocouples type J. For this purpose, holes (\varnothing 0.5 mm) are made at the corresponding points with a suitable CNC milling machine. Eight measuring points are provided per plate, Fig. 22.6 left. A thermocouple is inserted into the polymer surface to determine the polymer surface temperature (0.0 mm (P)). Another thermocouple is positioned at a distance of 0.1 mm from the polymer surface to measure the gas temperature on the polymer surface (+0.1 mm (G)). The other six thermocouples are placed 0.5 mm below the polymer surface (-0.5 mm (P)) with a distance of 3.3 mm.

The investigations in this work are focused on polyamide, which is mainly used for technical components in the industrial and automotive environment. Polyamides are semi-crystalline engineering thermoplastics. PA6 and PA66 are composed of the

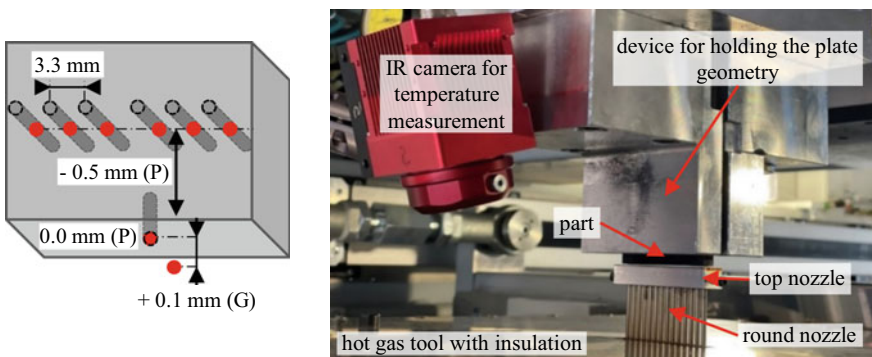


Fig. 22.6 Measuring points in the left half of the polymer plate (dark gray: polymer plate, red: measuring points), left; test setup, right; IR measurement is performed after moving out the hot gas too; +0.1 mm (G): gas temperature on polymer surface; 0.0 mm (P): temperature of polymer surface; -0.5 mm (P): temperature of polymer in 0.5 mm depth

Table 22.3 Selected properties (dry) of PA66-GF35 (Zytel® 70G35HSLR BK416LM-DuPont)

Name	Stress at break	Tensile modulus	Melting temperature	Glass transition temperature
PA66-GF35	210 MPa	11,000 MPa	263 °C (10 K/min)	70 °C (10 K/min)

same empirical formula $(C_6H_{11}ON)_n$. The two polyamides differ in their structural composition. The different molecular structure explains the higher melting point and lower water absorption of PA66 (Lanxess Deutschland GmbH 2009). Due to the high solidification temperature and shorter crystallization time, PA66 has a very short cycle time compared to PA6. The rapid solidification of the PA66 melt is more of a disadvantage with glass fiber-reinforced grades, because poorer surface quality and distortion of the components are to be expected (Lanxess Deutschland GmbH 2009). The investigations are carried out with a PA66 with 35% glass fibers (Zytel® 70G35HSLR BK416LM-DuPont). The tested material is widely used on the market (Table 22.3).

22.4.2 Validation of the Simulated Shape of the Molten Polymer

Differences in the melting evolution caused by the round nozzle and the top nozzle are investigated using a PA66-GF35 and compared with the simulation. For this purpose, thin sections of the specimen (micrographs through the weld, transmitted light microscopy) heated by the round nozzle and the top nozzle system are created (weld width 4 mm). The simulations for the round nozzle and the top nozzle show a melting evolution comparable to the thin sections.

The different heating behavior of the two nozzle systems can be seen in the cross-section of the polymer below the nozzle opening. With the conventional round nozzle, the melting zone of the polymer is shaped convexly, and only a few amounts of polymer is melted at the edges of the weld seam (Fig. 22.7). The melting zone is identified by local temperatures above the melting temperature of 260 °C.

In contrast, the top nozzle melts the polymer concavely (Fig. 22.8), as it is known from hot plate or IR welding (Ehrenstein and Ahlers-Hestermann 2004; Gehde et al. 2008; Fuhrich et al. 2011a, b; Fuhrich and Gehde 2014). The simulation results (Fig. 22.7 and Fig. 22.8, left) and the experimental results (Fig. 22.7 and Fig. 22.8, right) show similar shapes of the melting zone. With the top nozzle, a deeper melting at the edges of the weld seam is evident. The enclosing of the weld seam with the top nozzle can explain this behavior.

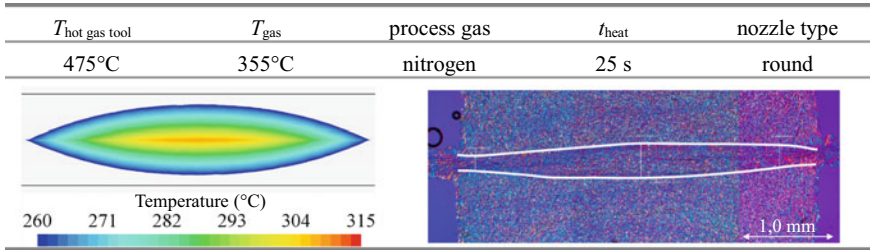


Fig. 22.7 Simulation (left) and thin section image (right, white line) of a weld heated with the round nozzle

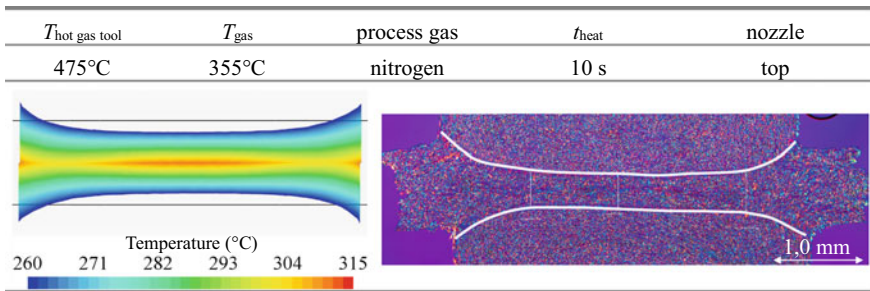


Fig. 22.8 Simulation (left) and thin section image (right, white line) of a weld heated with a top nozzle

22.4.3 Validation of the Simulated Transient Heating Behavior

The temperature evolutions on the surface and in the polymer are investigated during the welding process to validate the simulation. The gas temperature applied to the polymer is measured with thermocouples. The polymer surface temperature is determined using thermocouples and an IR camera system. The temperatures arising in the polymer at a depth of 0.5 mm are determined using thermocouples. The simulated transient heating behavior is validated for the round and the top nozzle. The focus of the simulations carried out is to investigate the behavior of the top nozzle with a 4 mm weld width.

The simulation results in the case of the round nozzle of the gas temperature (+0.1 mm (G)) and the temperature of the polymer (PA66-GF35) on the surface (0.0 mm (P)) can be compared with the temperatures measured during the process (Fig. 22.9). It is assumed that the thermocouples, which measure the gas temperature, need a specific time to be heated by the hot gas (0–5 s). This thermal inertia leads to a delayed heat up of the measured temperature values compared to the simulation results in the first five seconds of the process. After five seconds, the influence of the thermal inertia decreases significantly. The effect of thermal inertia is significant

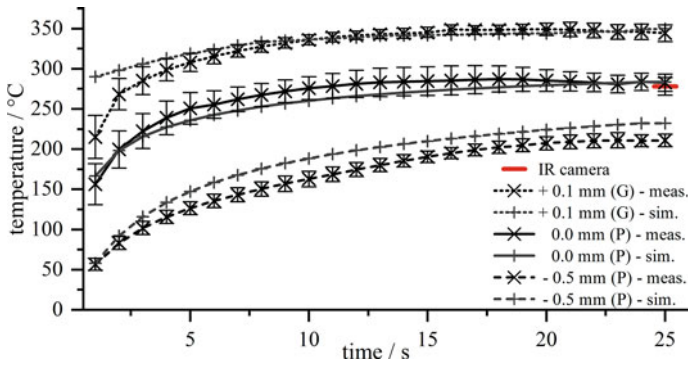


Fig. 22.9 Comparison of temperature measurements and simulation results using the round nozzle system ($T_{\text{gas}} = 355 \text{ }^{\circ}\text{C}$; $\dot{V} = 1.11 \text{ (l/min)/tube}$; PA66-GF35)

when measuring the gas temperature since the heat transfer between the gas and the thermocouple (gas/solid) is significantly lower than the heat transfer between the thermocouple and the polymer (solid/solid). This effect can be neglected since the first five seconds of the heating phase are not relevant for the investigations. The temperature predictions after 10–25 s are more relevant for the investigations, as these influence the welding result. The temperatures measured at a depth of 0.5 (–0.5 mm (P)) are lower than those calculated in the simulation. It is also assumed that the thermocouples must be heated and thus cool the polymer. The surface temperature measured with the IR camera matches the simulation results and the temperature measurements with the thermocouples at $t = 25 \text{ s}$ quite well.

The simulated results of the gas temperature (+0.1 mm (G)) and the temperature of the polymer (PA66-GF35) on the surface (0.0 mm (P)) can be compared with the temperatures measured in the process (Fig. 22.10). It is assumed that the thermocouples, which measure the gas temperature, need a specific time to be heated by the hot gas (0–5 s). This thermal inertia leads to a delayed heat up of the measured temperature values compared to the simulation results. The reason for this is similar to Fig. 22.9. The surface temperatures measured by the IR camera at $t = 12.5 \text{ s}$ and the temperatures measured at a depth of 0.5 mm (–0.5 mm (P)) are slightly lower than those in the simulation calculated but within the standard deviation of the measurements.

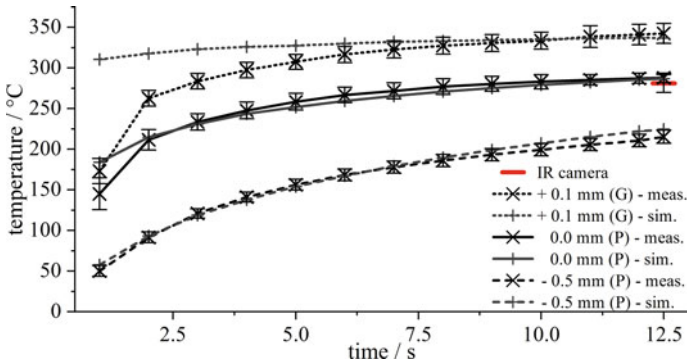


Fig. 22.10 Comparison of temperature measurements and simulation using the top nozzle system ($T_{\text{gas}} = 355\text{ }^{\circ}\text{C}$; $\dot{V} = 1.67\text{ (l/min)}$ /tube; PA66-GF35)

22.5 Investigation of the Influence of 3D-Shaped Weld Contours

The hot gas welding process analysis with the top nozzle for 2D-shaped welding contours using CFD simulations is performed in (Schmid et al. 2022). The simulations provide comparable results with the temperature measurements for two polyamides with different base polymers and different glass fiber contents (PA6-GF40 and PA66-GF35) at varying heating times, temperatures of the hot gas tool and volume flows. Measurements validate the results of the simulations with an IR camera system and lost thermocouples. The simulations show that an increase in the process parameters gas temperature, heating time or volume flow leads to a correspondingly higher polymer temperature (Schmid et al. 2022).

The geometrical variation of the gap distance between polymer and top nozzle shows that a smaller gap leads to higher temperatures on the surface and inside the polymer. A gap between nozzle and polymer $< 1.0\text{ mm}$ does not appear to be practical for manufacturing reasons and leads primarily to the fact, that fewer tolerances can be compensated for the components to be welded (Fig. 22.11). An immersion depth of -0.5 mm into the polymer is recommendable. A deeper immersion of the polymer does not lead to a better heating behavior and no immersion leads to a significant temperature drop inside the polymer (Fig. 22.11) (Schmid et al. 2022).

Varying the distance between the nozzle opening and the polymer surface shows that the distance between the nozzle opening and the polymer surface has no significant influence. However, a moderate distance is advisable for low viscosity materials, since otherwise, the impact flow can cause crater-like structures to form on the polymer surface. The temperatures on the surface and inside the polymer decrease with larger tube diameters. Small tube diameters have the highest flow velocity, which can lead again to crater-like structures on the surface of the polymer in case of low viscosity materials. The study of the geometrical parameters of the top nozzle indicates that tube diameter between $1.7\text{ and }2.0\text{ mm}$ leads to an efficient heating

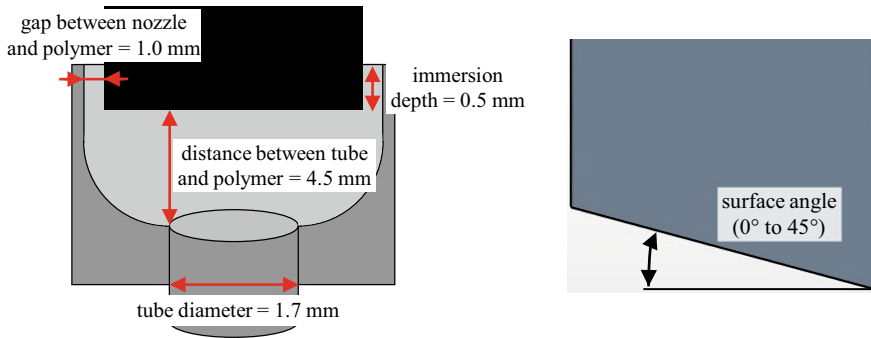


Fig. 22.11 Sketch with the geometric parameters of the top nozzle system (left) and the polymer (right) used in the simulation

process with simultaneously low temperature ranges in the polymer for a 4 mm wide weld seam. From a manufacturing point of view, larger tube diameters are preferable, since this means lower manufacturing costs. A gap of 1.0 mm between nozzle and polymer is recommendable, and a distance of 4.5 mm is currently selected between the nozzle opening and the polymer surface (Fig. 22.11) (Schmid et al. 2022).

The study carried out in this paper deals with the simulative investigation of the round and top nozzle on inclined welds with a surface angle between 0° and 45°. All further investigations in this study are performed with a top nozzle with the geometric parameters shown in Fig. 22.11. The manufacturing of hot gas tools with varied geometrical parameters is very complex and expensive. Therefore, the further investigations of the influence of various geometric parameters are performed using validated simulation.

22.5.1 Simulation Results of Inclined Weld Contours

In this chapter, the influence of an inclined weld contour on the heating behavior of the polymer is investigated with the round and the top nozzle. First, the different flow behavior of the two nozzle systems is briefly explained. More detailed investigations of the two nozzle systems can be found in (Schmid et al. 2021a, 2021d, 2022).

The round nozzle system (gas outlet) has a distance of 2.0 mm and the top nozzle a distance of 4.5 mm to the polymer surface (Fig. 22.12 top). The top nozzle encloses the polymer, which is covered 0.5 mm by the nozzle. It must be taken into account that the flow velocity with the top nozzle is 1.5 times higher than the round nozzle. Only lower volume flow rates are possible with the round nozzle system, since the distance between the nozzle opening and the polymer is smaller compared to the top nozzle. With the round nozzle system, a distance between 1.0 and 3.0 mm has become target-oriented in practice. With distances higher than 3.0 mm, the free jet is broadened and delayed by the interaction with the surrounding gas (see also

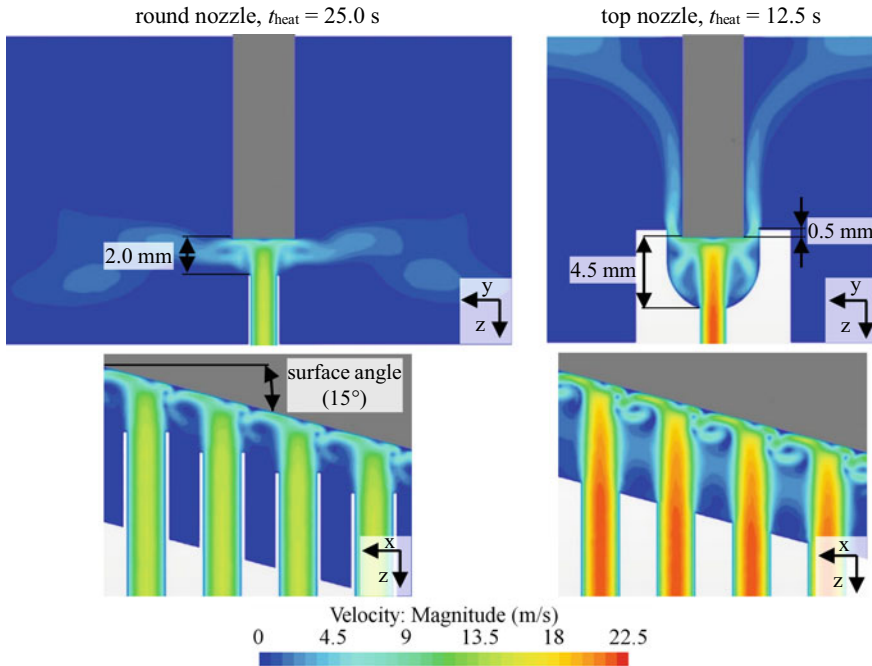


Fig. 22.12 Developing impingement flow for the round nozzle system and the top nozzle system, section in y -direction (top) and x -direction (bottom)

chapter 2). Higher volume flows lead to crater-shaped structures below the nozzle opening (stagnation point of the impingement flow) in the case of low viscosity materials, such as polyamide.

Due to the differences between the two nozzle systems, the flow field differs significantly. The heating and melting of the edge areas and of the center of the polymer are more homogeneous with the top nozzle due to the more controlled flow field. Furthermore, this flow field leads to a more homogeneous temperature distribution in the polymer in the case of the top nozzle. The angle of 15° of the polymer surface and the free jet leads to a lateral flow of the hot gas for both nozzle systems (x -direction in Fig. 22.12, bottom). In contrast, the impingement flow is symmetric in the y -direction.

The difference between the two nozzle systems can also be seen in the temperature field of the polymer surface (Fig. 22.13). The lateral flow of the hot gas leads to an unsymmetrical formation of the stagnation point and thus to an inhomogeneous heating of the plastic (Fig. 22.13 left). The round nozzle's stagnation points with a steep temperature gradient occur below the nozzle openings. This leads to crater-like structures forming on the polymer surface, and the edge areas are heated less intensively. The temperature gradient is reduced below the nozzle openings with the top nozzle. In addition, the edge areas are heated much better with the top nozzle

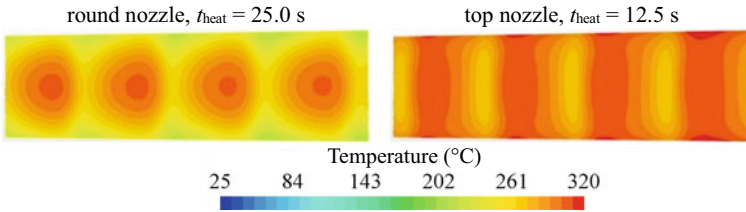


Fig. 22.13 Developing temperature profile on the polymer surface for the round nozzle system and the top nozzle system at a surface angle of 15°

compared to the round nozzle, and a more homogeneous temperature distribution can be observed.

The investigation of inclined welds between 0° and 45° of the two nozzle shows that the temperature of the polymer is reduced with larger angles (Fig. 22.14). A reduction in temperature is expected as the angle of impingement and the area to be heated increases. With the round nozzle system, the temperature of the polymer surface decreases up to 39 K (45° surface angle in Fig. 22.14 left). In comparison, using the top nozzle, the surface temperature decreases only up to 21 K (45° surface angle in Fig. 22.14 right). The temperature range on the surface is significantly larger in the case of the round nozzle. In addition, the temperature difference between the gas temperature at the nozzle outlet and the gas temperature on the polymer surface (+0.10 mm (G)) is significantly higher for the round nozzle system (47 (0°)–104 K (45°)) than for the top nozzle system (21 (0°)–40 K (45°)).

The heated surface area per round tube increases with larger surface angles up to 70% (Table 22.4). To keep the ratio between the volume flow and the surface to be

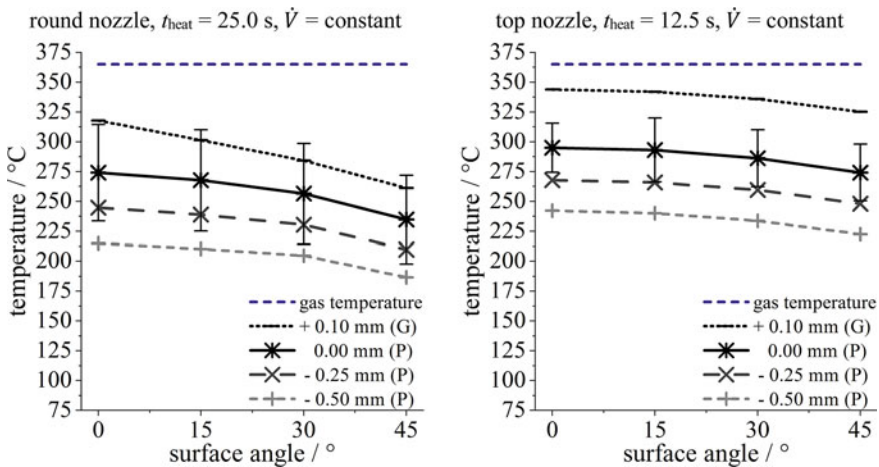


Fig. 22.14 developing temperature of the polymer at varying surface angles with a constant volume flow

Table 22.4 Surface area and volume flow with varying surface angles

Surface angle	Surface (mm ²)	Nozzle type	Flow velocity (m/s)	Nozzle type	Flow velocity (m/s)
0°	79	Round nozzle	9.0	Top nozzle	13.5
15°	82		9.3		13.9
30°	91		10.4		15.5
45°	111		12.7		19.0

heated constant, the volume flow of the round nozzle and the top nozzle system is increased accordingly.

In the case of the top nozzle system, the temperature drop of 21 K at a 45° surface angle (Fig. 22.15 top) can be minimized to 9 K at a 45° surface angle (Fig. 22.15 bottom) through an increase of the volume flow in relation to the surface increase (Fig. 22.15 right). By further increasing the volume flow by 20%, the temperature drop can be reduced to 4 K at a 45° surface angle. With the round nozzle system, the surface temperature is reduced up to 25 K (45° surface angle) even with an increased volume flow concerning the surface increases (Fig. 22.15 bottom). Without an increased volume flow, the surface temperature decreases for the round nozzle system up to 39 K (at 45° surface angle) (Fig. 22.15 top). The temperature drop of the round nozzle may be further reduced to 18 K at a 45° surface angle by increasing the volume flow by 20%. The effect of an increased heat transfer coefficient is the higher volume flow, which increases the heat input into the polymer. However, larger volume flows generate higher flow velocities, which can lead to crater-like structures on the surface of the polymer in case of low viscosity materials (e.g. PA66-GF35). Increasing the volume flow in ratio to the increasing surface of the polymer keeps the temperature profile for the top nozzle system with larger surface angles almost constant. This is not possible with the round nozzle system.

The simulations show that the top nozzle system can reliably heat the polymer even at increasing inclination angles of up to 45°. In contrast, the heating behavior of the round nozzle shows a temperature drop at the surface of up to 25 K with increasing inclination angles. Furthermore, the heating times for the round nozzle are 100% longer, and the temperature range on the polymer surface is 70% larger, which shows a more inhomogeneous temperature distribution.

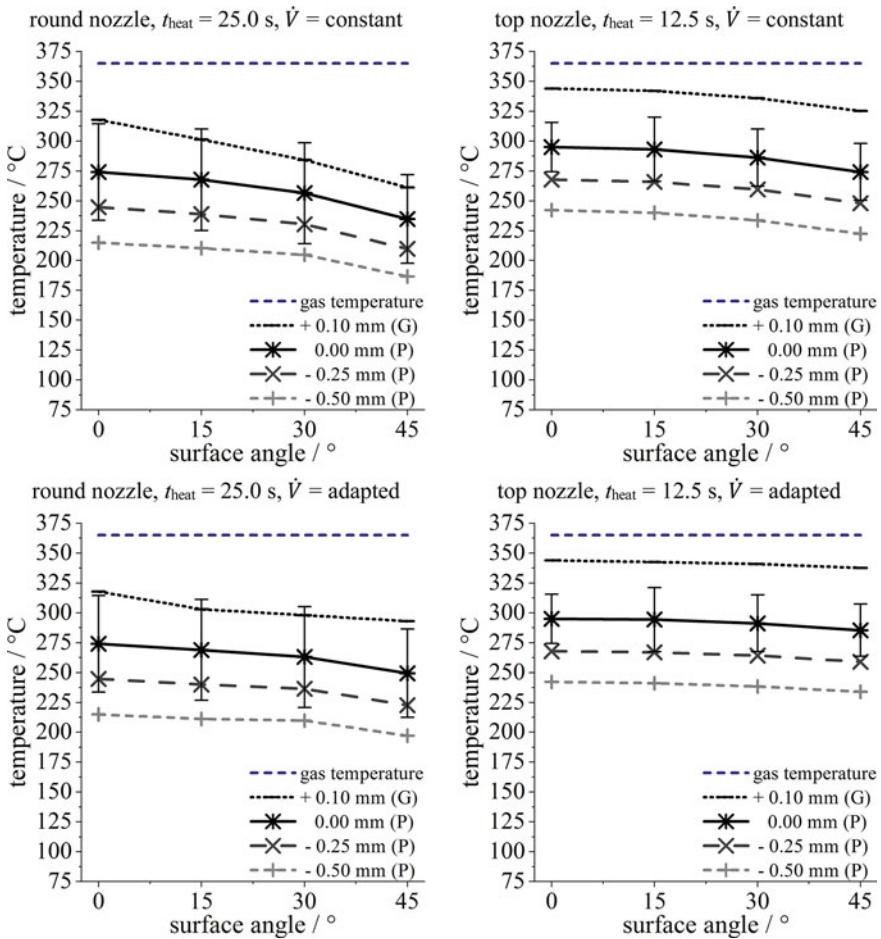


Fig. 22.15 Developing temperature of the polymer at varying surface angles with a constant volume flow (top) and an adapted volume flow (bottom)

22.5.2 Simulation Results of Hybrid Weld Contours

In this chapter, the heating behavior of the interface between an even and an inclined weld contour with a positively (Fig. 22.16 left) and negatively inclined weld (Fig. 22.16 right) will be investigated. The surface angle will be varied by 15°, 30° and 45° and investigated for the round and top nozzle system. To heat a hybrid weld, there are two options:

- Constant angle of the individual tubes—varying impingement angle ($\neq 90^\circ$)
- Varying angle of the individual tubes—constant impingement angle ($= 90^\circ$)

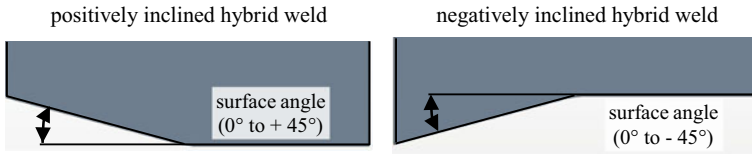


Fig. 22.16 Sketch of the geometric shape of the investigated hybrid weld contour

A constant angle of the individual round tubes is comparatively easy to manufacture. In contrast, if the angle of the individual round tube varies, each tube must be adjusted in order to guarantee a 90° angle of the impingement flow. This means each individual tube must be bent and separately adapted. With the top nozzle system, this complex adaptation of the individual round tubes can be provided by the top nozzle (GMB Kunststoffteile GmbH 2020). For a negative angle of the hybrid weld, it is difficult to achieve a 90° impingement angle since the individual round tubes would intersect with each other in the transition area. For an industrial implementation of a round nozzle system, the individual tubes are bent elaborately from the side. In the case of the top nozzle system, the individual round tubes can be adapted within the top nozzle without intersecting each other (GMB Kunststoffteile GmbH 2020). This procedure is significantly simpler and more efficient but will not be examined separately in this section.

Constant Angle of The Individual Tubes at a Positively Inclined Hybrid Weld

One possibility to heat a hybrid weld is to keep the angle of the individual tubes unchanged. Consequently, the angle between the impingement flow and the polymer surface changes in the inclined region of the polymer (Fig. 22.17). The volume flow is adjusted according to the larger area underneath the tube (see Table 22.4). The surface angle of 15° of the inclined part of the hybrid weld creates a 105° angle between the polymer surface and the free jet. This leads to a lateral flow of the hot gas for both nozzle systems in positive x -direction in Fig. 22.16. No significant turbulences are formed between the inclined and horizontal weld contour in the transition area.

Significant temperature drops occur in the edge area of the inclined welding contour using the round nozzle, despite the increased volume flow in relation to the larger polymer surface (Fig. 22.18, left). In the case of the top nozzle, only areas with a slight temperature increase are apparent in the inclined area. This can be explained by the correspondingly increased flow velocity and consequently higher heat input due to the increased heat transfer coefficient.

For the round nozzle system, the temperature decreases with increasing surface angle up to 7 K at 45° . In contrast to that, the temperature is almost constant for the top nozzle system (Fig. 22.19 right). Furthermore, the polymer surface temperature is more inhomogeneous for the round nozzle. By increasing the volume flow by 20%, the temperature rises 3 K at a 45° surface angle. The slight temperature increase with a higher inclination angle can be explained due to the reduction of the polymer volume in the transition area between the horizontal and the inclined weld contour area.

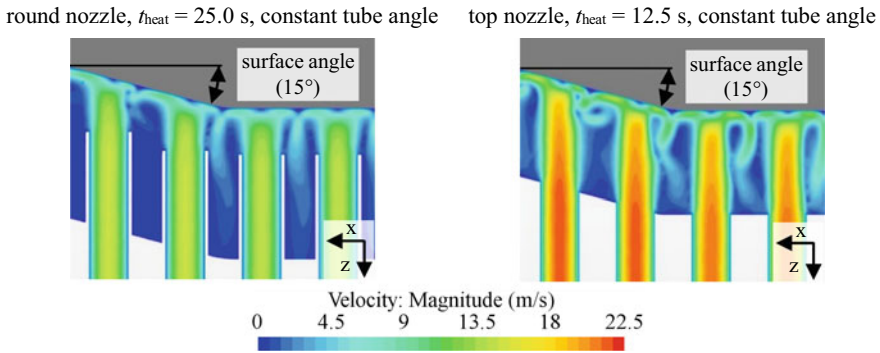


Fig. 22.17 Developing impingement flow for the round nozzle and the top nozzle system with a constant angle of the tubes for a positively inclined hybrid welds

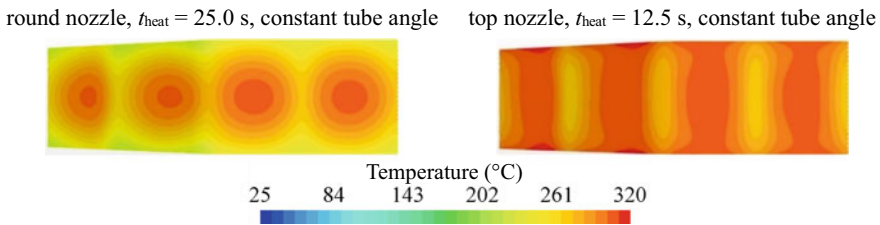


Fig. 22.18 Developing temperature profile on the polymer for the round nozzle and the top nozzle system with a constant angle of the tubes for a positively inclined hybrid welds

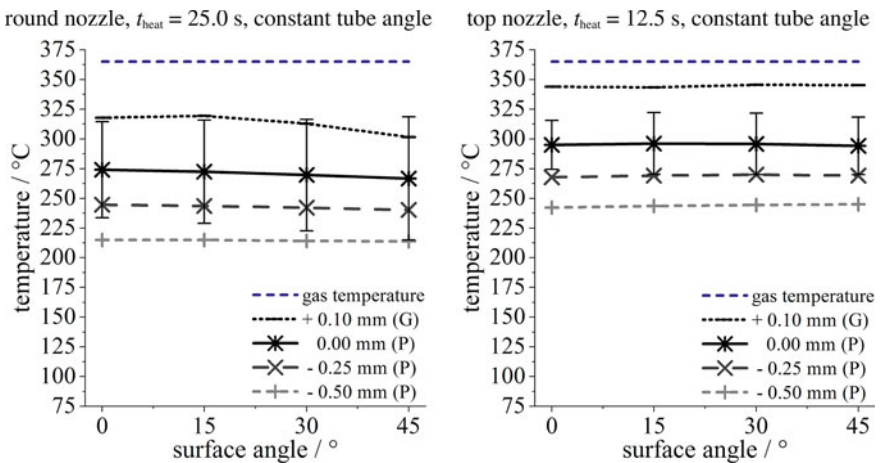


Fig. 22.19 Temperature profile of the polymer for the round nozzle and the top nozzle system with a constant angle of the tubes for a positively inclined hybrid welds

round nozzle, $t_{\text{heat}} = 25.0$ s, varying tube angle top nozzle, $t_{\text{heat}} = 12.5$ s, varying tube angle

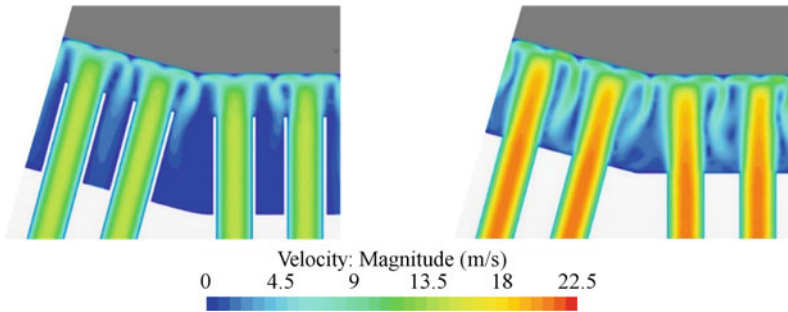


Fig. 22.20 Developing impingement flow for the round nozzle and the top nozzle system with a varying angle of the tubes for a positively inclined hybrid weld

The simulations show that the top nozzle system with a constant angle of the tube bores can homogeneously heat a hybrid weld with increasing surface angle.

Varying Angle of the Individual Tube at a Positively Inclined Hybrid Weld

A second possibility is to keep the impingement angle of the tubes constant at 90° (Fig. 22.20). Therefore, the angle of the tubes must be adjusted to the angle of the polymer surface. To guarantee a 90° impingement angle, the individual tubes must be bent and individually adapted. With the top nozzle, this complex adaptation of the individual round nozzles can take place within the top nozzle (GMB Kunststoffteile GmbH 2020). This procedure of manufacturing the hot gas welding tool is significantly more straightforward and more efficient.

There are no significant turbulences formed in the transition area between the inclined and the horizontal weld contour like in the case of the constant angle (Fig. 22.20).

The temperature profile of the hybrid weld contour is comparable to a straight weld for both nozzle systems. Only the differences in the homogeneity of temperature distribution in the polymer of the two nozzle systems are noticeable (Fig. 22.21).

For a 90° impingement angle, the temperature of the polymer is almost constant at different surface angles for the round and the top nozzle system (Fig. 22.22). The

round nozzle, $t_{\text{heat}} = 25.0$ s, varying tube angle top nozzle, $t_{\text{heat}} = 12.5$ s, varying tube angle

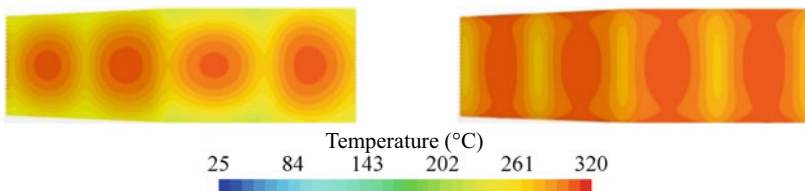


Fig. 22.21 Temperature profile on the polymer surface for the round nozzle and the top nozzle system with a varying angle of the tubes for a positively inclined hybrid weld

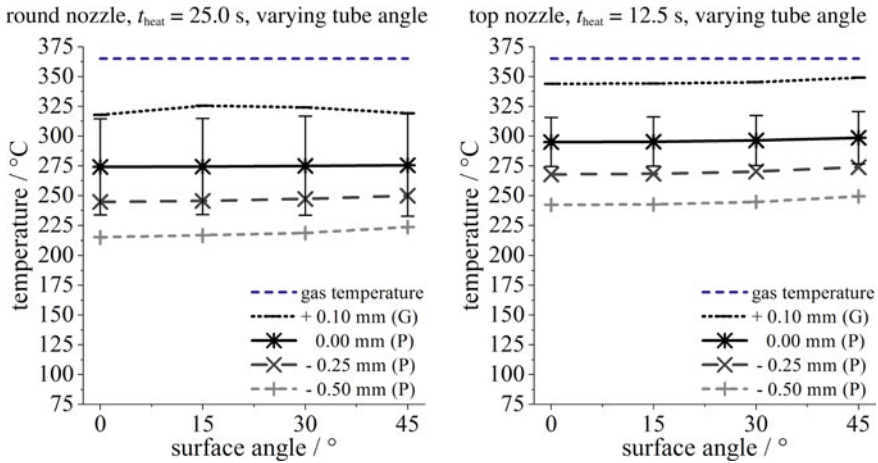


Fig. 22.22 Developing temperature of the polymer (even and angled area) for the round nozzle and the top nozzle system with a varying angle of the tubes for a positively inclined hybrid weld

slight temperature increase with a higher surface angle can be explained due to the reduction of the polymer volume in the transition area between the even and the inclined weld contour area. Nevertheless, the basic heating behavior of the round nozzle is more uneven and inefficient.

The simulations on a hybrid weld with a positive surface angle show that the top nozzle system heats the polymer more uniformly and efficiently than the round nozzle system. Furthermore, the top nozzle with a variable impingement angle can heat the polymer faster and more homogeneously than the round nozzle with an orthogonal impingement angle. From a manufacturing point of view, it is much easier not to bend and individually adjust the individual round nozzles. If a 90° impingement angle with the top nozzle is required, adapting the individual round nozzles is significantly easier. The bore angle in the top nozzle can be easily adjusted on a CNC milling machine, and therefore, the individual round nozzles do not have to be bent. To produce complex geometries, additive manufacturing can be advantageous.

Constant Angle of the Individual Tubes at a Negatively Inclined Hybrid Weld

To heat a hybrid weld with negative surface angles, only one possibility is investigated since the round nozzles would intersect in the transition area. For an industrial implementation with the round nozzles, the individual tubes are bent elaborately from the side. With the top nozzle system, the individual round nozzles can be adapted within the top nozzle without intersecting each other (GMB Kunststoffteile GmbH 2020). This procedure is significantly more straightforward and more efficient but will not be examined separately in this section, as the round and top nozzle systems will be compared.

The surface angle of -15° of the inclined part of the hybrid weld creates a 75° angle between the polymer surface and the free jet. This leads to a lateral flow of

round nozzle, $t_{\text{heat}} = 25.0$ s, constant tube angle top nozzle, $t_{\text{heat}} = 12.5$ s, constant tube angle

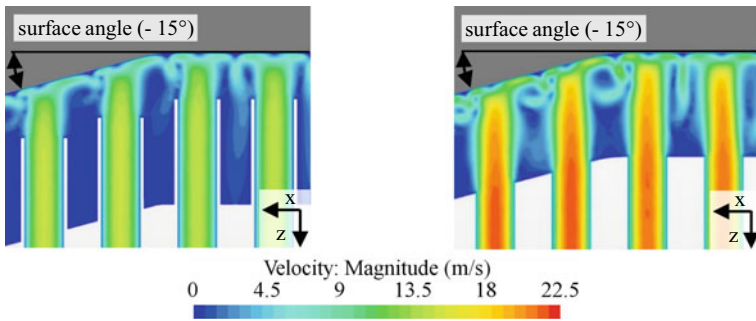


Fig. 22.23 Developing impingement flow for the round nozzle and the top nozzle system with a constant angle of the tubes for a negatively inclined hybrid weld

the hot gas for both nozzle systems in the negative x-direction in Fig. 22.23. No significant turbulences are formed in the transition area between the inclined and even weld contour.

Significant temperature drops occur in the edge area of the inclined welding contour with the round nozzle like with a positive-inclined weld (Fig. 22.18, left and Fig. 22.24, left). The heating behavior with the top nozzle is suitable for a positive and negative angled hybrid weld.

With the top nozzle system, the temperature drop can be minimized from 14 to 9 K at a 45° surface angle if the volume flow is increased concerning the surface increase (Fig. 22.25 right). With the round nozzle system, the surface temperature drops by up to 19 K (45° surface angle) even with an increased volume flow (Fig. 22.25 left). By increasing the volume flow of the top nozzle by 20%, the temperature drop can be reduced to 6 K at a 45° surface angle. Increasing the volume flow increases the heat transfer coefficient and thus increases the heat input into the polymer. However, larger volume flows generate higher flow velocity, which can lead to crater-like structures on the surface of the polymer in the case of low viscosity materials.

The heating behavior of hybrid welds with positive and negative angles differs in different changes in the polymer temperature in the transition area. The reason is

round nozzle, $t_{\text{heat}} = 25.0$ s, constant tube angle top nozzle, $t_{\text{heat}} = 12.5$ s, constant tube angle

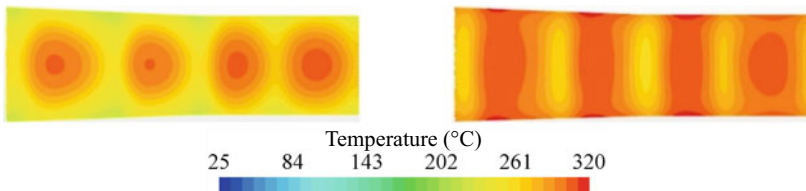


Fig. 22.24 Temperature profile on the polymer surface for the round nozzle and the top nozzle system with a constant angle of the tubes for a negatively inclined hybrid weld

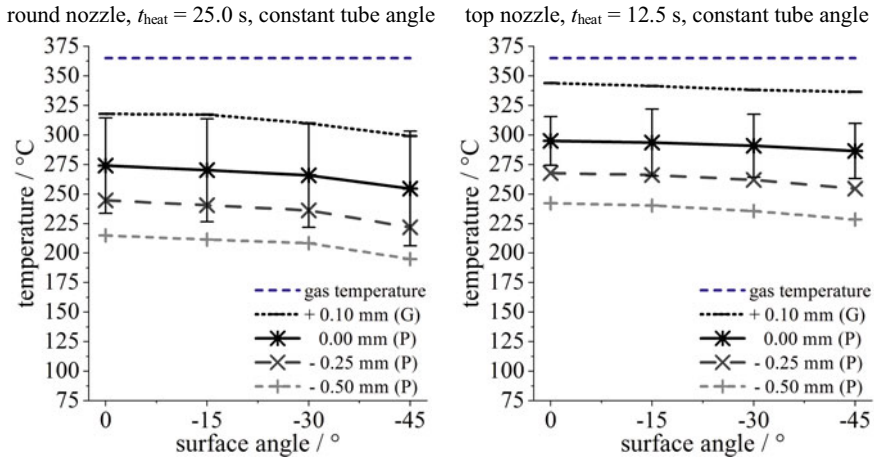


Fig. 22.25 Temperature profile of the polymer for the round nozzle and the top nozzle system with a constant angle of the tubes for a negatively inclined hybrid weld

the different volume of the polymer, which has to be heated in the transition area. The slight temperature increase for positive-inclined hybrid welds originated from a reduction of the polymer volume in the transition area (Fig. 22.26 left). The volume of the polymer increases in the transition area for negative inclined hybrid welds, which on the other hand leads to slightly lower temperatures (Fig. 22.26 right).

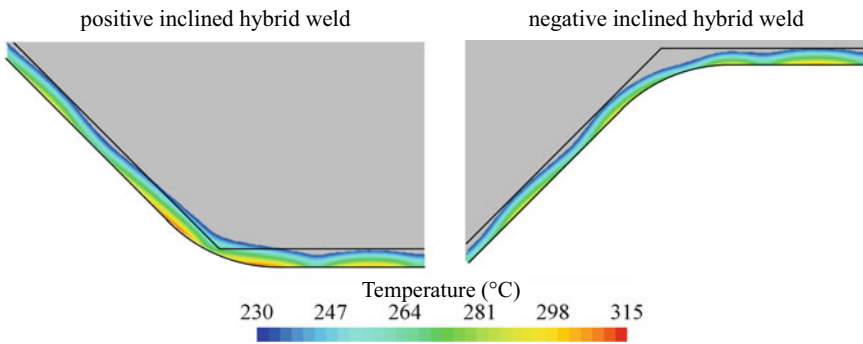


Fig. 22.26 Developing temperature profile in the polymer for the top nozzle at a heating time of 12.5 s; the black lines have a 0.5 mm spacing

22.6 Summary and Outlook

Today, hot gas welding processes often show limited processing windows and therefore are challenging to control and adjust. One reason for this problem is that the gas flow is difficult to control by using the ordinary round nozzle design, and thus, the welding of the weld joint is less uniform. Using the next generation top nozzle design, the weld joint is entirely covered by the nozzle. As a result, the heat loss is minimized and the hot gas flow could be guided and controlled much better. This behavior has been investigated and confirmed by many simulations and welding experiments including temperature measurements (Schmid et al. 2021a, 2021b, 2021c, 2021d, 2022). Overall measurements of the weld strength show that for the new top nozzle design, good results could be achieved for various materials even with varying hot gas temperatures and heating times (Schmid et al. 2021a, 2021b, 2021c, 2021d). The more homogeneous melting of the welding joint and the simultaneous absence of overheating and decomposing the polymer is mainly responsible for this.

The simulation of the hot gas welding process provides comparable results with the temperature measurements for two polyamides with different base polymers and different glass fiber content (PA6-GF40 and PA66-GF35) at varying heating times, temperatures of the hot gas tool and volume flows. The results of the simulations are validated by measurements with an IR camera system and lost thermocouples. Thus, the simulation provides reliable results for the investigated polyamides at the studied gas temperatures, heating times and volume flows (Schmid et al. 2022).

The simulation results for the round nozzle and the top nozzle system for inclined weld contours show that the top nozzle system can reliably heat the polymer even at increasing inclination angles of up to 45°. In contrast, the heating behavior of the round nozzle system shows a temperature drop at the surface of up to 25 K with increasing inclination angles. Furthermore, the heating times for the round nozzle system are 100% longer, and the temperature range (and therefore the inhomogeneity) on the polymer surface is 70% larger.

To heat a hybrid weld consisting of a horizontal and an inclined area, two options are investigated for the round nozzle and the top nozzle system: constant angles of the tubes and varying angles of the tubes. Both options are studied for the round nozzle system as well as the top nozzle system. For both options, the temperature profile of the polymer is almost constant at different inclination angles for the top nozzle system. In the case of the varying (impingement) angle, the temperature range on the polymer surface is larger compared to a constant (impingement) angle. Therefore, a constant (impingement) angle leads to less temperature inhomogeneity. For a positive-inclined hybrid weld, there is a slight temperature increase with increasing inclination angles, which can be explained by the reduction of the polymer volume in the transition area between the horizontal and the inclined weld contour. For a negative inclined hybrid weld, there is a slight temperature reduction due to an increase of the polymer volume in the transition area. Furthermore, the simulations for hybrid welds show that the top nozzle system heats the polymer more uniformly and efficiently compared to the round nozzle system. The top nozzle system with varying

(impingement) angle actually heats the polymer faster and more homogeneously than the round nozzle system with a constant (impingement) angle.

Concerning the manufacturing of hot gas tools, the conclusions are great improvements and lead to a more economic welding process. It is much simpler not to bend and adjust the tubes to the weld contour individually. If a 90° impingement angle for the top nozzle system is required, adapting the individual tubes is significantly easier. The bore angles of the individual tubes in the top nozzle can easily be adjusted in the case of using a CNC milling machine, and the individual round nozzles do not have to be bent. For complex geometries, additive manufacturing can be advantageous.

From the economical point of view, the advantage of the new top nozzle design is a reduced heating time and therefore a reduced welding cycle time as well as a reduced hot gas consumption. The broader process window and the shorter heating time of the top nozzle system lead to a higher reliability of the hot gas welding process. Using the top nozzle design, it is also possible to weld inclined and hybrid welds with a constant angle of the individual tubes of the hot gas welding tool.

The CFD simulation of the hot gas welding process for horizontal welds provides reliable results. In this study, the CFD simulation is applied to 3D welds, i.e., inclined and hybrid welds.

Furthermore, CFD simulation can help to analyze the flow field of the hot gas, to optimize the flow guidance and the heating behavior of the gas inside the hot gas welding tool. Thus, the top nozzle system and the hot gas welding tool can be better tailored to the welding process and the components to be welded. Therefore, the shape of the top nozzle can be improved by means of CFD simulation in the future.

Acknowledgements In a joint research project between GMB Kunststoffteile GmbH and Esslingen University of Applied Sciences on hot gas welding (funded by the “Zentrale Innovationsprogramm Mittelstand (ZIM)” from the Federal Ministry for Economic Affairs and Energy—funding code: ZF4166303FH8), the investigated new nozzle system—the top nozzle—has been invented and protected (GMB Kunststoffteile GmbH 2020). In a further joint research project between GMB Kunststoffteile GmbH, robomotion GmbH, Chemnitz University of Technology and Esslingen University of Applied Sciences on hot gas welding (funded by the “Zentrale Innovationsprogramm Mittelstand (ZIM)” from the Federal Ministry for Economic Affairs and Energy—funding code: KK5052604W00), the top nozzle system will be further developed for 3D weld contours.

All CFD simulations are performed on the bwUniCluster using STAR-CCM+. BwUniCluster is Baden-Württemberg’s general-purpose tier 3 high performance computing cluster (HPC) within the bwHPC project. The authors acknowledge support by the state of Baden-Württemberg through bwHPC.

References

- Albrecht M, Bialaschik M, Gehde M et al (2021) Hot gas butt welding of plastic. *Joining Plast* 15:162–169
- Albrecht M, Bialaschik MO, Gehde M et al (2020) Hot gas welding—influences of the tool design. AIP conference proceedings 2289.020006. <https://doi.org/10.1063/5.0029478>

- Barkhoff R, Happel J (2019) Quadralux: Hybrid heating procedure for the welding of plastics. *Joining Plast* 13:161
- Baudrit B, Schmitt M, Kressirer S et al (2014) Energy efficiency during heated tool welding. *Joining Plast* 8:197–203
- Belmann A (2017) Reducing contaminations during the joining of plastics. *Joining Plast* 11:34–41
- Bonten C (1998) Beitrag zur Erklärung des Wirkmechanismus in Schweißverbindungen aus teilkristallinen Thermoplasten. Dissertation Universität Gesamthochschule Essen, Essen
- Deckert MH, Schmid J, Weißer DF (2019) Neuartiges Heißgasschweißen von Kunststoffbauteilen. Hochschule Esslingen—Spektrum 48:21–23
- Egen U (1985) Gefügestruktur in Heizelementschweißnähten an Polypropylen-Rohren. Dissertation Universität Kassel, Kassel
- Ehrenstein GW, Ahlers-Hestermann G (2004) Handbuch Kunststoff-Verbindungstechnik. Carl Hanser Verlag, München
- Friedrich N, Schöppner V (2012) Reducing the cycle time in heated tool welding without any loss in quality as a result of forced cooling using compressed air. *Joining Plast* 6:134–141
- Friedrich S (2014) Lineares Vibrationsschweißen von Kunststoffen im industriellen Umfeld. Einflüsse und Restriktionen. Dissertation Technische Universität Chemnitz, Chemnitz
- Fuhrich R, Gehde M (2014) Contour-following infrared radiator for the welding of plastics with high time and energy efficiencies. *Joining Plast* 8:204–211
- Fuhrich R, Gehde M, Friedrich S (2011a) Process temperature measurement in infrared welding. *Joining Plast* 5:34–39
- Fuhrich R, Gehde M, Friedrich S (2011b) Mechanical properties of infrared-welded joints. *Joining Plast* 5:216–221
- Gardon R, Akfirat JC (1965) The role of turbulence in determining the heattransfer characteristics of impinging jets. *Int J Heat Mass Tran* 8:1261–1272
- Gehde M, Friedrich S, Motshev S (2008) Radiant heating during plastics welding with infrared radiation. *Joining Plast* 2:58–63
- GMB Kunststoffteile GmbH (2020) DE 20 2021 101 884 U1—Gebrauchsmusterschrift: Vorrichtung zum Schweißen von Kunststoffteilen, Pleidelsheim
- Hofmann HM (2005) Wärmeübergang beim pulsierenden Prallstrahlen. Dissertation Universität Karlsruhe, Karlsruhe
- Klein HM (2001) Laserschweißen von Kunststoffen in der Mikrotechnik. Dissertation RWTH Aachen, Aachen
- Kreiter J (1987) Optimierung der Schweißnahtfestigkeit von Heizelementstumpfschweißungen von Formteilen durch verbesserte Prozessführung und Selbsteinstellung. Dissertation Universität Paderborn, Paderborn
- LANXESS Deutschland GmbH (2009) The twins amongst the polyamides. Properties comparison of PA 6 and PA 66. Technical information—Lanxess Deutschland GmbH
- Mochev S (2018) Heißgasschweißen—Aktuelle Entwicklungen und Möglichkeiten. Carl Hanser Verlag, Landshut, Tagungsbeitrag—Fügen von Kunststoffen im Automobilbau
- Mochev S, Endemann UM (2016) Mehr als nur heiße Luft. Systematische Prozessoptimierung Für Das Heißgasschweißen Kunststoffe 10:76–79
- Mochev S, Endemann UM (2018) Faster and better welding: tools adaption reduces process times and improves weld quality. *Kunststoffe Int* 9:57–59
- Potente H, Schöppner V, Hoffschlag R et al (2008) Saving cycle time by means of intensive cooling during heated tool welding. *Joining Plast* 2:50–56
- Potente H, Schöppner V, Hoffschlag R (2010) Investigations into the melt adhesion during heated tool welding. *Joining Plast* 4:102–107
- Ratke M, Natrop J (2007) Infrared heating in plastics welding technology. *Joining Plast* 1:58–63
- Ratke M, Natrop J (2008) Newly developed convection welding process on a natural gas basis. *Joining Plast* 2:129–133
- Rzepka G (2021) Solid connection under a special atmosphere. How low-particle, non-contact welding of technical to high-performance plastics works. *K-PROFI Int* 2:30–35

- Schlarb AKH (1989) Zum Vibrationsschweißen von polymerwerkstoffen. prozess—struktur—eigenschaften. dissertation universität—gesamthochschule Kassel, Kassel
- Schmid J, Weißer DF, Mayer D et al (2021a) Reduction of the heating time for hot gas welding. Reduktion Der Erwärmungszeit Beim Heißgasschweißen. *Kunststofftechnik* 17:112–128
- Schmid J, Weißer DF, Mayer D et al (2021b) Heißgasschweißen in der Komfortzone. Neuartige Düsendesigns Eröffnet Vielfältige Möglichkeiten. *Kunststoffe* 50:80–82
- Schmid J, Weißer DF, Mayer D et al (2021d) Increase of the efficiency in hot gas welding by optimization of the gas flow. *Technol Lightweight Struct* 5:32–40
- Schmid J, Weißer DF, Mayer D et al (2021c) Reduktion der Erwärmungszeit beim Heißgasschweißen. *Technomer* 2021c—27. Fachtagung über Verarbeitung und Anwendung von Polymeren, Chemnitz
- Schmid J, Weißer DF, Mayer D et al (2022) Analysis of two different nozzle systems for hot gas welding using CFD simulations and measurement results. *Kunststofftechnik* (submitted 2022)
- Schulz JE (2002) Werkstoff-, Prozess- und Bauteiluntersuchungen zum Laserdurchstrahlungsschweißen von Kunststoffen, Dissertation RWTH Aachen, Aachen
- Simionescu Ş-M, Tănase N-O, Broboană D et al (2017) Impinging air jets on flat surfaces at low reynolds numbers. *Energy Proc* 112:194–203
- Tüchert C (2005) Einfluss der inneren Eigenschaften von Schweißverbindungen auf die langzeitige Schweißnahtgüte. Dissertation RWTH Aachen, Aachen
- VDI (2013) Verein Deutscher Ingenieure, VDI-Gesellschaft Verfahrenstechnik und Chemieingenieurwesen VDI-Wärmeatlas. Springer Vieweg, Berlin

Chapter 23

Modeling the Inelastic Behavior of High-Temperature Steels Using a Two-Time-Scale Approach



Katharina Knappe and Holm Altenbach

Abstract The aim of this work is to derive the constitutive equations needed to model inelastic material behavior of the high-temperature steel X20CrMoV12-1, which is commonly used for power plant components. Therefore, an Armstrong–Frederick model is considered, taking a constitutive equation for the inelastic strain rate and an evolution equation for the backstress tensor into account. Furthermore, applying a two-time-scale approach will reduce the computational time significantly by still capturing the material’s response to a cyclic loading profile. The material model is implemented in the finite element software ABAQUS to simulate the creep test of a bar at elevated temperatures.

Keywords Frederick-Armstrong equations · Two-time-scale approach · Creep

23.1 Introduction

Nowadays, power plants are mostly operating according to the actual needs and therefore have to be very flexible. Once invented, they were supposed to be running for a long period of time under the same operating conditions, thus having a stationary loading regime. This new, efficient kind of usage results in highly frequent start-ups and shut-downs of the system, subjecting their components to varying mechanical and thermal loading conditions. The materials of which the gas turbines, turbine rotors, and pipe systems, for example, are made out of, have to withstand periodic stress and strain states and, in addition, are exposed to very high surrounding temperatures, also leading to creep behavior. This process is characterized as a relatively slow time-dependent deformation due to changes in the microstructure occurring over a long period of time. The combination of fast and slowly changing loading

K. Knappe (✉) · H. Altenbach
Institute of Mechanics, Otto von Guericke University Magdeburg, Universitätsplatz 2, 39104
Magdeburg, Germany
e-mail: katharina.knappe@ovgu.de

H. Altenbach
e-mail: holm.altenbach@ovgu.de

conditions is considered to have a great impact on the material's and, therefore the component's lifespan. In order to be able to predict the remaining lifetime or adapt the maintenance intervals, a reliable simulation of the material's response to the rapidly varying loading condition is obligatory.

Therefore, a constitutive model reflecting the creep, plasticity as well as cyclic hardening and softening processes has to be derived. The paper at hand focuses on a macroscale-based model where the needed materials parameters can be determined by fitting experimental data (Eisenträger 2018). Any microscale model could represent the local deformation better; however, computing the stress-strain state of a real turbine is connected to a tremendous numerical effort.

The commonly used approach for unified constitutive modeling was originally proposed by Frederick and Armstrong (1966). It considers a backstress with a kinematic tensorial evolution equation and a constitutive equation for the inelastic strain rate tensor. Chaboche expanded the idea of the backstress tensor by introducing the superposition of several backstresses where each of them has its own evolution equation (Chaboche 1989), leading to a higher complexity due to the increasing number of material parameters, which is not helpful considering the effort needed their identification. In the past, unified constitutive models have been used to describe various mechanical and thermal loading conditions, but the prediction of the material behavior under cyclic loading remains challenging, especially from the numerical point of view (Altenbach et al. 2018). These calculations often result in very high computational time due to very small time increments during the time integration procedure so efficient solving methods have been suggested to be implemented in the finite element code avoiding a cycle-by-cycle integration. In Labergere et al. (2015), the cycle jumping method is introduced, calculating internal variables over many loading cycles after a stabilization of the integration procedure. Once that is achieved, their rate of change with respect to the loading cycles can be estimated hence there is no need to look at every single cycle separately. Another approach for analyzing inelastic material behavior under periodic loading conditions can be found in Joseph et al. (2010). Here, a wavelet transformation-based multi-time scaling method is introduced to model crystal plasticity.

Within this paper, the two-time-scale approach is used. Originally, the time scale and time averaging procedures were developed to solve differential equations of dynamical systems but are now also applied to evaluate the inelastic material response after it was firstly used to describe dynamic creep behavior (Altenbach et al. 2018). The approach is based on the introduction of several time scales accounting for the different kinds of processes (Oskey and Fish 2004). So, beginning with the Armstrong–Frederick model and applying the two-time-scale asymptotic method, the constitutive equations will be derived and afterward used to simulate a bar under high-temperature creep.

23.2 Constitutive Equations

In order to derive the constitutive equations needed to represent inelastic material behavior, the widely known Armstrong–Frederick type model is applied. It includes a constitutive equation for the inelastic strain rate tensor and a nonlinear kinematic hardening rule for the backstress tensor. The material parameters can be found for several materials, such as tempered martensitic steel in Eisenträger (2018) and Altenbach et al. (2018). Typically, the high-chromium steel X20CrMoV12-1 is known to have high tensile strength, low coefficient of thermal expansion, and a high thermal conductivity, which is why it is often used for turbine tubes or shafts (Eisenträger et al. 2018a).

23.2.1 Elasticity

As a starting point, assuming small strains, the additive decomposition of the strain $\boldsymbol{\varepsilon}$ into an elastic $\boldsymbol{\varepsilon}^{\text{el}}$ and inelastic $\boldsymbol{\varepsilon}^{\text{in}}$ part is introduced

$$\boldsymbol{\varepsilon} = \boldsymbol{\varepsilon}^{\text{el}} + \boldsymbol{\varepsilon}^{\text{in}} \quad (23.1)$$

where Hooke's law describes the elastic behavior including the bulk modulus K and the shear modulus G

$$\boldsymbol{\sigma} = K \operatorname{tr}(\boldsymbol{\varepsilon}^{\text{el}}) \mathbf{I} + 2G\boldsymbol{\varepsilon}^{\text{el}}, \quad (23.2)$$

with the stress tensor $\boldsymbol{\sigma}$, Young's modulus E and the Poisson's ration ν , tr denotes the trace (first invariant of the stress tensor) and \mathbf{I} is the unit tensor

$$K = \frac{E}{3(1-2\nu)}, \quad G = \frac{E}{2(1+\nu)}. \quad (23.3)$$

The stress tensor can be separated into a spheric $\boldsymbol{\sigma}_m$ and a deviatoric part $\boldsymbol{\sigma}'$ as can be seen in Eq. (23.5). In the following, deviators of the tensors will always be marked with a prime.

$$\sigma_m = \frac{1}{3} \operatorname{tr}(\boldsymbol{\sigma}), \quad (23.4)$$

$$\boldsymbol{\sigma}' = \boldsymbol{\sigma} - \sigma_m \mathbf{I}. \quad (23.5)$$

Now, the equation for the elastic strain yields

$$\boldsymbol{\varepsilon}^{\text{el}} = \frac{\sigma_m}{3K} \mathbf{I} + \frac{\boldsymbol{\sigma}'}{2G}. \quad (23.6)$$

23.2.2 Inelasticity

The inelastic strain ε^{in} is a function of the potential, which itself is dependent on the three invariants J_1 , J_2 and J_3 of the stress deviator considering \det as the determinant of a tensor

$$J_1 = \text{tr}(\boldsymbol{\sigma}'), \quad (23.7)$$

$$J_2 = \frac{1}{2} [\text{tr}(\boldsymbol{\sigma}')^2 - \text{tr}(\boldsymbol{\sigma}' \cdot \boldsymbol{\sigma}')], \quad (23.8)$$

$$J_3 = \det(\boldsymbol{\sigma}') \quad (23.9)$$

and can therefore be written as

$$\dot{\varepsilon}^{\text{in}} = \frac{\delta \psi(J_1(\boldsymbol{\sigma}'), J_2(\boldsymbol{\sigma}'), J_3(\boldsymbol{\sigma}'))}{\delta \boldsymbol{\sigma}'}. \quad (23.10)$$

Assuming that the inelastic deformation does not result in a significant change of volume, only the stress deviator is considered in the following equations, and this also leads to the first invariant being equal to zero (Eisenträger 2018). Furthermore, the influence of the third invariant is often neglected because it accounts only for so-called second-order effects in the material belonging to the tensorial-nonlinear behavior (Reiner and Abir 1964). So the inelastic strain is only dependent on the second invariant of the stress tensor

$$\dot{\varepsilon}^{\text{in}} = \frac{\delta \psi(J_2(\boldsymbol{\sigma}'))}{\delta \boldsymbol{\sigma}'}. \quad (23.11)$$

Evaluating the given equation then leads to

$$\dot{\varepsilon}^{\text{in}} = \frac{3}{2} \dot{\varepsilon}_{\text{vM}}^{\text{in}} \frac{\boldsymbol{\sigma}'}{\sigma_{\text{vM}}} \quad (23.12)$$

where σ_{vM} describes the von Mises stress calculated according to Eq. (23.13)

$$\sigma_{\text{vM}} = \sqrt{\frac{3}{2} \boldsymbol{\sigma}' : \boldsymbol{\sigma}'} \quad (23.13)$$

and $\dot{\varepsilon}_{\text{vM}}^{\text{in}}$ denotes the von Mises inelastic strain rate

$$\dot{\varepsilon}_{\text{vM}}^{\text{in}} = \sqrt{\frac{2}{3} \dot{\varepsilon}^{\text{in}} : \dot{\varepsilon}^{\text{in}}}. \quad (23.14)$$

The inelastic strain rate is temperature dependent, so a separation ansatz is used combining the stress response function f_σ and the temperature response function $R(\vartheta)$ depending on the absolute temperature ϑ . Both of them can be identified

examining the inelastic material behavior under monotonic loading

$$\dot{\varepsilon}^{\text{in}} = f_{\sigma}(\tilde{\sigma}_{\text{VM}})R(\vartheta) \quad (23.15)$$

where

$$R(\vartheta) = a_0 e^{\frac{\alpha}{\vartheta}} \quad (23.16)$$

with $a_0 = 4.641^{23} \frac{1}{\text{h}}$ and $\alpha = 6.121^4 \frac{1}{\text{K}}$ (Altenbach et al. 2018). The tensor's active part is denoted by $(\tilde{\cdot})$. The stress deviator is decomposed into an active $\tilde{\sigma}$ and a backstress part β

$$\beta = \sigma' - \tilde{\sigma}. \quad (23.17)$$

Here, an Armstrong–Frederick type backstress (Altenbach et al. 2018) is chosen, where B_i are material parameters calculated by fitting experimental data

$$\dot{\beta} = B_1 \dot{\varepsilon}^{\text{in}} - B_2 \dot{\varepsilon}_{\text{VM}}^{\text{in}} \beta. \quad (23.18)$$

The second term on the right-hand side of Eq. (23.18) is called dynamic recovery term and improves the numerical results significantly (Eisenträger 2018). In order to also be able to capture cyclic behavior, the superposition of backstresses according to Chaboche is used

$$\beta = \sum_{i=1}^n \beta_i, \quad (23.19)$$

$$\dot{\beta}_i = B_1 \dot{\varepsilon}^{\text{in}} - B_2 \dot{\varepsilon}_{\text{VM}}^{\text{in}} \beta_i. \quad (23.20)$$

23.3 Two-Time-Scale Approach

The aim of applying a time-scale technique is to reduce the computational time when solving a system of differential equations which in general has the following form

$$\frac{d\mathbf{x}}{dt} = \mathbf{X}(t, \mathbf{x}), \quad \mathbf{x}(0) = \mathbf{x}_0 \quad (23.21)$$

where \mathbf{x} represents a set of unknown variables. Now, two times scales T_0 and T_1 are introduced (Altenbach et al. 2000). The first, slow time scale, is often referred to as ‘natural time’ or ‘physical time’ and it accounts for quasi-static loading and long-term behavior such as creep

$$T_0(t) = t. \quad (23.22)$$

Similarly, a fast or fine time scale is defined with the help of the parameter μ depending on the total time considered t_{end}

$$T_1(t) = \tau(t) = \frac{t}{\mu} \tag{23.23}$$

$$\mu = \frac{T}{t_{\text{end}}} \ll 1. \tag{23.24}$$

The total time derivative can be defined as

$$\frac{d}{dt} = \frac{\delta}{\delta t} + \frac{1}{\mu} \frac{\delta}{\delta \tau} \tag{23.25}$$

yielding in a system of partial instead of ordinary differential equations. To solve them, an asymptotic series expansion (Oskay and Fish 2004) is applied to \mathbf{x} with respect to the factor μ

$$\mathbf{x}(t, \tau) = \mathbf{x}^{(0)}(t, \tau) + \mu \mathbf{x}^{(1)}(t, \tau) + \mu^2 \mathbf{x}^{(2)}(t, \tau) + \dots \tag{23.26}$$

The right-hand side of the differential equation system is expanded in the same manner inserted into the total time derivative, Eq. (23.25) yields a set of differential equations sorted with respect to the order of μ

$$\mu^{(-1)} : \frac{\delta \mathbf{x}^{(0)}}{\delta \tau} = 0, \tag{23.27}$$

$$\mu^{(0)} : \frac{\delta \mathbf{x}^{(0)}}{\delta t} + \frac{\delta \mathbf{x}^{(1)}}{\delta \tau} = \mathbf{X}(t, \tau, \mathbf{x}^{(0)}), \tag{23.28}$$

$$\mu^{(1)} : \frac{\delta \mathbf{x}^{(1)}}{\delta t} + \frac{\delta \mathbf{x}^{(2)}}{\delta \tau} = \frac{\delta \mathbf{X}(t, \tau, \mathbf{x}^{(0)})}{\delta \mathbf{x}} \mathbf{x}^{(1)}. \tag{23.29}$$

Evaluating the first equation shows that the mean solution $\mathbf{x}^{(0)}$ is only depending on the slow time scale t (Altenbach et al. 2018; Doghri and Haouala 2015).

Now, the time averaging operator of Eq. (23.30) is applied (Altenbach et al. 2018)

$$\langle f(t, \tau) \rangle = \frac{1}{T} \int_0^T f(t, \tau) d\tau \tag{23.30}$$

leading to the following system of differential equations to find the mean solution

$$\frac{d\mathbf{x}^{(0)}}{dt} = \bar{\mathbf{X}}(t, \mathbf{x}^{(0)}). \tag{23.31}$$

The solutions according to the higher orders of μ can also be calculated using the methods shown in Sanders and Verhulst (1985). For the remaining part of this work, the mean solutions will be derived. To do so, the stress tensor is assumed to be of the following form

$$\boldsymbol{\sigma}(t, \tau) = \boldsymbol{\sigma}^{(0)}(t) + \boldsymbol{\sigma}^{(1)}(\tau) \quad (23.32)$$

with a mean part $\boldsymbol{\sigma}^{(0)}(t)$ and a periodic part $\boldsymbol{\sigma}^{(1)}(\tau)$. The same separation was also applied to the stress deviator and the backstress tensor. In Altenbach et al. (2018), the backstress tensor for isothermal loading conditions is derived as follows

$$\dot{\boldsymbol{\beta}} = \frac{2}{3} R(\vartheta) \left[\dot{\boldsymbol{\varepsilon}}^{\text{in}} - \frac{3}{2} \dot{\varepsilon}_{\text{vM}} \frac{\boldsymbol{\beta}}{h(\sigma_{\text{vM}}, \vartheta)} \right]. \quad (23.33)$$

Taking the separation of mean and periodic variables into account gives the following set of constitutive equations with $C_h(\vartheta) = 8.84$ (Altenbach et al. 2018)

$$\dot{\boldsymbol{\varepsilon}}^{\text{in}(0)} = \frac{3}{2} R(\vartheta) \left\langle \frac{f_\sigma(\tilde{\sigma}_{\text{vM}})}{\tilde{\sigma}_{\text{vM}}} (\boldsymbol{\sigma}'^{(0)} - \boldsymbol{\beta}^{(0)} + \boldsymbol{\sigma}'^{(1)}) \right\rangle \quad (23.34)$$

$$\dot{\boldsymbol{\beta}}^{(0)} = \frac{2}{3} C_h(\vartheta) \left\langle \dot{\boldsymbol{\varepsilon}}^{\text{in}(0)} - \frac{3}{2} \boldsymbol{\beta}^{(0)} \left\langle \frac{\dot{\varepsilon}_{\text{vM}}^{(0)}}{h(\tilde{\sigma}_{\text{vM}}, \vartheta)} \right\rangle \right\rangle \quad (23.35)$$

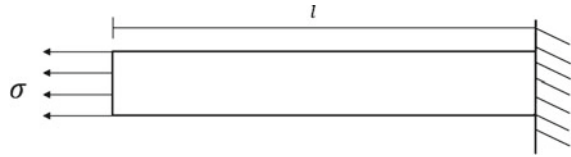
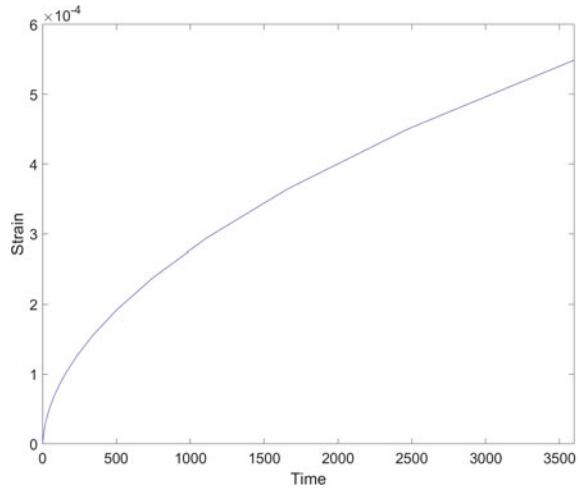
and

$$\tilde{\sigma}_{\text{vM}} = \sqrt{\frac{3}{2} \text{tr}(\boldsymbol{\sigma}'^{(0)} - \boldsymbol{\beta}^{(0)} + \boldsymbol{\sigma}'^{(1)})^2} \quad (23.36)$$

$$\dot{\varepsilon}_{\text{vM}}^{(0)} = \sqrt{\frac{2}{3} \text{tr}(\dot{\boldsymbol{\varepsilon}}^{\text{in}(0)})^2}. \quad (23.37)$$

23.4 Modeling Creep Behavior

To model the inelastic behavior, the finite element program ABAQUS is used. The material properties were implemented through an UMAT, an user-defined subroutine containing the specific data for X20CrMoV12-1 (Eisenträger et al. 2018b, 2020). For now, only creep behavior is examined where three stages can be observed (Naumenko and Altenbach 2016). During the first or primary creep stage, the creep strain rate decreases, and hardening effects are dominant. On a microstructural level, dislocation movements are hindered which leads to an increase in the material's strength. Once the strain rate reaches a minimum value, it stays constant for a certain amount of time, called the steady-state or secondary creep stage. After that, when entering the tertiary creep stage, the strain rate starts to increase again. This behavior can be traced back to

Fig. 23.1 Model of the bar**Fig. 23.2** Creep curve strain versus time of the bar loaded with $\sigma = 100$ MPa

the so-called softening, which describes the increasing strain rate with the increase of time and deformation eventually leading to failure. It is important to note that high-temperature steels such as X20CrMoV12-1 typically show no secondary creep behavior. The derived constitutive equations are now considered for a bar, clamped on one side as can be seen in Fig. 23.1.

The bar is subjected to a load of $\sigma = 100$ MPa. As initial condition, the temperature is kept constant at 873 K, which is assumed to be the highest operating temperature of a power plant (Altenbach et al. 2018). Furthermore, the elastic and inelastic strain are zero in the beginning of the simulation.

The diagram in Fig. 23.2 represents the strain versus time graph called creep curve. The stress distribution is shown in Fig. 23.3. Figure 23.4 pictures the elongation of the bar as expected.

23.5 Conclusion

Within this paper, creep behavior as an inelastic material response of high-temperature steels is investigated. Therefore, the widely known Armstrong–Frederick constitutive equations were used and the two-time-scale approach was applied to them. Afterward, a finite element simulation was carried out using ABAQUS to depict the creep

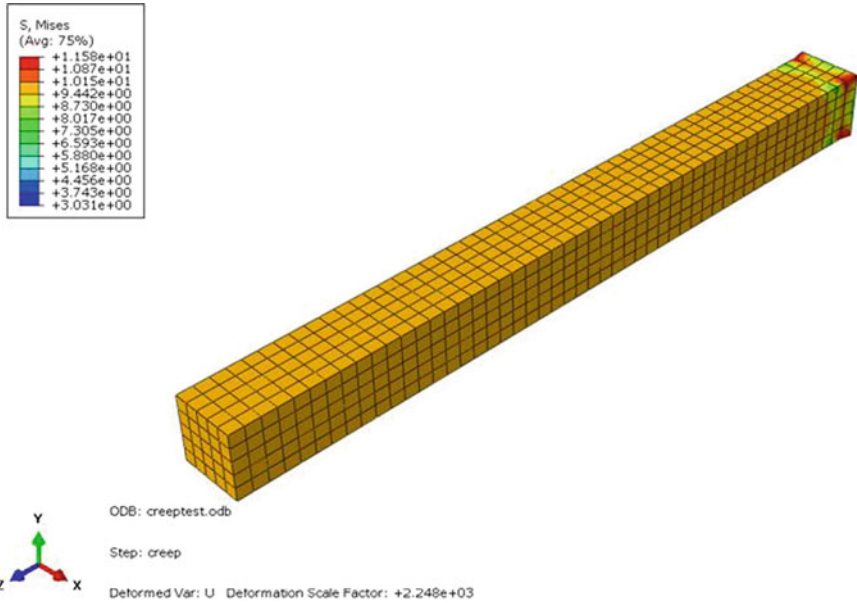


Fig. 23.3 Bar under creep load simulated with UMAT ind ABAQUS

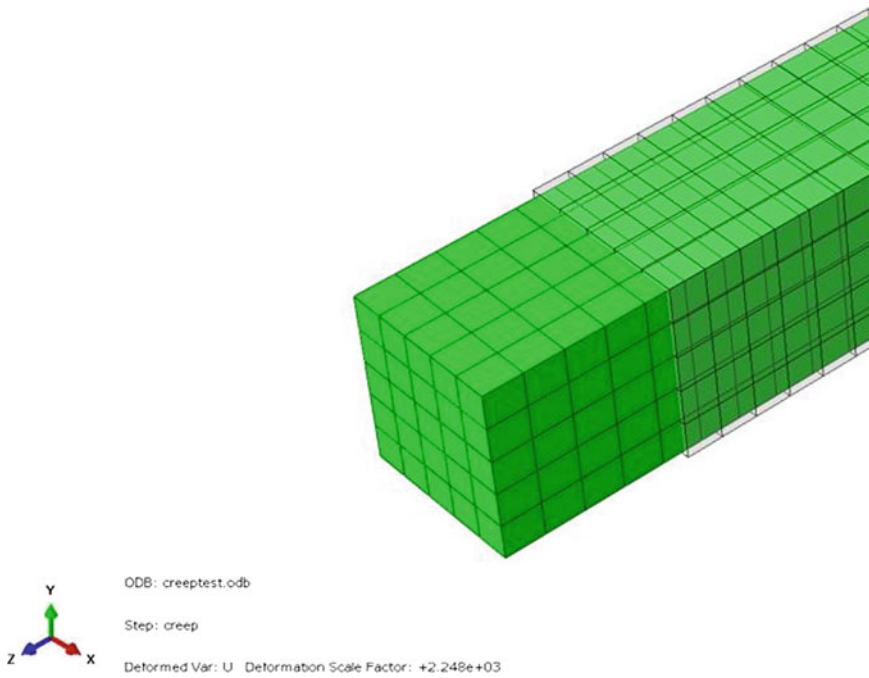


Fig. 23.4 Comparison between deformed (green) and undeformed (transparent) shape

behavior under elevated temperatures for a bar. The result of the simulation shows the expected creep curve which is in good agreement with the data found in Altenbach et al. (2018).

Future examinations of the material's inelastic response need to at first include cyclic loading conditions to further adapt the model to reality. Additionally, the rapidly varying temperatures have to be taken into account since they have a great impact on the remaining lifetime of the power plant components. The benefit of applying the two-time-scale approach is an easy adaption of the procedure to multi-axial stress states with a combination of static and cyclic loading without numerically complex cycle-by-cycle integration.

References

- Altenbach H, Breslavsky D, Morachkovsky O, Naumenko K (2000) Cyclic creep damage in thin-walled structures. *J Strain Anal Eng Des* 35:1–11. <https://doi.org/10.1177/030932470003500101>
- Altenbach H, Breslavsky D, Naumenko K, Tatarinova O (2018) Two-time-scales and time-averaging approaches for the analysis of cyclic creep based on Armstrong–Frederick type constitutive model. *J Mech Eng Sci* 233:1690–1700. <https://doi.org/10.1177/0954406218772609>
- Asai M, Ghosh S, Manchiraju S (2007) A dual-time-scale finite element model for simulating cyclic deformation of polycrystalline alloys. *Int J Mech Sci* 42:183–200. <https://doi.org/10.1243/03093247JSA233>
- Chaboche J (1989) Constitutive equations for cyclic plasticity and cyclic viscoplasticity. *Int J Plast* 5:247–302. [https://doi.org/10.1016/0749-6419\(89\)90015-6](https://doi.org/10.1016/0749-6419(89)90015-6)
- Doghri I, Haouala S (2015) Modeling and algorithms for two-scale time homogenization of viscoelastic-viscoplastic solids under large number of cycles. *Int J Plast* 70:98–120. <https://doi.org/10.1016/j.ijplas.2015.03.005>
- Eisenrager J (2018) A framework for modeling the mechanical behavior of tempered martensitic steels at high temperatures. PhD thesis, Otto-von-Guericke-Universitat Magdeburg, urn:nbn:de:gbv:ma9:1-11971
- Eisenrager J, Naumenko K, Altenbach H (2018a) Calibration of a phase mixture model for hardening and softening regimes in tempered martensitic steel over wide stress and temperature ranges. *J Strain Anal Eng Des* 53:156–177. <https://doi.org/10.1177/0309324718755956>
- Eisenrager J, Naumenko K, Altenbach H (2018b) Numerical implementation of a phase mixture model for rate-dependent inelasticity of tempered martensitic steels. *Acta Mech* 229:3051–3068. <https://doi.org/10.1007/s00707-018-2151-1>
- Eisenrager J, Zhang J, Song C, Eisenrager S (2020) An SBFEM approach for rate-dependent inelasticity with application to image-based analysis. *Int J Mech Sci* 182(105):778. <https://doi.org/10.1016/j.ijmecsci.2020.105778>
- Frederick C, Armstrong P (1966) A mathematical representation of the multi axial Bauschinger effect. CEBG report RD/B/N 731, Central Electricity Generating Board. The report is reproduced as a paper: *2007 Mater High Temp* 24:1–26. <https://doi.org/10.1179/096034007X20758>
- Joseph D, Chakraborty P, Ghosh S (2010) Wavelet transformation based multi-time scaling method for crystal plasticity FE simulations under cyclic loading. *Comput Methods Appl Mech Eng* 199:2177–2194. <https://doi.org/10.1016/j.cma.2010.03.020>
- Labergere C, Saanouni K, Sun Z, Dhifallah M, Li Y, Duval Y (2015) Prediction of low cycle fatigue life using cycles jumping integration scheme. *Appl Mech Mater* 784:308–316. <https://doi.org/10.4028/www.scientific.net/AMM.784.308>
- Naumenko K, Altenbach H (2016) Modeling high temperature materials behavior for structural analysis. Part I: continuum mechanics foundations and constitutive models. In: *Advanced struc-*

- tured materials, vol 28. Springer International Publishing. <https://doi.org/10.1007/978-3-319-31629-1>
- Oskay C, Fish J (2004) Fatigue life prediction using 2-scale temporal asymptotic homogenization. *Int J Numer Methods Eng* 61:326–359. <https://doi.org/10.1002/nme.1069>
- Reiner K, Abir D (1964) Second order effects in elasticity, plasticity and fluid dynamics. Pergamon Press, Oxford
- Sanders J, Verhulst F (1985) Averaging methods in nonlinear dynamical systems. In: *Applied mathematical sciences*. Springer, New York. <https://doi.org/10.1007/978-1-4757-4575-7>
- Zhu X, Chen H, Xuan F, Chen X (2017) Cyclic plasticity behaviors of steam turbine rotor subjected to cyclic thermal and mechanical loads. *Eur J Mech A/Solids* 66:243–255. <https://doi.org/10.1016/j.euromechsol.2017.07.012>